Numerical modelling of rockfall evolution in hard rock slopes

SIOBHAN KATHLEEN WHADCOAT

Numerical modelling of rockfall evolution in hard rock slopes

Siobhan Kathleen Whadcoat

Department of Geography

Durham University

Thesis submitted for the degree of Doctor of Philosophy

December 2016

Numerical modelling of rockfall evolution in hard rock slopes

Siobhan Kathleen Whadcoat

Abstract

The aim of this thesis has been to model small rockfalls in order to better understand where, when and why they occur. High-resolution monitoring of rock slopes has revealed clustering of rockfalls through space and time, suggesting interactions, whereby one detachment from a rock slope influences the nature of those that follow. This observation contrasts with the more conventional idea of rockfalls as time-independent, discrete events that occur in response to an identifiable trigger. As the processes that give rise to observations of rockfall clustering are not well established, this thesis takes the opportunity to bring together current understanding of the controls on rockfalls with ideas around the progressive development of failure in brittle rock in an attempt to explain these patterns. The representation of these processes at scales comparable to high resolution field monitoring has not previously been attempted. Therefore this thesis has developed an approach using numerical modelling to simulate rockfalls as spatially and temporally-dependent sequences of events, to better explain the underlying mechanisms.

This study begins with the analysis of a high-resolution inventory of rockfalls, concentrating on identifying patterns in rockfall occurrence. Analyses of this data reveals patterns of rockfalls that cannot be explained by environmental conditions or local geology alone. Evidence has been collected that demonstrates that rockfalls cluster in space and time, and that through time rockfall scars grow upward and outward in a consistent manner. The results of this analysis are used to inform numerical modelling that explores the mechanics driving small rockfalls, focussing upon the impact of a detachment on the location and timing of future rockfalls. Numerical modelling of idealised rock slope sections was conducted using Slope Model and demonstrated that the timing and location of failure in a rock slope could be considered as a function of accumulated damage, represented by fracture. The results suggest that time-dependent failure and associated mechanisms of stress redistribution and damage generation are one possible explanation for the propagating sequences of contiguous failures observed.

Finally, this thesis has taken an exploratory approach to modelling rockfalls through the development of a new deterministic, numerical model that simulates rockfall evolution using

cellular automata. This rockfall model allows the patterns and associated underlying mechanics of small rockfalls to be explored in detail using a reduced complexity approach. Critically rockfalls are modelled in a 2.5D slope face perspective to allow both rockfalls and their effects to interact across the rock slope through time. The model operates at a relatively high spatial and temporal resolution to consider the full range of rockfall characteristics that have been observed. The outputs of the model are compared with the two-year monitoring data to address key questions regarding the competing roles of endo- and exogenic forcing on rockfall occurrence. The results of the rockfall modelling shows that a consideration of stress redistribution from small scale rockfalls and time-dependent weakening provides a possible explanation for the size distribution of rockfalls, their location and timing, and the resulting changes to slope profile form as observed in the field. This has implications for how rock slopes are monitored and modelled to determine the potential for future rockfalls to occur.

Contents

Contents		i
List of figures		vii
List of tables		xiii
List of equations		xv
Declaration		xvi
Acknowledgements		xvii
1	**Introduction**	1
1.1	Context and rationale	1
1.2	A new approach to modelling rockfalls	5
1.3	Research aim and objectives	6
1.4	Organisation of the thesis	6
2	**Rockfall mechanisms and processes**	9
2.1	Controls on rockfalls	9
2.1.1	Structural controls	10
2.1.2	The role of slope morphology	11
2.1.3	Environmental controls on rockfall	12
2.1.4	The role of fracture mechanics	15
2.2	Observations of progressive failure in rock slopes	22
2.2.1.	Statistical analysis of rockfalls	25
2.3	Numerical modelling of rock slopes	27
2.3.1	Model scales and methods of discretization	31
2.3.2	Simulating damage in numerical rock slope modelling	32
2.3.3	Limitations of rock slope models for simulating contiguous rockfall	36
2.4	Conceptual approach	38
2.4.1	Modelling Objective 1: Modelling at a slope face view (2.5D), rather than in profile	39
2.4.2	Modelling Objective 2: Modelling at a high spatial resolution	39

2.4.3 Modelling Objective 3: The model should be dynamic through time and operate across a range of temporal scales 40

2.4.4 Modelling Objective 4: Modelling an evolving process, allowing stress to transfer and damage to accumulate 40

2.5 Summary 41

3 Rockfall occurrence on hard rock cliffs 44

3.1 Field Site: North Yorkshire, UK 45

3.1.1 Site descriptions 47

3.2 Rockfall Inventories 50

3.2.1 Data collection 50

3.2.1.1 Two-year dataset (2012-14) 50

3.2.1.2 Ten-year dataset (2003-13) 52

3.2.2 Data processing 53

3.2.2.1 Quantifying uncertainty 58

3.3 Spatial and temporal analysis 60

3.3.1 Arc model builder 61

3.3.1.1 Failure proximity and rock type 62

3.3.1.2 Failure geometry and cliff morphology 63

3.3.2 Cluster analysis 66

3.4 Results 69

3.4.1 Ten year dataset (2003-13) 69

3.4.2 Two year dataset (2012-14) 73

3.4.2.1 Magnitude-frequency distribution of rockfalls 78

3.4.3 Area of investigation 80

3.4.4 Spatial variations in rockfall distribution 83

3.4.5 Examples of rockfall evolution 87

3.4.5.1 Rockfall evolution 1: transition from inundation zone to above 87

3.4.5.2 Rockfall evolution 2: transition between geological units 91

3.4.5.3 Rockfall evolution 3: lateral propagation of rockfall 95
3.4.5.4 Rockfall evolution 4: Failure footprint – small pre-cursors to larger failures 98
3.4.5.5 Rockfall evolution 5: Arch development (around the periphery of failed zones) 101
3.4.6 Temporal behaviour 104
3.4.6.1 Time series of erosion 104
3.4.7 Influence of slope surface morphology 112
3.4.7.1 Rockfall distribution and local scale curvature 112
3.4.7.2 Rockfall characteristics and local curvature 115
3.4.8 Clustering of rockfalls 117
3.4.8.1 Ripley's K-function 117
3.4.8.2 Distance between rockfalls 121
3.4.9 Rockfall propagation 124
3.5 Summary 129

4 Numerical modelling - Slope Model 134
4.1 Introduction 134
4.2 Model specification 136
4.3 Slope Model 138
4.3.1 Model formulation 138
4.3.1.1 Flat joint model 143
4.3.1.2 Spring Failure Latency 144
4.3.2 Previous work 144
4.4 Model Performance 145
4.4.1.1 Displacement threshold 145
4.5 Experimental Design 150
4.6 Stage One: Conditions for failure 153
4.6.1 Experiment setup 153
4.6.1.1 Joint properties 153

4.6.2 Results 159

4.6.2.1 Joints 159

4.7 Stage Two: Progressive failure 175

4.7.1 Observations from Stage One experiments 175

4.7.2 Experiment setups 182

4.7.3 Results 184

4.7.3.1 Longer time periods 184

4.8 Discussion 197

5 Introduction to Rockfall Model 202

5.1 Modelling Philosophy 202

5.1.1 Exploratory modelling 203

5.1.2 Cellular automata models 204

5.2 Conceptual Model Design: Rockfall model 206

5.2.1 Model inputs 209

5.2.2 Interaction laws 211

5.2.3 Driving forces 213

5.2.4 Model outputs 215

5.3 Model Formulation 216

5.3.1 Boundary conditions 220

5.3.2 Initial conditions 221

5.3.3 Governing equations 223

5.3.4 Model outputs 227

5.4 Model development 1: Application of weathering, stress transfer and loss of structural support 230

5.4.1 Weathering and stress transfer and damage 231

5.4.2 Loss of structural support 235

5.4.3 Model validation/verification: 238

5.4.4 Sensitivity Analysis 245

5.4.4.1 Single parameter sensitivity analysis 245
5.4.4.2 Two-parameter sensitivity analysis 249
5.5 Model development 2: Application of time-dependent damage accumulation 253
5.5.1 Time-dependent damage accumulation 254
5.5.2 Rockfall size 257
5.5.2.2 Rockfall volume-area scaling law 260
5.5.2.3 Temporal resolution of data acquisition 262
5.6 Discussion 266
5.6.1 The applicability of the cellular rockfall model 267
5.6.2 Implications for rockfall modelling 268

6 Discussion and applications 272
6.1 The advantages of modelling rockfalls from a slope face perspective 272
6.2 The importance of small rockfalls for wider rock slope failure 274
6.3 Time-dependent failure associated with rockfalls 275
6.4 The spatial dependence of rockfall evolution 276
6.5 Simulating rock slopes with a reduced complexity model 277
6.6 Applications 279
6.6.1 External and internal process competition 279
6.6.2 The role of enhanced weathering zones for driving rockfall occurrence 290
6.6.3 Structural controls and the persistence of features 293
6.6.4 Are rock slopes likely to behave deterministically through time? 298

7 Conclusions 302
7.1 Evaluation of the aim 302
7.2 Conclusions 302
7.3 Recommendations for future research 307
7.3.1 Monitoring rockfalls in hard rock slopes 307

7.3.2 Numerical modelling of rockfalls 308

Appendices 310

Appendix 1: TLS rockfall data 310

1.1 Summary of rockfall dataset from *Boulby* 310

1.2 Summary of rockfall dataset from Section 1 311

1.3 Summary of rockfall dataset from Section 2 312

1.4 Summary of rockfall dataset from Cowbar 313

1.5 Elevation plots for individual monthly datasets 314

1.6 Recurrence interval data 318

Appendix 2: Slope Model 323

2.1 Full numeric formulation of Slope Model 323

2.2 Model performance 329

2.3 Model parameters 338

Appendix 3: Matlab script for Rockfall Model 340

References 351

List of figures

Chapter 1

Figure 1.1: Observations of rockfall scars and associated features on a cliff face (N. Yorkshire, UK) 2

Figure 1.2: A sequence of rockfalls in the Rhombus Wall (eastern Yosemite Valley, California): Stock *et al.* (2012, p.551) 3

Chapter 2

Figure 2.1: Conceptual graphs of weathering rate variations: Viles (2013). 14

Figure 2.2: [a] Factor of safety and [b] probability of failure: Kemeny (2003 p.33, 35). 18

Figure 2.3: Stress-strain curve: Eberhardt et al. (1999, p.363) 19

Figure 2.4: Schematic model of a large slope failure: Rosser *et al.* (2007a, p.12) 21

Figure 2.5: Cumulative annual change on a coastal rockface: Rosser *et al.* (2013, p.940). 22

Figure 2.6: Examples of time-dependent sequencing of failures 24

Figure 2.7: Elfen model showing an advanced stage of a 2D model of underground block caving: Pine *et al.* (2007, p.764)) 34

Figure 2.8: [a] Superimposed plots of inverse velocity and horizontal displacement; [b] Rock mass damage at the onset of failure: Havaej and Stead (2016, p.185). 36

Chapter 3

Figure 3.1: Field site location on North Yorkshire coast. 46

Figure 3.2: Geological section of the cliff exposure at the field site 47

Figure 3.3: Aerial view of the TLS point cloud data 48

Figure 3.4: Photographs of the cliff sections at each site 49

Figure 3.5: Setup of the RIEGL VZ1000 terrestrial laser scanner 52

Figure 3.6: TLS data processing workflow 55

Figure 3.7: Point cloud registration 56

Figure 3.8: Digital Elevation Model (DEM) generated from the point cloud data 56

Figure 3.9: Generating rockfall polygons in ArcMap 57

Figure 3.10: Images of the cliff sections used for uncertainty analysis 60

Figure 3.11: Workflow used for data analysis 61

Figure 3.12: Distance and direction analysis 62

Figure 3.13: Computing the geometric intersection between rockfall polygons 63

Figure 3.14: Calculating the mean depth of each rockfall 64

Figure 3.15: The statistics that describe the geometry of each rockfall polygon 64
Figure 3.16: Rockfall geometry types 65
Figure 3.17: Curvature outputs 65
Figure 3.18: The Ripley's K-function analyses 67
Figure 3.19: Rockfall centroids used for the Ripley's K-function analysis. 68
Figure 3.20: Rockfall polygons of a section of the cliff at Boulby from 2003 – 2013 71
Figure 3.21: Area-frequency density plot for rockfalls from the 10-year period 72
Figure 3.22: Rockfalls across the cliff face over the two year monitoring period 77
Figure 3.23: Magnitude-frequency plots for all rockfalls in the two year period 79
Figure 3.24: Plots illustrating data representation 1 80
Figure 3.25: Plots illustrating data representation 2 82
Figure 3.26: Variations in rockfall count and surface area failed with elevation 86
Figure 3.27: Transition out of the inundation zone (visual plots) 89
Figure 3.28: Transition out of the inundation zone (profiles) 90
Figure 3.29: Transition between geological layers (visual plots) 92
Figure 3.30: Transition between geological layers (profiles) 94
Figure 3.31: Rockfall propagation and bridging of rockfalls (visual plots) 96
Figure 3.32: Lateral rockfall propagation (visual plots) 97
Figure 3.33: Smaller rockfalls delineating the footprint of the larger rockfall (visual plots) 99
Figure 3.34: Smaller rockfalls delineating the footprint of the larger rockfall (profiles) 100
Figure 3.35: Examples of arch features that develop in hard rock cliffs 102
Figure 3.36: Arch feature development (visual plots) 103
Figure 3.37: Time series' of cumulative surface averaged erosion for each site 104
Figure 3.38: Time series' of cumulative surface averaged erosion for each geological layer 107
Figure 3.39: Location of AOIs along the cliff at Boulby 108
Figure 3.40: Time series' of cumulative surface averaged erosion for each AOI 109
Figure 3.41: Time series' of cumulative surface averaged erosion for different size rockfalls 111
Figure 3.42: Cumulative density function (cdf) of the slope curvature (pre-failure) 112
Figure 3.43: Cumulative density function (cdf) of the slope curvature (failed areas) 114
Figure 3.44: Rockfall area plotted against the pre-failure curvature values 115
Figure 3.45: Rockfall depth plotted against the pre-failure curvature values (by site) 116
Figure 3.46: Boxplot (outliers removed) of pre-failure curvature values for rockfalls in different geometry classes 117
Figure 3.47: The L(r) function computed for all rockfalls between 2003 and 2013. 118
Figure 3.48: The L(r) function computed for rockfall datasets at Boulby 119
Figure 3.49: The cross-K function computed for data over different time periods 120

Figure 3.50: The cross-K function computed for rockfalls ≥ 1 m^2 121
Figure 3.51: The distance between failures 122
Figure 3.52: Contiguous rockfall data 123
Figure 3.53: Rose plots: direction from rockfalls in one dataset to another 125
Figure 3.54: Rose plots: direction from rockfalls in one dataset to another (contiguous rockfalls) 126
Figure 3.55: Rose plots: direction from rockfalls in one dataset to another (non-contiguous rockfalls) 126
Figure 3.56: Rose plots: direction from rockfalls in one dataset to another (by rockfall size) 127
Figure 3.57: Rose plots: direction from rockfalls in one dataset to another (by rockfall size: contiguous rockfalls) 128
Figure 3.58: Rose plots: direction from rockfalls in one dataset to another (by rockfall size: non-contiguous rockfalls) 128

Chapter 4

Figure 4.1: Schematic of the lattice based structure of Slope Model 140
Figure 4.2: Bench setup in Slope Model 141
Figure 4.3: Illustration of the Flat Joint Model in Slope Model 143
Figure 4.4: Stress-strain curve showing the stages of crack development: Eberhardt *et al.* (1999) 146
Figure 4.5: Failing wedge shown in Slope Model 148
Figure 4.6: Plot of inverse velocity and displacement at the centre of the failing wedge 149
Figure 4.7: 1,000 m^3 block setup in Slope Model 151
Figure 4.8: Discontinuity sets used in Slope Model simulations 154
Figure 4.9: Surface morphologies used in Slope Model 157
Figure 4.10: Displacement (m) of each history point within the model 160
Figure 4.11: Total failed area through time for experiments 1.1 – 1.3 161
Figure 4.12: Displacement superimposed with inverse velocity (exp. 1.1 – 1.3) 162
Figure 4.13: Displacement (m) of each history point for experiments 1.4 – 1.7 164
Figure 4.14: Total failed area through time for experiments 1.4 – 1.7 165
Figure 4.15: Displacement superimposed with inverse velocity (exp. 1.4 – 1.7) 166
Figure 4.16: Displacement (m) of each history point for experiments 1.8 – 1.10 169
Figure 4.17: Displacement (m) of each history point for experiments 1.11 – 1.13 170
Figure 4.18: Total failed area through time for experiments 1.8 – 1.10 171
Figure 4.19: Displacement superimposed with inverse velocity (exp. 1.8 – 1.10) 172
Figure 4.20: Total failed area through time for experiments 1.11 – 1.14 173

Figure 4.21: Displacement superimposed with inverse velocity (exp. 1.11 – 1.14) 174
Figure 4.22: Location and timing of fractures and failed nodes; time series of cumulative failed area and fracture count for experiments 1.1 – 1.3. 177
Figure 4.23: Location and timing of fractures and failed nodes; time series of cumulative failed area and fracture count for experiments 1.4 – 1.5. 178
Figure 4.24: Location and timing of fractures and failed nodes; time series of cumulative failed area and fracture count for experiments 1.8 – 1.10. 179
Figure 4.25: Location and timing of fractures and failed nodes; time series of cumulative failed area and fracture count for experiements 1.11 – 1.14. 181
Figure 4.26: Illustration of the excavated areas (exp. 2.4) 183
Figure 4.27: Displacement (m) of each history point for experiments 2.1 – 2.3 186
Figure 4.28: Location and timing of fractures and failed nodes; time series of cumulative failed area and fracture count for experiements 2.1 – 2.3. 188
Figure 4.29: Displacement (m) of each history point for experiment 2.4 191
Figure 4.30: Location and timing of fractures and failed nodes; time series of cumulative failed area and fracture count for experiemen 2.4 192
Figure 4.31: Displacement (m) of each history point for experiments 2.5 – 2.7 194
Figure 4.32: Location and timing of fractures and failed nodes; time series of cumulative failed area and fracture count for experiements 2.5 – 2.7. 196

Chapter 5

Figure 5.1: Conceptual model of the rock slope environment 206
Figure 5.2: Illustration of discretising the rock slope 207
Figure 5.3: Temporal evolution of the driving and resisting forces in an unstable rock mass: Gischig. (2011, p.4) 209
Figure 5.4: Conceptual illustration of structural support 212
Figure 5.5: Conceptual sketch of the rock slope model 216
Figure 5.6: Workflow of the different stages in the rockfall model 218
Figure 5.7: Graphical illustration of the increase of damage in one cell over time 224
Figure 5.8: An illustration of stress transfer 227
Figure 5.9: Time series of rockfall count for 50,000 time steps 230
Figure 5.10: The model workflow used in simulations 1 - 2 231
Figure 5.11: Mean rockfall count and failed area per time step for: (a) simulations 1.1 – 1.16; (b) simulations 2.1 – 2.11. 233
Figure 5.12: Power law fits for magnitude-frequency plots for: (a) simulations 1.1, 1.6, 1.11, 1.16; (b) simulations 2.1, 2.4, 2.8, 2.11 234

Figure 5.13: The model workflow used in simulations 3 – 16 235
Figure 5.14: Mean rockfall count and failed area per time step for: (a) simulations 3.1 – 3.10; (b) simulations 4.1 – 4.10. 236
Figure 5.15: Power law fits for magnitude-frequency plots for: (a) simulations 3.1, 3.4, 3.7, 3.10; (b) simulations 4.1, 4.4, 4.7, 4.10 237
Figure 5.16: Time series of rockfall count for each simulation run with a different topographic grid 239
Figure 5.17: Magnitude-frequency of rockfall volume for: (a) simulation 4.10; (b) field data 241
Figure 5.18: Recurrence intervals for different rockfall volumes (m^3) 242
Figure 5.19: Variations in surface failures for different time periods 244
Figure 5.20: Average profile of the rock face at the end of model simulation 4.10 245
Figure 5.21: Percentage change of different model outputs (Sensitivity analysis) 248
Figure 5.22: Percentage change of model outputs (*ß*-value and r^2-value) 249
Figure 5.23: Mean rockfall count and mean failed area per time step for simulations 9 – 12 251
Figure 5.24: Mean rockfall count and mean failed area per time step for simulations 13–16 252
Figure 5.25: The model workflow used in simulations 17 – 21 253
Figure 5.26: Mean rockfall count and failed area per time step for: (a) simulations 17.1 – 17.11; (b) simulations 18.1 – 18.10 255
Figure 5.27: Power law fits for rockfall volume magnitude-frequency for: (a) simulations 17.1, 17.6 and 17.11; (b) simulations 18.1, 18.4, 18.7 and 18.10 256
Figure 5.28: Power law fits for rockfall magnitude-frequency for: (a) simulations 19.1 – 19.4; (b) simulations 20.1 – 20.5 258
Figure 5.29: Average slope profiles at the end of model simulations 19.1 – 19.4 259
Figure 5.30: Average slope profiles at the end of model simulations 20.1 – 20.5 260
Figure 5.31: Magnitude-frequency plot for simulation 21 261
Figure 5.32: Average slope profiles at the end of model simulation 21. 262
Figure 5.33: Visual plots of rockfalls that occurred over 9 time steps in simulation 21 264
Figure 5.34: Power law fits for rockfall volume magnitude-frequency for simulation 21 265
Figure 5.35: *ß*-values of the power law fits in Fig. 5.34, plotted against temporal resolution 265

Chapter 6

Figure 6.1: Average slope profiles at the end of a model simulation run without *pd* 280
Figure 6.2: Magnitude-frequency data for the model simulation run without *wi* 281
Figure 6.3: Rockfalls at the rock slope surface for combinations of *wi* and *pd* values 282
Figure 6.4: Spatially averaged slope profiles for combinations of *wi* and *pd* values 283
Figure 6.5: Vol.-freq. plots for model simulations run at different values of *wi* and *pd* 284

Figure 6.6: Rockfall behaviours identified for different combinations of *wi* and *pd* 286
Figure 6.7: Changes in spatially averaged erosion in a rock slope as a result of increasing weathering intensity (*wi*) and increasing values of damage transfer (*pd*). 288
Figure 6.8: Slope profiles generated from airborne LiDAR data of the North Yorkshire coastline: Swirad *et al.* (2016, p.614) 289
Figure 6.9: Changes to the cliff profile as a result of increasing *pd* and *wi* to simulate zones of enhanced weathering 291
Figure 6.10: Spatially averaged erosion plotted against the *wi* ratio for zones of enhanced weathering 292
Figure 6.11: Rockfall count and slope profiles for simulations run with a stronger layer of rock 295
Figure 6.12: Rockfall count and slope profiles for simulations run with a stronger layer of rock of different thicknesses 296
Figure 6.13: Average slope profiles for a simulation run with a stronger layer of rock 298
Figure 6.14: Average slope profiles model simulations run at *pd* = 95%, with *wi* = 1; *wi* = 1.5 300

List of tables

Chapter 2

Table 2.1: Comparison of the rock slope modelling capabilities 29

Chapter 3

Table 3.1: Scan collection dates 51
Table 3.2: Values for different parameters used during TLS data processing. 58
Table 3.3: Summary of rockfall statistics for the ten year dataset 70
Table 3.4: Summary of rockfall statistics for each of the geological layers (ten year dataset) 72
Table 3.5: Summary of rockfall statistics for each of the field sites (two year dataset) 73
Table 3.6: Summary of rockfall statistics for each of the geological layers (two year dataset) 84

Chapter 4

Table 4.1: Numerical modelling approaches capable of simulating brittle fracture 138
Table 4.2: Slope Model input parameters 142
Table 4.3: Material properties of the geological layers at Boulby, N Yorkshire: Lim *et al.* (2010) 152
Table 4.4: Mean orientation and spacing of discontinuity sets at Boulby, N Yorkshire 155
Table 4.5: Joint strength classifications in Slope Model 156
Table 4.6: Joint material properties used in the first set of Slope Model experiments 156
Table 4.7: Changes to the rock mass and joint strength applied to simulate weakening 158
Table 4.8: Failed area, onset of failure and critical slope failure for each experiment run with different joint properties 159
Table 4.9: Failed area, onset of failure and critical slope failure for each experiment run with a different surface morphology 163
Table 4.10: Critical displacement threshold for failure 167
Table 4.11: Failed area, onset of failure and critical slope failure for each experiment run to simulate weakenin 168
Table 4.12: Fracture count and the failed area at 2 second intervals for each experiment in Stage One. 176
Table 4.13: Fracture count and the total failed area at 1, 5, 10, 15 and 20 seconds of model time for experiments 2.1 – 2.3. 185
Table 4.14: Onset of failure and critical slope failure; and fracture count and failed area at 1, 5 and 10 seconds of model time for experiments 2.4 and 1.14 190

Table 4.15: Fracture count associated with excavations 190

Table 4.16: Onset of failure and critical slope failure; and fracture count and failed area at 1, 5 and 10 seconds of model time for experiments 2.5 – 2.7 193

Chapter 5

Table 5.1: Physical and mechanical properties of each cell in the rockfall model 217

Table 5.2: Terminology used throughout this study to describe different model attributes 219

Table 5.3: Model validation criteria 229

Table 5.4: Input conditions and model parameters for the simulations used in Model development 1 232

Table 5.5: *k* (coefficient) and *ß* (exponent) values for each model simulation in Fig. 5.13. 234

Table 5.6: *k* (coefficient) and *ß* (exponent) values for each model simulation in Fig. 5.15 237

Table 5.7: The range of outputs values generated by varying different model parameters 240

Table 5.8: Input conditions and model parameters for single parameter sensitivity analysis 247

Table 5.9: Input conditions and model parameters for multi-parameter sensitivity analysis 250

Table 5.10: Input conditions and model parameters for simulations used in the application of time-dependent damage accumulation 254

Table 5.11: *k* (coefficient) and *ß* (exponent) values for each model simulation in Fig. 5.27. 256

Table 5.12: *k* (coefficient) and *ß* (exponent) values for each model simulation in Fig. 5.28 259

Table 5.13: *k* (coefficient) and *ß* (exponent) values for model simulation 21 over different temporal resolutions 266

List of equations

Chapter 2

2.1 Stead *et al.*'s (2004) Quantification of damage 17

2.2 Power law fit 25

2.3 Stead and Eberhardt's (2013) Damage intensity parameters 34

Chapter 3

3.1 TLS distance (*time-of-flight*) 50

3.2 Ripley's (1976) K-function for clustering 66

3.3 Tonini *et al.*'s (2013) Modified L-function for clustering 66

Chapter 4

4.1 Translational and rotational components of displacement (1) in Slope Model 139

4.2 Translational and rotational components of displacement (2) in Slope Model 139

4.3 Angular velocities in Slope Model 139

4.4 Sakurai's (2001) calculation for critical strain 145

4.5 Torres' (2014) relation of tensile strength and friction angle for Slope Model 155

4.6 Palmström's (1995) application of a weathering factor to reduce compressive strength 158

Chapter 5

5.1 Distance of cell protrusion from the mean slope surface in the rockfall model 222

5.2 Increase in damage resulting from weathering in the rockfall model 223

5.3 Increase in damage resulting from loss of structural support in the rockfall model 225

5.4 Conditional statements for the increase in damage beyond failure onset in the rockfall model 225

5.5 Stress transfer in the rockfall model 226

5.6 Volume-area scaling law (based on the field dataset in Chapter 3) 260

Declaration

I confirm that no part of the material presented in this thesis has previously been submitted for a degree in this or any other university. In all cases the work of others, where relevant, has been fully acknowledged.

Siobhan Whadcoat

Acknowledgements

This thesis would not have been possible without the support of so many, none more so than my supervisors: Nick Rosser, Rich Hardy and Matt Brain. I am grateful to them for giving me the opportunity to do the PhD and for the advice, encouragement, helpful feedback and unending patience along the way. Nick has been very generous with his time, providing many interesting ideas that have shaped this project. Rich has been an invaluable source of advice for the modelling aspects of this work and has provided insightful feedback from a different perspective. Matt has provided sound technical advice and kindly guided me through the rock mechanics aspects of this work. Thank you also to Dave Petley for valuable supervision, discussions and ideas in the early stages of this project.

This project has been possible thanks to the funding provided by ICL Fertilizers (UK) Ltd, who continue to fund the monitoring of the coastline in North Yorkshire. The use of Slope Model was generously provided by Itasca CG. Particular thanks to Loren Lorig and Maurilio Torres for help in the initial stages of learning how to use Slope Model, and for advice and discussions around a somewhat unconventional application of the model.

I am privileged to be part of such a supportive, inspiring and vibrant department. So many folk in the Geography department at Durham have supported me over the past four years. In particular, thanks to Sam Waugh and Emma Vann Jones for taking me out on fieldwork, teaching me how to use the scanner, and making a cold, snowy day on the North Yorkshire coast much more fun than it sounds. Thanks also to Emma for your sound advice at so many stages along the way. Thanks to my fellow PhD cohort - you have been excellent friends and made even the most difficult days more enjoyable. Particular thanks to Jack for setting the bar high, and for unending advice and moral support as we've navigated our way through the PhD journey together.

I would also like to thank Doug Stead and Mohsen Havaej for hosting me at Simon Fraser University for a month and for valuable discussions about my work in the context of geological engineering. Particular thanks also to Mohsen for helping me get to grips with Slope Model and the world of dxf files. I would like to thank Greg Stock for an extremely fascinating and fun few days exploring rockfalls in Yosemite National Park and for the insightful conversations about large scale rock slope failures.

Finally, thanks to friends and family who have supported, encouraged and endured me through the last four years. Particular thanks are owed to my parents, for their constant

support and unwavering confidence in me and in what I can achieve. Thanks also to those friends who have adventured outdoors with me and kept me sane; to lovely housemates who have made home life full of fun and laughter; to the most wonderful, fun community on Neville Terrace that has shown me what good neighbours really look like; to friends who have been ahead of me on the PhD journey and provided wisdom and motivation along the way; and to Ruth & Col, Beth & Luke, and Katy, who have been like family to me and have supported me in so many ways - you are the very best of friends and I feel privileged to know you.

Thanks be to God for His grace and strength and ultimately, for creating such a fascinating and complex world for us to explore.

1 Introduction

1.1 Context and rationale

Rockfalls are one of the principal mechanisms of erosion that control the development of rock slopes (natural and engineered) through time (Dussauge *et al.*, 2003; Rosser *et al.,* 2007a; Moore *et al.,* 2009; Stock *et al.,* 2012; Zimmer *et al.,* 2012). With recent developments in data acquisition and monitoring (Abellán *et al.,* 2014) spatial sequencing and temporal patterns in rockfalls have been observed (Rosser *et al.,* 2007a, 2013; Abellán *et al.,* 2010; Stock *et al.,* 2012; Royan *et al.,* 2013). These observations have generated an appreciation of the role of small rockfalls in the overall larger scale stability and behaviour of rock slopes. Despite these observations, our understanding of the controls on the sequencing and propagation of small rockfalls, and how this behaviour is modelled, is under represented and limits our ability to understand when, where and why rockfalls occur.

Rockfalls are a subset of landslides (Varnes, 1978) and defined as sudden movements of rock, driven by gravity, that become detached from steep rock slopes (Dussauge *et al.*, 2003), such as coastal cliff faces as shown in Figure 1. Rockfalls often occur along existing weaknesses in the rock (Fig. 1.1e), but evidence for the distribution of failures beyond and outside of existing weaknesses is also observed (Fig. 1.1). Rockfalls propagate in sequence across the rock face through time (Fig. 1.1b), generating spatial clusters of rockfall scars (Fig. 1.2) that evolve over time (Stock *et al.,* 2012). The propagation of small rockfalls relative to the size of the rock slope, can extend across the entire rock face, whereby small rockfalls can eventually dominate the erosional behaviour of the slope (Fig. 1.1b). At times rockfall scars can therefore appear to grow (Fig. 1.2), such that an observed failure scar, rather than reflecting a single instantaneous event (Dewez *et al.,* 2007), instead may reflect multiple contiguous rockfalls that coalesce over a period of time (Stock *et al.,* 2012; Rosser *et al.,* 2013). Temporal patterns in rockfalls are also observed in the form of precursors to slope failure or rockfalls, either in the form of spalling (Rosser *et al.,* 2007a) and deformation, or creep (Abellán *et al.,* 2010). The interaction of rockfalls with both structural and morphological features on the rock face is apparent via the emergence of characteristic surface features, such as overhangs (Fig. 1.1a), protrusions (Fig. 1.1c) and arches (Fig. 1.1d). These features appear to develop as a result of rockfall activity and then these features influence the location and development of future rockfalls, presenting an interesting feedback. However, such features do not develop as might be expected. For example, on coastal cliffs the lack of notching by waves (Fig. 1.1c) in the zone where the efficacy of erosion is assumed to be higher, questions the dominant drivers of rock slope

failure (Lim *et al.*, 2010; Vann Jones *et al.*, 2015) and points to a non-environmental control on rockfalls.

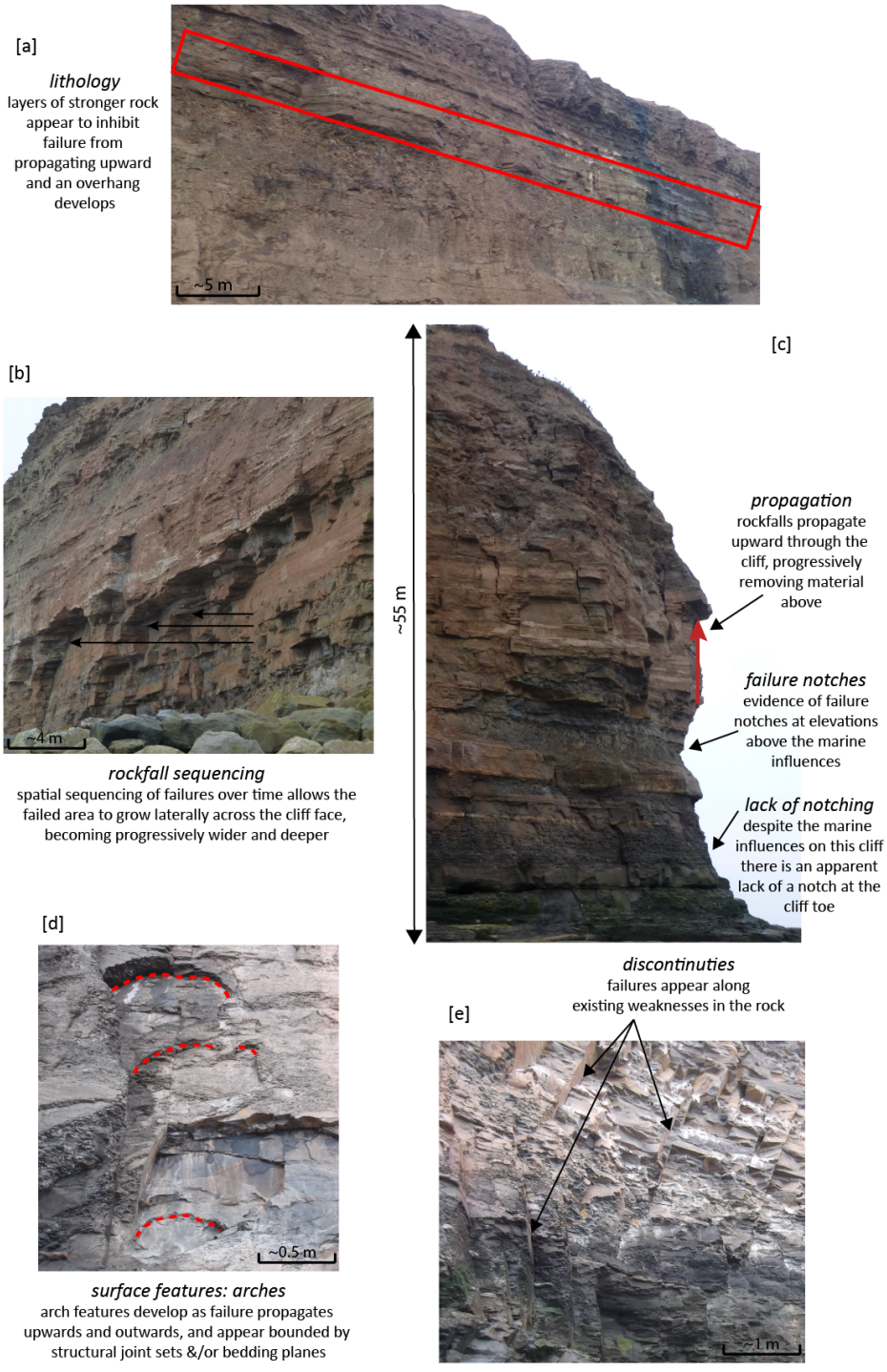

Figure 1.1: Observations of rockfall scars and associated features on a cliff face (N. Yorkshire, UK), illustrating: [a] the structural surface features associated with lithology; [b] widening spatial sequencing of rockfalls; [c] evidence of upward propagation and notching in the cliff profile (this is a coastal cliff with a tidal inundation zone at the base); [d] structural surface features as arches that form from rockfall propagation; [e] the influence of discontinuities in driving failure location

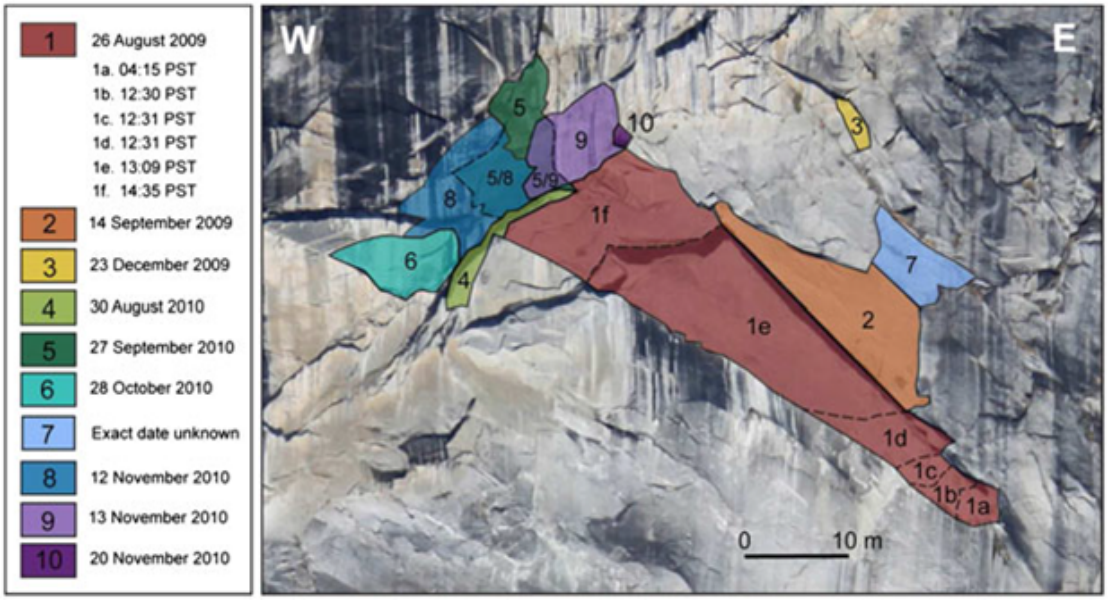

Figure 1.2: A sequence of rockfalls in the Rhombus Wall (eastern Yosemite Valley, California) from Aug 2009 – Nov 2010, illustrating an example of an apparently time-dependent sequencing of failures. Reproduced with permission from: Stock *et al.* (2012, p.551)

These observations (Fig. 1.1 and 1.2) are not fully explained or supported by the current process understanding of rockfalls. As highlighted in Zimmer *et al.* (2012), studies often assume that rockfalls occur as independent, isolated events in both time and space, in contrast to the observations of spatial and temporal sequences of rockfalls described above. A well-developed understanding exists around rockfalls as discrete and independent events (Hoek and Bray, 1977), including characteristic observations of the triggering mechanisms that lead to failure, and the subsequent changes to the landscape (Selby, 2005). However, an understanding of the mechanisms driving the behaviour outlined, rather than treating rockfalls as individual events in isolation, is poorly developed (Senfaute *et al.,* 2009).

The links between failures and environmental controls can be difficult to establish (Dewez *et al.,* 2007; Lim *et al.,* 2010) particularly when trying to account for failures that occur with no direct trigger (Senfaute *et al.,* 2009). Recent studies have established links between environmental conditions and both rockfall size characteristics (Strunden *et al.,* 2015; Vann Jones *et al.,* 2015), and frequency (D'Amato *et al.,* 2016) in specific environmental settings. Notwithstanding these links, relating rockfalls to environmental drivers more generally remains challenging (Vann Jones *et al.,* 2015) and the timing of the largest failures is difficult to predict or forecast (Rosser *et al.,* 2013). It is suggested that the difficulty in attributing failure

to trigger may be explained by the important role of internal rock mass processes and underlying time-dependent failure mechanisms that are less well understood in this context and scale (Stock *et al.,* 2012; Rosser *et al.,* 2013). Rockfalls, and particularly the spatial sequencing of contiguous rockfalls, have previously been attributed to progressive failure (Stock *et al.,* 2012): the underlying process of time-dependent fracture development in a rock mass, which occurs irrespective of (changes in) external forcing (Petley *et al.,* 2005).

Numerical models of rock slopes are well designed to simulate the structural controls on where failure can occur (Stead and Wolter, 2015) and to assess the importance of a range of rock mass properties on the possible or likely failure mechanisms (Kimber *et al.,* 1998; Brideau and Stead, 2010; Styles *et al.,* 2011; Havaej *et al.,* 2014a). However, models have not been designed to consider the underlying processes that may be driving the spatial sequencing and propagation of rockfalls observed, and therefore do not represent processes relevant to failure evolution at a spatial resolution corresponding to failure size (Stead and Coggan, 2012). For example, in the cliffs shown in Figure 1.1 the mean failure size is 0.001 m^3 (Rosser *et al.,* 2013), which is far smaller than the discretization used in many rock slope models. In addition, models do not fully represent stress redistribution, whereby stress is transferred from a zone of failure to the neighbouring areas of a rock slope surface, and the instant or perhaps more importantly, the lagged consequence of this, which has been posited as a driver of the space and time-dependent sequencing of rockfalls (Stock *et al.,* 2012). Many current rockfall models necessarily reduce the dominant structural controls to a 2D profile view (Styles *et al.,* 2011), thus not considering kinematic lateral confinement and block interactions at the rock face.

This thesis is focused on rockfall evolution in hard rock slopes, defined as slopes with a high mechanical strength that fail in a brittle manner through gravity driven mass movements (Dussauge *et al.,* 2003), focussing on circumstances where rockfall sequencing and propagation is observed. This study explores the spatial and temporal interactions of rockfalls, the possible (mechanical) controls on the rate and nature of rockfall interactions, and the implications that this has for rock slope evolution. Herein the term 'rock slope evolution' is used to describe the changes over time to the entire rock slope as a result of both rockfall and other mass wasting processes. Understanding the spatial and temporal interactions of rockfalls and the possible controls on this will have the potential to improve how well numerical models of rock slopes reflect the reality of rockfall and their role as an erosional mechanism in rock slopes, over short to medium timescales (10^{-1} to 10^{2} years).

1.2 A new approach to modelling rockfalls

With recent developments in monitoring of rock slopes (Abellán *et al.,* 2014), data is now available to inform the boundary conditions of numerical models that operate at a resolution and perspective closer to failure size. Spatial and temporal length scales established from analysis of monitoring data can be used to improve process representation within the models. This study uses high resolution monitoring of coastal rock slopes in North Yorkshire (UK) collected over two years, to inform the development of a new approach to modelling rockfalls. Importantly, the approach developed focuses at the scale of small rockfalls (sub-metre), which can evolve through time, and considers the interactions between these rockfalls and the surrounding rock slope surface. This builds on the understanding developed in conventional rock slope models, which consider the structural controls on where a failure can occur, whilst the remainder of the slope remains stable as longer term weakening is generally not simulated.

To model how small rockfalls and their interactions can influence wider rock slope behaviour (Fig. 1.1b), the spatial sequencing of rockfalls and time-dependent weakening of the rock mass must be represented within the model. By operating at a resolution comparable to failure size, the model allows small rockfalls to evolve and interact to simulate incremental sequences at the scale of small (sub-metre) rockfalls. The efficacy of the driving processes, such as time-dependent fracture propagation due to stress redistribution following a previous rockfall (Stock *et al.,* 2012), is here referred to as 'rock mass connectivity' and defines the impact of a rockfall on the wider slope.

Incorporating spatial sequencing in modelling has been demonstrated by conceptual models (e.g. Bak *et al.,* 1988; Chapius and Tetzlaff, 2014), which are based on principles of self-organised criticality (SOC) (Bak *et al.,* 1988), whereby small instabilities are able to propagate through a system as an avalanching type process. Both Bak *et al.* (1988) and Chapius and Tetzlaff (2014) represent the systems they are modelling using a reduced complexity model, where concepts are characterised by simplified variables and their interactions. In doing so, several more processes and their interactions can be modelled that could not be predicted from the individual components alone. Although simplistic, reduced complexity modelling has been shown to provide alternative explanations of mass movement processes that cannot be explained by more conventional numerical modelling alone (Hergarten, 2003). It is anticipated that modelling at a scale that could incorporate spatial sequencing of rockfall events, has the potential to improve upon current numerical rock slope models' ability to emulate the high resolution observations from rock slopes described above. This also has the potential to allow

wider questions regarding rock slope behaviour over both short to medium timescales (10^{-1} to 10^{2} years) to be addressed, such as: the interaction between rockfalls and external environmental processes (Lim *et al.,* 2010; Viles, 2013; Krautblatter and Moore, 2014); the controls on 2D slope profile form (Emery and Kuhn, 1982); the importance of slope surface topography for rock slope evolution (Rosser *et al.,* 2007a; Stock *et al.,* 2012); and the response of rock slopes to future changes in climate (Murphy *et al.,* 2009).

1.3 Research aim and objectives

The overall aim of this thesis is to simulate rockfalls as a temporally- and spatially-dependent process in order to better understand where, when and why small rockfalls occur.

To address this aim, the research will be conducted by addressing the following four research objectives:

- O1: To look for patterns of rockfall distributions from field monitoring data that are indicative of a progressive failure mechanism.
- O2: To evaluate when and under what conditions, time-dependent and spatially-dependent failure influences the characteristic scales of rockfalls.
- O3: To develop an approach to simulating rockfalls as an evolving process that allows redistribution of stress and accumulation of damage through time.
- O4: To use the new methodological approach to predict the evolution of rockfalls to demonstrate where and when rockfalls occur as a function of both external forcing and internal rock mass interactions.

1.4 Organisation of the thesis

The thesis is divided into six chapters (2 – 7) following this introduction. The content of these chapters is as follows:

Chapter 2 reviews recent advances in understanding and characterisation of rockfalls that underpin this research, with a particular emphasis on the space and time-dependent nature of rockfalls and the ability of current rock slope models to predict this behaviour. The chapter shows that the way rockfalls are observed to evolve through time and across space is not fully explained by the established understanding of the controls on rockfalls. The chapter argues for

a new approach to modelling rockfalls at the spatial and temporal scales of the small (sub-metre) rockfalls that are observed to evolve, in order to improve understanding of the controls on these rockfalls.

Chapter 3 presents a two-year rockfall dataset collected using terrestrial laser scanning (TLS) and explores the spatial and temporal patterns in rockfalls. The dataset has been collected from four coastal cliffs sites in North Yorkshire (UK), which were selected for the opportunity they provided to collect a high spatial and temporal resolution dataset of actively failing rock slopes. Whilst these observations are specific to the coastal cliff site in North Yorkshire, the analysis of the data has implications for steep, hard rock slopes in other environments, such as waterfalls, bedrock rivers and steep gorges. Analysis of this rockfall dataset addresses the first research objective by identifying the scales at which rockfalls are observed to cluster and propagate across the cliff surface and through time. The results from this chapter are also used to inform both the process understanding and boundary conditions of the numerical modelling undertaken in Chapters 4 and 5.

Chapter 4 applies Slope Model (Itasca, 2010b), a 3D brittle fracture code, to explore the influence of rock slope conditions, including joint properties, slope surface topography and rock mass weakening, on the timing of failure. Slope Model is a discontinuum model and was used here for its capability to simulate both brittle fracture through intact rock and failure along discontinuities. Slope Model is used to simulate a hypothetical section of rock slope (1,000 m^3), whereby strain in the rock slope resulting from stress is observed as deformation (displacement, mm) and brittle fracture growth. Using measures of displacement and inverse velocity different failure stages are identified alongside the timing of brittle fracture growth, which is considered an indication of time-dependent failure in the rock mass. The results provide an indication of the conditions when fracture growth influences the timing and location of failure events, thereby addressing the second research objective.

Chapter 5 presents the design, formulation and development of a cellular rockfall model, hereafter referred to as the 'rockfall model'. The development of the rockfall model addresses the third research objective by focussing on simulating small scale (< 0.1 m^3) rockfalls as a function of incremental damage accumulation through time. The rockfall model considers the interactions between rockfalls, which represent mechanisms of stress transfer and lateral confinement of the slope surface. Both a single and multi-parameter sensitivity analysis is conducted and the model is validated with respect to field data to ensure that both the rockfall behaviour and the overall slope averaged erosion agree with observations.

Chapter 6 brings together the findings of Chapters 3 – 5 in a discussion of the new approach that this research has developed to modelling rockfalls. This chapter incorporates the significant and novel aspects of this approach into a wider review, discussing the perspective and temporal and spatial scales of the reduced complexity modelling approach. Following this, an application of the rockfall model to answer the questions outlined at the end of Chapter 2 is presented, addressing the fourth research objective.

Chapter 7 presents the conclusions of this study in the context of the four research objectives. The overall aim is evaluated and recommendations for future research are given.

2 Rockfall mechanisms and processes

Rock slopes fail in a variety of ways depending on lithology, rock mass structure, environmental conditions and the inheritance of damage within the slope (Agliardi *et al.*, 2013). Rockfalls, rock slides and rock avalanches are all types of rapid movement that originate from steep rock slopes (Dussauge *et al.*, 2003). These modes of failure are a subset of the more general classification of landslides as described by Varnes (1978). This study is concerned with rockfalls: sudden movements of rock, driven by gravity, that become detached from steep and sub vertical rock slopes (Dussauge *et al.*, 2003). Rockfalls occur in a range of geomorphic environments and over a range of scales from frequent, small failures (10^{-4} m^3) (e.g. Rosser *et al.,* 2013), up to large, infrequent failures (>10^5 m^3) such as those that fall from the granitic slopes of Yosemite National Park (e.g. Matasci *et al.*, 2011). At all scales, rockfalls present a range of hazards that vary dependent on the location and timing of failure.

Recent advances in monitoring (e.g. terrestrial laser scanning (TLS); Abellán *et al.*, 2014), have allowed high spatial and temporal resolution data describing rock slopes to be captured, which have revealed spatial clustering and temporal sequencing of rockfalls (Rosser *et al.*, 2013). The complexity observed in both the location and timing of failures likely pertains to the non-linear controls and the interactions of multiple processes on the behaviour of rock slopes (Krautblatter and Moore, 2014).

This chapter reviews advances in understanding and characterising rockfall, with a particular emphasis on the time-dependent nature of rockfalls. The concepts of progressive failure, stress redistribution and damage accumulation within a rock slope are discussed and this critique demonstrates how these concepts have been used in advancing understanding of when, where and why rockfalls occur. The developments in numerical modelling of rock slopes are reviewed with particular consideration of the ability of current models to simulate time-dependent rockfall behaviour that is observed in the field, which motivates the third and fourth research objectives outlined in Chapter 1.

2.1 Controls on rockfalls

It is well established that the stability of a rock slope is dependent upon rock mass strength (Hoek and Bray, 1977). The global strength of a rock mass is a function of the intact rock strength (Hoek, 1994) and the character (spacing, persistence, orientation) of any discontinuities (Cai *et al.*, 2004). The presence of discontinuities within the rock mass modifies

overall rock mass strength significantly (Selby, 1982), such that failure is often observed at stresses below the unconfined compressive strength of the intact rock (Terzaghi, 1962; Eberhardt *et al.*, 1999). Alongside internal rock mass characteristics, the stability of a rock slope and the likelihood of rockfall occurrence are also dependent on the magnitude and type of external forcing that acts to weaken the rock mass through time, or to perturb the rock mass.

2.1.1 Structural controls

The rate of erosion of a rock slope, as the spatially averaged sum of mass wasting, is dependent on both geomorphological and geotechnical characteristics (Kimber *et al.*, 1998). The importance of structural rock properties have long been recognised as significant controls on failure size and mode (Terzaghi, 1962; Hoek and Bray, 1977; Selby, 1982), as emphasised by Stead and Wolter (2015) in their review of rock slope failure mechanisms. In addition to lowering rock mass strength (Krautblatter and Dikau, 2007; Böhme *et al.*, 2013), discontinuities provide release surfaces for failures to be released from the mass (Brideau and Stead, 2010; Zimmer *et al.*, 2012); change local stress concentrations (Martel, 2011); and provide an opening along which weathering processes can act (Viles, 2013). The orientation of the slope surface relative to discontinuity orientations determines which discontinuities daylight at the surface, and strongly influences the susceptibility of individual block release from the slope surface (Krautblatter and Moore, 2014).

General and traditional analysis of rockfalls focus on determining existing failure planes that form in part or in whole along pre-existing discontinuities (Willenberg *et al.*, 2002). Through determination of the failure planes, the mode of failure, and an assessment of failure size can be estimated. The work of Allison and Kimber (1998) and Kimber *et al.* (1998) used a 2D numerical model (UDEC) to determine the limiting conditions for different failure mechanisms for rockfall and rock slope failures from and in jointed rock masses. Their work demonstrated that principles based on single-block movements, as developed by De Freitas and Watters (1973) and Hoek and Bray (1977), are not always geomechanically similar to larger, rock slope failures. With the advancement of 3D modelling capabilities, such as 3DEC (Itasca, 2008), Brideau and Stead (2010) determined combinations of discontinuity orientations that result in 3D toppling failures, extending existing 2D criteria. Brideau and Stead (2012) showed that the orientation of specific release surfaces, the block size and the persistence of discontinuities, also influenced the size and mechanism of failure.

Advances in the application of high spatial and temporal-resolution monitoring technologies has improved the characterisation of rock slopes (e.g. Sturzenegger and Stead, 2009a; Petley, 2012), allowing previously inaccessible areas to be mapped at a high level of accuracy. Sturzenegger and Stead (2009b) provide a comprehensive evaluation of the use of remote sensing technologies (photogrammetry and TLS) for characterising discontinuities at the slope surface. Oppikofer *et al.* (2009), Sturzenegger and Stead (2009a), Matasci *et al.* (2011), Matasci *et al.* (2013), and Agliardi *et al.* (2013) have demonstrated the use of these advances in remote sensing technology to develop structural characterisations of rockfall source areas and determine the key discontinuity sets that promote failure. Agliardi *et al.* (2013) used this information to develop and quantify a topographic signature of damage, by mapping Geological Strength Index (GSI) values onto the structural characterisations of the rock slope. The information gained from remote sensing technologies, and subsequent assessments of damage, can then be used to inform the boundary conditions of numerical models (Stead *et al.*, 2012) for predicting the location and mode of future failures (e.g. Matasci *et al.*, 2013; Havaej *et al.*, 2015).

2.1.2 The role of slope morphology

The topography of a rock slope reflects rock mass properties and environmental forcing, and is modified by the location, shape and size of rockfalls (Krautblatter and Moore, 2014). The influence of topography on rock slope failure has been identified at a regional (10^3 km^2) scale by Leith (2012) where topographic perturbations across the range of an Alpine valley affect local stress fields and associated slope displacements. Martel (2006) demonstrated that topographic differences at the local slope scale (10^1 m) can also significantly influence rockfall occurrence, showing that the convexity of the slope surface changes the local stress concentrations in the near surface. Subsequently local stress concentrations have been shown to be fundamental in the formation of surface-parallel fractures, which then generate rockfall (Martel, 2011). In this way the likelihood of failure of individual areas of the slope can be associated with the degree of curvature of the slope surface at that location.

Microtopographic surface features such as overhangs, protrusions and arches also influence the mechanics of rockfall. They can be identified at a range of scales within rock slopes, from sub-metre features in sedimentary cliffs (Rosser *et al.,* 2007a) to arch features spanning 10^2 m in the granite slopes of Yosemite National Park (Matasci *et al.,* 2011). Where such features generate high stresses, rock disintegration can be enhanced (Krautblatter and Dikau, 2007). Bruthans *et al.* (2014) demonstrated the role of the stress field in controlling the evolution of

arches and bridges in sandstone landforms using small scale analogue modelling. Their findings show that small protrusions, where stress is sub-critical, are more prone to erosion. In sedimentary coastal cliffs in the UK, Rosser *et al.* (2007a) observe that overhangs and protrusions are accentuated by mass wasting due to rockfall, which can often cause such features to coalesce to form larger structures, or collapse. The interaction and feedbacks between microtopographic surface features and rockfalls is complex, but the importance of these features in driving or inhibiting rockfall has not been addressed in rockfall modelling. Where rockfalls are a predominantly surficial process, such surface topographic effects may be significant in controlling the rate and nature of rockfall from the cliff face, and therefore topographic effects should be considered in rockfall modelling.

2.1.3 Environmental controls on rockfall

Environmental factors that contribute to rockfall occurrence include a wide range of processes (Gischig, 2011; Strunden *et al.,* 2015) relating to changes in temperature and precipitation, wind and associated storms, the presence of water, such as waves and tides; seismic activity, and biological and chemical weathering. Each of these processes lead to strength and stress changes within the rock mass and are defined as preparatory factors (Gunzburger *et al.,* 2005). The effect of these factors on the time-dependent nature of slope failure is summarised by Gunzburger *et al.* (2005) and Gischig (2011). Some factors will increase the driving forces in a rock mass, both rapidly, such as seismic activity, and more slowly over time, such as seasonal temperature changes, to bring the rock mass to the conditions for failure (Gischig, 2011). Other factors will act to decrease the resisting forces in a rock mass, lowering the rock strength over time. Again this can occur rapidly, such as intense rainstorms, or more slowly, such as weathering and microscopic damage in the rock mass. Thus, the transition between preparatory and triggering factors can be continuous (Gischig, 2011) such that it is not always possible to directly attribute trigger to failure (Senfaute *et al.,* 2009).

Establishing links between environmental conditions and rockfalls has been attempted in a variety of environmental settings, and some success has been demonstrated in coastal cliffs (Rosser *et al.,* 2007a; Lim *et al.,* 2010; Vann Jones *et al.,* 2015) and high mountain rocks slopes (Strunden *et al.,* 2015; D'Amato *et al.,* 2016). Environmental controls, even when weak (Rosser *et al.,* 2007a) appear to be scale-bound such that the environmental control signal diminished with increasingly large rockfalls, as supported by Strunden *et al.* (2015). In a deglaciated alpine environment, Strunden *et al.* (2015) found a two-month lag between minimum air temperature and rockfall activity, seen most clearly in rockfalls < 1 m^3. By using microseismics

as a proxy for environmental forcing, Vann Jones *et al.* (2015) were able to demonstrate significant relationships between environmental forcing and rockfall occurrence, illustrating the range of processes in the coastal environment that contribute to erosion. For example, Vann Jones *et al.* (2015) demonstrated a marine control on the size characteristics of rockfalls and the total volume of material removed, that extended far above the inundated marine zone of the cliff. In addition to relationships between environmental controls and the size characteristics of rockfalls, D'Amato *et al.* (2016) have shown that rockfall frequency can also be associated with environmental factors. They demonstrate links between rockfalls and both temperature changes and rainfall intensity, such that the frequency of rockfalls is observed to be 7 times higher during freeze-thaw episodes and up to 26 times higher with a mean rainfall intensity greater than 5 mm h^{-1}.

Ultimately, the action of environmental factors in driving rockfall occurrence is via processes of weathering and erosion, whereby the rock mass is broken down and subsequently removed as a rockfall. Rock slopes are often considered to be weathering-limited, such that weathering is the rate-limiting process that determines slope form (Viles, 2013). Conventionally defined as the *in-situ* breakdown of rocks (Viles, 2013), weathering acts over a wide range of spatial and temporal scales. Broadly, the intensity of weathering can be linked to rock slope strength and the rate of weathering linked to the stresses acting on the slope, as weathering can act as a preconditioning, preparatory and/or triggering factor for rockfalls (Krautblatter and Dikau (2007). The wide range of weathering processes, spanning mechanical, chemical and biological weathering (Viles, 2013), will degrade intact rock via reducing the compressive strength of the rock, and lowering the shear strength of the joints (Barton, 1973). Weathering can generate new fractures and exacerbate and exploit existing weaknesses in the rock mass (Krautblatter and Moore, 2014) via the dilation of exisiting fractures (Collins and Stock, 2016). As a result of the breakdown of rock associated with instability, the surface area exposed will increase, again increasing the efficacy of weathering. In this way, potential for the impact of weathering on a rock slope is modulated by the rock mass properties, which in turn are altered by the action of weathering. A summary of the current understanding of the relationship between weathering and rockfalls is given in Viles (2013), which highlights the complexities in trying to produce any generalised models of how weathering contributes to whole slope (in)stability.

A more general relationship between weathering and time, hereafter referred to as the weathering rate (*wr*), is observed to be punctuated by rockfall events and changes in climate, as illustrated in conceptual graphs from Viles (2013) (Figure 2.1). The *wr* peaks in wet weather or climatic periods and drops to a background rate during dry periods. Whilst this conceptual plot is demonstrating changes over decadal timescales, field data of rockfalls over month to

annual timescales display a more complex relationship with weathering (e.g. Lim *et al.*, 2010; Vann Jones *et al.,* 2015; Strunden *et al.,* 2015; D'Amato *et al.,* 2016). Figure 2.1b illustrates the idea that *wr* is reset following a rockfall due to the fresh surface exposed by the rockfall. Within each cycle it can be observed that the initial *wr* is slow, thought to represent the development of a weathering layer (Wells *et al.*, 2008). Beyond this, *wr* increases to a near-equilibrium state until the next rockfall event, which resets the surface. This process is highly variable between different lithologies and environments as the depth of the weathering layer varies (Viles, 2013). Most processes operate across the near-surface zone and along discontinuities, whilst a much smaller selection of processes operate through a deeper, more extensive weathering profile (Viles, 2013).

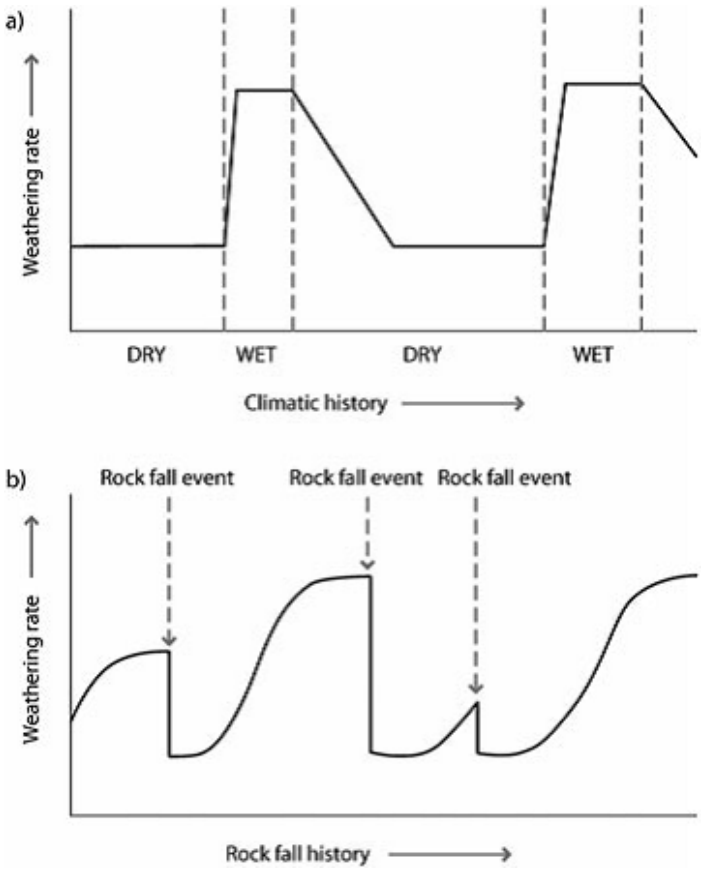

Figure 2.1: Conceptual graphs of weathering rate variations on a rock slope as a response to decadal changes in rainfall (a); and to rockfall events over an annual timescale. Figure reproduced from Viles (2013).

2.1.4 The role of fracture mechanics

Many slope stability analysis techniques rely on the assumption that failure surfaces develop along persistent and continuous planes (Yan, 2008). In reality a combination of pre-existing discontinuities and fracture propagation through intact rock bridges is required for failure to occur. Fracture mechanics, which focuses on the study of crack propagation in a range of materials, was first developed by Griffith (1921), who later demonstrated that there is a threshold stress level at which enough energy is available to produce a rupture surface (Griffith, 1924). Subsequently the stress intensity factor (Irwin, 1957), thresholds for stable and unstable crack propagation (Bieniawski, 1967), and the extension strain criterion (Stacey, 1981) have applied the work of Griffith (1924) to describe critical values at which crack propagation can begin. This has provided a way of assessing the initiation of damage accumulation in the form of crack growth, which is important for establishing thresholds of critical failure.

A large body of literature has demonstrated the application of fracture mechanics to analysing rock slope stability in field-based, laboratory and numerical modelling studies (Jennings, 1970; Einstein *et al.*, 1983; Scavia, 1990; 1995; Kemeny, 2003; Eberhardt *et al.*, 2004; Stead *et al.*, 2004; Brideau *et al.*, 2009; Tuckey *et al.*, 2012; Havaej *et al.*, 2013). Conventional slope stability analysis (Jennings, 1970) uses the joint persistence, which is the ratio of the total joint length to the intact rock, to adjust the parameters in the conventional Mohr-Coulomb failure criterion and define the factor of safety along a failure plane. This approach has been criticised by Einstein *et al.* (1983) who stipulate shortcomings of the approach, namely that it restricts failure to the joint planes. Incorporating the principles of fracture mechanics in evaluating slope stability addresses this by allowing failure surfaces to propagate beyond pre-existing joint planes, and by defining the factor of safety in terms of the stress intensity factor required for fracture initiation and propagation (Saouma, 2010). Further applications of fracture mechanics in rock slope stability have demonstrated that a fracture mechanics approach could predict a slope to be stable, where a limit equilibrium analysis approach would predict the same slope to fail (Tharp and Coffin, 1985), that maximum slope height decreases as a function of increasing crack length (Singh and Sun, 1989), and that the use of numerical modelling to simulate crack propagation and coalescence can be used to determine slope stability as individual fractures are shown to grow and coalesce into larger fractures, that ultimately form a failure surface (Scavia, 1995).

Failures that require the development of fracturing to occur can be termed partially structure-controlled failures, whereby the rock is not kinematically free to move out of the slope without

fracture development (Hajiabdolmajid *et al.*, 2002). Partially structure-controlled failures include both in-plane (along a potential failure surface) and out-of-plane (in between pre-existing discontinuities) rock bridge failures (Einstein *et al.*, 1983). In assessing slope stability for these failures, it is important to be able to quantify rock bridges, and in particular the percentage of intact rock bridge content required to sustain stability. However, methods of quantifying rock bridges remain challenging and inconsistent (Tuckey *et al.*, 2012). Where studies have attempted rock bridge characterisation, estimates of intact rock bridges range widely from 0.2% to 45% (Tuckey *et al.*, 2012), which may reflect either reality or the inadequency of techniques for characterisation. Advances in numerical modelling provides a way of examining the rock bridge content required for failure in different scenarios, and when combined with field studies, can lead to a more accurate assessment of failure mechanisms. For example, Brideau *et al.* (2009) combined detailed field studies with numerical modelling to show how brittle fracture through intact rock and step-path failure mechanism were important for failure surface development in the 1965 Hope Slide (BC, Canada) and the Randa rockslides (Switzerland).

The ability for fractures to propagate is partly controlled by rock mass structure: a closely jointed rock mass may produce small scale rockfalls, inhibiting any significant growth or propagation of fractures, or conversely, in a more massively jointed rock mass, stress relief fracturing may dominate (Rosser *et al.*, 2007b). To date, adopting a fracture mechanics approach to investigate rock slope failure is principally focused on large slope failures such as rock slides 100s m in length, where fracture growth permits the development of a continuous or step-path failure surface (Eberhardt *et al.*, 2004; Brideau *et al.*, 2009; Sturzenegger and Stead, 2012; Havaej *et al.*, 2014b). Fewer studies have investigated the role of fracture development for individual, smaller rockfalls 10s m in length (Collins and Stock, 2016), where the principles of fracture mechanics that have been largely established at the whole slope scale may not apply.

Examining the effects of microfracturing and the associated evolution of the mechanical properties of the rock mass as fractures grow, has been defined as 'damage mechanics' (Mazars and Pijaudier-Cabot, 1996). Related to fracture mechanics, this field of study when applied to slope stability focuses on quantifying the change within a rock mass from its intact structure to a damaged fracture-induced state, with damage as the continuous parameter that reflects internal deformation or weakening of the rock (Eberhardt *et al.*, 1999). The measure of fracture intensity (L^{-1}) (Tuckey *et al.*, 2012), provides one means of quantifying damage within the rock mass. Conceptually this can be considered by the following equation:

$$D_{fs} = \frac{\partial S_D}{\partial S}$$

Equation 2.1 (Stead et al., 2004, p.5)

where, D_{fs} is the damage on a potential failure surface, ∂S_D is the sum of the areas (length) of microcracking on the failure surface, and ∂S is the total area of failure surface considered. As propagating fractures multiply over time and across the space of the rock mass, damage accumulates and can be correlated with an effective reduction in the cohesive strength of the material (Eberhardt *et al.*, 1999). This was illustrated by Kemeny (2003) who developed a fracture mechanics model to simulate the loss of rock joint cohesion as a result of rock bridges breaking, through subcritical crack growth. From this Kemeny (2003) demonstrated the importance of time-dependence for slope stability, as illustrated by the reduction in the factor of safety through time (Figure 2.2a), which translates to an increase in failure probability (Figure 2.2b). The time-dependent nature of fracture development in a rock mass acts to progressively induce damage, which can leave exposed rock more susceptible to surface erosional processes (Adams *et al.*, 2005). As such, damage accumulation can act as a both a trigger and a preparatory factor for rockfall (Krautblatter and Dikau, 2007).

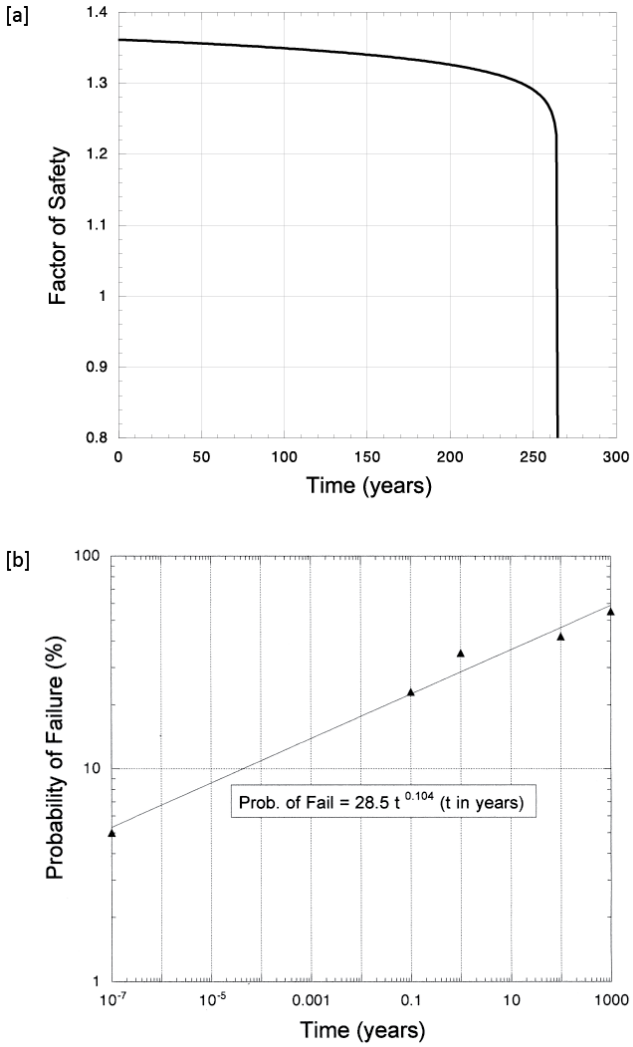

Figure 2.2: [a] Factor of safety as a function of time and [b] probability of failure vs time, for two different experiments. Reproduced with permission from: Kemeny (2003 p.33, 35).

2.1.4.1 Time-dependent damage accumulation within a rock slope

Time-dependent fracture development in a rock mass was first proposed by Bieniawski (1967) as a characteristic sequence of stages of failure in brittle rock. Although at the time much research existed on the fracture of rock, this was a new attempt at establishing a general mechanism to describe the processes taking place. Based on failure criterion equations and on laboratory experiments, Bieniawski (1967) proposed five stages of brittle fracture:

1. Closing of cracks;
2. Linear elastic deformation, leading to fracture initiation;
3. Stable fracture propagation followed by a critical energy release;
4. Unstable fracture propagation causing failure at maximum stress;
5. Forking and coalescence of cracks resulting in rupture, i.e. maximum deformation.

This development of fracturing within a rock mass can be summarised using the staged brittle failure model developed by Martin and Chandler (1994) and Eberhardt *et al.* (1999), where critical stages of fracture development are represented by thresholds in the model (Figure 2.3). Martin and Chandler (1994) conducted a range of laboratory tests on Lac du Bonnet granite to investigate the effect of accumulated damage on the crack initiation stress (σ_{ci}) and crack damage stress (σ_{cd}) (Figure 2.3). Their results showed that σ_{cd} is highly dependent on the accumulated damage, whereas σ_{ci} appears independent of the accumulated damage. This is because the unconfined strength of a material decreases as a function of the accumulated damage and the point at which unstable fractures form (σ_{cd}) is dependent on the unconfined strength (Martin and Chandler, 1994).

Figure 2.3 illustrates crack development through time based on changes in stress and strain within the rock mass under compressive loading. It is clear from figure 2.3 that fracturing observed in laboratory experiments is complex and that the peak stress alone does not capture the full fracturing process (Hoek and Martin, 2014), however boundaries within this process can be defined, as illustrated by the different stages on the curve (Figure 2.3). Each of these stages could be represented by a level of critical stress or strain.

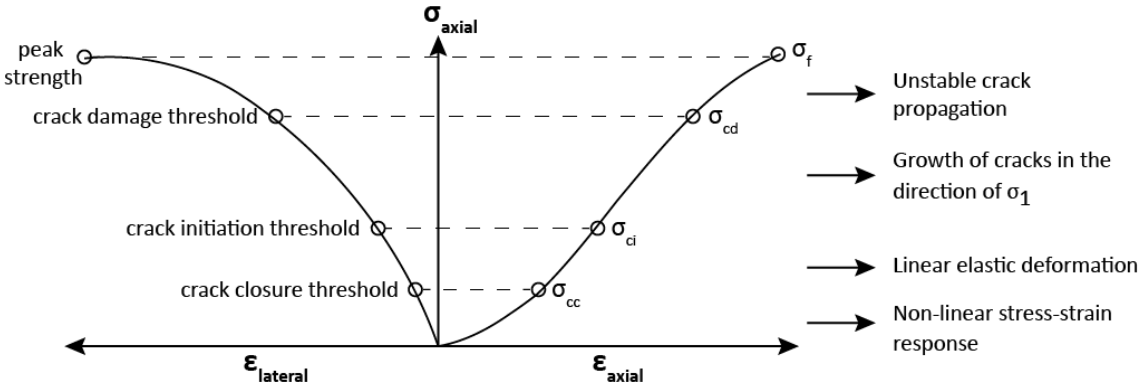

Figure 2.3: Stress-strain curve showing the stages of crack development: modified from Eberhardt et al. (1999, p.363). The second threshold (σ_{ci}) can be represented by a critical strain.

Critical strain levels in a rock mass are emphasised in many field and modelling studies, and have been linked to a range of environmental forces (Brain *et al.*, 2014), yet few studies have tried to quantify this. Petley *et al.* (2005) suggest that the crack initiation threshold, which marks the point at which microcracks interact and coalesce, may be well represented by a critical strain. Crucially the rock mass must reach this critical strain level at crack initiation (σ_{ci})

in order for cracks to coalesce before damage processes can then further influence rock mass strength (Brain *et al.*, 2014).

The crack damage threshold (σ_{cd}) (Figure 2.3), represents a second critical threshold of strain at which the shear strength of the rock mass has been exceeded and failure development moves from a regressive to progressive stage (Havaej *et al.*, 2015). The final stage of failure is characterised by unstable fracture propagation as the rock mass catastrophically accelerates to failure (σ_f) in a time dependent manner, regardless of the applied stress (Bieniawski, 1967; Eberhardt *et al.*, 1999). This has been shown to be characterised by linearity in inverse velocity (Λ) – time (t) space (Petley *et al.*, 2005), building on the earlier work of Saito (1965; 1969), who presented some of the first attempts to incorporate a temporal component into the prediction of brittle slope failures. Similar behaviour is observed in the fracture growth associated with post-earthquake seismic activity as energy is redistributed through the rock mass, as modelled by Narteau *et al.* (2000). They show that the external forcing (elastic potential energy) increases the fracture density up to a point, beyond which the fracture organisation (material properties) controls the fracture density.

The failure envelope, known as the S-shaped failure envelope, was developed by Diederichs (2003) and illustrates another example of progressive fracturing along a continuum by considering the ratio of compressive (σ_1) to confining (σ_3) stresses. This multiphase failure envelope consists of four zones, describing different states of damage and modes of failure. Through the failure envelope, the importance of intact rock bridges in providing short term stability is highlighted (Diederichs, 2003). Using the S-shaped failure envelope, Tuckey *et al.* (2012) provided a conceptual illustration of where different failure mechanisms could occur in relation to different zones of fracturing, thus applying the concepts of brittle fracture to characterise failure mechanisms at different locations at the sub-slope scale.

The concept of time-dependent damage accumulation within a rock slope is well illustrated by the schematic model of the development of a large slope failure (Rosser *et al.* (2007a) Figure 2.4.). Based on a continuous, time-dependent progression towards failure, this model incorporates environmental forcing and rockfall events to illustrate the accumulation of damage within the rock mass. As environmental events generate an increase in the number of rockfalls, redistribution of stress within the rock mass subsequently occurs, resulting in damage accumulation due to crack growth (illustrated in stage 'b' of Figure 2.4; Rosser *et al.*, 2007a). The horizontal dashed line (Figure 2.4) represents a critical strain threshold, equivalent to the crack damage threshold in Figure 2.3. Critically, stage 'd' of the model (Figure 2.4) illustrates how a rock mass may remain in a state close to the critical threshold for a significant

period of time before entering the final phase of failure (Rosser *et al.*, 2007a). This offers a potential explanation for failures that occur without any apparent trigger (Stock *et al.*, 2012) and for the absence of clear links between environmental forcing and rockfall occurrence (Lim *et al.*, 2010; Vann Jones *et al.*, 2015).

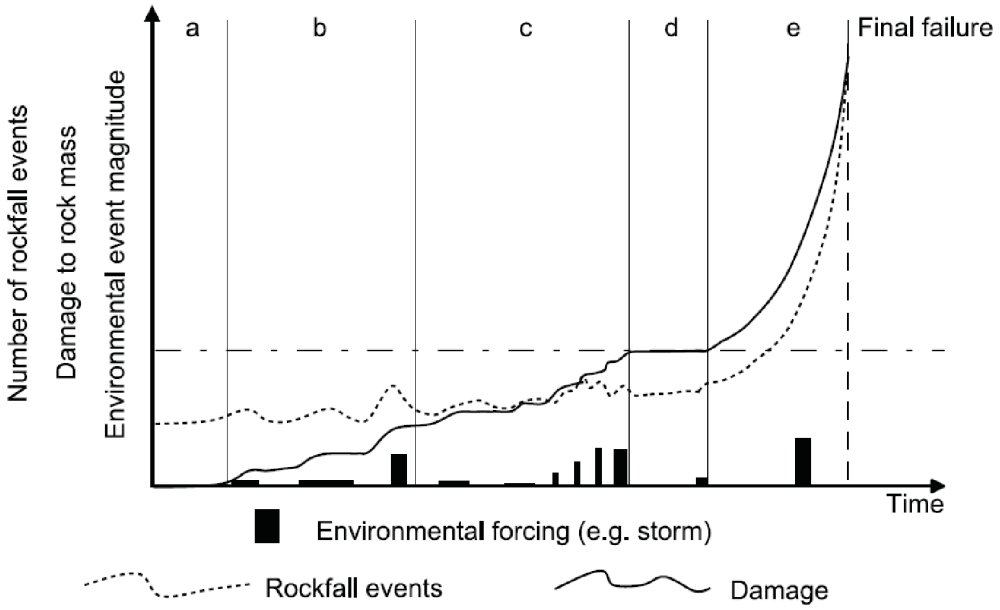

Figure 2.4: Schematic model of the development of a large slope failure via rockfall events and the accumulation of damage to the rock mass. Reproduced with permission from: Rosser *et al.* (2007a, p.12)

As the field of fracture mechanics has developed, it has been recognised that micro-scale processes are important drivers of larger scale phenomena that trigger rockfall. For example, a series of investigations (Diederichs, 2003; Diederichs *et al.,* 2004) into the behaviour of brittle rock during tunnelling reveals that micro-crack growth is a key driver in initiating the development of larger macroscopic features. Subsequently, Leith (2012) proposed that the onset of micro-crack growth through intact rock should be set as an additional threshold in the fracture growth process. Griffith's theory of fracture (Griffith, 1924) emphasised this through the concept of a *process zone* whereby microfractures form ahead of a propagating macrofracture. This idea can be extrapolated whereby small levels of damage within a rock mass may accumulate and redistribute, and eventually drive the propagation of larger failures (Lim, 2006; Brain *et al.*, 2014). Evidence for the results of this is seen in the field where smaller failures often act as precursors to larger failures (Rosser *et al.*, 2007a).

2.2 Observations of progressive failure in rock slopes

Assessment of rockfalls both in field observations and laboratory measurements has advanced mechanical understanding of rockfalls and has led to a well-developed understanding of how rockfalls occur as discrete events. The application of fracture mechanics to rock slope stability has challenged the assumption that rockfall are always discrete and that do not evolve through time (Dewez *et al.*, 2007), and that individual rockfall events always occur in isolation (Zimmer *et al.*, 2012). The progressive nature of failure in rock slopes may be manifest in several ways and is often postulated from observed behaviour of rockfalls, made possible through advances in monitoring technology. For example, Rosser *et al.* (2013) present evidence of patterns of contiguous rockfall evolution, observed in high-resolution monitoring of coastal cliffs in North Yorkshire using TLS (Figure 2.5). This pattern of clusters of rockfalls may be a surface expression of the progressive nature of failure wherein deformation acts to shed smaller rockfalls prior to larger rockfalls. Such time-dependent nature of changes within a rock slope act to drive a slope to fail over time via weakening of rock (Terzaghi, 1950).

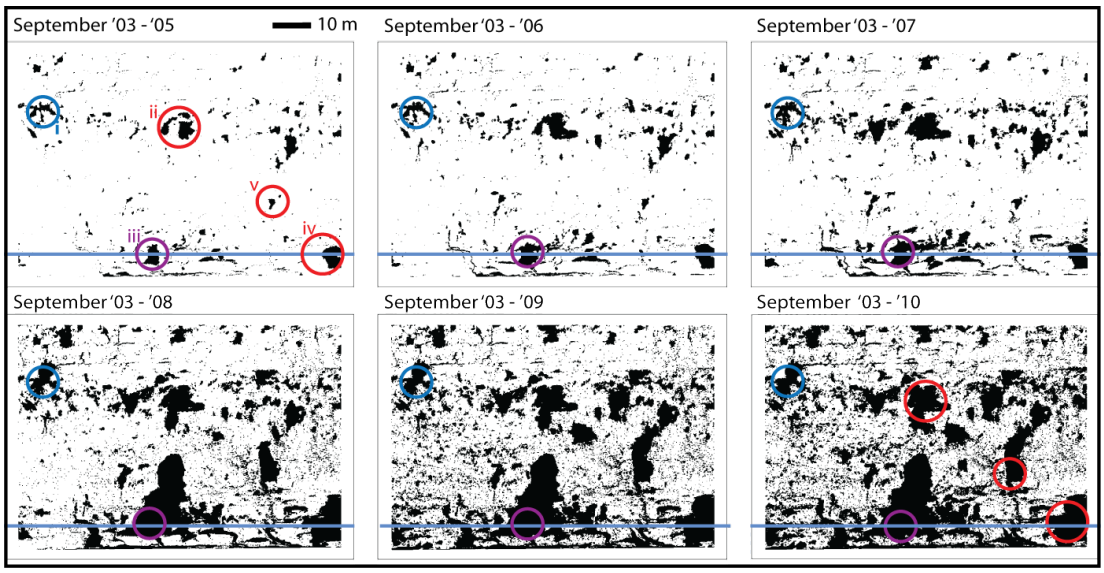

Figure 2.5: Cumulative annual change on a coastal rockface (N Yorkshire, UK) from Sep 2003 to Sep 2010, derived from TLS data. Areas within the circles show progressive rockfall evolution: i, ii – bridging and coalescence of failures; iii, iv – scars at the cliff toe which propagate up; and v – a small scar which grows to coalesce and form an upslope aligned feature. The blue line indicates the high annual tide. (Reproduced with permission from: Rosser *et al.* (2013, p.940).

Temporal sequencing of failures is observed in a variety of rock slope studies and displayed in the sequential failures that are contiguous or in close proximity (Fig. 2.6). Precursory rockfall activity was recognised in a pioneering study by Rosser *et al.* (2007a) where small rockfalls were observed as precursors to larger failures (Fig. 2.6b) in the form of spalling. Figure 2.6c shows another example of precursory activity in the form of slope deformation (creep) that increases in rate over time towards failure (Abellán *et al.*, 2010). Stock *et al.* (2012) present observations of a temporal sequencing of rockfalls (Fig. 2.6a) that provide one of the few quantitative studies of progressive rock slope failure, where both the timing and location of rockfall propagation is recorded. The temporal sequencing of rockfalls and spatial distribution of the rockfalls (Fig. 2.6a) offered new insight into the potential nature of progressive failure. Without any clear external trigger, these failures are postulated to have been driven by stress redistribution and crack propagation (Stock *et al.*, 2012). Stress re-distribution within a rock mass is particularly important for understanding contiguous rockfalls as post-failure stress re-distribution can create a damaged zone characterised by the increased presence of microcracks in the surrounding material. This relates to the concept of a *process zone* (Griffith, 1924) and the idea that small additional damage within a rock mass will accumulate and stress will redistribute, eventually driving the development of larger failures (Lim, 2006; Brain *et al.*, 2014). The ways in which this occurs, and the degree to which stress is distributed, arguably plays an important role in determining subsequent rockfall activity (Senfaute *et al.*, 2009; Stock *et al.*, 2012).

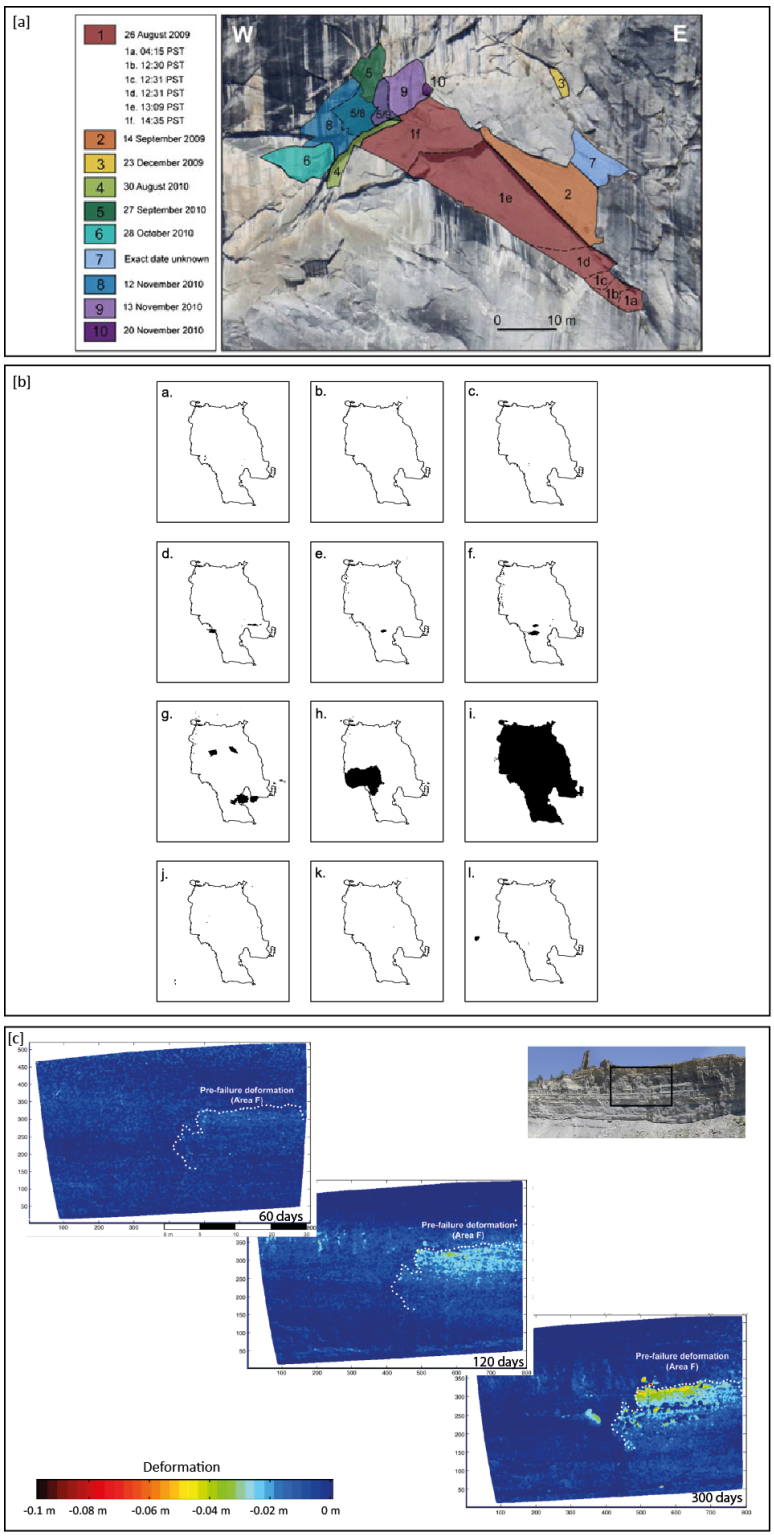

Figure 2.6: Examples of apparently time-dependent sequencing of failures as observed in the field, where deformation operates independent of environmental forcing: [a] sequence of rockfalls in the Rhombus Wall (eastern Yosemite Valley, California) from Aug 2009 – Nov 2010. Reproduced with permission from: Stock *et al.* (2012, p.551); [b] sequence of rockfalls in coastal cliffs (N Yorkshire, UK) from Nov 2004 to June 2005. Each image (10*11.5 m) covers 1 month. Reproduced with permission from: Rosser *et al.* (2007a, p.10); [c] pre-failure deformation monitored over 300 days on a rockface that forms part of a larger landslide scar (see inset) (Catalonia, Spain). Reproduced with permission from: Abellán *et al.* (2010, p.169)

2.2.1. **Statistical analysis of rockfalls**

Evaluating the characteristics and behaviour of rockfalls requires analysis of the location, size and timing of rockfall (Dussauge *et al.*, 2003). The size distribution can be used for hazard assessment, on the assumption that the distribution is consistent through time (Dussauge *et al.*, 2003). The size distribution, and in particular the fit to a power law, has also been considered indicative of the underlying processes driving rockfall occurrence.

A common approach to the statistical analysis of rockfall events is to develop magnitude-frequency distributions, based on rockfall inventories (Dussauge-Peisser *et al.*, 2002). Magnitude-frequency analysis provides a method of quantifying the erosive impact of geomorphic processes, especially for phenomena that occur over large spatial areas (Stark and Guzzetti, 2009). There has been a large body of research on the frequency distributions of rockfalls and landslides, with particular reference to the best methods of presenting the data (e.g. Stark and Hovius, 2001; Malamud *et al.*, 2004) and characterising the distributions observed, commonly using power laws (e.g. Stark and Hovius, 2001; Brunetti *et al.*, 2009; Stark and Guzzetti, 2009; Barlow *et al.*, 2012). Typically, negative power law scaling of magnitude (volume)-frequency distributions is observed, and a power law is often fitted to data as a way of describing the distribution and allowing comparisons of different datasets. The power law fit is of the form:

$$f = k \times {R_V}^{-\beta}$$

Equation 2.2

where f = frequency, k = coefficient, R_V = rockfall volume (or event magnitude, m^3), and β is the power law exponent. The power law exponent describes whether the erosion is dominated by the largest failures or the small failures (Stark and Guzzetti, 2009), and therefore can be used to suggest the dominant processes driving erosion in the landscape in question. Dussauge-Peisser *et al.* (2002) and Dussauge *et al.* (2003) compiled data on rockfall size distributions from a range of rockfall inventories from natural rock slopes, obtaining power-law distributions with an average exponent of 0.7 ± 0.3. Theoretically, the properties of a rock slope - rock strength, discontinuities, slope morphology - should constrain the exponents of distributions (Barlow *et al.*, 2012). However, exponent values obtained from the power law distributions of multiple rockfall inventories do not show a unique correlation with either geology, climate or triggering mechanisms (Hergarten, 2003; Barlow *et al.*, 2012).

In an attempt to understand the origin of power-laws observed in the frequency distribution of mass movements, self-organised criticality (SOC) has been applied in relation to slope dynamics and mass movements (e.g. Dussauge *et al.*, 2003; Hergarten, 2003; Chapuis and Tetzlaff, 2014). SOC describes a system that can organise itself towards a critical state where events of all sizes can occur and their statistical relationship is scale invariant (Hergarten, 2003). SOC was first illustrated for mass movements by the Bak-Tang-Wiesenfeld model (Bak *et al.* 1988). The model describes an abstract avalanching process, whereby an instability starts in small area and propagates through a pile of sand standing at a critical angle. This is similar to the phenomenon of progressive slope failure introduced by Bjerrum (1967), who identified the need for a shear surface to develop in order for cohesive materials to fail. The development of the shear surface was recognised as a progressive process occurring as the shear zone transitions from peak to residual strength, propagating through the slope. Within this process a critical point can be identified, beyond which failure development occurs rapidly (Petley *et al.,* 2005) and can be characterised by runaway crack coalescence leading to failure (Eberhardt *et al.,* 1999; Petley *et al.,* 2005), as previously illustrated (Fig. 2.3). Although SOC models are capable of simulating a propagating, unstable process, Hergarten (2003) demonstrate the difficulty in applying SOC based models on a quantitative level, and show that the power law distributions exhibit an over dependence on the largest events. This would mean that the models are not correctly representing the behaviour observed in mass movement events. Hergarten (2003) suggest that introducing a time-dependent weakening component can significantly improve the SOC based models for landslides, generating a power-law exponent within the range of those observed in natural systems. However this doesn't account for the variability observed in rockfall inventories, and Hergarten (2003) suggest that mechanics should be introduced to the models in order to ascertain whether the variability is driven by variations in rock mass properties, environmental conditions, or whether it is purely a statistically driven phenomena. Rosser *et al.* (2007a) propose an alternative approach in the form of analysis of the spatial and temporal patterns in precursory rockfall activity (Fig. 2.5 and 2.6) which they recognise as a visible expression of the time-dependent weakening and deformation within the rock mass, proposed by Hergarten (2003).

In all cases where power law scaling of magnitude-frequency distributions have been applied to geomorphic events, the magnitude-frequency analysis is sensitive to the spatial and temporal resolution of data collection (Barlow *et al.,* 2012), which often underrepresents the smallest events (Stark and Hovius, 2001; Dussauge *et al.*, 2003). Using an extensive dataset collected on the North Yorkshire coast (UK) Barlow *et al.* (2012) demonstrate the impact of the temporal resolution of monitoring when utilising approaches to analysis such as magnitude-

frequency distributions. Crucially, the results suggest that existing datasets may not be indicative of the long-term evolution of rock cliffs as the full volume distribution may not be captured in short-term monitoring datasets. Advances in monitoring technologies that have enabled higher spatial and temporal resolution data collection have gone some way to addressing these issues by increasing the ability to capture the smallest events at lower end of the rockfall distribution, and allowing more frequent data capture over longer monitoring periods. Together these deal with some of the previous concerns in sampling deficiencies associated with this type of analysis (Rosser *et al.*, 2007a).

2.3 Numerical modelling of rock slopes

Over the last decade progress has been made in the numerical modelling of rockfalls (Stead and Coggan, 2012). Recent advances in the spatial and temporal resolution that numerical models are able to operate at have demonstrated the importance of the spatial and temporal scale of investigation. For example, Pine *et al.* (2007) use a high resolution, 3D model to simulate rock slope failure at the scale of individual blocks and show how larger failures, often observed when modelling at a coarser spatial and/or temporal resolution, are in fact the sum of many smaller failures. This concept supports observations from field studies where rock slopes are monitored at a high temporal resolution, (Fig. 2.6), and is crucial in developing our understanding of rock slope evolution. Additionally, Brideau and Stead (2012) demonstrated that changing the spatial resolution of the rock slope face in the model, results in variations in the calculated displacement and failure mechanisms predicted by the model. This result is equally manifest in both 2D and 3D, and emphasises that the scale of investigation can determine the results.

The following section reviews a range of approaches to rock slope modelling, with a particular focus on the temporal and spatial scales of modelling, simulating damage in a rock slope, and the current limitations of rock slope models for simulating contiguous rockfall. The variety of numerical rock slope models can be broadly split into four methodological approaches, as defined by Stead and Coggan (2012): i) limit equilibrium methods; ii) continuum techniques; iii) discontinuum techniques; and, iv) hybrid techniques. Each of these approaches reflects a stage of development in the modelling of rock slopes, and more recently the inclusion of fracture, as both technical understanding and modelling capabilities have advanced. Table 2.1 summarises the advantages and disadvantages of each approach. Within each category some specific model codes have additional functionalities and can be considered more sophisticated (Styles

et al., 2011). The capabilities of those codes are considered specific to the codes and so are not included within the summary in Table 2.1, but are highlighted within the review below.

Table 2.1: Comparison of the rock slope modelling capabilities for the simulation approaches

Approach	Discretisation	Solution method	Advantages	Disadvantages	Application/Example
Limit equilibrium	Rigid blocks	Single analytical process	• Well established, industry standard models; • Low computational costs; • 2D and 3D capabilities;	• Only considers rigid blocks and simple failure geometry; • Intact rock fracture is not simulated; • No internal deformation.	Case examples: Hoek and Bray (1977) Collins and Sitar (2011) Numerical models: Rocscience (2013)
Continuum: Finite element method (FEM) Boundary element method (BEM) Finite difference method (FDM)	Finite elements	Implicit	• Intact rock mass is able to fracture; • Can simulate a progressive response of the rock mass to changes in stress/strain; • Can effectively handle heterogeneous and non-linear material; • 2D and 3D capabilities.	• Rotation/ detachment of material is not permitted; • Discontinuities are not explicitly modelled.	Case examples: Styles *et al.* (2011) Numerical models: Phase^2 (Rocscience, 2013) FLAC (Itasca, 2014)

Discontinuum: Discrete element method (DEM), Discontinuous deformation analysis (DDA)	Discrete elements (blocks/ particles) Either: Voronoi tessellation (polygonal) or Trigon (triangular)	Explicit	• Displacement and detachment are permitted; • Can effectively handle non-linear material; • Dynamic behaviour; • 2D and 3D capabilities; • Simulates failure along discontinuities; • PFC based models can simulate fracture.	• UDEC and 3DEC do not permit intact rock fracture.	Case examples: Allison and Kimber (1998); Nichol *et al.* (2002) Brideau and Stead (2010) Numerical models: UDEC, 3DEC, PFC, Slope Model (Itasca, 2014)
Hybrid: Continuum/ discontinuum methods	Finite elements mesh and discrete element discontinuities; transition between them is possible	Can use explicit or implicit (explicit commonly used to allow independent consideration of elements)	• Benefits of continuum & discontinuum; • Can simulate failure along discontinuities and fracture through intact material; • Existing discontinuities and new fractures can interact; • Can simulate stages of fracture development (full failure process); • 2D and 3D capabilities.	• Computationally intensive; limiting the number and range of simulations.	Case examples: Stead *et al.* (2004) Eberhardt (2004) Elmo (2006) Pine *et al.* (2007) Numerical models: Elfen (Rockfield, 2013)

2.3.1 Model scales and methods of discretization

The majority of applications of numerical models to slope stability are concerned with large scale, discrete events, rather than the iterative processes of contiguous rockfalls that develop across the slope face. Limit equilibrium methods (LEM) are the most common form of slope stability analysis for rock slopes (Stead and Coggan, 2012) and are designed for relatively simple translational failures such as planar, multi-planar and wedge type failure analysis at the scale of the large failures or even the whole slope, rather than for individual smaller rockfalls (Stead *et al.*, 2006; Collins and Sitar, 2011). Using a LEM approach to back-analyse failures in limestone cliffs, Frayssines and Hantz (2009) showed that the modelling results produced much lower rock cohesion values than observed in previous laboratory tests, emphasising the importance of both the spatial and temporal scale of investigation in slope stability analysis.

Continuum techniques simulate deformation of material without detachment. Models are able to operate dynamically, allowing the simulation of the rock mass response to changes in stress and strain (Styles *et al.*, 2011). Models that employ continuum techniques are well suited to simulating large scale slope deformation and failure and have been successfully employed in the back analysis of individual slope failures (Styles *et al.*, 2011; Agliardi *et al.*, 2013), and to simulate valley-wide response to long-term glacial loading and unloading (Leith *et al.*, 2014a; 2014b). Conversely, continuum techniques are not suited to simulating individual surficial failures, such as contiguous small rockfalls, particularly as detachment is not explicitly simulated. Recent developments to Phase^2 (Rocscience, 2013) have also allowed joints to be incorporated and therefore structurally controlled failures can now be simulated with this code (Stead and Wolter, 2015).

Discontinuum techniques are most appropriate for the accurate representation of jointed rock slopes and large scale displacements (Stead and Wolter, 2015). Discontinuum techniques encompass the Discrete Element Method (DEM), Discontinuous Deformational Analysis (DDA), Particle Flow Codes (PFC) and recently, lattice-based codes. In DEM models, which are most commonly used in rock slope modelling, the model space is discretised into elements, bounded by discontinuities so that the rock slope is composed of individual, free blocks that interact with surrounding blocks at the contacts between them (Stead *et al.*, 2012). These contacts are continually updated during the model process, in contrast to continuum approaches where the contacts between system components remain fixed (Jing and Hudson, 2002). The explicit solution scheme allows a large number of discontinuities to be explicitly considered in the model and both displacement and detachment are permitted (Stead *et al.*, 2012). Modelling rock slopes with a DEM can simulate movement along existing structures and

translation and rotation of blocks in 2D and 3D (Stead and Wolter, 2015) and thus movement of individual blocks up to whole slope failure can be simulated. Subsequently discontinuum methods can be applied at a range of spatial scales, where the model resolution will be restricted by the level of complexity required.

Early applications of UDEC, a 2D discontinuum based model code, include the work of Allison and Kimber (1998) and Kimber *et al.* (1998) who demonstrated the structural controls on failure mechanisms in jointed rock slopes. As numerical models advanced to include 3D capabilities, for example 3DEC (Itasca, 2014), the structural controls on failures were further investigated. Brideau and Stead (2010) and Brideau and Stead (2012) used 3DEC to investigate the influence of discontinuity orientation on block toppling, allowing the kinematics of toppling failures to be resolved at both the individual block and the whole slope scale. Brideau and Stead (2012) demonstrated the advantages of modelling in 3D and including a slope width of similar dimensions to its height and depth, allowing the block size, accurate discontinuity orientation and kinematic confinement to be included. This allowed model simulations to include failure across the slope face as well as in profile, demonstrating the advantages of this level of detail and perspective in rock slope modelling. Results from their study showed predictions of displacement across the slope face, which revealed spatial patterns of failure and associated changes in failure mechanism.

Adopting a high spatial resolution, hybrid modelling approach for a geotechnical application, Pine *et al.* (2007) also focused on the failure of individual blocks and considered joint properties in their model of block caving. Fracturing between blocks was observed, and similar to the modelling in Allison and Kimber (1998), they focused on the sequential failure of blocks over time and the resulting slope development. Uniquely Pine *et al.* (2007) modelled from an slope face perspective, allowing interactions between blocks across the slope to be observed. Modelling at the scale of individual blocks illustrates that larger failures, often observed when modelling at a coarser resolution, are in fact the sum of many smaller failures (Pine *et al.,* 2007).

2.3.2 Simulating damage in numerical rock slope modelling

Damage, a continuous measure of any weakening of the rock mass (Eberhardt *et al.,* 1999), is represented in numerical rock slope models by simulating brittle fracture, which has developed as numerical models have increased in sophistication. LEM take an analytical approach to modelling brittle fracture (Jennings, 1970). In considering the role of joint

persistence and rock bridge length, fracturing is implicitly considered; however intact rock fracture mechanisms are not explicitly considered (Stead *et al.*, 2007). Boundary element methods have advanced using purely analytical techniques and allow consideration of different fracture modes. This method has been used in the analysis of step-path failures in rock slopes, such as the fundamental work of Singh and Sun (1989) and Scavia (1995), as previously discussed (section 2.1.4).

In models that adopt continuum techniques the stages in fracture development associated with damage accumulation are characterised implicitly by considering the overall degradation of rock mass properties (Stead and Wolter, 2015). Conversely, brittle fracture is modelled explicitly in discontinuum-based model codes. For example, UDEC and 3DEC simulate brittle fracture by allowing cracks to develop when stresses in the model cause failure along the contacts between blocks (Stead and Wolter, 2015). However, these models do not permit fractures to develop through the intact rock, limiting the extent to which damage and stages of fracture development can be simulated.

The hybrid numerical model Elfen (Rockfield, 2013) uses a finite element mesh to model joint bounded blocks and discrete elements to model the joints (Elmo, 2006) (Table 2.1). This allows the model to simulate failure along discontinuities and through intact material. The model has been demonstrated to successfully simulate brittle fracture at a range of scales in both 2D, (Cai *et al.* 2004) and 3D, (Hamdi *et al.,* 2013). Furthermore the model is capable of simulating the stages of fracture development: initiation, growth and coalescence, making the model suitable for simulating progressive failure in rock slopes (Elmo, 2006). Elfen simulates failure based on the Mohr-Coulomb failure criterion and the time-integrated approach allows sequencing of individual failures resulting in whole slope collapse. Elfen is capable of simulating step-path failure, as demonstrated by Eberhardt *et al.* (2004) in their application of Elfen to an investigation of the 1991 Randa rockslide. Their results uniquely highlighted the role of fracture initiation and propagation in the development of the failure surface. Pine *et al.* (2007) used Elfen to model rockfalls associated with block cave mining and demonstrated that the model is able to simulate patterns of failure analogous to those observed in the natural environment (Fig. 2.7.). Their results further demonstrated the value of modelling brittle fracture processes to understand rock slope failure mechanisms.

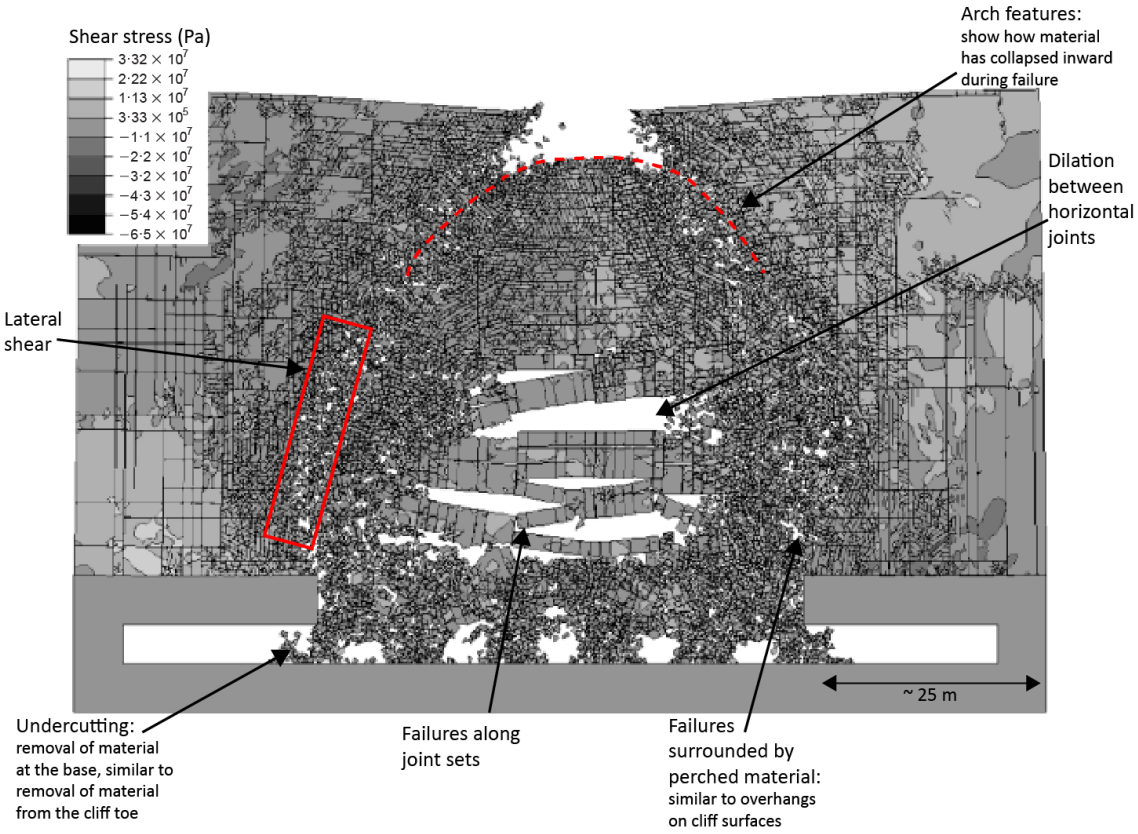

Figure 2.7: Elfen model showing an advanced stage of a 2D model of underground block caving, with shear stress values (Pa) (reproduced with permission from: Pine *et al.* (2007, p.764)). Annotations have been added to show features of evolving rockfalls, as seen in hard rock cliffs: failure along joint sets, arch features, lateral shear, failures surrounded by perched material, undercutting, and dilation between horizontal joints.

Various methods have been adopted to quantify damage within numerical models. Tuckey *et al.* (2012) describe measures of fracture density and intensity in 1D, 2D and 3D. These ideas have been translated by Stead and Eberhardt (2013) to damage intensity parameters in units of m^{-1} according to the following equations:

$$[a]\ D_{10} = \frac{number\ of\ cracks}{unit\ length}$$

$$[b]\ D_{21} = \frac{length\ of\ cracks}{unit\ area}$$

$$[c]\ D_{31} = \frac{area\ of\ cracks}{unit\ volume}$$

Equation 2.3 (Stead and Eberhardt, 2013)

Havaej and Stead (2016) have adopted Equation 2.3b and c to quantify damage within applications of the relatively new model code, Slope Model. Slope Model is a 3D brittle

fracture code, based on the Particle Flow Code (PFC) but replacing the balls and contacts of PFC with nodes and springs in a lattice setup (Itasca, 2010a). When the strength of a spring has been exceeded it breaks and is replaced with a fracture, in the same way that broken contacts are replaced by fractures in the PFC model. In this way, fractures can develop through intact rock and the model has the ability to simulate the initiation, growth and propagation of fractures. Havaej and Stead (2016) sought to quantify damage by measuring the intensity and extent of fracture development under different slope conditions. They present a new method, termed the 'damage ellipse', whereby damage is quantified based Equation 2.3b or c, using the size of the ellipse as the unit area or volume respectively (Fig. 2.8b). Quantifying damage in this way within a numerical model allows the relationship between failure kinematics and the resulting damage to be established. Using this to consider how damage evolves both spatially and temporally would further enhance understanding of how rockfalls evolve.

Until recently the final stage of failure (Bieniawski, 1967) (Fig. 2.3) was often unaccounted for in rock slope modelling studies due to the relatively low temporal resolution of monitoring data available to inform the models. Recent studies combining advanced observational and modelling techniques have explored this final stage of failure. For example, Elmo *et al.* (2011) applied multiple modelling approaches to simulate progressive failure, highlighting the impact of the different ways rock mass properties are represented. Their work utilising the hybrid modelling code Elfen, illustrates how the inclusion of rock bridges can alter fracture propagation to final failure. This has enhanced our understanding of the timing of the final failure stage as identified in the laboratory work of Martin and Chandler (1994) and Eberhardt *et al.* (1999).

Havaej and Stead (2016) also explored the final stage of failure by using Slope Model to identify a critical threshold of fracture intensity in a large open pit mine and determine the subsequent timing of failure under different slope conditions. The critical threshold was identified by plotting both inverse velocity and displacement against time (Fig. 2.8a). They identify the transition from regressive to progressive failure and refer to this point as the onset-of-failure. Examining the fracture intensity at this point in the model allows them to identify the critical threshold as a measure of fracture intensity and determine the subsequent time to failure under various slope conditions. Their results showed that models with shallower failures exhibit higher fracture intensity and a shorter time to failure. Using numerical models in this way to observe the rate and spatial extent of fracture growth during slope failure illustrates the relationship between damaged areas of the slope and the failure mechanisms produced. Importantly when considering progressive failure, these models also allow observation of post-failure fracture development.

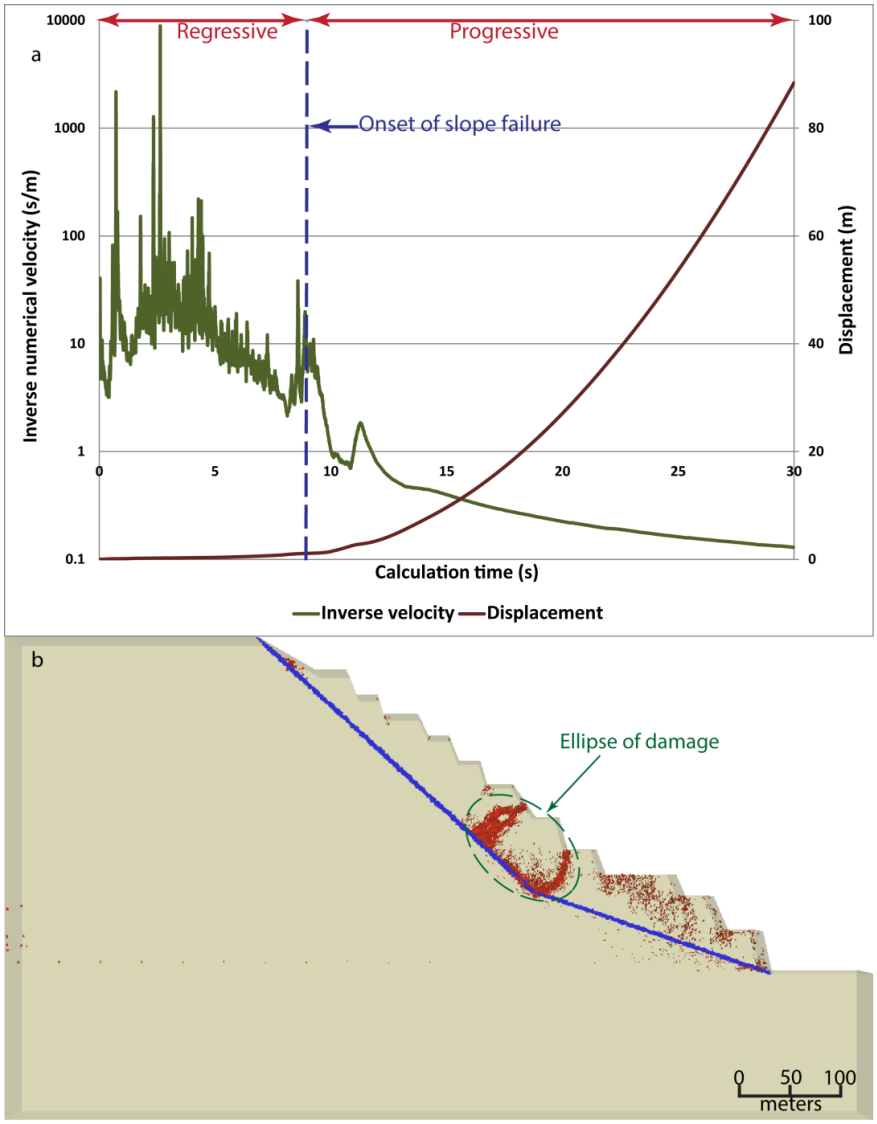

Figure 2.8: [a] Superimposed plots of inverse velocity and horizontal displacement. The onset of slope failure is identified (blue dashed line) as the time at which the stability of the slope changes from decelerating to accelerating behaviour, as evidenced by the sudden increase in slope displacement; [b] Rock mass damage at the onset of failure. The geometry of the damage zone is quantified as the ellipse of damage (here in 2D): the lengths of the two axes of the ellipse are used to quantify damage within the model at any stage. Figure reproduced with permission from: Havaej and Stead (2016, p.185).

2.3.3 Limitations of rock slope models for simulating contiguous rockfall

There is a noticeable gap in current research of studies that are using the most recent numerical codes, such as Slope Model and Elfen, to model sub-metre to 10s of m scale rockfalls on natural rock slopes. The typical frequency distribution of rockfall size exhibited by failures in a range of studies (Hungr *et al.,* 1999; Rosser *et al.,* 2007a; and Barlow *et al.* 2012), suggests that a significant amount of geomorphological work via rockfalls is achieved at the

sub-metre scale. The following section will summarise the limitations of current rock slope models to the task of simulating patterns of contiguous rockfall, (Fig. 2.6), at the sub-metre scale.

2.3.3.1 Perspective and scale

Stead and Coggan (2012) demonstrate that much of the current rock slope modelling is at a coarser scale than needed to detect widely observed features of shallow (sub-metre depth) rockfalls (Fig. 2.5) and as such, models fail to represent stress redistribution as a mechanism of failure at the appropriate spatial and temporal scales.

The application of many current rock slope models reduce the dominant structural controls to a 2D profile view (Styles *et al.,* 2011; Havaej *et al.,* 2014a). This perspective is appropriate for a kinematic analysis of whole slope failure, or the failure of discrete features, such as a cantilevered overhang. For example, analysis of the Joss Bay failure by Styles *et al.* (2011) clearly demonstrated the progressive nature of the slope failure as the stresses resulting from the notch at the cliff base caused tensile failure in the upper slope. However this approach does not consider the boundary conditions imposed by lateral confinement across the rock face, the rock face structure or its variability, as identified as potentially important factors from field observations (Fig. 2.5, 2.6). Subsequently, the profile view may not be representing important controls on failures that occur, which are in turn essential for modelling rockfall evolution. High-resolution monitoring of rock slopes is also captured with a slope face perspective, making any comparison with profile view model outputs problematic. Recent applications of sophisticated discontinuum and hybrid codes, such as 3DEC (Brideau and Stead, 2012), Slope Model (Havaej and Stead, 2016) and Elfen (Pine *et al.*, 2007), have begun to model rock slopes in 3D, from a slope face perspective. The results of these applications demonstrate the advantages of modelling from this perspective as outlined in section 2.3.1 and 2.3.2.

In addition to the spatial resolution of the modelled rock slope, the inclusion of external processes such as weathering in rock slope models is also sensitive to the model resolution. As illustrated by laboratory tests (Lajtai *et al.* 1987) and field experiments (Collins and Stock, 2016), the influence of environmental forcing can be observed at the scale of individual fractures, suggesting that numerical models should apply environmental processes at a scale relative to failure size. Or more broadly, numerical models should represent processes at the scale at which they drive change. Lim *et al.* (2010) state that our understanding of cliff

behaviour is limited by our ability to identify, quantify and therefore simulate the full range of failures occurring on the rock face. Thus, the scale at which processes are considered or represented in rock slope models is a key research gap.

2.3.3.2 Stress redistribution and damage accumulation

At all scales, the majority of modelling studies consider rockfall as discrete events. Only the highest resolution modelling studies (e.g. Pine *et al.,* 2007; Havaej and Stead, 2016) begin to consider the process of evolving rockfall, adopting fracturing as the measurement of damage. However, fracturing is often simulated at metre-scale resolution (Fig. 2.8b) and the role of microfracturing, as observed in laboratory tests, is seldom simulated in numerical modelling.

The staged brittle failure model developed by Martin and Chandler (1994) and Eberhardt *et al.* (1999) describe failure as a continuous process reflecting strain accumulation. Strain is often physically expressed as fracturing within a rock slope, yet the continual accumulation of strain is not simulated.

Stress redistribution within a rock mass is recognised as a potential driver of patterns of contiguous and propagating rockfalls (Stock *et al.,* 2012); however this process is difficult to quantify and therefore not explicitly included in current rock slope models. Conceptual models such as the sandpile model (Bak *et al.*, 1988), and a recent model simulating processes of glacier calving (Chapuis and Tetzlaff, 2014), have demonstrated how propagation of surficial events can be simulated. These examples have the potential to be adopted and adapted to simulating rockfall processes, and would allow stress redistribution to be explicitly included.

2.4 Conceptual approach

The combination of the mechanical understanding of fracture growth and propagation, and the observation of failure sequencing and propagation in the field has raised further questions regarding how rockfall evolve through time, the most appropriate scale to model at, and the conditions in which progressive failure may act to drive this process. Numerical modelling provides the potential to examine these questions as processes can be modelled over time and at appropriate scales not observable in the field. Furthermore, the interaction with rock mass structure, material properties and slope morphology can be investigated. A new approach is required if patterns of rockfall evolution are to be simulated in a way that is more analogous to

the most recent generation of quantitative field observations, as described in this chapter. Critically this approach should achieve the following modelling objectives:

2.4.1 Modelling Objective 1: Modelling at a slope face view (2.5D), rather than in profile

Monitoring and modelling studies that operate from a slope face perspective have demonstrated that the mode and process of failure is often more complex than can be observed in profile alone. In 2D profile models, spatial constraints on rockfall are limited to vertical (un)loading and loss of support. Ideally, rockfall modelling should consider a slope face view in 2.5D, with the grid oriented parallel to the cliff face, with each grid cell with an elevation relative to the mean plane of the surface. This model structure is able to account for rock mass properties and topography of the slope face, in order that the controls on failure that occur across the rock slope may be observed and modelled.

2.4.2 Modelling Objective 2: Modelling at a high spatial resolution

The spatial scale adopted in rockfall modelling should be set to allow for the distribution of observed failure sizes to occur, and so needs to be comparable to the resolution in the monitoring data. Currently the majority of numerical rock slope stability models are focused on the whole slope, not at the scale of the rockfall observed here. Field observations show that rockfalls range in size from 10^{-4} m^3 upwards (Rosser *et al.*, 2013), and even this figure may be a larger minimum size estimate, further limited by the frequency and resolution of data collection. Models focused at assessing the stability of the whole slope are likely to miss smaller failures, which are more widely suggested to contribute most of the geomorphic work (material loss) from slopes where stability is not predefined by larger structures and instability. By modelling down to the resolution of the smallest failure sizes, individual failures and how they interact can potentially be assessed.

Despite observations of spatially-dependent sequencing of rockfalls in various rockfall monitoring studies (Collins and Sitar, 2008; Abellán *et al.*, 2010; Stock *et al.*, 2012), these processes are not well represented in most rock slope models, in part because the models have not been designed for this purpose. Conceptual models, such as Bak *et al.* (1988), incorporate spatial sequencing and a recent study by Chapuis and Tetzlaff (2014) demonstrated the application of these ideas to glacier calving. The advantages of modelling at

a scale that could incorporate spatial sequencing for rockfall events is illustrated in the glacier calving study presented by Chapuis and Tetzlaff (2014), and can be summarised as follows:

i. The relationship between external drivers (e.g. weathering) and internal rock mass properties can be considered at the scale of individual rockfalls;
ii. Connectivity between surface topography and rockfalls can be considered, at a range of spatial resolutions;
iii. Failures are considered as part of a continuous process, not just an isolated event, and can be observed at a range of spatial scales.

2.4.3 Modelling Objective 3: The model should be dynamic through time and operate across a range of temporal scales

As demonstrated through the review of fracture mechanics (section 2.1.4) and the concept of damage in a rock slope, it is clear that failure within a rock mass can be considered, at least in part, a time-dependent process. Damage accumulates up to a critical point, beyond which the mass due to fail becomes unstable and accelerates to failure in a time dependent manner independent of external forcing, characterised by a linear trend in Λ–t space (Petley *et al.*, 2005). A model which is dynamic through time such that rock strength is not fixed, allows simulation of a time-dependent weakening of the rock mass, as suggested by Hergarten (2003). Furthermore, a model dynamic through time would allow model stages to be temporally constrained and the relative time scales of different driving processes to be observed. Additionally, the model should be able to simulate both longer term change as well as instantaneous rockfall. The temporal resolution of any model with this aim should be high enough to simulate sequencing of individual failures through time that build into a larger contiguous failure.

2.4.4 Modelling Objective 4: Modelling an evolving process, allowing stress to transfer and damage to accumulate

The process of post-failure stress redistribution through a rock mass is particularly important for understanding how rockfalls evolve. The impact of a rockfall on the wider slope is dependent on how efficiently, both in space and through time, this process occurs. The redistribution of stress can promote damage and weaken zones neighbouring previous rockfalls, as characterised by the increased presence of micro cracks in the surrounding

material, if the material is critically stressed (Brain *et al.*, 2014). For example, in their analysis of the 2009-'10 Rhombus Wall rockfalls (Yosemite National Park, CA), Stock *et al.* (2012) explore that how this process plays an important role in determining subsequent rockfall activity. Despite a recognised importance of rock mass connectivity, defined here as the ability for stress to transfer within the rock mass, for determining overall rock slope stability, most rock slope models don't operate at a resolution to allow stress transfer to trigger further failures. Without sufficient detail of the rock mass structure, surface topography and fracturing at the slope surface, stress transfer is unable to drive small scale failures as observed in the field (Fig. 2.5). Therefore stress transfer at the scale of small failures should form a crucial component of a new approach to rockfall modelling, meaning that rockfalls are modelled as a part of an evolving process, not just a series of isolated events. Further to this the interaction of stress with structure and slope morphology is shown to be a governing process at the scale of individual failures (Martel, 2006), and therefore also should be considered as a factor in how stress transfers and failures evolve.

2.5 Summary

The critique and synthesis of the literature presented has outlined advances in understanding and characterising rockfall that has been achieved through the development of numerical models and specifically the consideration of various manifestations of time-dependent weakening prior to rockfall. On the basis of the literature presented, the following research areas and key questions have been developed. By achieving the research objectives outlined in Chapter 1, our understanding of each of these areas below should be improved and the questions presented should be addressed:

1. Research on process zones and evidence of propagation suggests that stress redistribution, often resulting in time-dependent crack propagation, may be driving the progressive sequencing of contiguous rockfalls. This internal mechanism operates alongside external environmental forcing such as rainfall to drive rockfall failure. Conceptual models of the relationship between environmental forcing, rock mass damage and rockfall events (Fig. 2.4) suggest that the timing of rockfall events may be determined by the accumulation of damage rather than the timing of environmental events. Together internal and external processes contribute to the time-dependent accumulation of damage in the rock, that has some merits in explaining the variability in both observation and model outputs, where other approaches fall short. If the

conceptual models of the relationship between environmental forcing, rock mass damage and rockfall events are correct, this research seeks to address the competition between external and internal processes acting on the rock mass and how this impacts on rockfalls.

2. Monitoring cliff erosion from a 2.5D or fully 3D slope face perspective has generated observations of the spatial and temporal sequencing of rockfalls across the cliff surface (Rosser *et al.*, 2007a; Lim *et al.*, 2010; Abellán *et al.*, 2010). This raises questions about the dominant drivers of cliff erosion, which in part challenge previous notions of how (coastal) rock cliffs fail (Sunamura, 1982). This questions the role of the enhanced weathering at the base of coastal cliffs (Emery and Kuhn, 1982), through for example basal sapping, or enhanced weathering at the base of cliffs undercut by fluvial processes, knickpoints or uplift, and the resulting cantilever failure of material above. If established models of cliff erosion are not representative of field observations then this questions whether zones of enhanced weathering always create a notch, especially in environments where small rockfalls dominate cliff behaviour through processes of progressive failure. In cliffs where a notch is present, these observations of rockfalls initiating and sequencing across the cliff face, questions whether the notch dominates overall cliff behaviour, with regards to rockfall occurrence and spatially averaged erosion?

3. The occurrence of rockfalls is partly structurally controlled by rock mass strength and the presence of discontinuities (section 2.1). As demonstrated by the literature discussed, rockfalls can be observed as an evolving process, postulated to be driven by the redistribution of stress and their subsequent propagation across the rock slope surface. It remains unclear how this propagation of rockfalls is influenced by different rock types of different structure, and how this is reflected in the nature of rockfalls generated. In a rock slope where bands of rock with different strength and structural properties are interbedded, how does this change the behaviour of propagating rockfalls, and how does this impact more generally on the nature of rockfalls generated and the overall slope evolution?

4. Statistical analysis of rockfalls and monitoring of cliff erosion is vital for understanding rock slope failures and rockfalls as a hazard. Statistical distributions of rockfall magnitude and frequency are used to predict the likelihood of future rockfall occurrence. However, the size distribution generated can only be used for hazard

assessment on the assumption that the distribution is fixed through time (Dussauge *et al.*, 2003). As we seek to understand how rock slopes will respond under the predicted changing climate (Murphy *et al.,* 2009) it is important to establish whether rock slopes behave in a deterministic way and if so, what temporal and spatial extent of data is required to understand future patterns of change?

3 Rockfall occurrence on hard rock cliffs

The time-dependent process of rockfall propagation is observed in hard rock cliffs (Oppikofer *et al.,* 2008; Abellán *et al.,* 2010; Stock *et al.,* 2012; Rosser *et al.,* 2013) and appears to be an important driver for rock slope evolution. However observations of time-dependent rockfall propagation are limited and often only span short time periods and cover a limited spatial extent (Abellán *et al.,* 2010; Stock *et al.,* 2012). As a result the conditions where time-dependent rockfall propagation drives overall slope failure remain poorly understood.

By assessing the spatial and temporal distribution of rockfalls in hard rock cliffs, patterns of behaviour that characterise rockfall evolution can be identified. Crucially this allows empirical relationships to be established, which is important for accurate assessment of the mechanisms driving rock slope failure at the appropriate spatial and temporal scale. Linking the established empirical relationships to the structure and morphology of the cliff could begin to address the underlying mechanics of propagating rockfalls, such as identifying any preferential direction in rockfall scar growth.

In order to explore the spatial and temporal distribution of rockfall in hard rock cliffs, a high resolution monitoring dataset is required from an actively failing rock slope. Terrestrial laser scanning (TLS) provides an accurate way of capturing a high resolution 3D rockfall inventory, effectively characterising and monitoring rock slopes (Abellán *et al.,* 2014). Adopted in a wide range of monitoring studies, as discussed in Abellán *et al.* (2014), repeated data collection over time is capable of providing accurate quantification of rockfall rates across a rock slope. In this chapter, TLS is used to monitor cliff face erosion at a range of sites along an actively failing coastline in North Yorkshire (UK). Previous studies at this site have identified rockfall activity distributed across the entire cliff face (Lim *et al.,* 2010), propagation of rockfall over time (Rosser et al., 2013) and pre-cursory behaviour (Rosser *et al.,* 2007a), making this an ideal study site for this research.

The data presented in this chapter are used to examine the notion that rockfalls evolve as a result of progressive failure and internally driven failure propagation. This is achieved by addressing the following questions:

- Is there a temporal pattern to rockfall behaviour, observable at different spatial scales, which displays variability beyond rock mass strength and environmental conditions?
- Can a relationship be identified between slope morphology and the distribution and geometry of rockfalls?

- Over what scales do rockfalls show significant clustering?
- Is rockfall scar growth random or directional?

To answer these questions, this chapter analyses high resolution field monitoring data to identify spatial and temporal relationships in the observed behaviour, importantly providing information on the scales at which these findings are valid and thereby addressing the first research objective for this study.

3.1 Field Site: North Yorkshire, UK

The North Yorkshire coastline from Staithes to Boubly comprises a 2.5 km stretch of Jurassic, hard rock cliffs (Fig. 3.1). These are some of the highest, near-vertical cliffs on the east coast of the UK, reaching up to 90 m in places. Their northerly aspect exposes them to the waves of the North Sea, generating an actively eroding environment. The waves and high tidal range (approximately 6 m) submerges the shore platform along this stretch of coastline, preventing any long-term accumulation of rockfall debris at the base of the cliffs. Composed of predominantly clastic, sedimentary rocks, the near-horizontal bedded geological layers (mudstone overlain by shale, ironstone, siltstone and sandstone, see Figure 3.2) are easily distinguishable and are generally free from vegetation cover, allowing direct observation of the surface. The rocks are capped with up to 10 m of glacial till and dip shallowly (ca. 2°) to the east (Rawson and Wright, 2000).

This section of coastline retreats relatively slowly: a seven year monitoring study by Rosser *et al.* (2013) observed a mean retreat rate of 0.027 m yr^{-1} across seven sites along this coastline, notably lower than the rate of 0.05 m yr^{-1} established from the analysis of historic maps since 1856 (Agar, 1960). A number of previous studies into erosion along this coastline, as discussed in Chapter 2, have shown that erosion is driven by rockfalls that initiate across the entire cliff face (Rosser *et al.,* 2007a, Lim *et al.,* 2010), challenging the established conceptual model of coastal cliff erosion driven by the development of a wave-cut notch at the toe and subsequent cantilever failure of the material above (Sunamura, 1992).

This site was chosen to provide monitoring data for this project as it is actively failing, which allowed changes to be observed during the two years of monitoring. The exposure of the cliffs allows direct observation of the surface without obscuration by scree deposits, weathering crusts or vegetation growth. The coastline is a dynamic environment comprising both marine and terrestrial weathering zones and varied weather conditions throughout the year (Vann

Jones *et al.,* 2015). This allowed observation of rockfall behaviour through the full range of seasons. The headland-bay morphology along the coastline means that different sections of the cliffs have a different exposure and different slope morphology, allowing comparison of rockfall behaviour in these different morphological settings. Additionally, the heterogeneous lithology of the cliffs produces differing rockfall characteristics in the different lithological layers. Uniquely, a history of monitoring exists at this site and so previous data was available, as indicated in the references given in the introduction to this chapter. This also means that the site was accessible for regular monitoring and an established technique for data collection was already in place. The opportunity to monitor the site at a high spatial and temporal resolution was essential for providing observation of the spatial and temporal patterns of rockfall, and the associated structural and morphological characteristics of the cliff.

Figure 3.1: (left) Field site location on North Yorkshire coast. (right) Photograph of the cliffs at low tide.

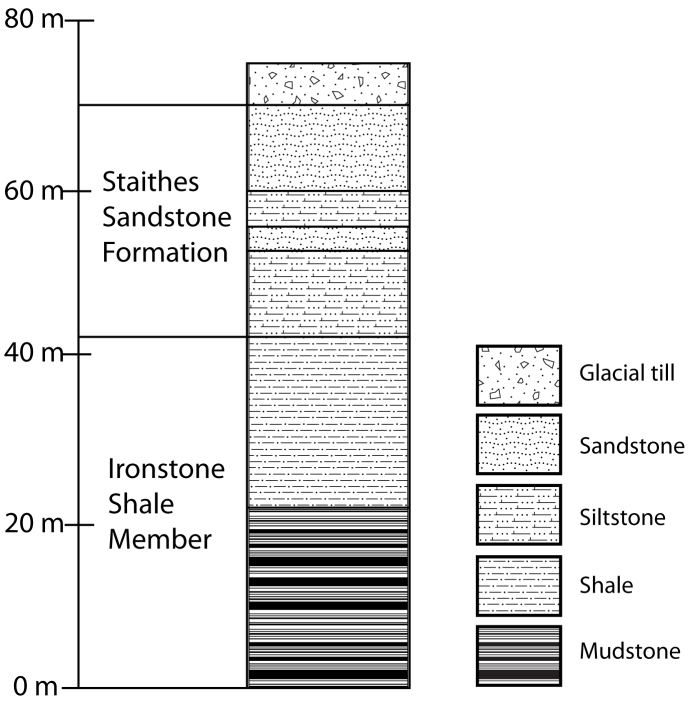

Figure 3.2: Geological section of the cliff exposure at the field site, showing height above ordnance datum.

3.1.1 Site descriptions

Four sites along this stretch of coastline were chosen to be investigated. These were selected as they provided a range of different exposures to the sea and different cliff face morphologies, whilst all are composed of the same geological layers. An aerial view of the TLS point cloud data, with an image for comparison, shows the location of the four sites in Figure 3.3; Figure 3.4 shows images of each site with corresponding geologic sections. From the images in Figure 3.4 the more resistant mudstone at the cliff toe and sandstone and siltstones towards the cliff top can be observed. At all sites the surfaces of the cliffs are heavily weathered: located within the tidal zone, the mudstone is typically smoother than the other layers of rock; the surface of the shale is rough, owing to an almost constant removal of small fragments from the cliff face and occasional larger failures; and the blockier siltstone and sandstone reflects the larger, joint controlled rockfall that occurs in this zone. Brief descriptions of the key features of each field site are given below:

- *Boulby* is a 300 m wide north-northeast facing stretch of coastline, with an average cliff height of 60 m (excluding glacial till). The mudstone layer at the base of the cliff ranges from 16-18 m thick, overlain by 20 m of shale and 22 m of interbedded siltstone and sandstone (Fig. 3.4a).

- *Site 3 – Section 1 (hereafter referred to as Section 1)* is a north facing bay, 130 m in width, with an average cliff height of 37 m (excluding glacial till). It is slightly sheltered by two headlands. The mudstone layer at the base of the cliff averages 4.5 m thickness, overlain by 16.5 m of shale, 15.5 m of siltstone and 1.5 m of sandstone (Fig. 3.4b).
- *Site 3 – Section 2 (hereafter referred to as Section 2)* is an 85 m wide, curved section of coastline on the edge of a bay, with a north-westerly aspect and an average cliff height of 37 m (excluding glacial till). The mudstone layer at the base of the cliff averages 4 m thickness, overlain by 13 m of shale and 20 m of interbedded siltstone and sandstone (Fig. 3.4c).
- *Cowbar* is a 220 m wide north-northwest facing stretch of coastline, with an average cliff height of 33 m (excluding glacial till). The mudstone layer at the base of the cliff averages 5 m thickness, overlain by 17.5 m of shale and 10.5 m of interbedded siltstone and sandstone (Fig. 3.4d).

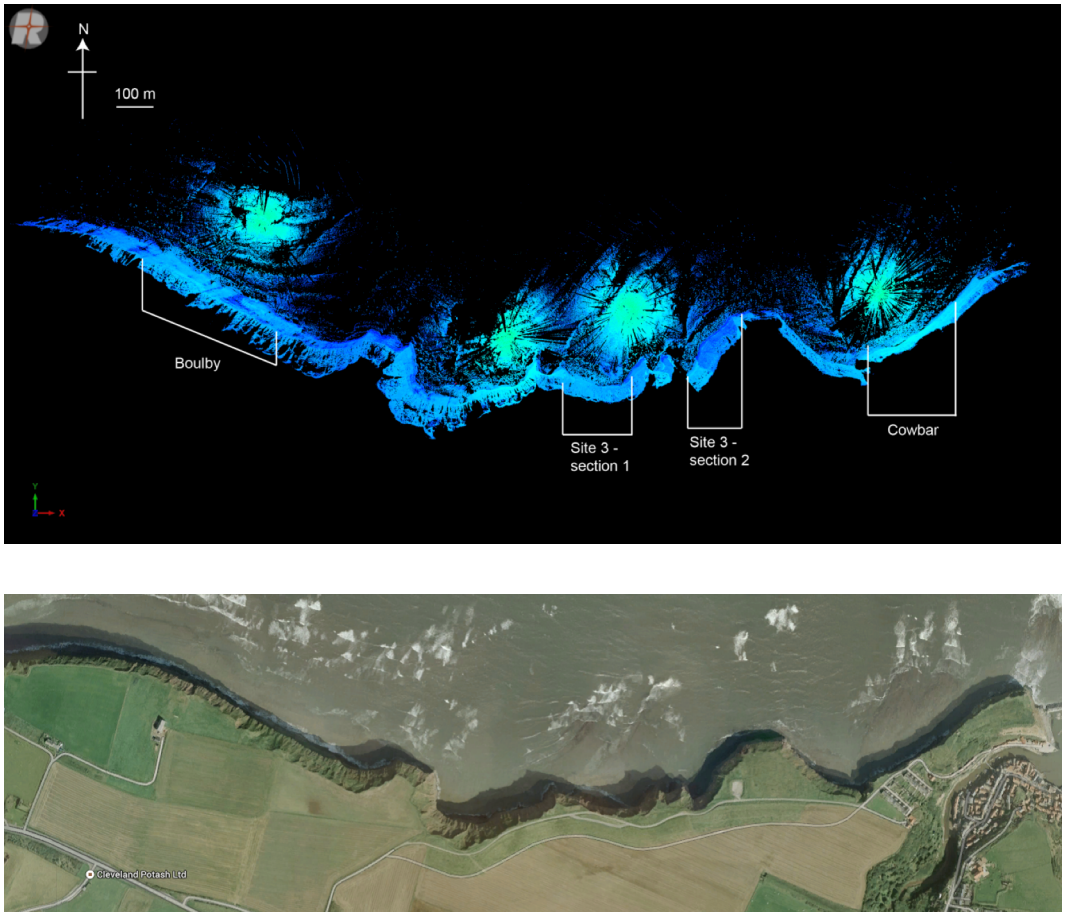

Figure 3.3: (top) Aerial view of the TLS point cloud data showing the four sites used for rockfall analysis. (bottom) Aerial imagery of the area shown above, sourced from *GoogleEarth*.

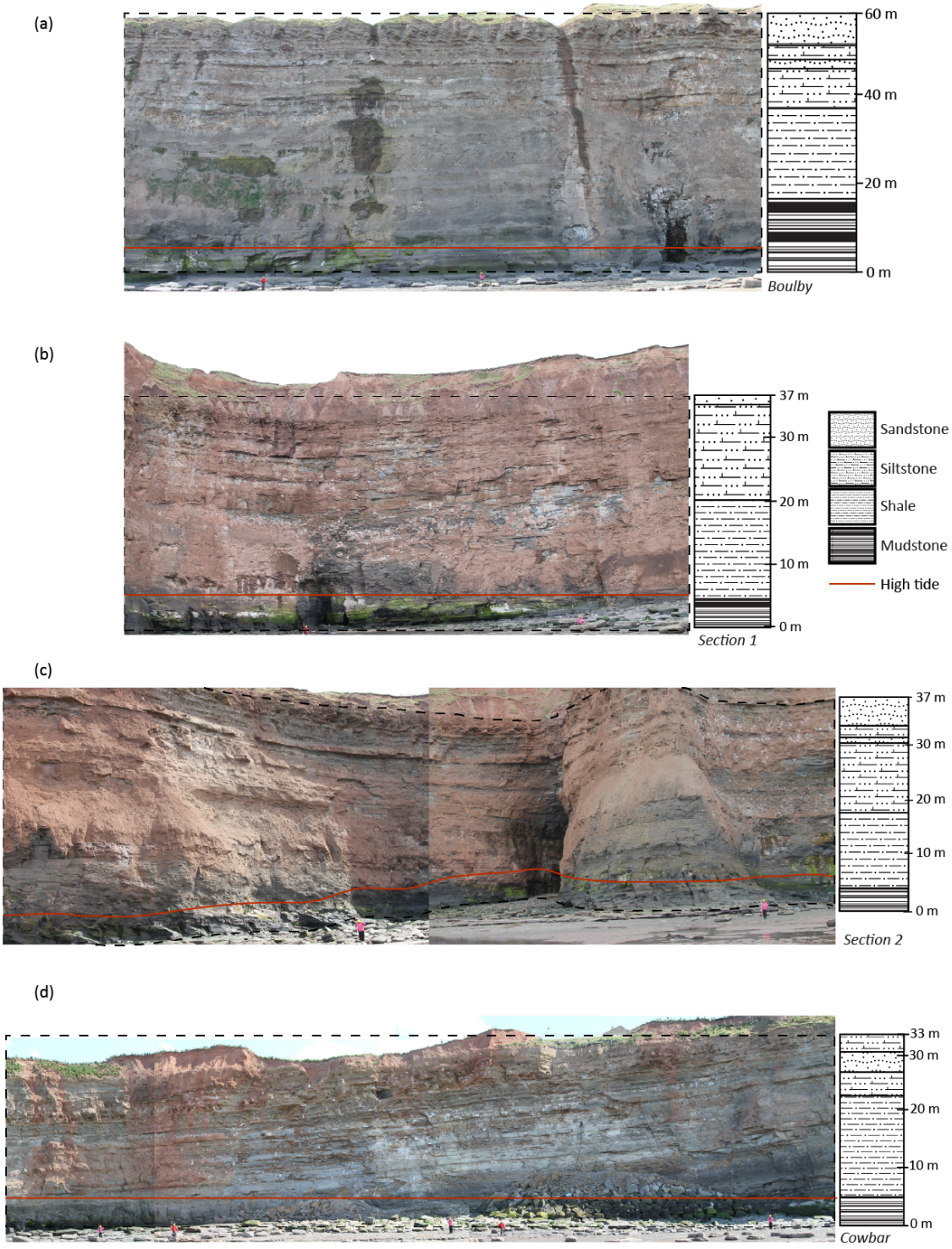

Figure 3.4: Photographs of the cliff sections at each site with corresponding geological sections of the cliff exposure, showing height above ordnance datum. (a) Boulby; (b) Section 1; (c) Section 2; (d) Cowbar.

3.2 Rockfall Inventories

Two rockfall inventories were compiled for this study: a monthly two-year dataset (2012-14) for each of the four field sites shown in Figure 3.4, and a ten-year dataset (2003-13) for Boulby (Fig. 3.4a). Details of the data collection and processing required to generate these datasets are given below.

3.2.1 Data collection

3.2.1.1 Two-year dataset (2012-14)

A RIEGL VZ1000 terrestrial laser scanner (TLS) was used to scan the cliffs every month from June 2012 to June 2014, collecting high resolution point clouds of the cliff surface. The RIEGL VZ1000 TLS has a measurement range of 1,400 m with 5 mm repeatable accuracy, collecting up to 122,000 measurements per second (RIEGL, 2015). The point clouds collected were processed using the DEM of Difference method (Lague *et al.,* 2013) to produce 3D surfaces of the cliff and change detection between them allowed individual rockfalls to be extracted and volumetric changes to be calculated. The timing of scanning each month was dictated by the low tide conditions, as access to the foreshore for 3-4 hours was required to complete the scanning at each site. Table 3.1 shows the date of scan collections and the sites that were scanned each time: any gaps in the data are primarily due to weather conditions, which restricted the availability of scanning time. For each successive scan the TLS was setup at the same, fixed position at each site at a distance of 110 m from the cliff toe, aided by the use of survey nails that are in place along the foreshore platform. Figure 3.5 shows an example of the typical setup. GPS located targets were placed around the scanning area, also in fixed positions, in order to allow a more accurate image registration (explained further below in Section 3.2.2). The TLS calculates the distance (*d*) to the surface using the time-of-flight technique (Abellán *et al.,* 2014), according to the following equation:

$$d = \frac{E_t * c}{2}$$

Equation 3.1

where d = distance, E_t = elapsed time of the laser pulse (return time to the scanner) and c = speed of light. The laser pulse is directed across the entire surface of the cliff area specified, with the spacing at which points are collected specified by the user. At each site in this study, the scanner was setup to produce a point cloud with 0.05 m point spacing, generating a high

resolution point cloud in which the 3D coordinates of each point are specified. The accuracy of the TLS data is discussed in Section 3.2.2 below.

Table 3.1: Scan collection dates and cumulative day (beginning at 120619, where change detection begins). The scan collected on 120509 provides the previous scan used for change detection on 120619. Cells in the four right hand columns are shaded for sites that were scanned at each date; white cells represent no scan taken. Months where scans were not collected are indicated with an 'X' in the ID column.

Scan date (yymmdd)	ID	Cumulative day	Boulby	Section 1	Section 2	Cowbar
120509	0	-				
120619	1	1				
1207xx	X	X				
120802	2	45				
120830	3	73				
121003	4	107				
121115	5	150				
121213	6	178				
130116	7	212				
130211	8	238				
130312	9	267				
130425	10	311				
1305xx	X	X				
130625	11	372				
1307xx	X	X				
130820	12	428				
130917	13	456				
131021	14	490				
131118	15	518				
131203	16	533				
1401xx	X	X				
140218	17	610				
140318	18	638				
140416	19	667				
140514	20	695				
140618	21	730				

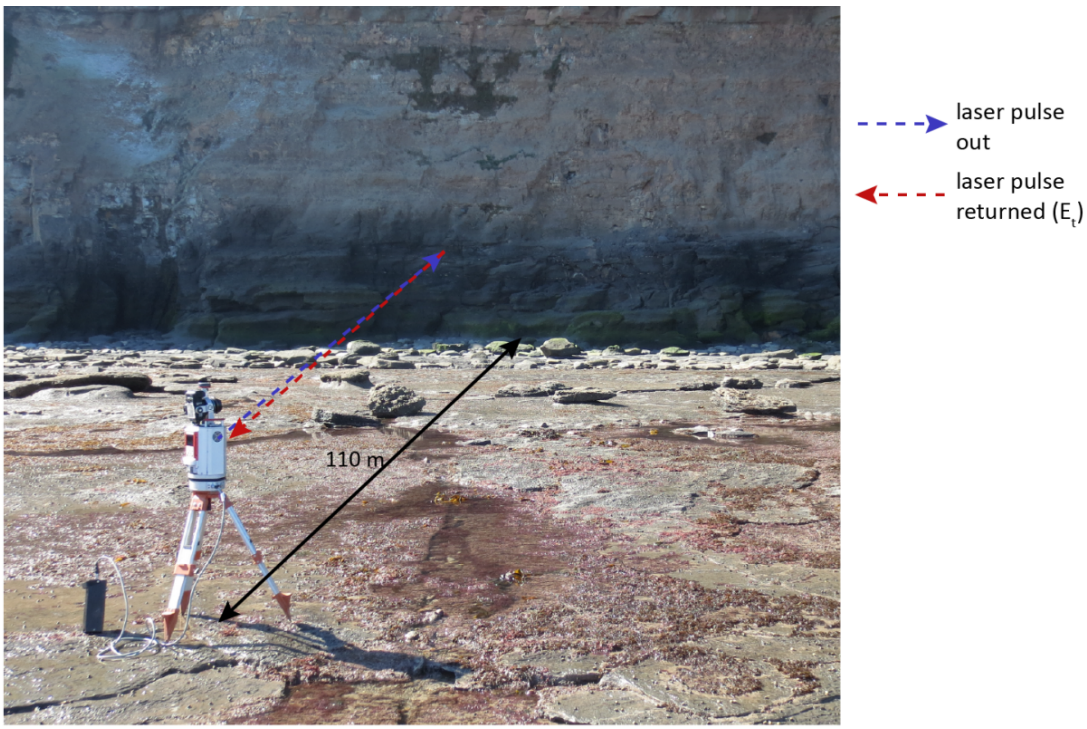

Figure 3.5: Setup of the RIEGL VZ1000 terrestrial laser scanner at Boulby. The scanner is centred above a permanent survey nail in the foreshore platform. The distance from the scanner to the surface of the cliff is calculated at a point spacing of 0.05 m, based on the elapsed time (E_t) of the laser pulse sent out from the scanner (red and blue arrows on the image).

3.2.1.2 Ten-year dataset (2003-13)

Owing to the range of previous studies along this coastline, notably the long-term monitoring studies from Rosser *et al.* (2007a), Lim *et al.* (2010) and Vann Jones *et al.* (2015), a large database of historic scans and inventory data was available for the Boulby site. Prior to 2010 these scans had been collected using a Trimble GS200 TLS and a MDL LaserAce 600 scanner. The point cloud spacing varied between different projects but in all cases was coarser than the two years of data collected as part of this study. Additionally, the time between scans varied dependent on the focus of previous studies, and therefore a separate inventory was generated with this data in order to show annual rather than monthly erosion. The data collected from 2003-10 had already been processed and rockfall inventories generated. These inventories were aligned in ArcMap in order that the rockfall data from each year could be compared. Scans collected as part of the two-year dataset provided the data from 2012-13, to extend this to a decadal dataset. Those scans were processed according to the method below before being added to this dataset. It should be noted that there is a gap in the dataset from 2010 – 2012.

3.2.2 Data processing

Point clouds collected with the TLS were processed according to the commonly used *DEM of Difference* method for point cloud comparison when the large scale geometry is planar (Lague *et al.,* 2013). The software packages and specific methods of processing used in this study had been well established for use at this field site (Rosser *et al.,* 2005, Lim *et al.,* 2009, Norman, 2012) in order to generate polygons of individual rockfalls from the raw point cloud data from which volumes are derived. An overview of the TLS data processing workflow is shown in Figure 3.6, and can be split into three stages:

- *RiScan Pro*

The point clouds are imported into *RiScan Pro*, the accompanying software for the TLS system. Each point cloud is cleaned up to remove vegetation and flying birds, and then trimmed to the relevant area of interest (AOI), defined for each site. The GPS located targets are highly reflective, making them easily detectable within the image. These are used to perform a coarse registration of the point clouds so that each can be aligned with previous and sequential scan images.

Within *RiScan Pro*, projects are created for each field site. Within each project the point cloud of the first scan, captured on 09-05-2012 is used as the 'base scan'. The scan is transformed so that it is oriented normal to the positive Z direction of the scanner, with Y vertical and X horizontal distances across the cliff face (Fig. 3.7). Each of the point clouds are then aligned to the base scan computationally using a multistation adjustment, which allows overlapping scans to be registered quickly together. A plane patch filter is used, where patches are created from the point cloud (from a user-specified number of points) and the scans are aligned by matching patches within a given search radius, producing a standard deviation in error between the two point clouds (Table 3.2 lists the values used for the settings in this process). This was performed repeatedly, reducing the search radius until a standard deviation in error ≤ 0.02 m was produced. The total area of the surface of the cliff scanned is large compared to the areas that have changed between scans, meaning that the areas of surface change do not significantly alter the alignment of sequential scans. Furthermore, aligning each sequential image to the base scan in this way avoids cumulative alignment errors that would arise through matching sequential scans and helps to avoid any errors resulting from variations in the positioning and orientation of

the scanner during data collection (Lim *et al.,* 2005). Once aligned, the point clouds were exported as ASCII files (X, Y, Z coordinates) and imported into *ENVI* imaging software.

- *ENVI*

In *ENVI* the point clouds were rasterised to grids with 0.05 m spatial resolution. In order to align the pixels, the grids were stacked and raster math used to calculate the change between successive DEMs: *difference = old – new,* such that negative change indicates erosion. The *DEM of Difference* was exported from *ENVI* and imported into GIS software *ArcMap*. In addition, the slope and aspect of each DEM pixel was generated and exported as topographic images. Figure 3.8 shows an example of the DEM generated from this data.

- *ArcMap*

Both the difference and topographic images were imported into *ArcMap* and clipped to the area of interest (AOI) for the field site, removing the till on top of the cliff and the boulders at the base. Figure 3.9a shows an example of the difference image for Boulby, where red indicates a negative difference (erosion) and blue indicates a positive difference (deposition). Areas of erosion are often located on protruding areas of the cliff face, and areas of deposition are often seen along ledges in the mudstone towards the cliff toe, and the sandstone towards the cliff top.

The original data was collected at a point spacing of 0.05 m and so the confidence level for significant change in the difference image was set to difference values ≥ 0.1 m (Lim *et al.,* 2009). In order to separate the significant change from the noise in the difference image the 'Raster Calculator' was used to remove any areas with a difference < 0.1 m. From the resulting raster, any areas of positive change (deposition) were removed, leaving only areas of erosion ≥ 0.1 m. This raster was then converted to polygons, which are shown in Figure 3.9b. The rockfall polygons show areas of erosion for each month of data collection and were used in a variety of spatial and temporal analyses as described in *Section 3.3: Spatial and Temporal Analysis*.

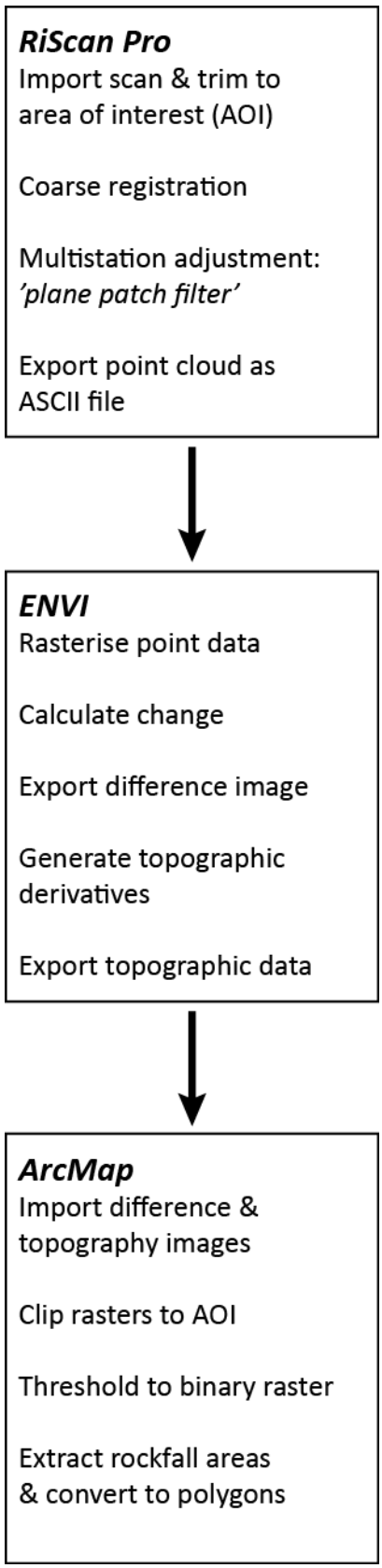

Figure 3.6: TLS data processing workflow

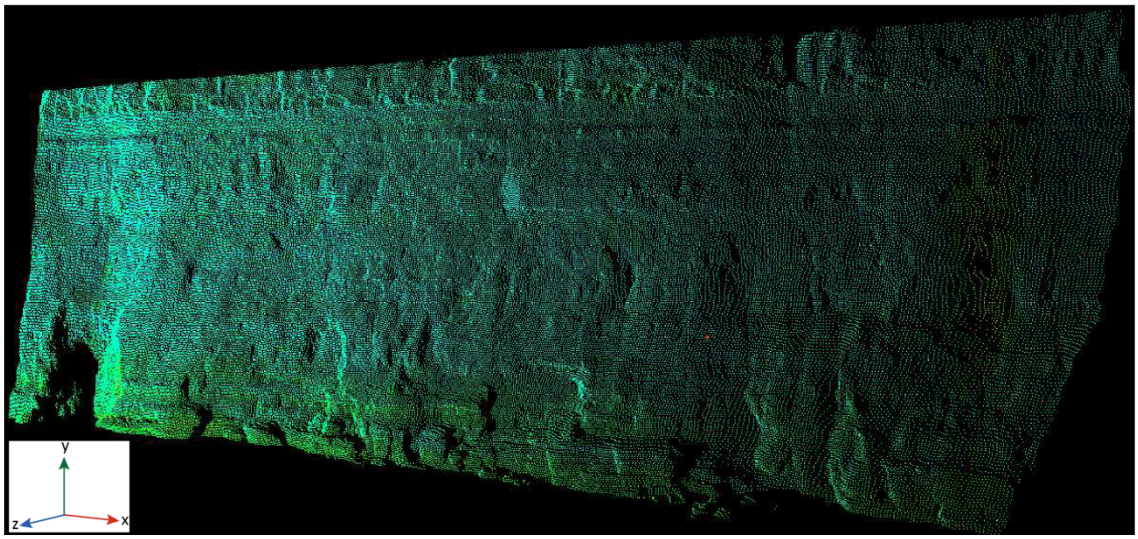

Figure 3.7: Point cloud registration: An example of a point cloud in RiScan Pro, coloured by surface reflectance, which has been registered and transformed so that the cliff surface aligns normal to the positive Z axis of the scanner, allowing the data to be easily projected in the plane [x, y].

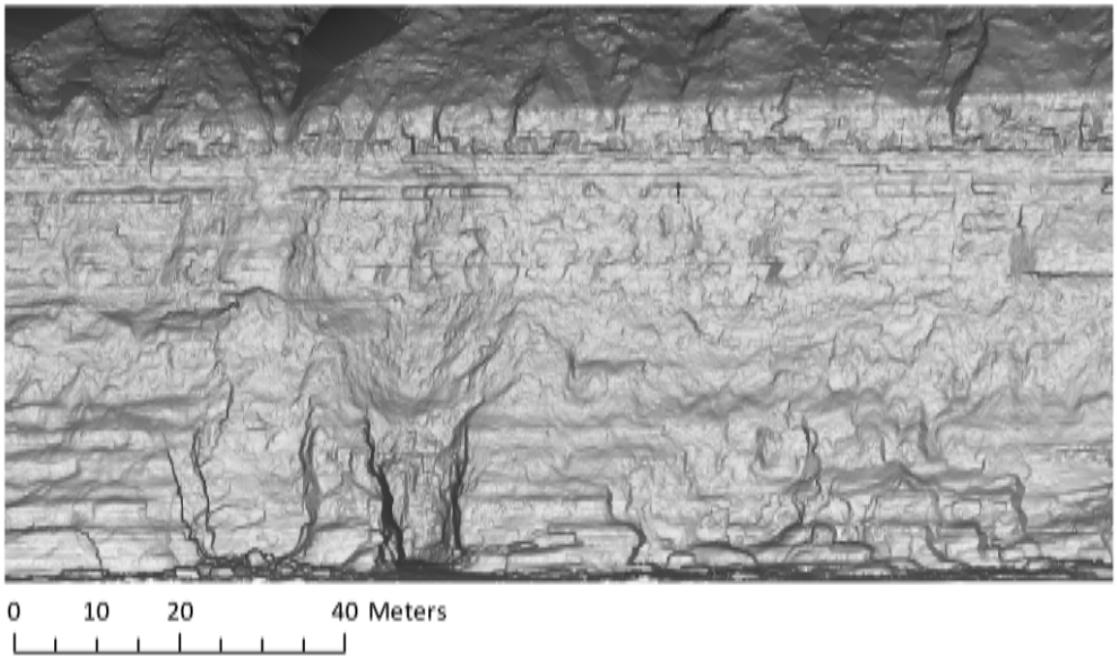

Figure 3.8: Digital Elevation Model (DEM) generated from the point cloud data at Boulby, shown by a hillshade image. The glacial till at the top of the cliff (darker grey) and boulders at the cliff toe are removed and not included in the rockfall calculations.

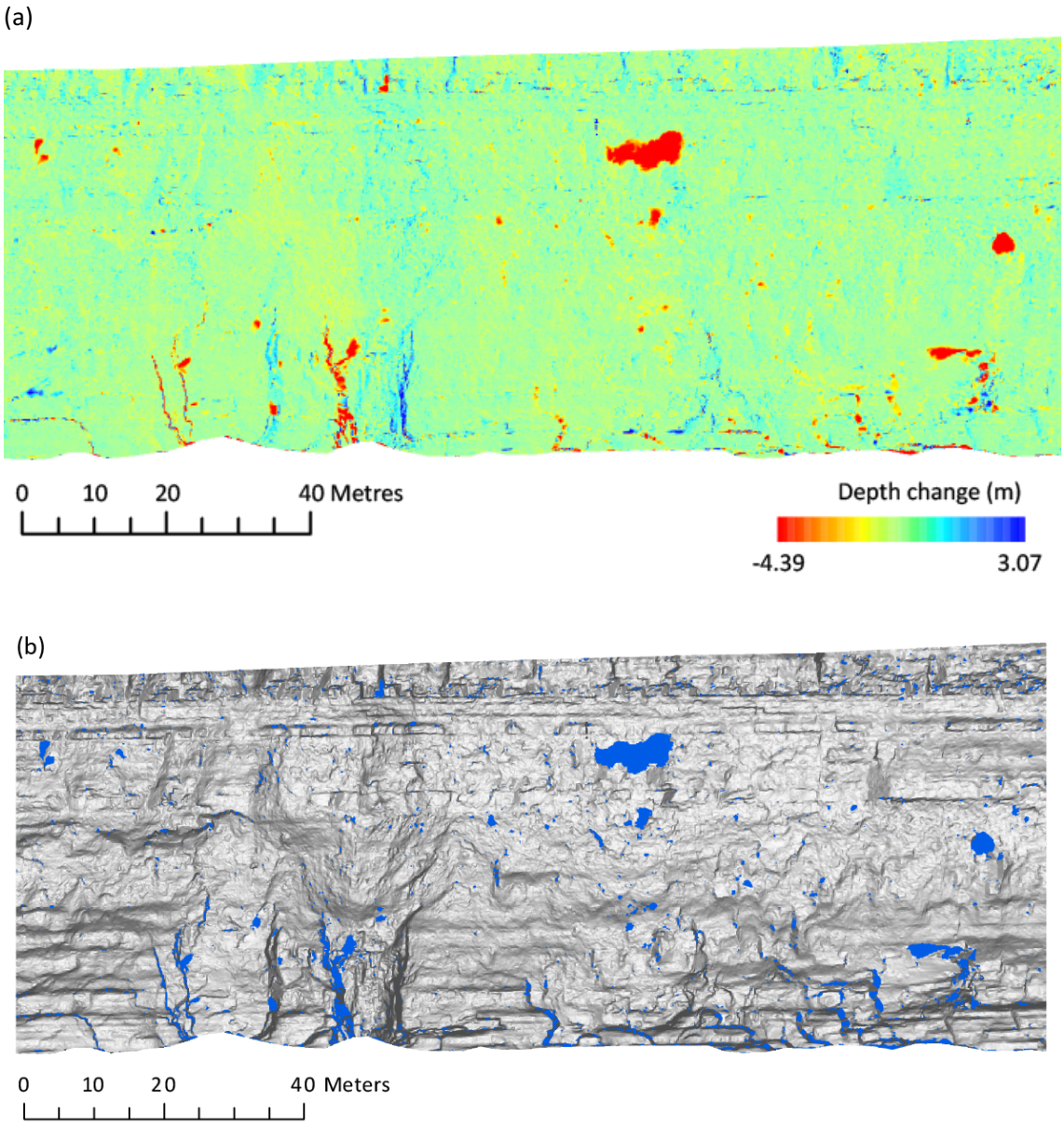

Figure 3.9: Generating rockfall polygons in ArcMap: (a) An example of the difference image exported from ENVI for the change calculated between 09-05-2012 and 19-06-2012 at Boulby. Red indicates negative change, i.e. areas of erosion, and blue indicates positive change, i.e. areas of deposition, as seen on the ledges near the top and toe of the cliff; (b) An example of the rockfall polygons (blue) generated for the same time period, often located on protrusions on the cliff surface.

Table 3.2: Values for different parameters used during TLS data processing.

Software	Tool	Parameter	Value
RiScan Pro	Multistation adjustment: plane patch settings	Maximum error (m)	0.15
		Points per plane	10
		Min/max search cube (m^3)	0.256/2.048
	Multistation adjustment: performance settings	Search radius: starting value (m)	2
		Maximum tilt (°)	15
		Minimum change of error (1): starting value (m)	10
		Minimum change of error (2): starting value (m)	1
		Outlier threshold	2
		Accepted standard deviation in error (m)	0.02 (from > 800 points)
ENVI	Rasterise point data	Spatial resolution (m)	0.05
	Topographic modelling	Sun elevation (m)	500
		Incidence angle (°)	45
ArcMap	Raster calculator	Significant change threshold (m)	0.1

3.2.2.1 Quantifying uncertainty

It is recognised that a number of factors can influence the accuracy of the generated surfaces that represent the cliff face, both in data collection and data processing. In a review of TLS for rock slope instabilities, Abellán *et al.* (2014) identify the main influencing factors during data collection as accuracy, resolution, range and survey set-up. The accuracy of the measurement can be influenced by the characteristics of the cliff surface, e.g. the roughness and wetness of the cliff face (Lim *et al.,* 2005, Sturzenegger *et al.,* 2007). Additionally, occlusion caused by uneven surfaces, large boulders and a high incidence angle of the scanner, can cause gaps in the point cloud, resulting in subsequent error in the distance measurements obtained (Lague *et al.,* 2013). The resolution of the data is defined by the point spacing, which can vary both with the quality of the scanner and the distance between the scanner and the target (Abellán *et al.,* 2014). As established techniques develop in the use and application of TLS, it is important to focus on the minimisation, identification and removal of errors (Lim *et al.,* 2009). This study adopted a well-established approach to data collection as described by Rosser *et al.* (2005), Lim *et al.* (2009) and Norman (2012) ensuring that any potential sources of error were minimised where possible. The surface characteristics of the cliff and the weather conditions that may affect the laser beam reflectance are unavoidable, although these effects are widely acknowledged to be negligible at this scale. However, the scanner location relative to the cliff (range) and the width of the scan were selected in order to minimise incidence angles and potential for occlusion. Abellán *et al.* (2014) suggest that the maximum range achievable on

natural rock slopes is approximately half of that suggested by the manufacturer: in this case the distance between the scanner and the cliff was kept significantly below the maximum 1,400 m range of the scanner, as suggested by RIEGL. The survey set-up included the use of GNSS targets, which ensured that scans were able to be aligned accurately. The root mean square (rms) separation between surfaces was lower than the point spacing (i.e. < 0.05 m) and therefore considered acceptable.

During data processing there is the potential for error in both the scan alignment and the subsequent change detection performed. As mentioned above, the alignment accuracy was improved by the use of GPS targets within the scans. Furthermore, the multistation adjustment used to match subsequent scans was performed until the standard deviation of error was ≤ 0.02 m.

As the change detection between successive scans was performed using an automated method (Figs 3.6 – 3.9), it was important to assess any potential uncertainty at this stage. Although the alignment precision may be within an acceptable degree of accuracy, Stock *et al.* (2011) highlight the additional uncertainty in the volumetric change that can arise from the interpolation methods used. They address this uncertainty by calculating the volumetric change for areas of the cliff face that, from high resolution photography, are known not to have experienced any rockfalls during the period of monitoring. Adopting this methodology, two cliff sections along the coastline were selected for examination: a flat stretch of coastline where the scanner is oriented normal to the surface (Fig. 3.10a); and a bay area of the coastline whereby the scanner is at an oblique angle to the surface (Fig. 3.10b). For both cliff sections, two photographs were taken a month apart, coinciding with scanning times. From these photographs, areas of the cliff where no change had occurred were identified: these areas (AOIs) can be seen as numbered red circles on the images in Figure 3.10 and have a diameter equivalent to the larger rockfalls detected at these sites. Using the results of the change detection analysis, the depth of change for each of these AOIs was calculated. For section A – the flat stretch of coastline –no change was incorrectly identified by the change detection in any of the six AOIs. Conversely in section B – the bay area of coastline – some error in the calculated depth of change was calculated, ranging from -0.015 m (AOI 4) to 0.098 m (AOI 1): in AOI 1 and 2 erosion of material (positive depth of change) is identified, whilst accretion of material (negative depth of change) is identified in AOI 3 and 4. It is likely that the error is highlighting the effect of the oblique angle of the scanner with respect to the cliff surface, which results in a lack of points within those areas. Subsequently the interpolation of the points to generate rasters results in error that propagates through to the final depth change calculated. However, the inaccurately calculated depth of change in all four areas is

smaller than the lower threshold set for rockfall depth (0.1 m) in the third stage of data processing (Figure 3.6 - *ArcMap*). Therefore, this is not considered to be a significant source of uncertainty in the method and the results for depth of change in this study are considered acceptable.

[a]

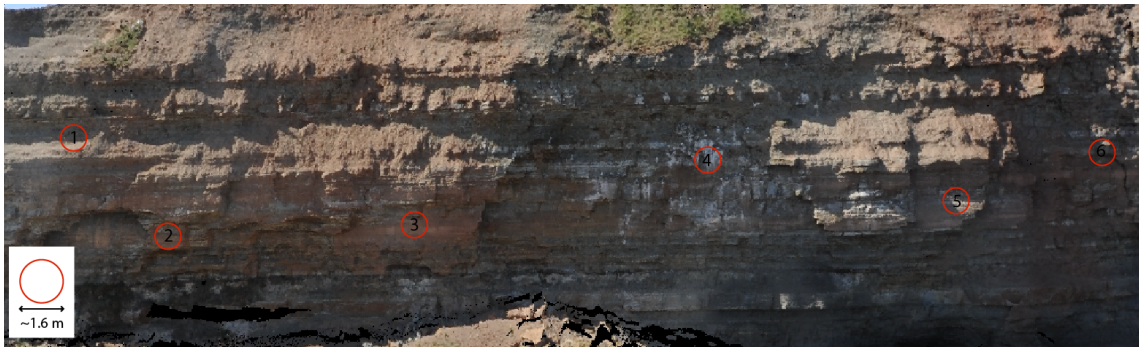

[b]

Figure 3.10: Images of the cliff sections (photographs draped over the point cloud in RiSCAN) used for uncertainty analysis: (a) flat section; (b) bay area. The numbers in red circles correspond to areas where depth change was measured – results are given in Table 3.3.

3.3 Spatial and temporal analysis

To identify the patterns within the rockfall inventory rockfall polygons were analysed to examine both spatial relationships between rockfalls, and the relationship between rockfalls and cliff characteristics. Most of the analysis was conducted using GIS, and is described in Section 3.3.1 below. Analysis of the clustering of rockfalls was executed manually and is described separately in Section 3.3.2.

3.3.1 Arc model builder

Within the GIS platform ArcMap, a workflow was created to efficiently run a series of analysis procedures on all of the data. Figure 3.11 illustrates the workflow where the blue rectangles show the analysis functions used for the five types of analysis performed. The workflow was run in two stages, as indicated on Figure 3.11, and each of the processes of analysis are described in detail below.

Rockfall polygons generated from each monthly scan at each site, are considered to be one dataset. Boulby and Cowbar each have twenty datasets, and Section 1 and Section 2 each have nineteen datasets (Table 3.1). The datasets were iteratively run through the workflow so that results were obtained for each site and each month (Section 3.4).

Figure 3.11: Workflow used for data analysis of the two year dataset: Red = inputs; Blue = Functions; Green = outputs.

3.3.1.1 Failure proximity and rock type

As can be seen in Figure 3.11, the first stage of the analysis examined the relationship between the rockfall polygons in one dataset and the nearest rockfall polygons in the preceding dataset. This first stage of analysis also determined the relationship between the rockfall polygons and the cliff lithology, represented by geological layers within the GIS database. The methods of analysis used are described below, with reference to the tools given in Figure 3.11.

The distance and direction was measured from the perimeter of each rockfall in 'dataset 2' to the perimeter of the nearest rockfall in 'dataset 1' (Fig. 3.12), where datasets 1 and 2 are from sequential scans and dataset 2 is the most recent. To explore the influence of rockfall size on failure proximity from one dataset to another, the analysis was run using subsets of the rockfalls in dataset 2, which were grouped by rockfall area.

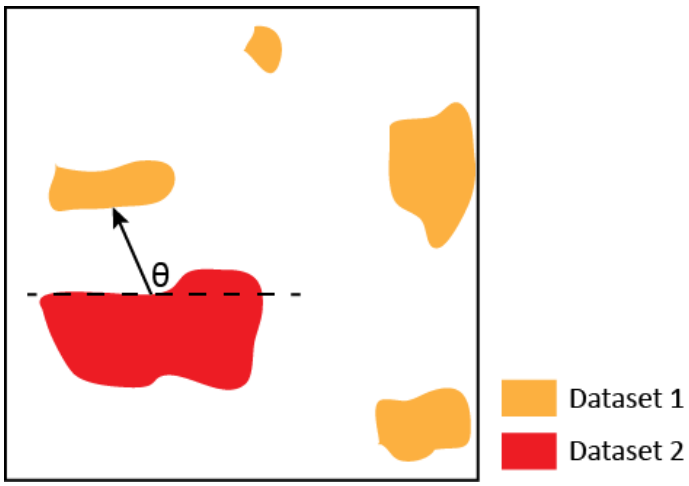

Figure 3.12: Calculating the distance and direction from rockfalls in dataset 2 to nearest rockfalls in dataset 1. The direction is measured from the horizontal plane (dashed line) of the rockfall in dataset 2 anticlockwise to the horizontal plane that aligns with the perimeter of the nearest rockfall in dataset 1, as indicated on the diagram by θ.

The rockfall polygons were overlaid on the geological layers and a geometric intersection of both features was computed to determine which geological layer each rockfall had occurred in (Fig. 3.13). The rockfall polygons were then assigned the geological ID of the layer that they overlapped with. If a rockfall overlapped with more than one geological layer then it was assigned the ID of the layer with the most areal overlap.

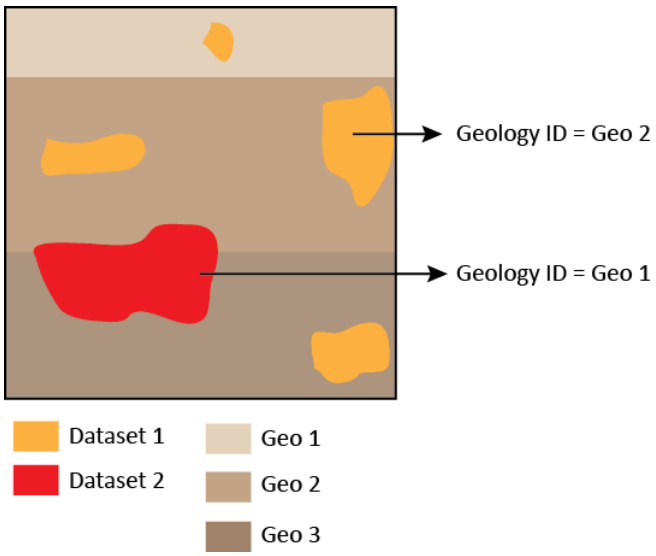

Figure 3.13: An illustration of the geometric intersection computed between the rockfall polygons and geological layers. Where a rockfall covers two geological layers (dataset 2 in the diagram), it is assigned the geological ID of the layer it overlaps most with.

3.3.1.2 Failure geometry and cliff morphology

The second stage of the analysis examined the statistics that describe the geometry of the rockfall polygons and the relationships between rockfalls and slope surface morphology. The methods of analysis used are described below, with reference to the tools described in Figure 3.11.

The mean depth (m) of each rockfall was calculated from the DEM of difference and the volume (m^3) calculated based on the sum of depth values within each rockfall polygon. The area (m^2) and length-to-width ratio of each rockfall polygon was calculated. The minor axis length, major axis length and orientation of the major axis were also computed for each rockfall polygon (Fig. 3.15). Each rockfall polygon was categorised as a geometrical form based on the length-to-width ratio and the orientation of the major axis (Fig. 3.16), in order to explore the different shapes of rockfall scars. The shape of a rockfall is shown to impact on its runout (Glover *et al.,* 2012) and therefore it is useful to establish what characteristics of the slope surface may determine the shape of a rockfall.

Slope surface morphology is defined here as the local curvature of the slope, calculated at the resolution of the slope face DEM (0.025 m^2 grid cell size). The curvature is calculated at the slope face view, rather than the normal plan view used when considering curvature of a landscape. This approach allows the interaction of the local cliff face topography and rockfalls to be explored. For each dataset the standard curvature (profile and planform combined) of

the cliff surface was determined from the DEM associated with the previous scan, allowing the curvature of the pre-failure surface to be identified for each rockfall polygon. The DEM of the cliff face (Fig. 3.8) was used as the surface input and the curvature of each raster grid cell calculated as the second derivative of the local slope, derived from the eight surrounding cells, and output as a curvature raster. The mean value of the curvature raster was taken within each rockfall polygon. Across the cliff surfaces used, curvature values ranged from -0.5 to 0.5, where negative values indicate the surface is concave; positive values indicate the surface is convex and a value of zero indicates that the surface is planar from a slope face perspective (Fig. 3.17).

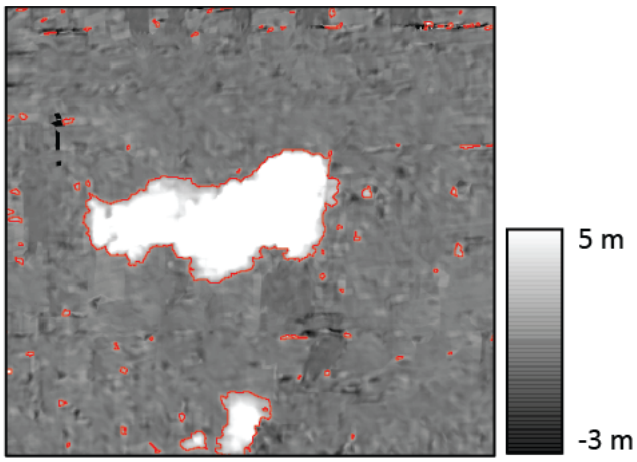

Figure 3.14: Mean depth of each rockfall calculated using the difference raster and rockfall polygons. The mean value of the difference raster is extracted from each zone defined by a rockfall polygon.

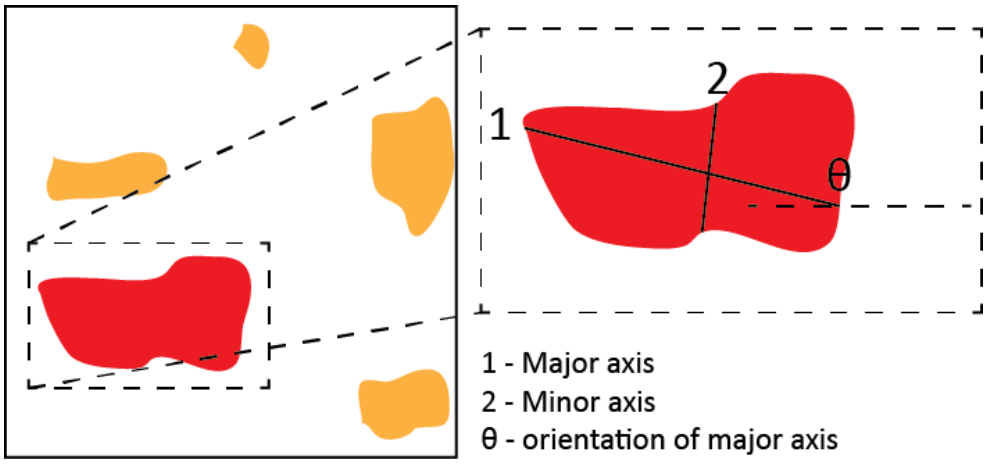

Figure 3.15: The statistics that describe the geometry of each rockfall polygon: The enlarged area shows the major axis (1), minor axis (2) and the orientation (θ) of the rockfall polygon. The orientation is measured from the horizontal plane (dashed line) anticlockwise.

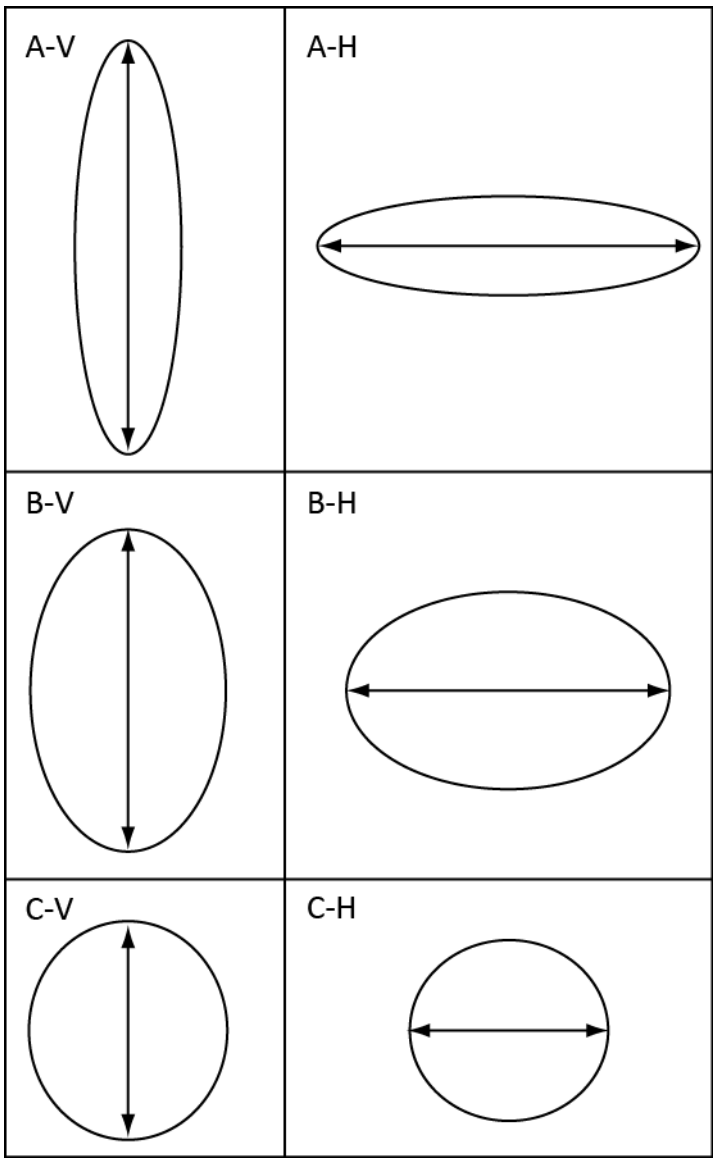

Figure 3.16: Rockfall geometry types identified by the length: width ratio and rockfall orientation (Fig. 3.15). From A to C the shape transforms from an ellipse to a circle; V and H denote a vertical and horizontal major axis respectively. The arrows within each shape represent the major axis.

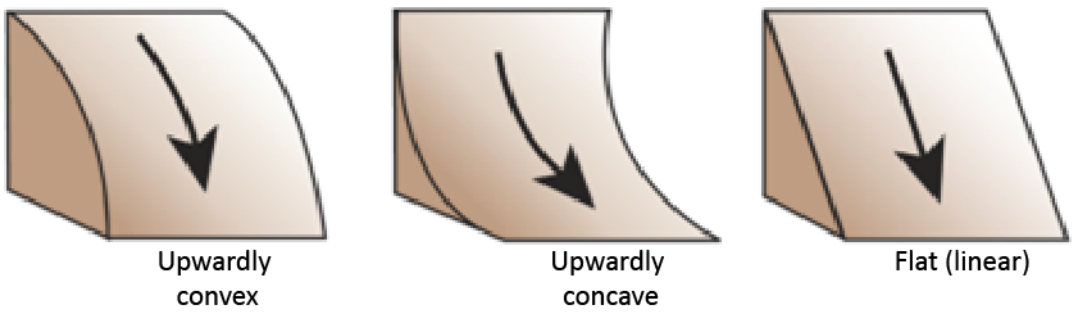

Figure 3.17: Curvature outputs range between [a] upwardly concave, [b upwardly convex and [c] linear (image modified from ESRI, 2016)

3.3.2 Cluster analysis

Clustering is defined as events with a density (spatially or temporally) higher than what would be expected in the surrounding area or time period if events were uniformly or randomly distributed (Tonini *et al.,* 2013). To explore the degree to which rockfalls appear to cluster both spatially and temporally, a modified version of the Ripley's K-function (Tonini *et al.,* 2013) was used and applied to the rockfall data from Boulby. This site was used for this analysis as both the high-resolution monthly datasets and the 10-year dataset were available, allowing investigation of clustering over monthly to decadal time scales and at a high spatial resolution. The 10-year dataset was not available for any of the other field sites and so this analysis was not performed on the rockfall datasets from those sites, as the comparison to clustering over decadal time scales would not have been possible.

The Ripley's K-function (Ripley, 1976) tests for spatial randomness of a spatial point process at a distance, *r*, between events. As a result it defines the distance, *r*, over which events are randomly distributed, clustered or dispersed. Ripley's K-function (*K(r)*) can be summarised as:

$$K(r) = \frac{E(r)}{\lambda}$$

Equation 3.2

where *E(r)* is the expected (observed) number of other events (rockfalls) within a given distance, *r*, from the investigated event divided by the intensity, λ. The intensity is defined as the average number of events within a given distance, *r*, from the central event if all events were evenly distributed (Figure 3.18). Under conditions of complete spatial randomness (CSR), such as a uniform Poisson distribution, *K(r)* would be equal to πr^2. Therefore, for any given value of *r*, $K(r) > \pi r^2$ indicates spatial clustering. Tonini *et al.* (2013) transformed the Ripley's K-function to the L-function in order to make it easier to compare estimated and theoretical (CSR) results. The L-function is defined by the following equation:

$$L(r) = \sqrt{\frac{K(r)}{\pi}}$$

Equation 3.3

This means that under CSR, *L(r)* is equal to zero at every distance, *r*.

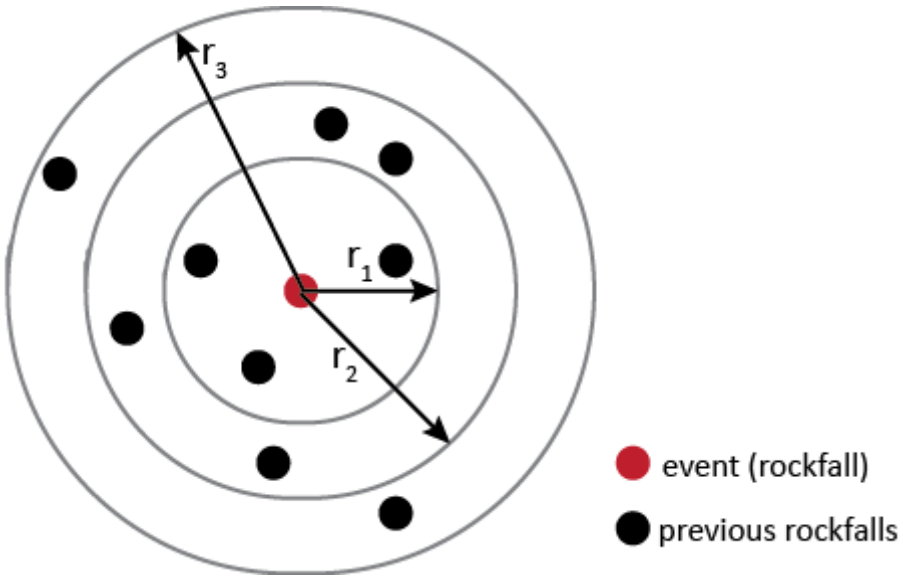

Figure 3.18: The Ripley's K-function analyses events (black dots) at increasing distances, *r*, from the central event (red dot). This figure is adapted from Tonini *et al.* (2013).

In order to apply the L-function to the rockfall data in this study, each of the rockfall polygons were converted to point data, using the rockfall centroid to represent each rockfall (Fig. 3.19). As the scale of each rockfall was small compared to the size of the field site, each rockfall was able to be considered as a point process (Tonini and Abellán, 2014). However, it is important to note that this is not an accurate representation for larger failures (Fig. 3.19a). The analysis was applied for a range of distances (r = 0.5 – 16 m): at each value of r a circle of that radius is generated around each rockfall event, and other rockfalls tallied within that circle. An edge correction was applied in order to deal with circles that fall partially inside the study area by weighting *E(r)* by the percentage of the circle area that fell inside the study area.

The L-function analysis was performed on each of the monthly datasets from the two-year dataset at Boulby and on the decadal dataset from the same site. This was used to determine whether rockfalls that occurred at the same time show significant clustering. In order to test for CSR, the *L(r)* value was computed for 99 Monte Carlo simulations of a realisation of an inhomogeneous random point process. This generated minimum and maximum Monte Carlo envelopes, allowing the significance of data randomisation to be assessed at each distance, *r*, making it possible to reject the null hypothesis (data randomisation) with statistical significance.

In order to test whether rockfalls cluster over time the cross K-function (L-function) was applied (Tonini *et al.,* 2013). Computationally, this counts the number of rockfalls in one time

period at distances, *r*, from rockfalls in a different time period. As with the standard function, the *K(r)* value from the cross function will equal πr^2 under CSR (Tonini *et al.,* 2013). The cross K-function was applied to the two-year dataset from Boulby to evaluate the strength of clustering over different timescales.

Finally, both the basic and cross K-function analyses were conducted on subsets of the data, grouped by rockfall size, in order to determine whether clustering in the data is evident for all rockfall sizes.

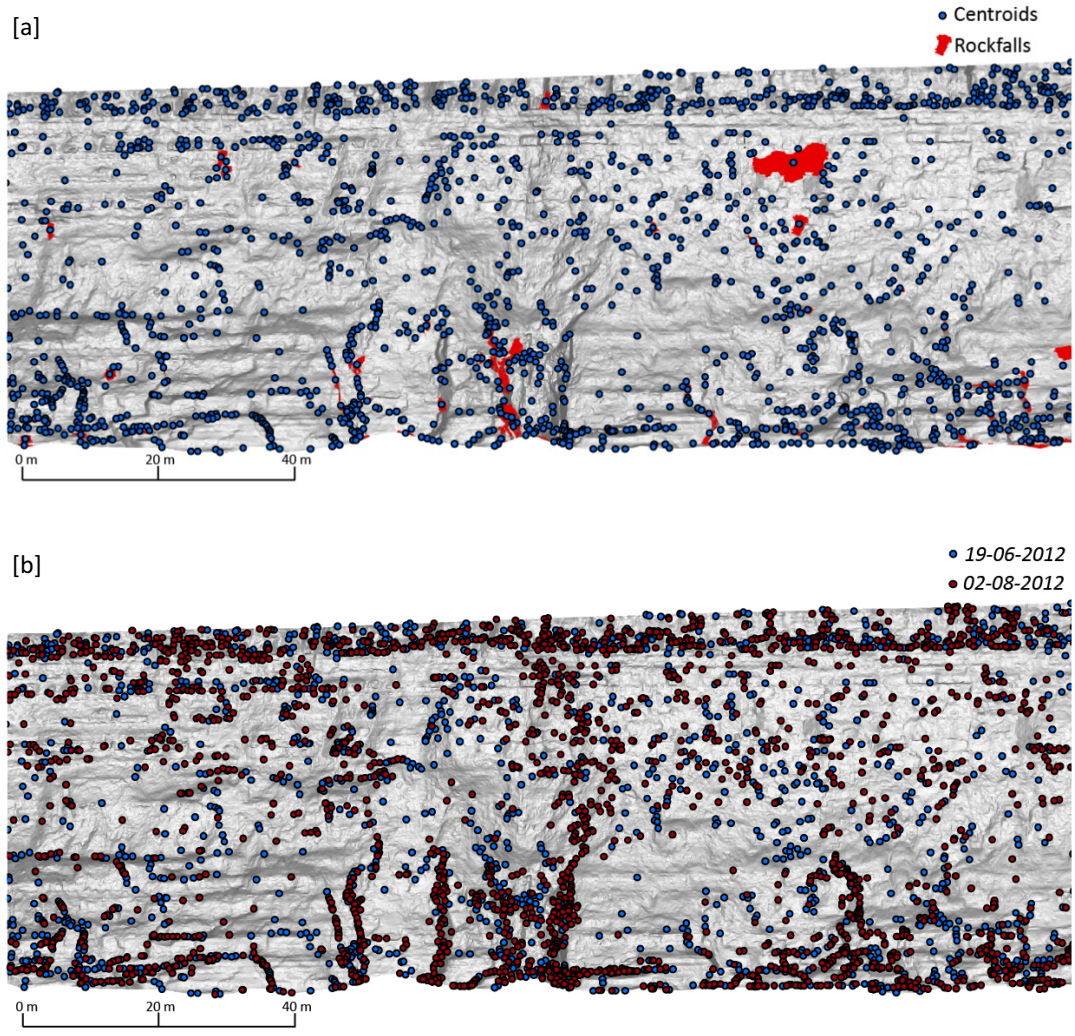

Figure 3.19: Rockfall centroids used for the Ripley's K-function analysis. [a] Rockfall centroids are overlaid on rockfall polygons, illustrating what each point represents: the majority of rockfalls are very small (< 0.1 m^2) and well represented by point data; however, 1D point positions become less representative of the actual 2D geometry of the rockfall polygon for larger rockfalls; [b] Rockfall centroids from two consecutive months are shown. This is an example of the data used for the cross-K function analysis, which assesses the clustering (attraction) between events.

3.4 Results

3.4.1 Ten-year dataset (2003-13)

The rockfall inventory data collected from 2003 – 2013 is shown sequentially in Figure 3.20, where each image includes an additional year of data contributing to the cumulative pattern of rockfalls at the site. Rockfall polygons are colour coded according to their 'age', where an age of 0 represents rockfall that occurred in 2013. The images are annotated with boxes and arrows to illustrate key patterns identified, as discussed below.

Over the ten year monitoring period 9,324 rockfalls ranging from 0.01 m^2 to 26.97 m^2 were identified over a 4,413 m^2 area of the cliff at Boulby, resulting in 33.4% of the cliff area failing (Table 3.3). Rockfalls are distributed widely across the cliff face throughout all of the geological layers (Table 3.3: *Total 2003 - 13*). On an annual timescale, the spatial distribution of rockfalls is sometimes more concentrated within certain geological layers, however this varies between years. The mean rockfall area and variability in rockfall area is highest in the mudstone and decreases with each layer moving up the cliff (Table 3.4). The largest rockfall recorded was in the shale, and was contiguous with rockfalls in the mudstone below.

A magnitude-frequency distribution of rockfalls areas, generated using the log-interval method (Pickering *et al.,* 1995) displays a negative relationship between rockfall area (R_A) and frequency density (f) (Fig. 3.21). A power law is fit through the data (Equation 2.2) and the *ß*-value of the power law fit is -0.76, which is comparable to rockfall size distributions from a variety of settings, which range from -0.4 to -1.07 as presented in Santana *et al.* (2012). The high r^2 value (0.96) demonstrates that the power-law relationship fits the data well over four orders of magnitude.

The progression of rockfall development between images in Figure 3.20 shows incremental failure across the cliff face and illustrates how the range of rockfall sizes is distributed in time and space. Smaller rockfalls appear widely distributed across the cliff face, initially concentrated in the siltstone towards the top of the cliff, and also in the shale and mudstone towards the cliff toe (Fig. 3.20a & b, respectively). Over time subsequent rockfalls occur, often located alongside existing rockfalls, demonstrating how existing failures appear to extend up and laterally across the rock face (Fig. 3.20c). From 2007 onwards a larger proportion of rockfalls appear in the mid-section of the cliff in the shale. Over time rockfalls in this area coalesce, connecting the areas of higher failure density at the top and base of the cliff (Fig. 3.20d). This demonstrates a dominant upward and outward directionality in the propagation of rockfalls across the cliff face. Examples of this are shown by the arrows on the final image

(Fig. 3.20e), which contains all rockfalls identified between 2003 – 2013. Each of the arrows illustrates the coalescence and bridging of rockfalls through time and the subsequent destabilisation of surrounding areas of the rock face. This growth and propagation of rockfalls demonstrates that what may be observed as a single large failure from widely spaced surveys, is in fact the sum of many rockfalls that have evolved over a decade. This supports many of the key findings from previous studies along this coastline, crucially that erosion is driven by rockfalls that initiate across the cliff face; and that there is a notable absence of a cliff toe notch that causes cantilever failure of the whole cliff above.

Table 3.3: Summary of rockfall statistics for the ten year dataset of rockfalls identified at Boulby: 2003 – 2013. 'Failure % by geology' shows the percentage of failures in each geologic unit; the percentage of the cliff area represented by each geologic unit is given in parentheses at the top of each column.

Year	Rockfall count	Total failed area (m^2)	% cliff area failed	Failure % by geology		
				Mudstone (26 .7 %)	**Shale (62.2 %)**	**Siltstone (11.1 %)**
2003 – 04	607	53.84	1.22	16.44	72.75	10.81
2004 – 05	669	53.19	1.21	15.71	65.80	18.49
2005 – 06	2529	217.01	4.92	20.22	67.23	12.55
2006 – 07	800	194.28	4.40	33.52	61.47	5.01
2007 – 08	1479	191.96	4.35	26.55	69.06	4.39
2008 – 09	1526	320.63	7.27	25.26	59.97	14.78
2009 – 10	*No data*					
2010 – 11	*No data*					
2011 – 12	571	49.69	1.13	18.20	71.39	10.40
2012 – 13	1143	392.52	8.90	32.05	55.18	12.77
Total: 2003 - 13	***9324***	***1473.11***	***33.4***	***23.49***	***65.36***	***11.15***

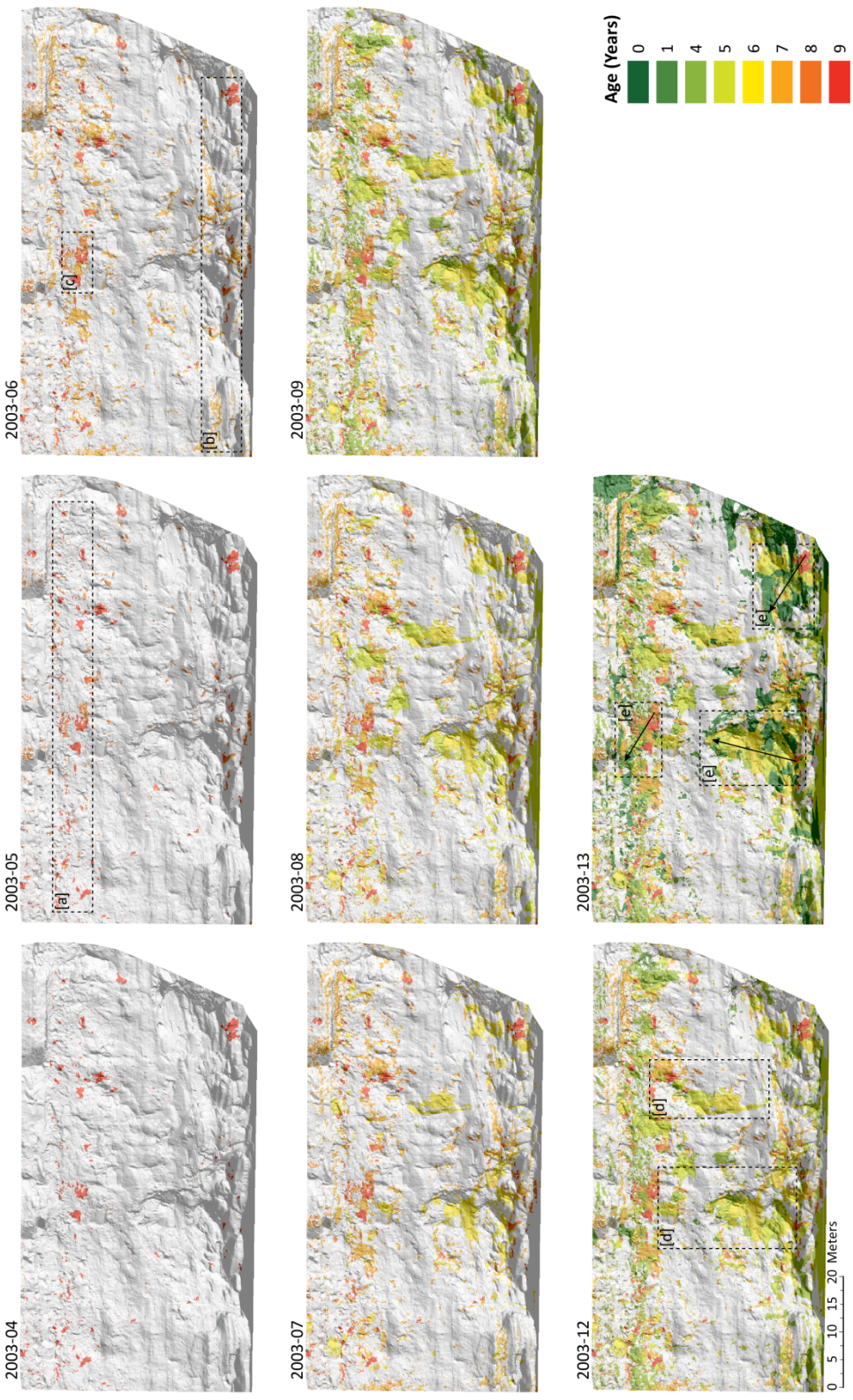

Figure 3.20: Rockfall polygons of a section of the cliff at Boulby from 2003 – 2013: polygons are colour coded by the age of the failure (green = youngest, red = oldest) and draped over a DEM of the cliff. Dashed line boxes refer to patterns identified and described in the text; arrows indicate growth of failure areas upward and outward across the cliff face and through time.

Table 3.4: Summary of rockfall statistics for each of the geological layers. Data is from the ten year monitoring period (2003 – 2013).

Geology	Surface area failed (%)	Mean rockfall size (m^2)	Minimum rockfall size (m^2)	Maximum rockfall size (m^2)	Standard deviation rockfall size (m^2)
Mudstone	68.35	0.253	0.01	23.760	1.135
Shale	41.13	0.196	0.01	26.964	0.974
Siltstone	42.22	0.104	0.01	9.979	0.402

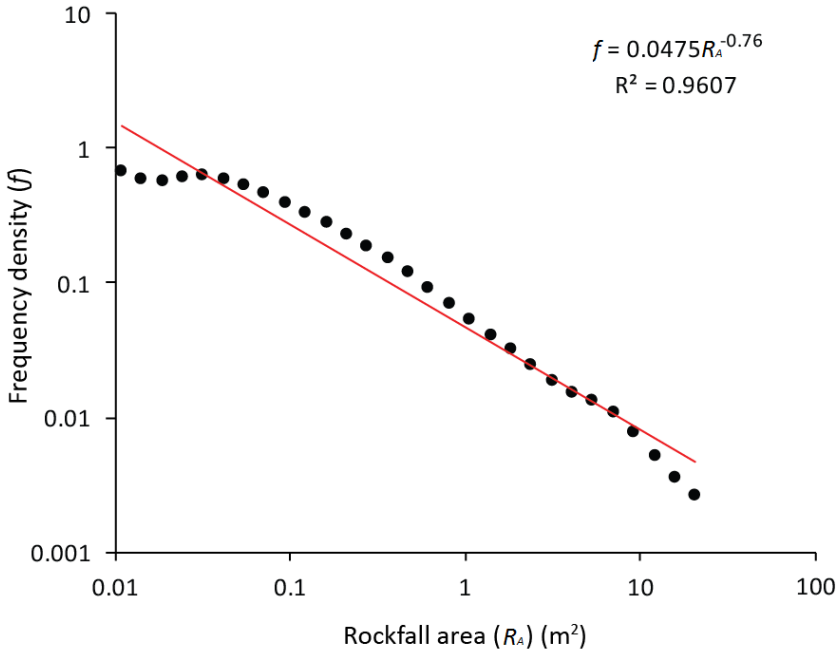

Figure 3.21: Area-frequency density plot for all rockfalls from the 10-year period (2003-13) at Boulby.

3.4.2 Two-year dataset (2012-14)

The rockfall inventory data collected from sequential laser scans between 2012 and 2014, show the evolution of rockfalls across the cliff face over this time (Fig. 3.22 a-d). For each of the sites monitored, rockfall polygons delineate the area of rockfall scars and are colour coded by the month in which they occurred, as indicated in the legend. Over the two years of monitoring, 46.2%, 46.9%, 19.1% and 33.4% of the cliff face is observed to have failed at Boulby, Section 1, Section 2 and Cowbar, respectively (Table 3.5). This number includes repeated failure of the same surface, whereas if repeated failures are ignored, the percentage of the cliff face that failed during the two year monitoring period and the actual surface change is much lower: 29.4%, 36.1%, 16.3% and 23.8% for each of the sites respectively. A measure of the spatially averaged erosion rate at each site, calculated as the *total volume of rock removed / total cliff surface area*, yields rates of 0.115 m yr^{-1}, 0.091 m yr^{-1}, 0.029 m yr^{-1} and 0.084 m yr^{-1} for Boulby, Section 1, Section 2 and Cowbar, respectively (Table 3.5).

Table 3.5: Summary of rockfall statistics for each of the field sites for the two year monitoring period (June 2012 – June 2014). The cliff area failed (%) includes repeated failures of the same surface and so could theoretically exceed 100% of the cliff face area; the area that has resurfaced (%), irrespective of repeated failure, is given in [ ] below. A detailed summary of the rockfall statistics for each acquired scan (monthly) can be found in Appendix 3.

Site	**Cliff area failed (%) [*resurface*]**	**Surface averaged erosion (m yr^{-1})**	**Mean rockfall vol (m^3)**	**Minimum rockfall vol (m^3)**	**Maximum rockfall vol (m^3)**	**Standard deviation rockfall vol (m^3)**
Boulby	46.167 [*29.396*]	0.115	0.068	0.001	701.977	3.567
Section 1	46.932 [*36.133*]	0.091	0.075	0.001	87.367	1.413
Section 2	19.093 [*16.265*]	0.029	0.038	0.001	42.080	0.714
Cowbar	33.376 [*23.773*]	0.084	0.068	0.001	319.685	2.851

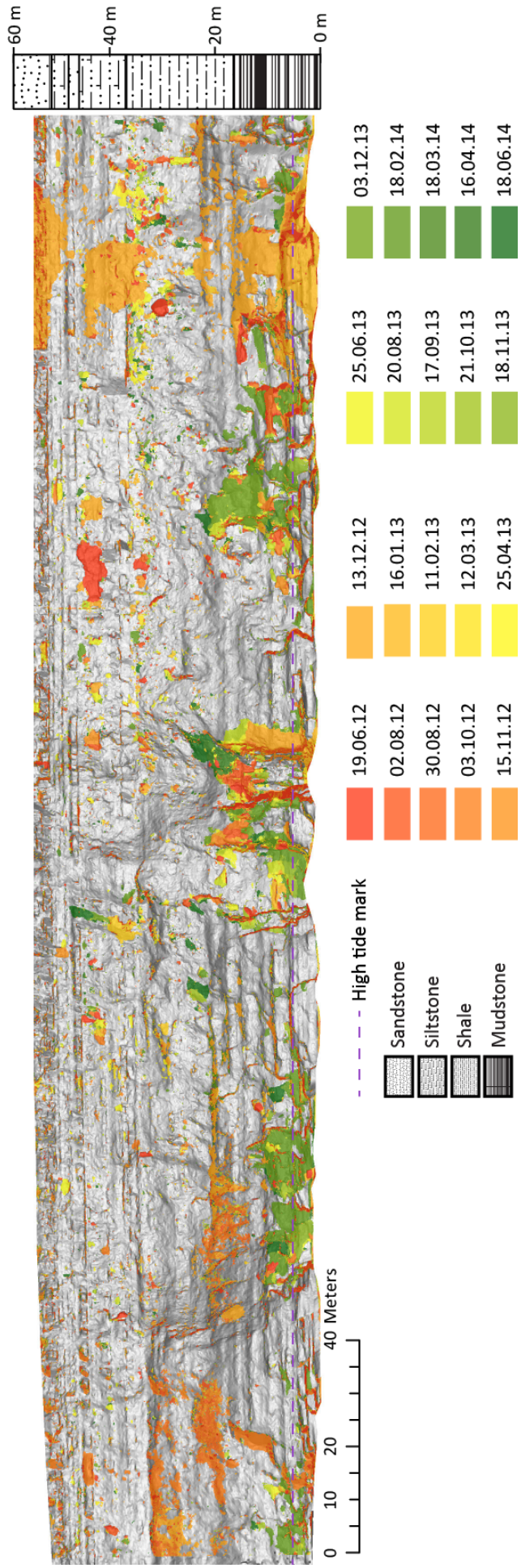
60 m
40 m
20 m
0 m
03.12.13
18.02.14
18.03.14
16.04.14
18.06.14
25.06.13
20.08.13
17.09.13
21.10.13
18.11.13
13.12.12
16.01.13
11.02.13
12.03.13
25.04.13
19.06.12
02.08.12
30.08.12
03.10.12
15.11.12
High tide mark
Sandstone
Siltstone
Shale
Mudstone
0
10
20
40 Meters

[a] Boulby

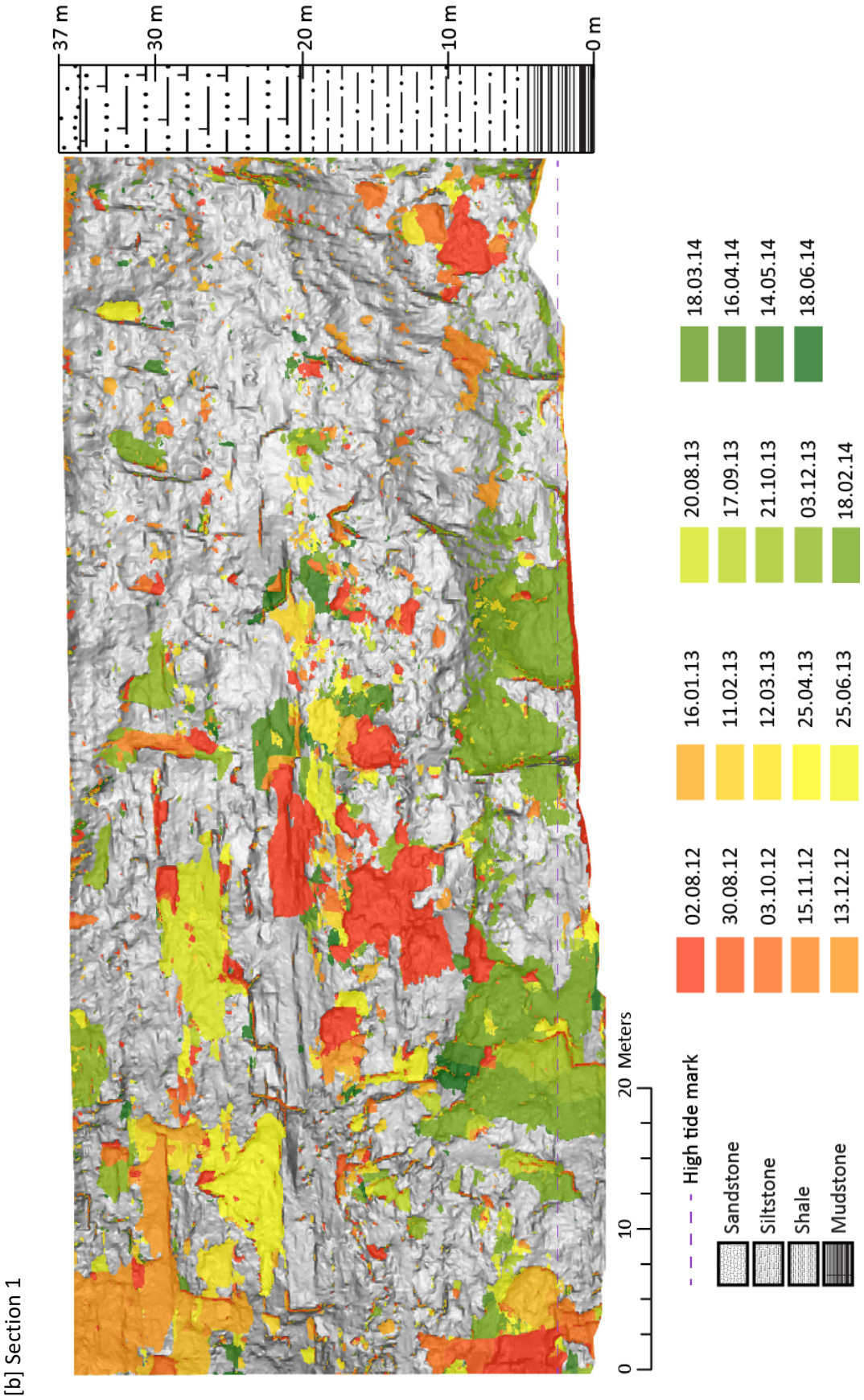
37 m
30 m
20 m
10 m
0 m
0
10
20 Meters
High tide mark
Sandstone
Siltstone
Shale
Mudstone
02.08.12
30.08.12
03.10.12
15.11.12
13.12.12
16.01.13
11.02.13
12.03.13
25.04.13
25.06.13
20.08.13
17.09.13
21.10.13
03.12.13
18.02.14
18.03.14
16.04.14
14.05.14
18.06.14

[b] Section 1

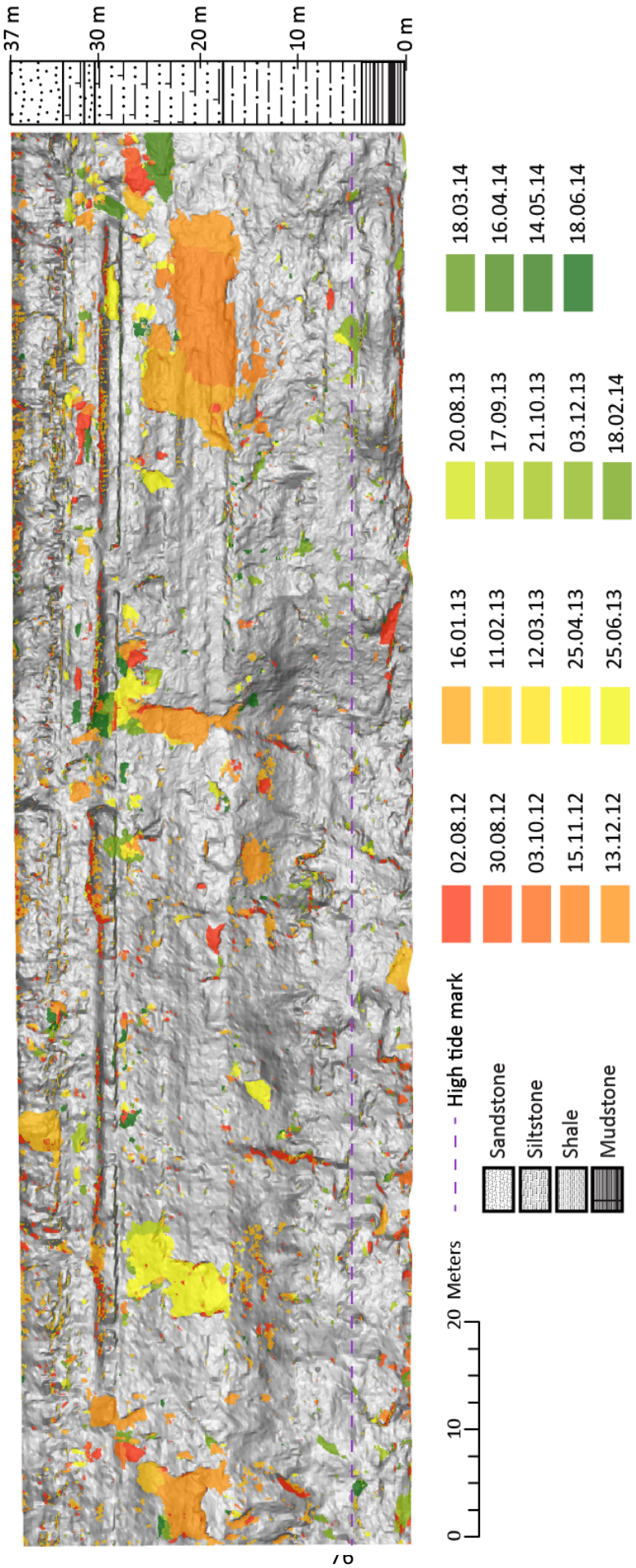
37 m
30 m
20 m
10 m
0 m
18.03.14
16.04.14
14.05.14
18.06.14
20.08.13
17.09.13
21.10.13
03.12.13
18.02.14
16.01.13
11.02.13
12.03.13
25.04.13
25.06.13
02.08.12
30.08.12
03.10.12
15.11.12
13.12.12
High tide mark
Sandstone
Siltstone
Shale
Mudstone
0
10
20 Meters

[c] Section 2

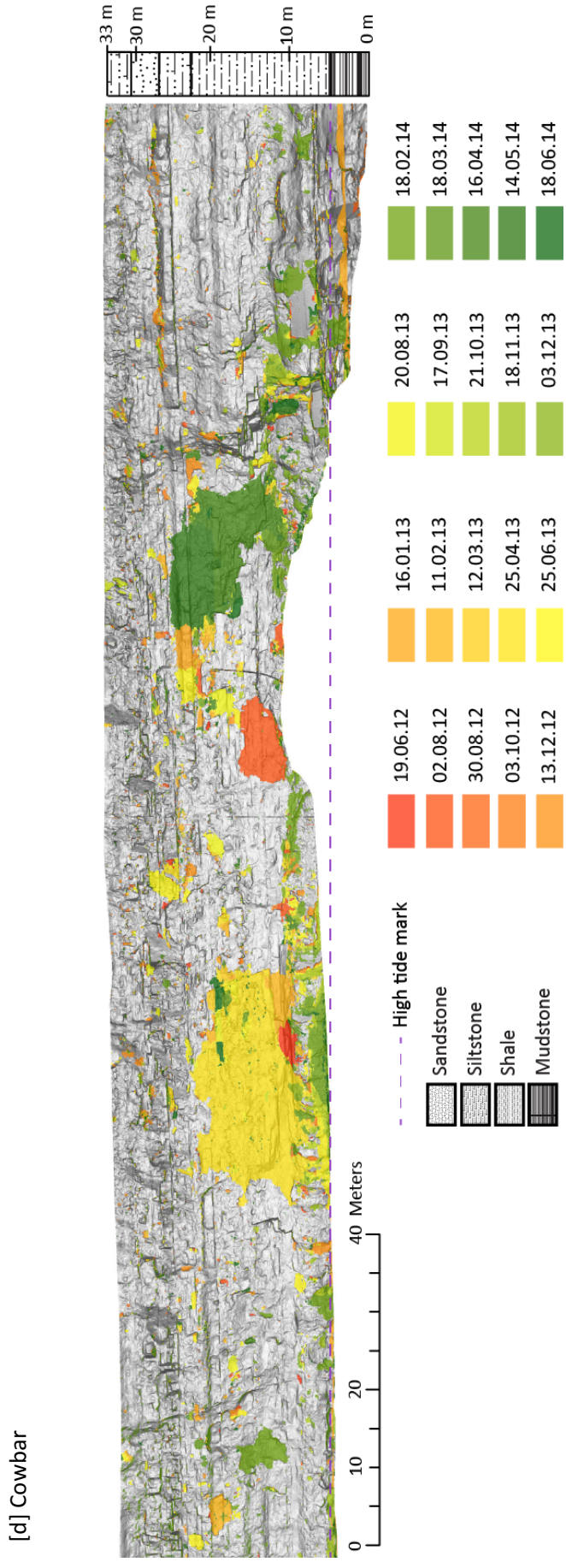

Figure 3.22: Rockfalls across the cliff face over the two year monitoring period (June 2012 – June 2014) for [a] Boulby; [b] Section 1; [c] Section 2; [d] Cowbar. Polygons delineate the area of each rockfall, colour coded by the month in which it occurred. The rockfall polygons are overlaid on a slope map of the cliff face to illustrate slope morphology. The purple dashed line indicates the high tide mark, distinguishing the inundation and non-inundation zones.

3.4.2.1 Magnitude-frequency distribution of rockfalls

Across the four sites rockfall sizes span five orders of magnitude, ranging from 10^{-3} - 10^{2} m^3 (Table 3.5, Fig. 3.23). This is two orders of magnitude less than the range of rockfall sizes identified by Lim *et al.* (2010) over a 20-month monitoring period along the same stretch of coastline. Partly this is due to the higher rockfall size cut-off imposed in this study: to avoid any error due to oblique scanning angles (Section 3.2.2.1) any rockfalls with a surface area < 0.01 m^2 were excluded from the data and the DEM generated from the point cloud data was gridded at 0.1 m resolution. Lim *et al.* (2010) imposed only the restrictions set by the resolution of the monitoring technique, allowing rockfalls as small as 10^{-4} m^3 to be captured. At the upper end of the rockfall range, the dataset produced by Lim *et al.* (2010) contained one failure c. 10^{3} m^3, whilst the largest rockfalls in this dataset are an order of magnitude smaller.

A magnitude-frequency distribution of rockfalls volumes, generated using the log-interval method (Pickering *et al.,* 1995) displays a negative relationship between the rockfall volume (R_V) and frequency density (f) (Fig. 3.22). The *ß*-values of the power law fits range from -0.707 to -0.863, which is comparable to rockfall volume distributions from a variety of settings, which range from -0.4 to -1.07 as presented in Santana *et al.* (2012), although higher than those presented for rockfall distributions in other sedimentary rocks (Dussauge-Peisser *et al.,* 2002). A power law is fit through the data (Equation 2.2) and the higher *ß*-value from this study might be attributed to the higher resolution of the TLS, which mean that smaller rockfalls are captured, whilst the distribution from Dussauge-Peisser *et al.* (2002) was based on historical data alone. There is a small rollover in the data at the smallest rockfall sizes seen at all sites, which is frequently seen in other inventories of rockfalls and landslides (Stark and Hovius, 2001; Guzzetti *et al.,* 2002; Santana *et al.,* 2012). This is often attributed to the under representation of the smaller events in a dataset (censoring) and in this case is possibly seen due to the removal of rockfalls < 0.001 m^3 from the inventory. At the upper end of the dataset a few outliers can be seen, representing large singular failures that occurred during the two year monitoring period, displaying a deviation from the power law fit. The outliers may be a result of the kernel used to determine the frequency density – the kernel determines the frequency at linear intervals in log-log space and the position of the points on the plot is a reflection of this.

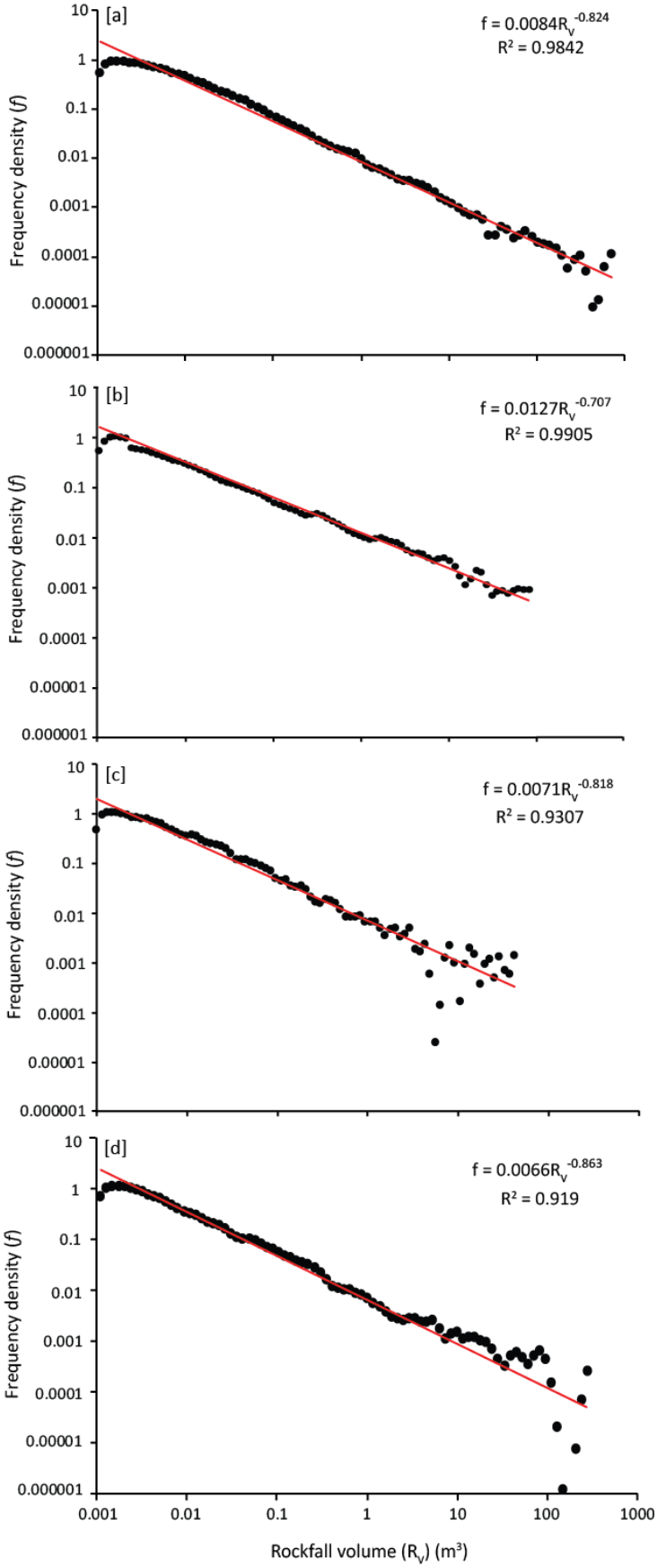

Figure 3.23: Magnitude-frequency plots for all rockfalls in the two year period (June 2012 – June 2014) at all four fieldsites: [a] Boulby (*ß*-value = -0.824), [b] Section 1 (*ß*-value = -0.824), [c] Section 2 (*ß*-value = -0.824), [d] Cowbar (*ß*-value = -0.824).

3.4.3 Area of investigation

Owing to the variability in the spatial distribution of rockfalls across the cliff (Fig. 3.22), the size of the area of investigation used in both monitoring and analysis will impact on how representative the data is of the whole cliff and wider coastline. In order to investigate this and to determine at what scale the data become representative of the whole cliff, the rockfall data from Boulby was analysed to determine how the average failed area varied at different spatial scales across the cliff. The rockfall count and size could also be used as measures of representation in future studies.

The rockfall polygon data was gridded to a cell size of 0.01 m^2 and the value of each cell equal to the number of times a rockfall had occurred there. A range of 'windows' of different sizes ranging from 4 m^2 to 15,700 m^2 were passed over the cliff face, moving at 0.1 m intervals, and the mean failed surface area calculated with each move. For each window the mean, standard deviation and 99th percentile of the data was calculated and compared to the mean failed surface area for the whole dataset. The ratio between the 99th percentile of the measured area data and the mean failed surface area of the whole dataset is used to indicate how representative the data in the measured area is of the whole cliff (Fig. 3.24).

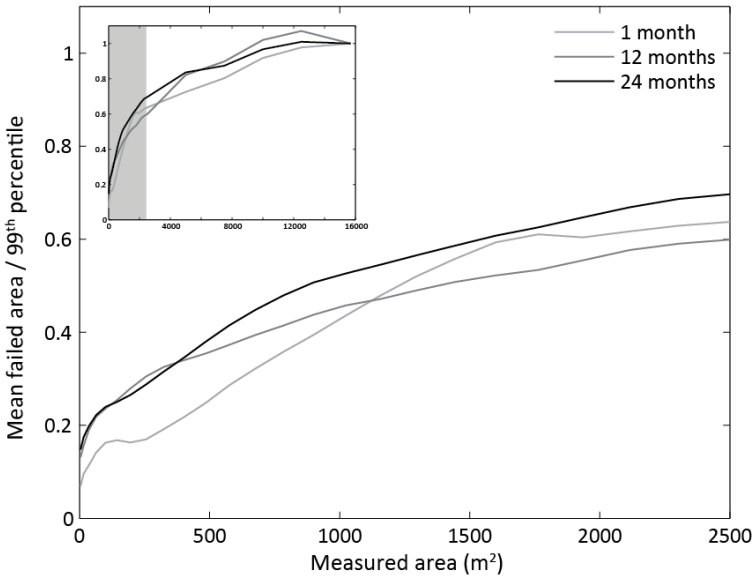

Figure 3.24: A measure of how representative the rockfall data is of the whole cliff when measured over different areas. The ratio between the mean failed area of the entire dataset and the 99th percentile of data from a measured area (vertical axis) is plotted against the measured area (horizontal axis) for datasets at three different timescales: 1 month, 12 months and 24 months of data. A ratio value of 1 represents a perfect correlation, indicating that the data within the measured area is at least 99% representative of the entire dataset. As most of the variation is seen at lower window sizes the data is shown for areas up to 2,500 m^2 with an inset showing the entire dataset up to area = 15,700 m^2, indicating that a perfect correlation is achieved at a measured area of ca. 12,000 m^2.

As the measured area increases the 99th percentile of the data becomes closer to the mean failed area of the whole cliff (Fig. 3.24). Using an area of 2,500 m^2 the ratio is above 0.6 for all three datasets; above an area of 9,000 m^2 the curve begins to flatten and the ratio is above 0.9 for all three datasets. Beyond an area of 10,000 m^2 for the 12 months' dataset and beyond 12,000 m^2 for the 24 months' dataset, the measured data overestimates the mean failed area. This suggests that 99 % of the time, measuring an area ≤ 63 % of the cliff size over 12 months will underestimate the failed area; over 24 months this increases to any area ≤ 76 % of the cliff size; and for only 1 month of data the failed area is underestimated at all measured areas.

By examining the change in the 99th percentile alongside the variability in the data, given by the standard deviation (Fig. 3.25, a-c), points can be identified where an increase in the measured area does not afford significant gains in the increase in data representation. This can be seen by subtle inflection points on the curve (red circles in Fig. 3.25), where the slope of the curve flattens and therefore the gain in data representation with increasing area becomes less. For example, in 1 month of data (Fig. 3.25a) subtle points of inflection can be seen in both curves at measured areas of 1,800 m^2 and 10,000 m^2. Over 12 months of data (Fig. 3.25b), inflection points can be seen at 5,000 m^2 and 10,000 m^2; and over 24 months of data (Fig. 3.25c) at 2,300 m^2, 5,000 m^2 and 10,000 m^2. Whilst no area smaller than the whole cliff provides a measure of failure that is completely representative of whole dataset, the uppermost inflection point in these observations illustrate that at all three timescales considered, there is little to be gained by measuring an area larger than 63% of the full cliff size at this site. This result is specific to the cliff at Boulby and may differ for different cliffs of varying sizes and rockfall characteristics.

In order to investigate this more fully a much longer dataset is required that allows for a complete resurfacing of the cliff face: from the field data it can be seen that many areas of the cliff fail repeatedly before an entire resurfacing would happen. A longer dataset that allowed for a total resurfacing would show how the location of the thresholds identified change with time, expecting that over much longer time periods the uppermost inflection point would decrease with respect to the measured area.

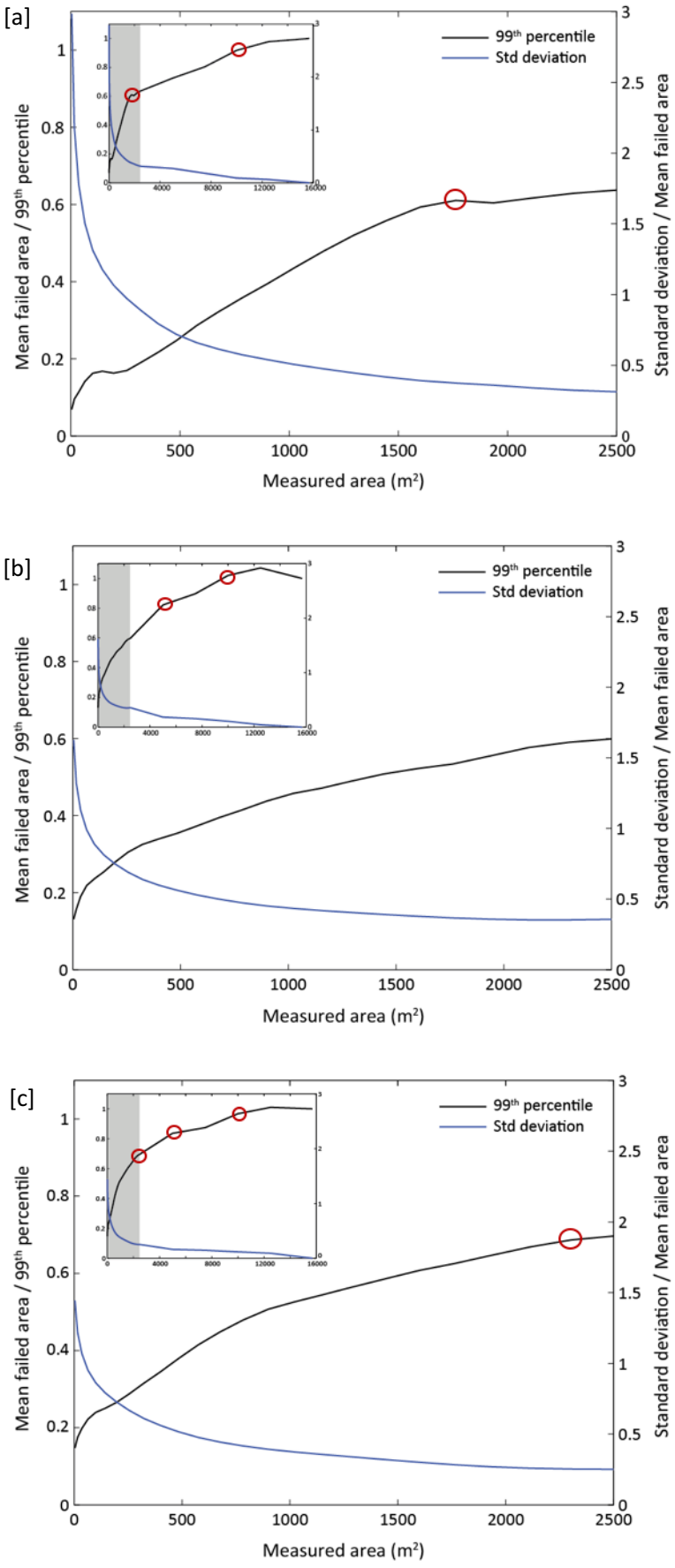

Figure 3.25: The ratio between the mean failed area and the 99th percentile of data (black line) and the ratio between the standard deviation and mean failure count (blue line), plotted against the measured area (window size). [a] 1 month; [b] 12 months; [c] 24 months. Subtle inflection points are in red circles.

3.4.4 Spatial variations in rockfall distribution

At all sites rockfalls are distributed widely across the cliff face (Fig. 3.22), with the highest surface averaged erosion rate in the mudstone and sandstone layers (Table 3.6). Rockfalls in the mudstone layer occurred over a large area – 69.51 % of the surface area failed over the two years of monitoring, and in contrast erosion in the sandstone layer occurred over only 30.66 % of the surface area. The mudstone layer coincides with the inundation zone (Fig. 3.4) and therefore is subject to tidally modulated inundation, wetting and drying across the entire surface area. This maybe the reason for the widely distributed rockfalls across this layer and the higher erosion rate, compared to the layers above which are exposed only to sub-aerial weathering. The coincident change in geological layers alongside the different weathering zones makes it difficult to ascertain which is the dominant control. The difficultly in attributing the variability in erosion to environmental controls is identified in Lim *et al.* (2010) and Norman (2012). The analysis presented in the remainder of this chapter distinguishes the inundation and non-inundation zones where appropriate, and a fuller exploration of the role of weathering is presented in the applications in Chapter 6.

The range of rockfall sizes also appears to vary spatially, modulated by the geology: the largest rockfall occurred in the sandstone layer, characterised by widely spaced joints and large, blocky structure, with a uniaxial compressive strength (UCS) of 34.2 MPa (Lim *et al.,* 2010); the maximum rockfall size was much lower in the shale and siltstone layers, which have more closely spaced joints compared to the sandstone and lower UCS values of 16.7 MPa and 30.2 MPa respectively. The mean rockfall volume was highest in the mudstone (0.079 m^3) and lowest in the siltstone (0.034 m^3), and 97% of the rockfalls are < 0.1 m^3, yet these smaller rockfalls only contribute to 12% of the total erosion, implying that the larger rockfall events dominate erosion along this coastline.

Table 3.6: Summary of rockfall statistics for each of the geological layers for all sites combined. The bottom row gives the average values for all sites and all geological layers. Data is from the two year monitoring period (June 2012 – June 2014). A detailed summary of the rockfall statistics for each acquired scan (monthly) can be found in Appendix 3.

Geology	Area failed (%)	Surface averaged erosion (m yr^{-1})	Mean rockfall vol (m^3)	Minimum rockfall vol (m^3)	Maximum rockfall vol (m^3)	Standard deviation rockfall vol (m^3)
Mudstone	69.51	0.188	0.079	0.001	302.654	2.528
Shale	18.46	0.032	0.051	0.001	107.704	1.224
Siltstone	12.19	0.021	0.034	0.001	133.818	1.344
Sandstone	30.66	0.115	0.062	0.001	701.977	5.807
All sites	36.39	0.080	0.062	0.001	701.977	2.136

The spatial variation in rockfall distribution between geological layers and between the inundation and non-inundation zones has been illustrated by a more detailed examination of the change in rockfall distribution and surface failure with cliff elevation (Fig. 3.26). At Boulby (Fig. 3.26a) and Cowbar (Fig. 3.26d) there is a peak in both rockfall count and failed area at the transition from the inundation zone to the non-inundation zone above. At Section 1 (Fig. 3.26c) the peak in both rockfall count and failed area is recorded towards the top of the shale layer, and in Section 2 (Fig. 3.26d) maxima in rockfall are recorded at the toe of the cliff and in the sandstone layers towards the top of the cliff. At each of the field sites there are locations on the cliff where large failed areas are accompanied by a low rockfall count, suggesting that the failure in these locations is achieved through fewer, larger failures. This behaviour is observed in the sandstone layers at Boulby and Section 1; in the siltstone layer at Section 2 and in the shale at Cowbar. In all cases this is supported by the observation of larger rockfalls in this layer, which can be seen in the rockfall polygons in Figure 3.22. Maxima in both the rockfall count and failed area are observed in narrow bands of rock, such as at Boulby and Section 2 where siltstone and sandstone are interbedded. This could be attributed to the closely spaced bedding or joint planes, along which rockfalls are able to propagate, and suggests that such transition zones between layers are more active zones of the cliff. Other transition zones between geological layers and from the inundated to non-inundated zone also display areas of increased rockfall activity. In some cases the rockfall count and failed area is higher below a transition zone and in some cases it is higher above a transition zone, but rarely is it consistent both above and below.

[a]

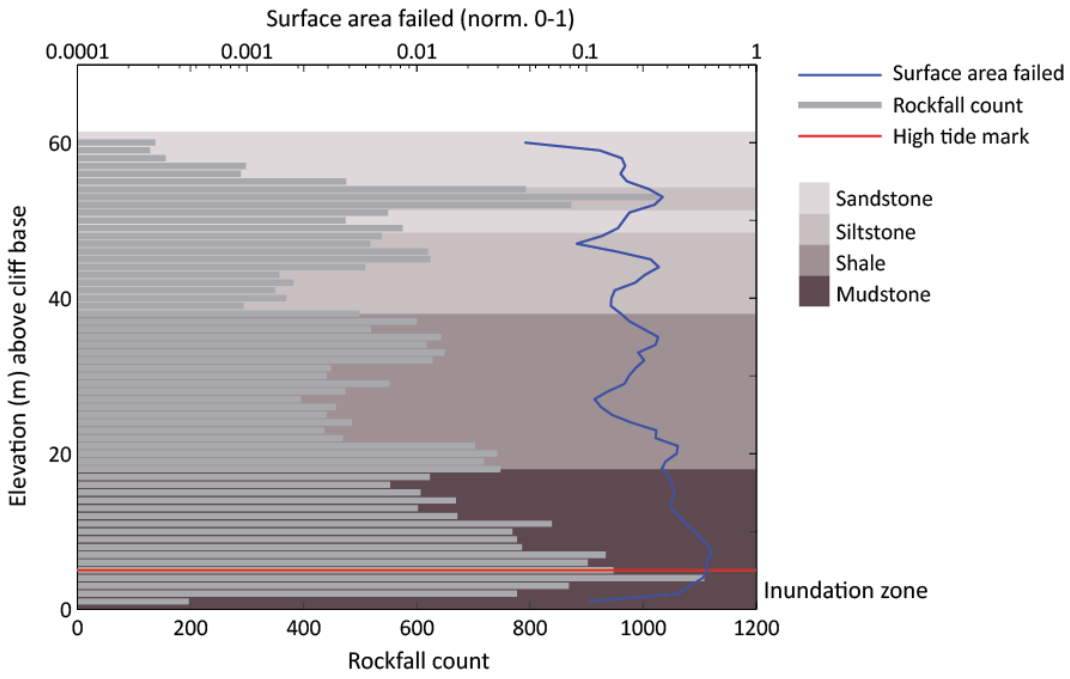
Surface area failed (norm. 0-1)
0.0001
0.001
0.01
0.1
1
Elevation (m) above cliff base
0
20
40
60
0
200
400
600
800
1000
1200
Rockfall count
Surface area failed
Rockfall count
High tide mark
Sandstone
Siltstone
Shale
Mudstone
Inundation zone

[b]

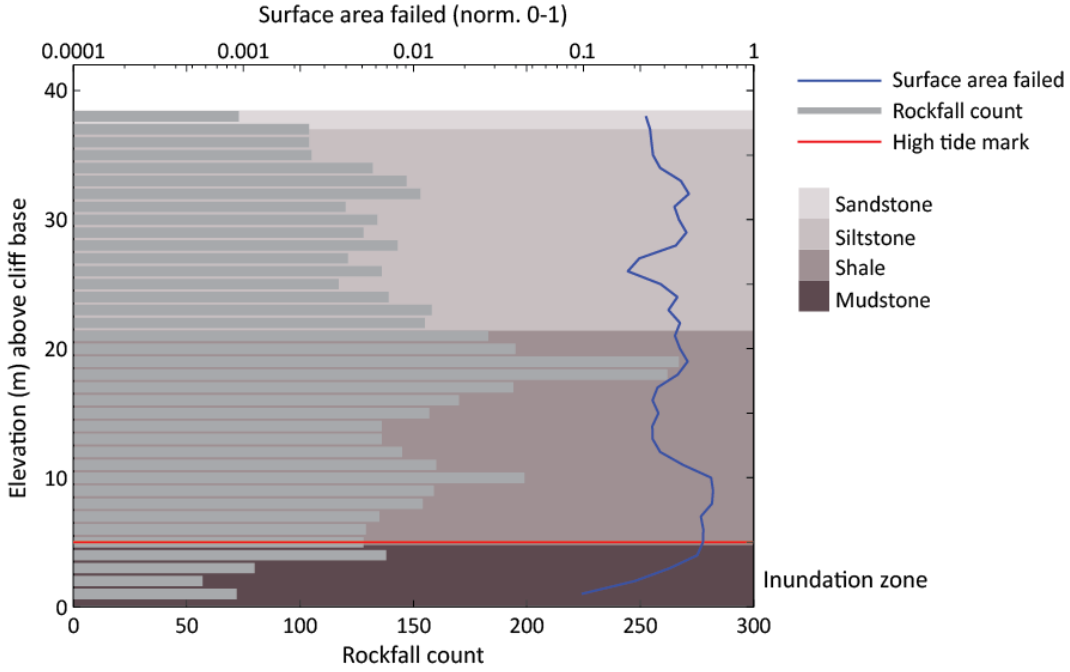
Surface area failed (norm. 0-1)
0.0001
0.001
0.01
0.1
1
Elevation (m) above cliff base
0
10
20
30
40
0
50
100
150
200
250
300
Rockfall count
Surface area failed
Rockfall count
High tide mark
Sandstone
Siltstone
Shale
Mudstone
Inundation zone

[c]

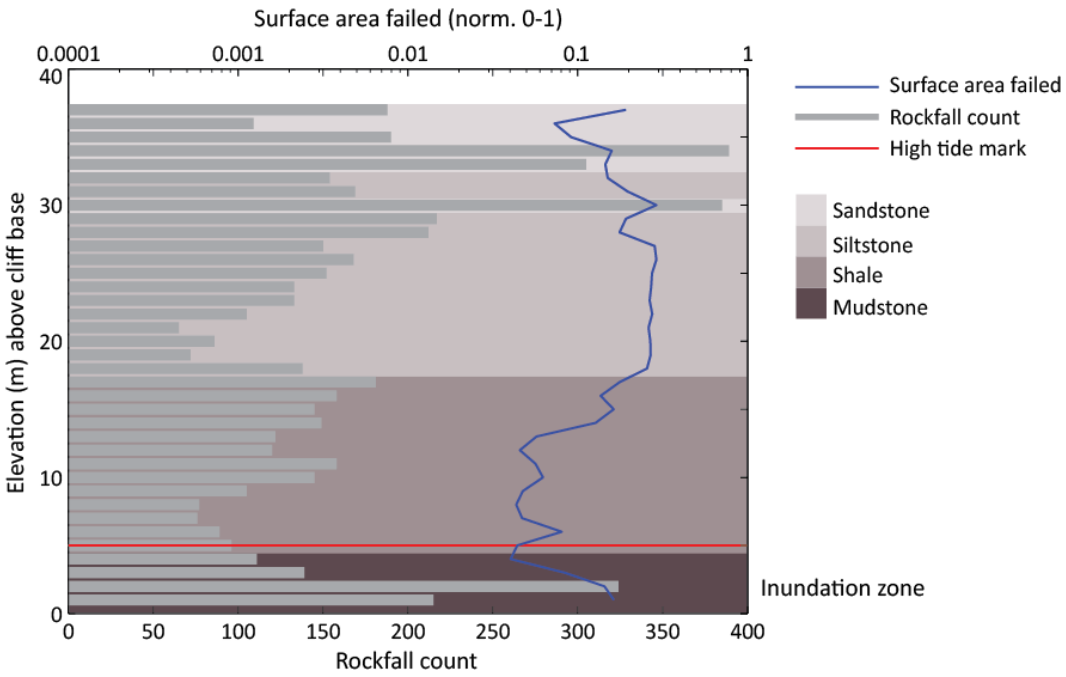

[d]

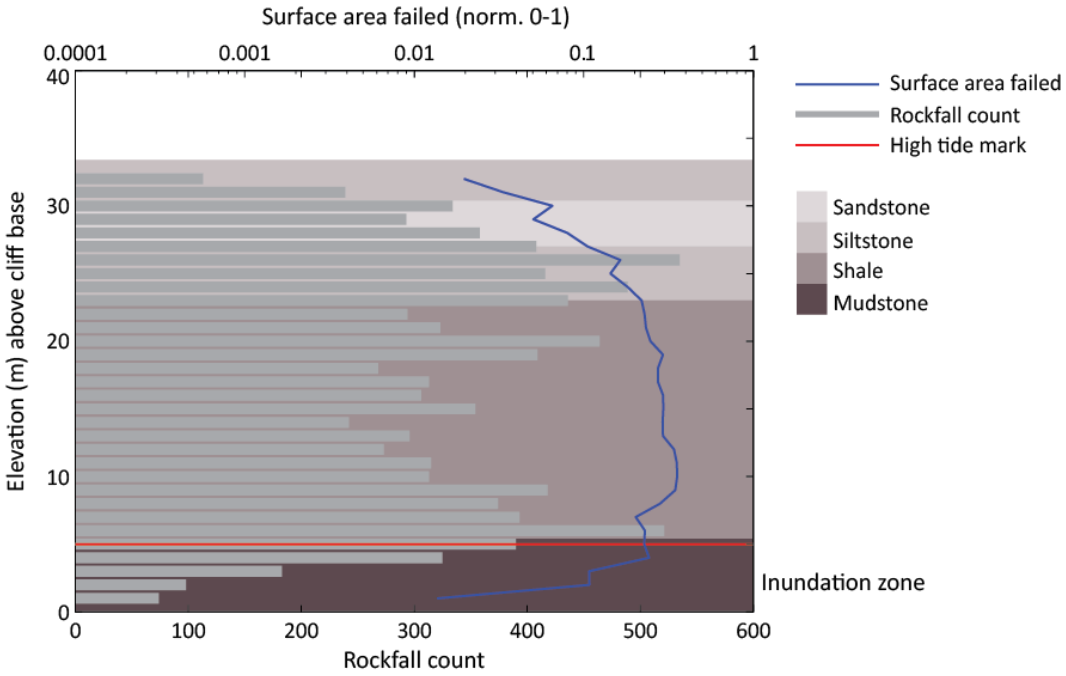

Figure 3.26: Variations in rockfall count (grey bars) and surface area failed (blue line) plotted against elevation (0 m = cliff base) for each site: [a] Boulby; [b] Section 1; [c] Section 2; [d] Cowbar. Shading delineates the geological layers as indicated in the legend. The high tide mark (red line) represents the top of the inundation zone, which is exposed to marine conditions at high tide (Norman, 2012). Moving up the cliff from the base, the number of rockfalls (lower horizontal axis; grey bars) and the percentage of the cliff face that had failed (top horizontal axis; blue line) were calculated for each 1 m elevation bin. Individual plots for each acquired scan (monthly) can be found in Appendix 3. *Note: surface area failed has been normalised so 1 = 100 % failure.*

The data presented thus far suggests large variability between geological units and with elevation, however has not accounted for the spatial variability across/within these layers. Such variability is clear from the images in Figure 3.22, which show the evolution of rockfalls across the cliff face over the two years of monitoring. For example, rockfalls concentrated appear along joints and along bedding planes, particularly at the transition between geological layers; larger rockfalls are contiguous with smaller, earlier rockfalls; later rockfalls can be observed adjacent to existing rockfalls, illustrating the coalescence of rockfalls through time; and structural surface features develop around the periphery of failed zones. Surface features such as overhangs, protrusions and arches are formed as a result of rockfall and develop through time to a consistent form, which then drive rockfall characteristics. These observations raise key questions regarding rockfall evolution and the processes driving erosion in these hard rock cliffs:

- How do rockfalls propagate vertically across transition zones and laterally across the cliff face?;
- What is the role of smaller rockfalls and are they indicative of the location and timing of larger rockfalls?;
- How do surface features and rockfalls interact?

Examples of rockfall evolution through time related to each of these questions have been provided in the analysis that follows.

3.4.5 Examples of rockfall evolution

3.4.5.1 Rockfall evolution 1: transition from inundation zone to above

This first example is from Section 1 (Fig. 3.22b) and illustrates how rockfall propagate vertically up the cliff, moving from the inundated to non-inundated section of the cliff (Fig. 3.27). Due to marine action at the base of coastal cliffs, it is expected that a large number of failures would initiate in this zone, however the set of conditions that allow the rockfalls to grow and propagate beyond this area are unclear.

The sequence of images in Figure 3.27 shows a failure initiate in the inundation zone in October 2012 (Fig. 3.27, 3rd image). Over three months the October 2012 rockfall in the inundation zone propagates upward towards the transition into the non-inundation zone. In February 2013 the propagation appears to trigger a larger failure that crosses the transition

into the non-inundation zone above (Fig. 3.27, 7th image). Next the rockfall continues to grow, generating smaller failures in the non-inundation zone and coalescing with a larger, existing failure (Fig. 3.27, 15th image).

Profiles taken through the middle of the image shown in Figure 3.27 are given in Figure 3.28, illustrating the events described. Erosion that has initially occurred directly as a result of marine action, destabilises the rock mass above, eventually triggering rockfall to occur in the non-inundation zone. This series of events occurs with some rockfall, however is not observed with every rockfall that occurs in the inundation zone. Potentially there are thresholds on rockfall size, the intensity of the marine action, and pre-existing damage in the surrounding rock mass, which determine whether or not this series of events occurs. Propagation across the inundation zone boundary is not the only mechanism of failure generation above the inundation zone and many rockfall initiate at various heights up the cliff face with no apparent link to what has previously occurred on the cliff below. Notably in the cliff profiles (Fig. 3.28) it can also be seen that large failures initiate at the top of the cliff at the same time as the larger failures towards the toe, as seen in February 2013, profile 3.

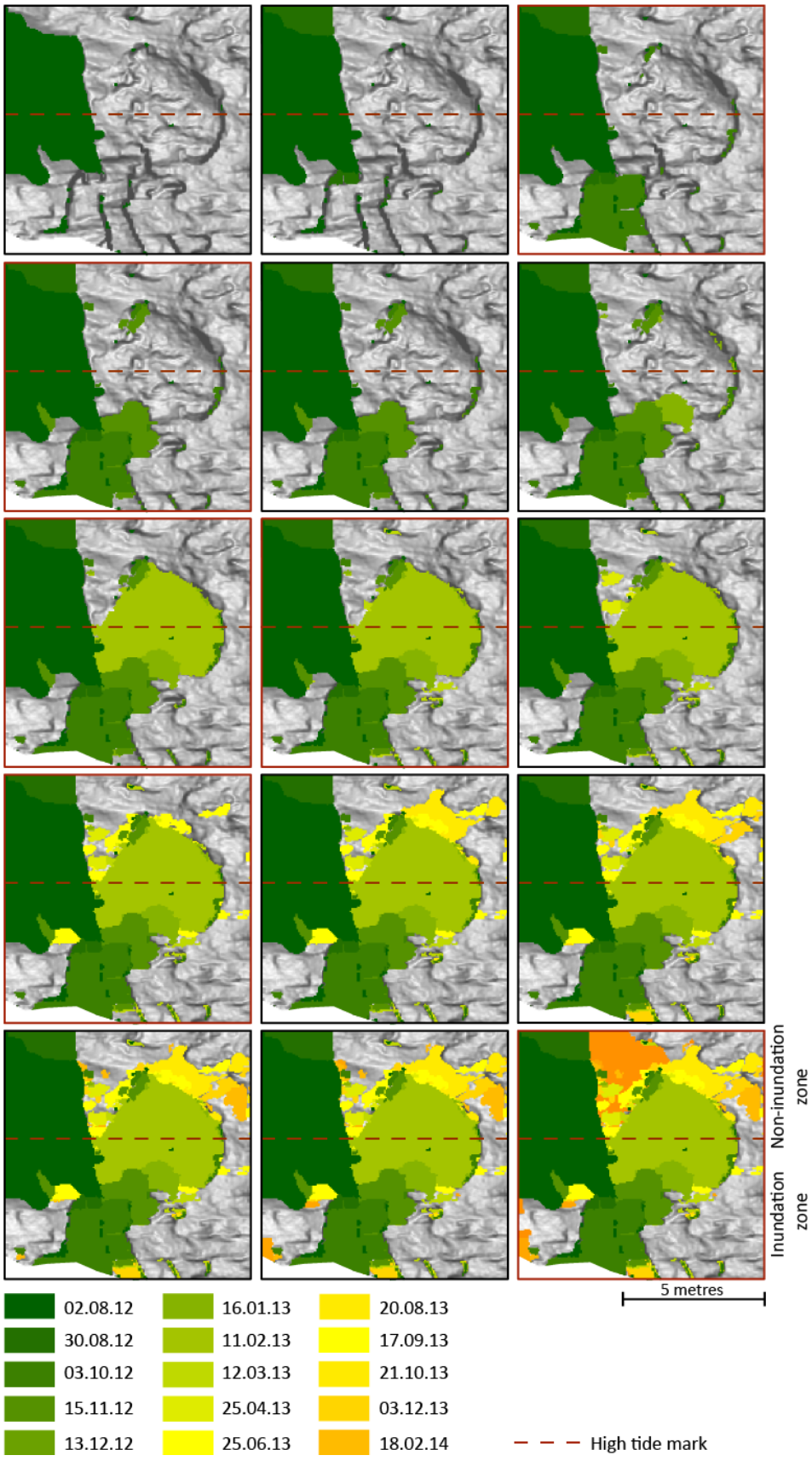

Figure 3.27: Sequential images (top left (row by row) to bottom right) taken from Section 1, illustrating the transition out of the inundation zone. Rockfall polygons are overlaid on a DEM of the cliff face. Red boxes denote images that profiles are taken from (Fig. 3.28).

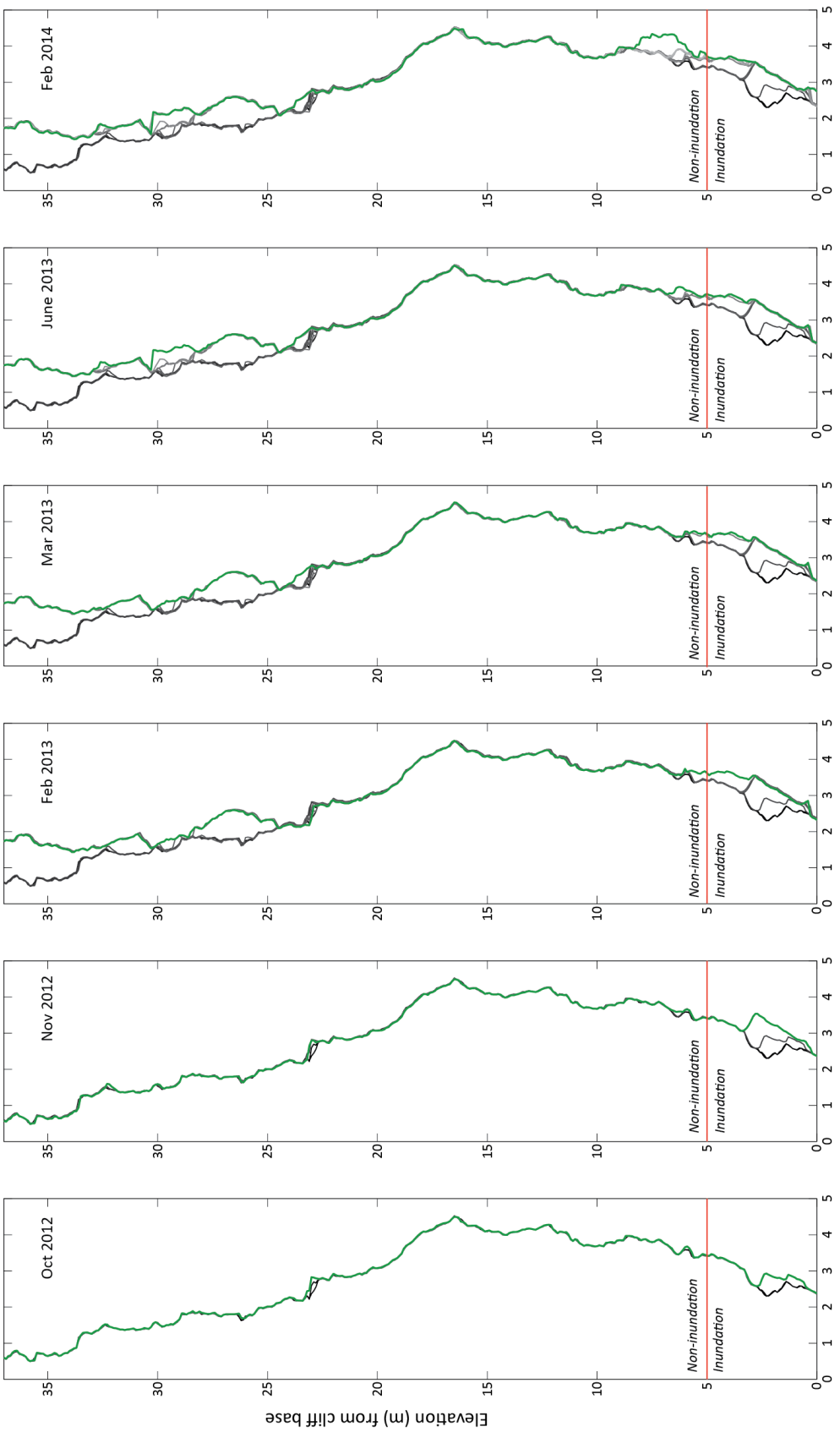

Figure 3.28: Profiles of the cliff surface taken through the area shown in Fig. 3.27 for the entire cliff height. In each plot the newest profile is shown in green and previous profiles in black – grey, where darker colours are older profiles. The high tide mark is depicted by the red line, separating the inundation and non-inundation zones. The distance back from the cliff face (x-axis) is measured from the most prominent point on the cliff surface.

3.4.5.2 Rockfall evolution 2: transition between geological units

The second example is from Boulby (Fig. 3.22a) and illustrates how rockfalls propagate across the boundary between geological units in the cliff. The first example (Fig. 3.29a) shows rockfalls propagating from the mudstone at the cliff toe into the shale above, and the second example (Fig. 3.29b) shows rockfall propagating from the shale into the stronger siltstone above. The two examples are at different heights on the cliff and separated 15.5 m apart across the cliff.

The first example shows a rockfall that has developed along the mudstone/shale boundary in June 2012 (Fig. 3.29a). Additional rockfalls initiate below the June 2012 rockfall in the mudstone, eventually propagating upwards and triggering a larger failure in the shale which coalesces with the initial failure (December 2012, Fig. 3.29a). This sequence of events can also be identified in a profile taken through the cliff (Fig. 3.30a) through the area shown in Figure 3.29. The final profile, taken in December 2012 shows a large rockfall occurring in the sandstone directly above the failure in the shale and in the same survey epoch, implying that the two rockfalls could be contemporaneous.

The second example shows the development of a rockfall across the shale/siltstone boundary (Fig. 3.29b). In this example, rockfalls are not observed to develop directly along the bedding plane. Instead, a series of smaller rockfall are observed to develop in the surrounding area both in the shale and siltstone (Fig. 3.29b, 1^{st} – 5^{th} image). In December 2012 (Fig. 3.29b, 6^{th} image), the smaller rockfalls appear to have destabilised the rock mass around the shale/siltstone boundary, allowing a larger rockfall occurred across the two geological units. The sequence of events can be seen in the profiles of the cliff (Fig. 3.30b) taken through the area depicted in Figure 3.29b. Again, in the final profile the large rockfall can be observed in the sandstone directly above (Fig. 3.30b, profile 6).

Both examples demonstrate the development of smaller failures around the boundaries between geological units, which often provide conditions for a larger failure to then cross this boundary, allowing rockfalls to propagate upwards. These examples have also illustrated potential connections between the base and the top of the cliff, as suggested by the apparently coincident timing of rockfalls at different elevations within the same profile (Fig. 3.30a and b, profile 6), possibly occurring as a result of tensile cracks that are commonly found towards the crest of steep cliffs as a result of unloading (Young and Ashford, 2008).

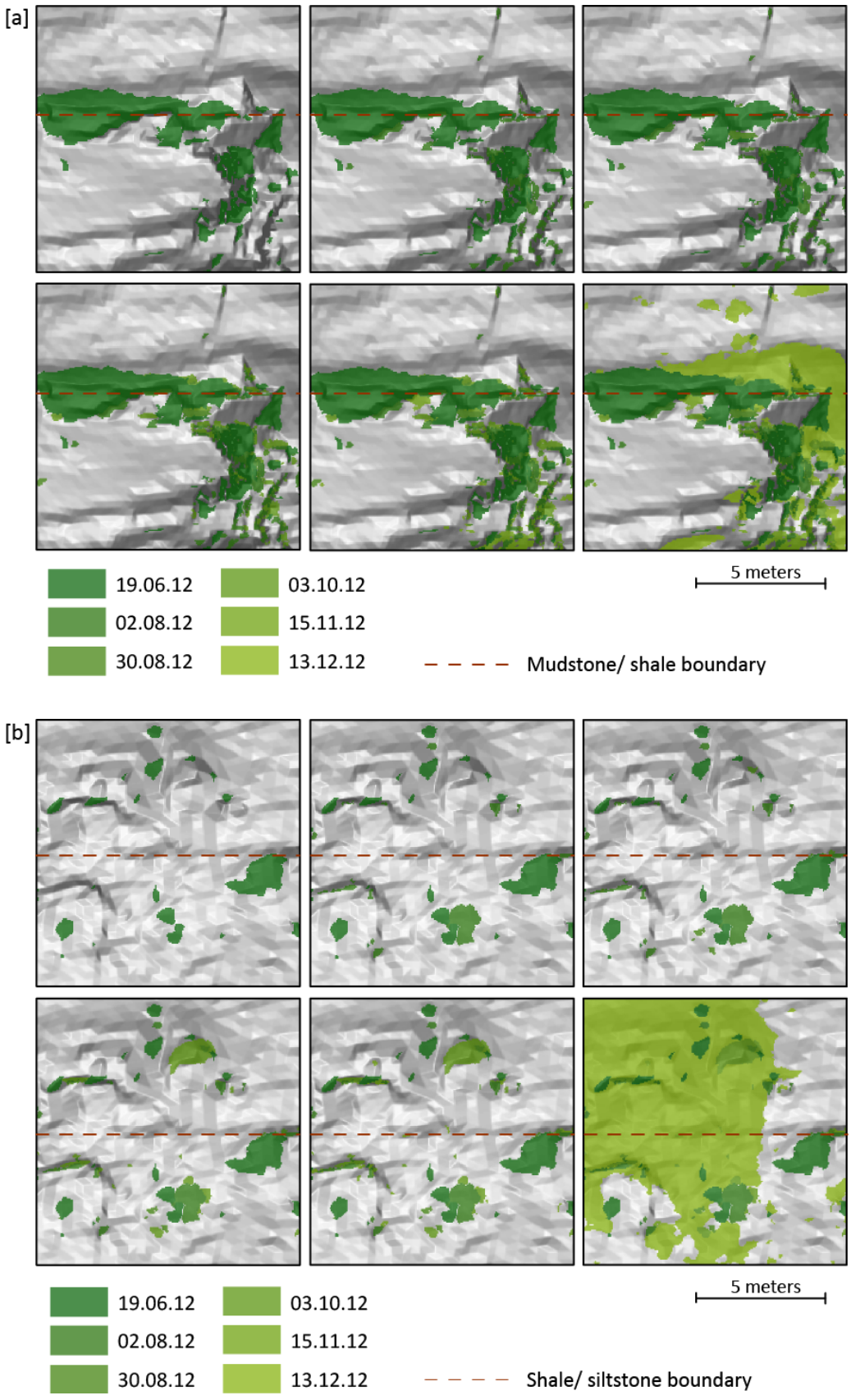

Figure 3.29: Sequential images (top left, row by row, to bottom right) taken from Boulby, illustrating: [a] The transition from mudstone to shale; [b] The transition from shale to siltstone. Rockfall polygons are overlaid on a DEM of the cliff face. Profiles of each image are shown in Fig. 3.27a and b.

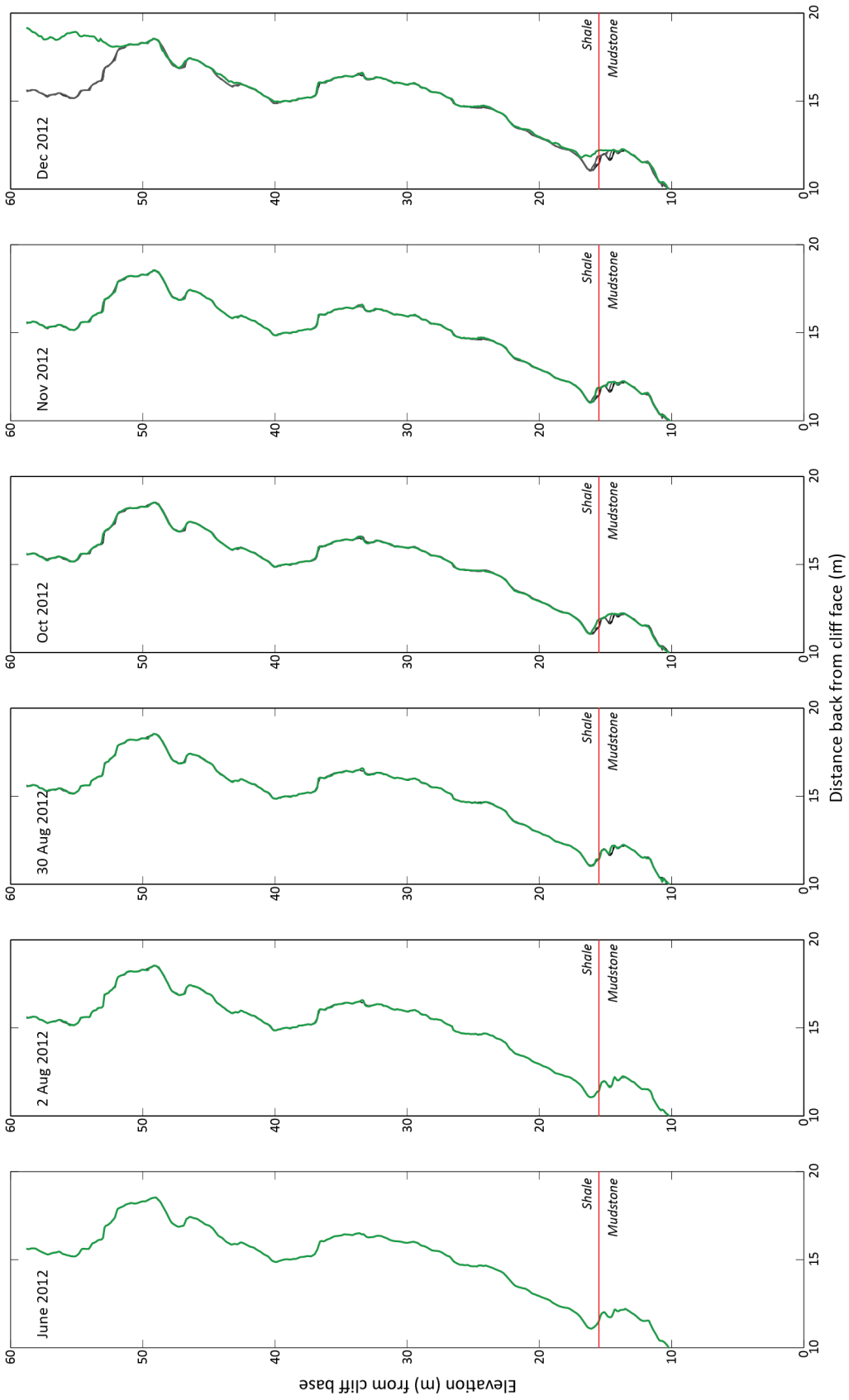
[a]
Elevation (m) from cliff base
Distance back from cliff face (m)
June 2012
2 Aug 2012
30 Aug 2012
Oct 2012
Nov 2012
Dec 2012
Shale
Mudstone
0
10
20
30
40
50
60
10
15
20

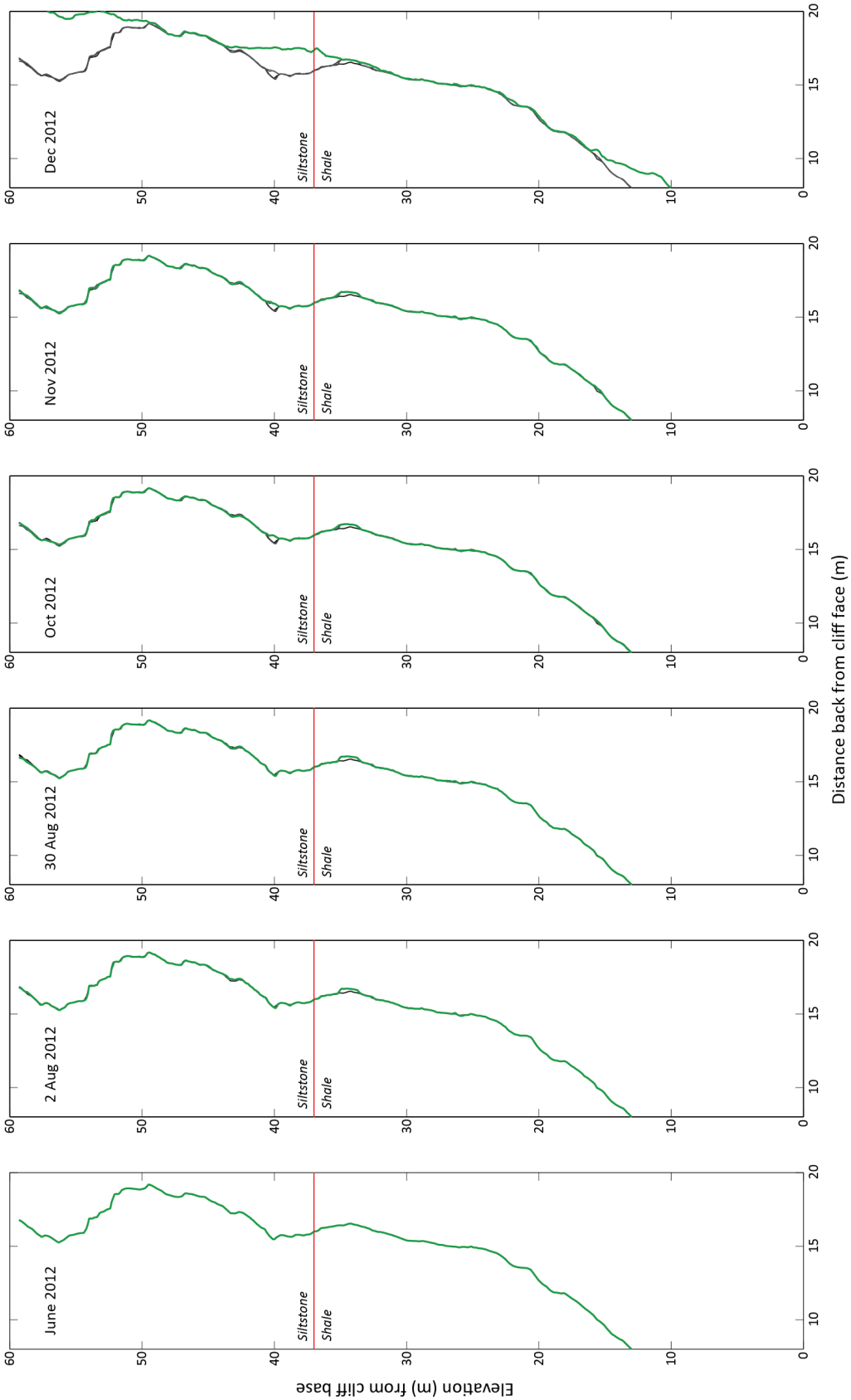

Figure 3.30: Profiles of the cliff surface taken through the area shown in Fig. 3.29 for the entire cliff height: [a] Mudstone to shale (Fig. 3.29a), [b] Shale to siltstone (Fig. 3.29b). In each plot the newest profile is shown in green and previous profiles in black – grey, where darker colours are older profiles. The geological boundaries are depicted by the red line. The distance back from the cliff face (x-axis) is measured from the most prominent point on the cliff surface.

3.4.5.3 Rockfall evolution 3: lateral propagation of rockfall

Rockfalls are observed to propagate across the cliff face, coalescing through time, as shown in Figure 3.22 and in many examples within the literature such as Stock *et al.* (2012, Fig. 7, p.551). The third rockfall evolution example illustrates the lateral propagation of rockfalls at Section 2 (Fig. 3.22c). The first example illustrates how rockfalls coalesce in the siltstone. Figure 3.31 shows rockfalls initiating in the siltstone and sandstone layers in close proximity to one another (Fig 3.31: Aug 2012, Nov 2012). Over the next five months these rockfalls begin to propagate outward and upward (Dec 2012, Apr 2013). In the final two images showing rockfalls from December 2013 and February 2014, additional rockfalls occur in between the existing rockfalls, bridging the gaps between them and generating a larger total failed area.

The second example demonstrates lateral propagation of rockfalls of varying sizes within the siltstone layer (Fig. 3.32). In the centre of the images in Figure 3.32, rockfalls ranging from 20 m^2 – 68 m^2 surface area propagate laterally from November 2012 to February 2013. In the top right of the images the same pattern of behaviour is displayed by rockfalls an order of magnitude smaller (0.3 m^2 – 4.8 m^2 surface area). In both cases there is significant overlap between the rockfalls and the time between contiguous rockfalls is approximately one month, however as this is the resolution of the monitoring data there may be an issue of superimposition, where multiple failures in close proximity may be observed as one failure (Barlow *et al.,* 2012). It is probable that some of the rockfalls identified as individual events are in fact the sum of smaller failures, although this is yet to be shown with monitoring at a temporal frequency greater than one month. Thus, this leads to the assumption that the spatial proximity and temporal frequency of propagating rockfalls is at, or above, the spatial and temporal resolution of the data presented here.

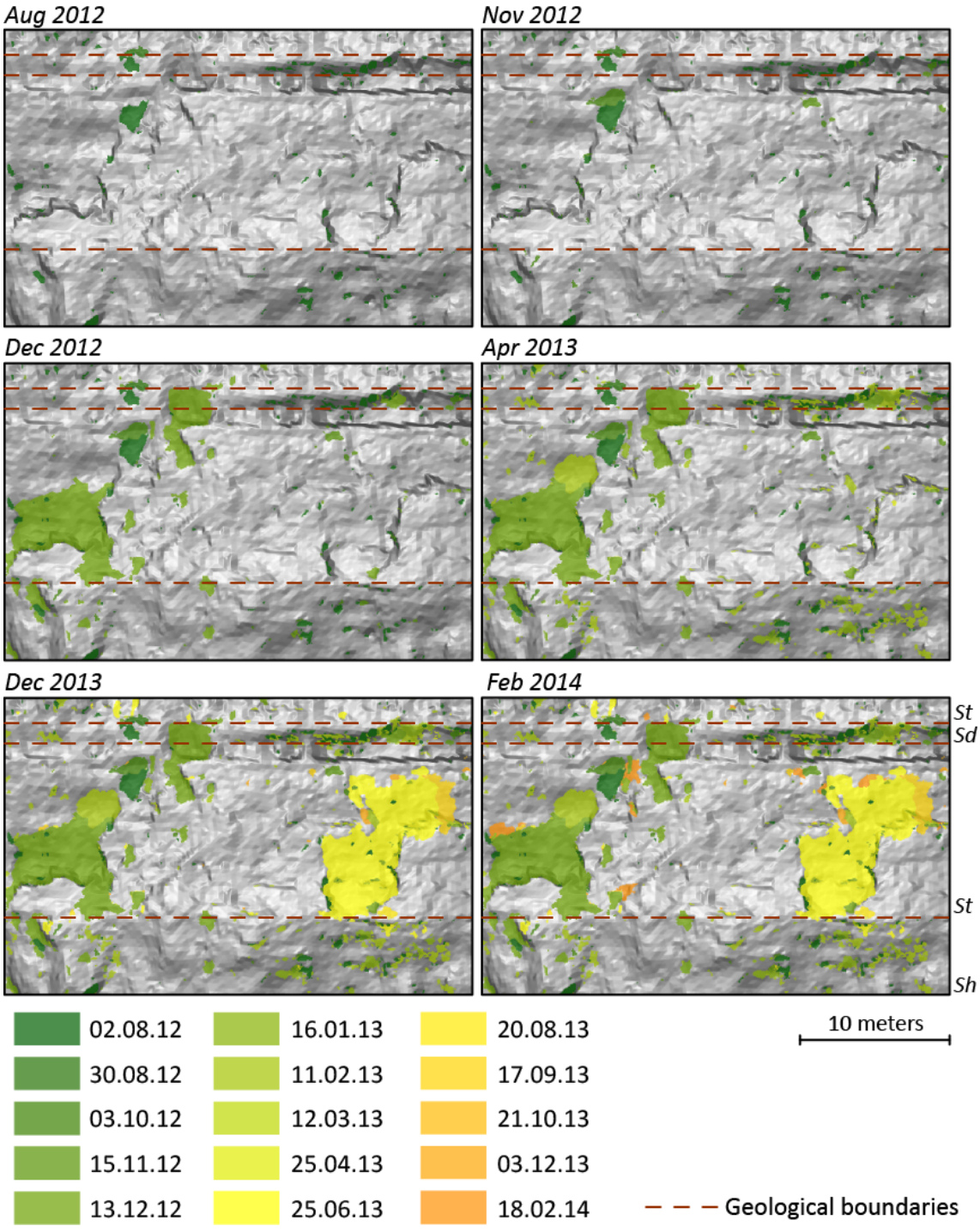

Figure 3.31: Sequential images of rockfall propagation and bridging of rockfalls at Section 2 (left hand side of the cliff) from Aug 2012 – Feb 2014. Rockfalls initiate in both the siltstone and sandstone and sequential rockfalls coalesce, bridging the original rockfalls. The different geological layers are denoted on the bottom image: Sh = shale; St = siltstone; Sd = sandstone. Rockfall polygons have been overlaid on a DEM of the cliff face.

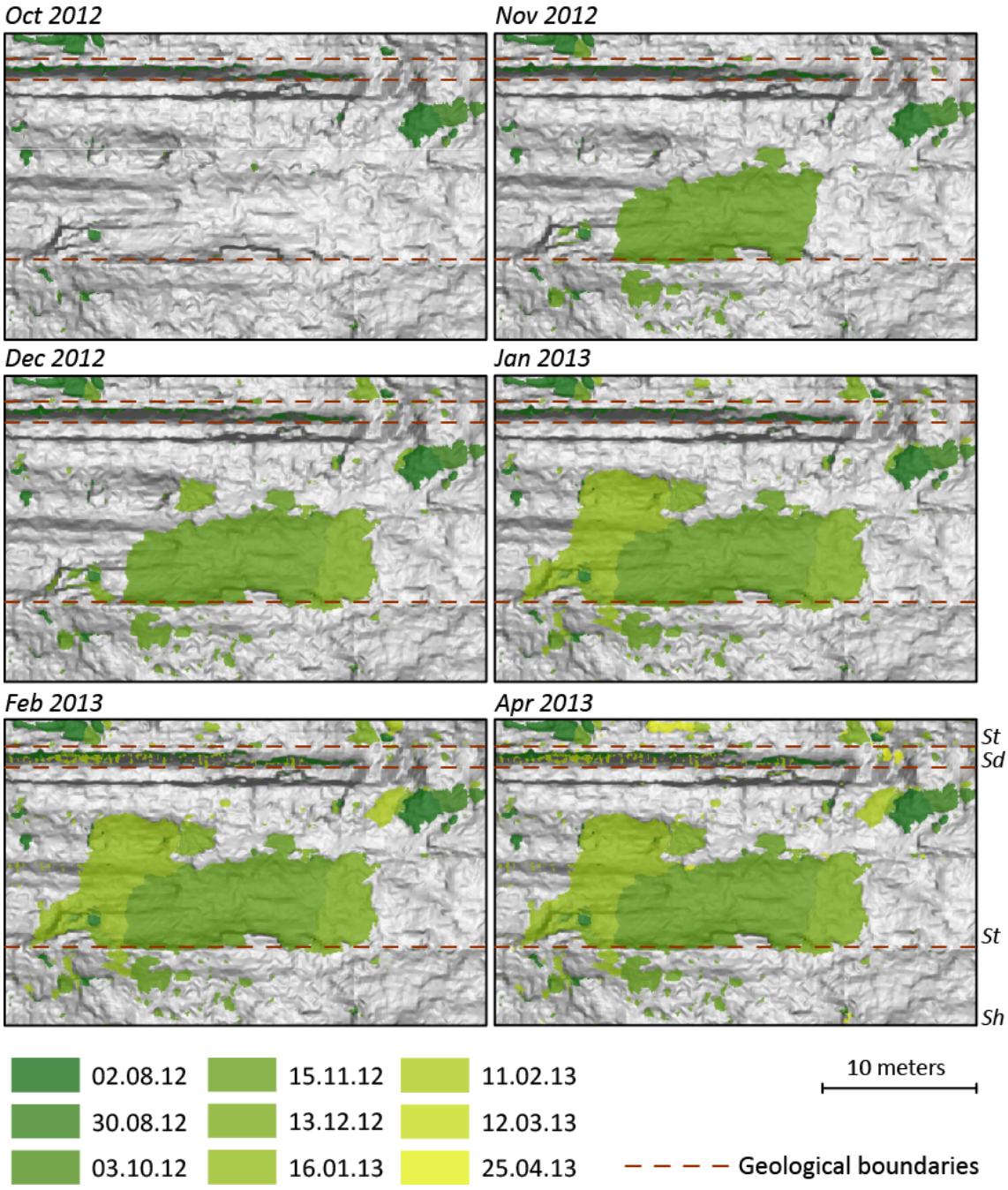

Figure 3.32: Sequential images of lateral rockfall propagation at Section 2 (right hand side of the cliff) from Aug 2012 – Apr 2013. Similar behaviour is seen in both larger and smaller rockfalls. The different geological layers are denoted on the bottom image: Sh = shale; St = siltstone; Sd = sandstone. Rockfall polygons have been overlaid on a DEM of the cliff face.

3.4.5.4 Rockfall evolution 4: Failure footprint – small pre-cursors to larger failures

The fourth example is taken from Boulby (Fig. 3.22a) and illustrates the development of a failure *footprint* in the mudstone layer, whereby small failures delineate the *footprint* (surface area) of a subsequent, larger failure. Other studies of failure in hard rock cliffs have reported how larger failures are often preceded by an increase in rockfall activity in the same area of the cliff (Rosser *et al.,* 2007a; Oppikofer *et al.,* 2008; Abellán *et al.,* 2010), illustrating that precursory failures often fall within the *footprint* of a future failure (Rosser *et al.,* 2007a). The example given here shows a range of small failures (< 1 m^2 surface area) occurring over fifteen months from August 2012 to November 2013 (Fig. 3.33, images 1-14). These failures delineate the area where a larger failure (91.5 m^2 surface area) then occurs in December 2013 (Fig. 3.33, image 15).

A profile of the cliff taken through the middle of the area shown in Figure 3.33 is shown in Figure 3.34. The rockfalls that occurred directly below the larger December 2013 rockfall can be seen developing from October 2012 onwards, however the rockfalls directly above are too shallow to detect in the profile view.

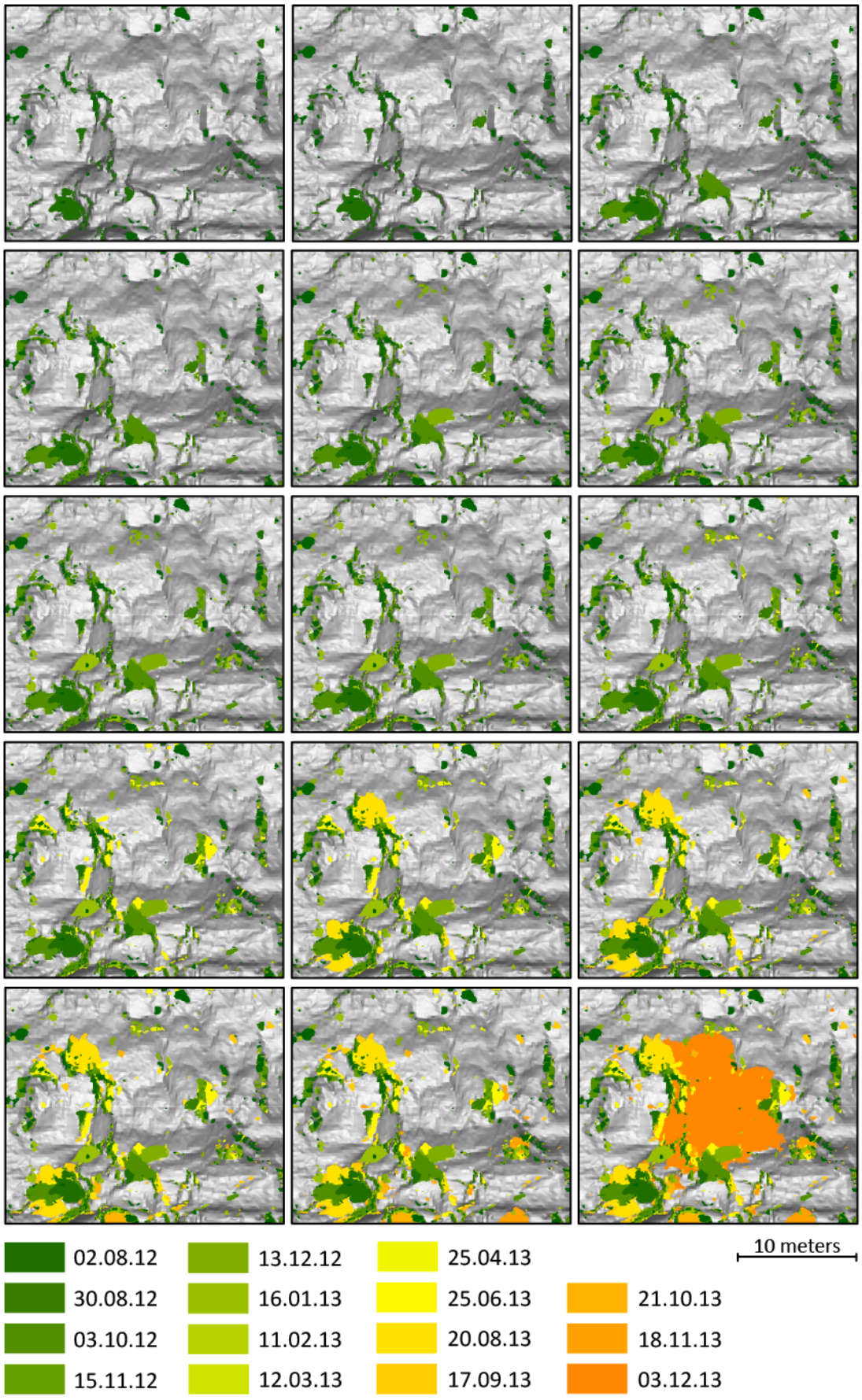

Figure 3.33: Sequential images (top left, row by row, to bottom right) of rockfall at Boulby (near cliff toe) from Aug 2012 – Dec 2013. Smaller rockfalls are observed to delineate the footprint of the larger rockfall seen in the final image. Rockfall polygons are overlaid on a DEM of the cliff face.

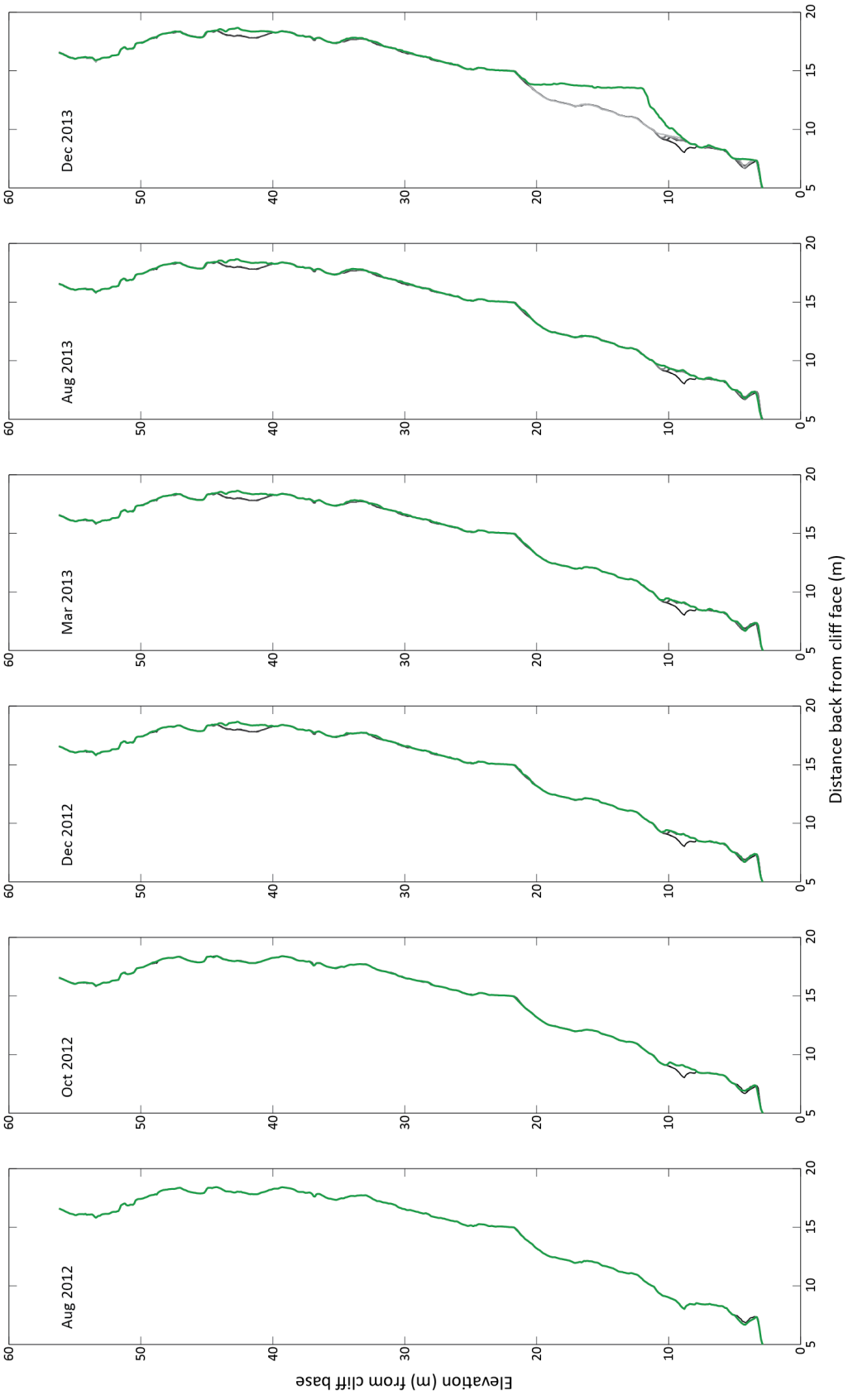

Figure 3.34: Profiles of the cliff surface taken through the area shown in Fig. 3.33 for the entire cliff height. In each plot the newest profile is shown in green and previous profiles in black – grey, where darker colours are older profiles. The distance back from the cliff face (x-axis) is measured from the most prominent point on the cliff surface.

3.4.5.5 Rockfall evolution 5: Arch development (around the periphery of failed zones)

Arch features are observed to develop on hard rock cliffs at a variety of scales (Fig. 3.35). The final case study provides an example of an arch developing around the periphery of a failed zone at Cowbar (Fig. 3.22d). The images in Figure 3.36 show the sequential development of a large arch feature over the two years of monitoring, from June 2012 to May 2014. Rockfalls initiate towards the cliff toe (October 2012) and towards the top of the arch (January 2013). These rockfalls then propagate upwards and outwards, across the cliff face, eventually coalescing with rockfalls to the right of the images shown (Fig 3.36, April 2014). As a result of the final arch feature that the rockfall scars delineate, an overhang is left above. These features can be seen in other locations along the N Yorkshire coastline (Fig. 3.36a), where over time smaller arches are seen to coalesce into larger arches. Arch features have also been observed in different environmental and geological settings, such as the Royal Arches wall in Yosemite National Park (Fig. 3.36b), where large failures occur along the face parallel exfoliation joints exposing arches of a range of sizes.

Upward and lateral propagation of rockfalls has been illustrated through these examples of rockfall evolution, showing that rockfalls are able to propagate across a transition zone in the cliff over time as a series of smaller rockfalls precede a larger rockfall that crosses the transition boundary. From the observations made in these case studies, smaller rockfalls appear to indicate that time-dependent weakening is occurring and therefore smaller rockfalls could be considered indicative of the location and timing of larger rockfalls. In order to further investigate the patterns of behaviour that have been identified, the spatial and temporal analysis of the two year rockfall dataset will be used to examine the temporal pattern in rockfall behaviour; the influence of surface morphology; the clustering of rockfalls in time and space; and the directionality of rockfall propagation. In doing so, the questions outlined at the beginning of this chapter will be addressed

[a]

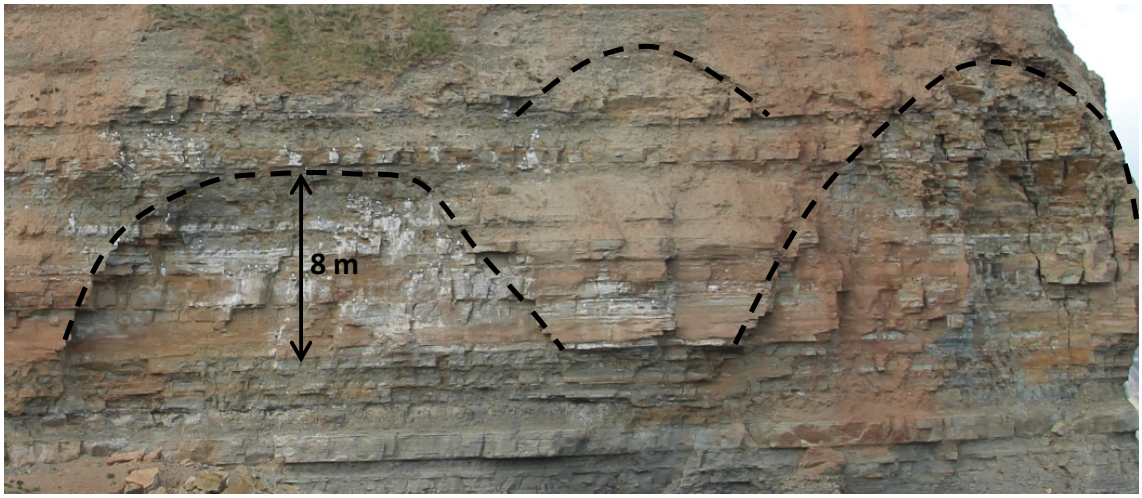

[b]

Figure 3.35: Examples of arch features that develop in hard rock cliffs: [a] At Cowbar, N Yorkshire coast; [b] Royal Arches, Yosemite National Park (c. 430 m high).

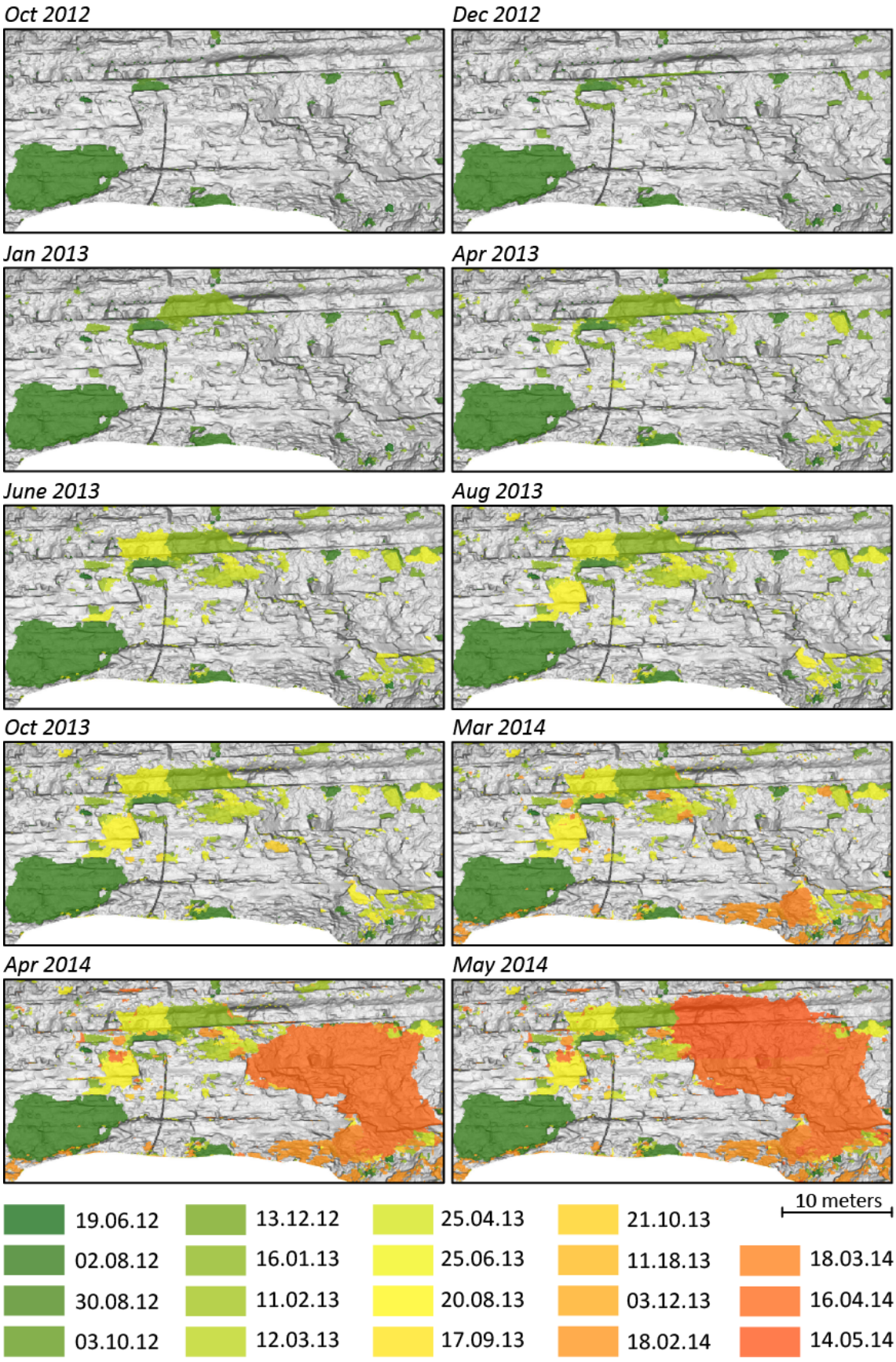

Figure 3.36: Sequential images of arch feature development at Cowbar in the shale, from June 2012 – May 2014. Rockfalls propagate across the cliff face from left to right, eventually coalescing with rockfalls to the right of the image (Apr 2014), leaving an overhanging arch feature above these rockfall scars.

3.4.6 Temporal behaviour

3.4.6.1 Time series of erosion

Surface averaged erosion through time displays a consistent pattern between each field site (Fig. 3.37). Two periods of acceleration in erosion are visible, which coincide with the winter months of the year (November – January) at each of the field sites, with the exception of Cowbar where acceleration in the rate of surface erosion is seen later, between March and April 2014. The later acceleration in surface erosion at Cowbar compared to the other field sites, suggests that site-specific internal processes, such as the speed of fracture propagation, have a significant role in driving erosion alongside external forcing related to environmental changes.

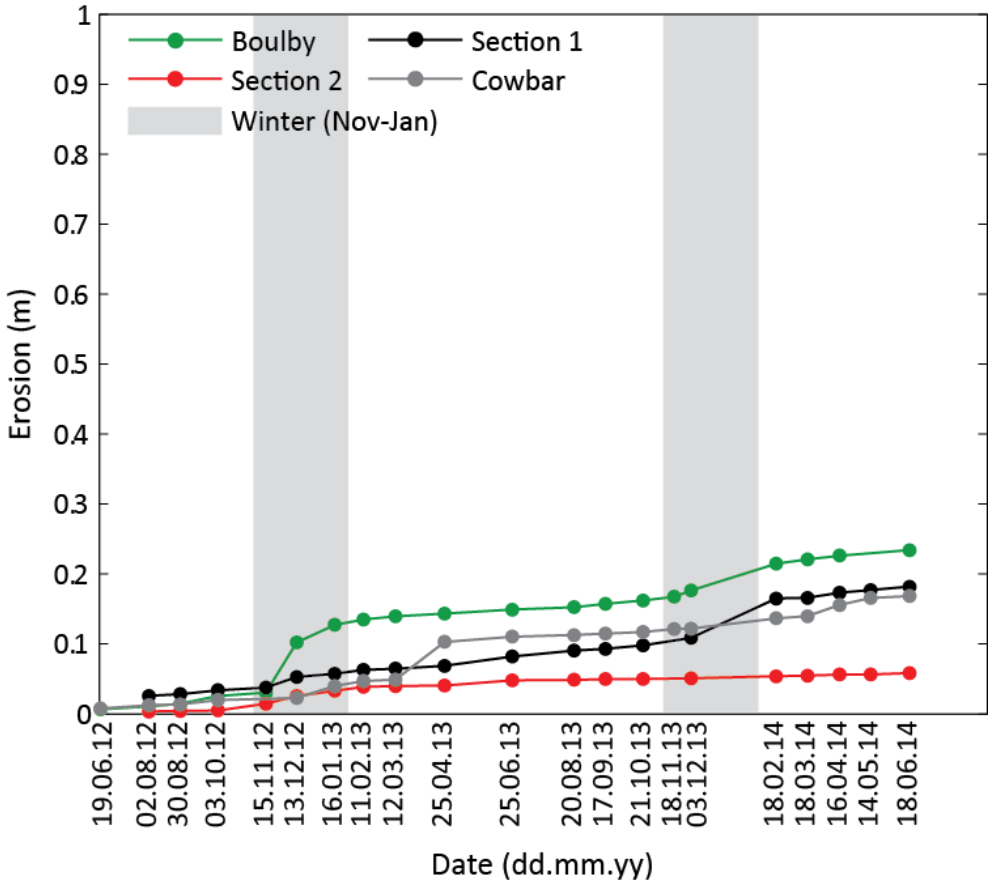

Figure 3.37: Time series of cumulative surface averaged erosion (m) (*total rockfall volume/ cliff surface area*) over the survey epoch length from June 2012 – June 2014 for Boulby, Section 1, Section 2 and Cowbar.

At each site the rate of surface averaged erosion, as presented in Figure 3.37, is variable between the different rock types in the cliff (Fig. 3.38). At each site the amount of erosion varies between layers and the amount of erosion per layer differs between sites. At Boulby the surface averaged erosion is greater than the mean in the sandstone and mudstone layers, and at Section 1 erosion is greater than the mean in the sandstone and shale layers. At both Boulby and Section 1, the mudstone, shale and siltstone show similar patterns of surface averaged erosion through time, which reflect the surface averaged erosion for the whole cliff (Fig. 3.37). Conversely, erosion within the sandstone layer is near stationary, punctuated by a large rockfall (702 m^3 at Boulby) between November and December 2012 (Fig. 3.38a), which achieved 87% of the total erosion in the sandstone layer at Boulby over the survey epoch. There is little distinction between the surface averaged erosion in each of the geological layers at Section 2 and the erosion in each layer is within 0.05 m of the mean. At Cowbar the surface averaged erosion in the shale layer is greater than the surface averaged erosion of the whole cliff and both display a similar pattern through time. This suggests that the erosion in the shale is dominating the erosion of the cliff for this site and time period.

[a]

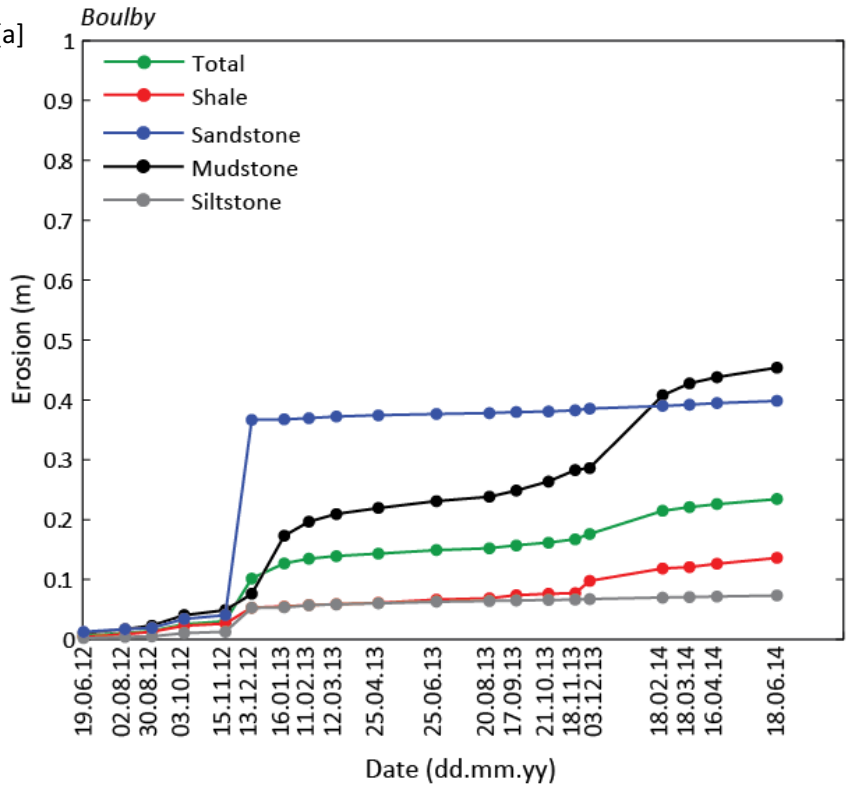
Boulby
Total
Shale
Sandstone
Mudstone
Siltstone
Erosion (m)
0
0.1
0.2
0.3
0.4
0.5
0.6
0.7
0.8
0.9
1
19.06.12
02.08.12
30.08.12
03.10.12
15.11.12
13.12.12
16.01.13
11.02.13
12.03.13
25.04.13
25.06.13
20.08.13
17.09.13
21.10.13
18.11.13
03.12.13
18.02.14
18.03.14
16.04.14
18.06.14
Date (dd.mm.yy)

[b]

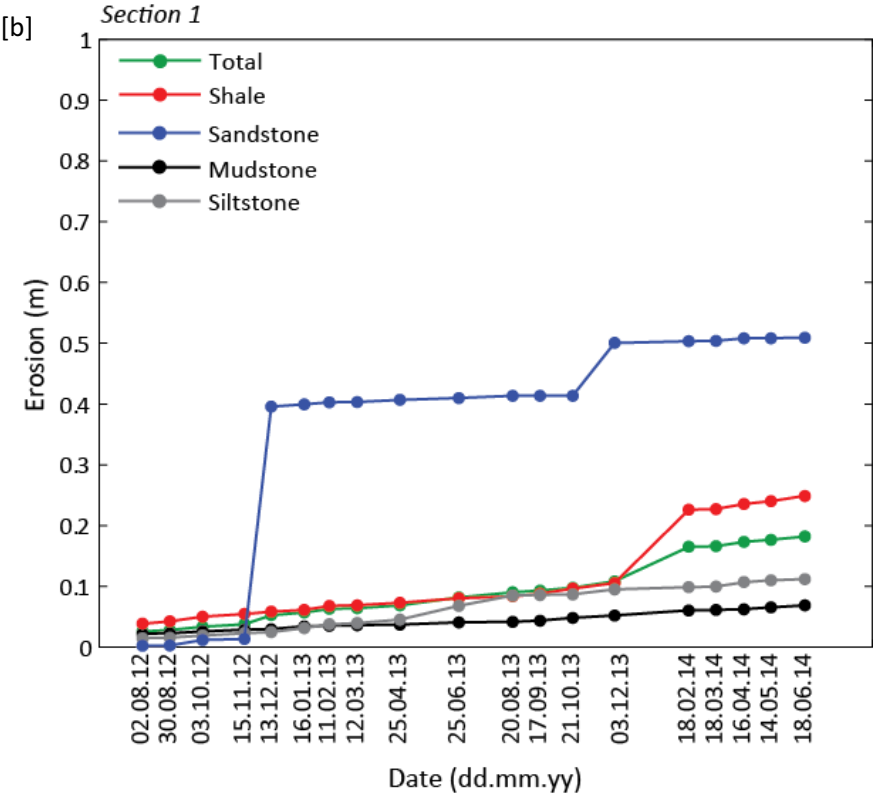
Section 1
Total
Shale
Sandstone
Mudstone
Siltstone
Erosion (m)
0
0.1
0.2
0.3
0.4
0.5
0.6
0.7
0.8
0.9
1
02.08.12
30.08.12
03.10.12
15.11.12
13.12.12
16.01.13
11.02.13
12.03.13
25.04.13
25.06.13
20.08.13
17.09.13
21.10.13
03.12.13
18.02.14
18.03.14
16.04.14
14.05.14
18.06.14
Date (dd.mm.yy)

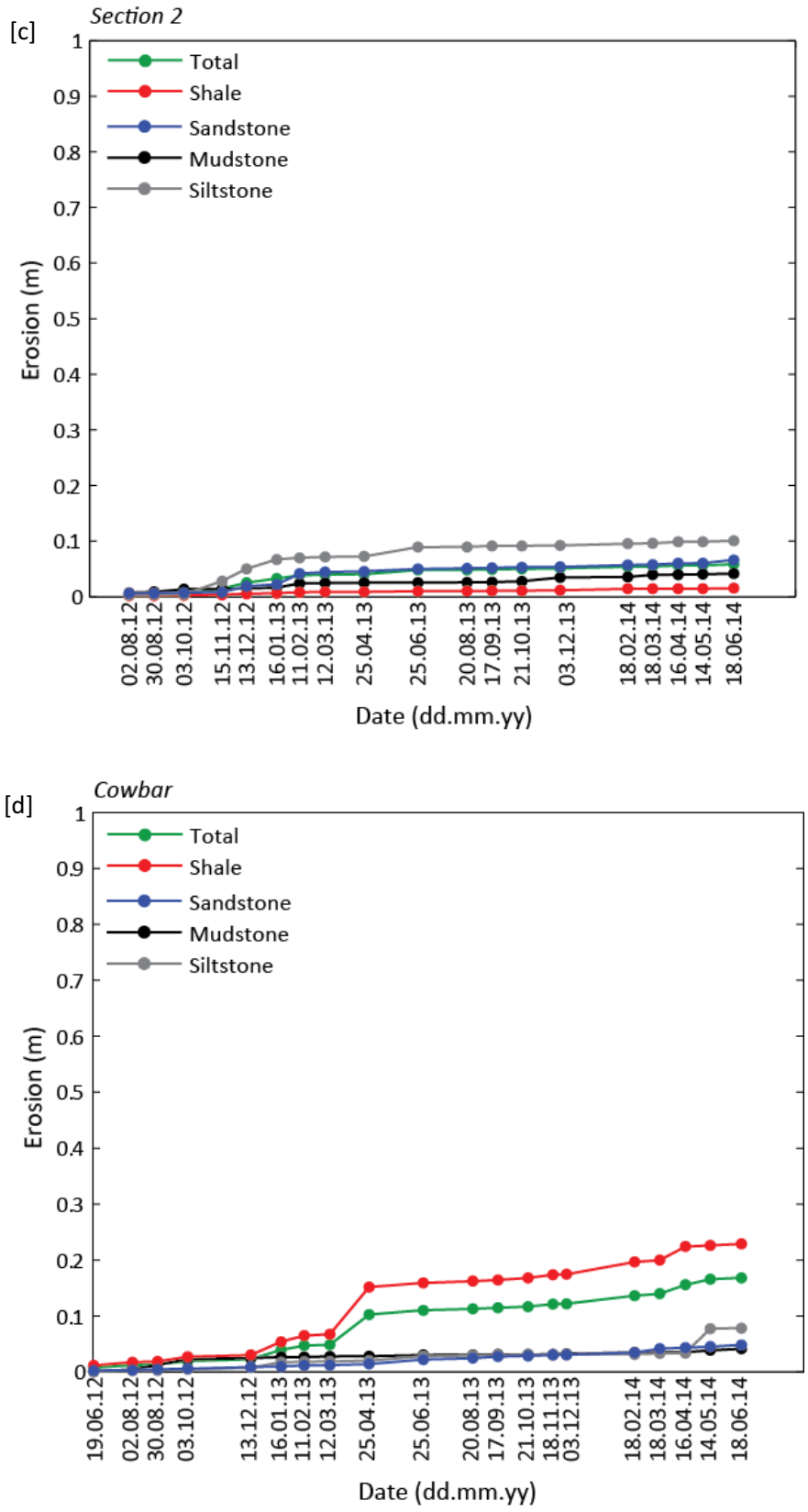

Figure 3.38: Time series of cumulative surface averaged erosion (m) over the survey epoch length from June 2012 – June 2014 for each geological layer at [a] Boulby, [b] Section 1, [c] Section 2 and [d] Cowbar. The green line is the averaged erosion for the whole cliff (Fig. 3.37), also referred to as the mean.

In addition to the variation seen between the geological layers, variation across the cliff face is observed (Fig. 3.22). In order to illustrate how erosion varies across the cliff face and to explore temporal behaviour at a different spatial scale, smaller areas of the cliff at Boulby were analysed. Boulby was chosen for this analysis as the entire stretch of the cliff face at this site is viewed normal to the scanner, avoiding any oblique angles that can result in areas of shadowing or obscuring. This avoids any potential uncertainty in measurements of depth as suggested in Section 3.2.2.1, and ensures minimal artificial differences between the smaller areas investigated. Four areas of interest (AOIs) were selected along the cliff at Boulby, to represent areas of different rockfall density, as illustrated in Figure 3.39. The data shown in Figure 3.40 represents erosion by the rockfalls extracted from each of these AOIs and highlights the significant spatial variability in surface averaged erosion across the cliff face. Within AOI 4 (the right hand side of the cliff) 1.05 m of erosion is achieved over the two years of monitoring, whilst less than 0.3 m of erosion is achieved in the other three AOIs. The changes in surface averaged erosion with time in each AOI, is similar to the surface averaged erosion over the entire cliff face (Fig. 3.37). Both periods of acceleration seen in Figure 3.37 can be identified in Figure 3.40. The first period of acceleration is seen in AOI 4 and the second period of acceleration is seen in AOIs 1-3.

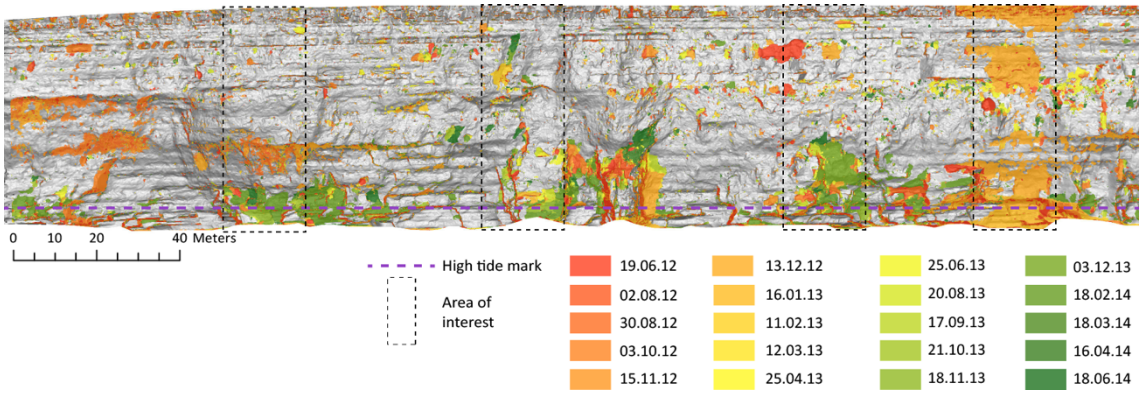

Figure 3.39: Location of AOIs along the cliff at Boulby, outlined by the black dashed line. AOIs are numbered 1-4 moving left to right along the cliff. The base image used is the rockfall polygons colour coded by date and overlaid on a DEM of the cliff (Fig. 3.22).

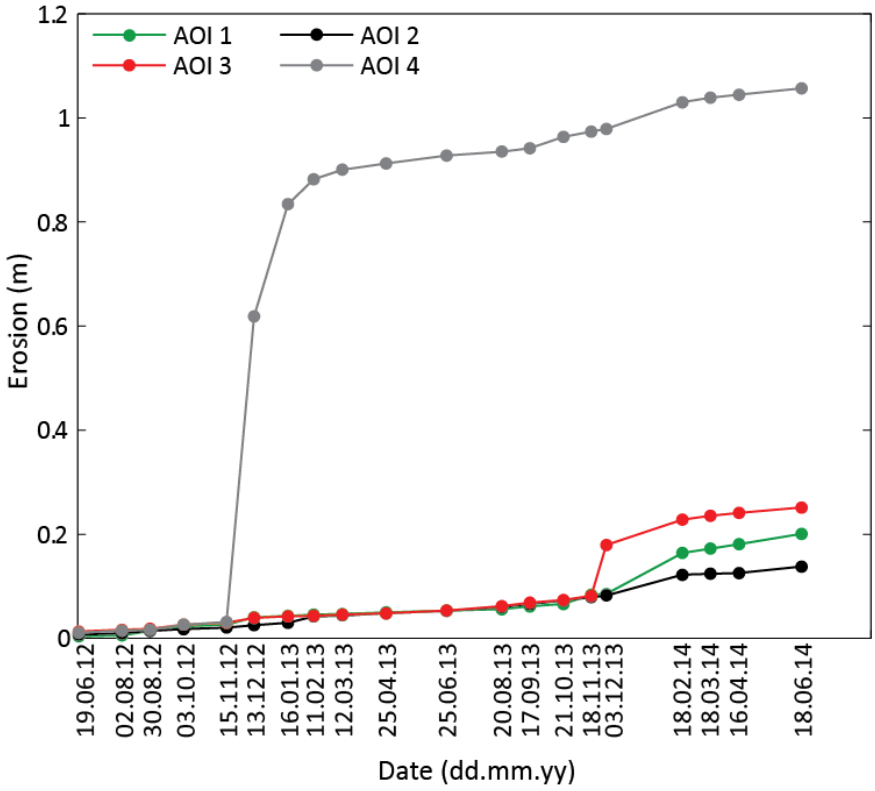

Figure 3.40: Time series of surface averaged erosion (m) over the survey epoch length from June 2012 – June 2014 for the four AOIs on the cliff at Boulby (Fig. 3.39).

The temporal behaviour in erosion that has been presented so far has used the entire rockfall inventory but subdivided for a range of different areas. The magnitude-frequency data presented in Figure 3.23, illustrates the negative relationship between rockfall volume and frequency density. The small rockfalls (< 0.1 m^3) contribute to 12% of the erosion volumetrically, which can be modelled from the magnitude-frequency curve, as per Barlow *et al.* (2012). However, the magnitude-frequency curve does not show the contribution to erosion from different rockfall sizes through time. In order to examine how the contribution of different rockfall sizes changes through time, the surface averaged erosion was calculated for subsets of the rockfall databases, grouped by rockfall size (surface area). Figure 3.39 presents plots of cumulative erosion at each site for rockfalls in different size categories. The temporal pattern for each size range is very similar and compares to the plot of surface averaged erosion for all rockfalls at each site (Fig. 3.35). The plot for all rockfalls ≥ 1 m^2, shows that the larger rockfalls are contributing the majority of the erosion achieved and dominating the temporal pattern that can be seen. Presenting the data in this way suggests that whilst smaller rockfalls (< 1 m^2) add to this trend, increasing the overall amount of erosion, the rockfalls smaller than 1 m^2 do not alter the overall behaviour observed.

[a]

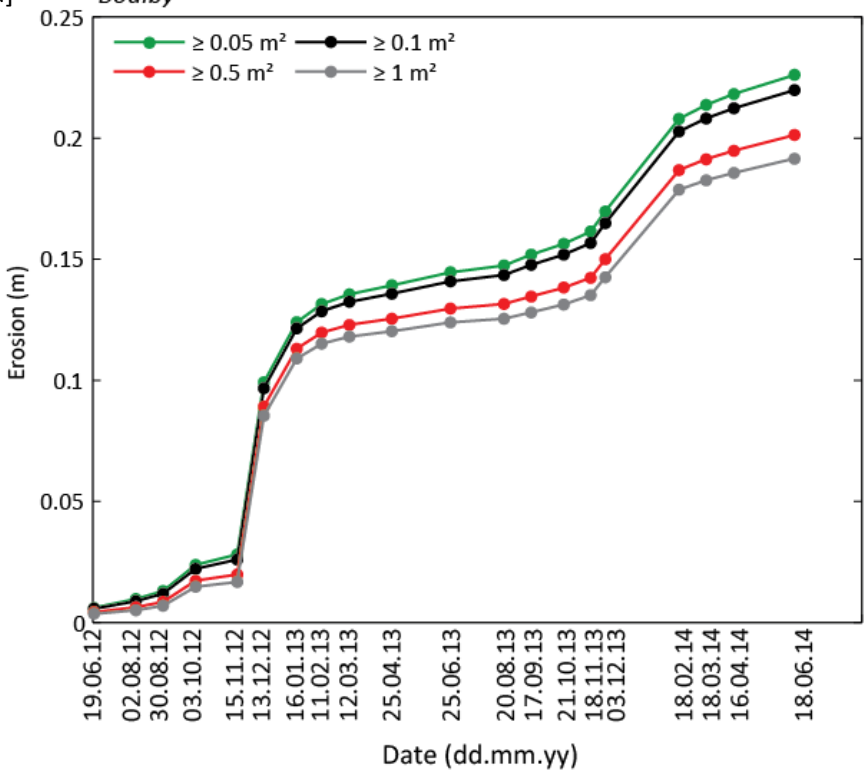
Boulby
≥ 0.05 m²
≥ 0.1 m²
≥ 0.5 m²
≥ 1 m²
Erosion (m)
0.25
0.2
0.15
0.1
0.05
0
19.06.12
02.08.12
30.08.12
03.10.12
15.11.12
13.12.12
16.01.13
11.02.13
12.03.13
25.04.13
25.06.13
20.08.13
17.09.13
21.10.13
18.11.13
03.12.13
18.02.14
18.03.14
16.04.14
18.06.14
Date (dd.mm.yy)

[b]

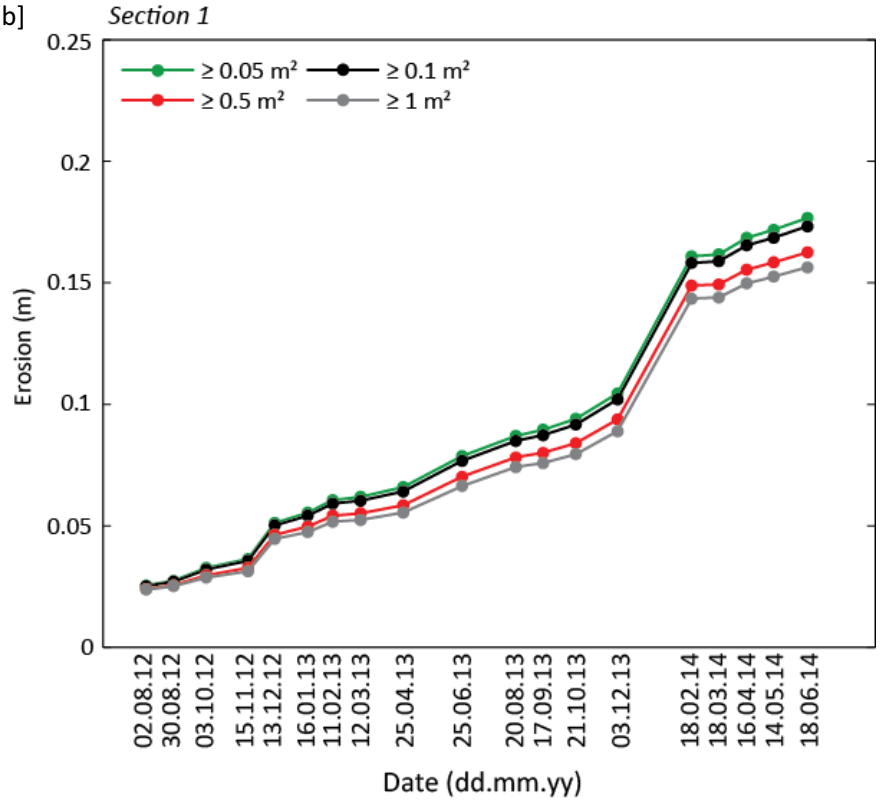
Section 1
≥ 0.05 m²
≥ 0.1 m²
≥ 0.5 m²
≥ 1 m²
Erosion (m)
0.25
0.2
0.15
0.1
0.05
0
02.08.12
30.08.12
03.10.12
15.11.12
13.12.12
16.01.13
11.02.13
12.03.13
25.04.13
25.06.13
20.08.13
17.09.13
21.10.13
03.12.13
18.02.14
18.03.14
16.04.14
14.05.14
18.06.14
Date (dd.mm.yy)

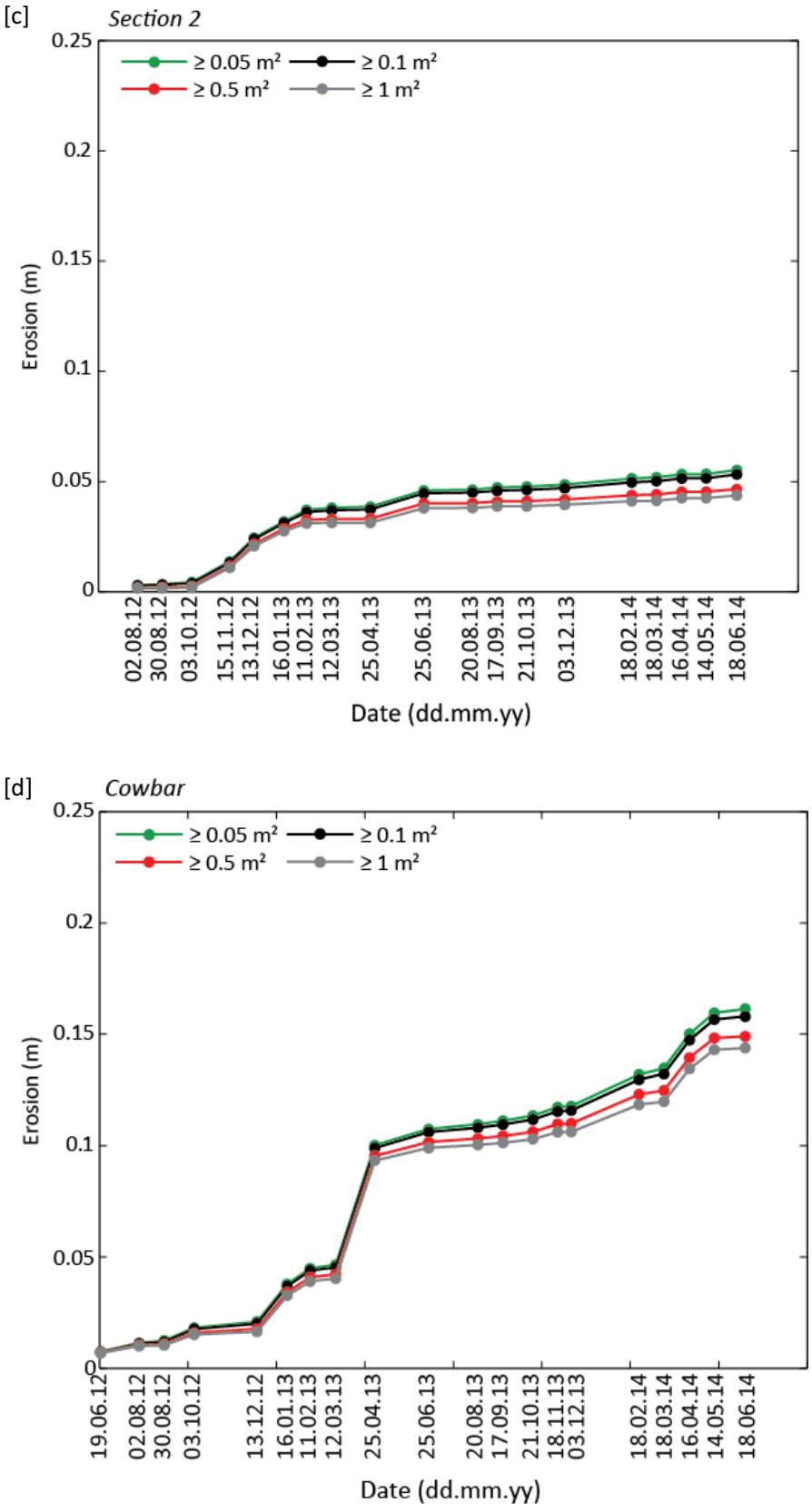

Figure 3.41: Time series of cumulative surface averaged erosion (m) over the survey epoch length from June 2012 – June 2014 for rockfalls of different sizes (as indicated in the legend) at [a] Boulby, [b] Section 1, [c] Section 2 and [d] Cowbar.

3.4.7 Influence of slope surface morphology

3.4.7.1 Rockfall distribution and local scale curvature

Slope surface morphology has been defined as the local scale curvature of the slope, calculated at the resolution of the slope face DEM (0.025 m^2 grid cell size), as described in section 3.3.1.2. Therefore, the following results and subsequent discussion of the data (Section 3.5) should be considered in the context of local slope curvature. Calculating slope curvature at a lower spatial resolution would likely produce different results but the investigation of curvature resolution is beyond the scope of this study. Here the local curvature values are used in order that the curvature data is at the resolution of the smallest failure size. Cumulative density functions (cdf) of the local scale slope curvature for all rockfall areas (pre-failure) are shown for each site in Figure 3.42. At all sites, more than 80% of the rockfalls are occurring in areas that are locally convex, as defined by a positive curvature value. As can be seen from the plots, the distribution of curvature values of rockfall locations is similar at all field sites, with a slightly higher frequency of rockfalls on the most convex parts of the slope occurring at Section 2 compared to the other sites.

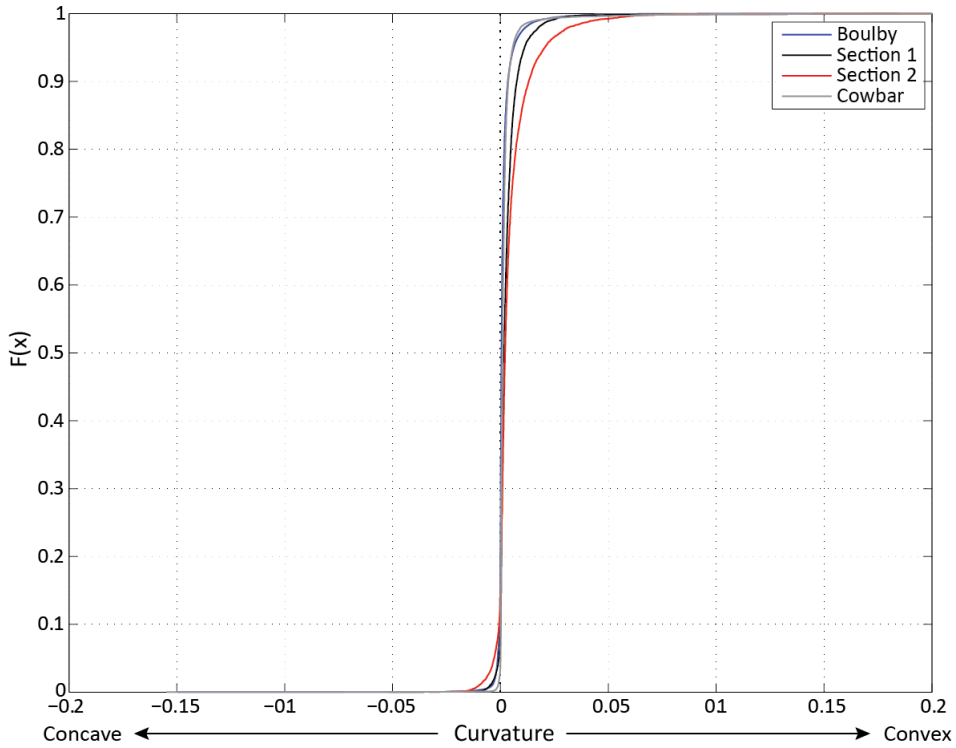

Figure 3.42: Cumulative density function (cdf) of the slope curvature (pre-failure) where rockfalls occurred. The curvature is calculated from the DEM (as described in Section 3.3). A cdf plot is shown here for each of the sites for all rockfalls that occurred from June 2012 – June 2014.

In order to assess the curvature of failed areas as compared to the overall slope morphology, the curvature values of the failed areas in the first and last monthly scan data for each site were compared with the curvature values of the whole slope for those time periods (Fig. 3.43), illustrating that rockfalls are more commonly occurring on convex areas of the slope.

Overall the cdf plots of curvature values across the whole slope show little change from June 2012 to June 2014 at all sites (Fig. 3.43). This suggests that whilst local areas of the slope are changing as a result of rockfall, the overall cliff morphology, as represented by the proportion of convex to concave areas, remains fairly consistent.

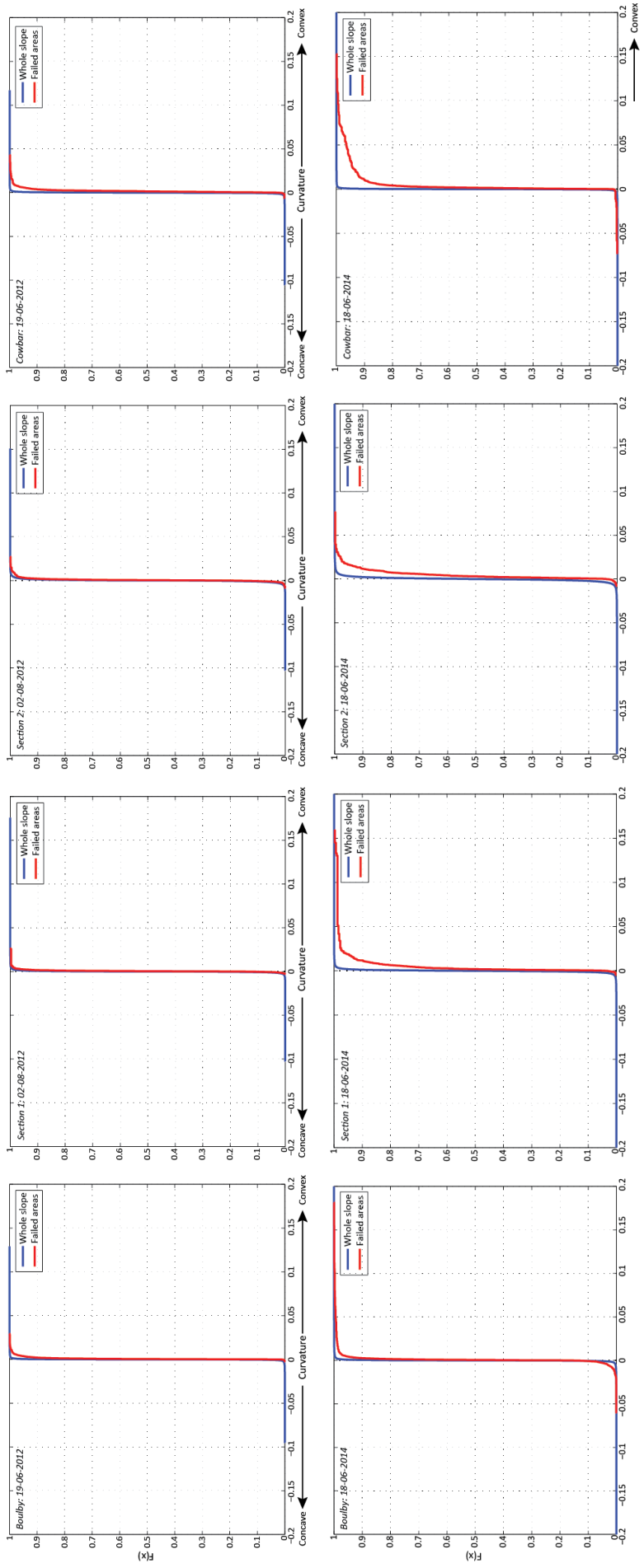

Figure 3.43: Cumulative density function (cdf) of the slope curvature for failed areas (red line) and for the whole slope (blue line), both taken from a DEM of the slope in the month preceding the rockfalls. Plots are shown for each field site from the first and final month of data collection as indicated on the plots.

3.4.7.2 Rockfall characteristics and local curvature

Having established that rockfalls more commonly occur on locally convex areas of the cliff face, the geometrical characteristics of the rockfalls – area, depth and shape – were analysed for any relationship with slope curvature, in order to determine whether the slope surface topography impacted on the rockfall characteristics as well as their location. Figure 3.44 show that rockfalls with a smaller surface area occur across the range of curvature values, with more rockfalls occurring on locally convex areas of the slope, whilst rockfalls with a greater surface area appear restricted to planar areas of the slope. This demonstrates that local curvature, at the resolution of the smallest failure size, is less important for the larger failures where it is likely that global slope curvature becomes more important. However, the local curvature does appear to influence the location of smaller rockfalls; this is particularly evident for rockfalls with a surface area < 1 m^2.

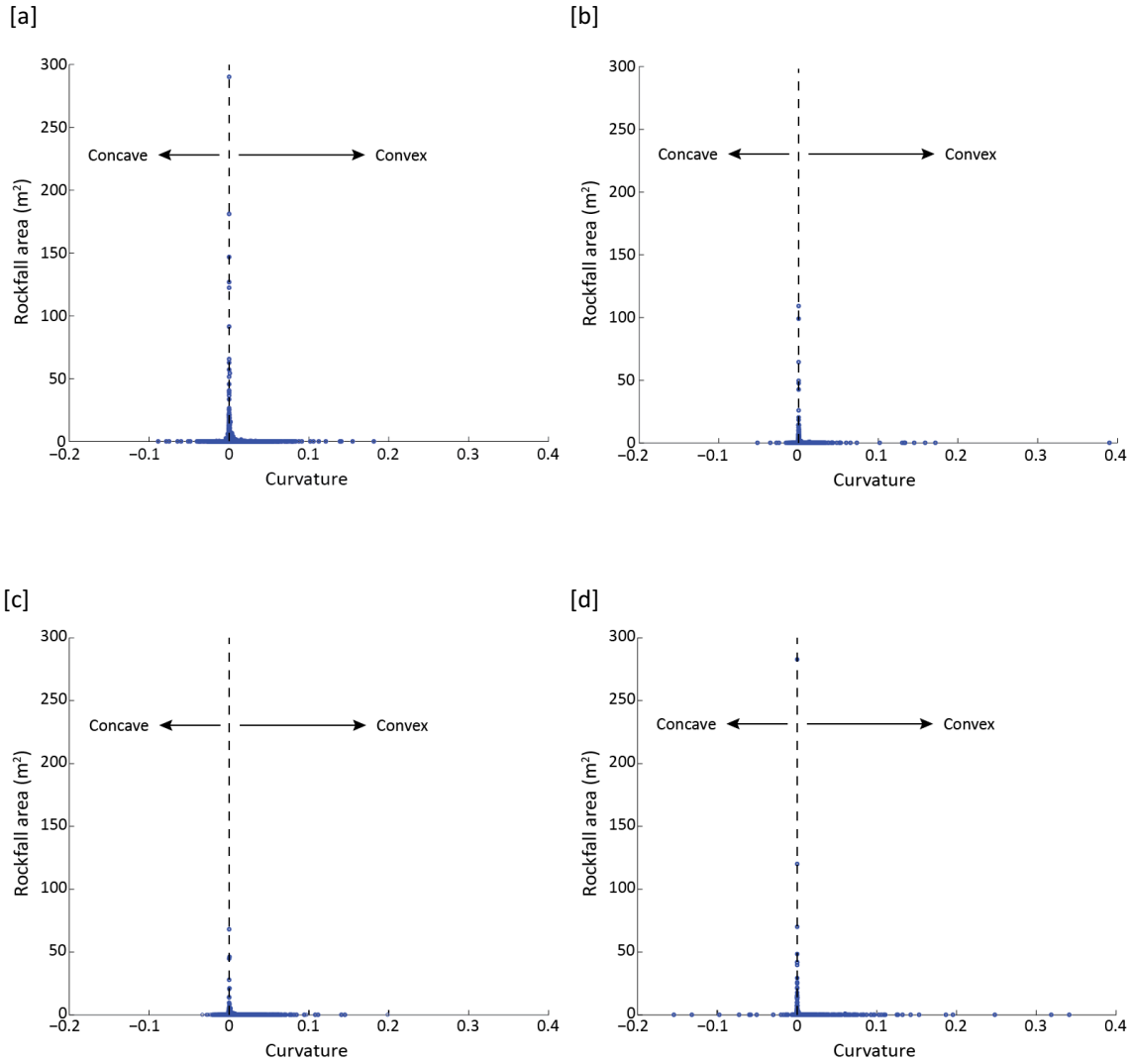

Figure 3.44: Rockfall area plotted against the pre-failure curvature values for all rockfalls that occurred at [a] Boulby, [b] Section 1, [c] Section 2 and [d] Cowbar from June 2012 – June 2014.

Figure 3.45 show that the deeper rockfalls more often occur on locally convex areas of the slope. Combined with the CDF plots of curvature values (Fig. 3.43), this suggests that not only are convex areas of the slope are more likely to fail than planar and concave areas, but also that the rockfall that occur from these areas is likely to be deeper. For example, at Boulby and Section 1 all rockfalls that occurred in areas with curvature values greater than 0.1 were more than 1 m deep. This might occur due to the higher concentration of stress in areas of local convexity (Martel, 2006), which allows a larger mass of rock to fail. Additionally, areas that are locally convex are protruding from the mean surface of the cliff and are likely to fail back to the mean surface, thereby removing a larger amount of material than areas that are already planar or concave with respect to the mean cliff surface.

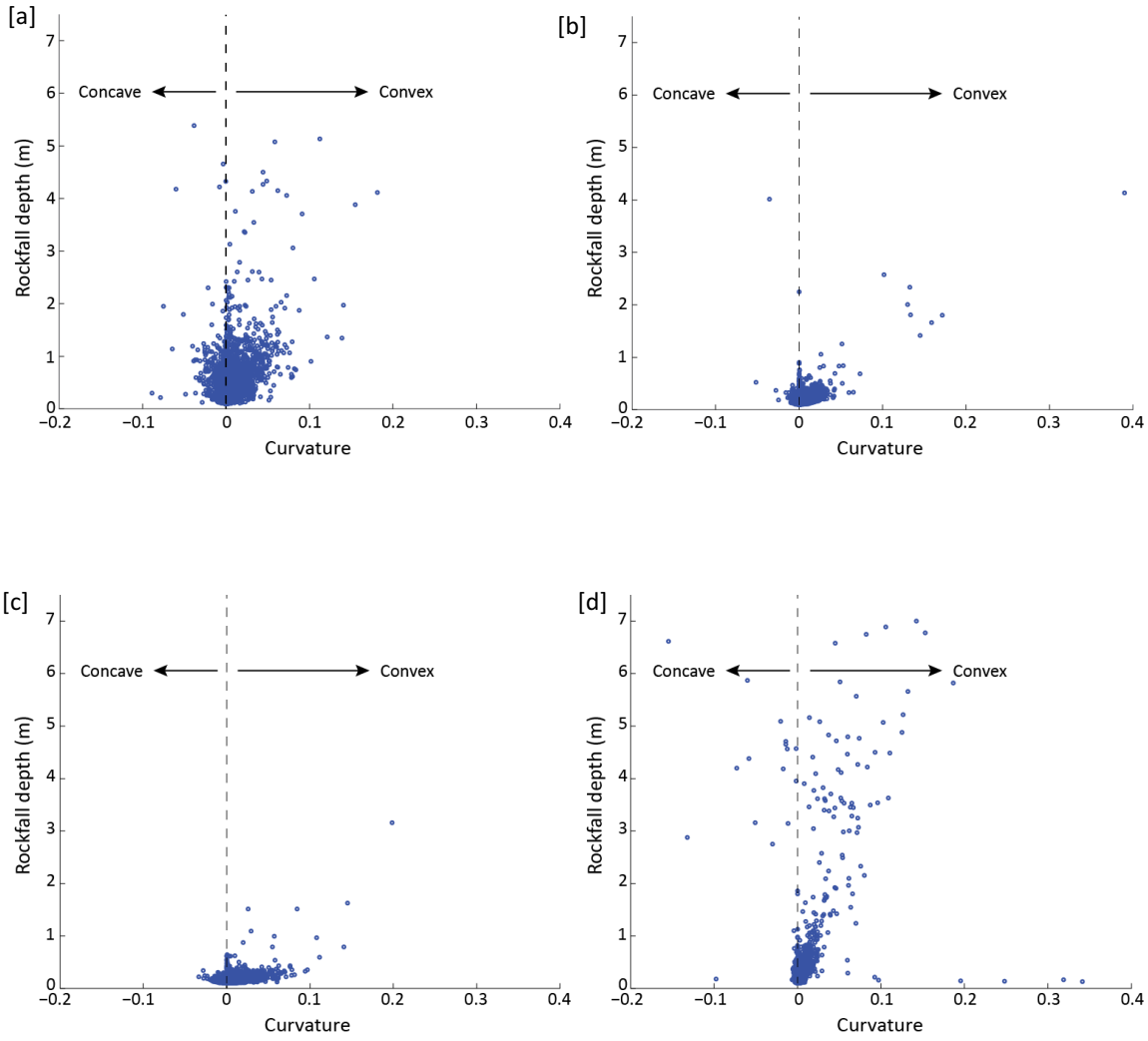

Figure 3.45: Rockfall depth plotted against the pre-failure curvature values for all rockfalls that occurred at [a] Boulby, [b] Section 1, [c] Section 2 and [d] Cowbar from June 2012 – June 2014.

As shown in Figure 3.46, no clear correlation appears between the shape of the rockfall and the local curvature of the slope at any of the sites. Thus, local curvature at the resolution of the smallest failure size, appears to have no observable influence on the shape of the rockfall.

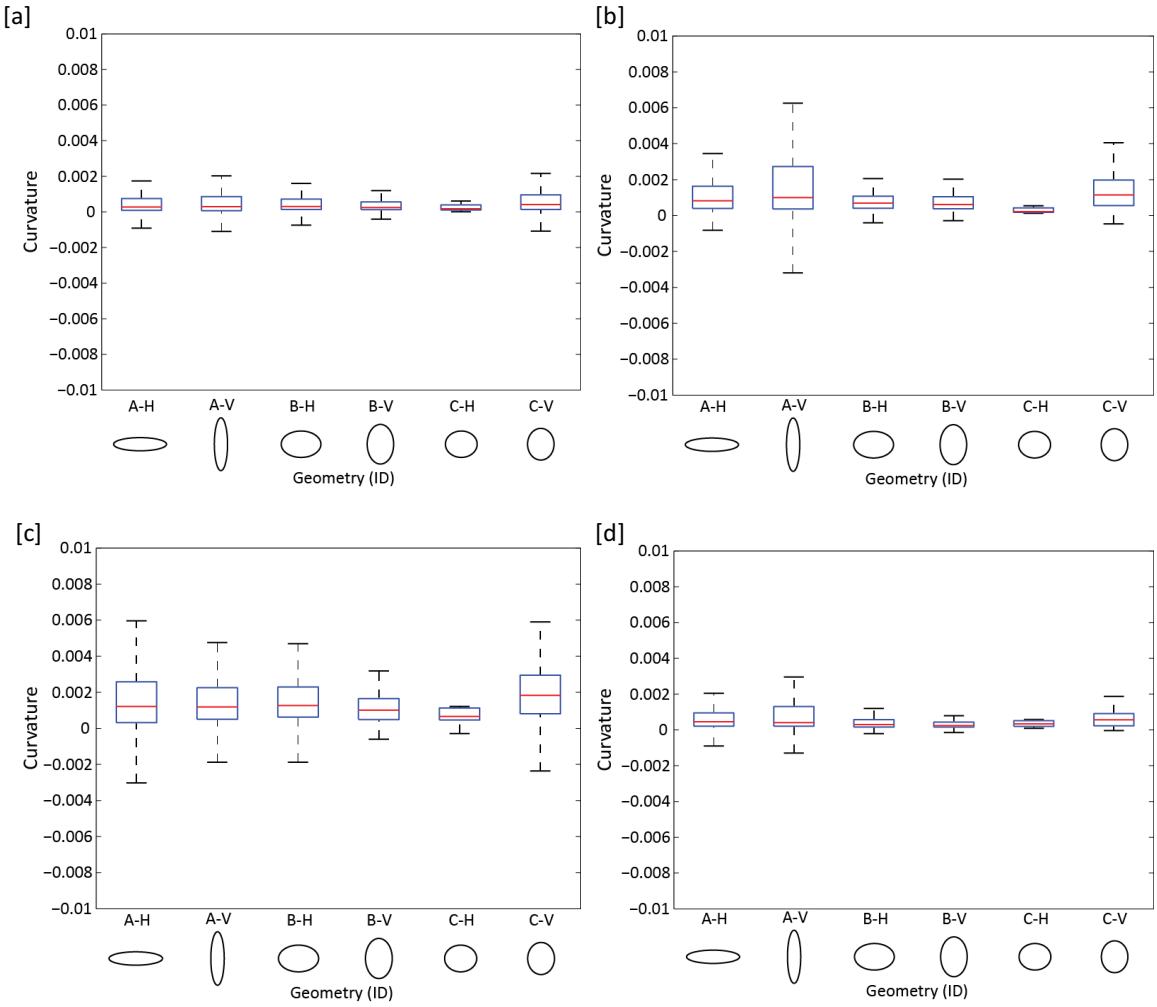

Figure 3.46: Boxplot (outliers removed) of pre-failure curvature values for rockfalls in different geometry classes, where geometry is relative to the strike of the cliff: the datasets include all rockfalls that occurred at [a] Boulby, [b] Section 1, [c] Section 2 and [d] Cowbar from June 2012 – June 2014. Geometry IDs are explained in Section 3.3, and depictions of each given here on the x-axis.

3.4.8 Clustering of rockfalls

3.4.8.1 Ripley's K-function

This section presents the results of the analysis of spatial rockfall clustering over different time periods at Boulby as given by the Ripley's K-analysis (see Section 3.3.2 for details of the method). Results show that rockfalls are not uniformly or randomly distributed across the cliff face but cluster. Figure 3.47 shows results of the basic analysis performed on the ten-year

dataset. The shape of the L(r) curve shows that rockfalls are significantly clustered compared to that expected for a random distribution up to a distance of 10 m, as the L(r) curve is outside of the confidence envelopes that surround the random distribution (Theo[L(r)-r]). Rockfalls are significantly dispersed above a distance of 12 m, and within the confidence envelopes in between 10 m and 12 m, suggesting a random distribution of rockfalls within this spatial range. A more pronounced clustering behaviour can be seen at a distance of 10 m. This can be regarded as a critical distance-value for this dataset, which may indicate a length scale that dominant failure mechanisms are operating at.

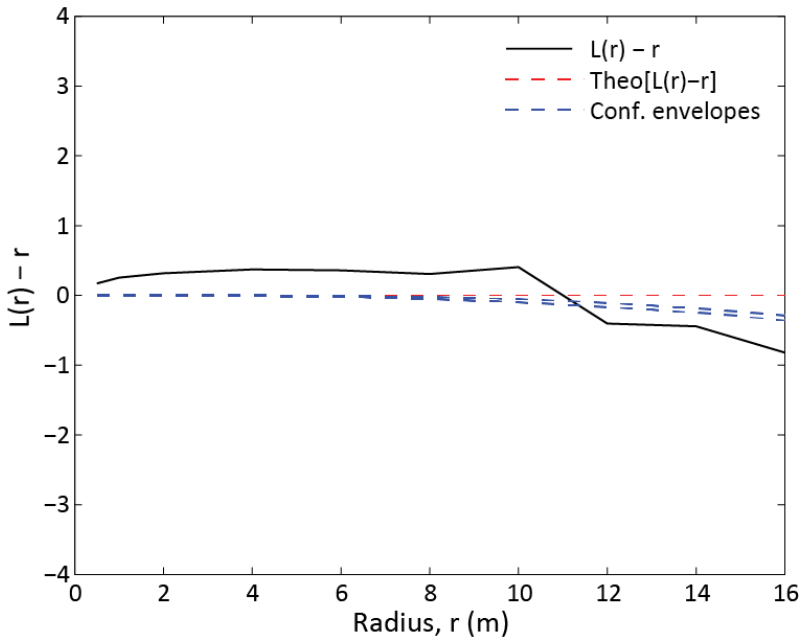

Figure 3.47: The L(r) function computed for all rockfalls between 2003 and 2013.

Four monthly datasets from the two-year dataset at Boulby were selected for analysis to represent different seasons throughout the year: 19-06-2012; 30-08-2012; 13-12-2012; 12-03-2013. Figure 3.48 shows results of the basic analysis performed on each of these datasets. The shape of the L(r) curve shows that rockfalls are significantly clustered compared to that expected for a random distribution up to a distance of 12 m for 19-06-2012 (Fig. 3.48a) and up to a distance of 14 m for 13-12-2012 (Fig. 3.48c) and 12-03-2013 (Fig 3.48d); significantly dispersed beyond 14 m for 19-06-2012 and beyond 16 m for 13-12-2012 and 12-03-2013. Critical distance values can be identified in each of these datasets at 4 m (Fig. 3.48a), 14 m (Fig. 3.48c) and 6 m (Fig. 3.48d) respectively.

The L(r) curve for the rockfalls from 30-08-2012 (Fig. 3.48b) shows significant clustering of rockfalls at all distances analysed. The strength of clustering, as defined by the L(r) value, is higher than the data from all other months analysed and increases at distances where other datasets display significant dispersion. Observation of the rockfall data for this month (Fig. 3.22a) shows that the majority of rockfalls were small and clustered together in multiple clusters across the cliff face. The increase in the L(r) value beyond a distance of 12 m may reflect the average distance between these areas of clustering.

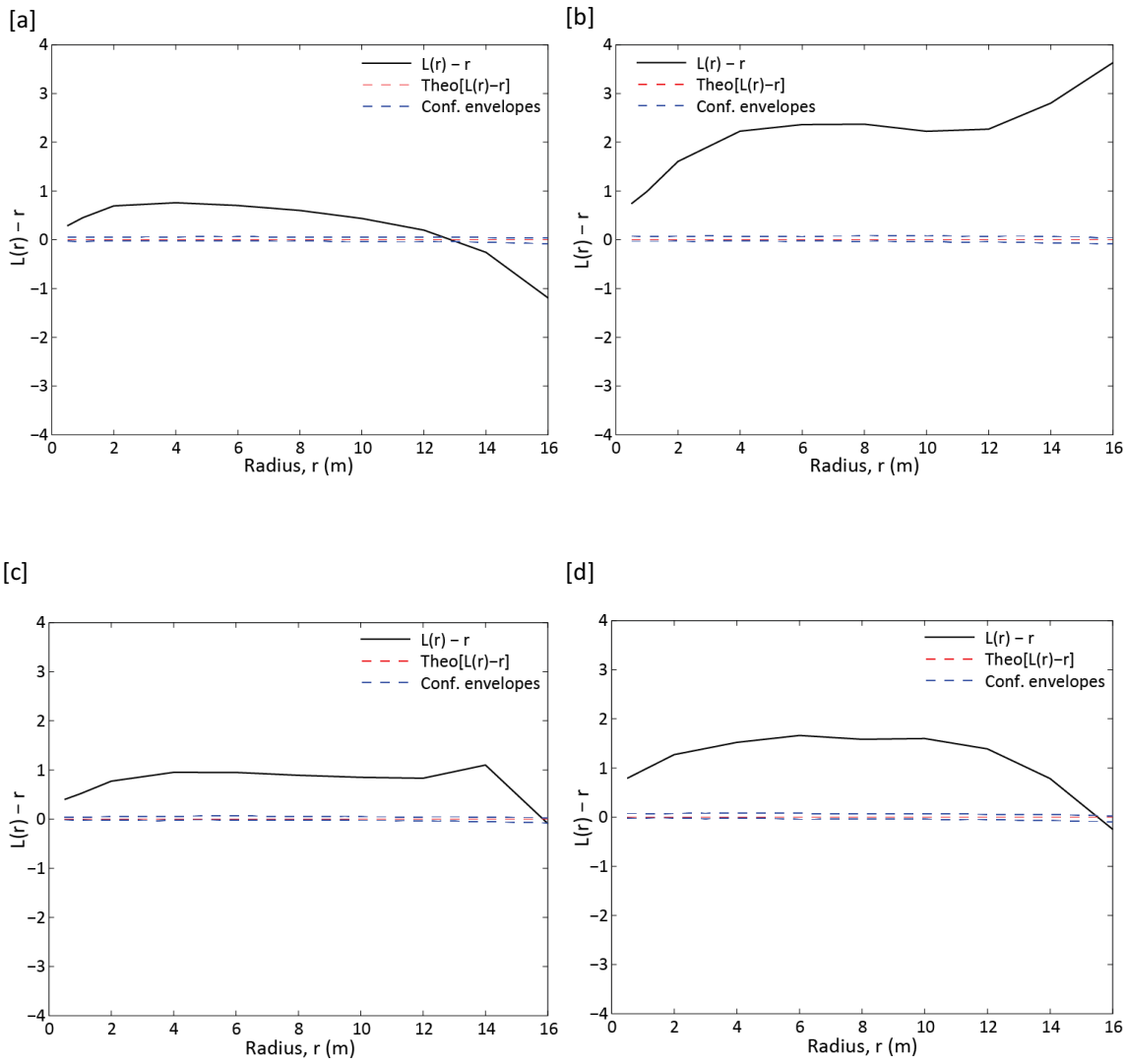

Figure 3.48: The L(r) function computed for rockfall datasets at Boulby from: [a] 19-06-2012 (3,613 rockfalls); [b] 30-08-2012 (2,533 rockfalls); [c] 13-12-2012 (3,618 rockfalls); and [d] 12-03-2013 (2,543 rockfalls)

The cross K-function analysis examines the clustering of rockfalls with respect to the rockfalls from another time period. All of the monthly datasets from August 2012 – June 2013 at Boulby

were compared to the data from June 2012. Beginning with the dataset from August 2012, each dataset was then incrementally added, increasing the size and temporal range of the dataset at each stage. Results in Figure 3.49 show that rockfalls are not randomly distributed at any temporal range around previous failures but cluster significantly. The shape of the L(r) curve shows that for all temporal ranges rockfalls are significantly clustered compared to that expected for a random distribution up to a distance of 10 m, and significantly dispersed above a distance of 12 m. More pronounced clustering behaviour can be seen at a distance of 2 m, suggesting a much lower critical distance-value for clustering of rockfalls over time compared to the individual datasets (Fig. 3.48). The significant clustering of rockfalls through time is observed at all timescales investigated (two months – twelve months). This may be because the mechanisms that allow rockfalls to cluster, for example stress redistribution surrounding a rockfall, occur over a range of short-term timescales.

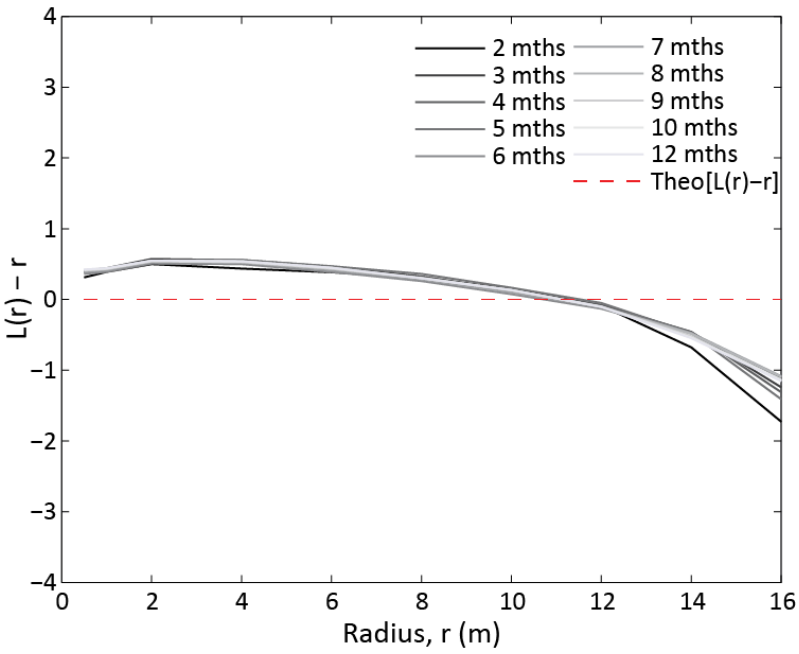

Figure 3.49: The cross-K function computed for data from 19-06-2012 compared to data from the following 2 months, 3 months etc, as indicated in the legend.

The Ripley-K analysis has represented each rockfall as point data as the size of the mean rockfall was small compared to the size of the field site (Tonini and Abellán, 2014). Therefore when the analysis is run on the entire rockfall dataset, the clusters of rockfalls are identified. However, if only the largest rockfalls (< 1 m^2) are considered, the point data is no longer an accurate representation of the areal extent of the rockfalls and clusters are not identified

(Fig. 3.50). From observations of the rockfalls in Figure 3.22a it is clear that rockfalls of this size do in fact cluster, further supported by the examples of rockfall evolution (Section 3.4.5). Therefore, in order to examine the spatial distribution of rockfalls in different size classes, the results of the proximity analysis were used.

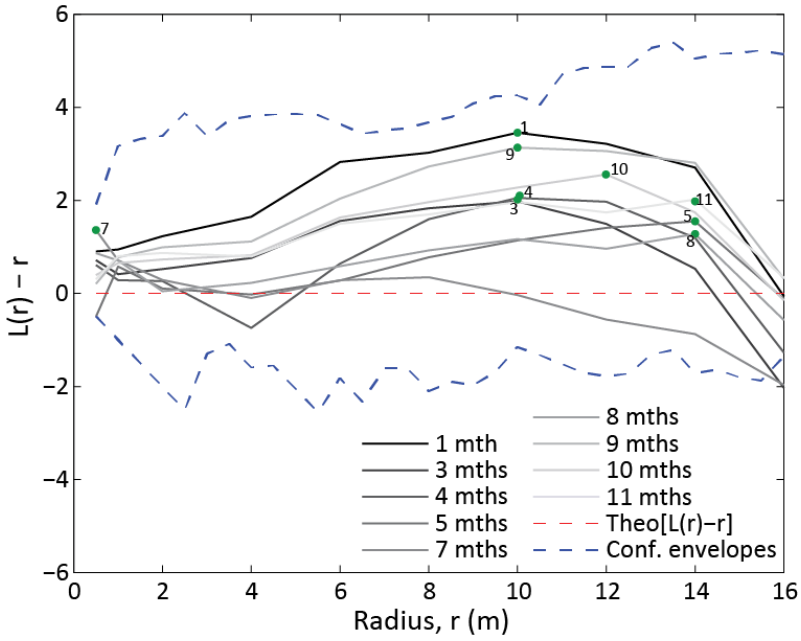

Figure 3.50: The cross-K function computed for rockfalls ≥ 1 m^2 that occurred in the month preceding 14-07-2014, compared to the previous month, 3 months, 4 months etc, as indicated in the legend. The green dots identify the peak L(r) value for each dataset and the numbers next to them refer to the months (as given in the legend).

3.4.8.2 Distance between rockfalls

Proximity analysis of rockfalls was used to examine the proximity of rockfalls from one dataset and the nearest rockfall in the previous dataset. The results from this are used in this section firstly to examine the distance between rockfalls of different sizes. At all rockfall sizes 30% of rockfalls are contiguous and 40% are within 0.1 m of another rockfall. As the size of rockfalls increases, the mean distance to the nearest existing rockfall decreases, as shown by the migration of the curve towards zero with increasing rockfall size (Fig. 3.51). If all rockfalls were uniformly randomly distributed as points the mean spacing would be 2.25 m. For all rockfalls, 89% are within 2.25 m from a rockfall that occurred in the previous month, indicating that rockfalls are occurring closer to previous rockfalls than would be expected for a random distribution. Again, the percentage of failures within this distance increases with the lowest

rockfall size considered (Fig. 3.51). Furthermore, the percentage of contiguous rockfall increases with increasing rockfall size.

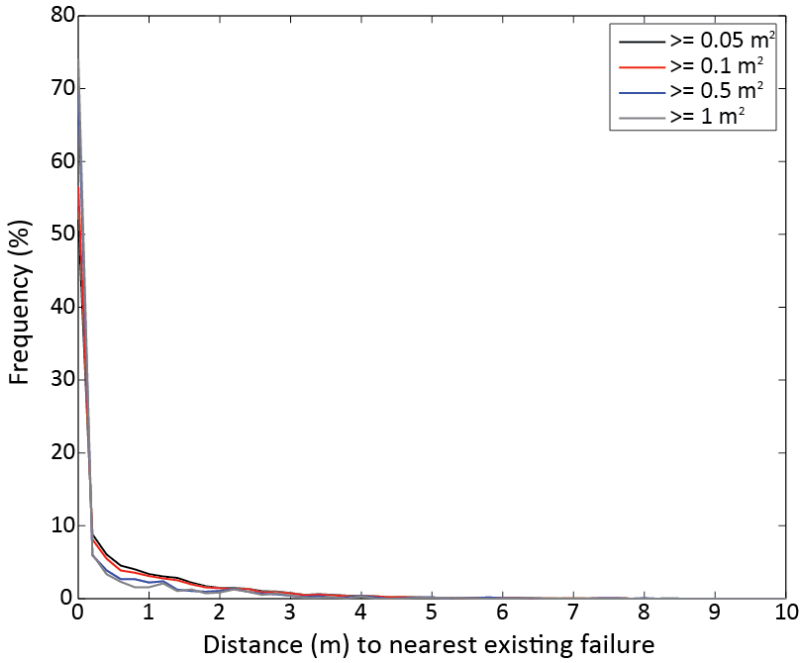

Figure 3.51: The distance between failures from one dataset and the nearest failure in the previous dataset presented for rockfalls of different sizes at Boulby. Each curve represents a different set of rockfall sizes, as indicated in the legend.

Considering the entire dataset (all rockfall sizes), the distance between rockfalls was examined over an increasing time frame in the same way that the cross K-function was applied. All rockfalls from an additional scan acquired on 14-07-2014 at Boulby were analysed for the distance to the nearest previous rockfall in a dataset that was incrementally increased. Beginning with the dataset from June 2014, each dataset was then incrementally added, increasing the size and temporal range of the dataset at each stage. The percentage of contiguous failures increases with time and the sharpest increase is seen over the first 5 months (Fig. 3.52).

The results of the failure proximity analysis are displayed as the ratio between the percentage of contiguous rockfalls and the failed area (as a percentage of the total cliff area) (Fig. 3.52). For the entire two-year survey epoch more rockfalls are contiguous than would be expected from a uniform or random distribution, demonstrating that rockfalls are more likely to occur contiguous to rockfall scar. Statistically, this supports the observations shown in Figure 5 and previous observations of contiguous failures at this site (Rosser *et al.,* 2007a) and elsewhere (Stock *et al.,* 2012; Royan *et al.,* 2013). The highest ratio (Fig. 3.52) is observed when four

months of cumulative rockfall data is considered and the ratio decreases as the size of the dataset increases beyond four months. This suggests that for this context, four months represents a critical temporal-value for contiguous rockfall growth.

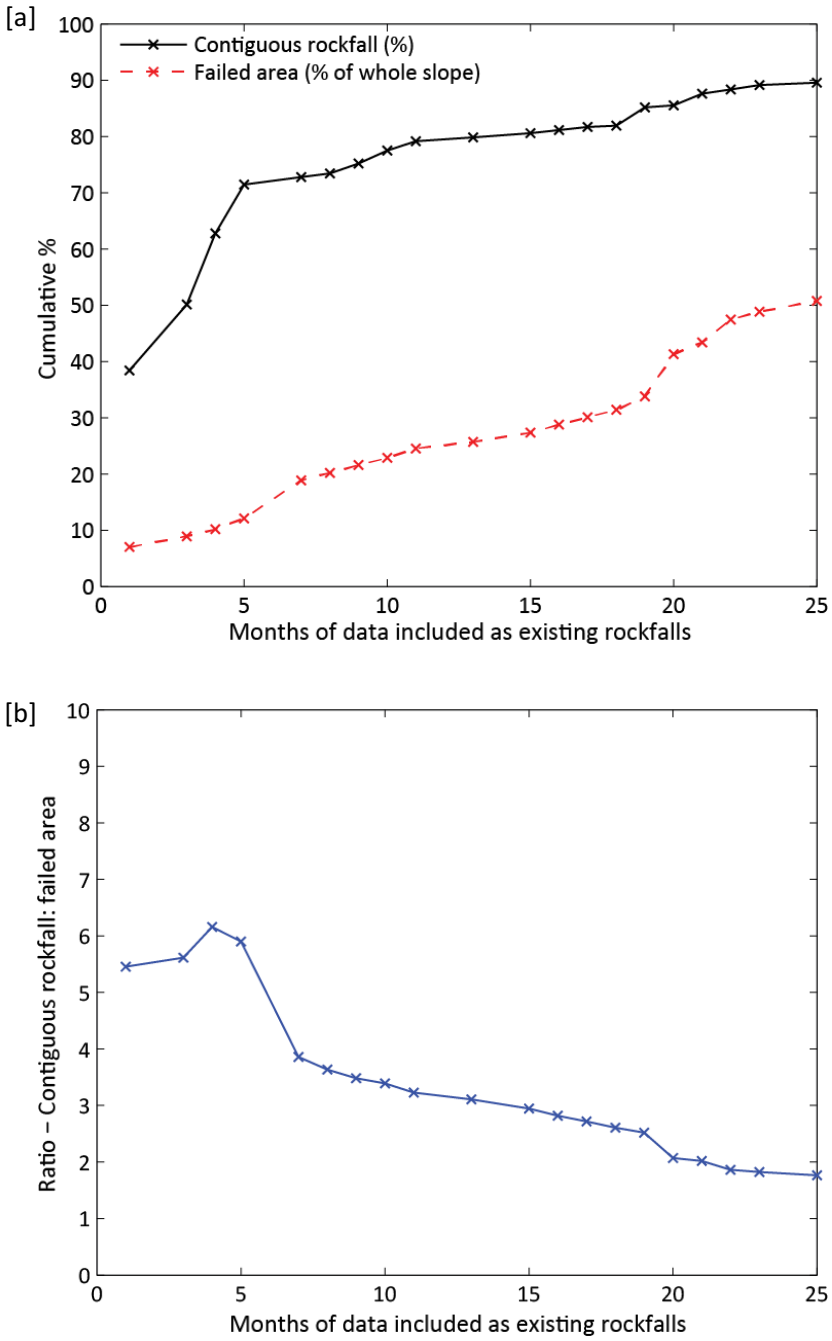

Figure 3.52: [a] The percentage of contiguous rockfall when data from 14-07-2014 at Boulby is compared to datasets from an increasing amount of months (black line). The dashed red line shows the failed area as a percentage of the whole slope, which does not account for overlapping failures between months and therefore is an overestimate of the surface area failed. [b] The ratio between the two plots in [a], calculated as: contiguous rockfall/ failed area. If rockfalls were uniformly or randomly distributed across the cliff face, a ratio of 1 would be expected. A ratio > 1 suggests that rockfalls are contiguous more than a uniform or random distribution would predict. *Note: contiguous is defined as any overlap between rockfall, i.e. edges touching.*

3.4.9 Rockfall propagation

This section of the results concerns the direction of rockfall propagation, calculated as the direction from existing rockfalls in one dataset to the nearest rockfall in the following (newer) dataset. Results are presented as rose plots and show no clear directional preference for the development of new rockfalls when considering the entire dataset. However, a directional preference emerges when contiguous rockfall are considered separately from non-contiguous rockfall.

Figure 3.53 shows the data for all the monthly datasets at each site. There does not appear to be a dominant directional preference and at all sites the newer rockfall are relatively evenly distributed above and below existing rockfall. This is supported by the data in Table 3.8 (column 1), which shows the percentage of rockfalls with a directional component above the left-right horizontal line on the rose plots. At Boulby, Section 2 and Cowbar there appears a slight preference for rockfall to develop outward (directly left and right) from existing rockfall. This could be associated with the influence of the near horizontal bedding planes along this coastline.

Table 3.8: Summary of the percentage of rockfall that are above the Left-Right horizontal line in the directional data plots presented in Figures 3.57 – 3.62. The corresponding figures for each statistic are given in brackets.

Dataset	**All (%)**	**Contiguous (%)**	**Non-contiguous (%)**
Boulby (all)	49.8 (Fig. 3.53)	52.1 (Fig. 3.54)	48.8 (Fig. 3.55)
Section 1 (all)	50.3 (Fig. 3.53)	54.2 (Fig. 3.54)	48.8 (Fig. 3.55)
Section 2 (all)	52.9 (Fig. 3.53)	60.6 (Fig. 3.54)	51.6 (Fig. 3.55)
Cowbar (all)	52.7 (Fig. 3.53)	59.0 (Fig. 3.54)	50.1 (Fig. 3.55)
Boulby ≥ 0.05 m^2	55.1 (Fig. 3.56)	61.8 (Fig. 3.57)	50.1 (Fig. 3.58)
Boulby ≥ 0.1 m^2	55.9 (Fig. 3.56)	62.9 (Fig. 3.57)	49.1 (Fig. 3.58)
Boulby ≥ 0.5 m^2	59.7 (Fig. 3.56)	64.8 (Fig. 3.57)	50.1 (Fig. 3.58)
Boulby ≥ 1 m^2	61.3 (Fig. 3.56)	65.3 (Fig. 3.57)	52.4 (Fig. 3.58)

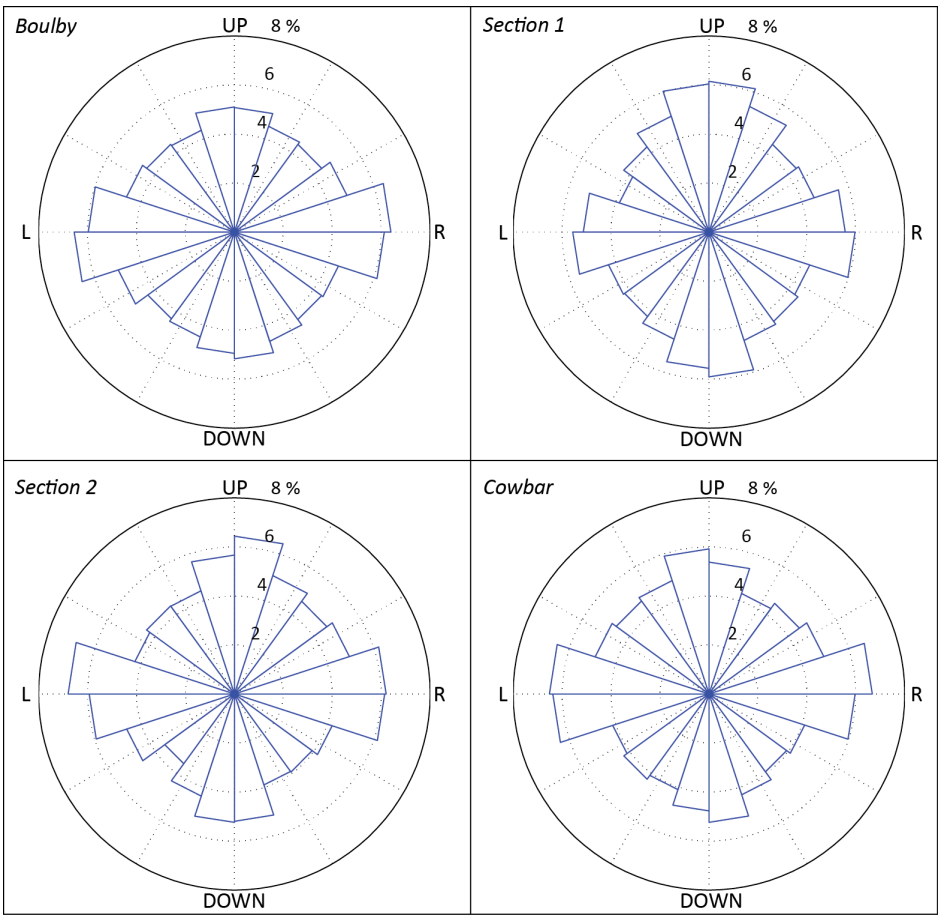

Figure 3.53: Rose plots showing the direction from existing rockfalls in one dataset to the nearest rockfall in the subsequent (new) dataset for each field site, as labelled. The data presented is a compilation of all the monthly data from June 2012 – June 2014.

Figures 3.54 and 3.55 present the same data, split according to whether new rockfall are contiguous (Fig. 3.54) or non-contiguous (Fig. 3.55) with existing rockfall (here contiguous is defined as any overlap between rockfall, such as edges touching). The plots in Figure 3.54 display clearer patterns than when all the data is plotted together (Fig. 3.53). Contiguous rockfall appear predominantly outward and upward from existing rockfall at all sites. This is supported by Table 3.8 (column 2), which show more than 50 % of rockfalls at all sites with a directional component above the left-right horizontal line. Conversely, the non-contiguous rockfalls show no clear directional preference as seen from the plots in Figure 3.55. This suggests that the non-contiguous rockfall are masking the directional preference of contiguous rockfall evolution when all the data is considered together and also that there are potentially two separate populations of rockfalls here: those which depend on what has happened previously at a timescale of months; and those which either have no link with previous events or operate over much longer timescales.

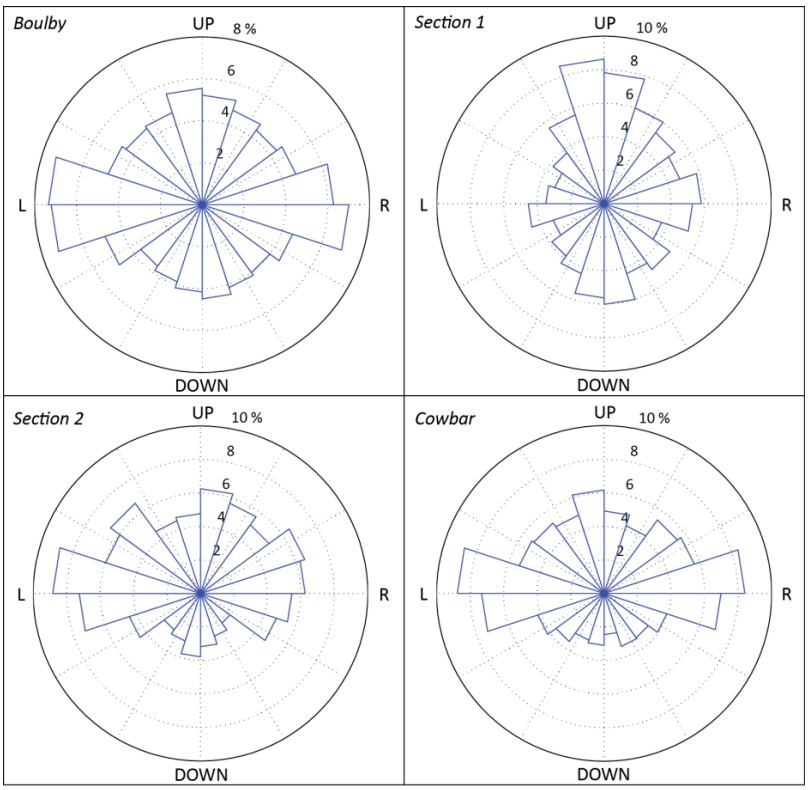

Figure 3.54: Rose plots showing the direction from existing rockfalls in one dataset to the nearest rockfall in the subsequent (new) dataset only for ***contiguous*** rockfalls, for each field site as labelled. The data presented is a compilation of all the monthly data from June 2012 – June 2014.

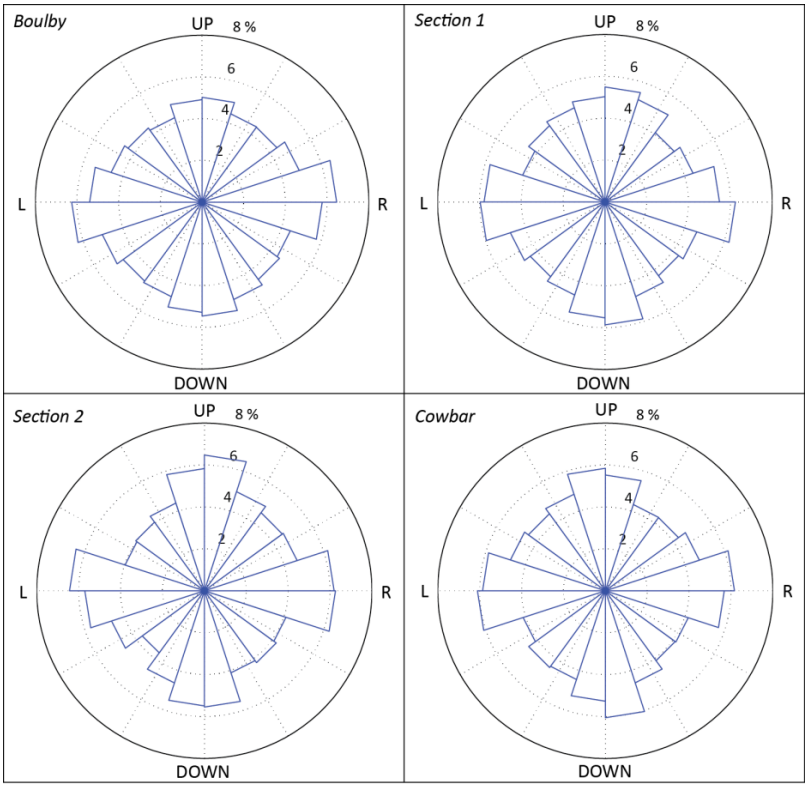

Figure 3.55: Rose plots showing the direction from existing rockfalls in one dataset to the nearest rockfall in the subsequent (new) dataset only for ***non-contiguous*** rockfalls, for each field site as labelled. The data presented is a compilation of all the monthly data from June 2012 – June 2014.

Finally, to examine the rockfall size ranges at which the directional behaviour can be observed, the data from Boulby was further analysed for different rockfall sizes. Boulby was used for this analysis as the length of the cliff face at this site is flat (not a bay or headland) and therefore normal to the angle of the scanner. This avoids any potential uncertainty in depth measurement error (Section 3.2.2.1) and ensures minimal artificial differences between the smaller areas investigated. For each set of analysis the rockfalls from the newer dataset were split into different categories based on rockfall size, whilst the entire dataset of the existing rockfalls was used.

Figure 3.56 shows that as the smallest size of the new rockfalls increases, the directional preference for rockfalls located upward and outward from existing rockfalls also increases (see Table 3.8, column 1). Repeating this analysis for contiguous (Fig. 3.57) and non-contiguous (Fig. 3.58) rockfall shows that the pattern identified in Figure 3.56 is reflecting the contiguous rockfall data. This is further supported by the data in Table 3.8 (column 2 and 3) which shows that more than 60 % of contiguous failures for rockfalls ≥ 0.05 m^2 have a directional component above the left-right horizontal line, which increases with increasing rockfall size.

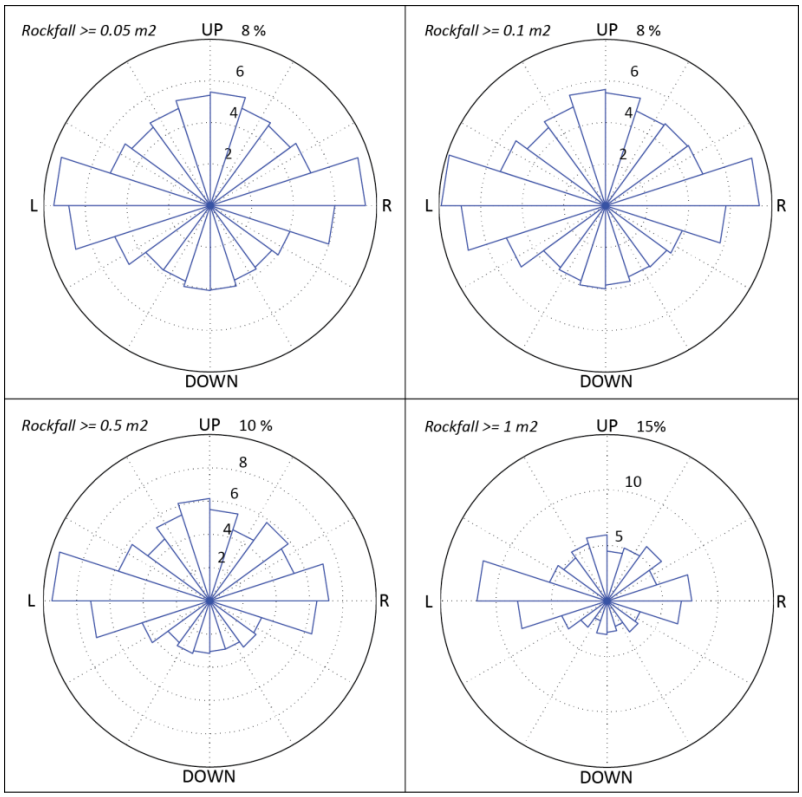

Figure 3.56: Rose plots showing the direction from existing rockfalls (all sizes) in one dataset to the nearest rockfall (size according to the label on the plots) in the subsequent (new) dataset for rockfalls at Boulby from June 2012 – June 2014.

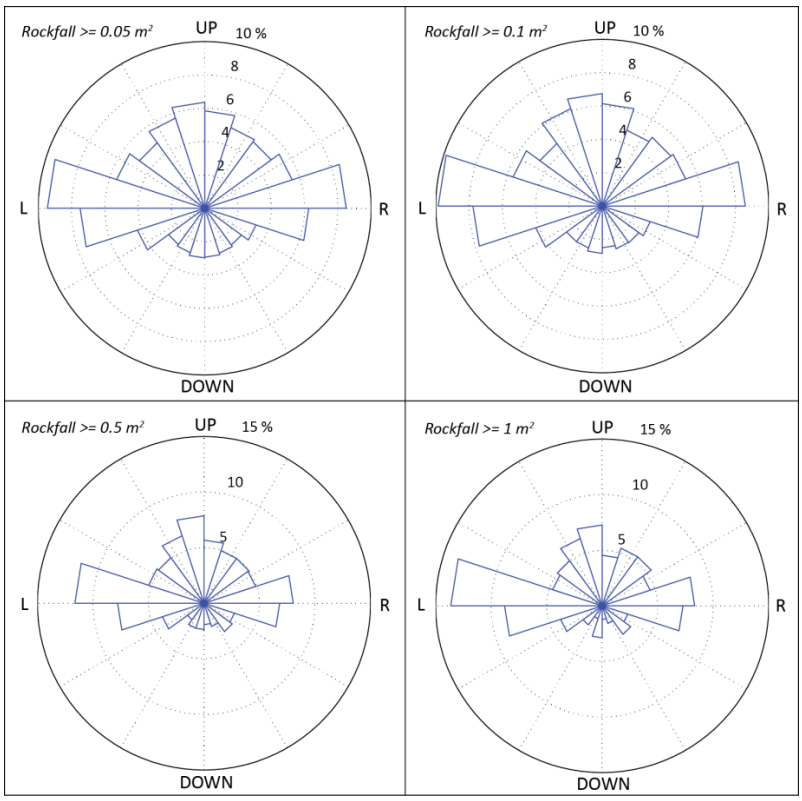

Figure 3.57: Rose plots showing the direction from existing rockfalls (all sizes) in one dataset to the nearest rockfall (size according to the label on the plots) in the subsequent (new) dataset for ***contiguous*** rockfalls only at Boulby from June 2012 – June 2014.

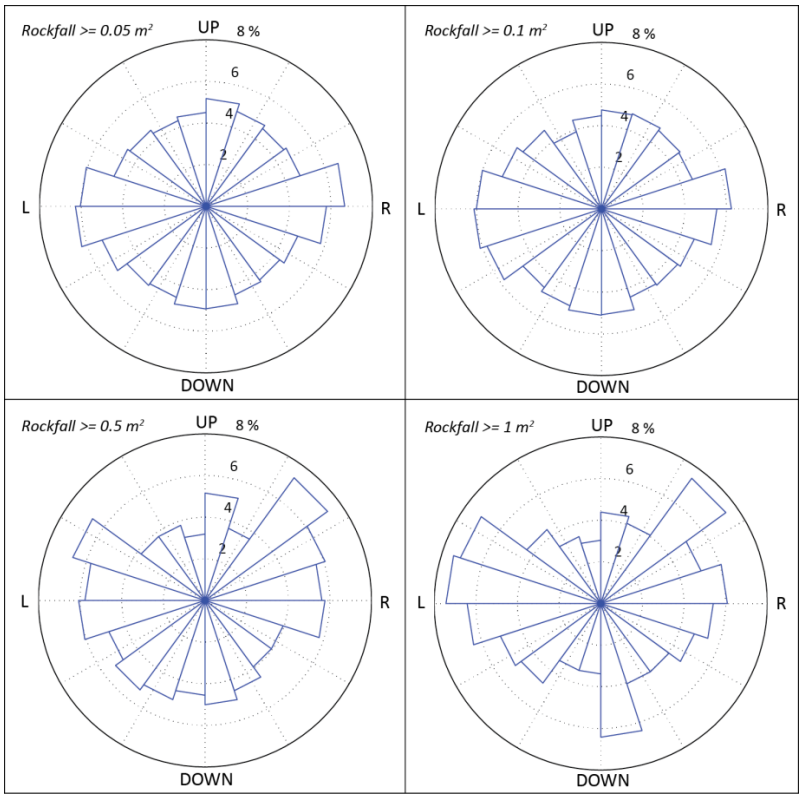

Figure 3.58: Rose plots showing the direction from existing rockfalls (all sizes) in one dataset to the nearest rockfall (size according to the label on the plots) in the subsequent (new) dataset for ***non-contiguous*** rockfalls only at Boulby from June 2012 – June 2014.

3.5 Summary

High resolution field monitoring data has been used to extract monthly rockfall datasets from the North Yorkshire coastline over two years from June 2012 to June 2014. Within the resulting rockfall datasets presented in this chapter, propagation of rockfalls across the cliff face appears to be an important mechanism that controls both when and where the cliff fails next. Evidence of this has been provided as visual observations of rockfall sequencing and in analysis of the spatial and temporal relationships identified above. These can be summarised by answering the questions set out at the beginning of this chapter:

Question 1: Is there a temporal pattern to rockfall behaviour, observable at different spatial scales, which displays variability beyond rock mass strength and environmental conditions?

Selby (1982) states that rock slopes will retreat based on their rock mass strength and weathering conditions, such that any variation from a uniform slope profile can be attributed to these factors. Although environmental conditions have not been explicitly considered in this research, the close proximity of the sites suggests that conditions are likely to be similar. However, it is acknowledged that there may be localised differences such as differences in the wave energy due to the fetch (Vann Jones *et al.,* 2015). Despite this, owing to the similar conditions, the temporal pattern of spatially averaged erosion is consistent between sites and shows heightened activity during the winter months when stronger winds and waves are evident along the North Yorkshire coastline (Vann Jones *et al.,* 2015). Within each site the marine and subaerial environmental process zones are the primary difference in environmental conditions. However, the variation in erosion with elevation (Fig. 3.26) shows no clear distinction between these two zones.

At each site there is considerable variability in the temporal pattern of erosion between lithological units and across the cliff face. The erosion rate in each lithological unit varies between field sites and the unit with the highest erosion rate over the two years is different at each site, suggesting that it is not only the material properties of the rock mass that are regulating the temporal pattern of erosion. The variation was evident within the same environmental process zones of the cliff (marine inundated and subaerial), thus emphasising the variability in rockfall occurrence that exists beyond what can be explained by environmental conditions.

The process length scale for cliff parallel retreat is much longer than the two years of data presented here and data from each field site is providing only a snapshot of a longer-term process. Over the short time scale, the variability between and within field sites is pointing to a non-environmental and non-lithological control on the timing of rockfalls at these field sites. Alternatively, the discontinuity network within the rock mass, the role of fracturing, or the process of stress redistribution may provide an explanation for the variability and temporal pattern observed. Such mechanisms may be controlling the occurrence and subsequent propagation of rockfalls. At this stage, with the data collected, it is not clear which mechanism is most dominant.

The temporal data presented for rockfalls of different sizes shows that the magnitude and pattern of cliff-averaged erosion is dictated by the largest rockfalls in this dataset, and that the smaller rockfalls only add to this pattern, but do not alter it significantly. However, observations from the case studies presented, and the clustering and directional analysis, show that these smaller rockfalls relate to the timing and location of larger rockfall. Precursors suggests that the rock mass is weakening, possibly indicating an ongoing progressive failure is occurring (Petley *et al.,* 2005).

Question 2: Can a relationship be identified between slope morphology and the distribution and geometry of rockfalls?

Rockfalls occur preferentially on locally convex areas of the cliff face. This is as expected based on the work of Martel (2006) who showed how local slope surface convexity (10^1 m) changes local stress concentrations in the near surface. An increase in stress promotes the generation of damage, increasing the likelihood of failure. Furthermore, the higher stress concentrations may also trigger larger scale failures, as documented here, where rockfalls that occur on locally convex areas are shown to be deeper than the mean rockfall depth.

This study has shown that local curvature, determined at a resolution relative to the smallest failure size, is a determining factor for the location and depth of rockfalls, and particularly the smaller failures (< 1 m^2 surface area). The surface area and shape of rockfalls does not, however, appear to be influenced by curvature at this resolution. These results point to the potential influence of the larger scale slope morphology, particularly for larger scale failures.

The influence of curvature at different scales has implications for how slope surface morphology could be included in rockfall modelling, as indicated by Stead and Coggan (2012)

who point to the need for models to represent processes relevant to failure evolution at a spatial resolution corresponding to failure size.

The propagation of rockfalls across the cliff face can also be linked to local slope morphology. As demonstrated in the case studies of rockfall evolution provided in Section 3.4.5, overhangs develop as a result of rockfalls in the space below, and develop through time to a consistent form that then dictates future rockfall character. Combining this with the observation that rockfalls more commonly occur on locally convex areas of the slope, then the most likely direction of rockfall propagation is therefore upward and outward, in the direction of the convex areas of the slope.

Question 3: Over what scales do rockfalls show significant clustering?

In this study the modified L-function and cross L-function, based on Ripley's K-function analysis (Ripley, 1976), provided an indicator of the range of distances and time over which rockfalls show significant clustering. Spatial clustering of rockfalls is identified as statistically significant up to distances between 10 m and 14 m for individual datasets over different timescales. Critical distance-values have been identified, which appear to correspond to the distances between small areas of clustering. The significant clustering of rockfalls through time exhibits a critical distance value of 2 m, which is potentially indicative of the spatial scale at which these mechanisms occur. These critical values can be retained for future analysis that aims to locate clusters (Tonini and Abellán, 2014), for example indicating process length scales to use within numerical modelling.

Examining the distances between subsequent rockfall using polygons, showed that a large percentage of failures are contiguous and that the average distance between rockfall decreases as rockfall size increases. This supports field observations from this study (Section 3.4.5), and previous studies (e.g. Rosser *et al.,* 2007a) that show a smaller rockfall occurring within a footprint of a later larger rockfall. Rockfalls are more distributed in a more contiguous manner than a random distribution over a range of time scales from 1 – 25 months. A critical temporal-value for this dataset was identified at 4 months, suggesting a potential timescale over which contiguous failures propagate.

Question 4: Is rockfall scar growth random or directional?

Rockfalls that are contiguous show a clear upward and outward directional preference as they propagate across the cliff face, however this directional preference is less apparent when looking at non-contiguous failures, which is logical. Additionally, these observations are seen more clearly when looking at rockfall of different size categories. As rockfall size increases, the strength of the directional signal between successive rockfall increases. Again, this is seen within contiguous failures, and is less apparent within non-contiguous failures.

The directionality observed in the propagation of contiguous rockfalls could also be used to inform modelling of the processes of rockfall propagation. The predominantly upward and outward propagation and the spatial distances over which clustering appears to occur, suggest the extent over which stress may be redistributed in and across the rock mass, promoting the generation of damage to trigger further rockfalls. The directional preference observed supports the idea that stress transfer would most likely cause upward and outward propagation of rockfalls, due to gravity (Lim, 2006), and this is most clearly expressed in the development of contiguous and larger rockfall.

Overall, the spatial and temporal distribution of rockfalls presented in this chapter has illustrated the progressive failure of rockfalls, suggesting that in many instances a rockfall can be viewed as precursory to the next, and that the propagation of rockfall on these rock faces appears to be a significant mechanism that controls the timing, location and nature of failure. Crucially, the field data has provided an indication of the spatial and temporal scales at which these processes operate, indicating that the spatial proximity and temporal frequency of propagating rockfalls is at, or above, the spatial and temporal resolution of the data analysed here. This has been demonstrated via observations of rockfall propagation across the cliff face, the temporal patterns in rockfall behaviour, evidence that rockfalls cluster significantly at a range of scales, and the directional preference expressed as rockfalls propagate and grow across the cliff face. These processes indicate areas of the cliff where future failures are most likely to occur. Building upon this, this research explores the degree to which this behaviour can be considered be a function of progressive stress redistribution through time that can promote the generation of damage within the rock mass, as suggested by amongst others, Stock *et al.* (2012). In order to further explore this, the current challenge for this research is to comprehensively investigate the role of structural and morphological parameters in driving rockfall, in the context of time-dependent failure. This is most appropriately addressed through numerical modelling that permits time-dependent fracture of the material.

Furthermore, the development of rock degradation remains largely unknown in the context of rockfall evolution in hard rock cliffs. Brain *et al.* (2014) discuss damage thresholds at the whole slope scale via the stress concentrations required to activate crack growth. However, at the sub-slope scale, where stress concentrations can be identified in relation to structure and morphology, damage thresholds are a significant unknown in the understanding of rockfall behaviour. Numerical modelling that considers time-dependent fracture will allow this process to be assessed under different conditions. Further examination of the degradation of intact rock required to trigger failure could be appropriately addressed through the development of a model that simulates damage to the rock mass through time. The information presented in this chapter not only contributes to an improved understanding of rock slope failure on a local scale, but also provides the necessary information to be used in developing an approach to rockfall modelling that is capable of simulating rockfall evolution in the manner observed here.

4 Numerical modelling - Slope Model

The field data presented in Chapter 3 demonstrated the spatial and temporal scales at which progressive failure appears to be driving rockfall occurrence via observations of rockfall propagation across the cliff face. These processes are postulated to be a function of progressive stress redistribution through time, possibly via sub-critical crack growth within the rock mass. This chapter aims to further ascertain the validity of this idea by using numerical modelling to investigate rockfall occurrence in the context of time-dependent failure. In particular this allows examination of rock degradation in the form of brittle fracture development.

Slope Model, a lattice spring code, is used to investigate the effect of structural and slope morphological input parameters on slope failure and on the development of fractures both pre- and post-failure. This is achieved through a range of model experiments whereby joint strength, slope morphology and material properties are varied to simulate weakening of the slope. The response of the model is observed through recording the timing and location of both failures and fractures within the model. Adopting brittle fracture growth as a representation of time-dependent failure allows the influence on the location and timing of rockfalls to be observed, thereby addressing the second research objective for this study.

4.1 Introduction

Rockfall studies using numerical modelling often make implicit assumptions that can be at odds with field observations. Studies often assume that rockfalls occur as individual events in both time and space (Zimmer *et al.,* 2012), and that failure is discrete, and that the manner in which failures evolve is not a significant control on the wider behaviour of the slope (Dewez *et al.,* 2007). This assumption is mainly derived from a low monitoring frequency relative to the frequency of event recurrence (Senfaute *et al.,* 2009, Abellán *et al.,* 2010), and models that don't represent stress redistribution and the associated propagation of failures at a scale relative to observed rockfall sizes (Stead and Coggan, 2012). The majority of current rockfall models reduce the dominant structural controls on rockfall to a 2D profile view (Styles *et al.,* 2011), thus not considering lateral confinement of failing blocks across the rock face, wider 3D structure or heterogeneity, and so do not fully represent failure mechanisms that operate across the rock face. Examples of such failure mechanisms that are not well-represented in most rockfall models include: contiguous rockfall; the spatially dependent sequencing of

propagating rockfalls (Abellán *et al.,* 2010); and progressive failure that includes the time-dependent development of fractures in a rock mass (Stock *et al.,* 2012; Rosser *et al.,* 2013). Patterns of rockfalls across the rock face that are indicative of these failure mechanisms are observed in rockfall monitoring studies, such as those presented in Chapter 3. Such observations are postulated to be driven by, amongst other factors, stress redistribution following rockfalls, which causes time-dependent fracture propagation (Senfaute *et al.,* 2009) that acts to reduce local stability and eventually leads to further rockfall (Stock *et al.,* 2012).

Numerical modelling provides a means to examine these processes over time at a range of spatial scales, from sub-centimetre fracture development to metre-scale rockfall, in ways that are not easily observable in the field or laboratory. Numerical modelling provides the potential to investigate the interaction between rock mass structure, material properties and slope morphology. In order to achieve this an explicit 3D model that simulates fracture is required. Within engineering geology and mining these models have been developed (Stead and Coggan, 2012) and have been used to advance understanding of how large rock slopes fail. In particular, this previous research has demonstrated the role of fracture development in failure, as illustrated by Elmo *et al.* (2011), who used the hybrid FEM/DEM code ELFEN to simulate the effects of rock bridge strength and fracturing on the failure of a wall of a large open pit mine slope. Building on this, Havaej *et al.* (2014b) quantified fracture development under different slope conditions by exploiting recent advances in numerical codes to calculate 'damage' based on fracture intensity and extent.

Within research on natural (non-engineered) rock slopes, there are fewer studies using numerical models to investigate the role of fracture mechanics, with most studies focussed at the macroscale (m to km), considering fracture development across entire slopes or valleys. Eberhardt *et al.* (2004) used ELFEN to reproduce the extent of the 1991 Randa rockslide and highlighted the role of fracture initiation and propagation in the development of the failure surface. Leith *et al.* (2014a; 2014b) demonstrated the role of fracture development across an Alpine valley using a finite difference model to simulate a 4 km cross section responding to a range of geomorphic and tectonic processes associated with long-term glacial loading and unloading.

There is a noticeable gap in the literature of studies using the most recent numerical codes to model fracture development associated with sub-metre failures from natural rock slopes. The typical frequency distribution of rockfall volume in this study (Chapter 3) and others, such as Hungr *et al.* (1999), Rosser *et al.* (2007a), and Barlow *et al.* (2012), suggests that at the sub-

metre scale a significant amount of geomorphological work in terms of net volume flux via rockfall is achieved by small rockfall.

To address this gap, this Chapter applies a 3D model to examine the role of fracture initiation and growth in driving individual small scale rockfall. Rather than using a 3D numerical model to recreate one particular rockfall or landslide, as most numerical rock slope models attempt (e.g. Eberhardt *et al.,* 2004; Stead *et al.,* 2004; Pine *et al.,* 2007; Styles *et al.,* 2011), this study applies a 3D rock slope model to conduct a scenario-based analysis, whereby the model is used to assess the emergent spatial and temporal behaviour of failures. This approach aims to establish a more general understanding about the key mechanisms and processes involved in how rockfalls behave. A similar approach has been previously illustrated by Kimber (1998), whereby UDEC was used in a similar manner to define the general characteristics of jointed rock masses. In this chapter, different weathering conditions and slope morphologies are simulated in order to investigate fracture development under various conditions. In doing so, this research addresses the following questions:

1. How does model behaviour (magnitude and timing of failure) vary in response to weakening of the rock slope due to fracturing?
2. Does fracture growth precede the point of failure, defined as the point at which displacement has exceeded the critical strain threshold of the rock mass?
3. How does fracture development vary pre- and post- the point of failure?
4. What is the spatial extent of damage (fracture development) surrounding a failed area of the slope?

4.2 Model specification

To answer the research questions outlined above, a 3D model capable of explicitly simulating time-dependent fracture at a sub-metre scale was required. Whilst both continuum and discontinuum models are capable of simulating brittle fracture, only discontinuum models explicitly simulate fracture (Stead and Wolter, 2015). A discontinuum-based approach was required for the model used in this study. This approach also allows simulation of motion along discontinuities, which is required for the model to fail along discontinuities as well as through intact rock. Further to simulating time-dependent fracture, the model was required to record the location and timing of fracture as an output to address research questions 2 – 4. Finally, to design model experiments to address research question 1, the rock mass properties, slope morphology and joint conditions of the model were all required to be user-definable.

A variety of discontinuum-based modelling approaches capable of simulating time-dependent fracture were available, as summarised by Stead and Wolter (2015). Table 4.1 uses the information from Stead and Wolter (2015) to present the advantages and limitations of the different modelling approaches against the requirements of the model in this study, as outlined. It is clear that both the hybrid and lattice spring model approaches are well suited, fulfilling the requirements of the model specification. Of the two models, the lattice spring model represents the most recent development in numerical modelling of brittle fracture, and prior to this study had not been used in geomorphological applications.

Slope Model (Itasca, 2014) was selected to be used in this study. It is a time-dependent, 3D brittle fracture code developed by Itasca (Itasca, 2010b; Lorig *et al.,* 2010) primarily designed to assess slope stability in large open pit mines. The model has fully coupled fluid interaction, with the capability of also allowing fracturing through intact rock. The model is not yet commercially available and the opportunity to use it was generously provided by Itasca. This study presents the first application of Slope Model for examining failure at the small scale (sub-metre) in natural rock slopes. In doing so this work explores a finer sensitivity of the model than has been demonstrated in previous studies.

Table 4.1: Summary of numerical modelling approaches that are capable of simulating brittle fracture, based on information from Stead and Wolter (2015). Advantages and limitations of each approach are relevant to the model specification for this study. The overall suitability is qualitatively defined.

Modelling approach (Examples)	**Advantages**	**Limitation**	**Overall suitability**
Distinct Element (UDEC, 3DEC)	• Records intact rock fracture • Operates in 3D	• Difficulty in incorporating discrete fracture networks (DFN, e.g. user defined joints)	Medium
Particle Flow Codes (PFC2D and 3D)	• Records brittle fracture • Can include DFNs	• Limited use of models in 3D • Computationally expensive	Medium
Synthetic Rock Mass (FLAC3D)	• Operates in 3D • Operates at a range of sizes	• Testing still required for some lithological units • Define strengths that are then applied to a continuum model where fracture does not occur	Low
Hybrid (FEM/DEM) (ELFEN, YGEO)	• Can simulate and record fracture from intact continuum to discontinuum • Can incorporate DFNs • Simulation incorporates continuous re-meshing	• Modelling primarily confined to 2D; developments ongoing in 3D	High
Lattice Spring Model (Slope Model)	• Simulates and records brittle fracture • Operates in 3D • User-defined inputs • Suited to small scale displacements	• Computationally intensive for large scale models • New code, so limited previous use especially in natural rock slopes	High

4.3 Slope Model

4.3.1 Model formulation

Slope Model has a lattice based structure, representing brittle rock as an assembly of nodes (masses) connected by nonlinear springs which simulate the density, elasticity and tensile strength of the rock (Fig. 4.1). The mean distance between nodes is the model resolution. This formulation is based on the Synthetic Rock Mass modelling approach (SRM), described by Pierce *et al.* (2007), which allows fracturing of intact rock in addition to deformation along joints. Importantly, rock mass behaviour is an emergent property of this modelling approach, in contrast to older approaches such as finite element modelling (FEM), whereby the behaviour is governed by constitutive laws (Lorig *et al.,* 2010). The application of a lattice based structure to modelling a jointed rock mass offers higher computational efficiency and

increased flexibility compared to both continuum and discrete element modelling (DEM) approaches (Pierce *et al.,* 2007).

Slope Model is a small strain code with a fully dynamic solution, suitable for simulating highly nonlinear behaviour such as rock fracture and joint deformation (Cundall and Damjanac, 2009). The law of motion is used to apply the following central difference formulas to each node to determine translational and rotational components of displacement:

$$\dot{u}_i^{(t+\frac{\Delta t}{2})} = \dot{u}_i^{(t-\frac{\Delta t}{2})} + \sum F_i^{(t)}\, \Delta t/m$$

Equation 4.1, from: Itasca (2010b)

$$u_i^{(t+\Delta t)} = u_i^{(t)} + \dot{u}_i^{(t-\frac{\Delta t}{2})} \Delta t$$

Equation 4.2, from: Itasca (2010b)

where $\dot{u}_i^{(t)}$ and $u_i^{(t)}$ are the velocity and position respectively of vector component *i* (*i* = 1,3) at time *t*, ΣF_i is the sum of all force components acting on the node of mass *m*, with the mechanical time-step Δt. Angular velocities, ω_i, of each vector component *i* (*i* = 1,3) at time *t* are calculated by applying the following central difference equation:

$$\omega_i^{t+\frac{\Delta t}{2}} = \omega_i^{t-\frac{\Delta t}{2}} + \frac{\sum M_i^t}{I} \Delta t$$

Equation 4.3, from: Itasca (2010b)

where $\sum M_i^t$ is the sum of all moment-components *i* acting on the node with moment of inertia I.

Joints are accepted into Slope Model through a DFN and overlaid on the lattice springs (Cundall and Damjanac, 2009). If a spring then forms part of a joint segment, it obeys a joint constitutive law – a modified version of the smooth joint model (Itasca, 2010a) – which is applied in normal and shear directions, allowing slip and opening of joints respecting the orientation of the joint, rather than local particle orientations (Itasca, 2010b). Intact rock fracture is simulated through the breakage of springs in both shear and tension (further details of the equations governing crack formation are given in the full numerical formulation in Appendix 2). Fluid flow through the joint network and rock matrix can also be modelled, with resulting pressures used to compute effective stresses on each joint element (Cundall and Damjanac, 2009). This allows Slope Model to simulate the time-evolution of the field of

pressures and flows due to external forcing, which was primarily intended to simulate mining activities. For the purposes of this study, the fluid/mechanical coupling is not included in the experimental design.

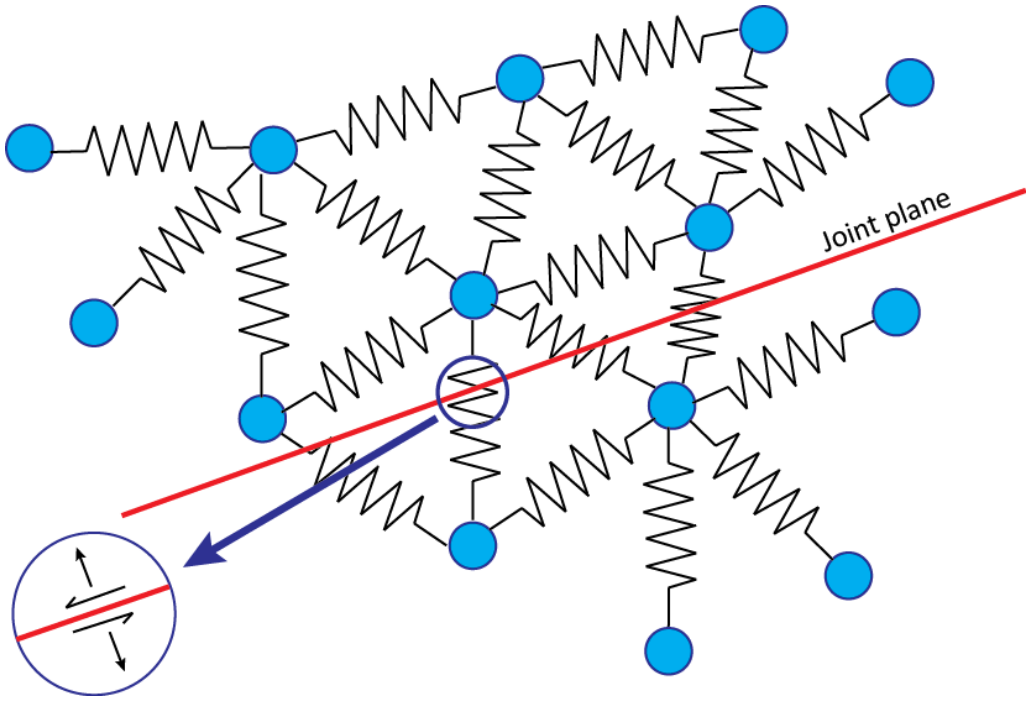

Figure 4.1: Schematic of the lattice based structure of Slope Model showing the assembly of nodes (blue circles) connected by nonlinear springs (black lines). A joint is shown cutting certain springs, where the constitutive joint law respects the direction of the joint plane, rather than the spring; slip and opening is modelled on the joint plane, as shown in the enlarged section of the diagram. This is based on Figure 1 from Cundall (2011 p.2).

Slope Model has a graphical user interface (GUI) that allows 'benches' to be defined and set-up as part of the slope (Fig. 4.2). Slope Model was primarily designed to simulate mining activities and the 'benches' represent the cuts made into large open pit mine slopes. The input parameters for this are outlined in Table 4.2. As shown in column 3 (Table 4.2), parameter values can be input directly via the GUI or via the use of input files: A Drawing eXchange Format (dxf) can be used to input bench geometry and importantly can be used to define the morphology of the slope surface; and, a DFN can be used to represent a probabilistic set-up of joint segments and discrete fractures within the model in 3D (Palleske *et al.,* 2013). Notably this allows the model to begin with a fractured rock mass, reflecting the inherent damage seen in natural rock slopes in the field. Once defined, the benches are constructed in the lattice

based structure described above. This is based on an inbuilt lattice data set, which is scaled to suit the resolution and material properties assigned.

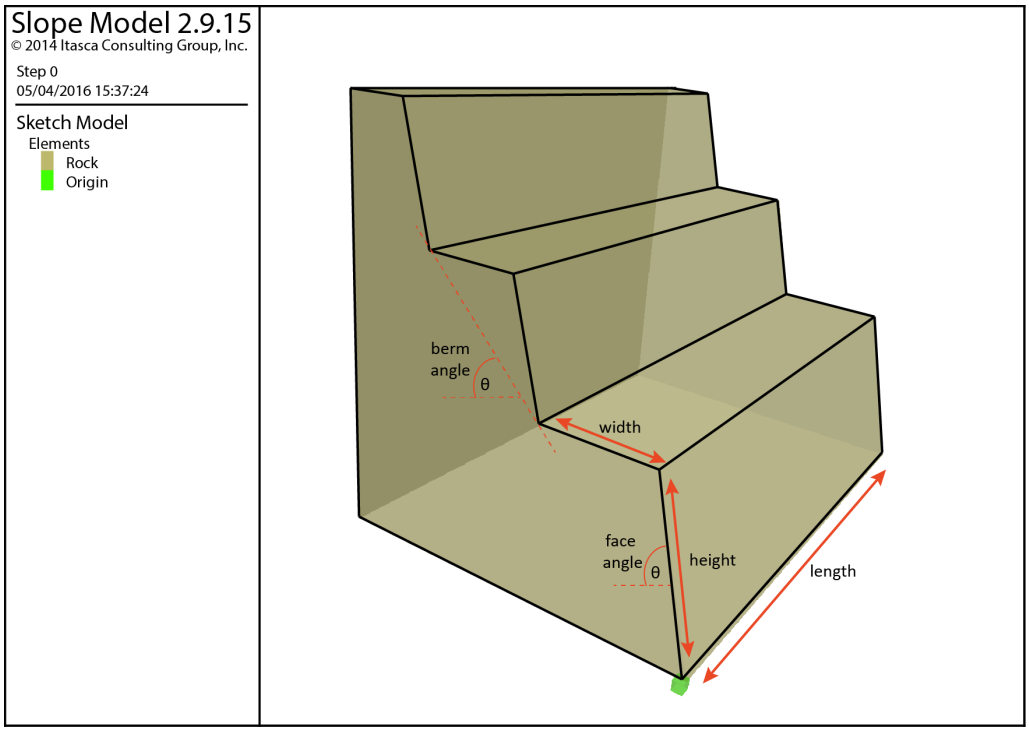

Figure 4.2: Bench setup in Slope Model

The outputs of *Slope Model* can be observed and recorded in the following ways:

- Displacement over time at specified nodes;
- Velocity over time at specified nodes;
- The velocity field for the entire slope (deformation) at specified times;
- The time series of microcracks (fractures);
- The location of microcracks (fractures);
- The values of stresses at specified nodes at any specified time.

Table 4.2: Slope Model input parameters
(*these are both recent (2014) additions to the model code and are explained in the following sections)

Category	**Parameter**	**Input method**
Main rock (geometry)	Dimensions - Bench set-up (length, width, height, face angle, berm angle – see Figure 4.2)	Direct (via GUI) OR, Indirect (via .dxf file)
	Rock type - Density, ρ (kg/m^3) - UCS, σ_c (MPa) - Tensile strength, σ_{ts} (MPa) - Young's modulus, E (GPa) - Poisson's ratio, v - Friction angle, φ (°) - Porosity, n (%) - Permeability, k (m^2)	Direct (via GUI): pre-set rock types or user-defined OR, Indirect (via .dxf file)
	Stress (MPa): σ_{xx}, σ_{yy}, σ_{zz}	Direct: 3 principal components, applied at top and base of model

Features (optional)	Joint sets
	- Material properties (σ_{ts}, φ, c)
	- Dilation: angle (°) & slip (mm)
	- Dip & dip direction (°)
	- Stiffness (GPa/m):
	  o K_n (normal)
	  o K_s (shear)
	- Spacing (m)
	- Reference point
	- Radius & aperture (optional)
		Direct (via GUI: built in DFN generator)
		OR, Indirect (via DFN file)

	Seams/excavations - Origin and orientation - Geometry - Material	Direct (via GUI)

	Fluid flow
	- Fluid type
	- Pressure:
	  o constant (Pa)
	  o gradient (water level, m)
		Direct (via GUI)

Solution	Resolution of the lattice (m)	Direct (via GUI)
	Fluid flow (active or not)	Direct (via GUI)
	Aperture change (max aperture)	Direct (via GUI)
	Flat Joint Model (disk radius & sub-contact points)*	Direct (via GUI)
	Spring Failure Latency* - Radius - Timestep	Direct (via GUI)

4.3.1.1 Flat joint model

The first version of Slope Model returned ratios of unconfined compressive strength (*UCS*) to tensile strength (σ_{ts}) that were much lower than those typical of hard rocks (Cundall, 2014). This was assumed to be because Slope Model was unable to model partial failure of a contact. In order to address this, a version of the Flat Joint Model originally developed by Potyondy (2012), was added to the code. Rather than the simple node and spring arrangement, a contact disk is assumed between nodes, with sub-contacts arranged around the circumference of the disk (Figure 4.3). Resulting normal and shear displacements at sub-contacts (computed from the translational and rotational motion of the corresponding nodes) produce forces that can then be compared to tensile and shear force limits, and therefore breaking, sliding or opening can occur separately at each sub-contact (Potyondy, 2012). Cundall (2014) state that including the Flat Joint Model within Slope Model has produced much higher UCS/σ_{ts} ratios, which correspond to those exhibited by most hard rocks. Further details of the formulation, verification and implementation of the Flat Joint Model are given in Cundall (2014). The Flat Joint Model can be optionally activated within Slope Model, and the disk radius and number of sub-contact points specified by the user. It has been used in this study in order to ensure that partial failure of a contact may be simulated and so that the UCS/σ_{ts} ratios generated are representative of hard rock.

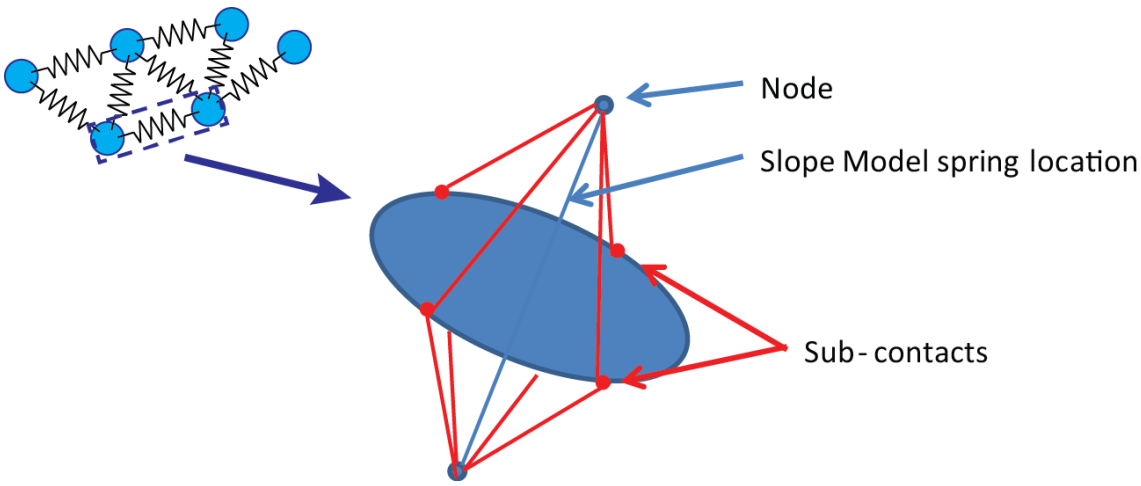

Figure 4.3: Illustration of the Flat Joint Model in Slope Model. The blue disk represents the contact disk between the two nodes, and the red lines indicate the vectors from nodes to contacts. The smaller inset shows this in the context of the lattice structure in Fig 4.1. (Modified from: Cundall, 2014)

4.3.1.2 Spring Failure Latency

Whenever a new microcrack is initiated in the model represented by a spring breakage, this parameter gives the option to set the distance (cm) and time (time steps) over which no new microcracks can appear. Inclusion of this in the model gives the user the ability to simulate a delay in the initiation of new microcracks once a microcrack has formed, either spatially, temporally, or both. This can be used to avoid runaway failure, whereby the initiation of a microcrack then transfers stress to surrounding springs causing further microcracks to rapidly appear; or can also be used to more easily examine the impact of specific microcrack initiation on subsequent slope failure. This is also optionally activated within Slope Model and was used in later stages of the model experiments in this study as a way of prohibiting microcrack development, as explained in Section 4.7.

4.3.2 Previous work

Slope Model was written as part of the Large Open Pit project (LOP) (CSIRO, 2014) with the primary application of assessing slope stability in large open pit mines. A large number of applications of the model code have therefore been to simulate slope and rock mass failure in large open pit slopes, such as Havaej *et al.* (2014b), Lorig *et al.* (2010) and Cundall and Damjanac (2009). Applications of the code beyond this have included: the reproduction of laboratory test results (Cundall, 2011); investigations of internal damage and dilation during slope failure (Tuckey *et al.,* 2012); and more detailed investigations into the role of damage in driving slope failure in both engineered and natural rock slopes (Havaej *et al.,* 2014b, Havaej *et al.,* 2013). Together these studies have demonstrated the applicability of the code to large scale slope failure analysis and its ability to critically evaluate the role of brittle fracture as a driving process in a range of slope conditions.

The work of Havaej *et al.* (2013) and Havaej *et al.* (2014b) uses Slope Model to highlight the close relationship between kinematics and damage required for rock slopes to fail. In doing this, they demonstrate the applicability of Slope Model outputs for assessing the magnitude of internal damage at the onset of failure. Inverse velocity and displacement are recorded as outputs in the model to determine the point of failure onset, and the extent of newly created cracks are also recorded for this point in time. Their work particularly illustrates the unique capability of Slope Model to examine the role of internal damage on failure. This capability of a model code is essential to achieving Research Objective 2, which focuses on the role of time-dependent failure. The work of Havaej *et al.* (2013), Havaej *et al.* (2014b) and other

applications of Slope Model are yet to apply the code to model rock slope failure at the smaller scale (< 10 m) in natural settings. This study applies Slope Model to evaluate the conditions when time-dependent fracturing, possibly indicative of progressive failure, acts to drive short-term rock slope behaviour, by exploiting the unique capabilities of Slope Model to examine the role of internal damage alongside surface expressions of failure.

4.4 Model Performance

Slope Model is a commercial model code that has been verified against standard modelled scenarios, as reported in Itasca (2010b). It has also been successfully used to model slope failure in a variety of studies, as previously discussed. This study is not focused on the development of the Slope Model code but is using it to develop process understanding of the role of time-dependent fracture associated with failure in natural rock slopes. Key aspects of model behaviour and demonstration of confidence in the model outputs, which build on previous work (Itasca, 2010b) are given in Appendix 2. Aspects of model behaviour that have been specifically developed for this study are detailed below.

4.4.1.1 Displacement threshold

Slope Model calculates displacement at each node within the lattice, however the explicit solution scheme of the model means that there is not an inbuilt threshold that defines failure. Therefore a displacement threshold, which represents the complete detachment of material from the slope, was determined for this study. This allows a finer threshold to be applied, enabling the model to be used for different purposes, such as for simulation of failures at a smaller scale, and for individual rockfalls rather than whole slope failure. A measure of critical strain, defined below, was adopted as an approach to calculate the displacement threshold and therefore the threshold is independent of the model resolution and applicable to any of the model scenarios to be tested. Critical strain (ε_0) can be used to represent the point at which a rock mass fails (Sakurai, 2001) and is defined as the ratio of the uniaxial compressive strength (σ_c, MPa) and Young's Modulus (E, GPa):

$$\varepsilon_0 = \frac{\sigma_c}{E}$$

Equation 4.4: from Sakurai (2001)

where ε_0 is expressed as a percentage. This can be translated to a displacement threshold, by assuming that once displacement has reached ε_0 % of the total length of the rock mass, then the block has failed. As emphasised by the research objectives stated at the beginning of this chapter, this study is concerned with different stages of failure development. Therefore it is important to consider whether this critical strain (displacement) threshold represents final failure or an intermediate stage.

Critical strain levels in a rock mass are emphasised in many field and modelling studies, and have been linked to a range of environmental forces (Brain *et al.,* 2014). In a stress-strain curve showing the stages of crack development for a uniaxial compressive strength test (Fig. 4.4), each of these stages could be represented by a level of critical stress or strain. Petley *et al.* (2005) suggest that the crack initiation threshold, which marks the point at which microcracks interact and coalesce, may be well represented by a critical strain value. Crucially the rock mass must reach this critical strain level at crack initiation (σ_{ci}) in order for cracks to coalesce before damage can then further influence rock mass strength (Brain *et al.,* 2014). The crack damage threshold (σ_{cd}), represents the point at which the shear strength of the rock mass has been exceeded and it then catastrophically accelerates to failure. This has been shown to be characterised by linearity in Λ-t space, where Λ is 1/velocity and t is time (Petley *et al.,* 2005). Havaej *et al.* (2014b) have identified this threshold in Slope Model by plotting both Λ and displacement against t. They refer to this point as the *onset-of-failure*. Finally, the peak strength identified in Figure 4.4 (σ_f) represents final failure.

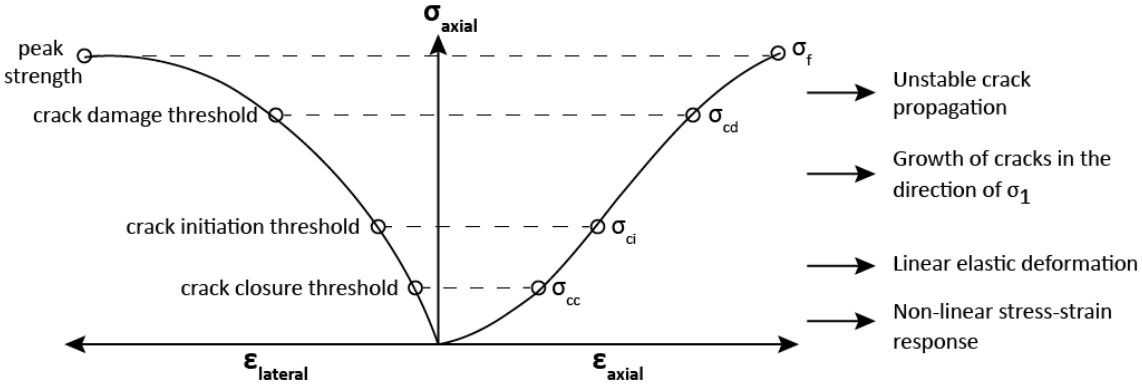

Figure 4.4: Stress-strain curve showing the stages of crack development: modified from Eberhardt *et al.* (1999). The second threshold (σ_{ci}) can be represented by a critical strain.

:

In order to determine which stage of failure is represented by the calculated critical strain (equation 4.4) a model scenario is set in Slope Model based on the conditions that satisfy an unstable slope, as identified by Itasca (2010b) and described in Appendix 2 (3D wedge stability). A 75°, 40 m high slope composed of 'test rock' (Appendix 2: Table A2.1) is simulated at a lattice size of 1 m, with two daylighting joint planes with dips of 40° and dip directions of 40° and 130° (Fig. A2.1). The material properties of the rock and joints are the same used in the model resolution experiments, given in Appendix 2: Table A2.1. This setup generates a failing wedge, with a long axis of 13 m as shown in Figure 4.5.

Adopting the approach of Havaej *et al.* (2014b), Figure 4.6 displays a plot of inverse velocity and displacement against time. As can be seen in Figure 4.6a the onset of slope failure (grey dashed line) is located between 0.1 and 0.2 seconds (numerical simulation time), as evidenced by the acceleration in slope displacement and the initiation of a more linear trend in the inverse velocity plot. Using equation 4.4 and the rock material properties in Appendix 2: Table A2.1, the critical strain for this material is: 200/70 = 2.86 %. Using this as the displacement threshold for the failing wedge (length 13 m) suggests that the point of failure is reached when displacement at the centre of the wedge reaches 0.372 m. As indicated in Figure 4.6b (black dashed line), this occurs at 2.8 seconds (numerical simulation time). This is far to the right of the onset of slope failure on the graph and within the region of the graph where displacement is accelerating and appears unstable. According to the thresholds identified in Figure 4.4, this would suggest that the calculated critical strain is representative of final failure (σ_f) and the detachment of material from the rock slope. The identified onset of slope failure most likely represents the crack damage threshold, σ_{cd} (Fig. 4.4) as this is where the acceleration in slope displacement begins. Subsequently, for the purposes of this study the calculated critical strain threshold is adopted as the displacement threshold. For those experiments that it is relevant to, the onset of slope failure is also identified in the same way (Fig. 4.6).

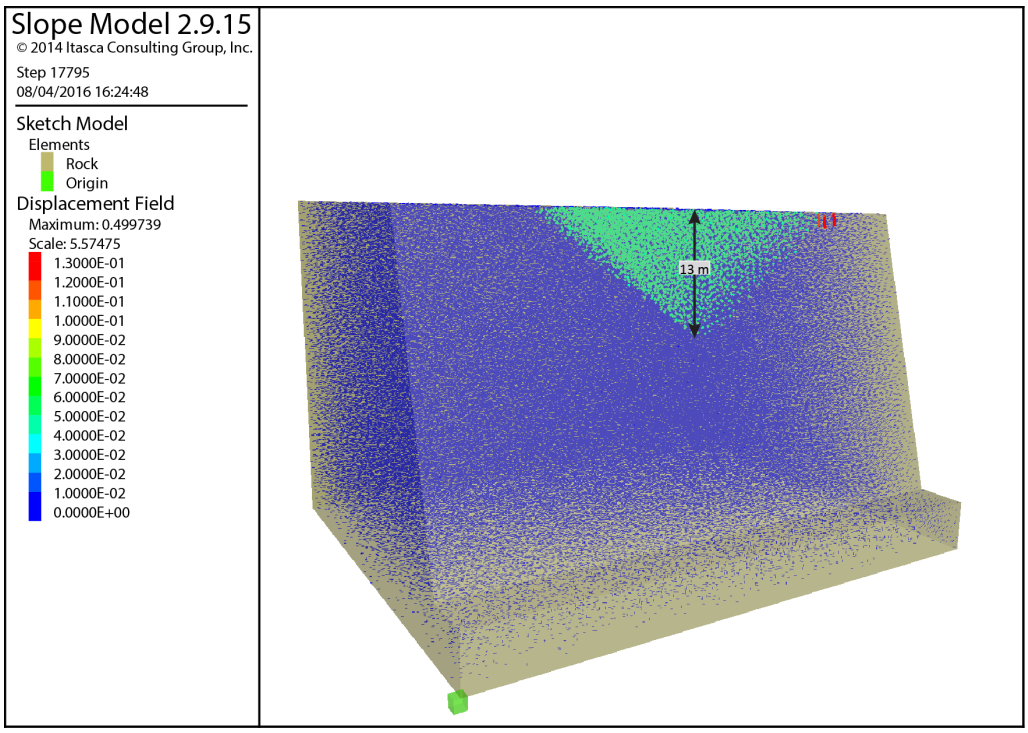

Figure 4.5: Failing wedge shown as light green nodes, with elevated displacement where the model comprises two joint planes (dips of 40° and dip directions of 40° and 135°) daylighting in the 40 m high slope.

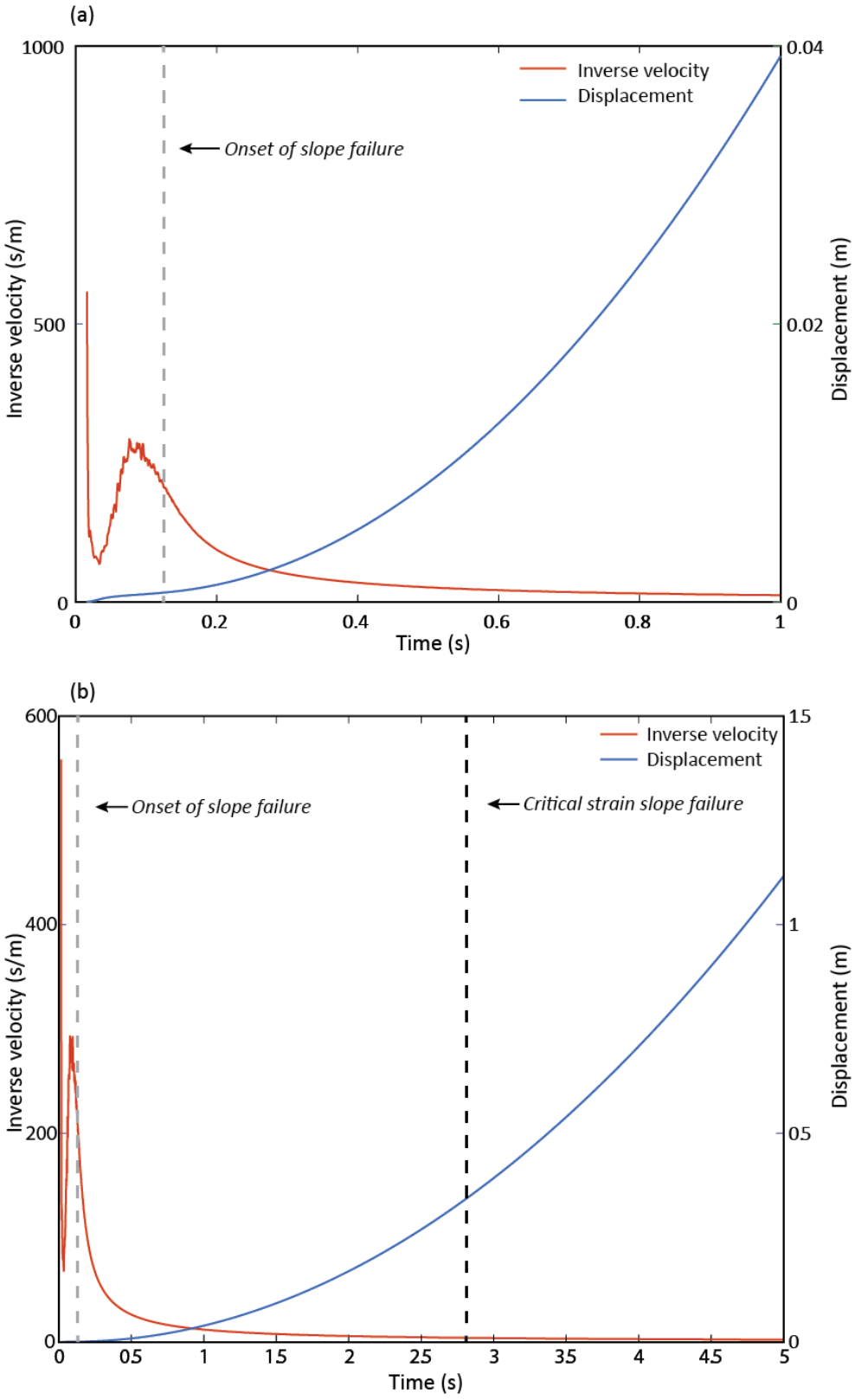

Figure 4.6: Plot of inverse velocity and displacement at the centre of the failing wedge (shown in figure 4.5) (a) for the first second of numerical simulation time; (b) for 5 seconds of numerical simulation time. The grey dashed line indicates the onset of slope failure, identified as the point at which slope displacement accelerates and inverse velocity initiates a more linear trend. The black dashed line indicates the critical strain slope failure threshold, calculated from equation 4.2.

4.5 Experimental Design

In order to answer the research questions outlined (Section 4.1), a variety of scenarios were developed in Slope Model to examine the conditions required for failure from the cliff face and the spatial and temporal extent of fracture growth around these failures. The scenarios developed focused on variations in joint strength, slope morphology and simulated weathering (weakening) of the cliff. Initially variations in these properties were simulated to establish how the model behaviour varied in response to weakening of the cliff (Section 4.6: Stage One). Following this, further experiments (Section 4.7: Stage Two) were developed to examine the extent of fracture growth in the model. As experiments were designed in this sequential manner, specific details of each experimental design are outlined in the relevant sections before each set of results are presented and details of all model parameters are given in Appendix 2.3.

For all model experiments, the material properties and boundary conditions were derived from field conditions at Boulby reported in Chapter 3 (Fig. 3.4a) in order to be representative of hard rock cliffs. The slope was modelled as a 1,000 m^3 block, 10 m in each dimension (*x,y,z*) with a curved surface at the slope face (Fig. 4.7a). The geometry was created using a .dxf file generated in *Rhino3D* (Robert McNeel, 2014). This was positioned within a larger cliff rock mass, as conceptually illustrated in Figure 4.7b. Less than 1 % of rockfalls identified in the field data in Chapter 3 were larger than 1 m^3 and less than 0.01 % of the rockfalls were larger than 100 m^3. Therefore, a model of this size (1,000 m^3) allows rockfalls of a similar size range to be generated, whilst operating at a high spatial and temporal resolution to allow for fracture growth and subsequent failure propagation. All models were run on a lattice with a node spacing of 0.2 m, which represents the finest spatial resolution for a model of this size that also allows a minimum of one simulation to run per day.

The stress values applied as boundary conditions to the model were defined in order to simulate the location of this block within a 60 m high slope, as illustrated in Figure 4.7. Basic calculations of stress due to loading were performed based on the material properties of the cliff at Boulby as described by Lim *et al.* (2010) (Table 4.3). The block was simulated to be located 7 m below the boundary between the shale and siltstone units (the dominant lithology in the cliffs at Boulby), which sits below 22 m of interbedded siltstone and sandstone, as illustrated in Figure 4.7. Based on the material properties of each of these layers, the vertical stress (σ_1) at the top of the block is 0.72 MPa, and 0.96 MPa at the base. Adopting an average *k*-ratio of 0.5 and assuming that horizontal stresses are equal, σ_2 and σ_3 are both equal to 0.36 MPa at the top of the block and 0.48 MPa at the base.

[a]

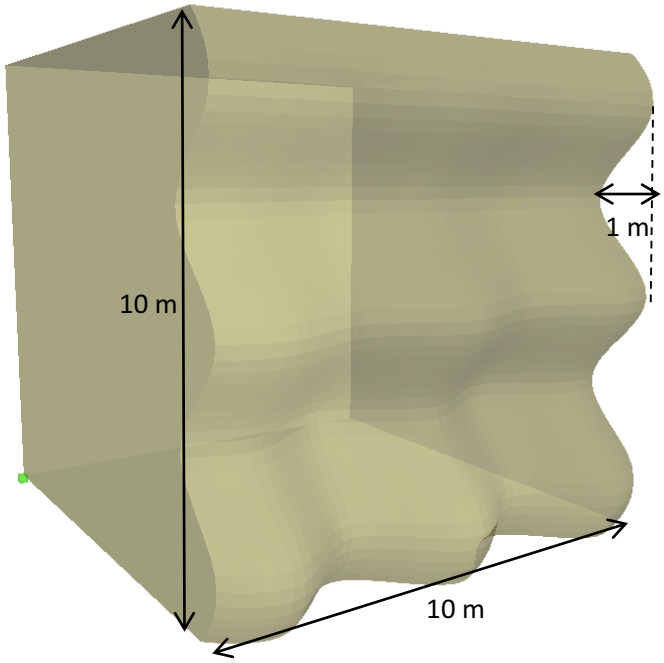

[b]

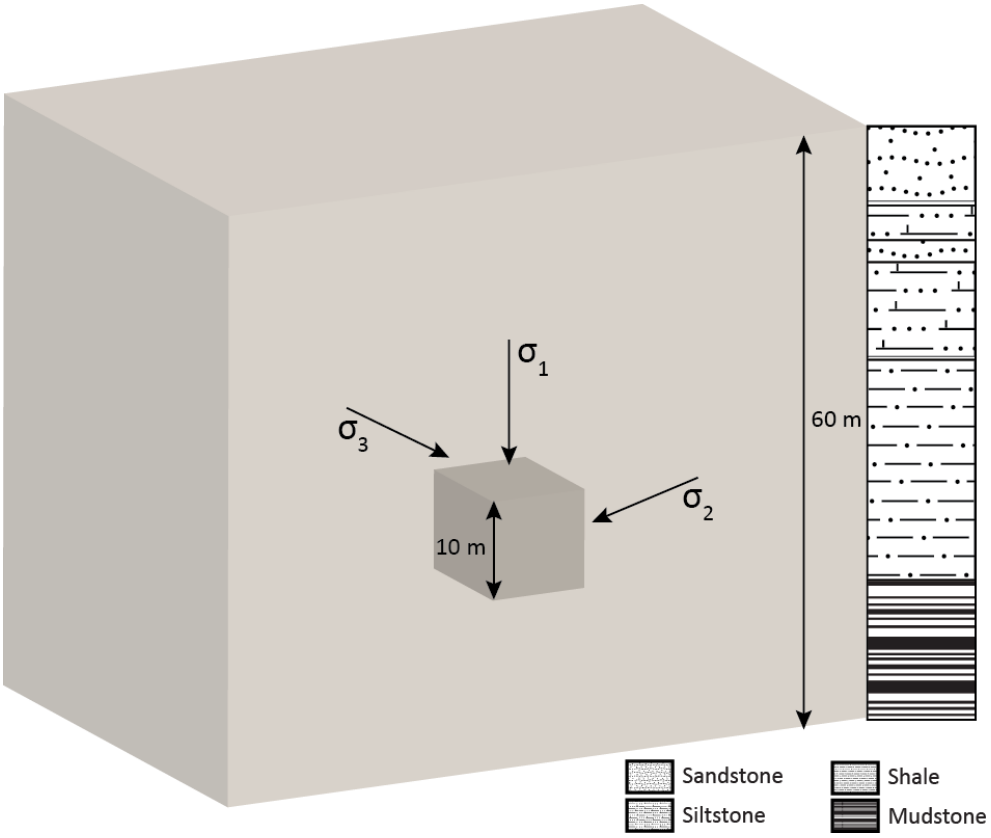

Figure 4.7: [a] Illustration of a 1,000 m^3 block with a curved surface morphology generated as a .dxf file. [b] Shows this block as simulated in the middle of a larger (60 m high) slope. The block is positioned 7 m deep within the shale rock and below the 22 m of interbedded siltstone and sandstone (based on the geology of Boulby, N Yorkshire, as described in Lim *et al.* 2010).

The following optional features (Table 4.2) were included in the model setup: joints, the Flat Joint Model (FJM) and Spring Failure Latency (SFL). Joints were included in all model experiments however the joint properties varied: this is described in Section 4.6. FJM was activated for all model simulations with a disk radius of 0.5 m and 3 sub-contact points. SFL was used in some of the later model experiments and the parameters used are given in Section 4.7, where relevant.

In all experiments a 1 m boundary around the edge of the model was set to account for boundary conditions: this zone was excluded from the results. Each experiment was run for 10 seconds of simulation time (note, this is model calculation time not real time) in order to allow multiple failures to develop. Initial tests have also shown that this allows for model equilibration if the model were to be stable (Appendix 2.2).

The outputs are recorded at designated history points within the model. For all experiments run, history points were set at a spacing of 0.2 m inside of the 1 m border boundary, so that the outputs were recorded at the resolution of the model lattice. For each experiment the following data were recorded:

- Horizontal and vertical displacement (m) at each time step (0.0004 seconds): these were resolved to provide an out-of-slope displacement measurement for each history point;
- Velocity (ms^{-1}) at each time step: from the resolved displacement values, the velocity of each history point was calculated;
- Fractures (cracks): the number of fractures within the model was recorded at each time step, including their location in 3D space. Note, the word fracture is used throughout this chapter and refers to what is sometimes called a 'crack' in the Slope Model literature (Itasca, 2010b).

Table 4.3: Material properties of the geological layers at Boulby, N Yorkshire (see Chapter 3). Reproduced with permission from: Lim *et al.* (2010).

	Elastic modulus (MPa)	**Bulk density (kg m^{-3})**	**Poisson's ratio**	**Tensile strength (MPa)**	**Uniaxial compressive strength (MPa)**
Sandstone	3480.55	2583	0.30	3.02	34.21
Siltstone	2206.32	2492	0.23	1.72	30.20
Shale	2137.38	2486	0.40	3.03	16.69
Mudstone	4126.33	2513	0.28	3.48	41.54

4.6 Stage One: Conditions for failure

The first stage of experiments was used to address research question 1 for this chapter: *How does the model behaviour (magnitude and timing of failure) vary in response to weakening of the rock slope?*

Slope Model is initially set up with material and joint properties reflecting the conditions in the field. As described above, the block is simulated as positioned within the shale layer of a 60 m high slope, reflecting the geological structure seen at Boulby, N Yorkshire (Chapter 3, Fig. 3.4a). The material properties used within Slope Model were taken from the properties of the shale rock as given in Table 4.3. Joints were input into the model via the built in DFN generator within Slope Model. The joint geometry and material properties were determined according to the methods described below. The model behaviour in response to the range of possible joint strengths and different surface morphologies was examined before then simulating weakening of the rock slope by lowering the material and joint strength.

4.6.1 Experiment setup

4.6.1.1 Joint properties

In order that the joints within Slope Model reflect field conditions, the orientation and spacing of the discontinuity sets at Boulby were determined. Figure 4.8a traces the discontinuity sets at Boulby based on field observations. Using RiSCAN (laser scan point cloud processing software) planes were manually fitted to multiple exposures of each discontinuity within the point cloud. Average values of the orientation of these planes were then used to define the orientation of each discontinuity set, given in Table 4.4. The cliff face at Boulby is near-vertical and strikes east-west at an orientation of 115°E. The spacing of each discontinuity set was estimated from field observations, photographs and the TLS point cloud. The surface of the cliff is highly weathered meaning that visible surface exposures of the discontinuities are limited. The spacing values given in Table 4.4 are given as a range of values based on the exposures available. Data was not available to measure the persistence of each discontinuity identified, however assuming at least a minimum joint persistence according to the classification of joint persistence from Bieniawski (1989), the joints are fully persistent through the 1,000 m^3 block, and were modelled as such. Within Slope Model the orientation of the joints are determined stochastically using a Gaussian distribution around the values in Table 4.4, in order to account for the uncertainty and spatial variability that are inherent to rock

mechanics problems (Havaej *et al.,* 2013). The median, upper and lower values of the range of the joint spacing (Table 4.4) are input into Slope Model. From these a DFN is generated based on a Gaussian distribution. The same DFN was used in all experiments (Fig. 4.8b).

[a]

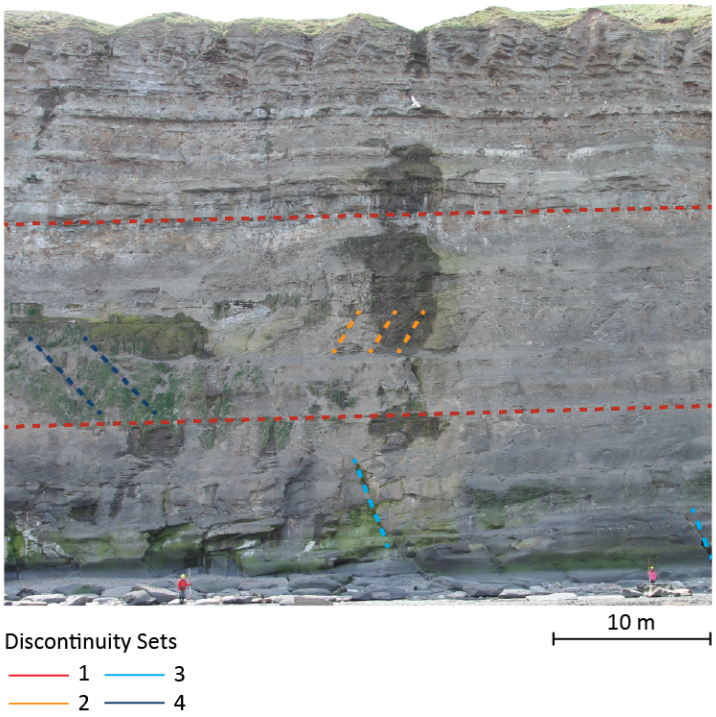

[b]

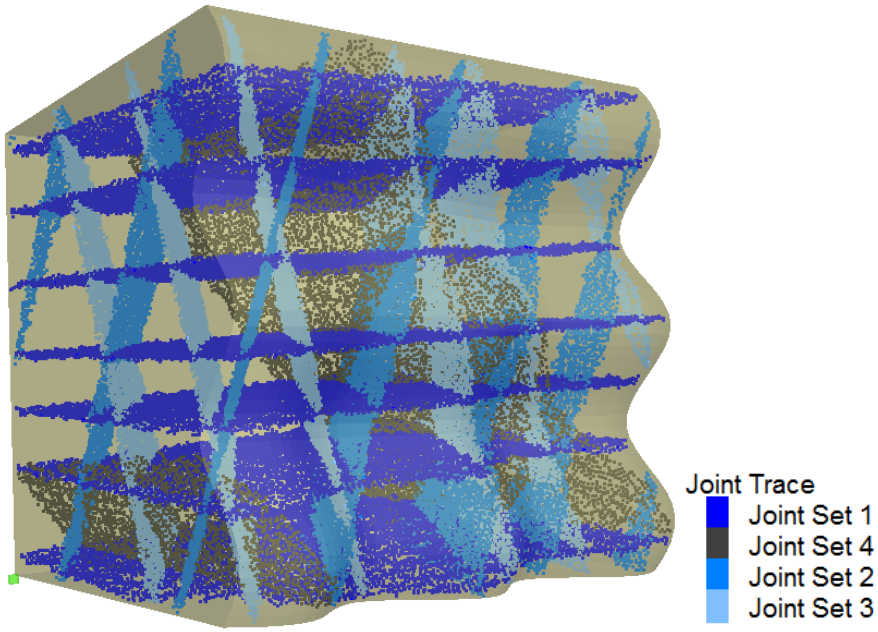

Figure 4.8: [a] Discontinuity sets identified in the cliffs at Boulby, N Yorkshire from field observations and analysis of the acquired scan data (details given in the main text). Orientation and spacing measurements of the discontinuities are given in Table 4.5. [b] Discontinuities represented as joint sets in Slope Model simulations

Table 4.4: Mean orientation and spacing of discontinuity sets at Boulby, N Yorkshire (Figure 4.8), as determined from multiple exposures of each discontinuity within the TLS point cloud data (details given in the text). Spacing is given as a range of values based on the exposures available.

Discontinuity Set	**Dip (°)**	**Dip Direction (°)**	**Spacing (m)**
1 (bedding planes)	6	53	Mudstone: 1.25 – 1.5 Shale: 1.5 – 2 Siltstone: 1.35 – 1.6 Sandstone: 0.9 – 1.1
2	74	118	1.3 – 2.5
3	78	300	1.2 – 2.4
4	53	268	6.5 – 7

The material properties of the joints were included in the model via a range of joint property classifications provided in Slope Model (Table 4.5) whereby the tensile strength is related to the tangent of the friction angle as follows:

$$\sigma_{ts} = \tan \Phi$$

Equation 4.5: Torres (2014)

where σ_{ts} is the tensile strength and Φ is the friction angle. The classification options range from σ_{ts} = 0.01 to σ_{ts} = 0.9 MPa as shown in Table 4.5. Within each classification option, the cohesion, dilation angle and zero dilation slip of the joints are set accordingly by the model. Additionally, the joint stiffness (shear and normal) is input by the user in units of GPa/m. As the material properties of the discontinuity sets at Boulby were unable to be measured as part of this study, average values were determined based on data for similar rock available within the literature. According to Barton (1973) the basic friction angle of joints in unweathered shale (when wet) is Φ = 27°, which equates to a tensile strength of σ_{ts} = 0.51 MPa according to Equation 4.5. This value will increase in dry material (Barton, 1973) and decrease when weathered, to a residual friction angle (Barton, 2013). The shear (k_s) and normal (k_n) stiffness of joints in sedimentary rocks were set at conservative values of k_s = 1 GPa/m and k_n = 3 GPa/m, based on the upper end of the range of strength properties for rock discontinuities, as published by Kulhawy (1975).

To explore the response of the model to the range of values for joint strength, three model experiments were run with different values of the joint strength classification used (Table 4.6). Details of all model parameters for each experiment are provided in Appendix 2.

Table 4.5: Joint strength classifications in Slope Model: the tensile strength and friction angle are related according to equation 4.5.

Joint strength classification	Tensile strength (MPa), σ_{ts}	Friction angle (°), Φ
Very weak	0.01	0.57
Weak	0.1	5.71
Medium-weak	0.25	14.04
Medium	0.5	26.57
Medium-strong	0.75	36.87
Strong	0.9	41.99

Table 4.6: Joint material properties used in the first set of Slope Model experiments.

Model experiment ID	Joint strength classification	Shear stiffness (k_s) (GPa/m)	Normal stiffness (k_n) (GPa/m)
1.1	Medium-weak	1	3
1.2	Medium		
1.3	Medium-strong		

4.6.1.2 Surface morphology

Surface morphology or slope curvature is often overlooked in 3D numerical simulations of rock slopes, resulting in oversimplified slope geometry and its influence on where and what fails (Havaej *et al.,* 2013). Field data analysis presented in Chapter 3 demonstrated a relationship between slope curvature and rockfall, highlighting the potential importance of considering slope curvature within numerical models. Here, the surface morphology was varied to simulate areas of different curvature. In order to achieve this, the .dxf file input option has been used to provide the slope geometry rather than the standard bench input option. Using *Rhino3D* (Robert McNeel, 2014), four .dxf files were generated using sine waves where the wave form was oriented normal to the rockface, with different periods in terms of length scale (*T*) to generate different surface roughness as illustrated in Figure 4.16. Four experiments were setup using each of the surface morphologies, as indicated in the caption of Figure 4.9. In each experiment all other conditions were kept constant at the values given for experiment 1.2 in the previous section. Full details of the model parameters used are provided in Appendix 2.

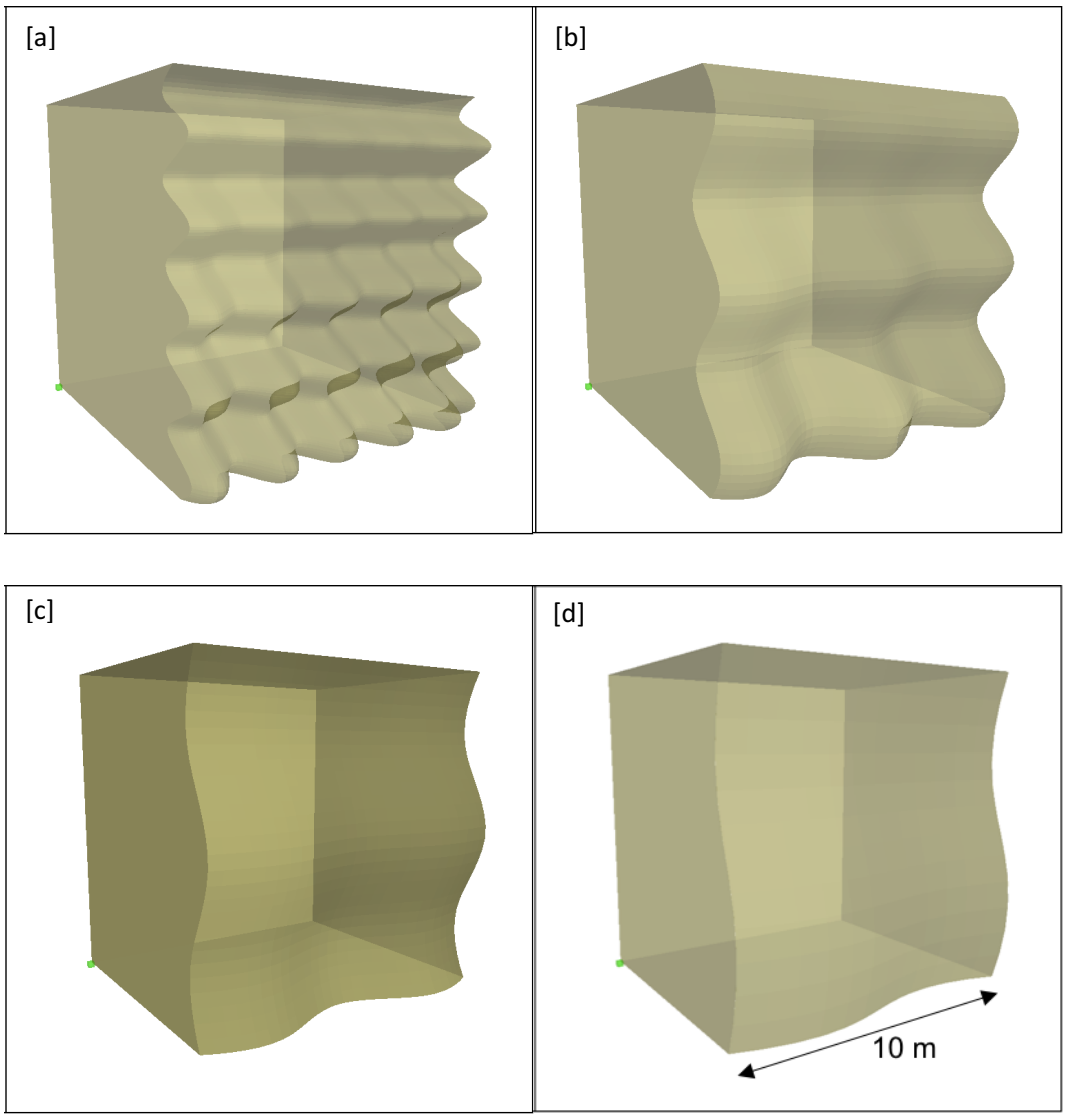

Figure 4.9: Illustrations of the four different surface morphologies generated from the dxf files: [a] $T = \pi/2$ m; [b] $T = \pi$ m; [c] $T = 2\pi$ m; [d] $T = 3\pi$ m, where T = sine wave period (in metres). The different morphologies were used in the following experiments: [a] exp.1.4; [b] exp.1.5; [c] exp. 1.6; [d] exp. 1.7.

4.6.1.3 Weakening the slope rock mass

In addition to considering the impact of possible variations in the material and structural properties of the cliff, the impact of external forcing (weathering) was also represented in the model by weakening both the material and joint strength. Environmental processes play an important role in driving slope failure (Viles, 2013), yet previous studies have shown that the relationship between weathering and rockfall is not clear (Lim *et al.,* 2010, Vann Jones *et al.,* 2015). The results from the field data in Chapter 3 suggest a broad link between the timing of erosion and environmental changes (Fig. 3.37), however this was variable between field sites and within sites there was considerable variability in the rates of erosion between geological layers (Fig. 3.38) and across the cliff face (Fig. 3.40), pointing to a non-environmental control.

Slope Model has been used to observe the changes in the timing and magnitude of failure (displacement) for different simulations of weathering intensity, represented by weakening of the cliff. As demonstrated through the use of laboratory tests by Lajtai *et al.* (1987), rocks in direct contact with water show a reduction in the uniaxial compressive strength (σ_c), fracture toughness (here represented as joint strength), and in the stress required to produce new cracks, represented by the tensile strength (σ_{ts}). To simulate weathering in Slope Model both material and joint strength were lowered to simulate the damage to the rock from weathering. As the model is set up to replicate the near surface region of the cliff (< 10 m depth), this was applied to the entire model.

Three experiments were run in which the strength of the rock mass was lowered by applying a weathering factor (*fW*) to the compressive (σ_c) and tensile (σ_{ts}) strength of the rock (Table 4.7). The *fW* is suggested by Palmström (1995) as a rough estimate of the strength reduction for the compressive strength in rocks, and is applied as follows:

$$\sigma_c = \frac{\sigma_{c\ fresh}}{fW}$$

Equation 4.6: Palmström (1995)

where σ_c is the reduced compressive strength; $\sigma_{c\ fresh}$ is the original compressive strength; and *fW* = 1.75 (slightly weathered), 2.5 (moderately weathered), and 10 (highly weathered). The same equation was applied to reduce the tensile strength simultaneously.

Following this, another three experiments were run, lowering the joint strength by applying lower classes of the joint strength classification, and a final experiment run where both the joint strength was lowered and a weathering factor applied (Table 4.7).

Table 4.7: Changes to the rock mass and joint strength applied to simulate weakening of the cliff, used in the second set of Slope Model experiments.

Model experiment ID	**fW applied to σ_c and σ_{ts}**	**Joint strength classification**
1.8 – 1.10	1.75 2.5 10	Medium
1.11 – 1.13	None (strength as given in Table 4.4)	Medium-weak Weak Very weak
1.14	1.75	Medium-weak

4.6.2 Results

The results of experiments 1.1 – 1.14 are presented in the context of the variable property: joints, slope face morphology, and weakening of the slope.

4.6.2.1 Joints

To identify areas that had failed in the model experiments, the critical strain threshold for failure was used. For model experiments 1.1 – 1.7 the rock mass had the properties of shale (Table 4.3) and therefore using Equation 4.4, the critical strain threshold was calculated as: 16.69/2.137 = 7.81%, which equates to a critical threshold for failure of 0.78 m for a 10 m high slope. Based on this threshold, Table 4.8 details the percentage of the history points that failed and the average timing of failure onset and critical slope failure for these failed areas. As joint strength is increased the failed area decreases as expected, particularly noticeable between experiments 1.1 and 1.2 (Table 4.8). This can be seen in the plots of displacement at the slope surface shown in Figure 4.10, which show a large failed area (red nodes) in the plots of models run at medium-weak joint strength (exp. 1.1). This failed area sits alongside one of the major joints in the model (Fig. 4.8b), indicating that failure has developed around and out from this joint. In the experiments where joint strength is higher (*Js* = medium or medium-strong) failure is seen across the cliff face and is not clustered around the major joints.

Table 4.8: Failed area (%) and the time (seconds) of onset of failure and critical slope failure for each of the model experiments run with different joint properties for 10 seconds of simulation time. Model scenarios are detailed in Table 4.6.

Model experiment ID	**Joint strength classification**	**Failed area (%)**	**Average onset of failure (secs)**	**Average critical slope failure (secs)**
1.1	Medium-weak	50.15	0.20	1.83
1.2	Medium	6.79	0.20	1.62
1.3	Medium-strong	5.54	0.23	1.57

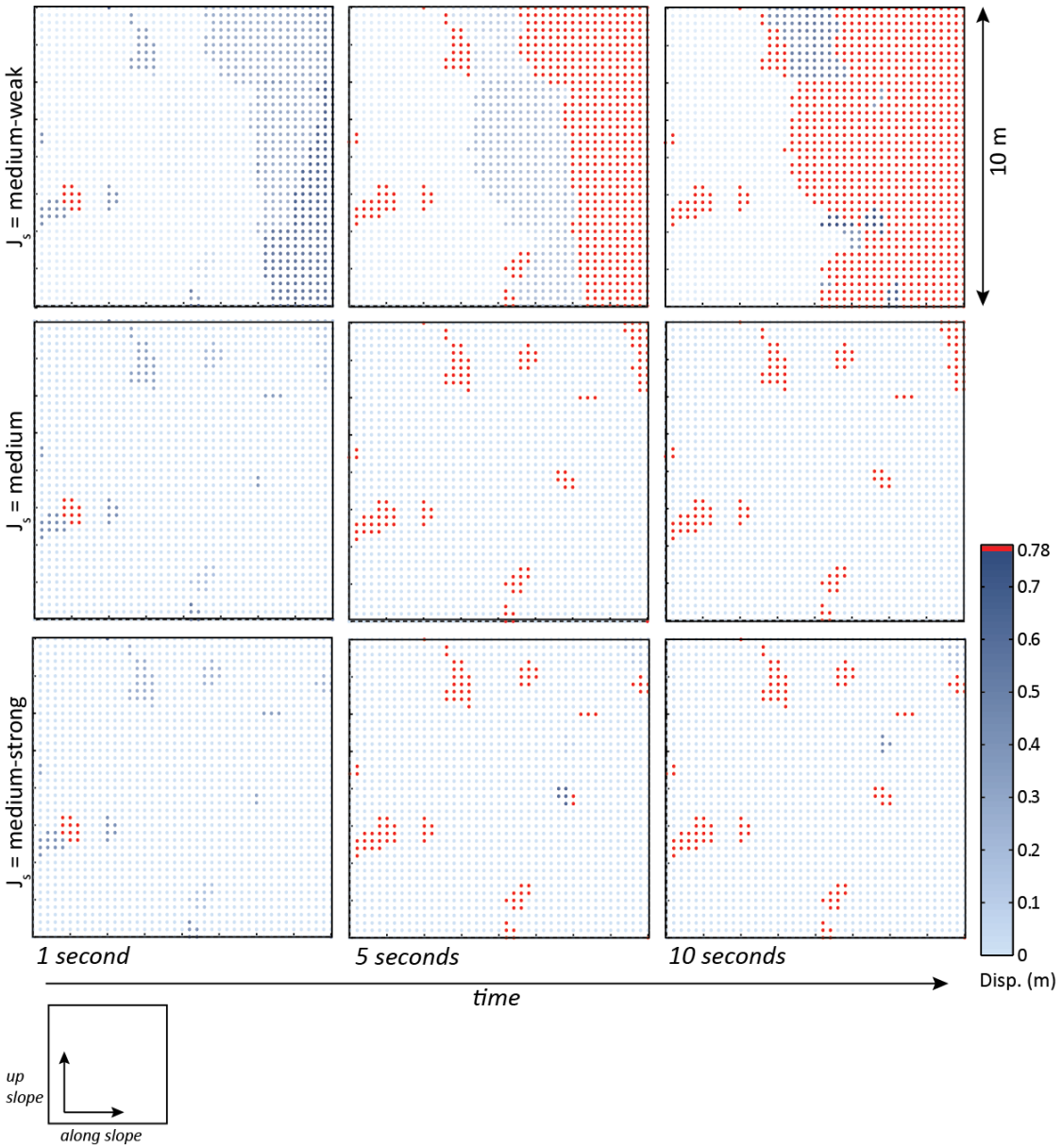

Figure 4.10: Resolved out-of-slope displacement (m) of each history point within the model at 1 second, 5 seconds and 10 seconds of simulation time. Displacement is shown for models run with different joint strengths. Each coloured dot represents a history point (Section 4.5) where displacement was recorded within the model and the value given by the colour illustrates the out-of-slope (horizontal and vertical components resolved) displacement (m) for the specified time, where red dots represent those nodes that have failed, and the blue scale represents deformation. Each plot is a face on view of the slope as illustrated in the sketch below the plots.

The variation in the timing of failure caused by changing the joint properties is shown by plots of failed area at the cliff surface over time for each experiment (Fig. 4.11). Areas of the cliff begin to fail at c. 1.2 seconds of model time in all three experiments. The failed area increases much faster in the experiment run with medium-weak joints compared to experiments run with stronger joints. After two seconds of model time, 33 % of the surface in experiment 1.1

has failed, compared to only 5 % of the surface in experiments 1.2 and 1.3. Although clear differences are seen in the extent of the failed area between experiments, the timing of failure is similar. This is supported in the plots in Figure 4.12, which superimpose inverse velocity onto plots of displacement and identify the average point of failure onset (defined as the time when dV/dt = 1) and the average point of critical strain failure. The timing of failure onset is similar in all three models, however the average time between failure onset and final failure declines as joint strength increases (Table 4.8, Fig. 4.12). In all three model experiments displacement increases smoothly and continuously up to the point of failure suggesting that the failure at these nodes is kinematically free, and so not constrained by confinement and interlocking of neighbouring blocks.

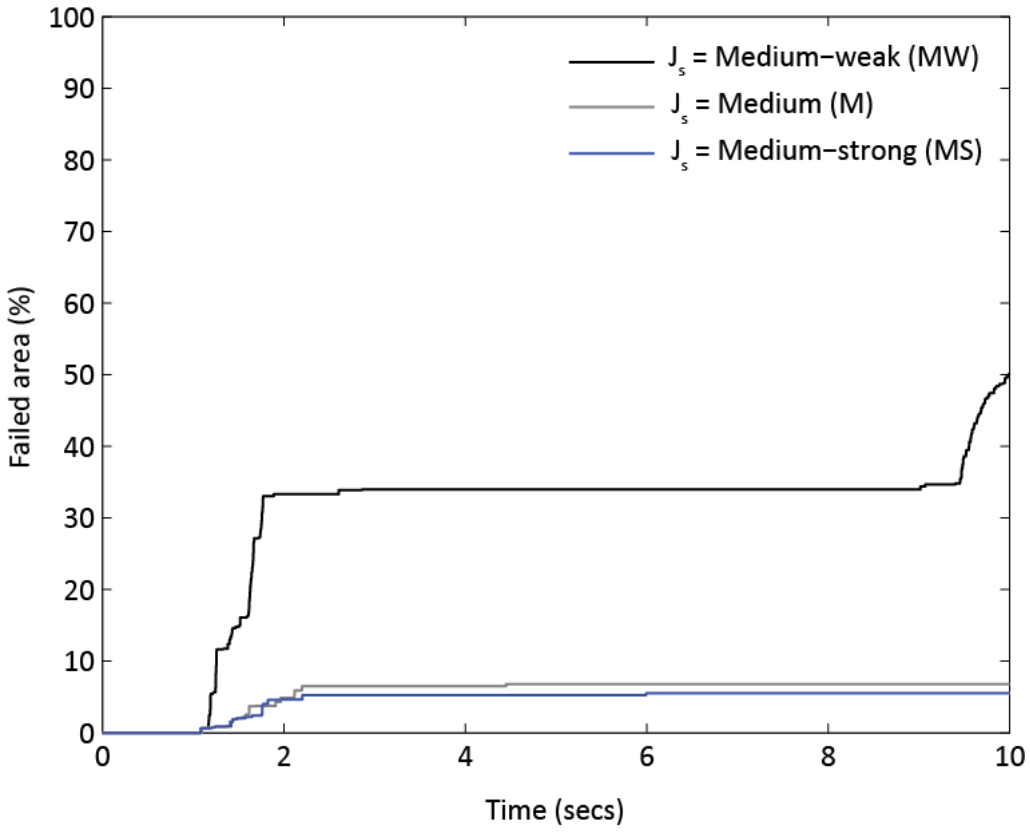

Figure 4.11: Plots of total failed area through time for experiments 1.1 – 1.3. The failed area is calculated as the percentage of history points that have reached the critical threshold for failure (e.g. the red dots in Figs. 4.12).

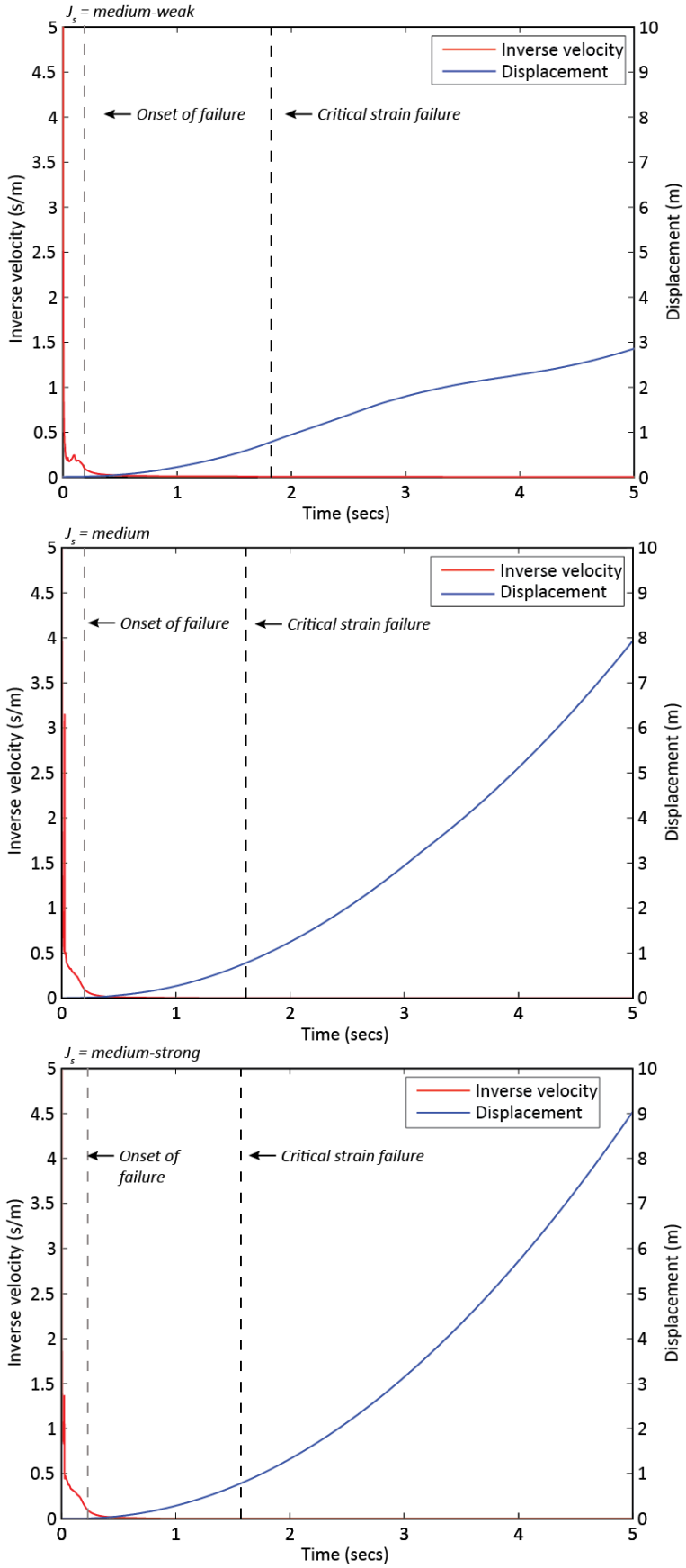

Figure 4.12: Plots of out-of-slope displacement superimposed with inverse velocity and points of failure, for exp. 1.1 – 1.3. Values of inverse velocity and displacement are the average of all the failed history points (e.g. the red dots in Figs. 4.11).

4.6.2.2 Slope face morphology

Models run with a higher surface roughness, represented by a smaller length scale sine wave period (T), generate a larger failed area in total (Table 4.9). When the slope is modelled as a nearly planar surface ($T = 3\pi$) the failed area is 62 % smaller than the failed area generated in the experiment with the most complex surface ($T = \pi/2$). This can be seen in the plots of displacement at the slope surface shown in Figure 4.13. Additionally, in experiments 1.4 – 1.6, many of the areas that have failed are on and around the periphery of the most locally convex areas of the slope surface, which are indicated by the shaded areas in Figure 4.13.

Table 4.9: Failed area (%) and the time (seconds) of onset of failure and critical slope failure for each of the model scenarios run with a different surface morphology: the values given for the surface morphology represent the period of the sine wave used (Figure 4.9).

Model experiment ID	**Morphology (*T*)**	**Failed area (%)**	**Average onset of failure (secs)**	**Average critical slope failure (secs)**
1.4	π/2	13.04	0.19	1.62
1.5	π	6.79	0.21	1.62
1.6	2π	6.08	0.04	1.44
1.7	3π	4.94	0.03	1.51

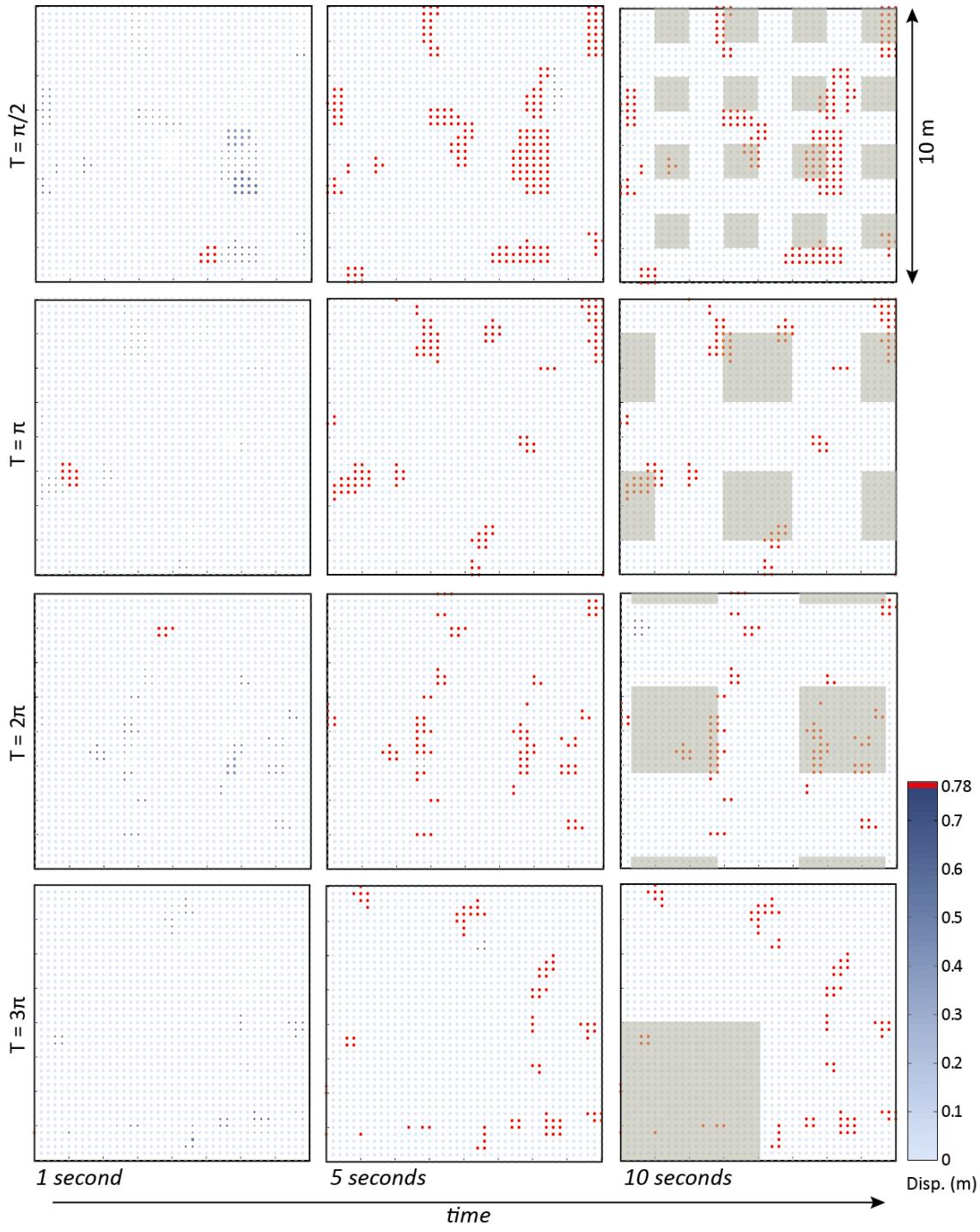

Figure 4.13: Resolved out-of-slope displacement (m) of each history point within the model at 1 second, 5 seconds and 10 seconds of model time. Displacement is shown for models run with different surface morphologies (e.g. *T = π/2:* Figure 4.9). Each coloured dot represents a history point (Section 4.5) where displacement was recorded within the model and the value given by the colour illustrates the out-of-slope (horizontal and vertical components resolved) displacement (m) for the specified time, where red dots represent those nodes that have failed. The shaded areas in the 10 second plots indicate the most locally convex (protruding) areas of the surface (see Figure 4.9).

The variation in the timing of failure caused by changing the surface morphology is shown by plots of failed area over time for each experiment (Fig. 4.14). Areas of the cliff begin to fail at the same time (c. 1.2 seconds) in all four experiments, with a faster increase in failed area seen in the experiment with the most complex morphology (Fig. 4.9a). Failures continue to occur for a longer time period in this experiment compared to the other three as shown by the curves in Figure 4.14. The average timing of failure onset and critical strain failure (Fig. 4.6) appears later in the experiments run with more complex morphology (exp. 1.4 and 1.5) as seen in the plots in Figure 4.15. However, the time between failure onset and critical strain failure is very similar for all four experiments (Table 4.9, Fig. 4.15), and in all experiments displacement increases smoothly and continuously up to the point of failure.

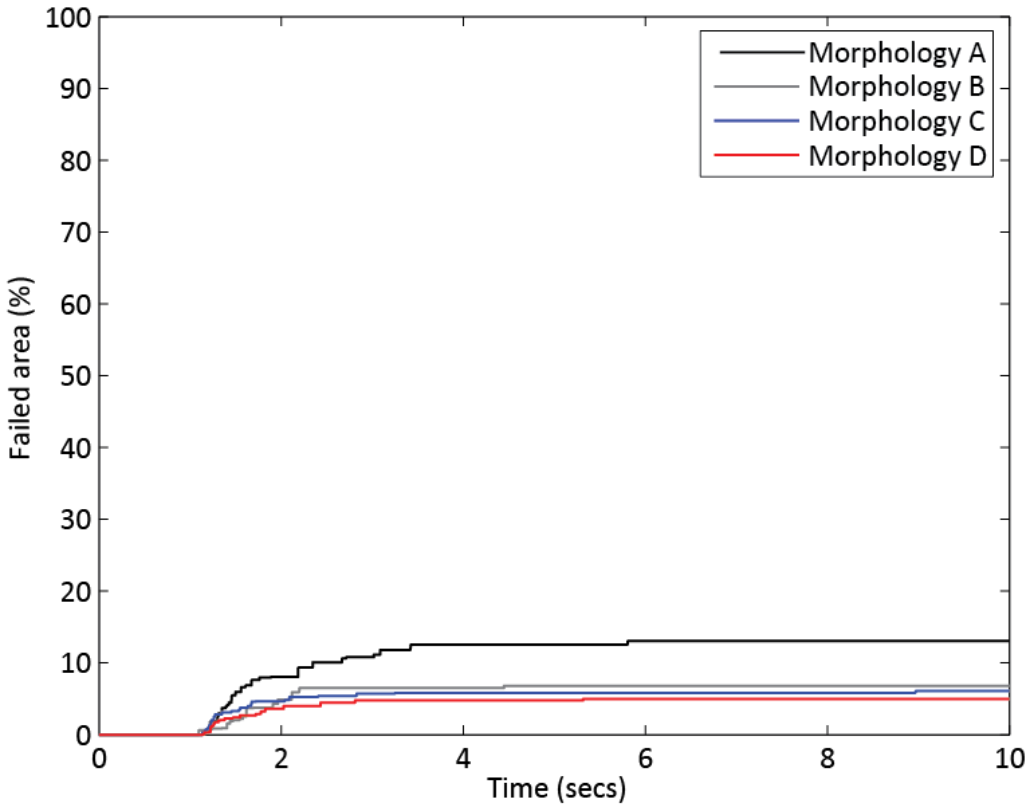

Figure 4.14: Plots of total failed area through time for experiments 1.4 – 1.7. Failed area is calculated as the percentage of history points that have reached the critical threshold for failure (e.g. the red dots in Figs. 4.20). Morphology A = π/2; Morph. B = π; Morph. C = 2π; Morph. D = 3π.

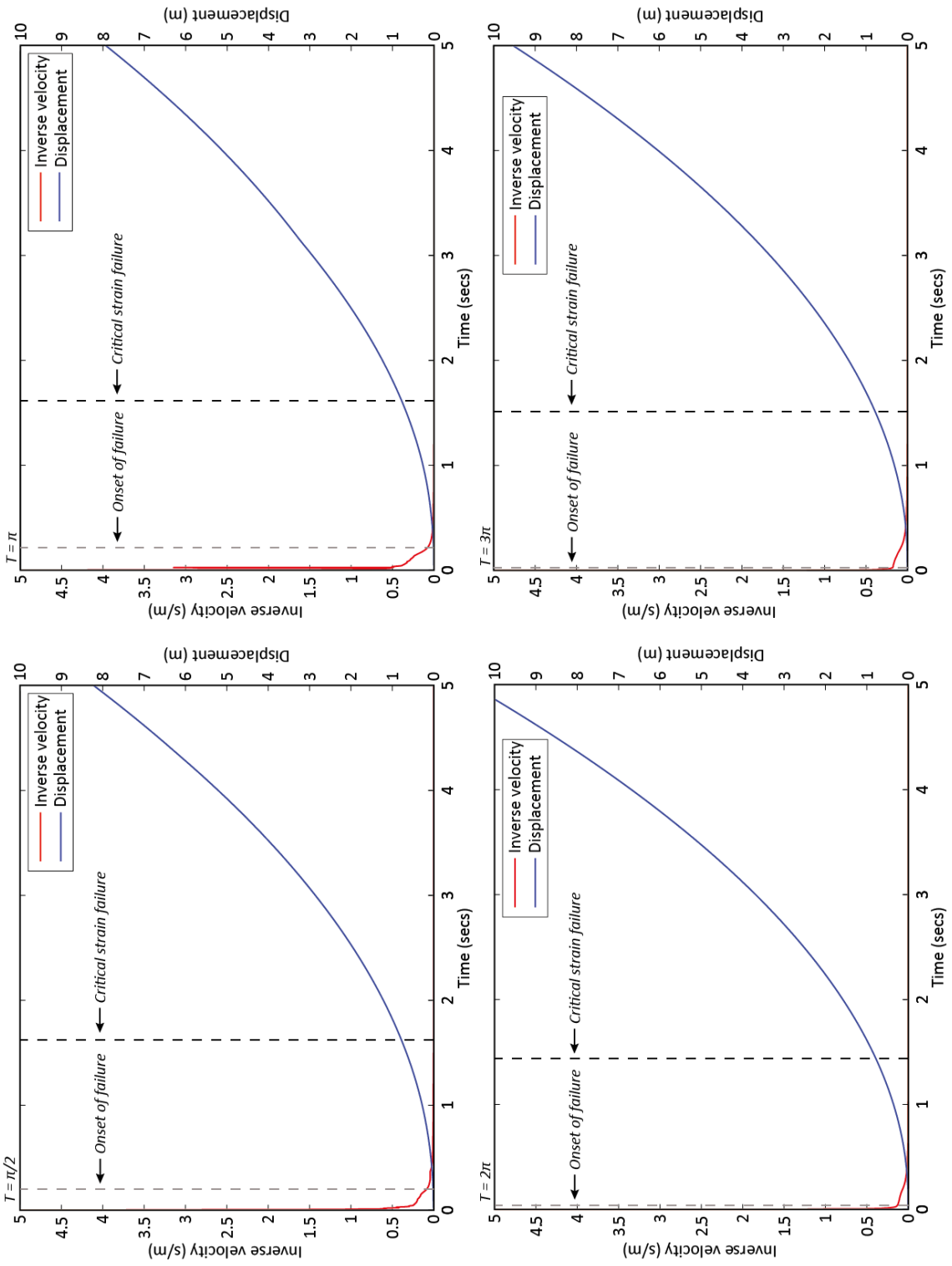

Figure 4.15: Plots of out-of-slope displacement superimposed with inverse velocity and points of failure, for exp. 1.4 – 1.7. The surface morphology of each experiment is indicated above each plot (*T = π/2; T = π; T = 2π; T = 3π)*. Values are the average of all the failed history points (e.g. the red dots in Figs. 4.13).

4.6.2.3 Weakening the slope

The rock mass properties were varied in experiments 1.8 – 1.10, and in experiment 1.14 through the use of the weathering factor (*fW*), which lowered the compressive (σ_c) and tensile strength (σ_{ts}) of the rock (Equation 4.6). Using equation 4.4, the critical threshold for failure for the 10 m high slope in these experiments was calculated (Table 4.10).

Table 4.10: Critical displacement threshold for failure (m) based on the critical strain (%) which is calculated using Equation 4.4, σ_c values listed and a Young's Modulus of E = 2.137 GPa.

Model experiment ID	***fW***	**σ_c (MPa)**	**ε_0 (%)**	**Critical displacement threshold for failure (m)**
1.8 & 1.14	1.75	9.54	4.46	0.45
1.9	2.5	6.68	3.13	0.31
1.10	10	1.67	0.78	0.078

For experiments 1.11 – 1.13, no *fW* was applied and therefore the critical threshold for failure remains at 0.78 m, as defined above. Based on these thresholds, Table 4.11 details the percentage of the history points that failed and the timing of failure onset and critical slope failure. Applying the *fW* to lower the compressive and tensile strength of the rock increases the failed area, as would be expected (Table 4.11), eventually generating almost entire slope failure with *fW* = 10 (Fig. 4.16). Likewise, lowering the joint strength also increases the failed area (Table 4.11) and generates almost entire slope failure at the weakest joint strength (Fig. 4.17). In the results of experiments 1.11 – 1.13 (Fig. 4.17), the growth of failures through time can be clearly seen. In all three experiments the initial failed areas are very similar (at t = 1 second) and as the joint strength is weakened the failure extends over a larger area more rapidly.

Variation in the timing of failure caused by weakening the material strength in the slope is shown by plots of failed area over time for each experiment (Fig. 4.18). Failure begins almost immediately in the experiment with the highest *fW* and increases rapidly for the first few seconds of the 10 seconds of simulation time. The failed area continues to increase until c. 5 seconds of model time. The experiments where *fW* is lowered (experiments 1.8 and 1.9) exhibit a much slower increase in the failed area through time: failure first appears in these experiments at c. 0.8 seconds and increases steadily until c. 3 seconds of model time. Beyond this point no additional failures are seen in these experiments. The average time taken for the failed areas to move from the onset of failure to critical strain failure for these experiments is

illustrated in Figure 4.19. As the *fW* increases, failure onset occurs earlier and the time from onset to critical failure decreases (Table 4.11, Fig. 4.19).

Weakening the slope by lowering the joint strength increases the rate of failure as shown by the plots in Figure 4.20. Failure begins earlier in the experiments run with a lower joint strength and continues to occur for longer than in experiments run with stronger joints. Lowering the joint strength also shortens the time between failure onset and critical failure as illustrated in Figure 4.21: for medium-weak joints the average time from failure onset to critical failure is 1.79 seconds, compared to 1.15 and 1.16 seconds for the experiments run with weak and very weak joints respectively (Table 4.11).

The effect of combining medium-weak joints with the lowest *fW* can be seen by comparing the red and black curves in Figure 4.20. Failure initially appears earlier when both are combined (red curve), and the failure event seen later in the model also begins earlier. No difference is seen in the average onset of failure, but the average critical slope failure appears earlier (Fig. 4.21).

Table 4.11: Failed area (%) and the time (seconds) of onset of failure and critical slope failure for each of the model scenarios run to simulate weakening of the slope.

Model experiment ID	***fW***	***Js***	**Failed area (%)**	**Average onset of failure (secs)**	**Average critical slope failure (secs)**
Weathering factor (*fW*)					
1.8	1.75	Medium	6.85	0.22	1.29
1.9	2.5	Medium	7.03	0.21	1.08
1.10	10	Medium	84.40	0.04	0.66
Joint strength (*Js*)					
1.11	-	Medium-weak	50.15	0.20	1.83
1.12	-	Weak	65.63	0.16	1.31
1.13	-	Very weak	94.52	0.14	1.30
fW and *Js*					
1.14	1.75	Medium-weak	52.05	0.20	1.66

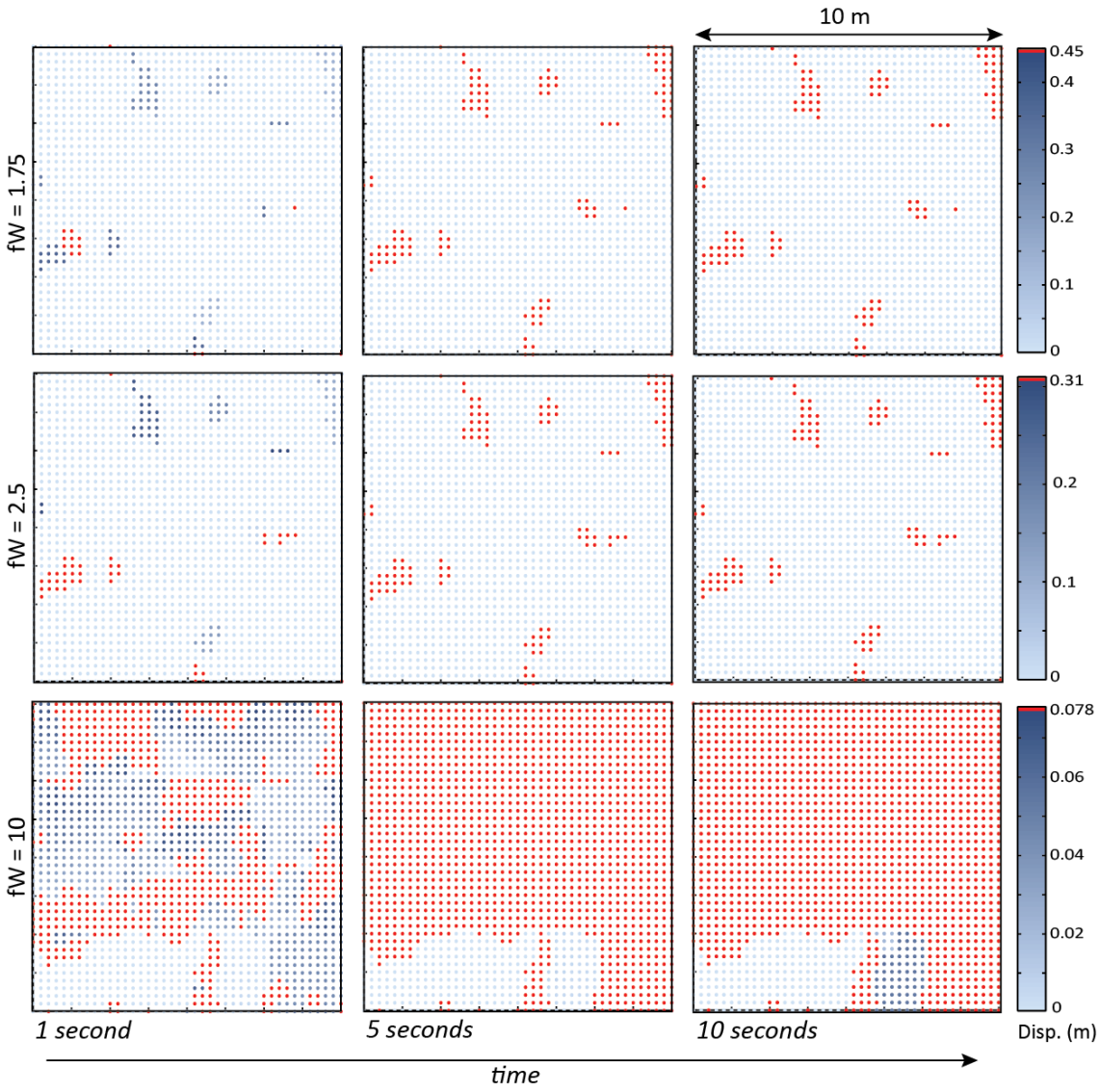

Figure 4.16: Changing material strength: Resolved out-of-slope displacement (m) of each history point within the model at 1 second, 5 seconds and 10 seconds of model time. Displacement is shown for models run different weathering factors (*fW*) applied, thereby lowering the tensile and compressive strength of the rock. Each coloured dot represents a history point (at each node) within the model and the value given by the colour illustrates the out-of-slope (horizontal and vertical components resolved) displacement (m) for the specified time, where red dots represent those nodes that have failed. Note that the threshold for failure changes with different *fW* as the threshold is dependent on the compressive strength.

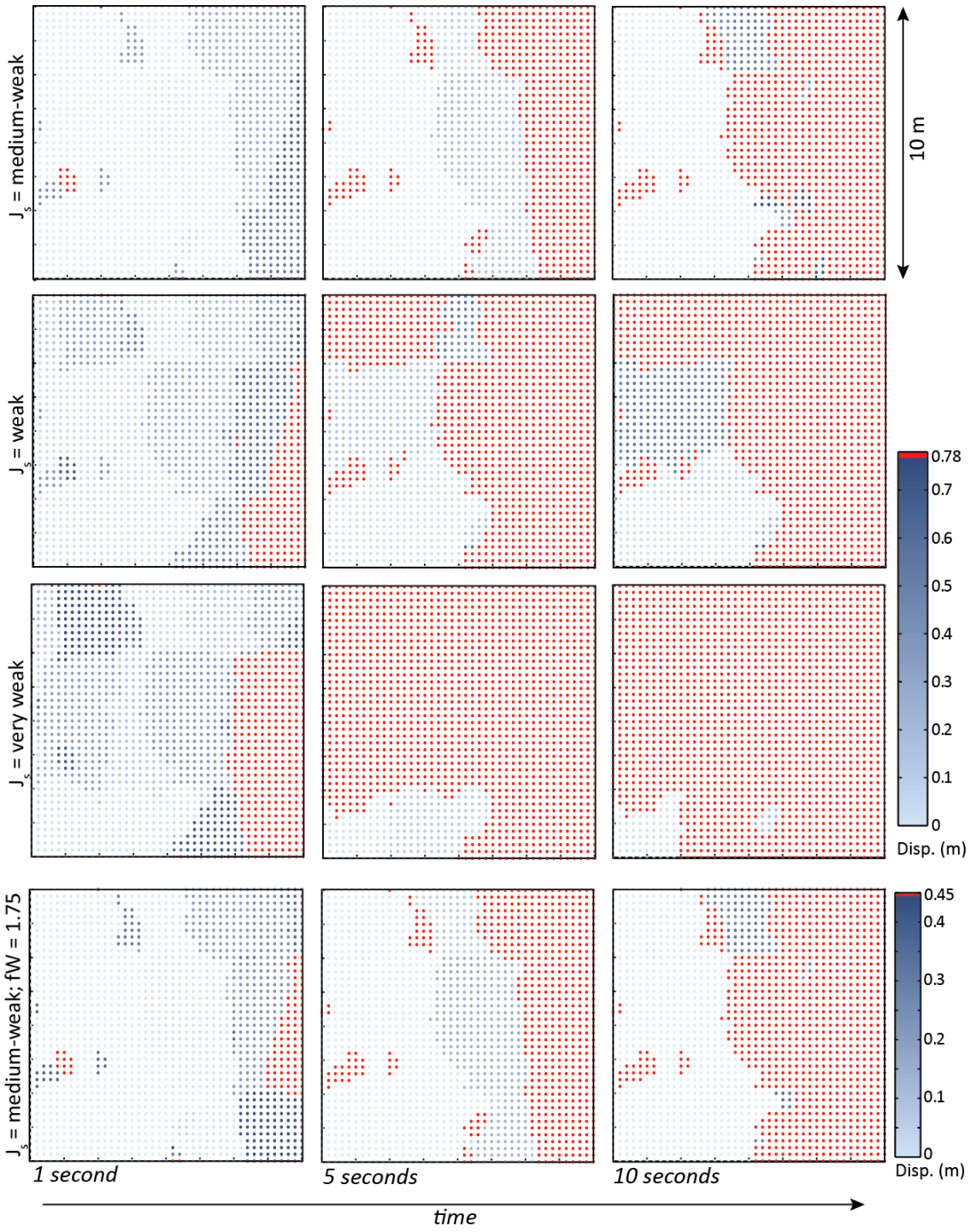

Figure 4.17: Changing joint strength: Resolved out-of-slope displacement (m) of each history point within the model at 1 second, 5 seconds and 10 seconds of model time. Displacement is shown for models run with different joint strengths, and for experiment 1.14 where both joint and material strength were lowered. Each coloured dot represents a history point (at each node) within the model and the value given by the colour illustrates the out-of-slope (horizontal and vertical components resolved) displacement (m) for the specified time, where red dots represent those nodes that have failed.

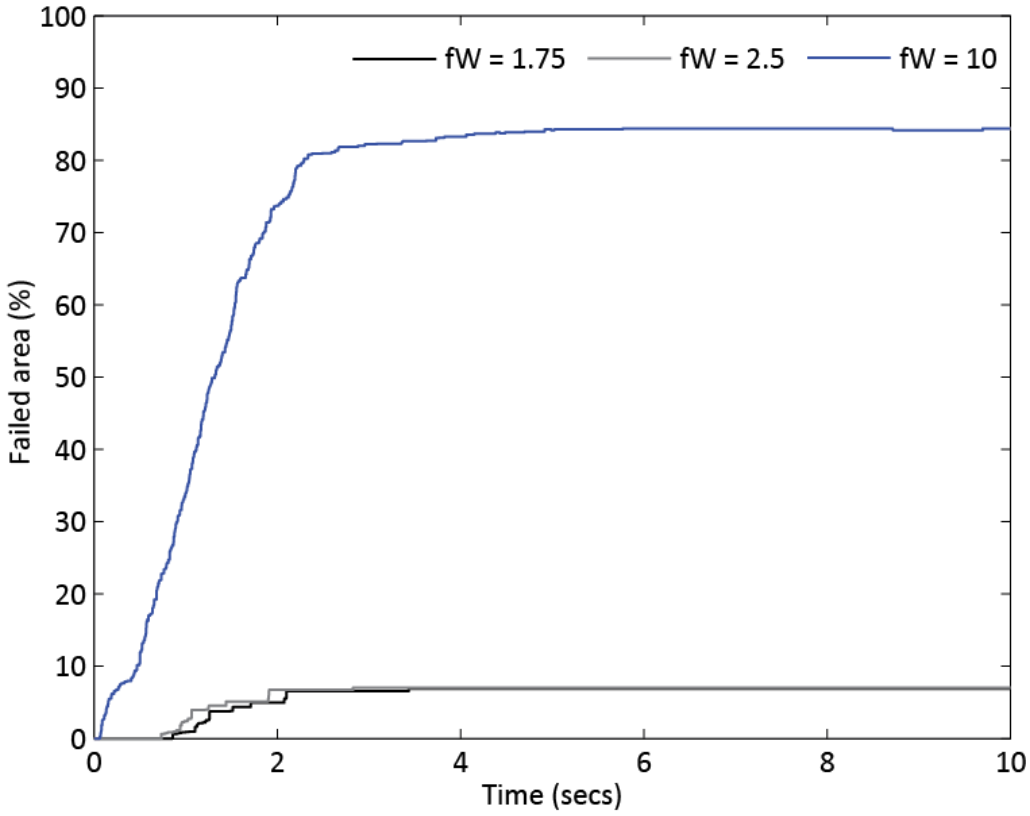

Figure 4.18: Plots of total failed area through time for experiments 1.8 – 1.10. Failed area is calculated as the percentage of history points that have reached the critical threshold for failure (e.g. the red dots in Figs. 4.16).

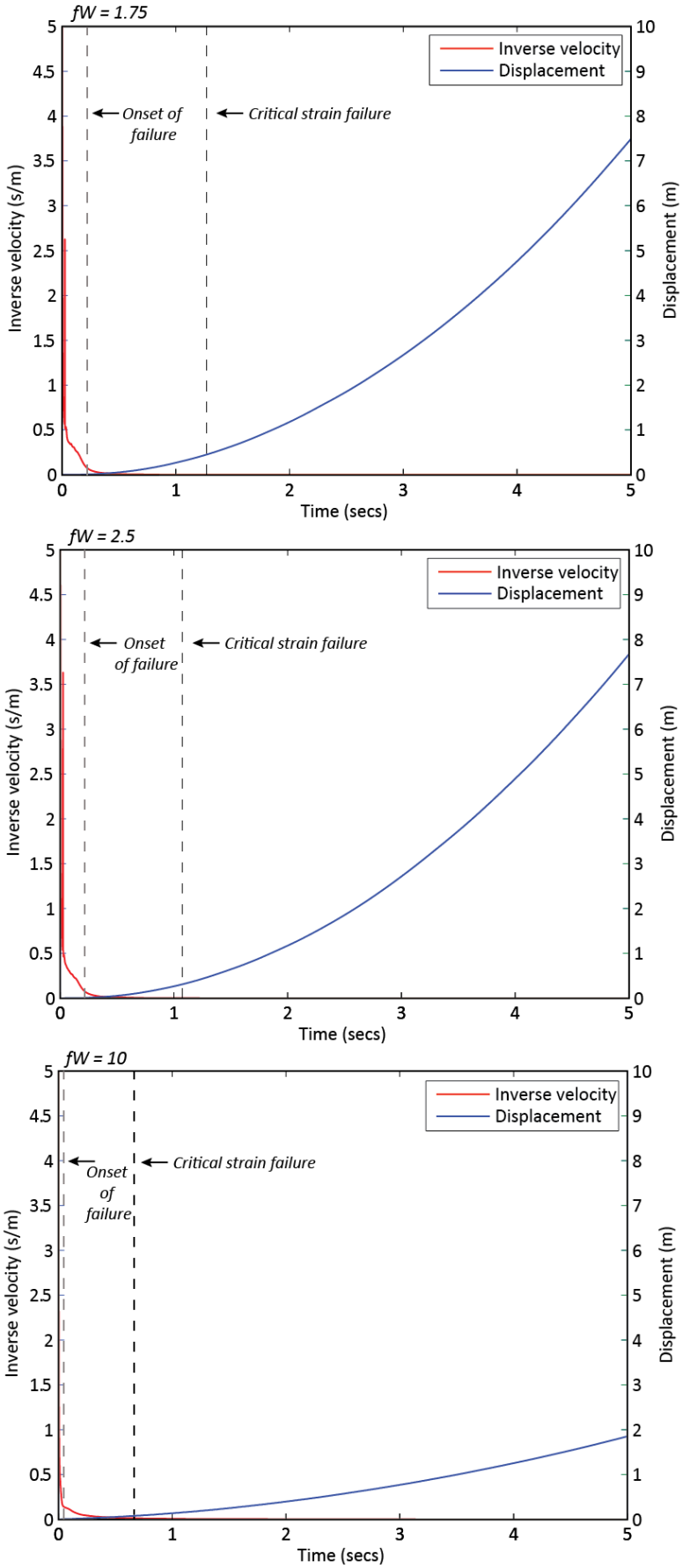

Figure 4.19: Out-of-slope displacement superimposed with inverse velocity and points of failure for experiments 1.8 – 1.10. Values are the average of all the failed nodes (e.g. the red dots in Fig. 4.16).

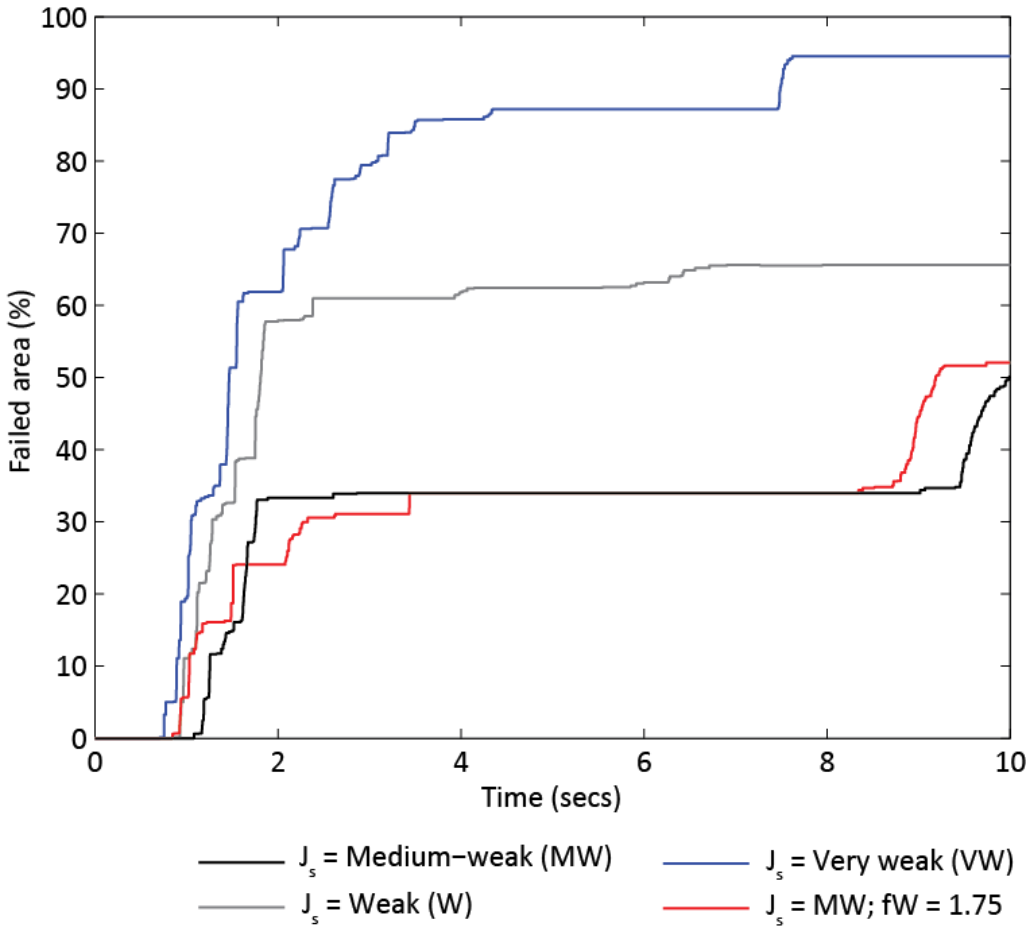

Figure 4.20: Total failed area through time for experiments 1.11 – 1.14. Failed area is calculated as the percentage of history points that have reached the critical threshold for failure (e.g. the red dots in Figs. 4.17).

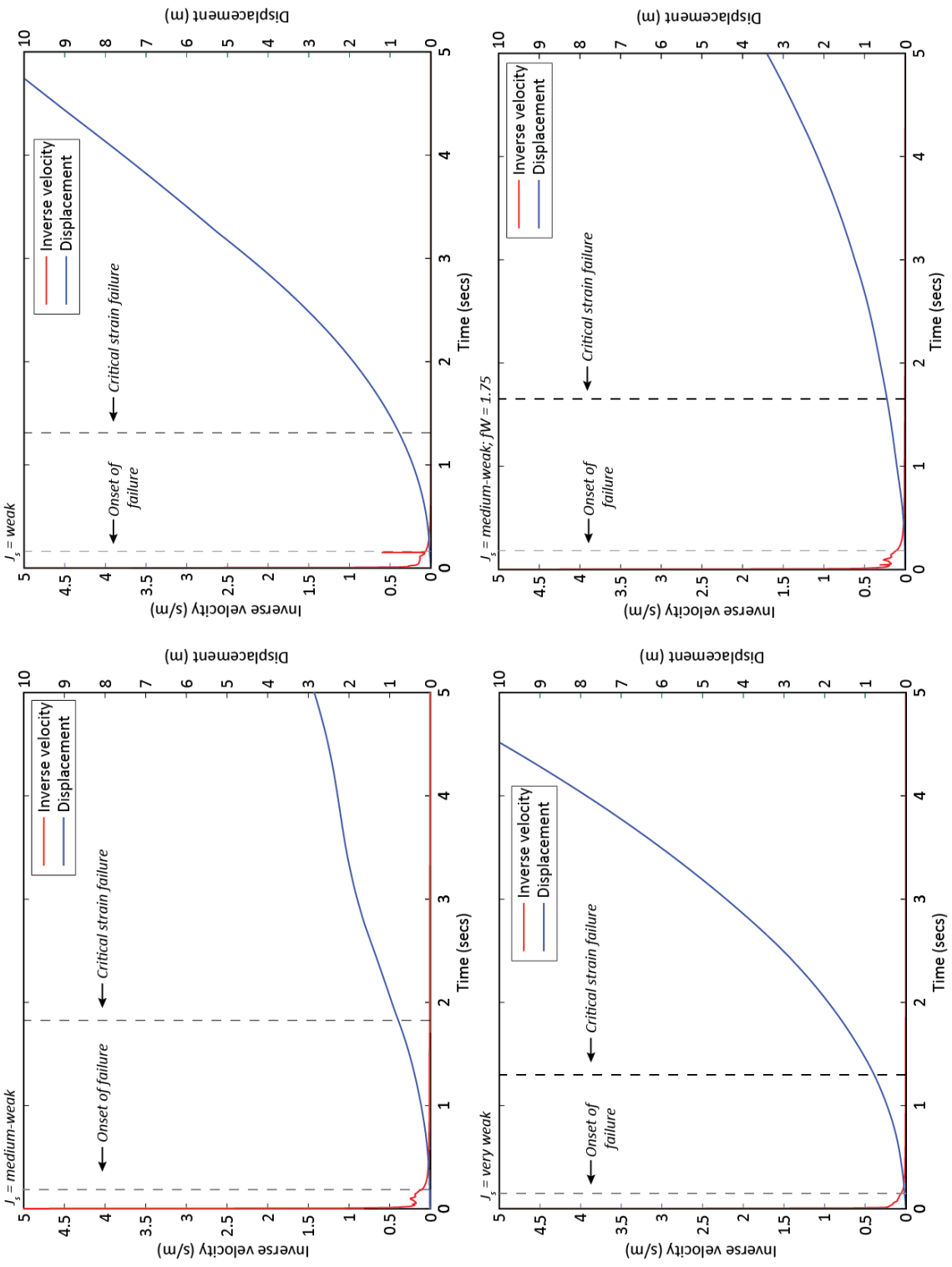

Figure 4.21: Out-of-slope displacement superimposed with inverse velocity and points of failure for experiments 1.11 – 1.14. Values are the average of all the failed nodes (e.g. the red dots in Fig. 4.17).

4.7 Stage Two: Progressive failure

This second stage of experiments builds upon the observations from stage one experiments, which are summarised below to introduce the second stage of experiments.

4.7.1 Observations from Stage One experiments

For each of the experiments run in stage one, the fracture count and failed area is given at two second intervals of model time (Table 4.12). Plots of failed area have been superimposed with plots of fracture count through time, and shown alongside the spatial distribution of failures and fractures (Figs 4.22 – 4.25). The results from experiments 1.1 – 1.7 show that for the range of joint properties and surface morphologies explored, failure had occurred in these experiments with very few fractures beforehand. This is particularly shown in the plots of failed area and fracture count (Fig. 4.22 – 4.23), which show that the first failure events are preceded by fewer than ten fractures in each instance. In the case of experiments 1.6 and 1.7 where the cliff surface had a lower surface roughness, failure occurred in a model completely absent of fracturing (Table 4.12).

When the slope was weakened using the weathering factor (*fW*), the model immediately generated fractures (Table 4.12, Fig. 4.24). As the *fW* increased, the tensile strength of the rock was lowered to a point where the initial overburden stress was enough to generate fracturing in the rock mass. The number of fractures generated and the failed area increased accordingly with the increase in *fW*. For these three experiments, fracturing is seen before failure, and the failed area increases in size with the increase in the number of fractures. When the slope was weakened by lowering the joint strength this also caused an increase in the number of fractures generated. Unlike when *fW* was applied, fracturing was not observed immediately but occurred episodically throughout the model simulation time (Fig. 4.25). Only when the model was run with very weak joints (exp. 1.13) is fracturing observed before failure at the beginning of the model run.

In experiment 1.14, where both the *fW* and a lower joint strength were combined, fracturing appears before failure at different temporal points throughout the model simulation, as shown in the plot of fracture count and failure (Fig. 4.25). Here a lag between fracturing and failure is observed throughout the model simulation, suggesting that fracture within the cliff could be related to failure occurrence in this experiment.

All plots of fracture location (Fig. 4.22 – 4.25) show that fracturing at the beginning of the model simulation is widely distributed across the cliff. Conversely, fracturing that occurs later in the simulation is concentrated within and around areas that have failed. The focal point of fracturing seems to move through time, propagating up and across the cliff, rather than fracture locations being completely spatially random.

Table 4.12: Fracture count (FC) and the failed area (%) given at 2 second intervals for each model experiment in Stage One.

Exp. ID	**Key variable**	**Fracture count (top) and failed area (below, %) at:**				
		2 secs.	**4 secs**	**6 secs**	**8 secs**	**10 secs**
1.1	J_s = med-weak	5 33.29	78 33.95	97 33.95	120 33.95	194 50.15
1.2	J_s = med.	3 4.88	3 6.49	3 6.79	3 6.79	3 6.79
1.3	J_s = med-strong	3 4.65	3 5.24	3 5.54	3 5.54	3 5.54
1.4	Morph. = π	4 8.04	4 12.51	4 13.04	4 13.04	19 13.04
1.5	Morph. = 2π	3 4.88	3 6.49	3 6.79	3 6.79	3 6.79
1.6	Morph. = 4π	0 4.65	0 5.84	0 5.84	0 5.84	0 5.84
1.7	Morph. = 6π	0 3.57	0 4.76	0 4.94	0 4.94	0 4.94
1.8	fW = 1.75	433 4.94	433 6.85	433 6.85	434 6.85	435 6.85
1.9	fW = 2.5	4044 6.73	4044 7.03	4044 7.03	4044 7.03	4044 7.03
1.10	fW = 10	154718 73.67	155527 83.26	156505 84.40	157360 84.40	158037 84.40
1.11	J_s = med-weak	5 33.29	78 33.95	97 33.95	120 33.95	194 50.15
1.12	J_s = weak	37 57.77	1413 61.82	1620 63.20	2299 65.63	2645 65.63
1.13	J_s = very weak	1032 61.88	1229 85.77	2623 87.20	3131 94.52	7311 94.52
1.14	J_s = med-weak; fW =1.75	334 24.06	523 33.95	558 33.95	571 33.95	611 52.05

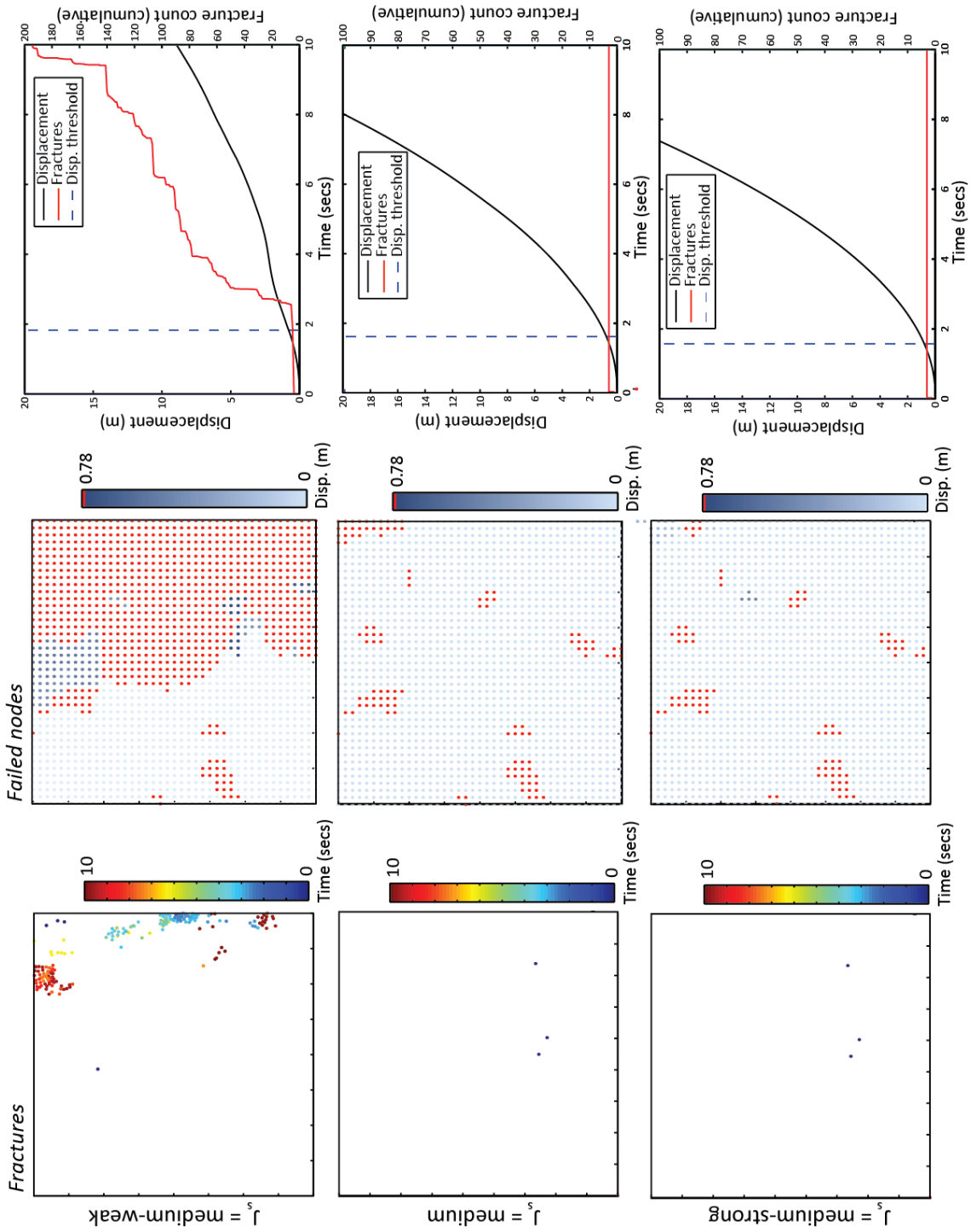

Figure 4.22: Location and timing of fractures (left) alongside images of the failed nodes (centre) and plots of cumulative failed area (%) and fracture count for experiments 1.1 – 1.3.

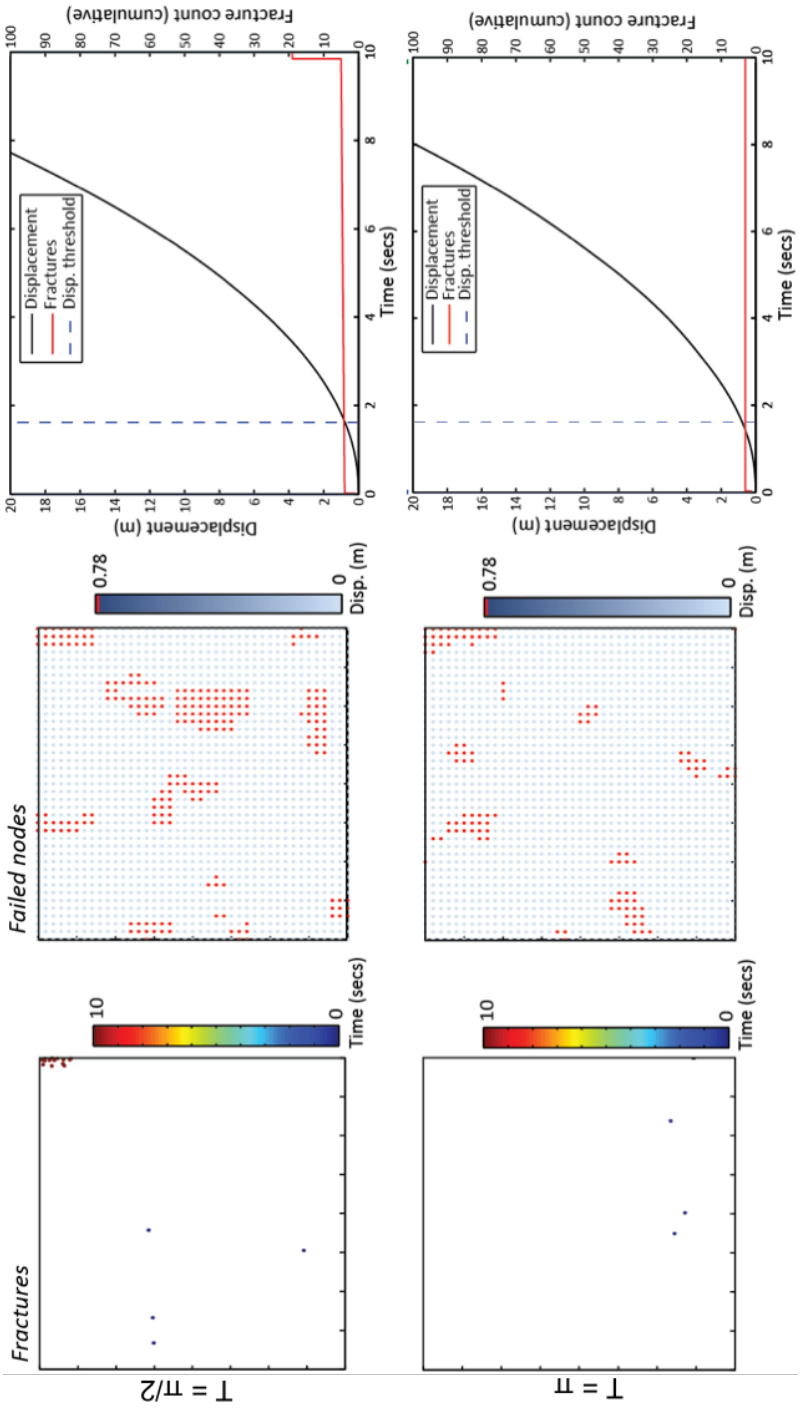

Figure 4.23: Location and timing of fractures (left) alongside images of the failed nodes (centre) and plots of cumulative failed area (%) and fracture count for experiments 1.4 – 1.5.

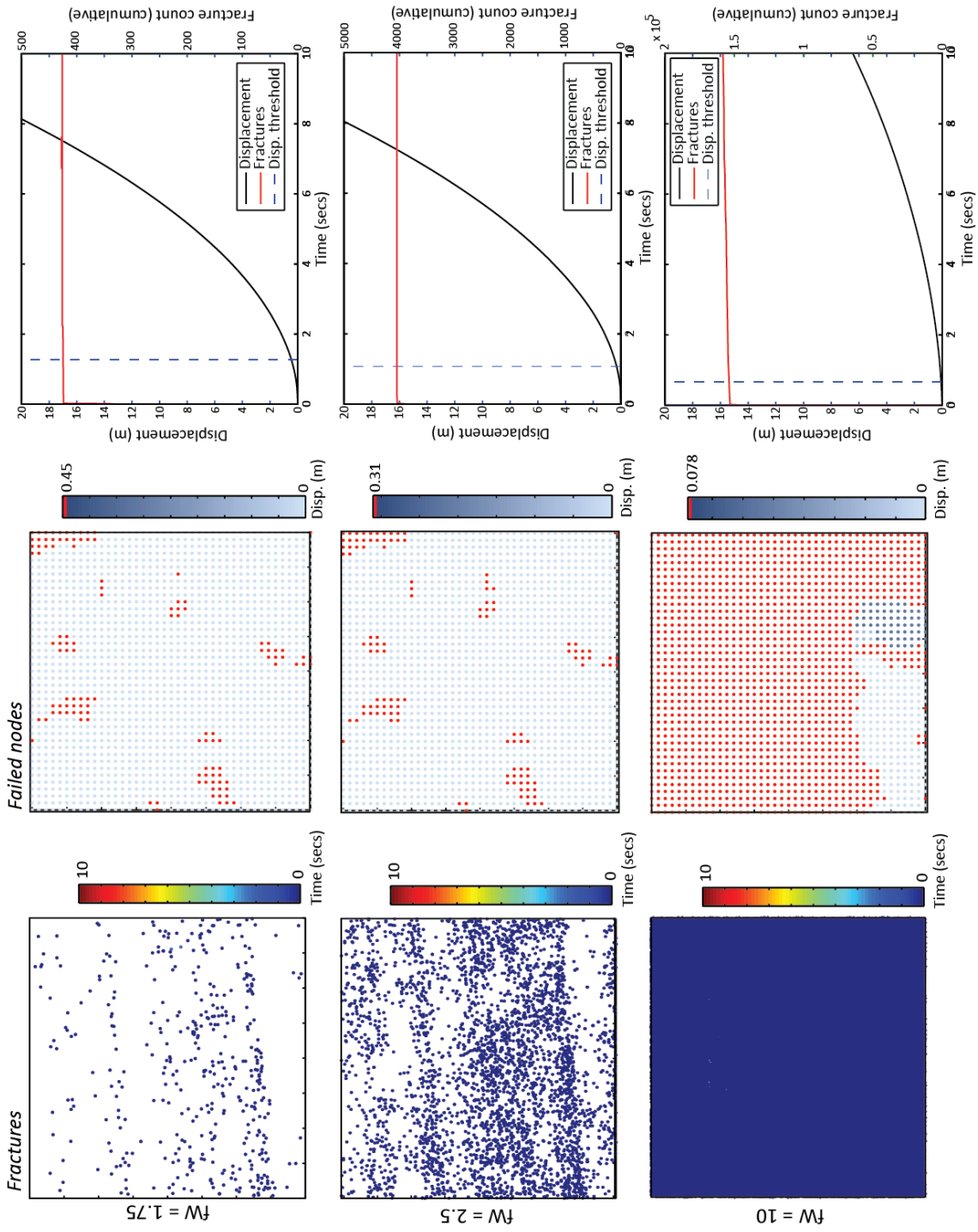

Figure 4.24: Location and timing of fractures (left) alongside images of the failed nodes (centre) and plots of cumulative failed area (%) and fracture count for experiments 1.8 – 1.10.

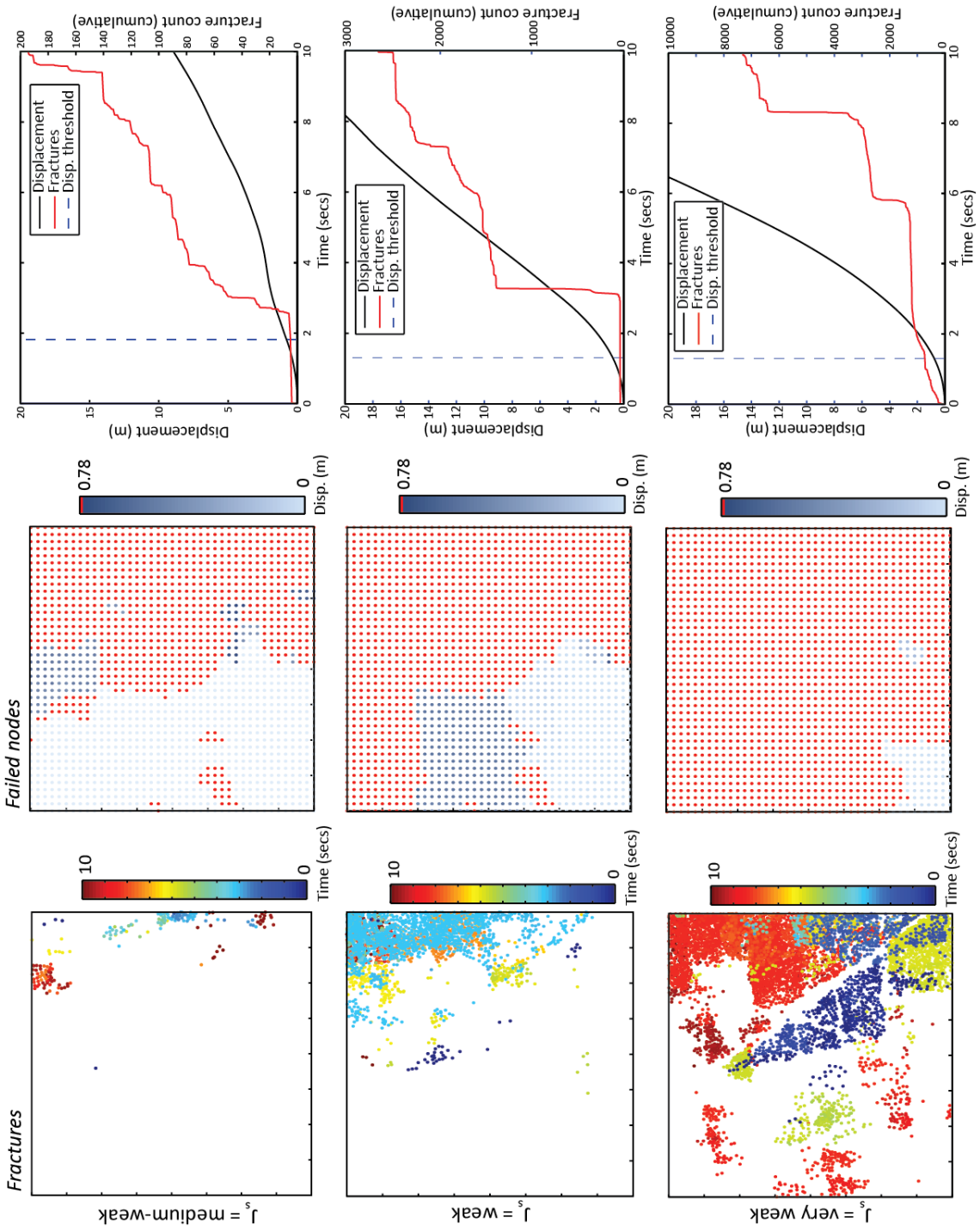
Fractures
Failed nodes
J_s = medium-weak
J_s = weak
J_s = very weak
Time (secs)
Disp. (m)
Displacement
Fractures
Disp. threshold
Displacement (m)
Fracture count (cumulative)
Time (secs)

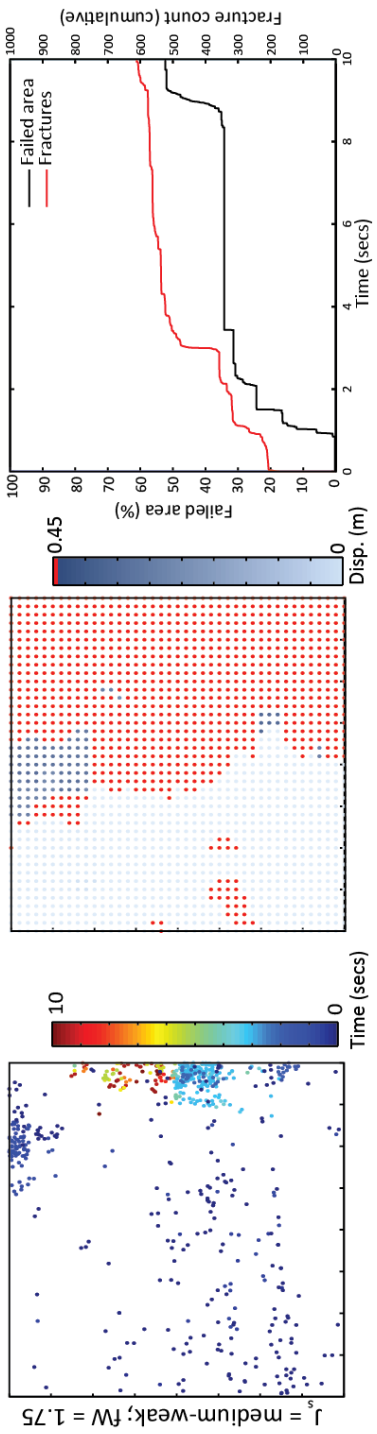

Figure 4.25: Location and timing of fractures (left) alongside images of the failed nodes (centre) and plots of cumulative failed area (%) and fracture count for experiments 1.11 – 1.14.

Based on the observations presented above, the second stage of experiments was used to address research questions 2, 3 and 4 for this chapter:

- *Q2: Does fracture growth precede the point of failure, defined as the point at which displacement has exceeded the critical strain threshold of the rock mass?*
- *Q3: How does fracture development vary pre- and post- the point of failure?*
- *Q4: What is the spatial extent of damage (fracture growth) surrounding a failed area of the slope?*

The outputs of model experiments run in stage one were used to examine the timing of fracture and failure. In order to observe fracture growth far beyond the point of failure, selected model experiments from stage one were then run for longer time periods. Finally, additional sets of experiments were set up to observe the spatial extent of fracture growth around failed areas: experiments that artificially triggered failures in the cliff; and experiments that used *Spring Failure Latency* in order to inhibit fracture development within specified spatial and temporal bounds.

4.7.2 Experiment setups

To observe fracture development both before and after occurrences of failure throughout the model and to examine the spatial extent of fractures around failed areas, further experiments were set up as detailed below.

4.7.2.1 Longer time periods

The experiments ran in stage one showed that fractures continued to develop throughout the duration of the experiment in cases where the joint strength was medium-weak or lower. This appeared to happen in stages, as indicated by the stepwise fracture count curves in Figures 4.22 – 4.25. In order to determine whether this pattern persisted and how fractures developed around later failures in the model, three of the experiments from stage one were run for twenty seconds of simulation time (as opposed to the ten seconds of simulation time that all previous experiments have run for). Experiments 1.8, 1.11 and 1.14 (Table 4.11) were chosen to show an experiment with *fW* applied; an experiment with the joint strength lowered; and a combination of the two. These three experiments ran for twenty seconds are hereafter referred to as experiments 2.1 – 2.3.

4.7.2.2 Excavation

One of the limitations of Slope Model is that it does not simulate detachment of material from the slope, limiting the opportunity to observe the impact of material completely removed from the slope. To resolve this, an experiment was setup whereby failures were artificially triggered and the material removed using the excavations tool in Slope Model, allowing the extent of fracture development in and around the failed (and removed) areas to be observed.

Furthermore, the results of stage one experiments showed that the spatial distribution of fractures was not confined to failed areas of the cliff surface. Where larger failures were observed, e.g. experiment 1.14 (Fig. 4.25), post-failure fractures appeared within this area however this was not the case with smaller failures. Therefore, to examine whether the size of failure indicates the magnitude and extent of post-failure fracture development, the experiment was designed with excavations of multiple sizes.

Three excavations (failures) of different sizes were triggered as shown in Figure 4.26. The excavations were 1 m^3, 8 m^3 and 27 m^3 in size and located at the cliff surface in the positions shown in Figure 4.26. The experiment run is referred to as experiment 2.4 and was setup with the same conditions as experiment 1.14 (Table 4.11) and run for ten seconds of model time.

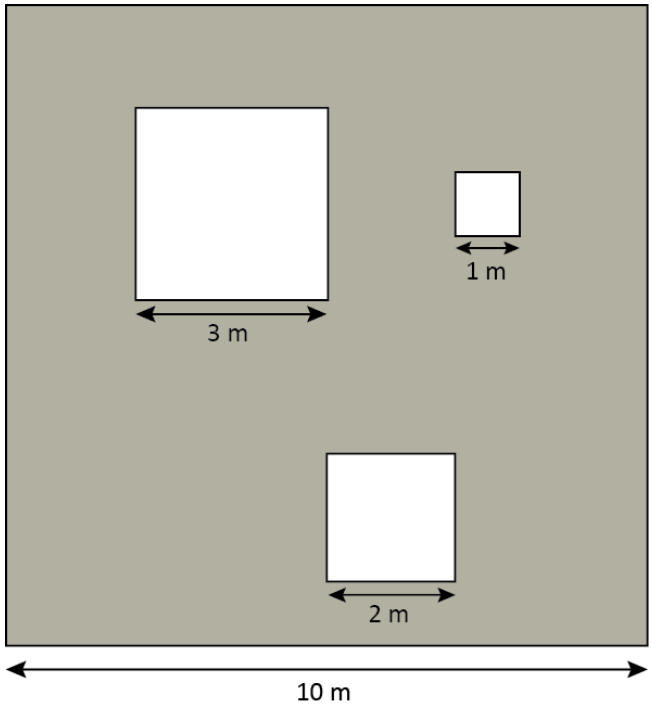

Figure 4.26: Illustration of the size and location of areas of the slope that were excavated to simulate failures on the cliff in experiment 2.4.

4.7.2.3 Spring Failure Latency

Previous experiments have shown the spatial extent of fracture development and failed areas, suggesting potential associations between the two. The *Spring Failure Latency* option in Slope Model was used to artificially inhibit fracture development within specified spatial and temporal bounds, in order to observe the effect this had on failure development. This was designed under the assumption that if fracture is driving failure occurrence within the model, then inhibiting fracture development should likewise inhibit failure development.

Three experiments were setup using the conditions given for experiment 1.14 (Table 4.11). For each experiment the distance and time over which fracture is inhibited is set by the radius and timestep multiplier respectively. For all three experiments the radius was set at a multiplier of 5 lattice nodes, which equates to a distance of 1 m at this spatial resolution. The timestep multiplier was varied in each experiment as follows:

Experiment 2.5: timestep = 100 (0.04 seconds);

Experiment 2.6: timestep = 1,000 (0.4 seconds);

Experiment 2.7: timestep = 10,000 (4 seconds).

4.7.3 Results

4.7.3.1 Longer time periods

For experiments 2.1 – 2.3, the fracture count and failed area is given at 1, 5, 10, 15 and 20 seconds of model time (Table 4.13). The images of failed nodes are also shown for these times in Figure 4.27. As with the previous results presented, plots of failed area have been superimposed with plots of fracture count through time, shown alongside the spatial distribution of failures and fractures (Fig. 4.28). Running the model for twenty seconds shows that both fracture count and the failed area continue to increase beyond ten seconds for experiments with medium-weak joints (Table 4.13). The development of failed areas through time (Fig. 4.27) shows that the increase in failed area during this time is small, whereas the number of fractures triples over this time period (Table 4.13).

When the model is run with medium-weak joints (exp. 2.1) fractures appear to develop post-failure, as indicated by the lag between the failed area and fracture curves in Figure 4.28. These fractures are spatially concentrated within the area of the largest failure and appear to propagate upwards and outwards over time (Fig. 4.28) in a zone proximal to one of the major

joints (Fig. 4.8b). Conversely, when *fW* is applied (exp. 2.2) there is no increase in fracture count or failed area beyond ten seconds of model time (Table 4.13, Fig. 4.28).

The results of experiment 2.3, where *fW* and medium-weak joints are combined, show that fractures initially precede failure, as indicated by the lag between the curves in Figure 4.28. At the point where 50 % of the surface area has failed, failure occurrences then appear to precede fractures. This pattern in the temporal behaviour of both fracture and failure development shows how both are contributing to the accumulation of damage within the slope through different stages of activity. The locations of fractures, particularly those that occur in the latter stages of the model simulation, are shown to be located within the area of the largest failure (Fig. 4.28). Again, the fractures appear to be propagating upward and outward through time (Fig. 4.28), proximal to some of the major joints (Fig. 4.8b).

Table 4.13: Fracture count (FC) and the total failed area (%) given at 1, 5, 10, 15 and 20 seconds of model time for experiments 2.1 – 2.3.

Exp. ID	**fW**	**Joint strength (Js)**	**Fracture count (top) and failed area (below, %) at:**				
			1 sec.	**5 sec.**	**10 sec.**	**15 sec.**	**20 sec.**
2.1	-	Med-weak	4 0	86 33.95	194 50.15	370 57.00	562 57.42
2.2	1.75	Medium	433 0.89	433 6.85	435 6.85	435 6.85	435 6.85
2.3	1.75	Med-weak	266 5.66	536 33.95	611 52.05	1933 57.30	2048 57.42

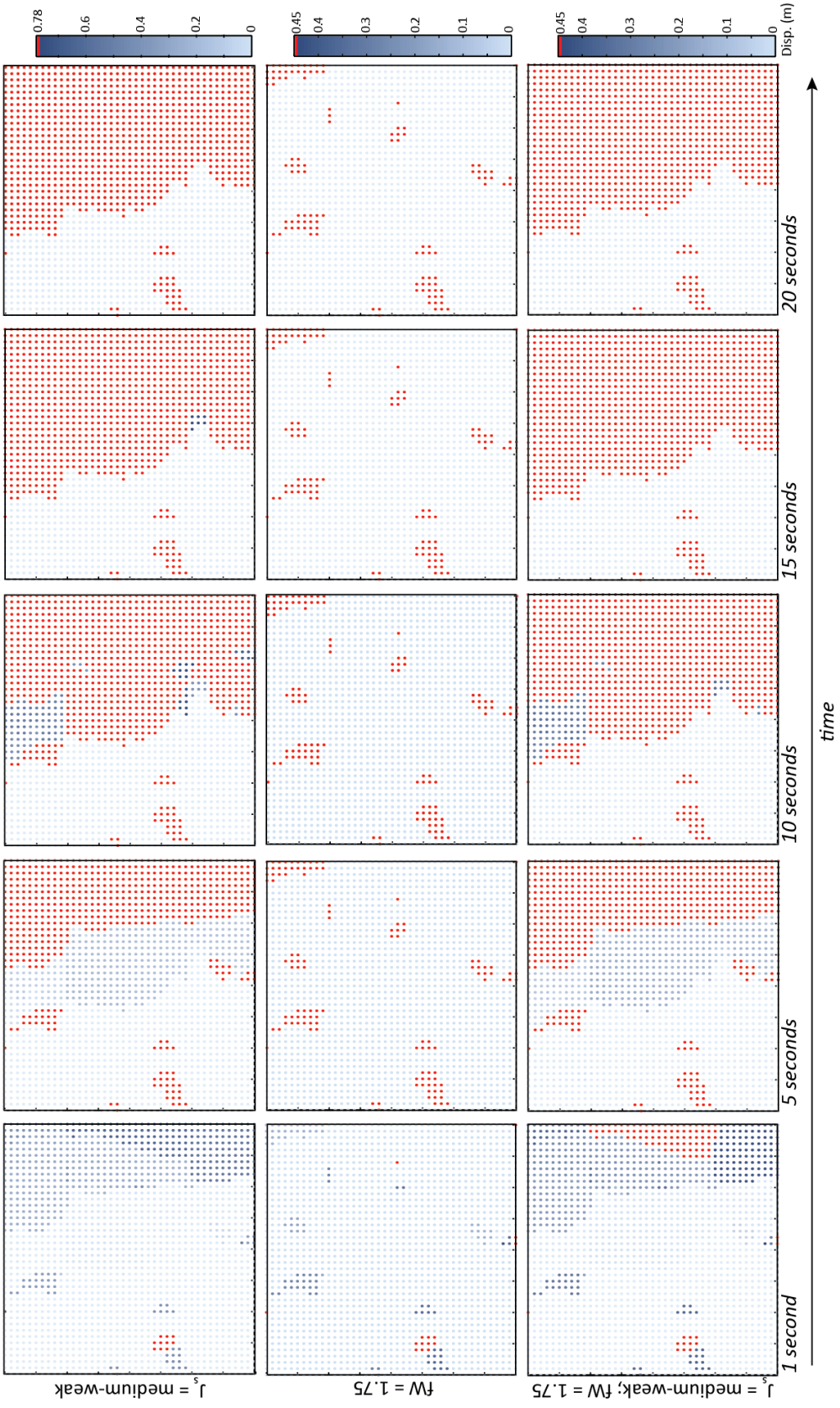

Figure 4.27: Resolved out-of-slope displacement (m) of each history point within the model at 1, 5, 10, 15 and 20 seconds of model time. Displacement is shown for model experiments 2.1 – 2.3. Each coloured dot represents a history point (at each node) within the model and the value given by the colour illustrates the out-of-slope (horizontal and vertical components resolved) displacement (m) for the specified time, where red dots represent those nodes that have failed.

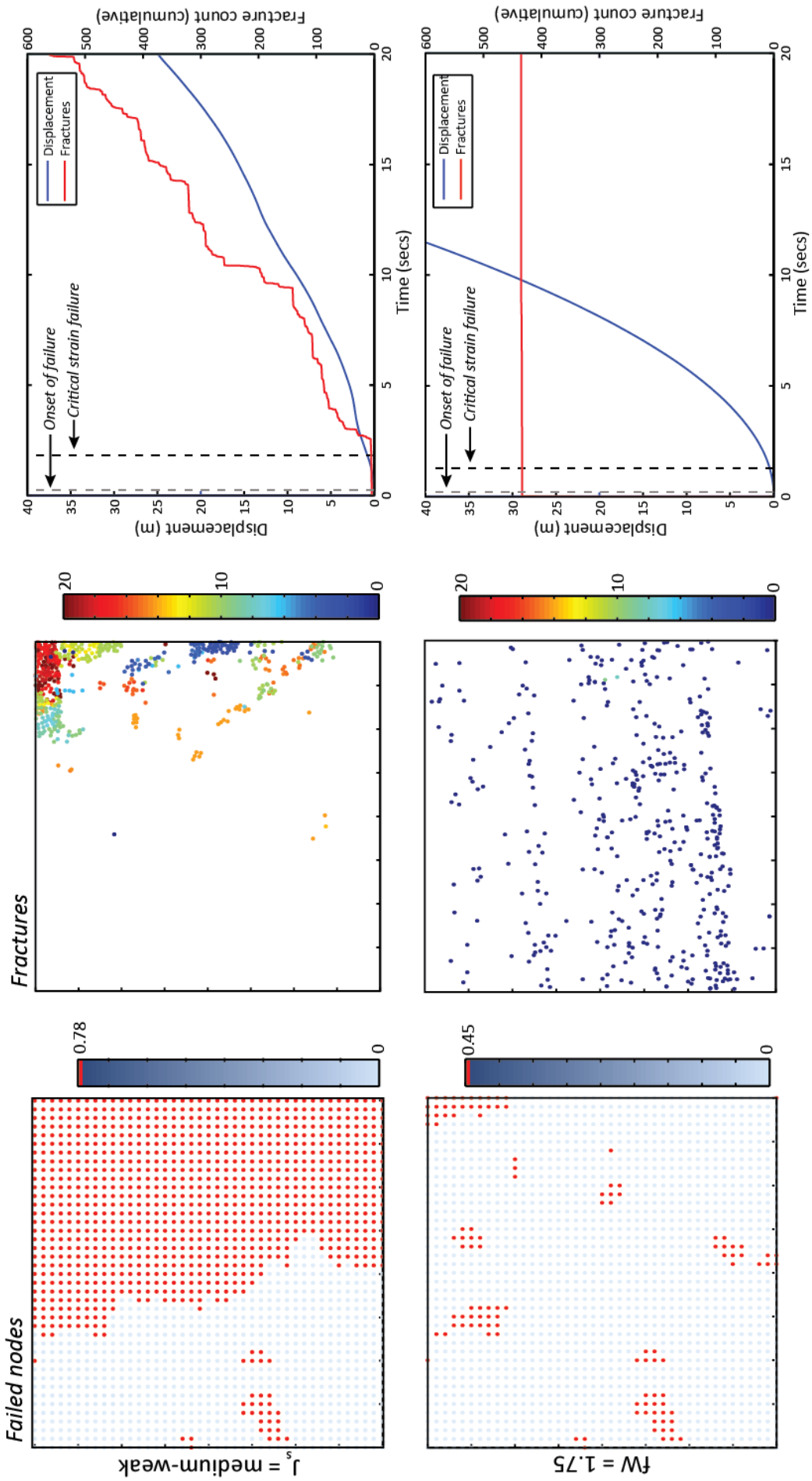
Failed nodes
Fractures
Displacement
Fractures
Onset of failure
Critical strain failure
Displacement (m)
Fracture count (cumulative)
Time (secs)
0.78
0.45
J_s = medium-weak
fW = 1.75

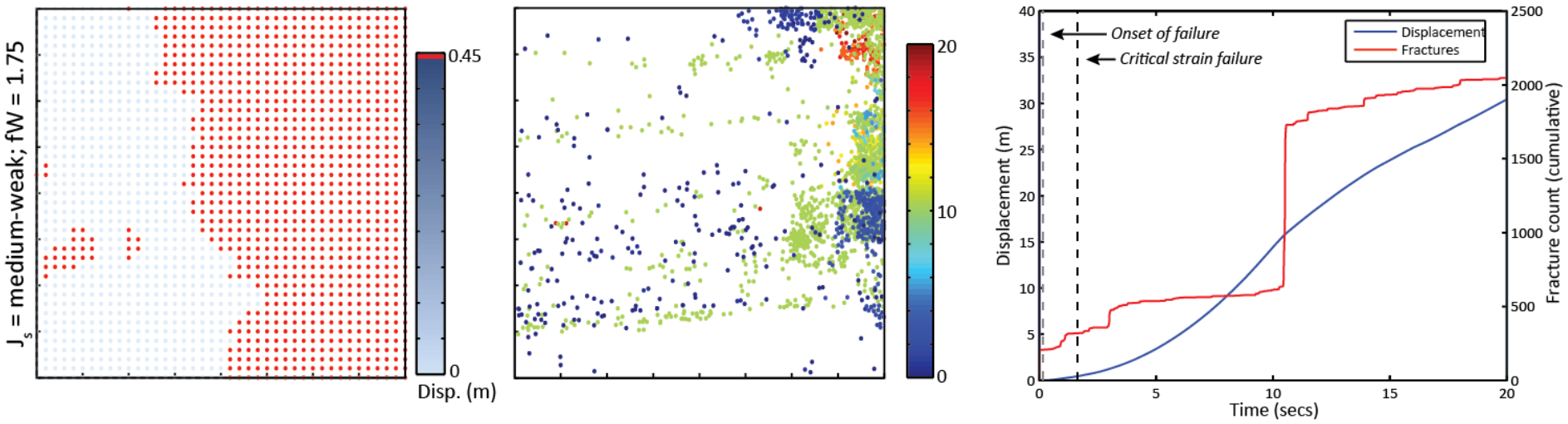

Figure 4.28: Images of the failed nodes (left) alongside the location and timing of fractures (centre) and plots of cumulative failed area (%) and fracture count for experiments 2.1 – 2.3.

4.7.3.2 Excavation

For experiment 2.4, the fracture count and failed area is given at one, five and ten seconds of model time (Table 4.14). Results from experiment 1.14 are also given in order to compare the results with the same setup without excavations. Fracture count within and around the excavated areas is presented in Table 4.15 and can be seen in the plots in Figure 4.30. When failures are artificially triggered as excavations at the beginning of the model, the fracture count is higher than in the same experiment without excavations (Table 4.14). As shown by the plots of failed area and fracture count (Fig. 4.30), this is mainly attributable to the initial spike in fracture generation in the model with excavations, presumably as a response to those failures. Despite a higher fracture count in experiment 2.4, the pattern of fracture development over time is very similar in both experiment 2.4 and 1.14 beyond the first few seconds of model time.

The fracture count surrounding the excavated areas does not correlate with excavation size as expected (Table 4.15). Owing to the different locations of the excavations, this demonstrates that other spatially variable parameters (e.g. joints, surface morphology) are exerting a stronger control over the amount of fracture development. However, the spatial distribution of fractures surrounding excavations (Fig. 4.30) show that fractures develop in higher concentrations both above and alongside the excavations compared to the same areas in the experiment without excavations. These areas of higher fracture concentration match areas of subsequent failures as illustrated in the plots of failure development through time (Fig. 4.29).

Table 4.14: The average time (seconds) of onset of failure and critical slope failure; and the fracture count (FC) and failed area at 1, 5 and 10 seconds of model time. Values are shown for both the experiment with excavations and without – experiments 2.4 and 1.14 respectively. *Note – the failed area does not include the area of excavations.*

Exp. ID	**Excavations**	**Average onset of failure (secs)**	**Average critical slope failure (secs)**	**Fracture count (top) and failed area (below, %) at:**		
				1 sec.	**5 sec.**	**10 sec.**
2.4	Yes	0.12	1.42	406 5.54	815 36.57	897 49.55
1.14	No	0.20	1.66	266 5.66	536 33.95	611 52.05

Table 4.15: Additional fracture count (FC) within the excavated areas ('FC inside'); within a 1 m perimeter of the excavated areas ('FC within 1m') and within a 2 m perimeter ('FC within 2m'). Values are shown as the difference between the experiment with excavations (exp. 2.4) and without excavations (exp. 1.14), e.g. a positive value indicates more fracturing in the experiment with excavations.

Excavation size	**FC inside**	**FC within 1m**	**FC within 2m**
1 m^3	8	129	173
8 m^3	3	71	-40
27 m^3	3	82	104

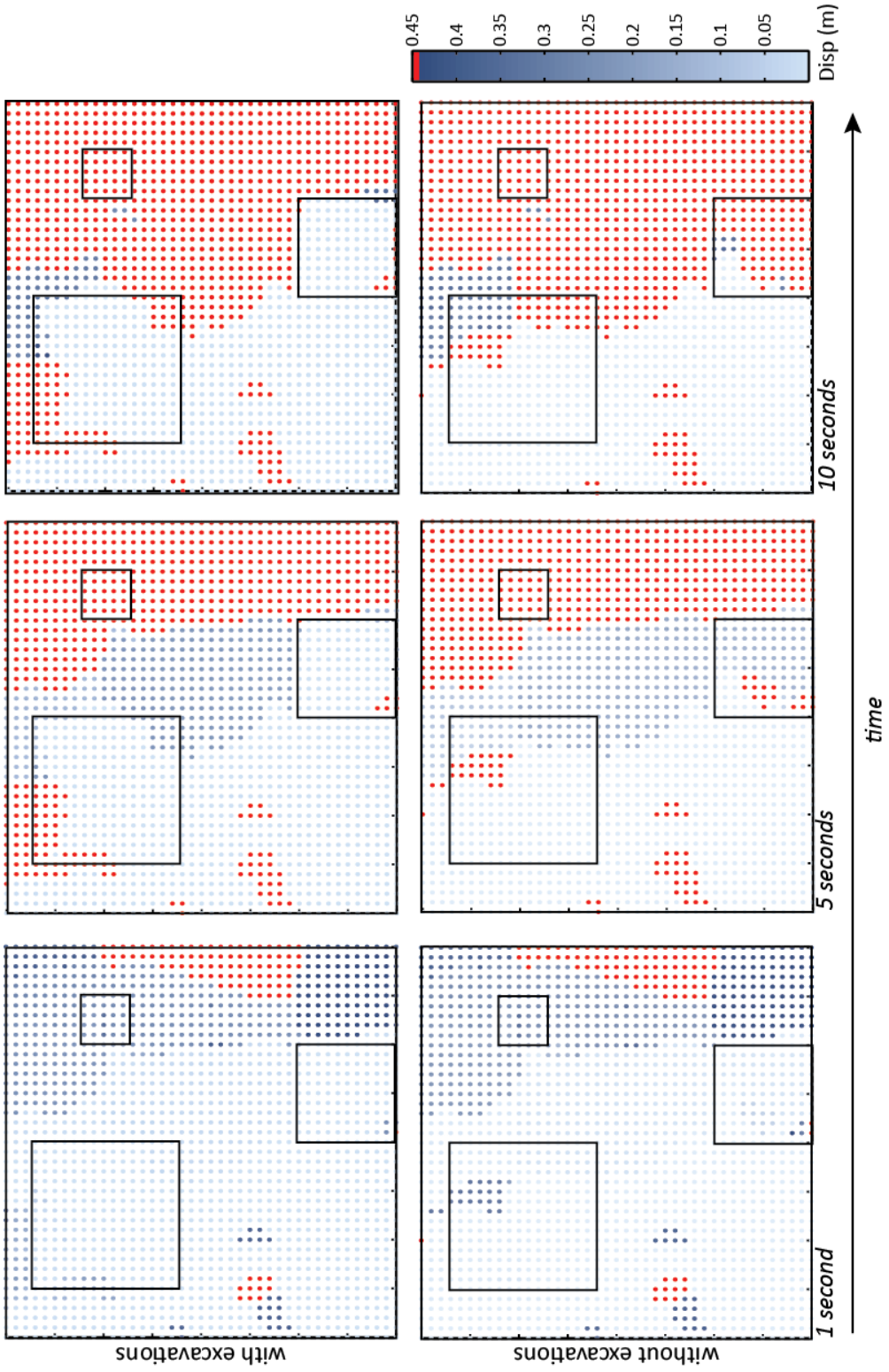

Figure 4.29: Resolved out-of-slope displacement (m) of each history point within the model at 1, 5 and 10 seconds of model time. Displacement is shown for model experiment 2.4 (top row) where the areas excavated are outlined in black. The bottom row shows the results of experiment 1.14 for comparison (the excavated areas are outlined on this for ease). Each coloured dot represents a history point (at each node) within the model and the value given by the colour illustrates the out-of-slope (horizontal and vertical components resolved) displacement (m) for the specified time, where red dots represent those nodes that have failed.

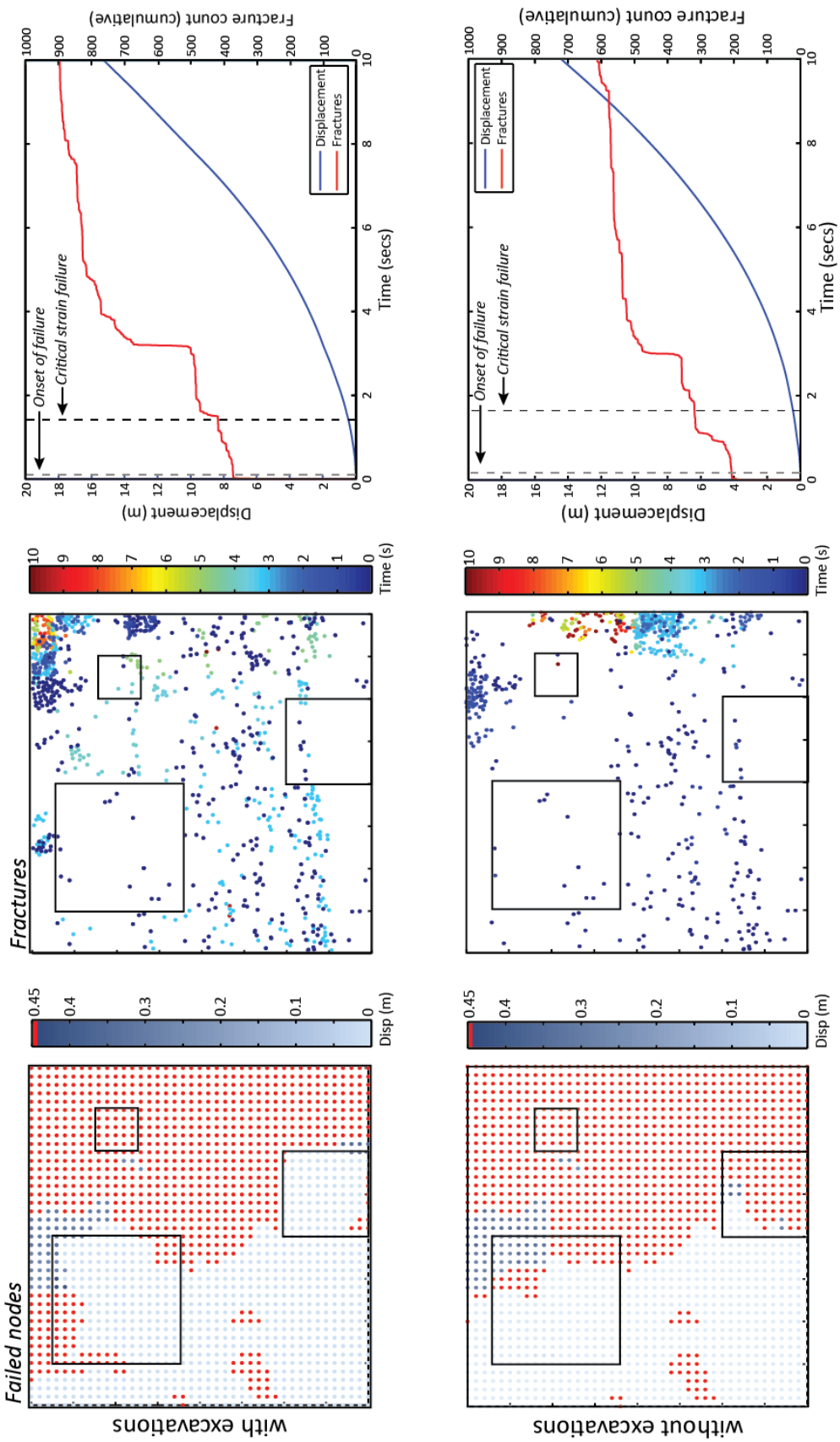

Figure 4.30: Images of the failed nodes (left) alongside the location and timing of fractures (centre) and plots of cumulative failed area (%) and fracture count for exp. 2.4 (top row) where the areas excavated are outlined in black. The bottom row shows the results of exp. 1.14 for comparison (the excavated areas are outlined on this for ease).

4.7.3.3 Spring Failure Latency

For experiments 2.5 – 2.7, the fracture count and failed area is given at one, five and ten seconds of model time (Table 4.16). As governed by the conditions set within the model, increasing the time for which fracture is inhibited (the timestep multiplier) results in fewer fractures generated in the model. However, the difference in the failed area between these experiments is minimal: increasing the timestep multiplier by two orders of magnitude reduces the fracture count by 74 % but only reduces the failed area by 0.83% (Table 4.16).

As the timestep multiplier increases, failure is observed to take longer to develop as seen in the plots of failed area through time (Fig. 4.31). Looking at the right hand column of Figure 4.31, the plots show areas of the cliff surface that are approaching the point of failure (dark blue nodes) in the model run with a timestep multiplier of 100 (top row). As the timestep multiplier is increased the displacement in these locations is lower (middle and bottom row) suggesting that inhibiting fracture development is slowing the development of failures.

Inhibiting fracture development within the model not only reduces the total fracture count, but also changes the temporal pattern of fracture development. This can be seen by comparing the plots of failed area superimposed with plots of fracture count in Figure 4.32. In all three cases there is an initial surge in fracture generation at the beginning of the model, however as the timestep multiplier is increased, subsequent increases in fracture development then occur at different times throughout the model. Despite these differences in fracture development, failure is still observed to occur at similar times, at a similar magnitude and in the same location(s). Overall, the development of failures appears dampened by inhibiting fracturing but the two do not appear directly correlated.

Table 4.16: The average time (seconds) of onset of failure and critical slope failure; and the fracture count (*FC*) and failed area (%) at 1, 5 and 10 seconds of model time. Values are shown for model experiments 2.5 – 2.7, where the timestep multiplier for SFL was increased, as indicated.

Exp. ID	**SFL multipliers**		**Average onset of failure (secs)**	**Average critical slope failure (secs)**	**Fracture count (top) and failed area (below, %) at:**		
	Radius	**Timestep**			**1 sec.**	**5 sec.**	**10 sec.**
2.5	5	100	0.22	1.17	107 5.65	249 33.95	951 34.78
2.6	5	1000	0.20	1.30	104 0.77	250 33.95	328 33.95
2.7	5	10000	0.23	1.17	70 5.48	120 33.95	244 33.95

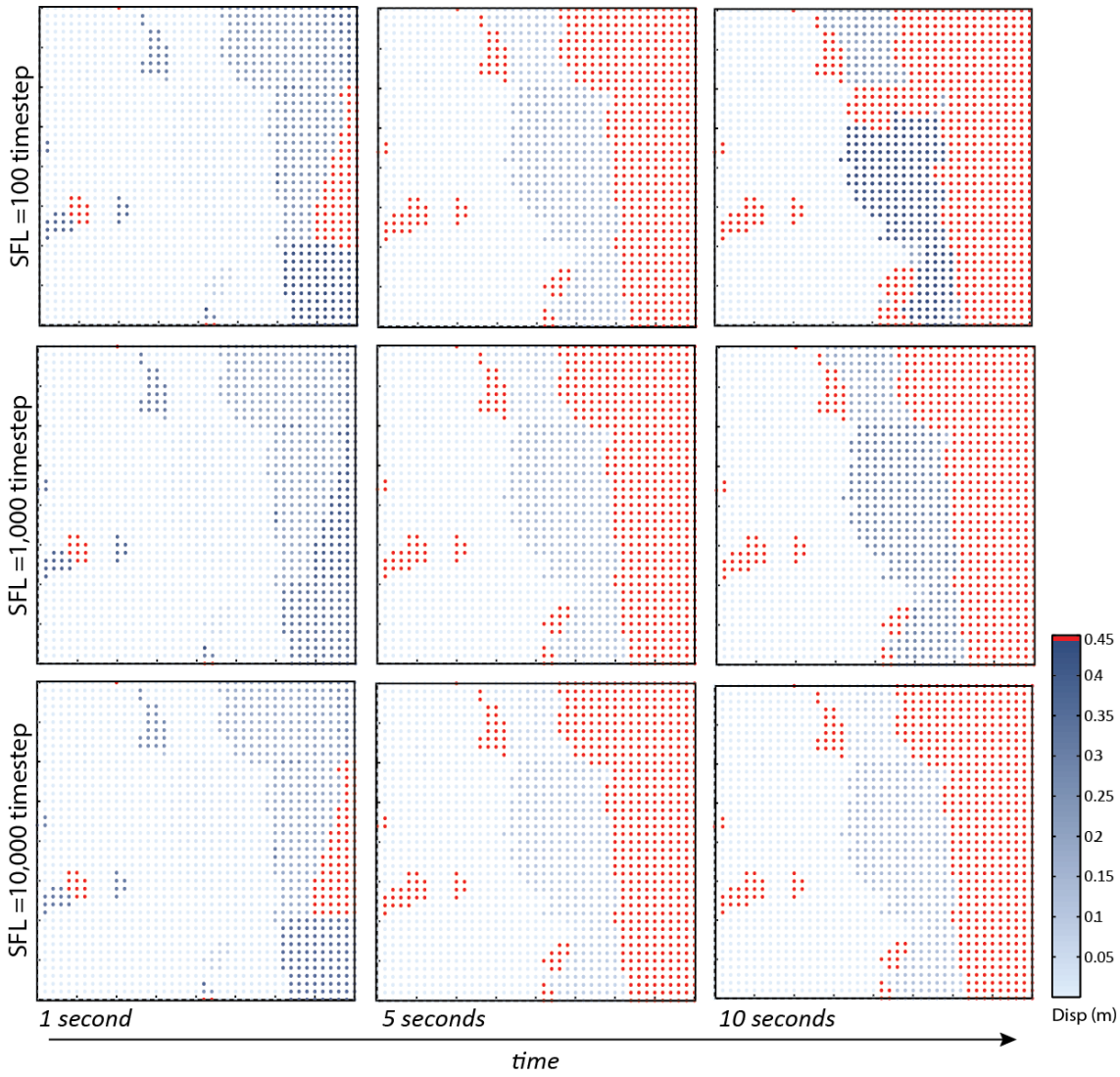

Figure 4.31: Resolved out-of-slope displacement (m) of each history point within the model at 1, 5 and 10 seconds of model time. Displacement is shown for model experiments 2.5 – 2.7, where the timestep multiplier for SFL was increased. Each coloured dot represents a history point (at each node) within the model and the value given by the colour illustrates the out-of-slope (horizontal and vertical components resolved) displacement (m) for the specified time, where red dots represent those nodes that have failed.

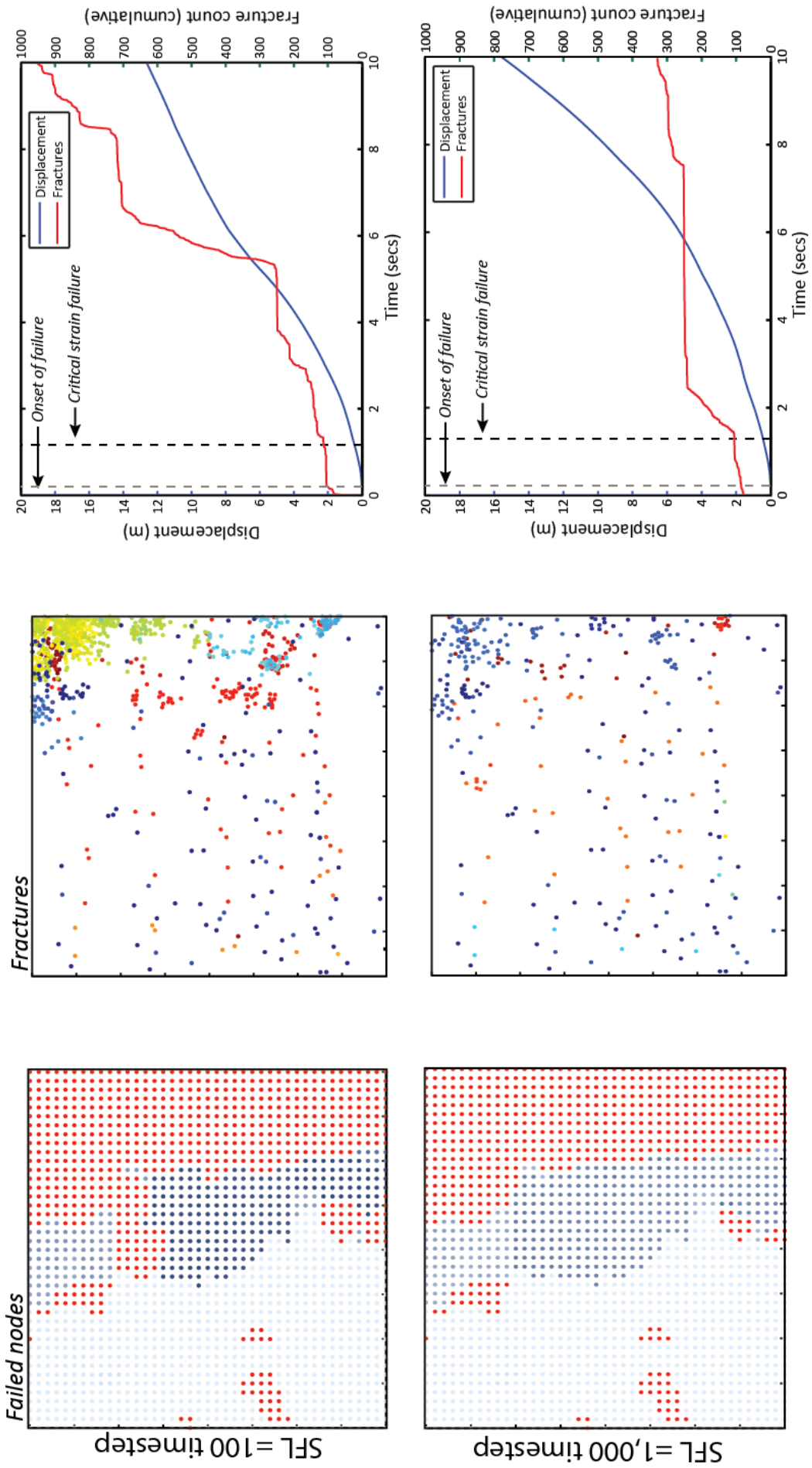
SFL = 1,000 timestep
SFL = 100 timestep
Failed nodes
Fractures
Displacement (m)
Fracture count (cumulative)
Time (secs)
Displacement
Fractures
Onset of failure
Critical strain failure

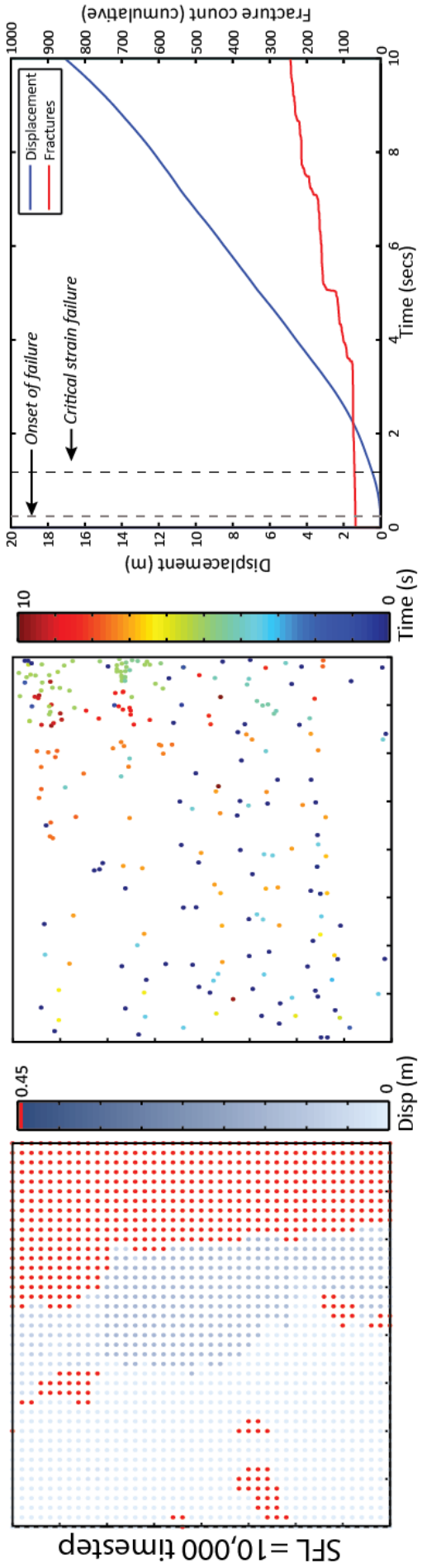

Figure 4.32: : Images of the failed nodes (left) alongside the location and timing of fractures (centre) and plots of cumulative failed area (%) and fracture count for experiments 2.5 – 2.7.

4.8 Discussion

Slope Model has been used to simulate a 10 m x 10 m section of vertical rock slope composed of shale rock, with conditions set to reflect the field site used in chapter 3. The slope has been simulated in range of scenarios in order to observe the response of the model to weakening of the slope and the role of fracture development alongside failure. Taking brittle fracture as a representation of time-dependent failure, the final stage in progressive failure (Petley *et al.,* 2005), the results presented in this chapter have shown how and when time-dependent failure can influence the location and timing of rockfall, as progressive failure represents one possible process generating rockfalls. This information can be summarised by answering the questions set out in Section 4.1:

Question 1: How does the model behaviour (magnitude and timing of failure) vary in response to weakening of the rock slope?

As the rock slope was weakened by lowering the material and/or the joint strength the number and size of failures increased, as would be expected. Without any weakening of the slope the failures generated were all < 10 m^2 in surface area. Failures ≥ 10 m^2 were only generated when the joint strength was lowered below *medium*, or when the material strength was lowered by an order of magnitude (*fW* = 10). The timing of failure was also altered as the slope was weakened. Failure occurred earlier in the model simulation and the time between failure onset and critical failure became shorter, indicating that the timing of the final stage of progressive failure (Petley *et al.,* 2005) is modulated by the rock mass strength.

The model response to weakening of the rock slope demonstrates the need for both external and internal forcing to weaken the slope from average field conditions (Lim *et al.,* 2010) in order to produce failure of a similar magnitude as observed in the field.

The magnitude of failure is also influenced by the complexity of the surface morphology, as shown by the larger failed area produced in experiments run with the most curved surface topography. The more complex surfaces have a higher concentration of locally convex areas, which will likely increase the stress in the near surface region (Martel, 2006), potentially promoting the generation of damage which will likely result in failure. This is supported by observations from the field data in Chapter 3 where rockfalls were shown to more commonly occur on locally convex areas of the slope. In all four experiments run with different surface morphologies the time between failure onset and critical failure was very similar, illustrating

that time-dependent failure in these experiments was not influenced by surface morphology and the potential associated changes to the near surface stress field. This suggests that the timing of failure is primarily driven by internal mechanisms, modulated by the rock mass conditions and less dependent on changes in the near surface stress field.

Question 2: Does fracture growth precede the point of failure, defined as the point at which displacement has exceeded the critical strain threshold of the rock mass?

The role of fracturing in rock slope failure can be observed at a variety of scales from shearing along joints (Yan, 2008) and breaking of intact rock bridges (Kemeny, 2005) to the development of large failure surfaces, as demonstrated by Eberhardt *et al.* (2004) in numerical analysis of the 1991 Randa rockslide. Most often these processes are associated with failure in large-scale slopes and demonstrate the role of fracturing in preceding rock slope failure. For example, Havaej *et al.* (2013) used Slope Model to illustrate how brittle fracture developed in an intact rock bridge at the toe of a slope in order to initiate failure. In this study, which is focused on small-scale rockfall events (10^{-3} - 10^{2} m^3) rather than whole slope failure, Slope Model has demonstrated that fracture growth is not always seen to precede the point of failure.

In many of the experiments run in this study, initial failures occur before any significant fracture growth is seen. In experiments run before *fW* is applied to lower material strength, the failure is joint controlled and slip along joints occurs without fracturing. Conversely, in experiments where *fW* is applied, the rock mass is able to fracture at lower stresses and fracture growth is then observed to precede failure under these conditions. This suggests that under conditions where joints are of an orientation and strength that allows slip to occur, then initial failure can occur without any fracturing of the intact rock. This is further supported by the experiments where the *Spring Failure Latency* (SFL) was employed, which showed that failure still developed even when the propagation and coalescence of fractures was inhibited for a range of time periods. Following the initial failure(s) seen in the model experiments, fracture growth is then observed to develop and precedes further failure occurrences within the simulations. Overall these results illustrate the role of fracture as part of the evolving failure process of damage in the rock slope rather than a distinct trigger as demonstrated in the cases of larger slope failures (Havaej *et al.,* 2013).

Question 3: How does fracture development vary pre- and post- the point of failure?

The results of experiments that ran for 20 seconds of model simulation time (exp. 2.1 – 2.3; Fig. 4.28) most clearly demonstrate the interplay of fracture development in relation to the points of failure within the model. When the joint strength was lowered to represent weakening, the rate of fracture development remained steady, interspersed with occurrences of rapid fracture development that were seen both pre- and post- points of failure. Lowering the material strength of the rock to represent weakening of the slope imposed less frequent, larger magnitude occurrences of rapid fracture development on the steady background rate set by the joint strength.

The magnitude of fracture development is not directly proportional to the magnitude of the failure(s) within the model. Similar temporal patterns are seen in the behaviour of fracture development and failure. The occurrences of rapid fracture development are observed in close temporal proximity to large failure events. Periods of slower, steady increases in fracture count coincide with a similar steady increase in smaller failures, and in situations where no new fractures develop for a period of time, this is reflected in no failures occurring during this time. The latter observation is most clearly demonstrated in the experiments that employed SF. As the time for which fracturing was inhibited was increased, the point at which the model stabilised became earlier.

Question 4: What is the spatial extent of damage (fracture development) surrounding a failed area of the slope?

Time-dependent fracture growth indicates that progressive failure is occurring (Petley *et al.,* 2005). Fracture growth is a physical expression of damage in the rock slope and therefore indicates areas of potential future failure. Subsequently, the extent of fracture development is important for understanding the spatial and temporal bounds on failure propagation through the rock mass. The extent of pre-failure fracture development has been quantified for large-scale slope failure by Havaej *et al.* (2014b). Through the novel application of an "ellipsoid of damage", they were able to describe both the extent and shape of the damage zone at the onset of failure. Application of the ellipsoid of damage was not appropriate for this study as there was not a single distinct zone of fracture development within the model. Rather, for smaller scale slope failure, this study has shown that post-failure fracture development concentrates within the area of the larger failures. Within these areas fractures are observed to propagate primarily upwards and secondly outwards over time, supporting the idea that

stress transfer would most likely cause upward and outward propagation of rockfalls due to gravity (Lim, 2006), and providing a potential explanation for the directionality observed in contiguous rockfall propagation in Chapter 3.

One of the limitations of Slope Model is that it does not simulate detachment of material from the slope. In this study an experiment was run whereby failures were artificially triggered and the material removed using the excavations tool in Slope Model (exp. 2.4). This allowed the extent of fracture development in and around the failed (and removed) areas to be observed. The intensity of fracturing that developed around the failures did not correlate with the failure size. The highest density of new fractures both within and around (2 m perimeter) the failed area was seen around the smallest failure. This is probably due to the different locations of the triggered failures and suggests that the intensity of fracturing is more sensitive to other spatially variable parameters such as jointing and surface morphology. Whilst the local fracture intensity did not appear influenced by the failures, the spatial distribution of fractures displayed a bias towards areas immediately above and alongside failures. The increase in fracturing when the excavations were triggered was highest within the immediate vicinity of the failure: the number of new fractures generated within 0 – 1 m of the failure was more than twice that generated within 1 – 2 m of the failure, offering a potential explanation for the contiguous failures observed in Chapter 3. Furthermore the concentration of new fractures was predominantly above and alongside the failures rather than below. These areas of higher fracture concentration delineated areas of subsequent failure, demonstrating a spatially sequencing process of failure development, driven by fracturing. This supports the concept of a process zone (Griffith, 1924) and the notion the post-failure stress redistribution (Stock *et al.,* 2012) will promote damage generation, which could result in the increased presence of fractures and subsequent failure in neighbouring areas. Here, this is observed to occur within the immediate vicinity of the failures and suggests that progressive failure processes and associated mechanisms of stress redistribution and damage generation are a possible explanation for the propagating sequences of contiguous failures observed at the slope surface.

Overall, the observations made from comparing the experiments with and without excavations have demonstrated that the spatial extent of post-failure damage decreases with distance away from the failure; is concentrated adjacent to the failure; and is not proportional to the size of the failure.

The use of Slope Model has demonstrated that the timing of failures can be considered as a function of damage in the rock slope and that the location of evolving rockfalls through time reflects an internal process of brittle fracture, thereby providing a basis for the development of the conceptual approach outlined in Chapter 2. The limitations of Slope Model for this study are chiefly that it does not simulate detachment of material from the slope and that it is very computationally intensive to run the model at a high spatial (sub-metre) and temporal (sub-second) resolution. Developing a simple, process based model that simulates rockfall as a function of damage through time, would extend the spatial and temporal range of the model simulations, and could be run in parallel with the sophisticated, mechanically-based understanding provided by Slope Model simulations.

5 Introduction to Rockfall Model

The field data presented in Chapter 3 questions the notion that areas of rock face that have recently failed will then remain stable for an extended period of time (Moore and Griggs, 2002), suggesting that the spatial character of episodic slope failure is more complex. Within the dataset small rockfalls have been shown to occur within the footprint of subsequent, larger rockfalls, and contiguous rockfall clusters have also been observed. Progressive failure and the notion of stress redistribution within a rock mass as a result of previous failures (Senfaute *et al.,* 2009) are suggested as mechanisms that may drive this behaviour (Stock *et al.,* 2012) and may explain some of the difficulty in attributing failure time to observable triggers (Vann Jones *et al.,* 2015). However, progressive failure and stress redistribution at the length scales of the rockfall observed in this research are not well accounted for in current rock slope models and therefore a new approach is required.

The approach adopted here is based on the criteria outlined at the end of Chapter 2 (Section 2.4), which suggests that a rockfall model that accounts for observations from field data should: (1) model in a 2.5D slope face view space, rather than in profile; (2) model at a high spatial resolution to simulate small rockfalls (sub-metre); (3) simulate a range of temporal scales; and (4) model an evolving process that allows stress to transfer and drive damage accumulation. Simulating rockfall as a time-dependent function or result of damage to the rock mass could be a suitable way to achieve this and is supported by the results of Slope Model simulations (Chapter 4), where relationships between fracture growth and failure occurrence demonstrated that the timing of failures can be considered as a function of damage in a rock slope.

Subsequently, this chapter outlines the background, development and validation of a 2.5D cellular rockfall model, where the rock slope face is discretised into a regular square cellular grid. This allows the spatial interactions of episodic rockfall behaviour on a rock face to be explored, thereby addressing the third and fourth research objectives for this study.

5.1 Modelling Philosophy

Achieving the aim of developing a new rockfall model that allows rockfalls to evolve across the cliff through time requires an innovative modelling philosophy, which considers the rockfall as part of a continuous rather than a discrete process. This philosophy is adopted in recent approaches to modelling pattern evolution in geomorphological settings (e.g. Chapuis and

Tetzlaff, 2014; Murray *et al.,* 2014) where the focus is not directed solely at defining the initial point of instability, but also in describing the patterns of events that follows as the system develops through time. As current rock slope modelling often aims to model failure of the whole slope, from an initial point of instability to a final point of total stability, a new approach is needed to consider the longer-term evolving process of rockfalls at the slope face as observed in field data. The high spatio-temporal resolution 4D data now available through advances in monitoring technologies such as terrestrial laser scanning (Abellán *et al.,* 2014), airborne LiDAR (Young *et al.,* 2010), and unmanned aerial vehicles (Giordan *et al.,* 2015), allows rockfall models to be designed in a way that is more analogous to field data.

5.1.1 Exploratory modelling

Exploratory modelling aims to analyse complex systems through the use of multiple computational simulations, rather than the use of a model to predict system behaviour (Bankes *et al.,* 2013). Exploratory models are developed over multiple stages where different combinations of parameter values and processes are used to determine conclusions, which are then validated (Bankes *et al.,* 2013). At each stage of development analysis of the outputs is used to inform further model development and to provide insight into the system being modelled.

Larsen *et al.* (2014) and Temme *et al.* (2015) identify a current major scientific challenge as a need to resolve causality, particularly in complex and non-linear systems. The challenge lies in not just identifying why a particular event occurs but to explore the underlying mechanisms that drive the observed behaviour. This is further complicated by the potential issue of equifinality whereby several combinations of processes and parameter values can produce the same emergent behaviour (Beven, 2002). For rock slopes, where rockfalls are often considered, observed and modelled as individual events, the challenge lies in exploring the underlying mechanisms that are driving continuous failure within the slope, such as the concept of progressive failure driven by, amongst other factors, fracture propagation and coalescence (Eberhardt *et al.,* 2004).

Reducing the complexity within a model by transforming complex concepts into simple variables and their interactions, substantially increases the speed of operation (Coulthard *et al.,* 2007), although this is at the expense of removing or simplifying physical details and potential issues and limitations associated with this, such as equifinality, should be accounted for (Ziliani *et al.,* 2013). By increasing the speed of operation, a large combination of

parameters and processes can be explored, which is not often computationally feasible with more complex, mechanical models such as *Slope Model* (Itasca, 2010b). Recent applications of exploratory modelling in geomorphology have been developed to include coupling between multiple environments, as demonstrated in the studies of Rozier and Narteau (2014), Coulthard *et al.* (2013) and Larsen and Harvey (2010), yet crucially a reduced complexity model of the physical processes is retained. Increasing the number of parameters and processes that can be simulated, or simulating multiple environments, will increase the likelihood of identifying the key causative process(es) if the representation of boundary conditions is increased accordingly. Additionally, exploratory modelling may serve as an indicator of where more detailed modelling of perhaps a different style, and field observations, should be directed (Oreskes *et al.,* 1994).

Within an exploratory modelling approach, the aim is not to simulate real world observations, rather to examine the combinations of inputs that produce similar and general behaviour to real world observations. This approach is well suited to rockfall evolution modelling where the goal is to understand the potential role of process drivers, the general resultant behaviour, and the resulting emergent characteristics, such as the development of topographic features on the cliff face.

5.1.2 Cellular automata models

Cellular automata (CA) models provide a method for simulating complex systems where the focus is on the interactions between components of the system through time (Wolfram, 1983). CA models idealise a physical system where both space and time are discrete and all physical properties have a finite set of discrete values. CA models are classed as reduced complexity and operate on a regular grid system where interaction rules cause the model to iteratively evolve over time, for example the landscape evolution model produced by Rozier and Narteau (2014). The interaction rules are based on a generalisation of the physics of the system being modelled. Originally developed by Von Neumann (Rozier and Narteau, 2014) for the purpose of modelling biological self-reproduction, CA models have since been developed and applied for a wide range of purposes (Murray and Paola, 1997, 1994; Narteau *et al.,* 2000; Rosser, 2002). Within geomorphology CA models can represent space, or a landscape as a grid of cells, whereby the interactions between cells determines how the landscape evolves (Coulthard *et al.,* 2007). Such models have been used based on concepts of self-organised criticality (Bak *et al.,* 1988) to simulate landslides (Hergarten, 2003) and mass loss from near vertical glacier

surfaces (Chapius and Tetzlaff, 2014). A similar type of model could be applied to the surface of a rock slope and allows the concept of progressive failure to be simulated at a reduced complexity as the interaction rules permit strain to transfer between model elements.

The components necessary for constructing a CA model are described by Rozier and Narteau (2014). A CA model can begin with an arbitrary length scale and time step, which should be informed in general terms by the real world environment or physical system that the model is simulating. A CA model allows for a diverse range of properties to operate at a single cell level, necessitating the dynamics of the model to be governed by small-scale interactions. Both the length scale and time step can later be parameterised or tuned in respect to real world data. Conventionally the models assign each individual element (cell) within the grid a scalar property, which is able to change as a result of exogenic and/or endogenic forcing. Within a CA model the exogenic forcing is often applied to the whole model, whereas endogenic forcing is represented by the interactions between model elements. This is well suited to modelling rockfalls development through time, allowing the role of both external (such as weather) and internal rock mass (such as runaway damage) dynamics to be considered.

A key feature of CA models is that the emergent behaviour is not calculable from an assessment or analysis of the individual model components alone, rather it emerges from the combination of interactions within the model. The iterative progression of a CA model over discrete time steps allows the emergent behaviour to be observed at each time step. The complexity of the model can also increase iteratively based on the analysis of the output at any stage.

5.2 Conceptual Model Design: Rockfall model

The following section outlines the conceptual basis and design of a rockfall model that allows rockfalls falling from the face of a rock slope to evolve over space and time. The concept for this model was based on a near vertical rock slope, as illustrated in Figure 5.1. Here the system definition of the rock slope is summarised as six components: rock mass properties; slope topography; interaction laws; weathering; damage; and rockfall. These components are linked and interact to drive the occurrence and development of rockfalls. Including a bulk term that describes rock strength as dynamic through time (damage) allows rockfalls to result from the progressive weakening resulting from stress transfer, fracturing, deformation and weathering, which each prepare any particular part of the rock face for failure.

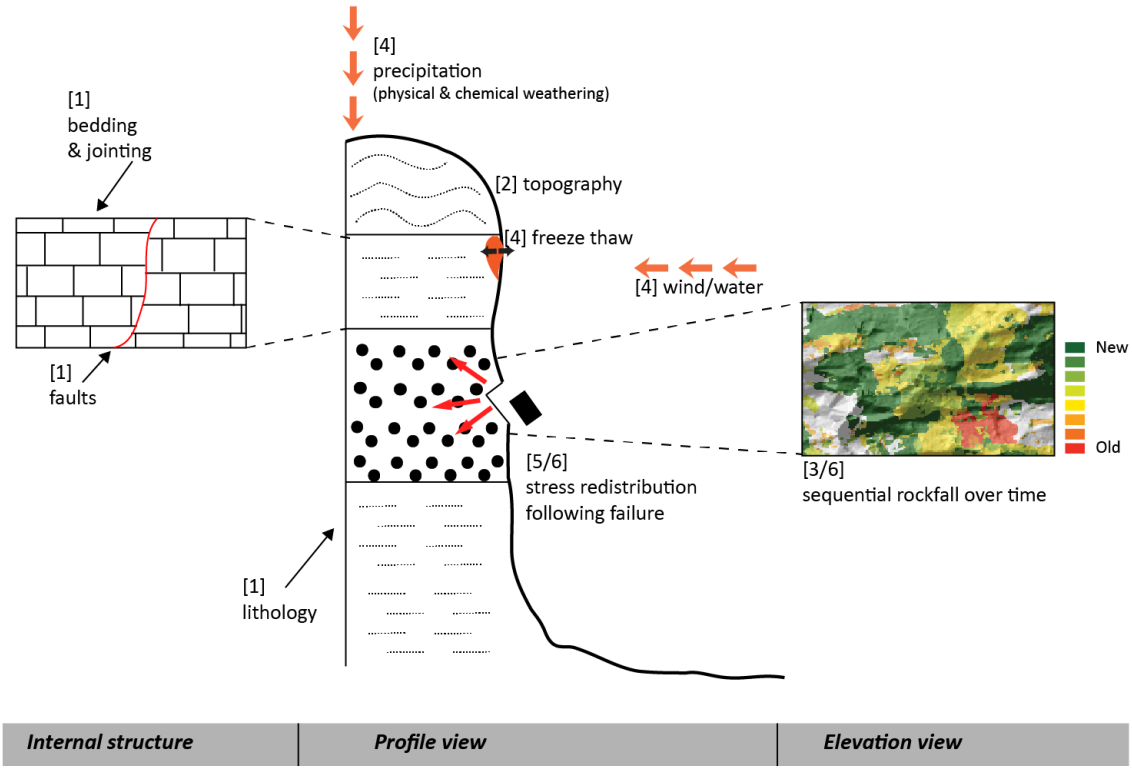

Figure 5.1: Conceptual model of the rock slope environment, demonstrating how the six model categories sit and interact within this environment: (1) Rock mass properties; (2) Slope topography; (3) Interaction laws; (4) External conditions (weathering); (5) Damage; (6) Rockfall

The manner in which the slope is modelled must incorporate the following key attributes:

- Modelling from a slope face view (2.5D), where cliff height and width define the model boundary, and change (rockfall) is simulated to remove mass normal to this plane;

- Modelling at a spatial resolution that the processes occur on;
- Considers time and operates across a range of temporal scales;
- Considers the evolving process of rockfalls, whereby the model responds to previous events by transferring stress, which can subsequently trigger damage generation.

A 2.5D cellular rockfall model has been developed, whereby the rock slope face has been discretised into a 2D grid, as illustrated in Figure 5.2. Each of the grid cells represents an individual element of the rock slope surface that has an elevation. The topography that these elevations define has a spatial resolution that can be set by the cell size. The model develops through time, and stress is able to transfer between model cells via interaction laws. The model is deterministic, however the emergent outputs are not directly calculable from the inputs.

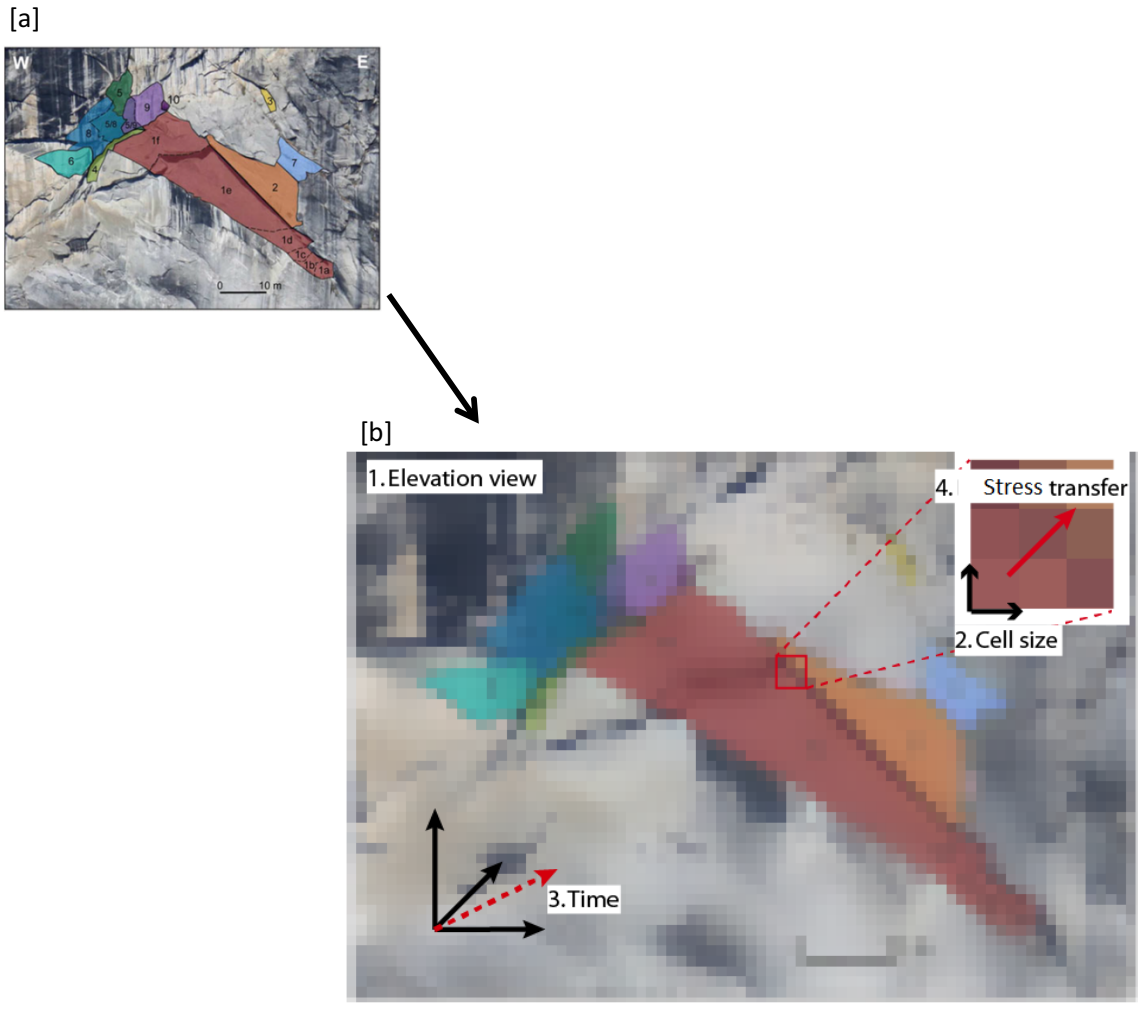

Figure 5.2: Illustration of the modelling approach of discretising the rock slope (a) into a 2D grid (b). The example (a) is reproduced with permission from: Stock *et al.* (2012, p.551). The numbers and labels used in (b) relate to the key achievements of this modelling approach, described in the text below.

Previously, changes to a rock slope have been conceptually modelled based on the notion of preparatory and trigger factors for rockfall (Krautblatter and Dikau, 2007). Preparatory factors change the driving stress or degrade the rock mass strength and trigger factors which include both external and internal drivers, are direct result in the final failure. The range of preparatory or preconditioning factors on failure is summarised by the conceptual model from Gischig (2011), shown in Figure 5.3, which either change the stress state (Fig. 5.3b-e) or the threshold for failure (Fig. 5.3f). The temporal evolution (Fig. 5.3a) illustrates how the point of ultimate failure occurs as a combined result of these factors as a function of rock strength and the magnitude of stresses. These principles are adopted in the rockfall model in this study by separating components of the model into boundary conditions (inputs); process drivers, which represent preparatory factors; interaction rules, which connect the drivers and accumulate damage; and outputs, which represent rockfalls. Each of the components of the rock slope environment shown in Figure 5.2 is incorporated into one of these model components as follows:

1. Rock mass properties	*INPUTS*
2. Slope topography	*INPUTS*
3. Interaction laws	*INTERACTIONS*
4. Weathering	*DRIVERS*
5. Damage	*DRIVERS*
6. Rockfall	*OUTPUTS*

By categorising each component of the rock slope environment in this way, the model seeks to simplify the interactions between them in order that the resulting feedbacks between each component and rockfall may be explored.

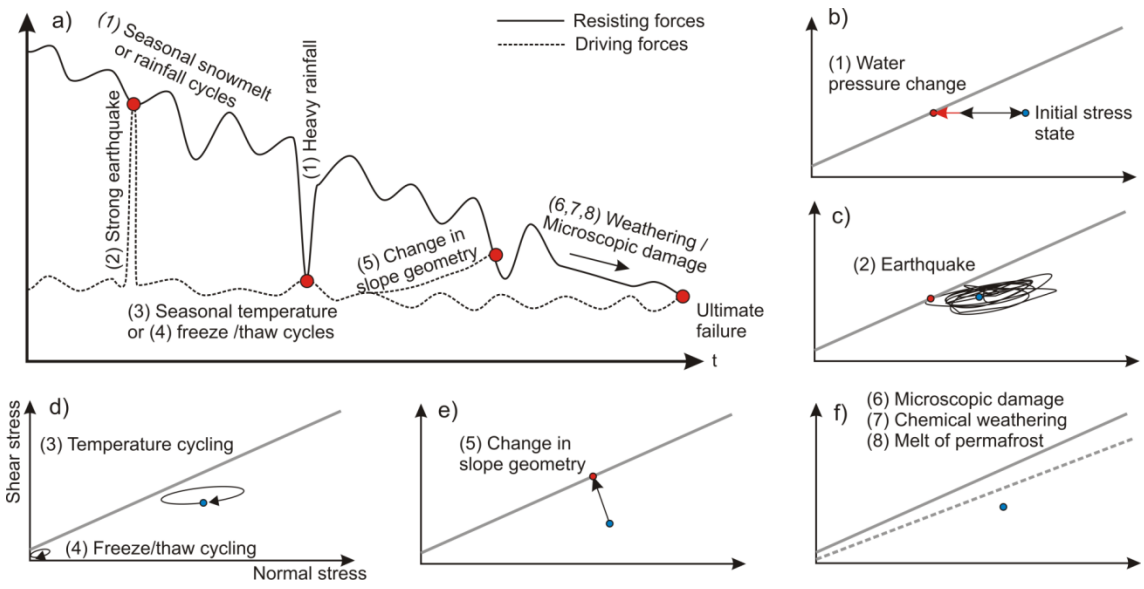

Figure 5.3: a) Temporal evolution of the driving and resisting forces in an entire unstable rock mass due to different preparatory factors; b – f) Changes in the stress state and strength at a single point in an unstable rock mass, due to changes in the different preparatory factors (reproduced with permission from Gischig., 2011, p.4; based on an earlier model from Gunzburger *et al.* (2005).

5.2.1 Model inputs

The model inputs include the rock mass properties and the slope surface topography (geometry). Together these properties define the initial conditions of the model. The model inputs can be changed in order that different conditions can be investigated.

5.2.1.1 Rock mass properties

The material properties of a rock slope, in particular the rock mass strength and the presence of discontinuities, determine slope stability and therefore are key parameters in determining the slope behaviour (Hoek and Bray, 1977; Selby, 1980). Within the rockfall model, both the drivers and interaction laws are modulated by the rock mass properties to reflect the influence of rock type on how damage can be accumulated.

Representation of rock mass strength within numerical models is typically complex and defined according to a number of different parameters, such as demonstrated in the application of Slope Model in Chapter 4. Representation of discontinuities often utilises a discrete fracture network (DFN) based on field observations (Elmo *et al.,* 2011, Tuckey *et al.,*

2012). Neither of these methods lends itself to representing global slope strength or stability by a single value.

Rock mass classifications such as the Geological Strength Index (GSI) (Hoek, 1994) and Rock Quality Designation (RQD) (Deere, 1964) allow rock mass properties to be reduced to fewer values that describe bulk rock mass strength and the stability effects of discontinuities. Additionally, the use of a rock mass classification system simplifies the complexity of discontinuity kinematics, and allows common behaviours to be identified within each of the classification groups. GSI quantitatively determines the strength of a rock mass based on structural rock mass characteristics and discontinuity properties where the resulting strength is a value between 0 and 100 (Cai *et al.,* 2004). Agliardi *et al.* (2013) demonstrate that by incorporating a degradation factor, the GSI values can be related to the level of damage within a rock mass. RQD is defined as the ratio of the length/area/volume of intact rock to the total length/area/volume of the sample (Deere, 1964; Zhang, 2016). The ratio is expressed as a percentage between 0 and 100% (Zhang, 2016).

For the purposes of this investigation GSI is used to define the rock mass properties for each cell within the model. Using GSI provides a representation of both strength and discontinuities that can be modelled. Applying GSI values at the scale of individual cells means that a spatial variation in rock mass properties can be applied at any scale, from individual cells to the whole slope. This enables a simplistic representation of rock slope conditions from a homogenous rock mass to highly jointed, or weak to stronger rock. GSI values are used to represent lithologies and it is assumed that the lithology of the rock at the surface persists back into the rock mass.

5.2.1.2 Slope topography

One of the aims of the model is to examine the relationship between failure and topographic features on the slope, which has previously been lacking from many rockfall studies (Krautblatter and Dikau, 2007). A common example of this interaction and feedback is the presence of inherently stable 'arch' features, forming parallel to the rock face (see Fig. 3.35). The manner in which such features are created by and then control rockfalls is a typical emergent property suited to exploration by cellular modelling. Martel (2006) shows that the range in topography and thus the roughness of the slope, expressed as the local curvature, impacts upon the likelihood of failure, when considering the surfaces of massive rocks (for example, 10^3 m in length, and 10^2 m in depth). The field data presented in Chapter 3 showed

that the influence of curvature can also be observed at a sub-metre scale, further supported by the numerical modelling undertaken in Chapter 4, which showed that failures preferentially occur in areas with a higher degree of curvature. However, the feedback between failure and topography is often overlooked. For example, the manner in which the removal of material then generates surface features such as overhangs, where the stress is likely to be higher. In this study, topography (cell elevation) is altered by rockfall, which then redistributes stress to surrounding cells.

5.2.2 Interaction laws

Within the rockfall model developed here, interaction laws allow the behaviour of one grid cell to impact the surrounding cells through stress transfer. The scales that stress transfer operates over are varied by changing both the magnitude of stress transfer and the distance over which the interaction rules search, for example beyond just the eight surrounding cells. As this interaction is not instantaneous, but rather triggers an accumulative process, this controls how the rock slope evolves. Two interaction laws are required to achieve this: the first to simulate the accumulation of damage in a cell (or group of cells) that is (are) kinematically free to fall; and second, to simulate the transfer of stress to surrounding cells when one cell fails. These are referred to from hereon as *loss of structural support (ss)* and (*post-failure) stress transfer (pd)*, respectively.

5.2.2.1 Loss of structural support

The cantilever beam theory, applied by Young and Ashford (2008) to coastal cliff failures, demonstrates how the presence of a notch within a cliff will eventually cause the overhanging block to fail as stresses accumulate in the cantilevered mass. The lack of support beneath means it is able to fail under lower stress conditions than when the support is in place, potentially triggering an upward propagation of rockfalls (Krautblatter and Dikau, 2007), as can be seen in a range of field observations both in this study (Chapter 3) and elsewhere (Styles *et al.,* 2011; Stock *et al.,* 2012; Rosser *et al.,* 2013). This concept of a cantilevered failure is adapted here into the rockfall model by allowing stress to transfer and then damage to accumulate in a cell that is regarded as unsupported, enabling overhanging cells to fail.

Within the rockfall model the forces between cells are regarded as equal and opposite (Fig. 5.4a) and therefore each cell is providing structural support to its surroundings. In the case

when a notch has developed into the slope profile (Fig. 5.4b), some of the structural support is lost as 'supporting cells' are removed. At this point there is an increase in the stress on the central cell (Terzaghi, 1962), resulting in damage.

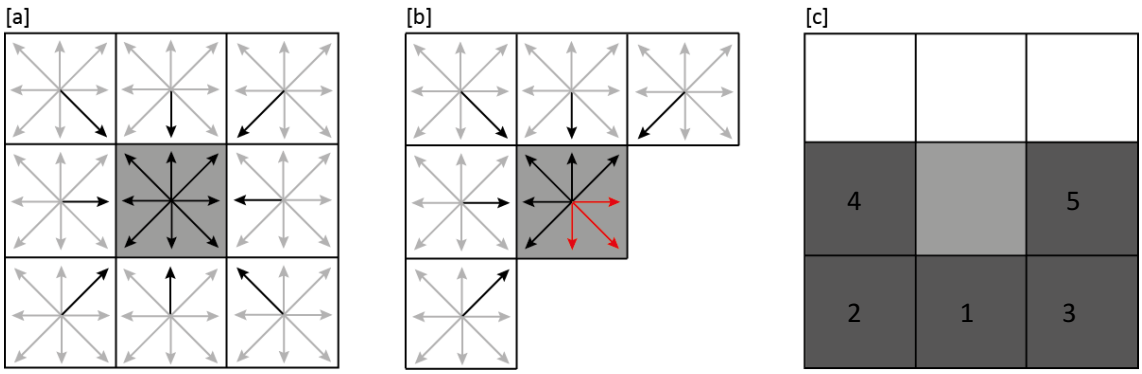

Figure 5.4: Conceptual illustration of forces acting to support the central (light grey) cell: (a) shows a balanced model; (b) shows the effect of removing structurally supporting cells: the red arrows are no longer opposed by equal and opposite forces, leaving the grey cell partially unsupported; (c) shows which cells the rockfall model considers supporting (dark grey).

5.2.2.2 Post-failure stress transfer and damage generation

The field data presented in Chapter 3 showed that rockfalls cluster both spatially and in time. Approximately 40% of failures were contiguous on the cliff between from one month and the next. Where contiguous rockfall are observed, propagation is also observed, primarily upwards and but also outwards from the previous rockfall scar. These observations were most evident for larger rockfalls, supporting the suggestion that smaller failures may be precursors to larger failures (Rosser *et al.,* 2007a). This behaviour is postulated to a function of post-failure stress redistribution (Stock *et al.,* 2012), which can cause damage to accumulate and weaken the surrounding material. Stress and the damage that it causes is most likely to propagate upwards and outwards due to gravity (Lim, 2006), and has been demonstrated through the use of numerical modelling in Chapter 4. In this study (Chapter 4), modelling showed immediate fracturing and subsequent failure in the area of the slope surface directly above and alongside a rockfall. Also using Slope Model, Havaej *et al.,* (2014b) demonstrated that fracturing occurs around a failure with a 'damage zone', termed a "damage ellipse". In the rockfall model presented here, the concept of the damage zone will be represented by the area which experiences increased stress and resultant damage, generating weakening.

The concept of stress transfer is included within the rockfall model via the post-failure stress transfer interaction law (equations in Section 5.3). Stress transfer from a failed cell to surrounding cells is simulated by increasing the damage value in the surrounding cells. Stress is transferred outwards and upwards from the failed cell to reflect the observations of failure scar growth in the field data and Slope Model results. The spatial extent and the speed of stress transfer is dependent on rock mass connectivity between cells in the modelled rock mass, which is influenced by rock mass properties.

Chapter 3 suggested that the critical timescale for which contiguous rockfall propagation was observed was around four months, which indicates that post-failure stress transfer is perhaps often not sufficient to trigger immediate further failure. Within the rockfall model, the total amount of damage increase in each cell resulting from stress transfer, must therefore be less than the critical threshold in damage required for failure.

5.2.3 Driving forces

The rockfall model simulates the evolution of the rock slope surface, which is influenced by both external conditions and internal changes to the rock mass such as damage accumulation. These are represented by the driving forces of the model, which bring the surface cells of the rock slope to failure.

5.2.3.1 External conditions: Weathering

External conditions encompass a range of long-term, iterative processes that act to weaken the cliff face and increase the susceptibility to failure, as illustrated in Figure 5.2. Broadly these conditions can be considered as weathering. Weathering is a key component of a slope failure that accounts for a reduction in rock mass strength with time due to weakening, reducing the strength of the rock and lowering the shear resistance of joints (Barton, 1973). The relationship between weathering and slope stability is non-linear (Viles, 2013), and varies in both time and space. The complexities associated with modelling the relationship between weathering and its impact on slope stability have been discussed in Chapter 2, and can be summarised as follows:

- Weathering can act as a preconditioning, preparatory and/or triggering factor for rockfalls (Krautblatter and Dikau, 2007);

- Weathering can be considered as a cyclic, dynamic load, and the amount of weathering required to trigger failure can be conceptualised using S-N curves (Brain *et al.,* 2014);
- Weathering can be spatially heterogeneous as a result of variations in local environmental conditions and the controls on weathering intensity;
- Weathering is temporally variable as a response to changes in weather, including for example, seasonality or diurnal cycles;
- Weathering impact on rock slope stability is modulated by the rock mass properties, which dictate the resistance of the rock to weathering, the opportunity for weathering to exploit the rock mass though for example discontinuities, and the exposure of the rock surface.

No single equation is able define the relationship between weathering and its influence on slope stability. Therefore, the rockfall model reduces weathering into a single non-dimensional value that acts to increases damage in the rock slope, in a manner that can be spatially and temporally variable. Weathering progressively increases damage in each cell according to a *weathering intensity (wi)*, the magnitude of weathering defined for each cell, and a *weathering rate (wr),* the amount of weathering applied per timestep. To represent the impact of the rock mass properties, the damage increase is inversely proportional to the *GSI* value and the elevation (depth into the rock face, as analogous to exposure) for each cell. Spatial variability in weathering is invoked via zones of different weathering intensity across the rock slope.

5.2.3.2 Time-dependent damage accumulation

External conditions and internal rock mass dynamics increase stress within a rock mass and cause damage to accumulate, often as fracturing, that may result in strain. The development of fracturing within a rock mass can be summarised using the staged brittle failure model developed by Martin and Chandler (1994) and Eberhardt *et al.* (1999), where critical stages of fracture development are represented by thresholds in the model. The discussion in Chapter 2 illustrated how the brittle failure model could be used to conceptually describe the accumulation of damage within a rock mass in response to rockfalls falling from the cliff surface.

The exceedance of the crack damage threshold in the brittle failure model marks the transition from secondary to tertiary failure (Petley *et al.,* 2005), whereby the growth of fractures accelerates in a time dependent manner, regardless of the applied stress (Bieniawski, 1967).

This final stage of failure is time-dependent, and is represented in the rockfall model by the time-dependent accumulation of damage once a critical threshold of damage accumulation has been exceeded. In order to achieve this, both a critical damage threshold and a relationship between damage accumulation and time are identified.

Damage mechanics provides one of the most useful illustrations of how stress in the rock mass allows linkages through space. The effects of micro-fracturing on the mechanical evolution of material (Martin and Chandler, 1994, Eberhardt *et al.,* 1999), results in changes to the material that are quantified with respect to a continuous measure of internal rock mass weakening.

Chapter 4 suggested that failure onset marks this transition from secondary to tertiary failure. The results showed that the time from failure onset to final failure completion was not instantaneous, and varied with the strength of the rock. This timing was not influenced by the slope surface morphology. Subsequently, the relationship between damage accumulation and time is set so that the time from onset to failure is always longer than one timestep in the model. This process is modulated by the rock mass strength, whereby the time from the failure onset threshold to final failure would be longer in a rock mass with higher GSI values. The results from Chapter 4 also showed that the magnitude of pre-failure fracturing was variable, and did not increase significantly in the time immediately preceding the point of failure, suggesting that the level of damage within the rock was already near the point of failure when failure onset occurred. This is reflected in the use of a critical damage threshold in the model to represent the point at which damage is sufficient to instigate the failure of that cell. The critical damage threshold is variable according to *GSI.*

5.2.4 Model outputs

The behaviour of the model is captured in the changes in topography of the rock slope surface through time, represented by rockfalls. A rockfall is defined here as the failure of a cell, which occurs when the cell reaches the critical damage value (Fig. 5.5). Cells that fail contiguously in one timestep are grouped as one rockfall. The occurrence of rockfalls, and their character, across the grid, and through time, is captured to allow comparison between runs and with field data. The evolution of rockfalls can be seen in visualisations of the model grid.

5.3 Model Formulation

The structure of the model was developed based on a 2D cellular grid where the grid value is elevation (depth into the rock face, as analogous to exposure) represented by *z*, as shown in Figure 5.5b. Model boundary conditions are represented as layers of values, which the interaction laws call upon. The rockfall model includes a bulk damage variable, *d*, that is calculated from all other model components. This is illustrated in Figure 5.5a, which shows how damage may evolve through time within a cell in the model.

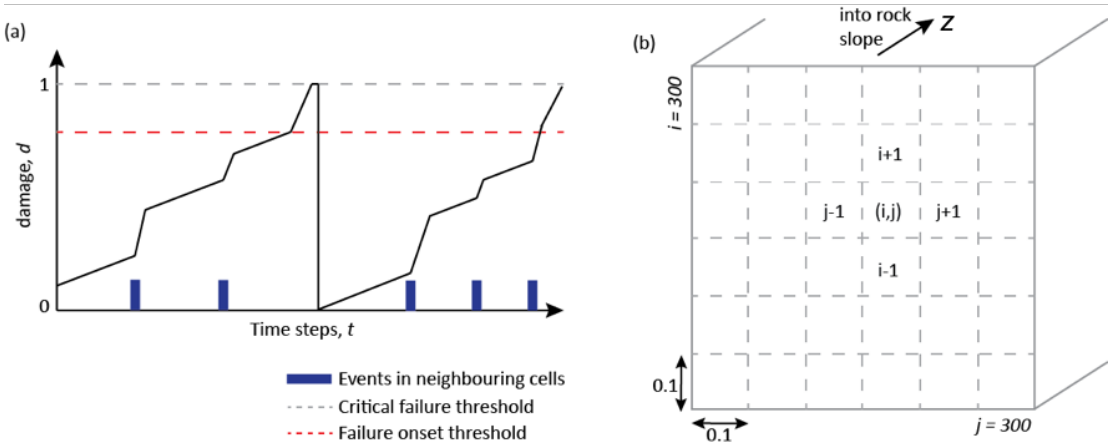

Figure 5.5: Conceptual sketch of the rock slope model, based on the sketch from Chapuis and Tetzlaff (2014, p.626; Figure 3). (a) The evolution of damage (*d*) over time in one cell. Damage accumulates through time set by the weathering rate (*wr*). This is punctuated by events in neighbouring cells, which can transfer stress to the cell, which then increases damage. Once damage exceeds the failure onset threshold (dashed red line) the cell proceeds to failure regardless of (external) forcing. Reaching critical failure (dashed grey line) triggers a rockfall. After failure the topography (*z*) is updated accordingly, and damage in the newly exposed rock face cells is reset to zero. (b) The rock slope face represented as a grid of 300 x 300 cells, with width and height = 0.1m, with ID based on the row (*i*) and column (*j*) position.

The interplay between damage and rockfall occurrence can be described as a positive feedback loop within the rockfall model. A cell fails if *d* reaches a critical value (*d = 1*). Once the cell fails it transfers stress to the surrounding cells due to removal of structural support. Elevated stress increases *d*, which eventually causes surrounding cells to exceed *d* = 1, and to also fail. The speed of this process is modulated by the topography of the slope surface (*z*), and the rock mass strength of each cell (*GSI*). External forcing, represented by the bulk weathering variable drives further damage in each cell that operates independently to inter-cell stress transfer. This positive feedback loop, alongside changes in rock mass properties and external dynamics,

allows the rockfall model to test whether the internal dynamics alone are sufficient to generate the rockfall behaviour seen in the field.

This approach to model development for rockfall was conceptually explored by Lim (2006), who outlined a 2D cellular model to explore rockfall development. The approach hypothesized a theoretical propagation of stress, and how this may lead trigger episodic failures from coastal cliffs. Here the basic premise of that model has been adopted and further developed to include a wider range of rock slope properties, and to examine the material interactions in more detail. An overview of the model workflow is given in Figure 5.6 that summarizes the description above. This describes the stages that each cell in the model experiences. The weathering component and loss of structural support are applied to all cells. The application of time-dependent damage accumulation and post-failure stress transfer and damage accumulation, are applied only when the *d* in the cell reaches the necessary failure onset threshold and critical failure threshold respectively. If a cell has not reached these failure thresholds (grey boxes in Fig. 5.6), then no further action is applied to that cell during that cycle of the model. Each cycle of the model is equal to one timestep (t_n).

Table 5.1: Physical and mechanical properties of each cell in the model, which are represented by a series of 2D grids.

Property (units)	**Description**	**Notation**
Geological Strength Index (0-100)	The Geological Strength Index is a commonly used way of identifying rock mass strength based on observable characteristics, e.g. surface condition, block size and joint condition (Cai *et al.,* 2004).	*GSI*
Elevation (m)	The depth into the rock face, as analogous to exposure, where the initial rock slope surface is $z = 0$ and positive values indicate depth into the rock mass.	*z*
Topography (protrusion: 0 - 2)	The amount that a cell protrudes from the mean rock slope surface, whereby the mean surface at any time can be considered as $p = 0$. This is used to represent curvature: 0 = concave (deepest); 1 = planar (mean slope surface); 2 = convex (most protruding).	*p*
Damage (0-1)	Used to represent the weakening of the rock mass, often physically seen as fracturing. Values range from 0 (no damage) to 1 (point of final failure).	*d*
Age (timesteps)	The time since each cell last failed, hence the surface exposure age of each cell. Age is described in units of model timesteps, e.g. one full cycle of the model, which broadly represents one day of real time.	*t*
Weathering intensity (1-10)	The intensity of weathering (external forcing) at each cell location. This ranges from 1 (low intensity) to 10 (max. intensity).	*wi*

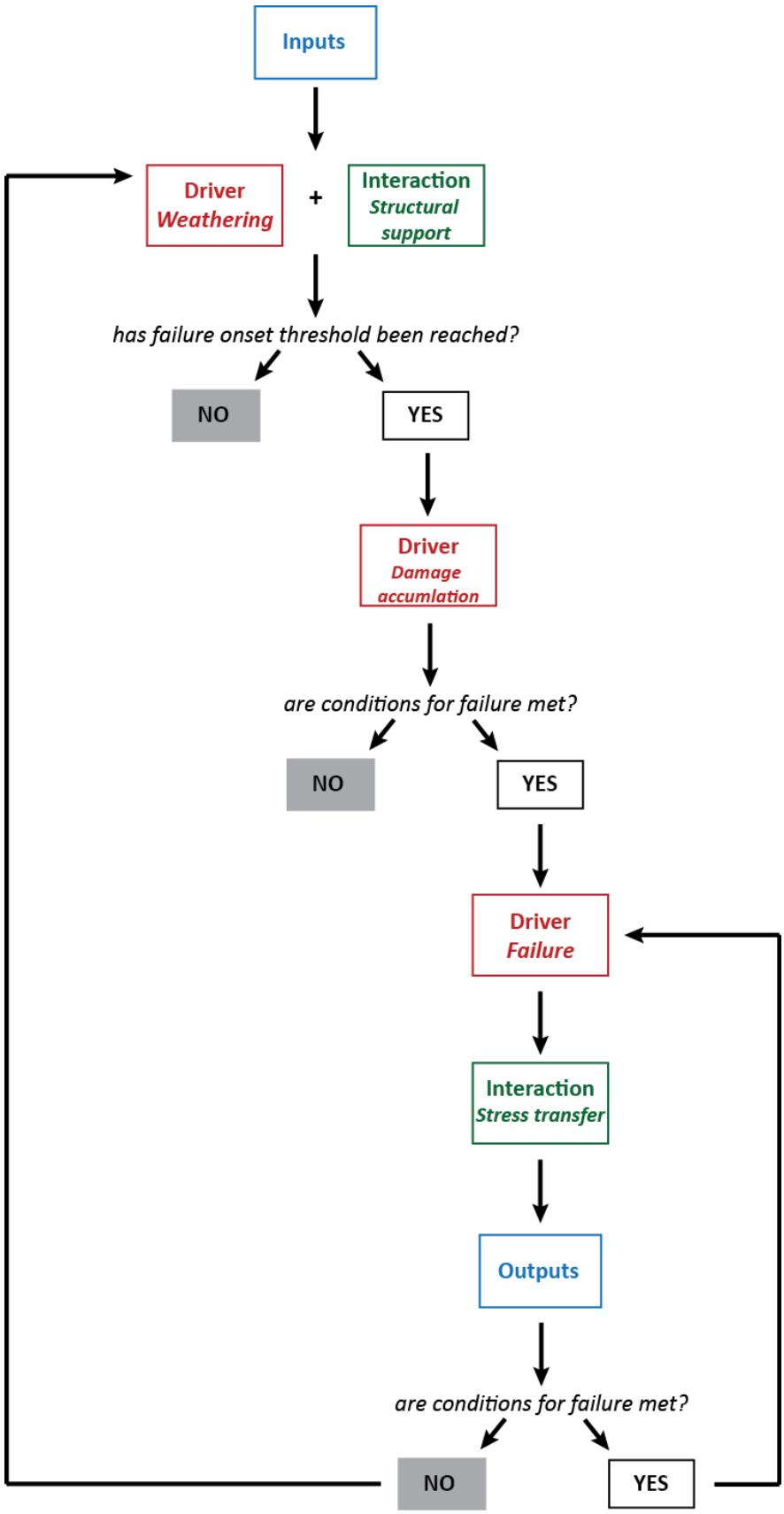

Figure 5.6: Workflow of the different stages in the rockfall model. Each cell in the model goes through this workflow for every cycle of the model and the grey boxes represent the different points at which the cycle can stop in an individual cell. Once the cycle has been stopped in every cell, the next model cycle begins.

Table 5.2: Terminology used throughout this study to describe different model attributes, here listed with the real world equivalent.

Model terminology	**Notation**	**Real world terminology/description**
Damage	*d*	A continuous measure of any weakening of the rock mass, which could be physically expressed as fracturing, grain scale damage, or deformation: d_n is the damage in a specific timestep (t_n)
Stress transferred (%)	*pd*	The amount of stress transferred from a failed block to surrounding areas
Range of *pd*	*e*	The distance in horizontal (*e1*) and vertical (*e2*) axis across the model grid that the stress can transfer
Modulated *pd*	pd_{mod}	The adjusted *pd* value such that when stress is transferred from one cell to neighbouring cells, the total stress transferred equals and cannot exceed the stress in the failed cell.
Distance to the failed cell	*dist(i, j)*	The distance from cell(i,j) to the failed cell (relevant to calculation of *pd*)
Number of cells in a given zone of surrounding cells	*f*cells	The number of cells within the same *dist(i,j)* from the failed cell
Failure/Rockfall		The detachment of material from slope once the critical damage level has been exceeded
Topography/Morphology	*z/p*	The elevation of each cell on the rock slope surface (see Table 5.1) *p* = protrusion from the mean slope surface
Time step	t_n	The time for one complete model cycle, broadly equivalent to one day real time
Model cycle	$t_n = 1$	One complete run of the workflow in Fig. 5.6. This stops when all cells are below the point of failure (*d* = 1).
Model simulation	*1.1*	A specific model setup that is run for a given number of time steps.
Length of model simulation	*L*	The length (t_n) of a model simulation
Refresh rate		Time taken for the entire surface of the rock mass to fail
Slope face view		Oblique, face-on view of a rock slope, where vertical (real-world) is the y axis, across cliff (real-world) is the x axis, and depth into the cliff is the elevation value (z)
Weathering rate	*wr*	The amount of weathering (*wi*) applied per t_n. This is defined as the number of timesteps it would take for a cell to fail by weathering alone, if the initial cell damage level (*d*) was 0.
Structural support	*ss*	The support provided to a block by the surrounding material, including lateral confinement and vertical support.
Notch threshold (m)	s_n	The depth of a notch required for the block above to be considered unsupported, e.g. no longer supported by surrounding material (*ss*)
Proportion of supporting cells lost (%)	*s*	The proportion of the supporting cells that have failed
Total structural support lost (%)	*sl*	The amount of support lost when a block is unsupported, e.g. when s_n is exceeded
Failure onset threshold	*fo*	The transition from secondary to tertiary failure in the brittle failure model, defined in terms of a percentage of *d*
Time to failure (t_n)	*tf*	The time from *fo* to final failure, defined as the number of timesteps
Time beyond failure onset (t_n)	*t_fail*	The number of timesteps that a cell has gone beyond *fo*
Overall slope angle (°)	α	The angle of the slope from vertical, e.g. 0° = a vertical slope

5.3.1 Boundary conditions

The boundary conditions are those factors which are not simulated or changed by the model equations (Mulligan and Wainwright, 2004). These include the area occupied by the model grid (model size); the boundaries of the model; the time the model runs; the rock mass properties defined for each cell in the grid; and the weathering conditions.

Model size

The model was required to be large enough for emergent features to develop. Rockfalls need sufficient space to grow and propagate, and for structural surface features, such as overhangs and arches, to emerge. Analysis of the field data has shown that within an area of c. 900 m^2, the distribution of rockfall sizes and the recurrence interval of rockfalls of all sizes is similar to wider behaviour of the entire slope (Appendix 1). The resolution of the rockfall model was set to the resolution of the field data, resulting in a cell size of 0.1 m (Fig. 5.5). In order to achieve an area of 900 m^2, this resulted in a 300 x 300 cell grid. The computational time for a model of this size is less than two minutes for 10,000 model cycles (excluding output processing time), allowing multiple model simulations to run quickly.

Model boundaries

As the cliff face is laterally continuous, to ensure that edge effects at the model lateral boundaries do not impact on the model outputs, a border of one cell was set around the edge of the model space where the cells were not included in model calculations and did not fail. This ensured that the interaction rules (post failure stress transfer and loss of structural support) could operate, as each cell included in model calculations was surrounded by all eight neighbouring cells. The cells in the model boundary are not included in the outputs of the model.

Model simulation time

The total amount of time that the model is able to run for is defined in terms of the number of model timesteps (t_n), where 1 t_n = 1 model cycle as per Figure 5.6. This is specified at the start of each model simulation and referred to as the length of the model simulation (L) in the model script in Appendix 3. The model simulation time was defined based on the initial performance of the model, as described in Section 5.4.

Rock mass properties

The Geological Strength Index (*GSI*) is based on both structural rock mass characteristics and discontinuity properties. For the rockfall model, estimated *GSI* values will be used to simulate rocks of varying strengths. For the initial developmental stages (sections 5.4 – 5.5), a single value of *GSI* = 50 is used to represent a homogenous, blocky rock mass of medium strength in good condition (Cai *et al.,* 2004). If the model were to be simulated based on field data from a specific environment, then the *GSI* classification developed by Cai *et al.* (2004) would be used.

Weathering conditions

Weathering is defined as boundary conditions for each model simulation as the weathering intensity (*wi*) and rate (*wr*).

wi varies between 1 and 10 in order to simulate *wi* variations over an order of magnitude. For the developmental stages of the modelling, a uniform grid of *wi* = 1 is used to simulate uniform weathering intensity. Applications of the model in Chapter 6 use the weathering grid to simulate different weathering zones across the rock slope in order to reflect different process zones.

wr sets the speed at which damage accumulates as a function of the number of weathering cycles that it takes for a cell to reach critical failure (*d* = 1) if no other factors were considered and the cell began with *d* = 0. This is varied in the developmental stages of the modelling to observe the behaviour of the model as a response to different weathering rates, which allows the temporal nature of external processes to be explored.

5.3.2 Initial conditions

The initial conditions of the model include the topography of the rock slope surface (*p*); the initial damage values of each cell (*d*); and the model timestep (*tn*). These variables change throughout the model simulation, evaluated in each model cycle, but need to be specified at the start ($t_n = 0$) (Mulligan and Wainwright, 2004).

Topography (protrusion, p)

Topography is calculated from depth values (*z*) normal to rock slope surface. From these values the amount that a cell protrudes from the mean slope surface (*p*) is calculated according to:

$$p(i,j) = z_{mean} - z(i,j)$$

Equation 5.1

where $p(i,j)$ is the distance that cell (i,j) protrudes from the mean surface; z_{mean} is the mean slope surface elevation; and, $z(i,j)$ is the surface elevation for an individual cell (i,j), which is scaled to range from 0 – 2. 1 represents the mean surface elevation, 0 is the deepest point into the slope, and 2 is the most protruding cell on the slope surface.

For the developmental stages of the rockfall modelling, a uniformly random topographic grid was generated with a range *z* = 0 – 0.5 m, approximately scaled on the roughness of the rock slope surface in the field data. This allows the influence of topography to be considered (section 5.3.4). Emergent topography as a result of rockfall, is analysed by capturing topography for each t_n. Applications of the model shown in Chapter 6 include varied slope topography, used to represent different types of rock slope profiles and geometry.

Damage (d)

Stress is either applied or redistributed within the model, and the consequent strain accumulation within each cell is referred to as damage (Tables 5.1 & 5.2). This is represented by values which can range from 0 to 1, where *d* = 1 represents 100 % damage at the point of final failure. At the beginning of each experiment, *d* for each cell was assigned using an array of uniformly distributed random numbers between 0 and 0.2. This was done to perturb the model and to represent pre-existing heterogeneous damage, at any given time. The range was chosen such that no cells were initialised with values beyond the critical threshold for failure (*fo*). Therefore, any failures observed were triggered by the model equations and interaction laws and not the starting conditions.

Model time step (t_n)

In simulating rockfall as an evolving process the relative timescales of those processes with a time-dependence are important, as illustrated in Figure 5.3 (Gischig, 2011). The time step for this rockfall model is set to be equivalent to one day of real time. Experiments with the model will later be used to explore the validity of the assumption. Simulations of the rockfall model begin at t_n = 0 and the outputs are captured on each timestep. Each cell is assigned an age value (*t*), which is the number of timesteps (t_n) since the cell last failed. Within the rockfall model a sub-loop during each iteration simulates post-failure stress transfer (see section

5.3.4.5 below). The duration of this loop is assumed to be infinitely small, representing the instantaneous nature of stress redistribution within a rock mass.

5.3.3 Governing equations

5.3.3.1 Weathering

Weathering increases *d* in each cell as a function of *wi* at the cell location, *wr*, *GSI* and *p*. Cells with a higher *GSI* value are assumed to be less influenced by weathering. This is reflected in the rockfall model by a slower accumulation of *d* for cells with higher *GSI* values. Conversely, those cells that protrude furthest from the mean slope surface are assumed to be more exposed to weathering. Additionally, these are likely to be locally convex areas of the slope where greater near surface stresses exist (Martel, 2006), and therefore the strength of the rock is further weakened. These factors are reflected in the CA model by a faster accumulation of damage for cells with a higher *p* value. Weathering is applied to each cell at every model time step according to the following equation (variables defined in Table 5.2):

$$d_n(i,j) = d_{n-1}(i,j) + \left[\frac{1}{wr} * wi(i,j) * p(i,j)\right]^{\frac{GSI(i,j)}{50}}$$

Equation 5.2

Equation 5.2 produces a linear increase in weathering with time (Fig. 5.7). A *wr* value is applied to the whole slope, defining the gradient of the line in Figure 5.7. All other factors are specific to each cell, and therefore moderate *wr* at a cell by cell level. As dictated by Equation 5.2, weathering grids with lower *wi* values result in a slower accumulation of *d* through time. Lower *wi* and *wr* values also allow the rock mass properties, *p* and *GSI*, to exert a more significant influence on the total rate of damage accumulation.

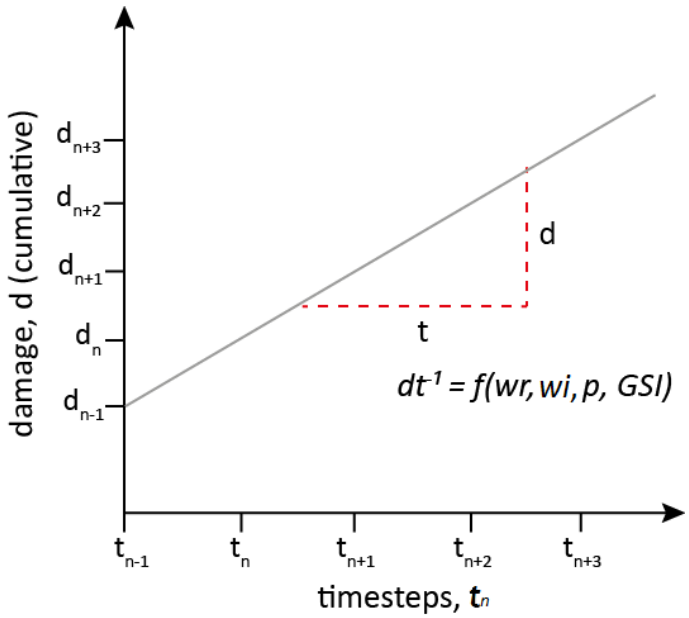

Figure 5.7: Graphical illustration of the increase of damage in one cell over time as a result of the weathering applied (Equation 5.2): the slope of the line is modulated by *wr, wi, p and GSI*.

5.3.3.2 Loss of structural support

The interaction rule for loss of support within the rockfall model increases *d* in the overhanging cell (*i, j*), as illustrated in Figure 5.4. The increase in *d* is dependent on the notch threshold (s_n); the proportion of supporting cells that have failed (*s*); and the support lost (*sl*). The support lost (sl) represents the total possible support that can be lost if all five supporting cells were deeper than s_n. Both *sl* and s_n are varied in the developmental stages of the modelling to observe the behaviour of the model in a response to different weathering rates.

This interaction rule is formulated within the rockfall model as follows:

- To determine whether a cell is unsupported, the five 'supporting cells' (Fig. 5.4) are queried to determine if the difference in their elevation (*z*) compared to the elevation of the central cell (*z*) is greater than s_n.
- The cells are queried in sequences: cell 1; 2 and 3; then 4 and 5 (Fig. 5.4). Cells 2 and 3 can only be examined if cell 1 is above s_n, and cells 4 and 5 only if cells 2 or 3 respectively are above s_n. The code that undertakes this sequencing is provided in Appendix 3.
- Once *s* (the proportion of supporting cells above s_n) has been determined, the interaction rule for loss of structural support is applied to each cell in every model iteration, according to the following equation (variables defined in Table 5.2):

$$d_n(i,j) = d_{n-1}(i,j) + [s(i,j) * sl]^{\frac{GSI(i,j)}{50}}$$

Equation 5.3

5.3.3.3 Time-dependent damage accumulation

Time-dependent damage accumulation drives a cell to the point of failure after the failure onset threshold (*fo*) has been reached, representing the final stage of progressive failure as time-dependent weakening. In order to do this, both a failure onset threshold (*fo*) and a time from this point to final failure (*tf*) are required. These are defined as follows:

- *fo* marks the point at which is cell becomes unstable (see sections 5.2.3.2). This is defined as a percentage of *d* and is set at the beginning of the model simulation. The *fo* value is varied between 85% and 95% damage (section 5.5).
- The time from failure onset (*fo*) to final failure is referred to as time to failure *(tf)* and is defined in terms of t_n. This is set at the beginning of the model and is also varied within the model development (section 5.5).

Once *d* in a cell reaches *fo*, then the time since this point is recorded within the model as the time beyond failure onset *(t_{fail})*. The cell fails after the defined number of time steps (*tf*) via the following conditional statement within the model (variables defined in Table 5.2):

$$if\ t_{fail}(i,j) \geq tf^{\frac{GSI(i,j)}{50}}$$
$$d_n(i,j) = 1$$

Equation 5.4

5.3.3.4 Rockfall failure

At the end of each model cycle (Fig. 5.6), all the cells are queried to see whether *d* has reached critical failure (*d* = 1). Where this is the case, then the cell is considered to have failed triggering a rockfall. This is based on the assumptions that all rockfalls detach from the rock slope and there is no intermediate storage on the cliff face, and that the rockfalls don't impact or damage any other part of the slope as they fall. In order to simulate failure, *z* is updated to reflect the material loss. *d* in the cell is reset to zero to represent the exposure of fresh rock. In the initial stages of model development, a consistent failure depth of 0.2 m was used,

reflecting field observations that most rockfalls are shallow and surface features, rather than deeper seated failures of the rock mass. This was later varied in the modelling development stage 2 (section 5.5).

5.3.3.5 Post-failure stress transfer (*pd*)

Once cells have failed, stress is transferred to surrounding cells, promoting the generation of damage in those cells. The consequence of this is simulated by increasing *d* in surrounding cells. The key variables are: the magnitude of damage that accumulates in response to stress transfer as a result of previous failure (*pd*); the cells that damage accumulates in after stress transfer (*e*).

The total ***damage accumulated*** is set as a percentage of the total damage required to initiate failure of the cell (*pd*), where 100% = 1. This value is modulated by the total number of cells that the damage is transferred to (pd_{mod}) such that when the stress in one cell is transferred to those neighbouring cells, the total stress transferred equals and cannot exceed the stress in the failed cell. pd_{mod} is user defined at the beginning of the model simulation and is varied within the modelling development (section 5.4).

The ***cells*** that stress is transferred to and damage accumulates in are specified by horizontal (*e1*) and vertical (*e2*) distances over which stress is transferred, as shown in Figure 5.5 and the ***spatial distribution*** of stress transfer and resulting damage accumulation is set as a function of distance from the failed cell. This is defined according to the position of each cell relative to the failed cell, as shown in Figure 5.8.

Stress is transferred to surrounding cells following each rockfall according to the following equation (variables defined in Table 5.2):

$$d(i,j)_{n+1} = d(i,j)_n + \left[\frac{pd_{mod}}{2^{dist(i,j)-1}} * \frac{1}{f_{cells}}\right]^{\frac{GSI(i,j)}{50}}$$

Equation 5.5

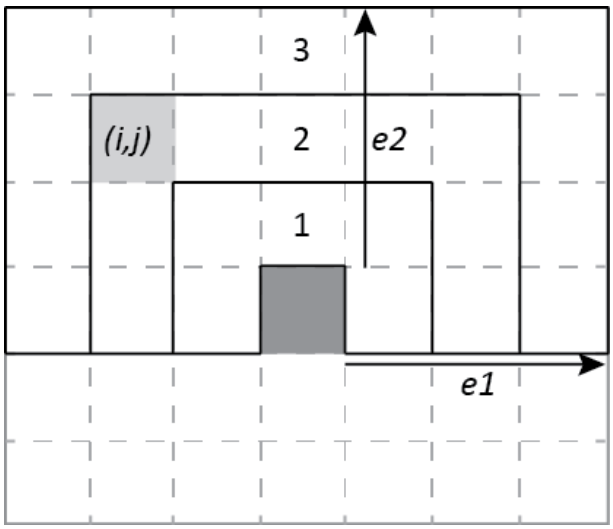

Figure 5.8: An illustration of the cells that stress is transferred that drives damage accumulation in neighbouring cells around a single failed cell (grey). Damage accumulates in zones of surrounding cells above and alongside the failed cell (layers 1, 2 and 3). The horizontal distance (e1) and the vertical distance (e2) from the failed cell define the geometry of layers 1 to 3. Example cell *(i, j)* identified on the figure, would be in layer 2, where *dist(i, j)* = 2 and f_{cells} = 9.

5.3.4 Model outputs

Failure events

At each time step the failed cells are identified and contiguous failed cells are grouped into rockfalls. For each rockfall identified the number of cells, surface area and volume are calculated. The total number of rockfalls per timestep is recorded in order to provide a time series of rockfalls. From this data, the recurrence interval of different rockfall sizes and magnitude-frequency relationships can be calculated.

Slope topography

At each time step a grid of the updated rock face topography is output, recoding elevation values (z). These grids are stored in an array so that the change in topography can be observed over any timescale within the model.

Visual plot of slope surface and rockfalls

Images of the model grid, with failed cells attributed by the time step of failure, are produced to show where and when rockfalls occurred. These grids are produced for any time period to show the development of rockfalls through time.

Slope profiles

At the end of each model simulation, the angle of the whole slope (model area) is calculated, from the crest to the toe and expressed as the angle from vertical, such that a slope angle of 0° = vertical. From the field observations and historical data, it is known that hard rock cliffs maintain an approximately near-vertical profile (see Chapter 3 and references therein), so a successful model is expected to replicate this behaviour. In addition, mean and sample slope profiles are generated from the topography data to show finer details and emergent changes in local scale profile form.

Model validation

To validate a model is to establish the legitimacy of the model outputs and to determine that the model does not contain any detectable flaws (Oreskes *et al.,* 1994). In this study, the rockfall model is validated against results from the field dataset presented in Chapter 3. The aim of this model is not to specifically replicate that environment, but to generate a model that demonstrates similar behaviour. For the purposes of this study it is important that both the overall erosion generated by the model and the process by which this is achieved are correct. The process(es) generating erosion can be examined by considering the distribution of rockfall sizes and the spatial distribution of rockfalls on the slope. The overall erosion can be examined using an erosion rate and the resulting slope profile. Subsequently the behaviour observed in the field data has been summarised and quantified according to four criteria that encompass these methods of analysis, which the model outputs will then be validated against the following variables, which are summarised in Table 5.3:

- Distribution and range of failure sizes

  The *distribution* of failure sizes is analysed by generating magnitude-frequency data of the rockfall volumes (logarithmic values to base 10) using the log-interval method (Pickering *et al.,* 1995) and fitting a power law through the data (Lim *et al.* 2010; Barlow *et al.* 2012) according to Equation 2.2. The range of failure sizes generated by the rockfall model is validated against the results from 30 x 30 m areas of interest from Boulby (Appendix 1), which represents an area the same size as the model space. The range of failure sizes are given in Table 5.3 and shown in Appendix 1.

- Erosion rate

  The spatially averaged erosion rate indicates whether the time step assigned to the model, and the rate of material loss, is reasonable. The rockfall model has been designed so that

each time step (t_n) is equivalent to approximately one day of real world time. The erosion rates observed in the field data, both from this study (Chapter 3) and previous studies at this site (Lim *et al.,* 2005, Rosser *et al.,* 2007a), range from 0.001 to 0.1 m a^{-1} depending on precise location and rock type. These values have been converted into an erosion rate with units of mm t_n^{-1} and a range of suitable values for the model outputs have been determined as 0.001 – 0.5 mm t_n^{-1} (Table 5.3).

- Total surface area failed

The failed surface area, expressed as a percentage of the total surface area, allows the mode time step to be adjusted to tune the net rate of behaviour of the model. Within the field dataset, the failed surface area ranged from 9.5 – 23.5% per year dependent on site monitored. These values have been converted to percentages per time step, and a range of suitable values for the model outputs have been determined as 0.01 – 0.1% (Table 5.3).

- Spatial distribution of failures

The cliffs described in Chapter 3 maintain near vertical profiles, despite spatial variations in erosion between different lithological layers, and variable up-cliff exposure to wave action, for example. Temporal patterns in erosion were highly locally (m scale) variable and no trend in erosion with height up cliff were observed. The distribution of erosion with elevation was variable between field sites. The spatial distribution of failures generated by the model can be examined in two ways: firstly, by considering the overall slope angle; and second, by examining the distribution of erosion with elevation. Field data suggest that the slope angle should remain close to vertical, and that the local-scar (m) distribution of erosion up the slope should be variable through time, which enables the slope profile to evolve in a way that permits up-cliff propagation of rockfalls.

Table 5.3: Model validation criteria based on field data presented in Chapter 3. For each parameter a range of suitable values is given, which the model outputs will be validated against.

Validation criteria	**Parameter(s)**	**Range of values**
Failure sizes	*ß*-value (dimensionless)	0.5 - 1
	Minimum volume (m^3)	0.001
	Maximum volume (m^3)	10
Erosion	Erosion rate (mm t_n^{-1})	0.001 – 0.5
Surface area failed	Failed area (%) per time step	0.01 – 0.1
Spatial distribution of failure	Slope angle (°)	< 10
	Distribution of erosion with elevation	Variable through time

5.4 Model development 1: Application of weathering, stress transfer and loss of structural support

The rockfall model was developed in stages, whereby different components of the model were introduced sequentially. This allowed the behaviour of the model in response to the addition of these components to be examined. The first stage introduced *weathering* and introduced two of the interaction rules: *post-failure stress transfer and damage generation* and *loss of structural support*, which are both necessary to enable the propagation of failures. The results from this stage were used to validate the model (section 5.4.3). Following this a sensitivity analysis was conducted to observe the relative response of the model (section 5.4.4). In the second stage of model development (section 5.5) further changes to the model were made, specifically to include progressive failure via a time-dependent damage accumulation function.

The rockfall model was run for 10,000 model time steps, allowing multiple simulations to be completed in one day on a standard MS Windows 64-bit operating system with 12GB of RAM in Matlab. After running the model for 10,000 time steps, approximately 60% of the surface area had failed at least once, which is almost twice the total failed area observed in ten years of field monitoring (total failed area = 33.4%). Running the model for 10,000 time steps was therefore assumed to give sufficient time to observe patterns in rockfall development similar to those in the field. Furthermore, running the model beyond 10,000 time steps shows that any longer-period cyclicity in rockfall occurrence repeats (Fig. 5.9) and the wider performance of the model is stable. Within 10,000 time steps, two cycles have completed suggesting that the model outputs for this time period will have captured a full representation of the behaviour of the model.

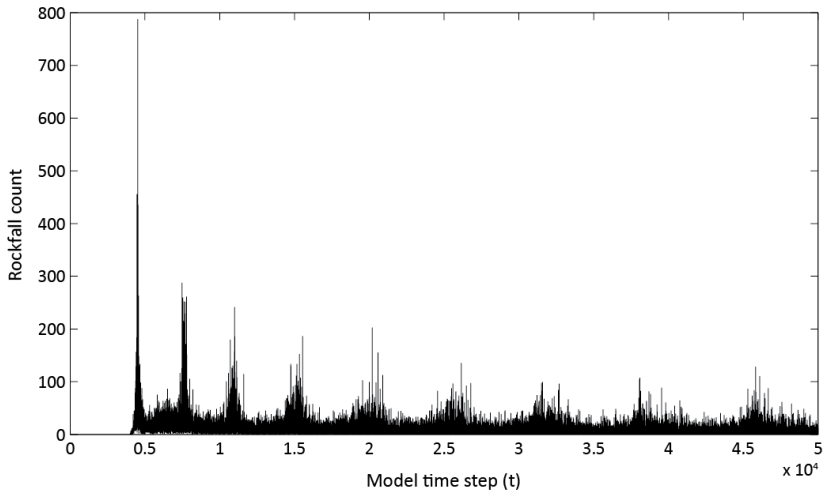

Figure 5.9: Time series of rockfall count (per time step) for a basic model setup run for 50,000 time steps

5.4.1 Weathering and stress transfer and damage

Initially, variable weathering rates (*wr*) and post-failure stress transfer (*pd*) functions were included within the rockfall model (Fig. 5.10), as described in Table 5.4.

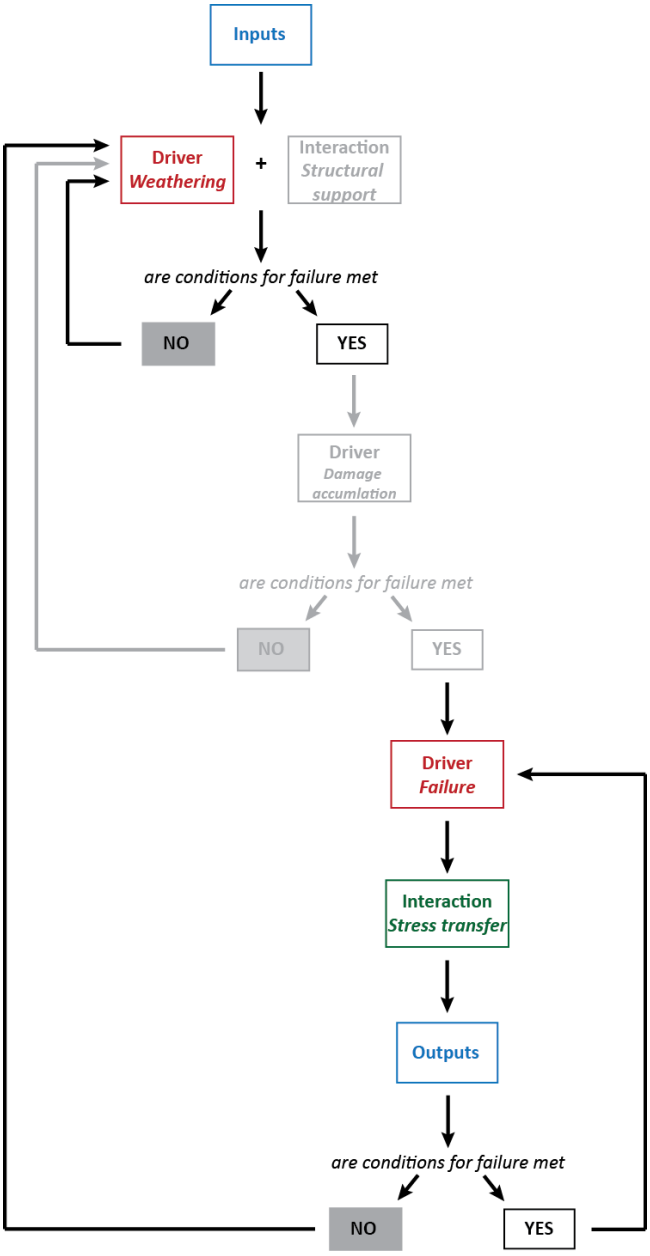

Figure 5.10: The model workflow used in simulations 1 - 2. The model components that have been faded are not used in these simulations. Where conditional statements are shown, this applies to all cells. If any cell meets conditions then the model moves on to the next stage in that cell, and once all cells no longer meet the condition then the model moves on one time step, and begins again at "Driver Weathering".

Results of these simulations show that as the *wr* is increased, both the rockfall count and failed area per time step decrease (Fig. 5.11a). However, the change in *wr* does not impact upon the distribution of rockfall sizes, as shown by negligible change in the magnitude frequency power laws (Fig. 5.12a). Here, a kernel density function (Bowman and Azzalini, 1997) has been used to generate a probability distribution of all rockfall volumes. The estimate is based on a normal kernel function evaluated across 100 logarithmically spaced rockfall volume bins between the minimum and maximum observed. The probability density is plotted against density and a power-law (straight line in log-log space) fitted (Equation 5.6).

As the *pd* is increased, the rockfall count increases, up to a value of *pd* = 95% where after it decreases. Failed area increases continually with increasing *pd* (Fig. 5.11b). This suggests that at higher *pd* values, fewer but larger rockfalls are generated, mirrored in the changing magnitude frequency distributions with increasing *pd* (Fig. 5.12b). As *pd* increases, the *ß*-value of the power law decreases (Table 5.5), indicating a more significant contribution of larger rockfalls to total erosion.

Table 5.4: Input conditions and model parameters for the model simulations used in Model development 1. The *GSI* (rock strength) and *wi* (weathering intensity) values were applied uniformly across the model grid. Where the range of model parameter values are given in the form *x* : *a* : *y*, *x* is the lowest value used, *y* is the highest value used, and *a* is the increment that the value is increased by for each model simulation. Notations used are given in Table 5.2.

Model simulation IDs	**Inputs**			***wr* (time steps)**	***pd* (%)**	***s_n* (m)**	***sl* (%)**	**Rockfall depth (m)**
	GSI	**Topography**	**wi**					
1.1 – 1.16	50	URD: 0 – 0.5	1	2500: 500: 10000	100	-	-	0.2
2.1 – 2.11	50	URD: 0 – 0.5	1	10000	75: 5: 125	-	-	0.2
3.1 – 3.10	50	URD: 0 – 0.5	1	10000	100	0.1: 0.1: 1	5	0.2
4.1 – 4.10	50	URD: 0 – 0.5	1	10000	100	0.4	5: 5: 50	0.2

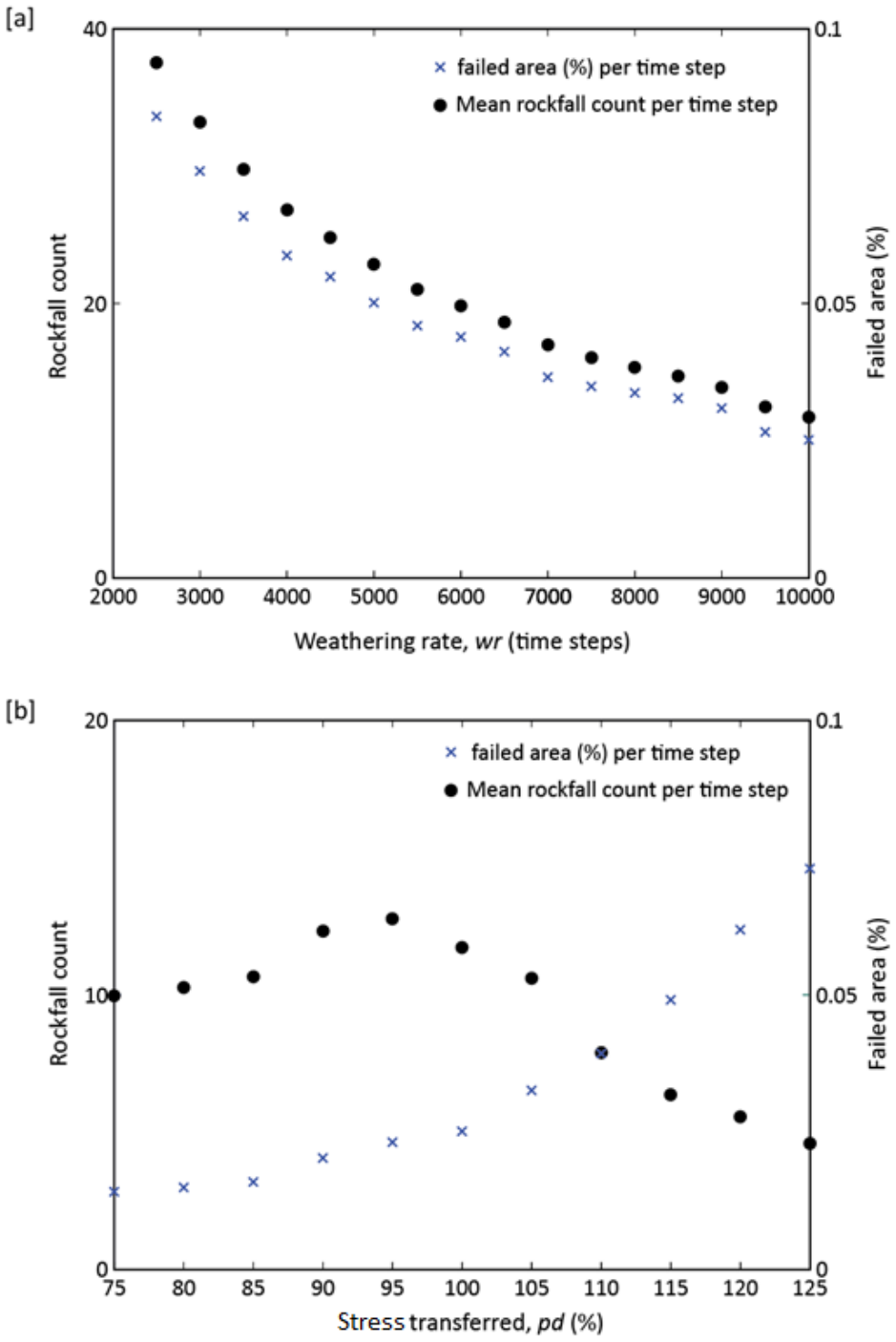

Figure 5.11: Mean rockfall count and failed area per time step for: (a) each model simulation run with different weathering rates in model simulations 1.1 – 1.16; (b) each model simulation run with different stress transfer (*pd*) values in model simulations 2.1 – 2.11.

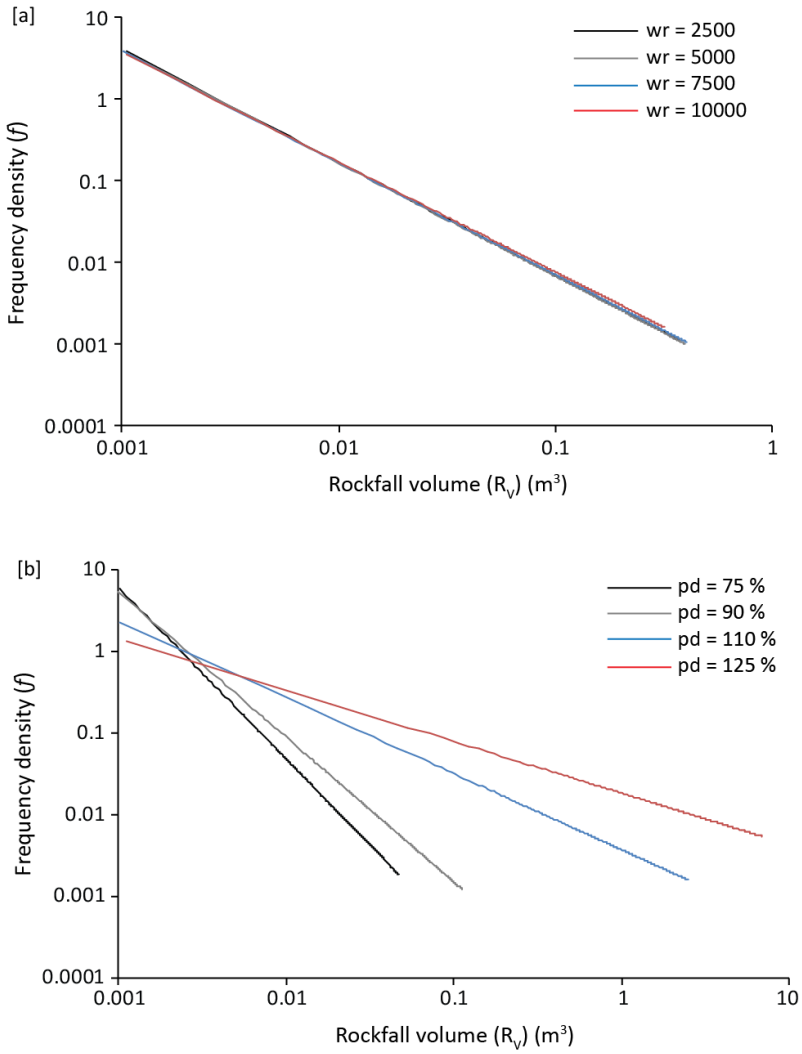

Figure 5.12: Power law fits for magnitude-frequency plots: (a) of all rockfalls from simulations 1.1, 1.6, 1.11 and 1.16 (*wr* ranging 2500 to 10000); (b) of all rockfalls from simulations 2.1, 2.4, 2.8, and 2.11 (*pd* ranging 75% to 125%).

Table 5.5: *k* (coefficient) and *ß* (exponent) values for the power law for each model simulation as shown in Figure 5.13.

Model simulation ID	***variable parameter***	***k value***	***ß* value**	**R^2 value**	**Max. rockfall size (m^3)**
1.1	*wr* = 2500	0.0003	-1.387	0.9509	0.37
1.6	*wr* = 5000	0.0003	-1.385	0.9476	0.39
1.11	*wr* = 7500	0.0003	-1.367	0.9512	0.40
1.16	*wr* = 10000	0.0003	-1.349	0.9589	0.32
2.1	*pd* = 75 %	0.000003	-2.103	0.8758	0.05
2.4	*pd* = 90 %	0.00003	-1.775	0.9161	0.11
2.8	*pd* = 110 %	0.0038	-0.932	0.9449	2.50
2.11	*pd* = 125 %	0.0186	-0.632	0.9347	6.85

5.4.2 Loss of structural support

The following set of models includes the structural support interaction rule (see Fig. 5.13). The notch threshold (s_n) and the amount of support lost (*sl*) are varied incrementally (Table 5.4). As *sn* is increased, the rockfall count and total failed area decrease (Fig. 5.14a). A sharp drop in both rockfall count and area is seen between a value of s_n = 0.1 m and 0.2 m, as this tends towards the 0.2 m failure depth used in the model. Beyond a threshold of 0.2 m, very little change in rockfall behaviour is observed. The range of rockfall sizes generated is largest in the model run with a threshold of s_n = 0.2 m (Fig. 5.15a). Conversely, the amount of support lost (*sl*) has a negligible effect on the model outputs (Fig. 5.14b; 5.15b).

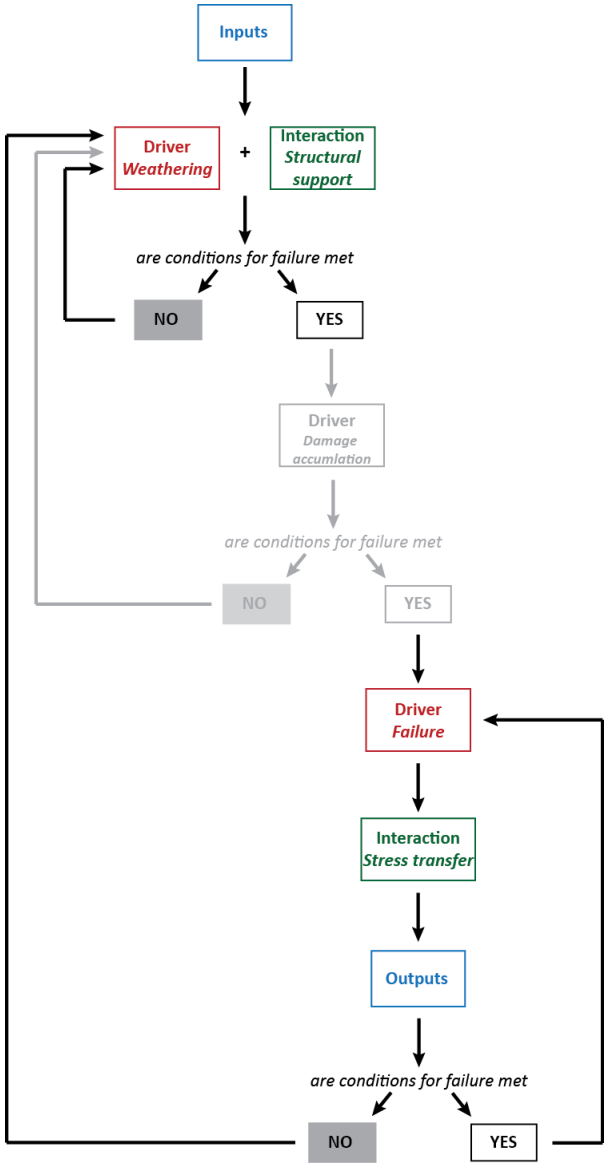

Figure 5.13: The model workflow used in simulations 3 – 16 (see Fig. 5.11 caption for details).

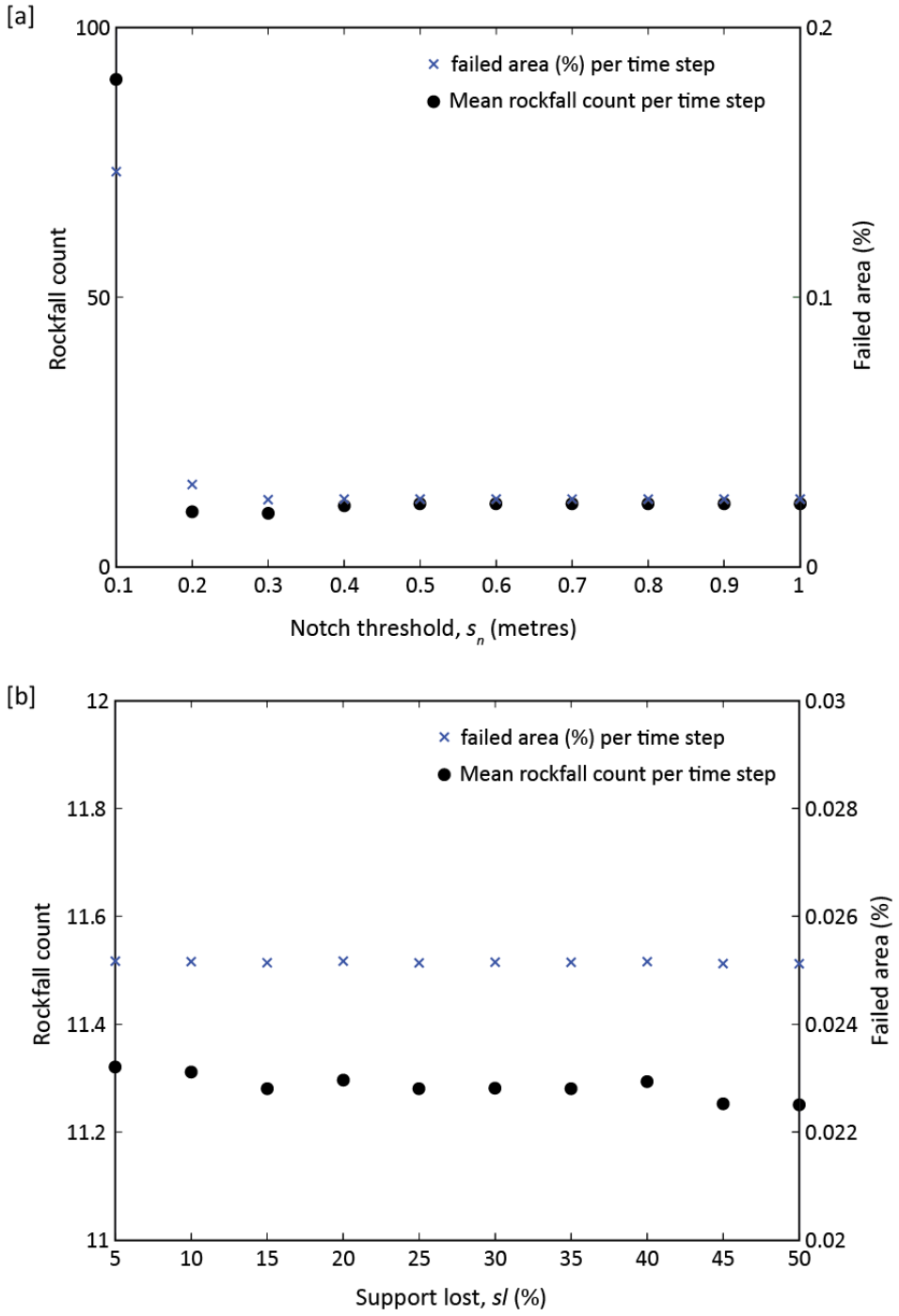

Figure 5.14: Mean rockfall count and failed area per time step for: (a) each model simulation run with a different notch threshold (s_n) in model simulations 3.1 – 3.10; and (b) each model simulation run with a different amount of support lost (*sl*) in model simulations 4.1 – 4.10.

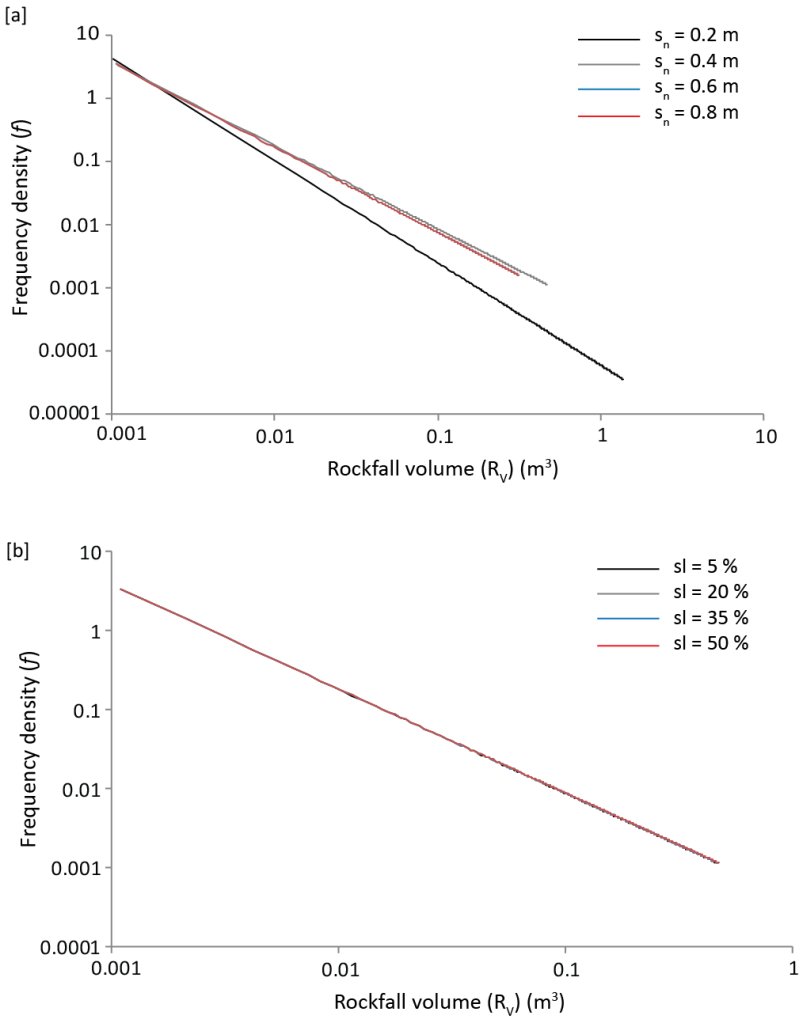

Figure 5.15: Power laws for rockfall volume magnitude-frequency plots: (a) of all rockfalls from model simulations 3.1 (s_n = 0.1 m); 3.4 (s_n = 0.4 m); 3.7 (s_n = 0.7 m); and 3.10 (s_n = 1 m); (b) of all rockfalls from model simulations 4.1 (sl = 5 %), 4.4 (sl = 20%), 4.7 (sl = 35%), and 4.10 (sl = 50 %).

Table 5.6: *k* (coefficient) and *ß* (exponent) values for the rockfall volume magnitude frequency power law (Fig. 5.15)

Model simulation ID	**variable parameter**	***k* value**	***ß* value**	**R^2 value**	**Max. rockfall size (m^3)**
3.1	s_n = 0.1 m	0.00006	-1.621	0.9848	1.38
3.4	s_n = 0.4 m	0.0004	-1.317	0.9668	0.47
3.7	s_n = 0.7 m	0.0003	-1.349	0.9589	0.32
3.10	s_n = 1 m	0.0003	-1.349	0.9589	0.32
4.1	sl = 5 %	0.0004	-1.317	0.9668	0.46
4.4	sl = 20 %	0.0004	-1.316	0.9669	0.46
4.7	sl = 35 %	0.0004	-1.316	0.9666	0.46
4.10	sl = 50 %	0.0005	-1.269	0.9689	0.46

5.4.3 Model validation/verification:

Two steps have been taken to verify and then validate the model outputs. Firstly, the impact of the initial topographic conditions in the model have been tested and compared to the response to parameter changes within the model. Secondly, to validate the model, the outputs from simulation 4.10 have been compared to the field data using the criteria outlined in Table 5.3. Simulation 4.10 was used as a representation of the average conditions of the model setup.

5.4.3.1 Initial conditions

To verify the impact of the initial topography on the model behaviour as compared to the impact of the *wr* and *pd*, outputs were compared for simulations run with different initial surfaces. 10 randomly generated grids of topographic values (*z*), ranging from z = 0 to 0.5, were used to sample the sensitivity of the initial conditions. Parameters from simulation 2.6 (Table 5.4) were used as the initial boundary conditions of model. The time series of rockfall occurrence resulting from each of these simulations were similar (Fig. 5.16). There are small differences in the peak values of rockfall count per time step (t_n), but the overall temporal pattern is very similar, with peaks of rockfall occurrence at t_n = ~4,500 and 7,750 in each simulation.

Comparing the results with a variable weathering rate (*wr*) and stress transfer (*pd*), different initial topography results in a much smaller range of both rockfall count and failed area outputs between runs, as shown in Table 5.7. Conversely, the variation in failure size distributions between the simulations is larger than produced from models with different *wr*, as shown by the beta values in Table 5.7. The variation in failure size distribution is much smaller than that produced from models run with different *pd* values. This result is unsurprising as changing the *wr* has been shown to alter the overall erosion (Fig. 5.11), but has a negligible impact on the distribution of rockfall sizes (Fig. 5.12). Together these results confirm, as so far as is possible, that the variations in model behaviour as a result of changes to the model process parameters, are real, exceed inherent variability in the model, and are more significant than any potential impact of the initial topographic surface used.

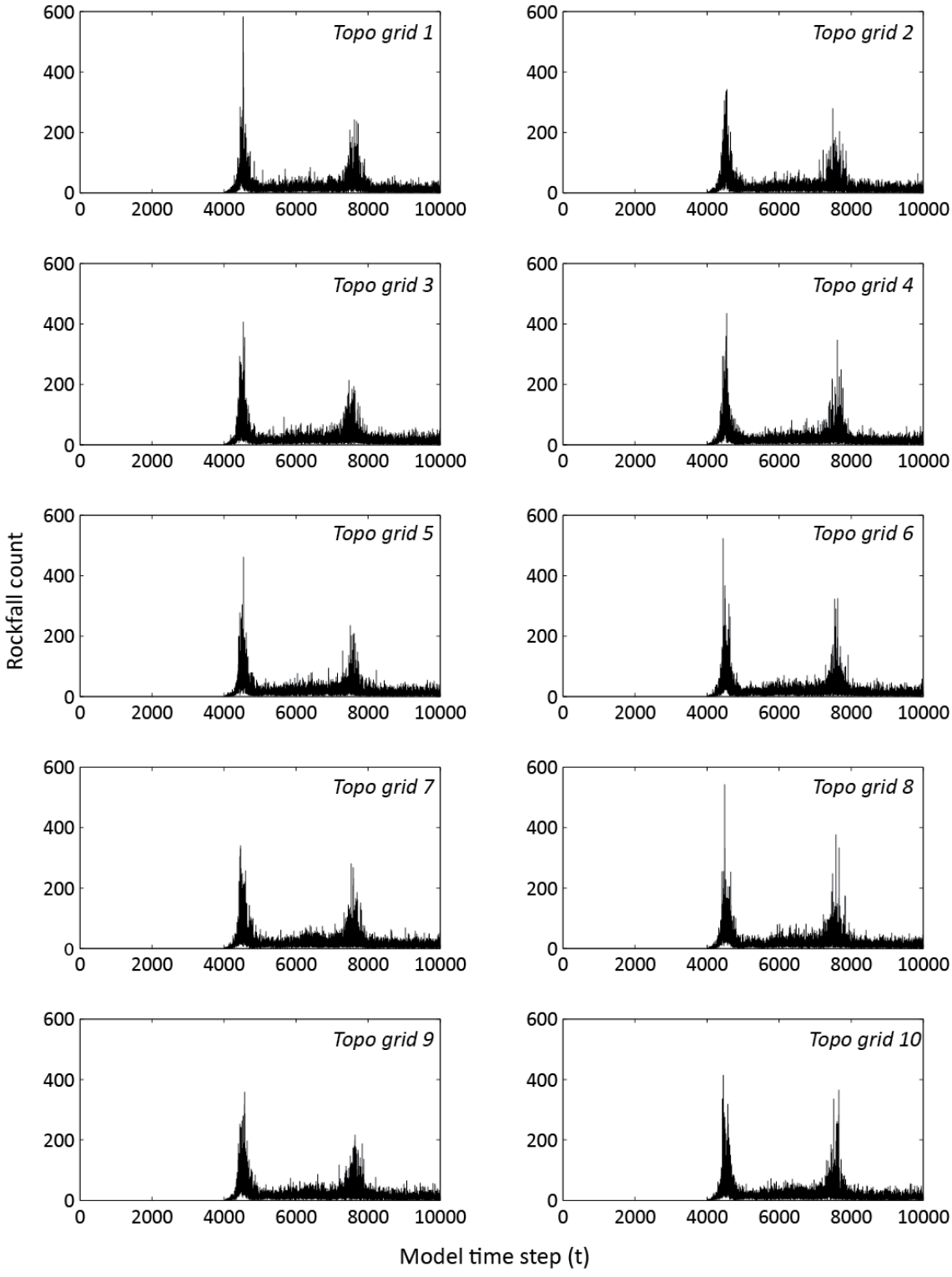

Figure 5.16: Time series of rockfall count for each simulation run with a different randomly generated topographic grid as initial conditions. Each grid was generated with cell elevations uniformly randomly distributed within the range $z = 0 – 0.5$.

Table 5.7: The range of outputs values generated by varying different model parameters: *z* (based on simulation 2.6); *wr* (simulations 1.1 – 1.16) and *pd* (simulation 2.1 – 2.11). The range of values presented are given in the units of the outputs values.

Output values	**Topographic grid (*z*)**	**Weathering rate (*wr*)**	**Stress transfer (*pd*)**
Rockfall count (number per t_n)	0.390	25.822	8.184
Failed area (% per t_n)	0.0005	0.059	0.059
Magnitude-frequency power law fits ($f = k*R_V^{ß}$)			
k-value	0.0001	0	0.019
ß-value	0.121	0.038	1.471
R^2-value	0.013	0.011	0.069

5.4.3.2 Distribution and range of failure sizes

The frequency distribution of rockfall volumes displays a negative relationship between rockfall volume and frequency density, similar to the field data, however the slope of the power-law fit is much steeper in the modelling results. This indicates a more significant contribution of smaller rockfalls to volume lost (Fig. 5.17), as reflected in the *ß*-value = -1.269, which exceeds the range defined in Table 5.3. An increasingly negative *ß*-value suggests that the processes generating rockfall are currently not capable of triggering larger rockfalls, and for these larger events to make a more significant contribution to erosion. This conclusion is supported by the recurrence interval for rockfalls of different sizes (Fig. 5.18), which shows that the range of rockfall sizes generated by the model is an order of magnitude lower than the field data over a comparable spatial extent of rock face (Fig. 5.18c).

The recurrence interval for rockfalls of different sizes displays a positive distribution with a power law fit exponent of *ß* = -0.7738, which is similar to a recurrence interval plot generated from the field data (*ß* = -0.7347) (Fig. 5.18c). The y-axis scale differs by an order of magnitude, however this can be resolved by resampling the model results to a resolution of 30 time steps or approximately one month (Fig. 5.18b) to allow better comparison with the monthly resolution field data. This implies that the temporal behaviour of the model is appropriate, and that the model time step can be considered as one day of real time.

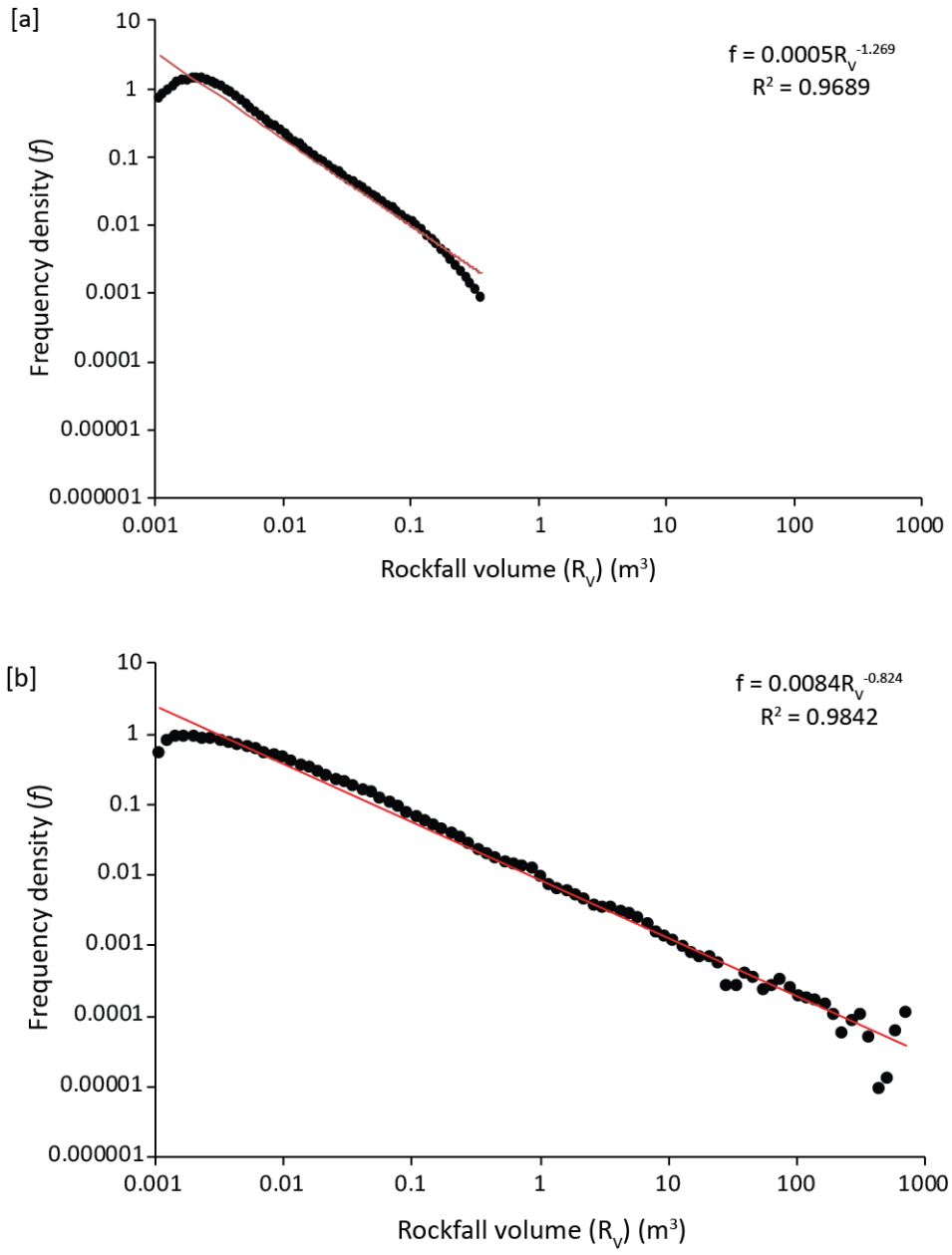

Figure 5.17: Magnitude-frequency of rockfall volume for: (a) all rockfalls in model simulation 4.10 (*ß*-value = -1.269); and, (b) all rockfalls observed during 2-year dataset at Boulby (*ß*-value = -0.824).

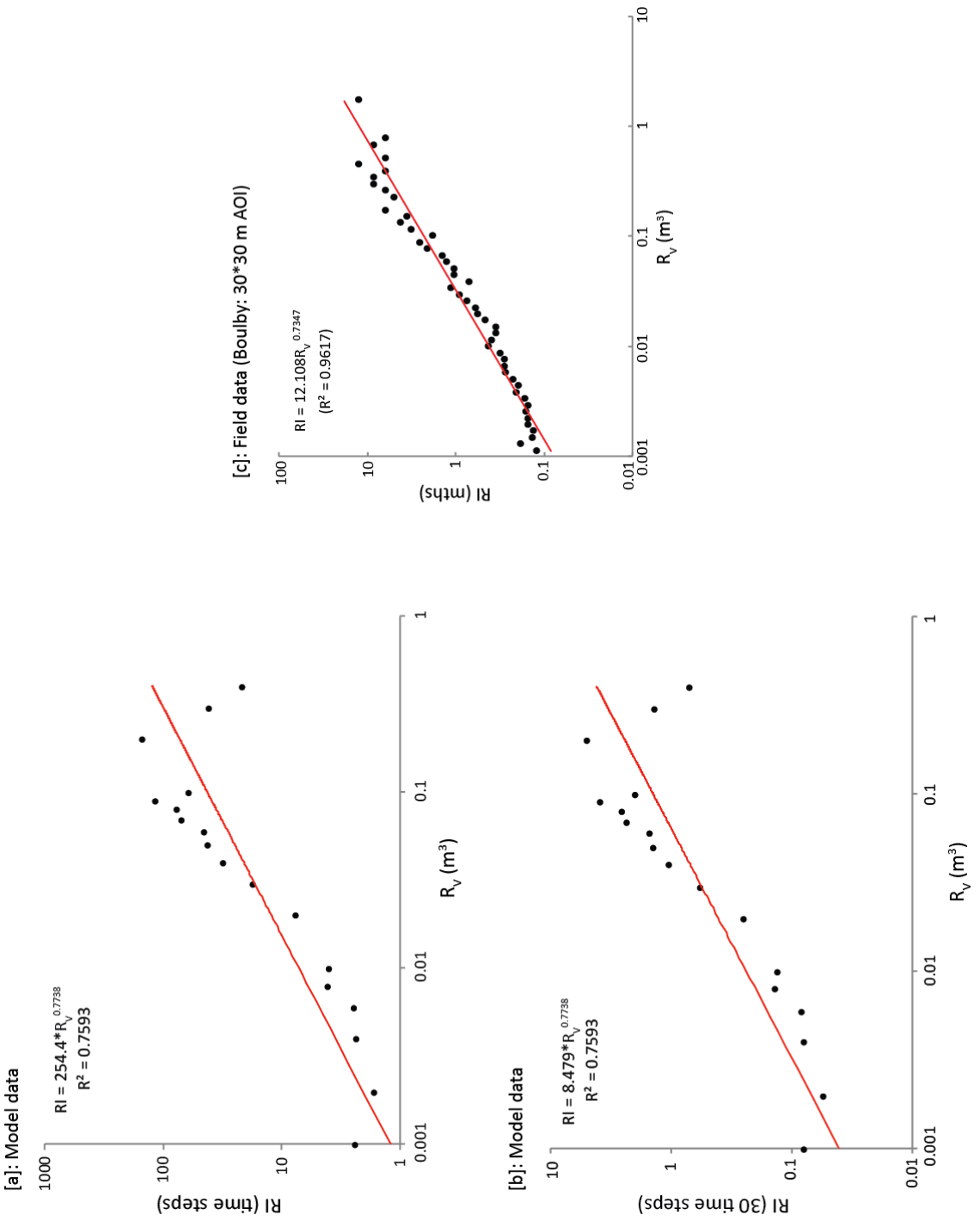

Figure 5.18: Recurrence intervals for different rockfall volumes (m^3) from model data (a & b) compared to rockfalls from the field data (c): (a) the recurrence interval in time steps for all rockfalls that occurred in simulation 4.10; (b) the recurrence interval per 30 time steps for all rockfalls in simulation 4.10, where one time step is assumed to represent one day; and (c) where the recurrence interval is in months for all rockfalls within a 30 x 30 m area of interest at Boulby, between June 2012 and June 2014 (Appendix 1.6)

5.4.3.3 Erosion rate and spatial distribution of rockfalls

The spatially averaged erosion rate for simulation 4.10 is 0.05 mm t_n^{-1}. This is within the range of suitable erosion rates specified (Table 5.3) and therefore further validates the model time step of t_n = 1 day. The failed area for simulation 4.10 averaged 0.025% per time step. This is within the range of suitable values specified in Table 5.3. Looking at the results from previous simulations (Fig. 5.11 & 5.14) indicates that in all cases the failed area is within the suitable range as outlined in Table 5.3.

Outputs from the rockfall model display a variable distribution of failed area when plotted against elevation for different time periods (Fig. 5.19a). Plots of rockfalls across the slope face (Fig. 5.19b) show that rockfall grow and evolve through time. Both plots imply that the concentration and location of erosion on the slope changes through time. The average slope profile remains near vertical (Fig. 5.20), at an angle of 0.03° from vertical, where positive angles are overhangs, and negative angles are the crest lying back. Again, these results satisfy conditions defined in Table 5.3, and suggest that the rockfall driven erosion generated by the model is spatially variable through time.

The model validation presented here demonstrates that the rockfall model performs well with respect to three of the four criteria set: erosion rate, surface area failed and spatial distribution of failures, and so the rockfalls generated by the model are within reasonable bounds determined from the field data. The rockfall model has not achieved the validation against the distribution and range of failure sizes, and requires further refinement to trigger a full range of failure sizes, that make a significant contribution to erosion. This is an issue of process, and cell interactions within the model and is addressed in section 5.5.2.

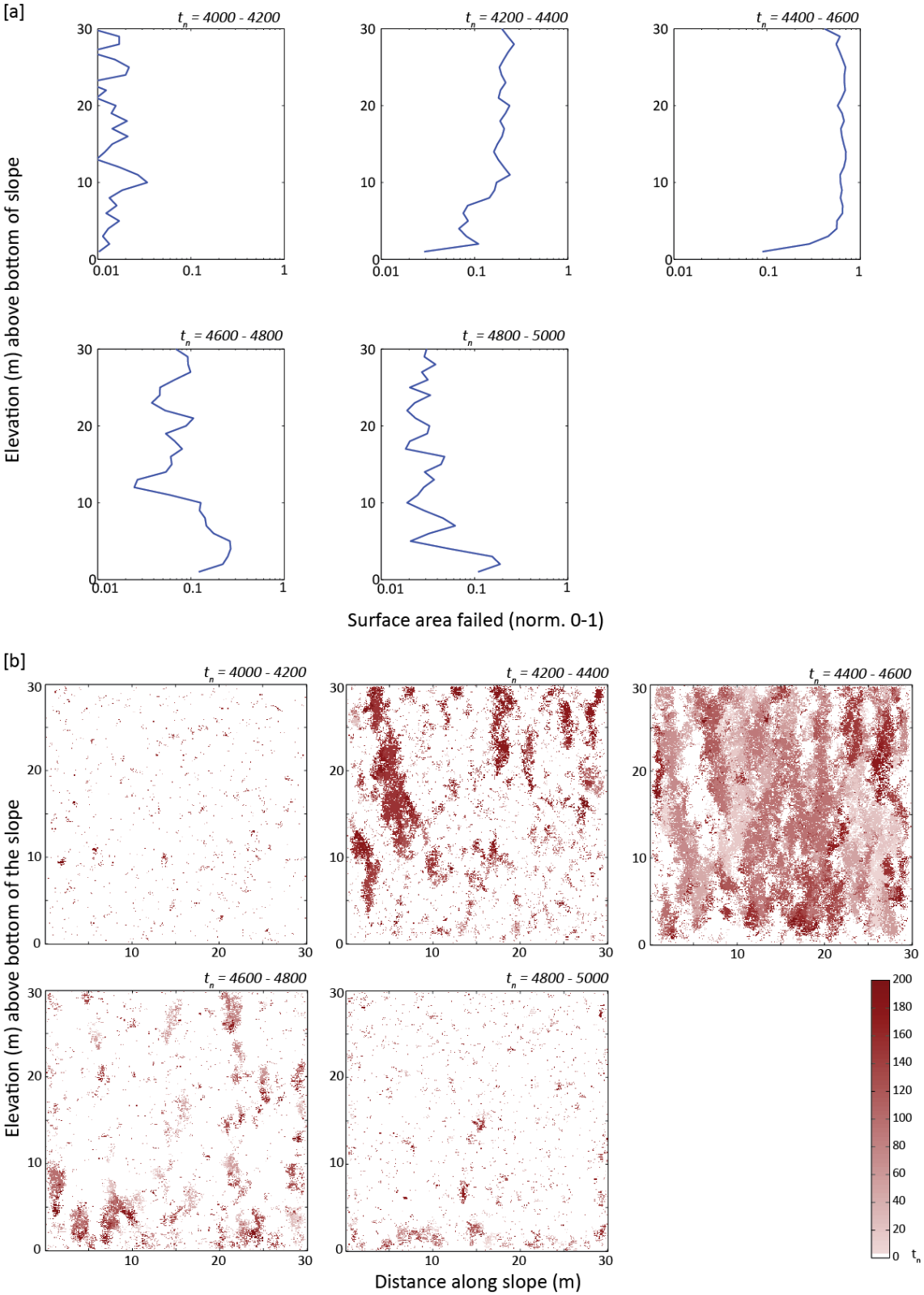

Figure 5.19: Variations in surface failures for different time periods (200 t_n each) in simulation 4.10: (a) surface area failed (normalised so that 1 = 100%) against elevation (m); (b) for the same time periods (as denoted above each plot) visual plots of the failures at the slope face coloured by the time step in which they occurred.

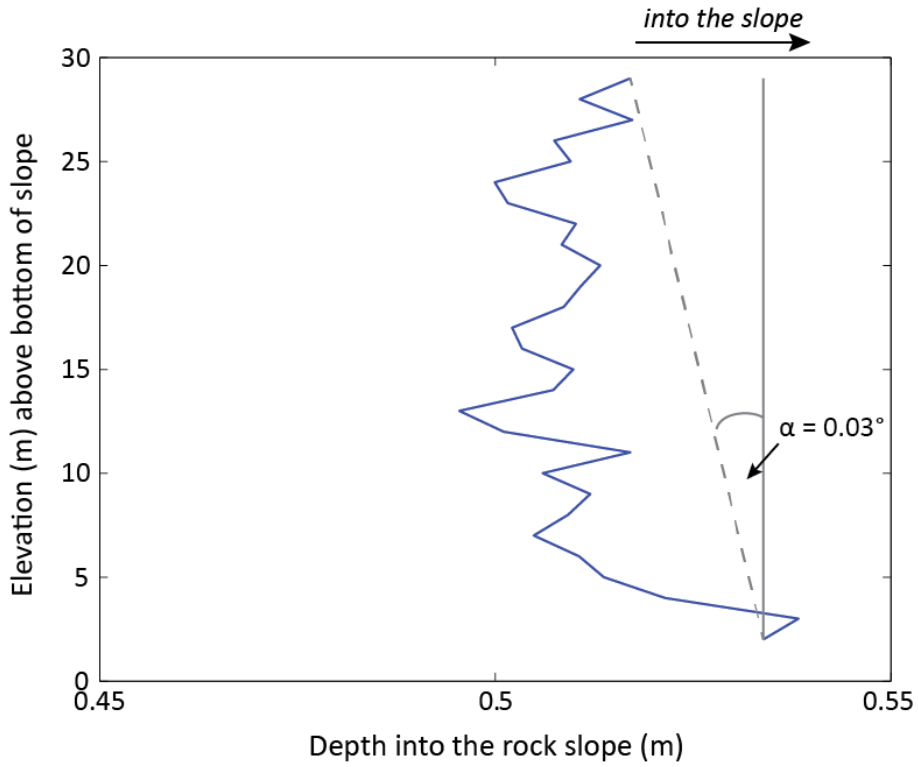

Figure 5.20: Average profile of the rock face at the end of model simulation 4.10 (t_n = 10,000). The profile is determined by taking the mean elevation across the slope face for every row of cells and this has then been smoothed to a 1 m resolution. The final model slope angle is 0.03°.

5.4.4 Sensitivity Analysis

The process of sensitivity analysis serves to define the sensitivity of the model output to changes in input parameters (Mulligan and Wainwright, 2004). In particular, it allows the interaction between parameters and therefore between processes in the model to be better understood. For the rockfall model both single parameter and multi-parameter sensitivity analysis was performed.

5.4.4.1 Single parameter sensitivity analysis

Using the model workflow shown in Figure 5.13, each parameter was varied incrementally around a base value, with all other parameters remaining unaltered at their respective base values (see Table 5.8). For each parameter, the proportional change in the outputs (rockfall count, failed area, largest rockfall size, and distribution of failure sizes) was recorded per percentage change in the input parameter (%). This allows the model response to each

parameter to be compared, and an order of magnitude of parameter sensitivity to be established, as the relative importance of each parameter is demonstrated.

Each of the outputs (Fig. 5.21a-c; 5.22) implies that the model is more sensitive to the *wr* and *pd* parameters, compared to the s_n and *sl*. The rockfall count is most sensitive to *wr*, where a positive exponential relationship is found (Fig. 5.21a), whereas the relationship between rockfall count and *pd* is variable (Fig. 5.21a). The failed area is observed to be more sensitive to parameter changes than the rockfall count (Fig. 5.21b-c). The total failed area (Fig. 5.21b) and the size of the largest rockfall (Fig. 5.21c) are most sensitive to changes in *pd*, where both outputs demonstrate an exponential increase as *pd* increases. Overall, the sensitivity of the model to *pd* is an order of magnitude greater than the sensitivity to other parameters, when rockfall area is considered. The total failed area increases with increases in *wr*, however the size of the largest rockfall is not significantly altered. This demonstrates that the rockfall size is most sensitive to *pd*, whilst the overall erosion in the model is driven by both *pd* and *wr*. The model sensitivity to s_n shown in Figure 5.21c, illustrating the effect of setting s_n much lower than the range in *z*.

The change in overall failure size distribution has been shown by plotting the rockfall volume magnitude frequency power law *ß*-value (Equation 5.6) against the r^2-value of the fit (Fig. 5.22). Again, the model displays the most sensitivity to *pd*, whereby an increase in this variable results in a higher *ß*-value, indicating a more significant contribution of larger failures to net erosion (Fig. 5.22b). A similar relationship is shown with changes to *wr* (Fig. 5.22a), however the increase in the *ß*-value is much smaller compared to Fig. 5.22b. The initial drop in *ß*-values as s_n is increased (Fig. 5.22c) indicate that larger failures are produced when s_n is close to the model resolution. Beyond a threshold of 0.5 m (-16% input change) there is no change in the *ß*-value or r^2-value outputs. Likewise, changing the amount of support lost has no impact on the failure size distribution generated by the model (Fig. 5.22d). In all cases the r^2-values demonstrate a good fit of the power law to the data, with the values ranging from $r^2 = 0.76 – 0.99$.

Table 5.8: Input conditions and model parameters for single parameter sensitivity analysis. The *GSI* (rock strength) and *wi* (weathering intensity) values were applied uniformly across the model grid; the topography (*z*) was generated from a uniform random distribution (URD) of values between 0 and 0.5 m. Where the range of model parameter values are given in the form x:a:y, x is the lowest value used; y is the highest value used; and a is the increment that the value is increased by for each model simulation. Notations are given in Table 5.2.

Model simulation IDs	**Inputs**			***wr* (time steps)**	***pd* (%)**	***s_n* (m)**	***sl* (%)**	**Rockfall depth (m)**
	GSI	***z***	***wi***					
5.1 – 5.16	50	URD: 0 – 0.5	1	2500: 500: 10000	100	0.6	30	0.2
6.1 – 6.13	50	URD: 0 – 0.5	1	6250	40: 10: 160	0.6	30	0.2
7.1 – 7.17	50	URD: 0 – 0.5	1	6250	100	0.2: 0.05: 1	30	0.2
8.1 – 8.17	50	URD: 0 – 0.5	1	6250	100	0.6	10: 2.5: 50	0.2

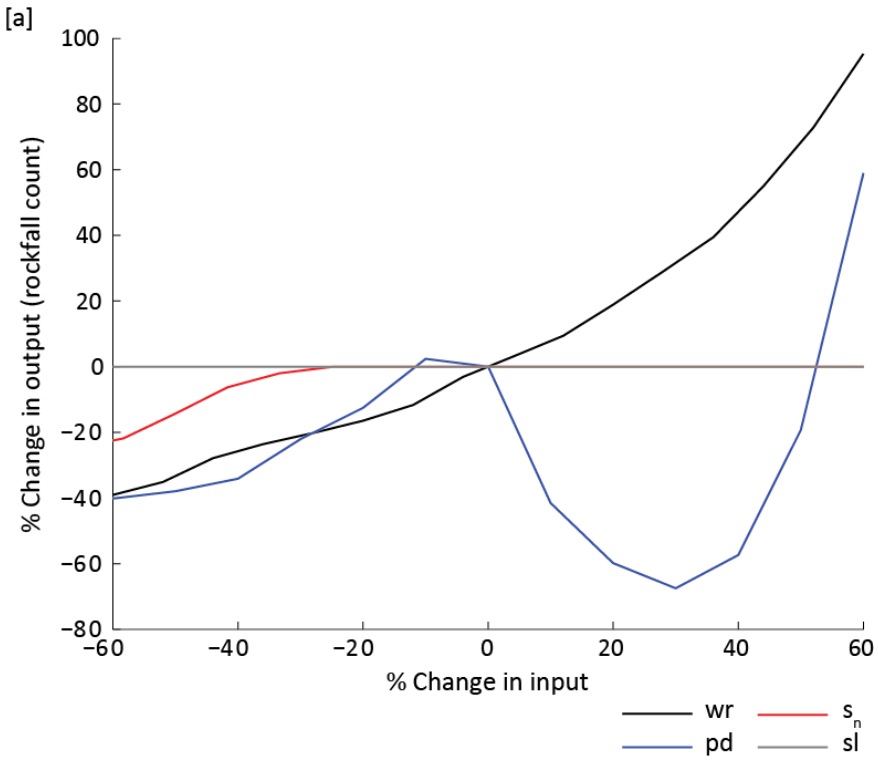

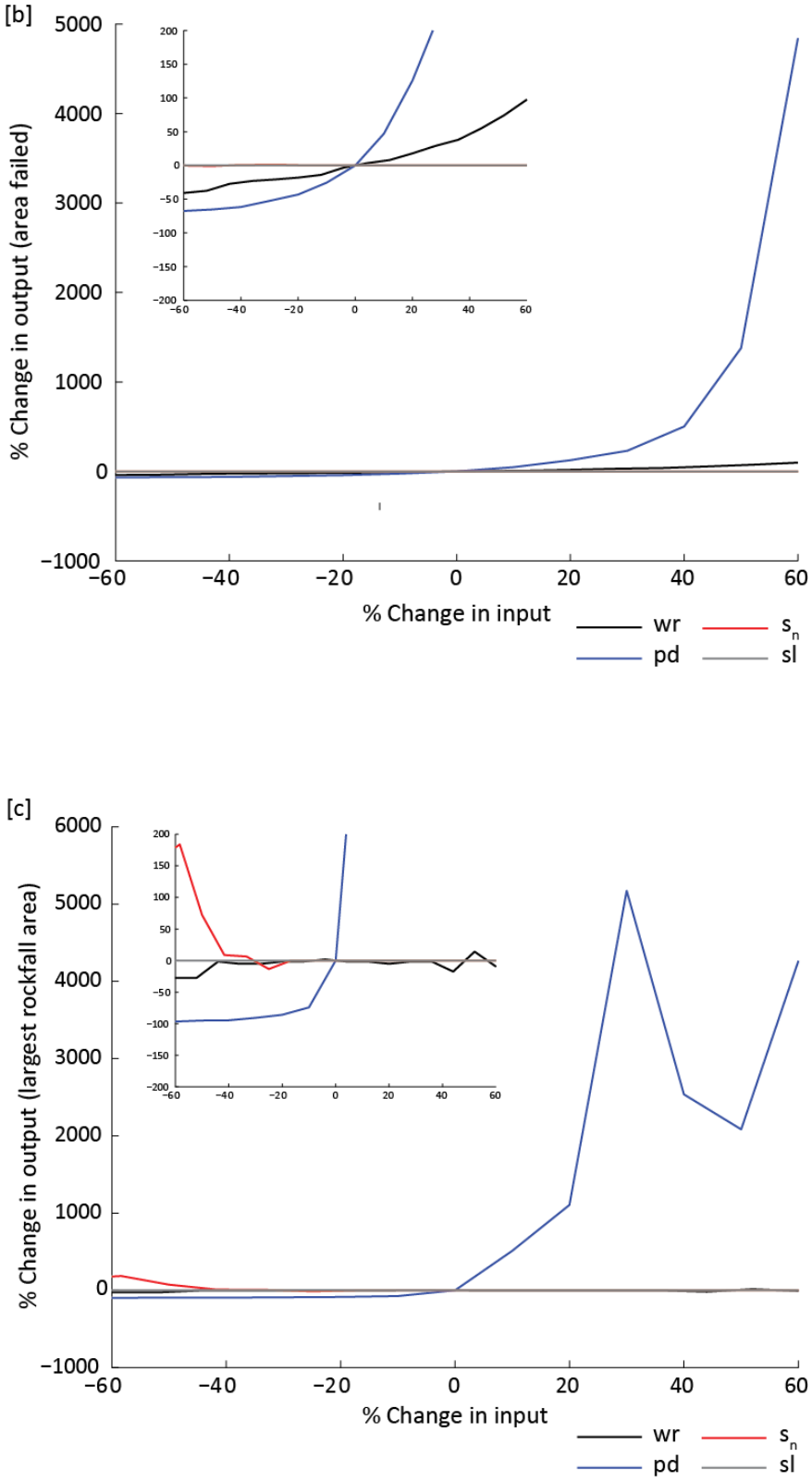

Figure 5.21: Percentage change of different model outputs: (a) rockfall count; (b) total failed area; (c) largest rockfall size, as each of the following input values are changed: *wr*, *pd*, s_n and *sl*. The initial values (0 % change) used for each of the inputs were: *wr* = 6250; *pd* = 100 %; s_n = 0.6 m; *sl* = 30 %. In plots (b) and (c) an insert shows the data for a smaller range of output change so that the detail can be seen in the results of changing *wr,* s_n and *sl*, which did not alter the model outputs as significantly as *pd*.

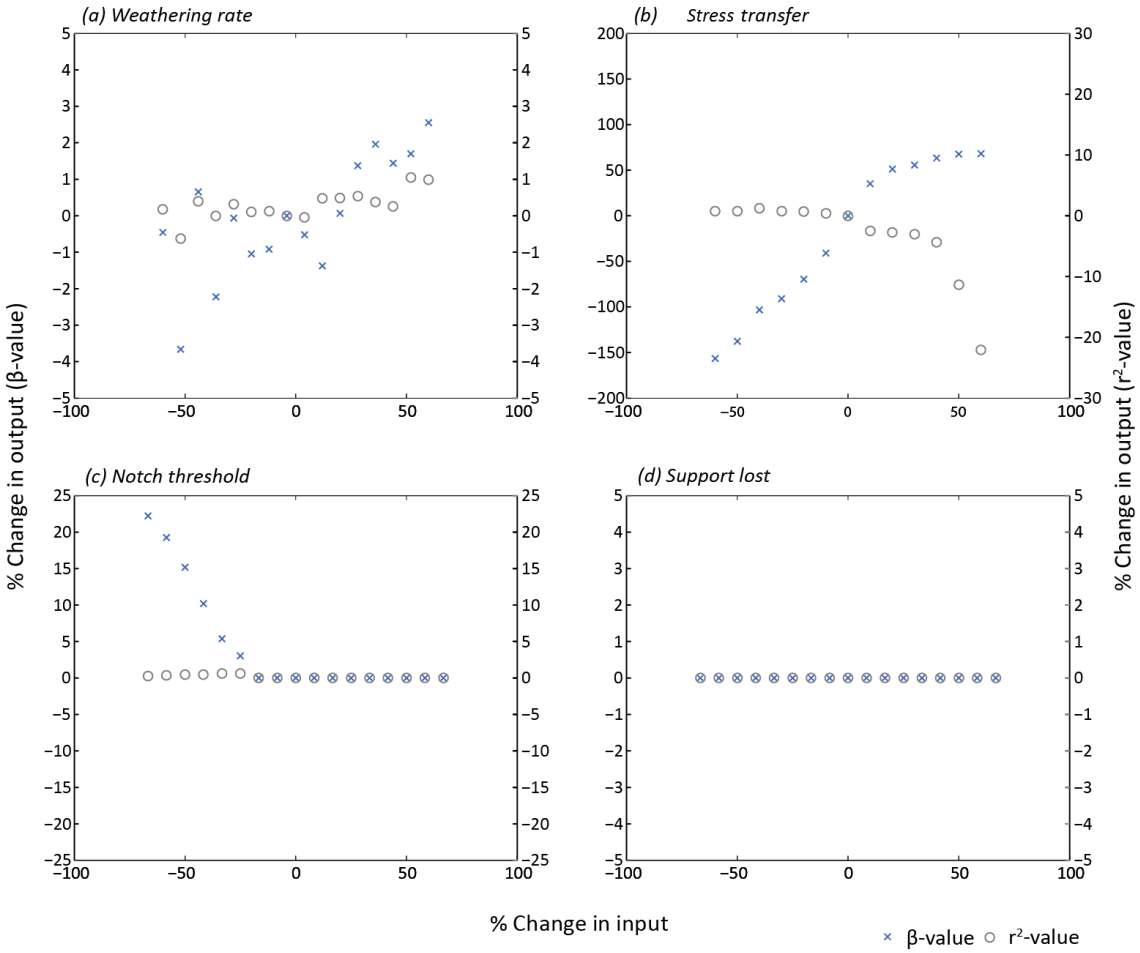

Figure 5.22: Percentage change of model outputs (*ß*-value and r^2-value) from magnitude-frequency power law fits of the form: $f = k*R_V^{ß}$, as each of the following input values are changed: (a) *wr*; (b) *pd*; (c) s_n; and (d) *sl*.

5.4.4.2 Two-parameter sensitivity analysis

Weathering and stress transfer, both resulting in damage accumulation, are the two key parameters driving the overall nature of rockfalls and behaviour of the model. These parameters have been compared as a representation of the model sensitivity to external and internal processes that are driving the rock mass towards failure. Subsequently, responses to variable notch threshold (s_n) and support lost (*sl*) were compared to examine the sensitivity of the model to the dependent parameters used in the structural support function. The model workflow in Figure 5.13 was used, and details of the values used in each model run are given in Table 5.9.

Changing *wr* and *pd* simultaneously (Fig. 5.23) reaffirms previous observations: *pd* changes the behaviour of the model, notably the failed area and distribution of rockfall sizes, and *wr* sets the overall rate of erosion. The plots in Figure 5.23 illustrate this as the curves that respond to

the *pd* function remain identical, but the magnitude and range of rockfall count and failed area both reduce as *wr* slows.

The impact of the structural support function (*ss*) on rockfall occurrence appears most sensitive to the notch depth threshold (s_n), which generates small changes in rockfall count and failed area for all values of *sl* (Fig. 5.24). Conversely, variations in *sl*, which represent the magnitude of stress transfer and damage accumulation when s_n is exceeded, result in negligible changes to the rockfall model outputs for all values of s_n (Fig. 5.24). This suggests that the size of the notch is more important than how long it remains a notch, an idea further explored in Chapter 6.

Table 5.9: Input conditions and model parameters for the model simulations run for two-parameter sensitivity analysis: *wr* and *pd* were varied simultaneously, and s_n and *sl* were also varied simultaneously.

Model simulation IDs	**Inputs**			***wr (time steps)***	***pd (%)***	***s_n (m)***	***sl* (%)**	**Rockfall depth (m)**
	GSI	***z***	***wi***					
9.1 – 9.16	50	URD: 0 – 0.5	1	2500	75: 5: 125	0.4	5	0.2
10.1 – 10.16	50	URD: 0 – 0.5	1	5000	75: 5: 125	0.4	5	0.2
11.1 – 11.16	50	URD: 0 – 0.5	1	7500	75: 5: 125	0.4	5	0.2
12.1 – 12.16	50	URD: 0 – 0.5	1	10000	75: 5: 125	0.4	5	0.2
13.1 – 13.10	50	URD: 0 – 0.5	1	10000	100	0.2	5: 5: 50	0.2
14.1 – 14.10	50	URD: 0 – 0.5	1	10000	100	0.4	5: 5: 50	0.2
15.1 – 15.10	50	URD: 0 – 0.5	1	10000	100	0.6	5: 5: 50	0.2
16.1 – 16.10	50	URD: 0 – 0.5	1	10000	100	0.8	5: 5: 50	0.2

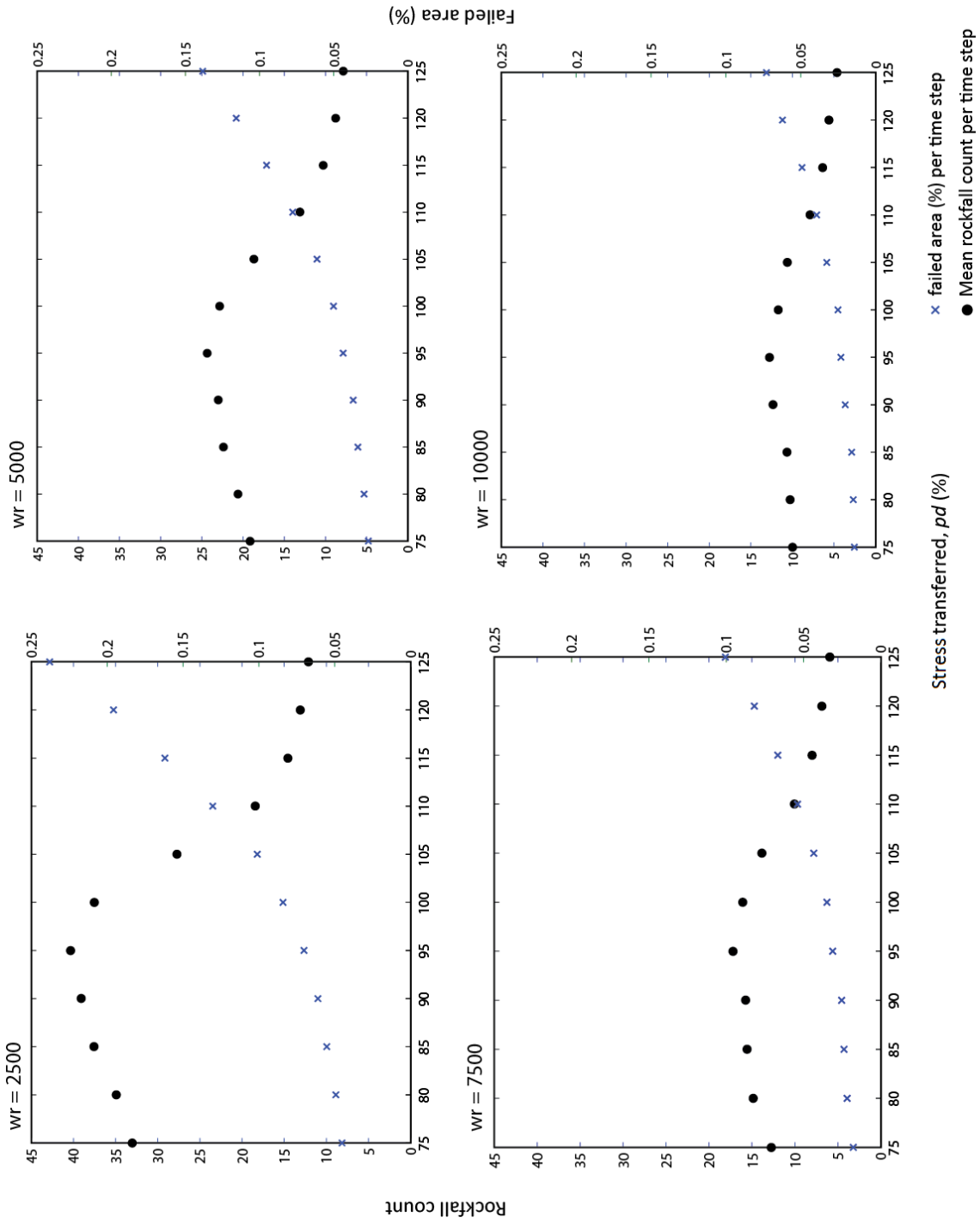

Figure 5.23: Mean rockfall count and mean failed area per time step for model simulations run with different *wr* and *pd* values for model simulations 9 – 12. Each plot shows the results for different *pd* values when run at a single *wr* value, as described above each plot.

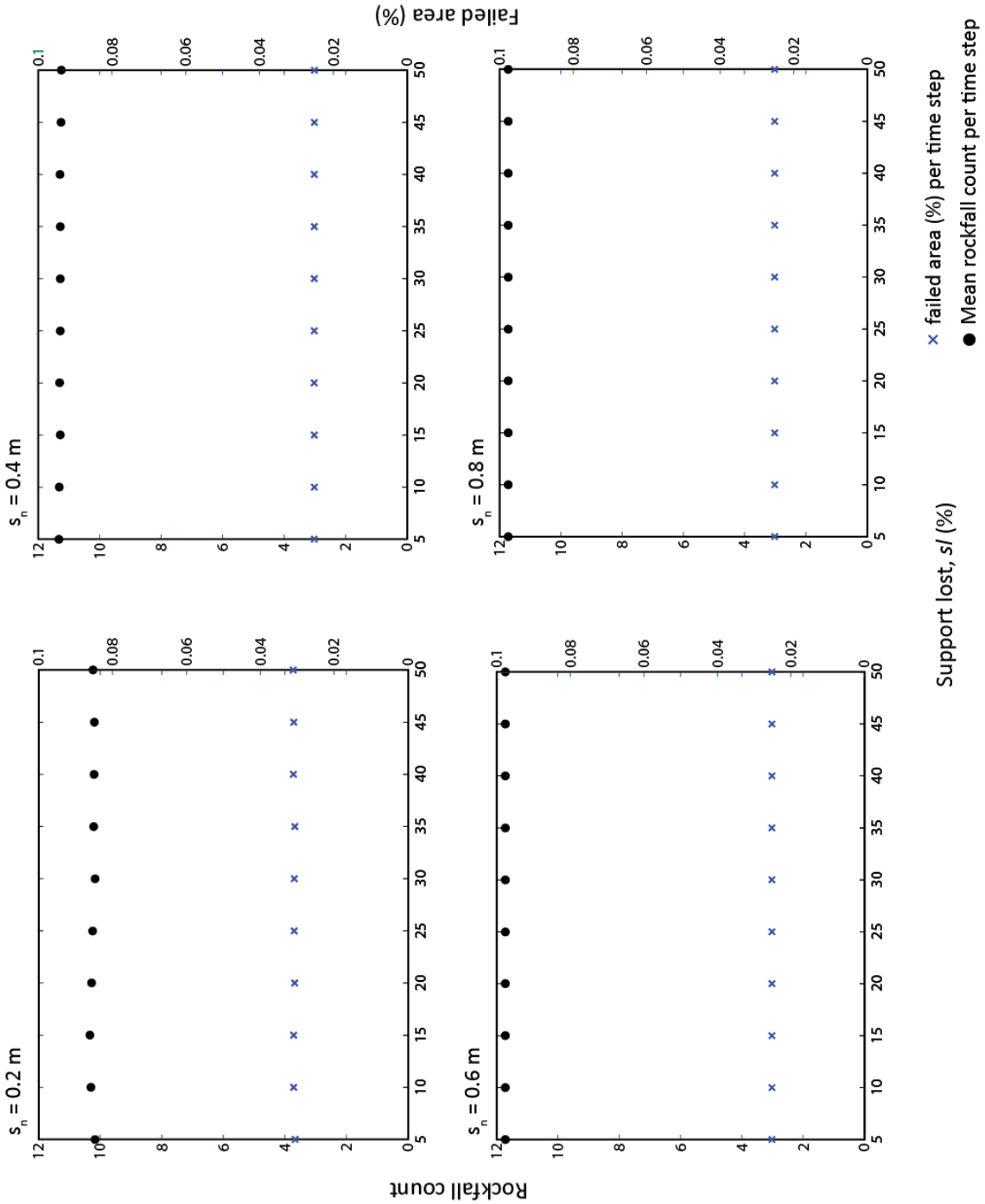

Figure 5.24: Mean rockfall count and mean failed area per time step for model simulations run with different notch thresholds (s_n) and support lost (sl) (model simulations 13 – 16): each plot shows the results for different amounts of support lost when run with a single notch threshold, as indicated above each plot.

5.5 Model development 2: Application of time-dependent damage accumulation

The second stage of model development incorporates the time-dependent damage accumulation function (Fig. 5.25). In response to the results of the model validation, a range of different approaches are explored to identify ways to increase the range of rockfall sizes generated by the model, to mirror observations from the field.

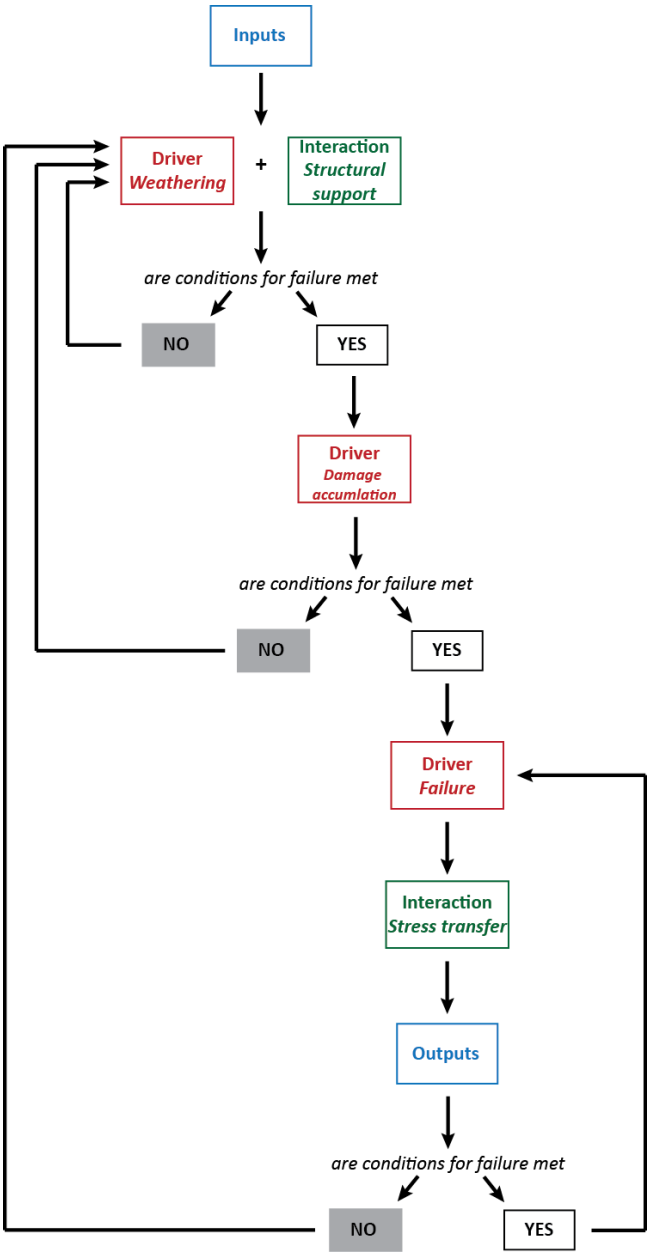

Figure 5.25: The model workflow used in simulations 17 - 21. Where conditional statements are shown, this applies to all cells. For example, if any cell meets conditions then the model moves on to the next stage, and once all cells no longer meet the condition then the model moves to the next time step.

5.5.1 Time-dependent damage accumulation

The damage accumulation function was introduced to the rockfall model and both the threshold for failure onset (*fo, %*) and the time from onset to final failure (*tf*) were varied. Details of the model simulations using this function are given in Table 5.10. The rockfall count and failed area for each simulation are presented in Figure 5.26, where the red markers indicate the model results when the damage accumulation function is not used. As *fo* and *tf* increase, the rockfall count and failed area per time step both decrease (Fig. 5.26). However in all cases, using the time-dependent damage accumulation function results in a small increase to the area of failure, as compared to the model outputs without this function. Although the failed area is observed to decrease with increasing *fo* and *tf* values, the distribution of rockfall sizes indicates a more uniform distribution of rockfall sizes as these parameters increase (Fig. 5.27). The plots in Figure 5.27 also show that including the time-dependent damage accumulation function results in a lower *ß*-exponent for the rockfall volume magnitude frequency, suggesting that this function enables contiguous individual cells near the point of failure to fail as a single larger rockfall. At all values of *fo* and *tf* the model outputs are within the bounds set in Table 5.3.

Table 5.10: Input conditions and model parameters for the model simulations used in the application of time-dependent damage accumulation. Where rockfall depth is given as an equation, *V* = volume and *A* = area. For all simulations *wr* and *ss* parameters were kept constant as follows: *wr* = 10,000; s_n = 0.4 m; *sl* = 50%.

Model simulation IDs	**Inputs**			***fo (%)***	***tf (time steps)***	***pd (%)***	***e (cells)***	**Rockfall depth (m)**
	GSI	***z***	***wi***					
17.1 – 17.11	50	URD: 0 – 0.5	1	85: 1: 95	2	100	3	0.2
18.1 – 18.10	50	URD: 0 – 0.5	1	80	1: 1: 10	100	3	0.2
19.1 – 19.4	50	URD: 0 – 0.5	1	85	2	125: 25: 200	3	0.2
20.1 – 20.5	50	URD: 0 – 0.5	1	85	2	100	1: 1: 5	0.2
21	50	URD: 0 – 0.5	1	85	2	100	3	$V = 0.22A^{1.105}$

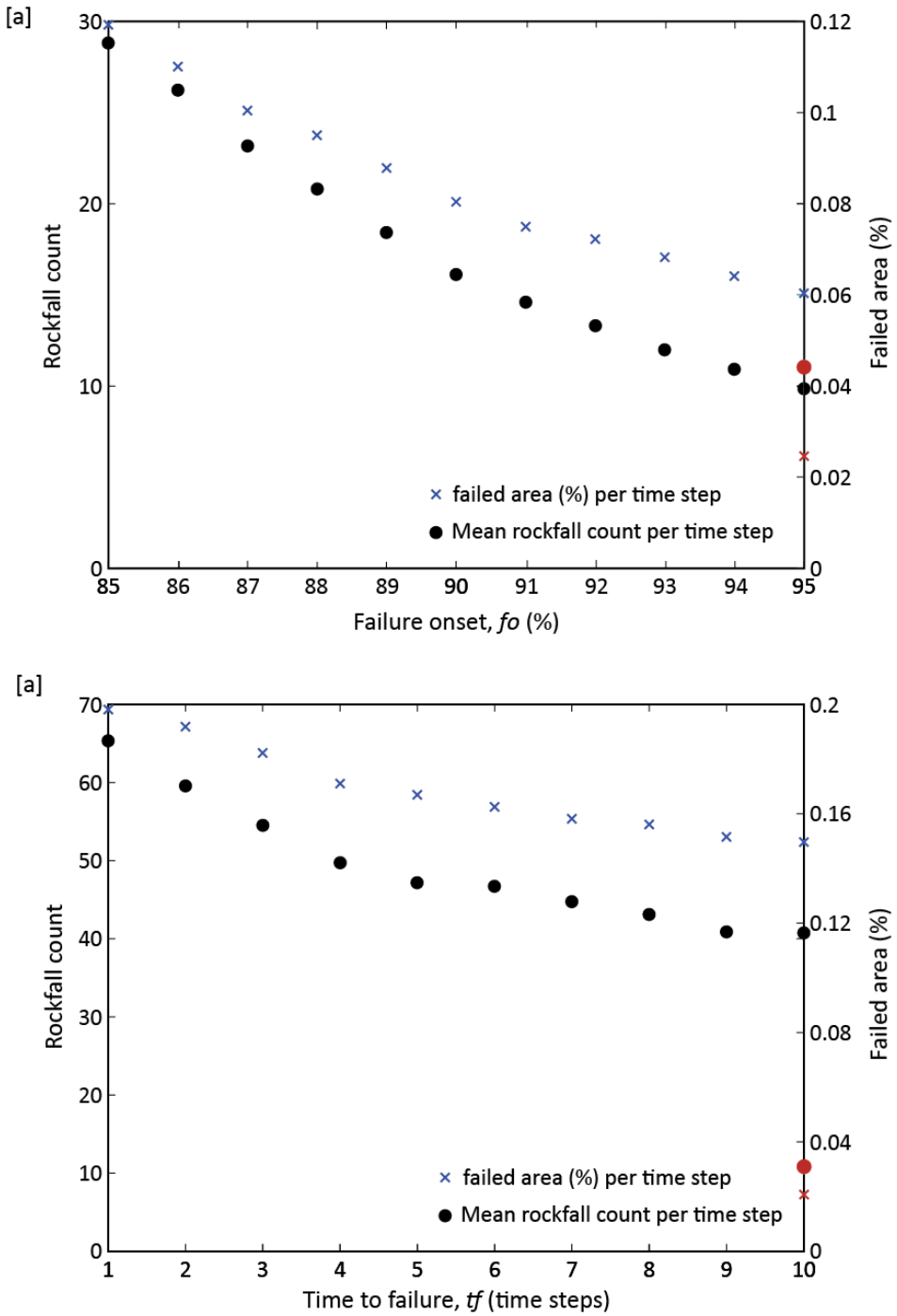

Figure 5.26: Mean rockfall count and failed area per time step for: (a) each model simulation run with a different *fo* value for model simulations 17.1 – 17.11; and (b) each model simulation run with a different *tf* value for model simulations 18.1 – 18.10. The red symbols indicate the mean rockfall count and failed area per time step for model simulation 4.10, where the model is run without the time-dependent damage accumulation function.

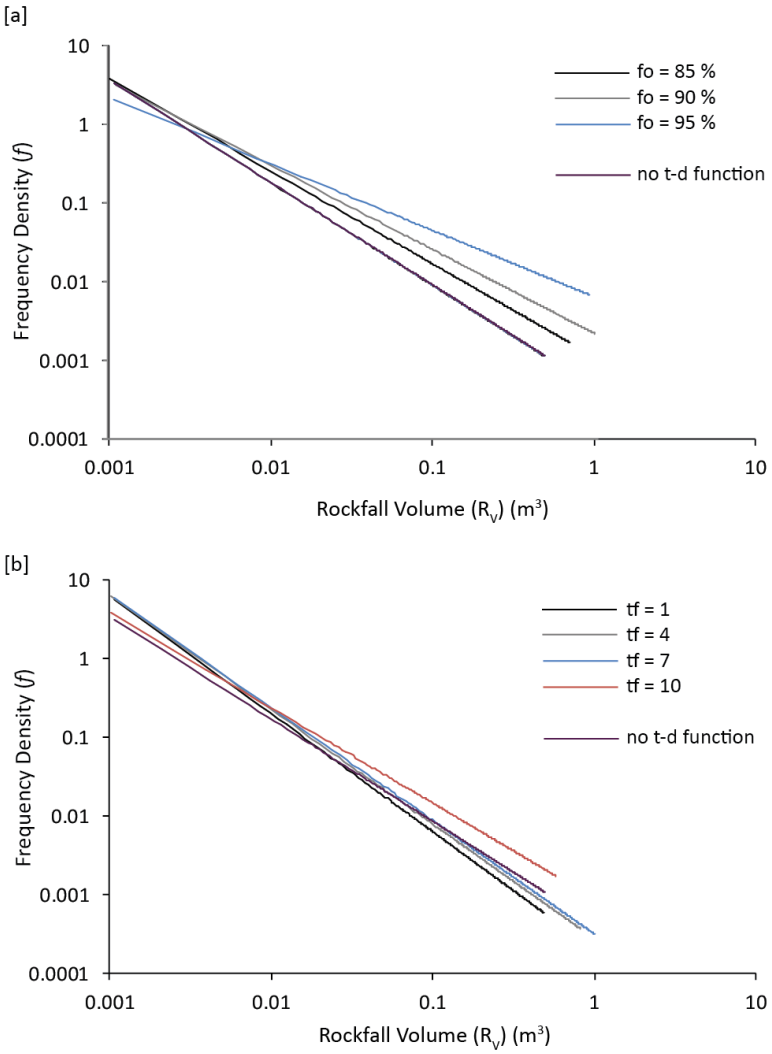

Figure 5.27: Power law fits for rockfall volume magnitude-frequency: (a) rockfalls from model simulations 17.1, 17.6 and 17.11 (*fo* = 85% - 95%); and (b) rockfalls from model simulations 18.1, 18.4, 18.7 and 18.10 (*tf* = 1 - 10). On each plot the power law fit for simulation 4.10 is shown (purple line), e.g. the simulation run with the same conditions but without the time-dependent damage accumulation.

Table 5.11: *k* (coefficient) and *ß* (exponent) values for the power law of the form: $f = k*R_V^{ß}$, which describes the power law fits as shown in Figures 5.27.

Model simulation ID	**variable parameter**	***k* value**	***ß* value**	**R^2 value**	**Max. rockfall size (m^3)**
17.1	*fo* = 85 %	0.0011	-1.179	0.8627	0.71
17.6	*fo* = 90 %	0.0022	-1.067	0.8796	1.00
17.11	*fo* = 95 %	0.0065	-0.844	0.9071	0.93
18.1	*tf* = 1	0.0002	-1.499	0.88	0.49
18.4	*tf* = 4	0.0003	-1.453	0.8683	0.82
18.7	*tf* = 7	0.0003	-1.44	0.8853	1.01
18.10	*tf* = 10	0.0009	-1.215	0.8813	0.58
4.10*	-	0.0005	-1.269	0.9689	0.46

*These values are for model simulation 4.10, where the model was run without the damage accumulation function (all other conditions were the same).

5.5.2 Rockfall size

Three different approaches were taken to improve the rockfall model to enable the generation of a wider range of rockfall volumes, including: increasing stress transfer and damage accumulation within the model; incorporating a rockfall volume-area scaling law; and altering the temporal resolution of data acquisition from the model. A summary of each approach and the resulting changes in model outputs are given below, and the outputs are validated against the criteria set out in Table 5.3.

5.5.2.1 Increasing stress transfer and damage accumulation

The total failed area and size of rockfalls are most sensitive to changes in *pd* (Fig. 5.21; 5.22). To determine whether the rockfall size was most sensitive to *pd* or the range of cells (*e*) over which stress is transferred and damage accumulates, simulations were run increasing the magnitude of both: *pd* was increased from 125% to 200%, and *e* was increased from 1 to 5 (Table 5.10). Increasing *pd* beyond reasonable values (> 100%) allowed the limits of the model to be explored.

Increasing the magnitude of *pd* increases the range of rockfall sizes up to 122 m^3 at *pd* = 200% (Fig. 5.28a; Table 5.12), and increases the *ß*-value of the rockfall volume magnitude frequency power law (Table 5.12) to within the range of suitable values set in Table 5.3, with the exception of *pd* = 200%. The erosion rate and surface area failed in this model setup (Table 5.12) are within reasonable values for *pd* = 125%. Above this, both the erosion rate (mm t_n^{-1}) and the failed area (%) become larger than the upper bounds set in Table 5.3. Likewise, at values greater than *pd* = 125%, the mean modelled slope profile inclines to more than 10° from vertical, as shown in Figure 5.29. As the slope becomes sub-vertical, such that it inclines further away from a vertical slope, the local stress in the slope would not be high enough for failure propagation to continue. This suggests that above *pd* = 125% the model results are no longer valid, and so *pd* = 125% is considered an upper threshold on stress transfer and damage accumulation conditions.

Increasing the distance over which *pd* operates results in a small increase in the largest rockfall sizes. Above *e* = 2, rockfalls greater than 1 m^3 are generated (Table 5.12), and the *ß*-value of the rockfall magnitude frequency power law (Table 5.12) is within the range of suitable values set in Table 5.3. However, as the range of cells (*e*) increases, the power laws steepens (Fig. 5.28b; Table 5.12) demonstrating a more significant contribution of smaller rockfalls in the overall distribution. This suggests that allowing stress to transfer and damage to accumulate

from one cell over a large distance and or area, may inhibit the development of large rockfalls as the magnitude of stress redistributed to neighbouring individual cells becomes very small. The erosion rate and surface area failed (Table 5.12) are within the bounds set in Table 5.3 for all values of *e*. Likewise, the resulting slope profiles from these simulations (Fig. 5.30) show that for all values of *e* the mean slope profile remains near vertical, ranging between 0.06° to 0.26° from vertical.

Increasing *pd* has a more significant impact on the model outputs. As the results have shown, only at *pd* = 125% are the results still within the suitable bounds set out in Table 5.3. Conversely, increasing the spatial range of stress transfer and damage accumulation has a much smaller impact on the model outputs.

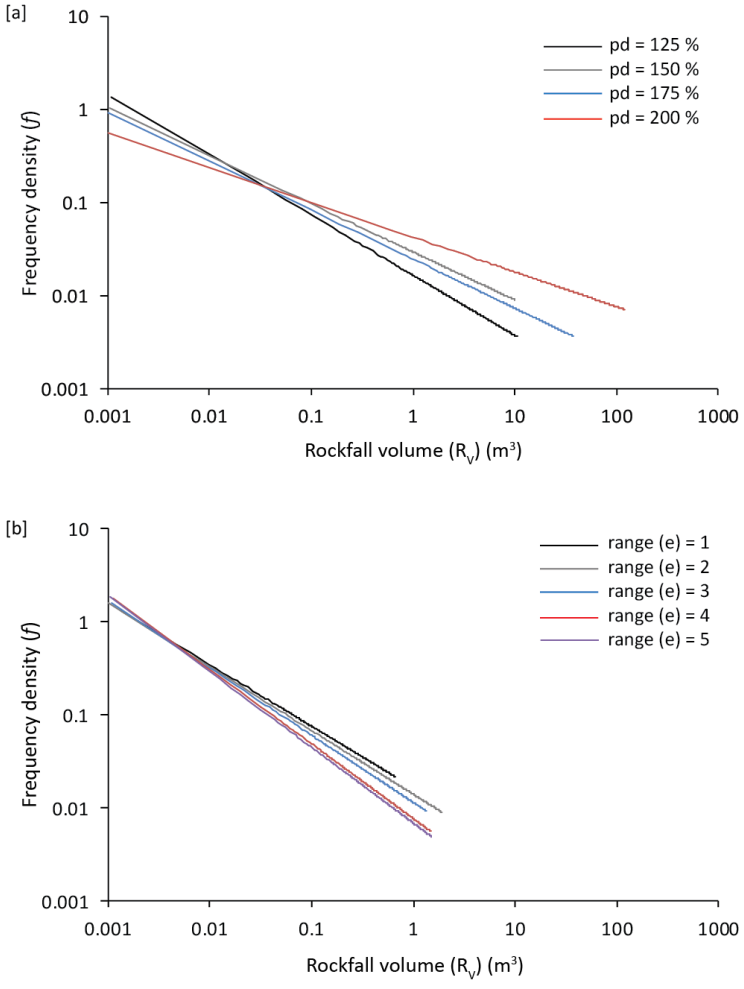

Figure 5.28: Power law fits for rockfall magnitude-frequency: (a) rockfalls from model simulations 19.1 – 19.4 (pd = 125% - 200%); and (b) rockfalls from model simulations 20.1 – 20.5 (*e* = 1 - 5).

Table 5.12: *k* (coefficient) and *ß* (exponent) values for the rockfall volume magnitude frequency power law, as shown in Figures 5.28.

Model run simulation ID	variable parameter	*k* value	*ß* value	R^2 value	Max. rockfall size (m^3)	Failed area (% t_n^{-1})	Erosion rate (mm t_n^{-1})
19.1	*pd*= 125 %	0.0167	-0.648	0.9555	10.55	0.08	0.156
19.2	*pd*= 150 %	0.0297	-0.516	0.9004	10.03	0.44	0.881
19.3	*pd*= 175 %	0.0248	-0.525	0.7998	37.32	9.75	19.510
19.4	*pd*= 200 %	0.0429	-0.374	0.737	122.35	103.30	206.680
20.1	range (*e*) = 1	0.0166	-0.661	0.6419	0.67	0.04	0.069
20.2	range (*e*) = 2	0.014	-0.686	0.9086	1.92	0.04	0.071
20.3	range (*e*) = 3	0.0115	-0.72	0.9394	1.33	0.04	0.086
20.4	range (*e*) = 4	0.0077	-0.803	0.9445	1.48	0.04	0.087
20.5	range (*e*) = 5	0.0069	-0.814	0.9519	1.51	0.05	0.089

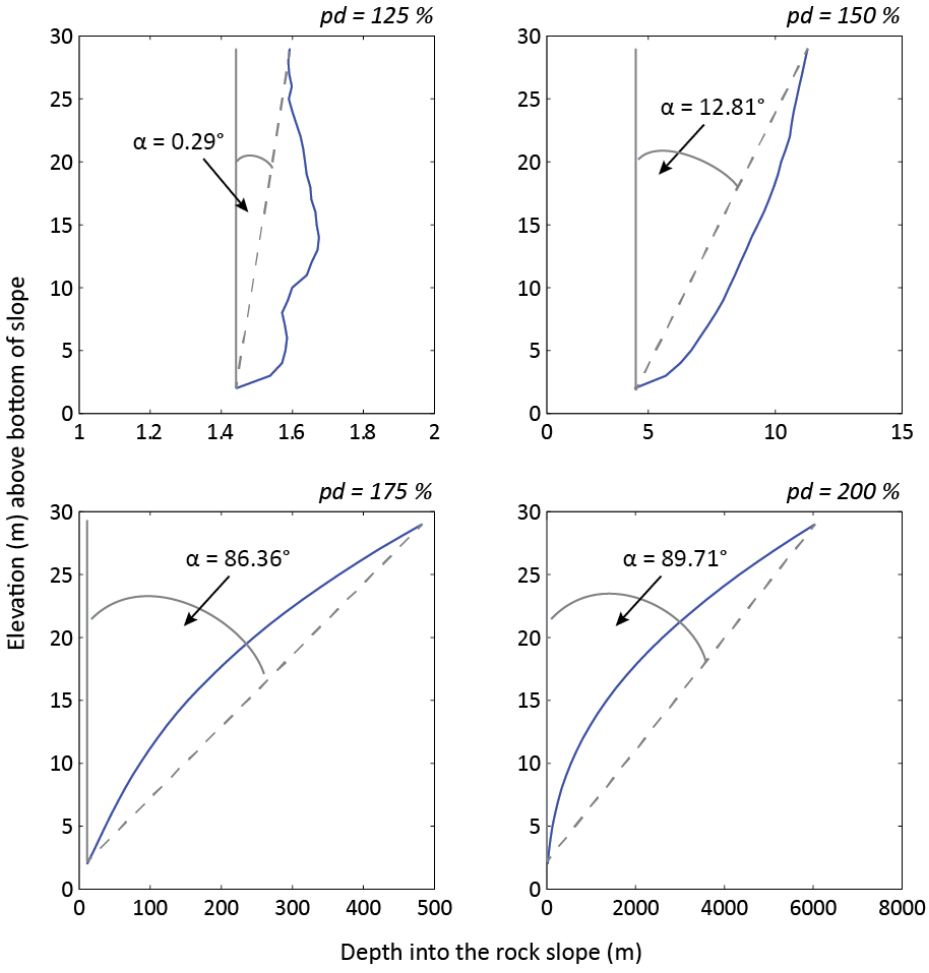

Figure 5.29: Average slope profiles at the end of model simulations 19.1 – 19.4 (*pd* = 125 – 200 %).

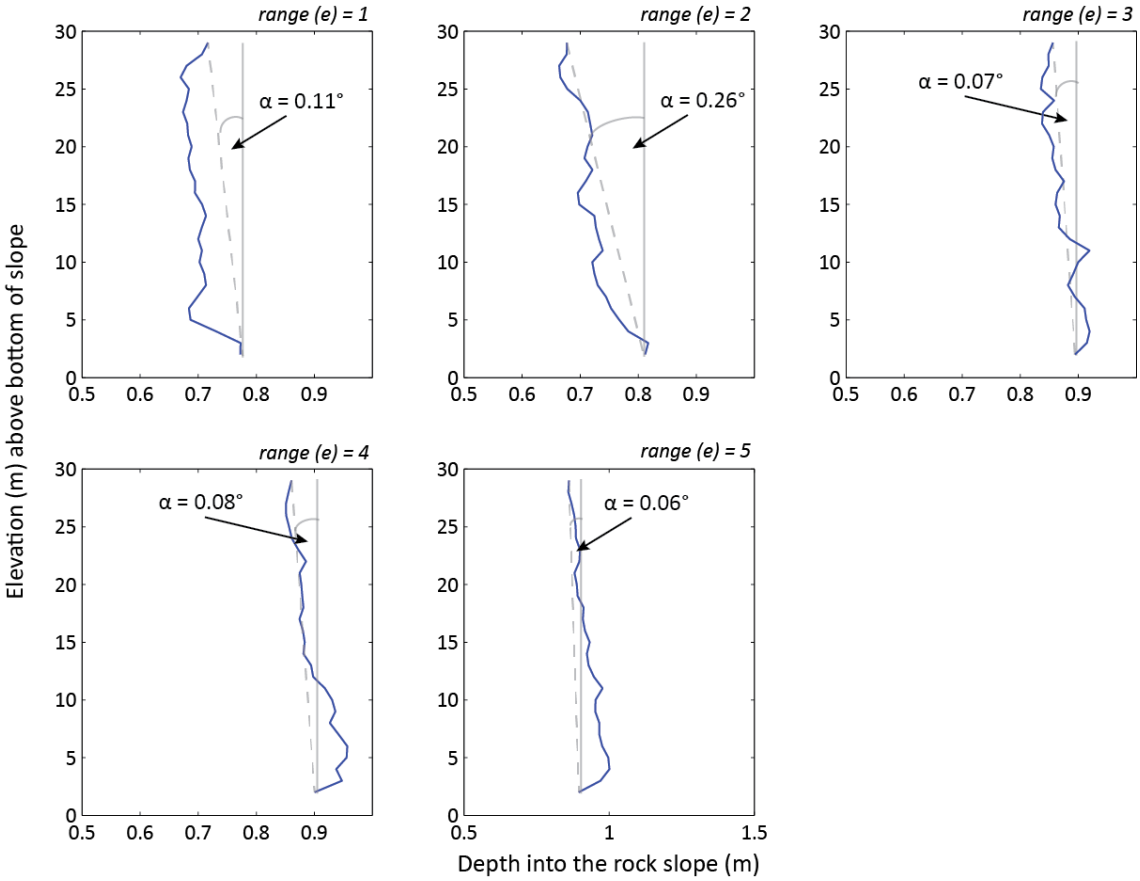

Figure 5.30: Average profile of the rock face at the end of model simulations 20.1 – 20.5 (*e* = 1 - 5).

5.5.2.2 Rockfall volume-area scaling law

In the first stage of model development the depth of all rockfalls was set to 0.2 m, constraining the rockfall volumes (*V*) to a linear relationship with rockfall area (*A*). In order to increase the range of rockfall volumes generated, a power-law describing the relationship between *V* and *A* was developed based on the field data results. The relationship between *V* and *A* for the field data, can be expressed as the following power law:

$$V = 0.22A^{1.105}$$

Equation 5.6

This relationship has a significant r^2 value of 0.92 and has the same form as other area volume scaling laws for a range of landslide inventories, (Rosser *et al.,* 2007a; Larsen *et al.,* 2010; Parker *et al.,* 2011). This relationship is applied to the rockfall model in order to calculate volumes based on surface area. Once rockfall areas have been determined by grouping contiguous failed cells, the volume is calculated and then the cell elevations uniformly reduced

within the scar area, and the surface topography updated accordingly. Rather than a fixed rockfall depth for all rockfalls, this approach increases rockfall volumes to greater than 1 m^3 (max. rockfall size = 2.10 m^3) and produces a power law fit with an exponent of -0.775 (Fig. 5.31). Both of these values are within the ranges set in Table 5.3.

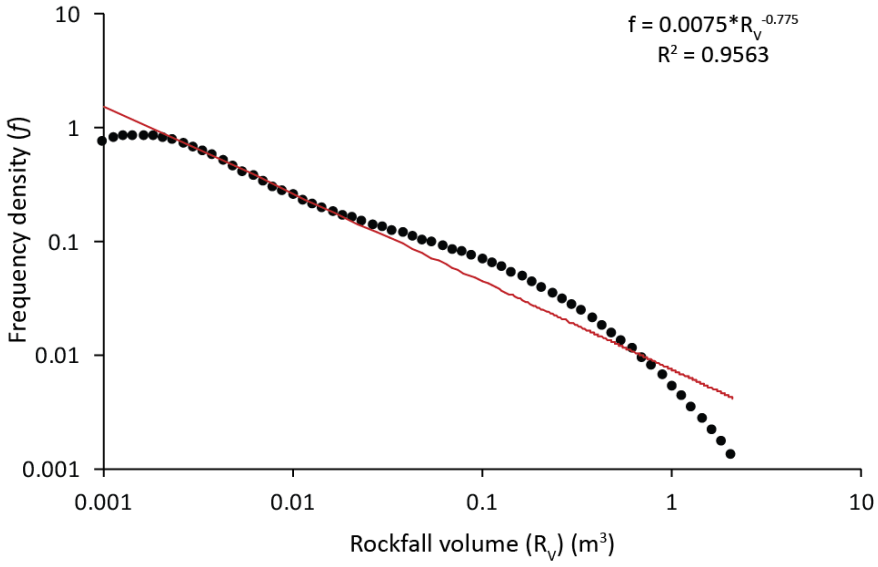

Figure 5.31: Magnitude-frequency plot (black circles) and power-law fit (red line) for all rockfalls in model simulation 21 (*ß*-value = -0.775).

The results of this simulation also validate the erosion generated by the model. The spatially averaged erosion rate is 0.124 mm t_n^{-1} and the average failed area is 0.06 % per time step. The average slope profile remains near vertical at an angle of 0.26° from vertical (Fig. 5.32), which satisfies the conditions set out in Table 5.3, and demonstrates the desired spatially variable erosion with elevation.

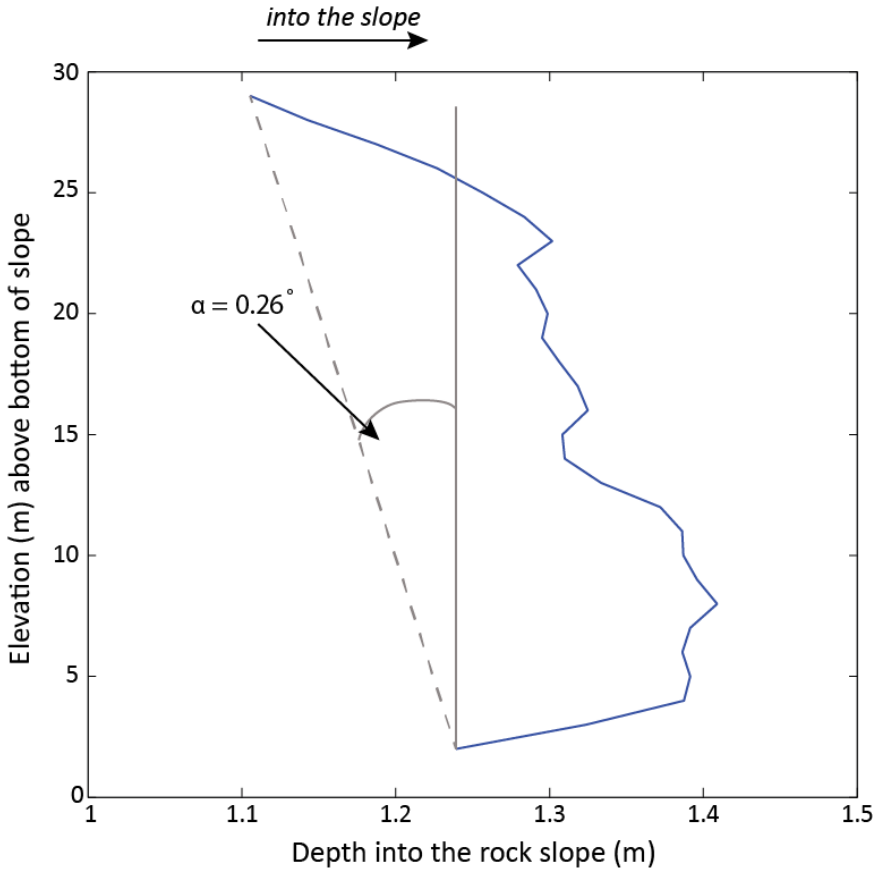

Figure 5.32: Mean rock face slope profile at the end of model simulation 21.

5.5.2.3 Temporal resolution of data acquisition

Rockfall data from field observations is usually based on a relatively low temporal resolution due to the logistics of data collection. For example, monthly TLS scans were acquired for this study (Chapter 3). One of the limitations of this approach is that rockfalls likely become superimposed, where those identified as single events may actually be the sum of many smaller events (Barlow *et al.,* 2012), and thus the relative contribution of small events is underrepresented (Rosser *et al.,* 2007a). This is illustrated in Figure 5.33 using results from simulation 21. Visual plots show how smaller rockfalls identified at individual time steps could be identified as one larger rockfall when considered at a lower temporal resolution.

In order to demonstrate the effect of the temporal resolution of data acquisition, results from model simulation 21 were presented for different temporal resolutions, using a range of sampling windows equal to t_n = 10, 20, 50 and 100 (Fig. 5.34, 5.35). As the temporal resolution decreases as t_n increases, the power law is less steep (*ß*-value reduced), indicating overall, a more significant contribution of larger failures (Fig. 5.34). The exponent (*ß*-value) plotted

against the temporal resolution (Fig. 5.35) shows that the increase in the *ß*-value becomes smaller for resolutions > 20 t_n, and very little change in response is observed for 50 and 100 t_n (Fig. 5.35). Conversely, the maximum rockfall size increases significantly between a temporal resolution of 50 and 100 t_n (Table 5.13). This suggests that the effect of increasing or reducing the temporal resolution of the data on the overall rockfall size distribution, is more apparent at higher temporal resolutions, whilst the increase in maximum rockfall size is more sensitive to lower temporal resolutions.

Across all temporal resolutions tested, the *ß*-values (Table 5.13) are within the range specified in Table 5.3 (model validation), and the maximum rockfall size remains in the range 1 to 10 m^3. Lowering the temporal resolution of the data does not affect the total failed area, but it does marginally increase the erosion rate (Table 5.13). Again, in all cases these values are within the suitable ranges defined in the model validation (Table 5.3).

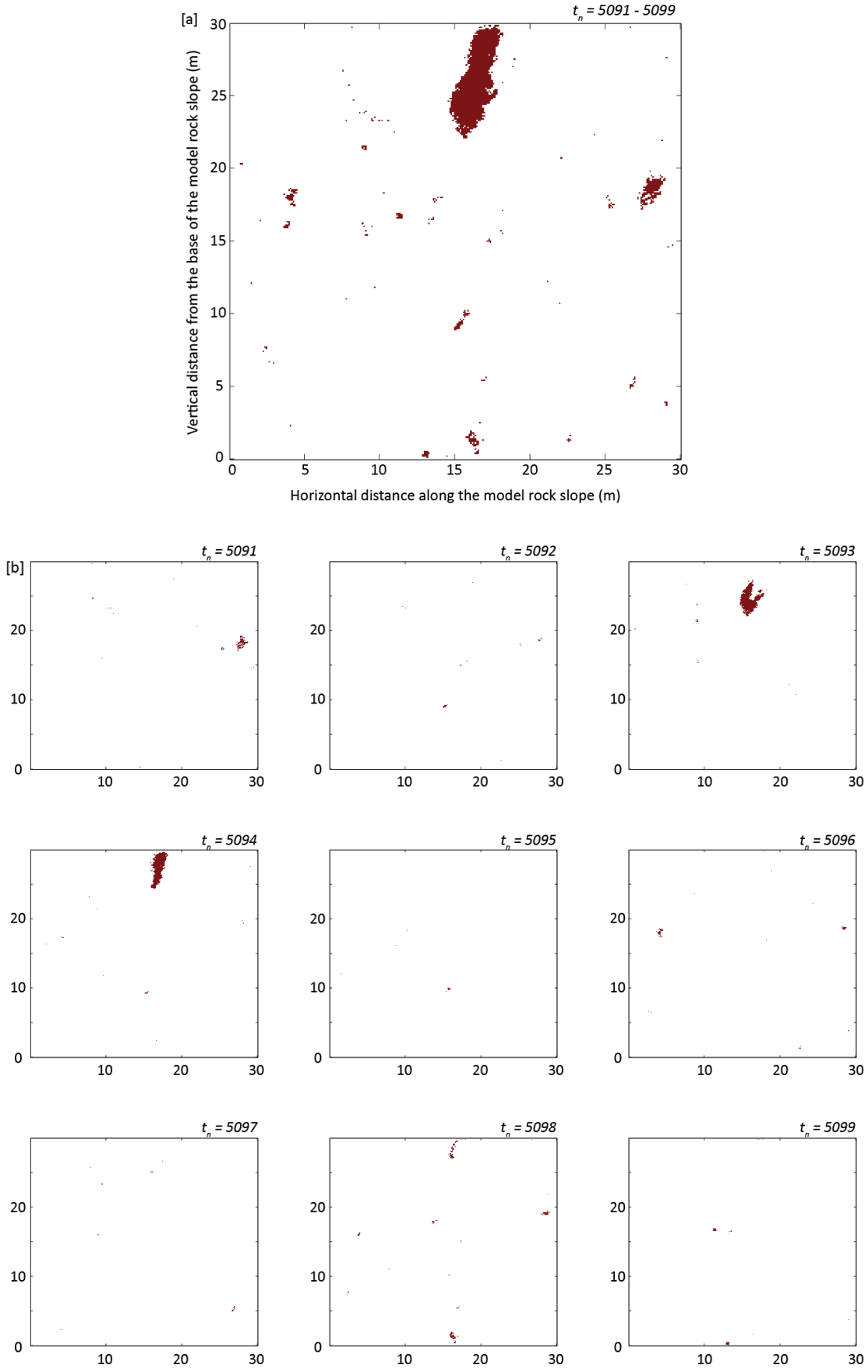

Figure 5.33: Visual plots of rockfalls that occurred over 9 time steps in simulation 21: (a) is the amalgamation of all rockfalls; and (b) shows the rockfalls as they occurred in each time step, from top left (t_n = 5091) to bottom right (t_n = 5099).

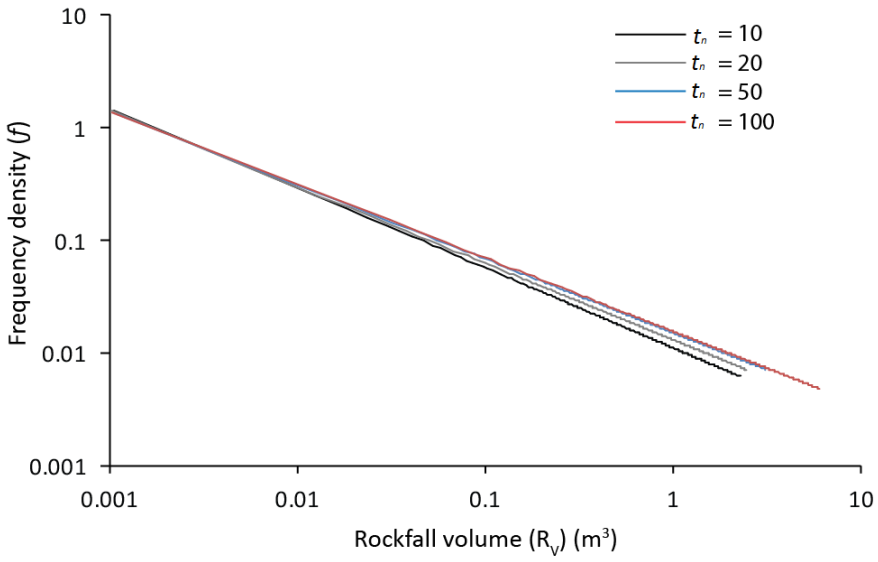

Figure 5.34: Power law fits for rockfall volume magnitude-frequency of all rockfalls from simulation 21. Each line depicts the power law fit for the rockfalls when identified over different temporal resolutions, given in time steps (t_n = 10; 20; 50; and 100).

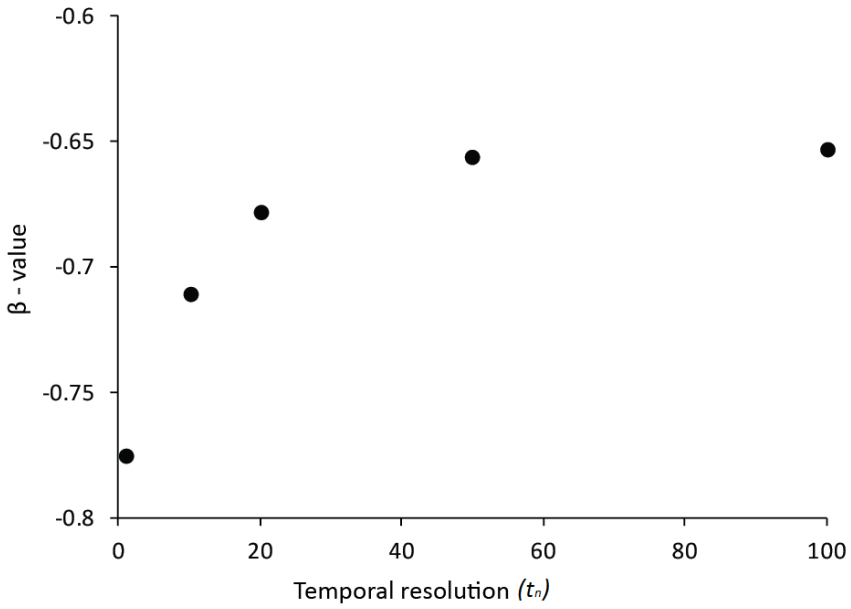

Figure 5.35: *ß*-values of the power law fits in Fig. 5.34, plotted against the temporal resolution at which rockfalls were identified. The *ß*-value increases, indicating a more significant contribution of larger rockfalls, as the temporal resolution increases up to t_n = 50. This demonstrates that the larger rockfalls observed at t_n = 50 are an amalgamation of smaller rockfalls in the model.

Table 5.13: *k* (coefficient) and *ß* (exponent) values for the power law from simulation 21 when identified over different temporal resolutions. The power law fits are shown in Figure 5.34.

Model simulation ID	**variable parameter**	***k* value**	***ß* value**	**R^2 value**	**Max. rockfall size (m^3)**	**Failed area (% t_n^{-1})**	**Erosion rate (mm t_n^{-1})**
21	temp. res. = 1 t_n	0.0075	-0.775	0.9563	2.10	0.06	0.124
21	temp. res. = 10 t_n	0.0112	-0.711	0.94	2.25	0.06	0.126
21	temp. res. = 20 t_n	0.0132	-0.678	0.9329	2.45	0.06	0.127
21	temp. res. = 50 t_n	0.0152	-0.656	0.9291	3.10	0.06	0.129
21	temp. res. = 100 t_n	0.0157	-0.653	0.916	6.02	0.06	0.132

Three different approaches have been used in an attempt to increase the volume range of rockfalls generated by the model. Increasing *pd* generated a rapid increase in rockfall size, however beyond *pd* = 125%, the rockfall model no longer produced reasonable outputs. Lowering the temporal resolution of the data increased the maximum rockfall size, however the larger rockfall sizes represent an amalgamation of smaller rockfalls superimposed over multiple time steps. This contradicts one of the key purposes of the model: to consider how rockfalls grow and evolve through time. However, the result presents an interesting consideration for field studies, suggesting that there is a monitoring frequency after which the data quality does not alter significantly. In Figure 5.35 this threshold would be at 50 time steps. Adopting the use of the volume-area scaling law provided the best results in terms of rockfall size distribution. Using this scaling law, and the equations presented in the first half of this chapter, the model can be applied to investigate scenarios involving rockfall failures from steep cliffs.

5.6 Discussion

The development of this rockfall model has demonstrated that the general and cumulative characteristics of rockfalls can be simulated in a reduced complexity model by considering the variables that replicate the interplay between stress transfer and damage accumulation, and external forcing. This model is able to reproduce the distribution and range of failure volumes,

the spatially averaged erosion rates of the slope, and the spatial distribution of failures across the rock slope.

Power law rockfall magnitude-frequency distributions are abundant in data that describes the natural environment (Chapuis and Tetzlaff, 2014), and have been widely applied to observe the distribution of different geomorphic events, including earthquakes (Bak *et al.,* 2002), landslides (Guzzetti *et al.,* 2002, Malamud *et al.,* 2004), glacier calving (Chapuis and Tetzlaff, 2014), and rockfall (Barlow *et al.,* 2012). Through the use of laboratory sand-pile experiments Bak *et al.* (1988) demonstrated how power law distributions can arise from systems that have reached a "self-organized critical state" (Bak *et al.,* 1988, pp.373) and how perturbations can propagate through that system. By allowing perturbations, such as stress transfer, to propagate through the rock slope, the rockfall model described has generated rockfall volume distributions that fit a power law ($r^2 > 0.95$). The exponent (β-value) of these power law fits are within the suitable range determined from field observations and published literature.

Spatially averaged erosion rates describe the erosion of a rock slope. The rockfall model has shown that whilst the distribution of rockfall sizes is sensitive to how rockfall grow and develop on the rock face, the net erosion rate is more sensitive to the intensity of external forcing. Here, the rate and intensity of weathering within the rockfall model sets the spatially averaged erosion rate of the slope.

By simulating rockfalls as a function of stress transfer and damage accumulation, the rockfall model has reproduced rockfalls that initiate, grow and coalesce across the entire rock slope surface as the area of maximum erosion on the slope changes through time. This spatial distribution represents a process of contiguous rockfall development that is commonly observed in rock slope monitoring studies, such as Rosser *et al.* (2007a), Abellán *et al.* (2010), and Stock *et al.* (2012). More recently, such behaviour has been shown to also occur in calving of a glacier terminus (Chapuis and Tetzlaff, 2014).

5.6.1 The applicability of the cellular rockfall model

The rockfall model is designed to simulate individual rockfalls and to demonstrate how these evolve through time as part of continuous damage accumulation within a rock mass. The model focuses on the preparation of the cliff face prior to failure, and then how failure influences the surrounding rock face, governed by the interactions between cells only on the near surface region of the rock slope. Due to the reduced complexity approach of the model

developed, it is able to simulate rockfall processes across a rock slope (10^2 – 10^3 m^2) and over relatively long time periods (10^2 years), whilst maintaining high spatial and temporal resolution.

The dominant processes operating in the model (weathering, stress transfer and damage accumulation, structural support amongst surface blocks, and time-dependent damage accumulation) make the model applicable to simulating rockfalls at the slope surface. As has been demonstrated, these processes work in symphony, and if one process becomes overly dominant, the model is no longer applicable. For example, Figure 5.30 shows the slope profile over steepens due to a large increase in stress transfer and damage accumulation, which results in propagation and excessive loss of the material at the cliff profile top. As the profile steepens the profile becomes unrealistic, and develops a form where the failure mechanisms the model is aiming to simulate become unlikely. Conversely, many existing slope models that are well-suited to simulating large-scale slope failure, such as 3DEC and Slope Model (Itasca, 2014), are not applicable to simulate individual rockfall at the slope surface over the time scales and at the resolution considered here.

5.6.2 Implications for rockfall modelling

The review of current rock slope modelling approaches provided in Chapter 2, describes the limitations associated with each approach taken to modelling rock slopes and rockfalls. The key limitations relevant to this study, which the rockfall model developed here has attempted to address, are (1) the perspective and scale of the model operation, (2) the ability for stress transfer to drive damage accumulation across the surface of the modelled slope, and (3) the complexity and high computational costs of modelling high numbers of rockfall at high spatial and temporal resolution.

Perspective and scale

Rockfall modelling capabilities have previously been limited by the available resolution of monitoring data, whereby measurements of discrete events are used to infer on-going changes within a rock slope and to the behaviour that is used to constrain rock slope models (Styles *et al.,* 2011). Low temporal and spatial resolution monitoring data has been shown to overlook small events as they are masked or subsumed by larger events, such that patterns of contiguous rockfall development are overlooked (Barlow *et al.,* 2012). This is supported by Stead and Coggan (2012) who demonstrate that much of the current rock slope modelling is at

a coarser scale than needed to detect widely observed features of rockfall evolution. By utilising the advances in terrestrial laser scanning for monitoring (Abellán *et al.,* 2014), this study has developed a rockfall model that simulates the processes of contiguous rockfall development at the spatial and temporal scales that they are observed to operate at.

Altering the temporal resolution of the model (Fig. 5.35) demonstrated how smaller rockfalls are only detected at higher temporal resolutions, as expected. The results suggest that there is a threshold in the temporal resolution of rockfall detection, above which the data quality does not significantly improve with increased frequency monitoring. These limits on temporal resolution of rockfall detection could be applied both to monitoring data and numerical modelling of rockfalls.

Many rockfall models operate in profile and those that operate in 3D are seldom used to consider the processes operating at as fine a scale as here. Results of the field data analysis emphasised the importance of across cliff rockfall interactions, supporting the results of previous studies such as Stock *et al.* (2012), Abellán *et al.* (2010) and Rosser *et al.* (2007a). The rockfall model operates from a slope face perspective, considering the interactions and processes that occur across the slope face as rockfalls occur.

Accumulation of damage and transfer of stress

The staged brittle failure model developed by Martin and Chandler (1994) and Eberhardt *et al.* (1999) describes failure as a continuous process, whereby strain accumulates up to the point of failure. Often physically expressed as fracturing within a rock slope, the accumulation of strain has been represented in the rockfall model as damage. The final stage of time-dependent failure in the brittle failure model has been represented in the rockfall model by incorporating time-dependent damage accumulation. This function has demonstrated how time-dependent failure can influence both the failure volume, as well as the timing of failures. Including the time-dependent damage accumulation within the model increased the surface area that failed as the sum of all rockfall, and the maximum rockfall size. Furthermore, the model has demonstrated the differences in rockfall and overall slope behaviour when weathering, stress transfer and damage accumulation, structural support amongst surface blocks, or time-dependent damage accumulation cause the damage threshold to be exceeded. This is explored further in chapter 6.

The role of stress transfer and damage accumulation in rock slope failure is often described (e.g. Stock *et al.,* 2012), yet this represents a relatively unknown quantity as a driver of small-scale rockfall, as it is hard to observe or measure. Subsequently, existing rock slope models are

not able to simulate at the resolution presented here, although ways of quantifying accumulated damage within a rock slope model has been developed by, for example, Havaej et al. (2014b). Including stress transfer and damage accumulation as a single function in the rockfall model, has shown how this mechanism can impact on the process of rockfall occurrence, the distribution of failure sizes, and changes to the overall slope.

Model complexity and computational costs

A range of existing numerical rock slope models are able to simulate progressive failure and include brittle fracture such as the hybrid finite-discrete element code Elfen (Rockfield, 2013); Particle Flow Codes (Itasca, 2010a); and the lattice spring code Slope Model (Itasca, 2014). These models are complex and the computational cost is high, particularly when simulating processes in 3D (Stead and Wolter, 2015). By developing the rockfall model in a reduced complexity approach, the key physical processes are represented but the complexity is reduced so that a large combination of parameters and processes can be explored. This is not often computationally feasible in the more complex, mechanical models.

The use of Slope Model in Chapter 4 provided a mechanically-based understanding of some of the processes included in the rockfall model, which has been incorporated into the stress transfer and damage accumulation and the time-dependent damage accumulation functions (see sections 5.2 and 5.3). The development of a simple, process based model that simulates rockfall as a function of this accumulative damage through time has extended the spatial and temporal range of the model simulations compared to Slope Model.

Simulating rockfalls in a simplified, homogenous rock mass with uniform weathering conditions has allowed rockfalls to be examined under fixed and relatively simple conditions. The results of the modelling have demonstrated that the observed rockfall behaviour is not solely a result of the spatial and temporal variability in external environmental conditions, and/or large-scale rock mass structure. Instead the observed rockfall behaviour in the rockfall model relies on relatively simple geometrical interaction rules that allow the transfer of stress to drive subsequent damage accumulation, through the near surface of the rock slope. Whilst the model has not explicitly modelled joints as failure surfaces, it has demonstrated the significance of internal rock mass character (stress transfer and damage accumulation), as the model has reproduced largely realistic rockfall size distributions without the explicit representation of joints.

Overall, the scientific value of this model is in taking the concepts of interaction driven, cellular, self-organising systems (Bak et al., 1988, Rozier and Narteau, 2014, Chapuis and Tetzlaff, 2014) and applying these concepts to near-surface rockfall dynamics to better understand how rock slopes fail at the scale of rockfalls commonly observed in new high resolution datasets. In doing so, the model has demonstrated the significance of a variety of time-dependent controls on rockfall triggering that act to differentially exploit internal characteristics of the rock mass. The model has addressed some of the limitations of current rock slope models for simulating small surface rockfall, and has been developed to a stage where it can be applied to answer questions around how rock slopes and cliffs change through time, and how various types of control on their behaviour interact. Through incorporating the role of stress transfer and damage accumulation, the model is positioned to address questions regarding: (1) the links between externally controlled processes such as weathering and rockfall occurrence; (2) the role of internal rock mass controls in preparing for and triggering failure; (3) links between rockfall and surface morphology; and, (4) overall rock slope evolution under changing conditions. Chapter 6 applies the model to address some of the key research questions for this study.

6 Discussion and applications

The aim of this thesis has been to simulate rockfalls as temporally and spatially-dependent to better understand where, when and why rockfalls occur. Building on previous work (Rosser *et al.,* 2007a; 2013; Oppikofer *et al.,* 2008; Abellán *et al.,* 2010; Stock *et al.,* 2012) that has identified spatial and temporal sequencing of rockfalls leading to a progressive failure mechanism as a potential explanation, this work has shown that considering stress redistribution from small-scale rockfalls as a key component in numerical modelling of rockfall is advantageous. Models that include interactions between successive rockfalls are able to explain the size distribution and location of rockfalls, and the resulting changes to rock slope profile form. In this thesis I have shown that the clustering and propagation of rockfalls operates over identifiable length scales in space and time. By incorporating these length scales into a new cellular rockfall model it is also possible to replicate the spatial and temporal sequencing of rockfalls.

Using the rockfall model presented in Chapter 5, I will now consider how this model can be used to improve understanding of rockfalls. Firstly, I discuss the outcomes of this study specifically in the context of the unique characteristics of the modelling approach developed. This includes the model discretization, the scale at which it operates, the temporal and spatial-dependence between rockfalls, and the advantages of the reduced complexity approach. Secondly, by using a series of experimental applications of the rockfall model, I address key research areas that apply to a wider range of research on rockfalls and rock slopes and discuss the findings that this approach generates.

6.1 The advantages of modelling rockfalls from a slope face perspective

The majority of rock slope studies are concerned with 2D profile form changes and longer-term retreat (Emery and Kuhn, 1982; Collins and Sitar, 2008; Young and Ashford, 2008; Trenhaile, 2011; Joyal *et al.,* 2016) or with the large scale stability of the wider slope. Such 2D approaches assume that the mass wasting is continuous across, or more widely representative of the whole slope face. Fundamentally this ignores the role of cliff face structure and topography, and how failures may interact and evolve. Variability in the location and sequencing of rockfalls as a result of these factors has been demonstrated in this study and elsewhere (Rosser *et al.,* 2007a; Lim *et al.,* 2010; Abellán *et al.,* 2010; Stock *et al.,* 2012; Rohmer and Dewez, 2013). The field dataset presented in this study showed that: rockfalls more frequently

occurred on locally convex areas of the slope; rockfalls cluster significantly in space and over time; patterns of rockfalls observed at the cliff face, such as the directional behaviour of rockfall sequencing, were not necessarily seen in profile; and variability in rockfalls observed across different rock types over the two-year survey was not consistent between study sites.

Considering rock slope failure in terms of 2D profiles collapses the erosion of the slope at any given elevation to a single spatially averaged value. Within a coastal environment, such models have been used to infer the nature of the dominant processes driving changing in slope profile form such as the dominance of marine versus sub-aerial weathering (Emery and Kuhn, 1982; Nunes *et al.,* 2009). Selby (1982) states that under uniform weathering conditions rock slopes will retreat in a way that is defined by their rock mass strength. However, non-planar rock slope profiles as identified in the field dataset presented (Figs 3.28, 3.30, 3.34) and from previous studies at this site (Rosser *et al.,* 2013; Swirad *et al.,* 2016), show variability beyond that which can be attributed directly to either variations in weathering or rock mass strength. Furthermore, the same profile form can be observed under different rock mass and environmental conditions, indicating equifinality in rock slope profile form.

By simulating the rock slope from a slope face view, this work has highlighted that rockfalls, at the individual event scale and cumulatively through time, can be as much a function of the lateral development and interaction of rockfalls across the cliff face, as it is a process that develops primarily up profile with no significant lateral control (e.g. Styles *et al.,* 2011). This is considered here to be due to the lateral transfer for stress following failure, structural confinement, and cascading behaviour triggered by rockfalls, which all have a fundamentally across cliff component. Using the rockfall model to simulate the rock slope from a slope face view has shown that the interactions between failing blocks at the slope surface might be a controlling factor on the size and location of rockfalls that are able to develop.

Consequently, short-term variability in rockfall and the erosion that they accumulate, which drives the evolution of the slope, is not adequately represented when rock slopes are considered from just a 2D profile perspective. If the across slope variability in rockfalls is overlooked then the spatial and temporal clustering and propagation of small rockfalls (Chapter 3), which can eventually widen out to dominate slope failure (Fig. 1.1), are also overlooked. Ignoring the sequencing of rockfalls across the slope can mean that areas of potential instability in the short-term are not detected. For example, neighbouring areas of the slope surface immediately above and alongside a rockfall have been shown to subsequently fail over monthly (and possibly shorter) timescales (Fig. 3.52).

6.2 The importance of small rockfalls for wider rock slope failure

Rock slope failures are often characterized by the size and temporal frequency of events (Dussauge-Peisser *et al.,* 2002; Barlow *et al.,* 2012) and size frequency distributions of rockfall sizes emphasise the net significance of numerous small events that fall from rock slopes, often characterised by a power law (Barlow *et al.,* 2012). However until recently, smaller rockfall events (< 0.1 m^3) were not detected due to the spatial and temporal resolution of monitoring data (Abellán *et al.,* 2014) and larger, discrete events were assumed to dominate rock slope erosion (Zimmer *et al.,* 2012). Owing to issues of superimposition at lower spatial and temporal resolutions, where multiple failures in close proximity may be observed as one failure (Barlow *et al.,* 2012), large rockfalls may not actually fail as a single mass, rather as a sequence of smaller rockfalls.

The analysis of the rockfall inventory presented in this thesis (Chapter 3) has shown that small rockfalls cluster and propagate both across and up the rock face. Clustering of rockfalls is identified at distances < 10 m and 30% of rockfalls are contiguous with a previous rockfall. Overall, rockfalls identified at a monthly sampling resolution are occurring closer to previous rockfalls than would be expected for a random distribution, implying that sampling at a lower resolution (temporal or spatial) would characterise the smaller rockfalls as fewer, larger failures. Smaller rockfalls are also shown to precede larger events, suggesting a progressive failure (Petley *et al.*, 2005) is occurring and whereby the patterns of rockfall potentially provide an indication of the location and timing of larger rockfalls (Rosser *et al.,* 2007a; Abellán *et al.,* 2010). Further evidence of a progressive failure process is seen in the fracturing that precedes small failures in Slope Model simulations. With the exception of simulations run with weak joint sets, whereby the joints accommodated the strain in the slope, all simulations recorded fracture growth before the point of critical failure, indicative of the final stage of progressive failure (Eberhardt *et al.,* 1999; Petley *et al.,* 2005). If small failures are occurring in response to brittle fracture growth, as the results from Slope Model are potentially suggestive of, then the timing of failures will be determined by the fracture growth rate. Consequently, it may not be possible to make a direct link between the timing of rockfalls and environmental conditions.

Despite these observations, smaller rockfalls are seldom modelled and the mechanisms driving failure at the appropriate spatial and temporal scales are poorly understood (Stead and Coggan, 2012). The analysis of the field data presented in Chapter 3 provided information that has been used to represent the processes of small rockfall propagation within numerical

modelling. The distances over which clustering occurs suggest that stress may be redistributed at sub-metre scales in the rock mass, promoting the generation of further rockfalls. The rockfall model has simulated small scale stress redistribution via the stress transfer function, which has been informed by the upward and outward directionality observed in propagation of contiguous rockfalls (Figs 3.54, 3.57). By simulating stress transfer at the scale of small failures (0.1 m), thereby allowing further small rockfalls to be triggered in neighbouring cells, the rockfall model has produced rockfalls with size characteristics similar to those observed in the field (Fig. 5.17-5.18). Stress redistribution at a sub-metre scale is therefore shown to be a potential mechanism driving the sequencing of small rockfalls.

6.3 Time-dependent failure associated with rockfalls

The time-dependent nature of changes within a rock slope act to drive a slope to fail over time via weakening of the rock (Terzaghi, 1950). This is illustrated in the model of progressive failure (Bjerrum, 1967; Petley *et al.,* 2005) that describes the underlying process of time-dependent fracture development in a rock mass. Progressive failure in rock slopes is described in four stages (Eberhardt *et al.,* 1999; 2004; Petley *et al.,* 2005), where the final stage characterises the time period when the rock mass weakens under its own mass, where rock mass damage is an accelerating, runaway process that progresses at a rate independent of external forcing (Petley *et al.,* 2005). Rockfall events mark the end point of this runaway process of fracturing and as such rockfalls are considered to develop through time (Eberhardt *et al.,* 2004; Petley *et al.,* 2005; Rose and Hungr, 2007; Rosser *et al.,* 2007a; Abellán *et al.,* 2010; Royan *et al.,* 2013).

By using Slope Model, temporal patterns of fracture growth and failure occurrence have been generated both up to and beyond the point of failure (Figs 4.22-4.25, 4.28-4.32), illustrating the evolving nature of failure events through time indicative of progressive failure. The temporal patterns of fracture growth and failure are similar with short lags between the two observed when either fracture growth precedes failures, or failure precedes further fracture development. Areas of fracture growth contiguous to previous failures were observed to delineate the location of future failures, reflecting the concept of a process zone (Griffith, 1924) operating at the scale of individual failures, as suggested by Brain *et al.* (2014). Crucially, the application of Slope Model in this study moves beyond the focus on pre-failure behaviour, exhibited in the applications of numerical models to simulating time-dependent behaviour (Havaej and Stead, 2016) where the successive evolution of a failure is only considered as an

instantaneous consequence, rather than something that may evolve over a longer period. In focusing on the time-dependent behaviour of a rock mass both up to and beyond the point of failure, Slope Model has replicated the successive evolution of failures both as a result of and as a trigger of time-dependent fracture growth.

Subsequent development of the rockfall model that simulates rockfalls as a function of damage accumulation arising from external forcing and interactions between blocks, has shown that variability in the volume frequency distribution of rockfalls and the maximum rockfall size respond to variations in the rate (*tf*) and magnitude (*fo*) of damage accumulation in the final stage of progressive failure (Fig. 5.27 and Table 5.11). This response of rockfall behaviour to the time-dependent accumulation of damage in the rockfall model supports Hergarten (2003) who suggest that introducing a time-dependent weakening component can significantly improve the size frequency distributions generated from self-organised criticality (SOC), cellular based models for mass movements. The rockfall model shows that it is possible to explain the occurrence of some rockfalls based upon a model that includes time-dependent weakening. Furthermore, the variations in rockfall behaviour associated with time-dependent failure imply that any individual location on the rock face at any point in time, may be at a different stage of a time-dependent process of damage accumulation, due to the history of what that location has experienced. Adjacent and seemingly similar locations on the rock face may therefore generate rockfall quite differently. This offers a potential explanation for non-parallel profile retreat of a rock mass beyond what can be explained by environmental conditions or rock mass strength (Rosser *et al.,* 2013; Swirad *et al.,* 2016).

6.4 The spatial dependence of rockfall evolution

Variability in rock mass strength, the presence of discontinuities and the environmental conditions influencing the stability of a rock slope, act together to control slope profile form (Terzaghi, 1962; Selby, 1982; Emery and Kuhn, 1982). Selby (1982) acknowledges the potential for a lag in response of the slope profile form to changes in rock mass strength as a change in one parameter, for example the opening and closing of joints, may require further action, such as exploitation of the joint via weathering processes, in order to generate an alteration in the local topography. In addition to the lag between a change in rock mass strength and observed profile response, similar slope profiles can reflect different conditions.

Both individual slope profiles and the rate of slope profile retreat through time can be indicative of rock mass properties (Moore *et al.,* 2009; Nunes *et al.,* 2009), and to an extent

can inform about process competition within the rock slope (Emery and Kuhn, 1982). Variability in the distribution of rockfalls and the spatially averaged erosion between geological layers (Figs 3.26 & 3.37) shows how rates of erosion can be modulated by rock mass properties; however the variability between field sites (Fig. 3.38) illustrates that this is not a simple relationship. Marine and sub aerial process zones in a coastal environment are shown to impact on the volume of erosion and size characteristic of rockfalls, but do not result in a classic wave-induced notch and subsequent cantilever failure (Vann Jones *et al.,* 2015). The field data presented in this thesis (Chapter 3) support the findings of Vann Jones *et al.,* (2015) and additionally show that failure notches are apparent at a range of elevations on the cliff, migrating through time (Section 3.4.5). When spatially averaged across the cliff face, the focus of erosion, measured as the surface area failed (Fig. 3.26), is not consistent with elevation between sites. Rather, the variation in erosion with elevation illustrates a dependence on spatial interactions both vertically through the slope profile and laterally across the rock face as illustrated in the example of rockfall evolution in Chapter 3 (Section 3.4.5). Together these results show that changes to the slope profile are not uniform through space or time.

The spatial dependence of one rockfall in generating another has been demonstrated in this study through numerical modelling. Slope Model predicts areas of fracture growth above and alongside previously failed areas, which delineates areas of future failure. The cellular rockfall model shows how the magnitude of stress transfer (*pd*) and the resulting propagation of rockfalls across the slope can increase the roughness in a near planar slope profile, allowing surface features to emerge (Fig. 5.30). At very high magnitudes of *pd* the propagation of rockfalls across the slope can cause an originally near-vertical rock slope profile to incline away from vertical, leading to collapse (Fig. 5.29). The role of *pd* in altering profile form, acts in combination with components of rock mass strength and environmental forcing. Combinations of these processes that result in different slope profiles have been alluded to in Chapter 5 and are explored in more detail in Section 6.6 of this chapter. Consequently, this research suggests that the fundamental work of Emery and Kuhn (1982) and subsequent models of cliff erosion (Sunamura, 1992; Collins and Sitar, 2008; Nunes *et al.,* 2009) should be re-assessed by using the rockfall model approach to simulate changes in slope profile form. This should be simulated as a result of variations in the spatial interactions between rockfalls at the slope surface, as well as the impact of variations in rock mass strength, structure and environmental conditions.

6.5 Simulating rock slopes with a reduced complexity model

Numerical models are capable of simulating complex 3D rock slopes with a full simulation of fracture development (Pine *et al.*, 2007; Havaej *et al.*, 2014b). Rock slope models can simulate failure both along existing discontinuities and through intact rock at a range of spatial scales (Stead and Coggan, 2012; Stead and Wolter, 2015) and thus are mechanically complex and computationally intensive. Consequently, the spatial and temporal resolution of the model is often restricted and as such these models are not designed to consider an entire rock slope (10s of metres) at a resolution sufficient to simulate individual, small failures (< 0.1 m^3). The importance of small failures and particularly in modelling at a resolution capable of simulating small failures has been outlined in Section 6.2. In order to extend the temporal and spatial resolution of rockfall simulations, the rockfall model presented in Chapter 5 developed the principles of a cellular based, interaction focused model, similar to the principles of SOC (Bak *et al.,* 1988; Hergarten, 2003; Chapuis and Tetzlaff, 2014). In doing so, the propagation of small events has been simulated via simple interaction rules. By simulating rock slopes with simplified variables, the rockfall model has included a representation of rock mass strength and strength reduction, structure, local and global slope stability, environmental processes (weathering), and stress transfer. In doing so, this study has demonstrated that developing a rockfall model, where the focus is at the scale of small (< 0.1 m^3) rockfalls and their interactions, rather than the overall global stability of the slope, can reproduce the behaviour complex observed in the field.

The reduced complexity of the rockfall model has allowed processes to be simulated at multiple timescales, whereby the *pd* function operates instantaneously, alongside external forcing (*wi*) that operates at the timestep of the model, equivalent to approximately one day of real time. The rockfalls generated by the model can be evaluated, and the slope topography updated accordingly, at a range of timescales (Section 5.5.2.3). In doing so the model has been able to replicate superimposition at lower temporal resolutions, suggesting that the superimposition observed in monitoring studies (Barlow *et al.,* 2012) is a result of the amalgamation of contiguous rockfalls driven by stress transfer.

Alongside the outlined advantages of simulating rockfalls with a reduced complexity model, there are limitations to this approach that should be considered. In reducing complex concepts to simple variables, the multiple factors that combine to determine, for example, rock mass structure are reduced to one variable. Therefore, whilst the rockfall model illustrates the different combinations of processes that contribute to rockfall characteristics, it cannot disentangle the specific factors or processes that may be driving each of these. Thus the purpose and applicability of the rockfall model lies in highlighting the combinations of key processes that produce different rockfall behaviour.

6.6 Applications

Having demonstrated how the key aspects of the modelling approach contribute to our understanding of how rockfalls evolve through time and across the space of a rock slope, the following section will now apply the rockfall model to key research areas for the study, addressing questions outlined at the end of Chapter 2.

6.6.1 External and internal process competition

Stress redistribution is suggested to be a cause of the progressive sequencing of contiguous rockfalls that are observed to fall from hard rock cliffs (Senfaute *et al.*, 2009; Stock *et al.*, 2012). Stress redistribution is represented in the rockfall model as stress transfer (*pd*), which can cause damage to accumulate, possibly via crack formation, and weaken the surrounding material. This internal process is operating alongside external environmental forcing to drive failure within the rock mass, represented within the rockfall model as weathering, where the weathering intensity is denoted as *wi*. Conceptual models of the mechanisms and forces controlling rock slope behaviour (Rosser *et al.*, 2007a; Norman, 2012), have suggested that the timing of rockfalls is determined by the resulting accumulation of damage in the rock mass, rather than the timing of discrete events such as storms. If these conceptual models are correct then it is important to establish how the competition of external and internal processes impacts on rockfall and the resulting cliff form? Addressing this question will show the potential rockfall distributions and cliff profiles that could result from different combinations of external and internal processes.

The explicit representation of *pd* within the rockfall model alongside *wi,* allows the competition between internal and external processes to be examined. Initially the rockfall model has been run with only *wi* or *pd*; following this the model is applied to simulate changes in both *wi and pd,* and variations in rockfall size distributions, slope profile form, and rockfalls at the slope surface are examined. Running the model without *pd* generates a slow erosion rate and a consistent slope profile through time (Fig. 6.1). Only two sizes of rockfall were generated: 0.0014 m^3 and 0.0029 m^3, suggesting that the size distribution of rockfalls observed in monitoring studies, spanning four to five orders of magnitude, cannot be reproduced by *wi* alone. Further simulations with varying maximum *wi* also produced similar size distributions, indicating that the expected size distribution of rockfalls relies on *pd*.

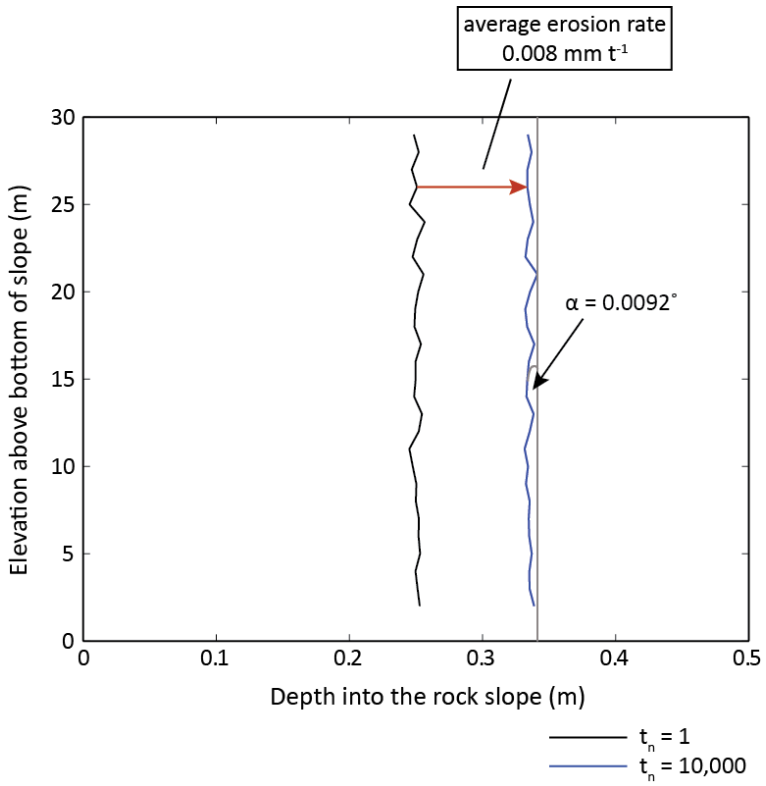

Figure 6.1: Average slope profile at the end of a model simulation run without *pd* (blue line). The slope profile is averaged over the entire cliff face, and the top and bottom 1 m are removed to avoid any boundary effects of the model. The x axis is relative to an arbitrary and fixed datum at zero, which represents the most protruding part of the slope at the beginning of the model. The profile has been exaggerated in the horizontal direction to display the local roughness up the slope. The initial model profile is shown by the black line. This shows that the slope has eroded in a largely uniform manner as a result of *wi*, with an average erosion rate of 0.008 mm per time step. The final global slope angle (calculated from crest to toe) is 0.0092° from vertical as indicated on the plot.

Running the model without *wi* generates a distribution of failure sizes within the range suggested from field observations (Fig. 6.2), indicating that a better representation of the field data is generated with *pd* alone compared to *wi*. However, the cliff does not maintain a near vertical profile as erosion towards the top of the cliff outpaces erosion at the base, resulting in a slope angle of 7.51° (2 dp), which is not representative of what is seen in the field. To run the model without *wi* a percentage of cells were initialised at the point of failure (*pd* = 1) to perturb the model. The percentage of cells set at failure ranged from 0.1% to 90% to explore how much external perturbation was required before *pd* would take over in a self-critical manner (Bak *et al.,* 1988). In all cases rockfalls stopped occurring within 250 time steps, suggesting that the model is not self-critical at any point. Therefore *pd* appears to control the

distribution of failure sizes and sequencing of rockfalls but *wi* is required to initiate and maintain the rate of failure.

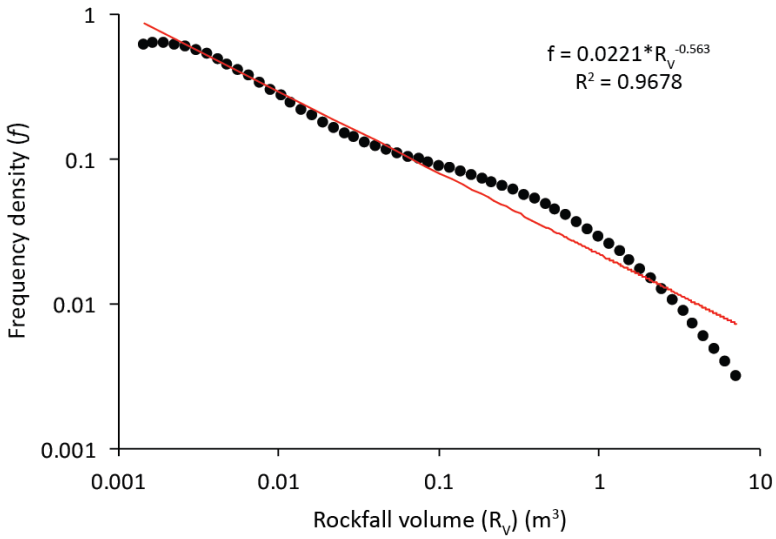

Figure 6.2: Magnitude-frequency data and power-law fit (red line) for all rockfalls in the model simulation run without *wi* and with 60% of cells initialised at the point of failure, as this model simulation ran for the longest time before rockfalls stopped occurring (*ß*-value = -0.563).

Having established that both external and internal processes are necessary for generating a distribution of failures and profile form that are representative of the field data, the rockfall model has been applied to simulate changes in both *wi* and *pd*. The visual observation of rockfalls in the model at the rock slope surface (Fig. 6.3) illustrate the increase in rockfalls as both *wi* and *pd* increase, with a more noticeable change observed as *pd* increases compared to *wi*. Patterns of rockfall propagation can be seen beyond *pd* = 70%, and are even more noticeable beyond *pd* = 80%. As *wi* increases the size of the failed area increases for the same time period, indicating that an increase in the rate of rockfalls is associated with increasing *wi*. A transition to almost complete slope failure occurs between *pd* = 95% and 100%, and the consequence of this can be seen in the final slope profiles after 10,000 timesteps (Fig. 6.4), where the slope surface collapses at *pd* = 100% for all *wi* values greater than 0.5.

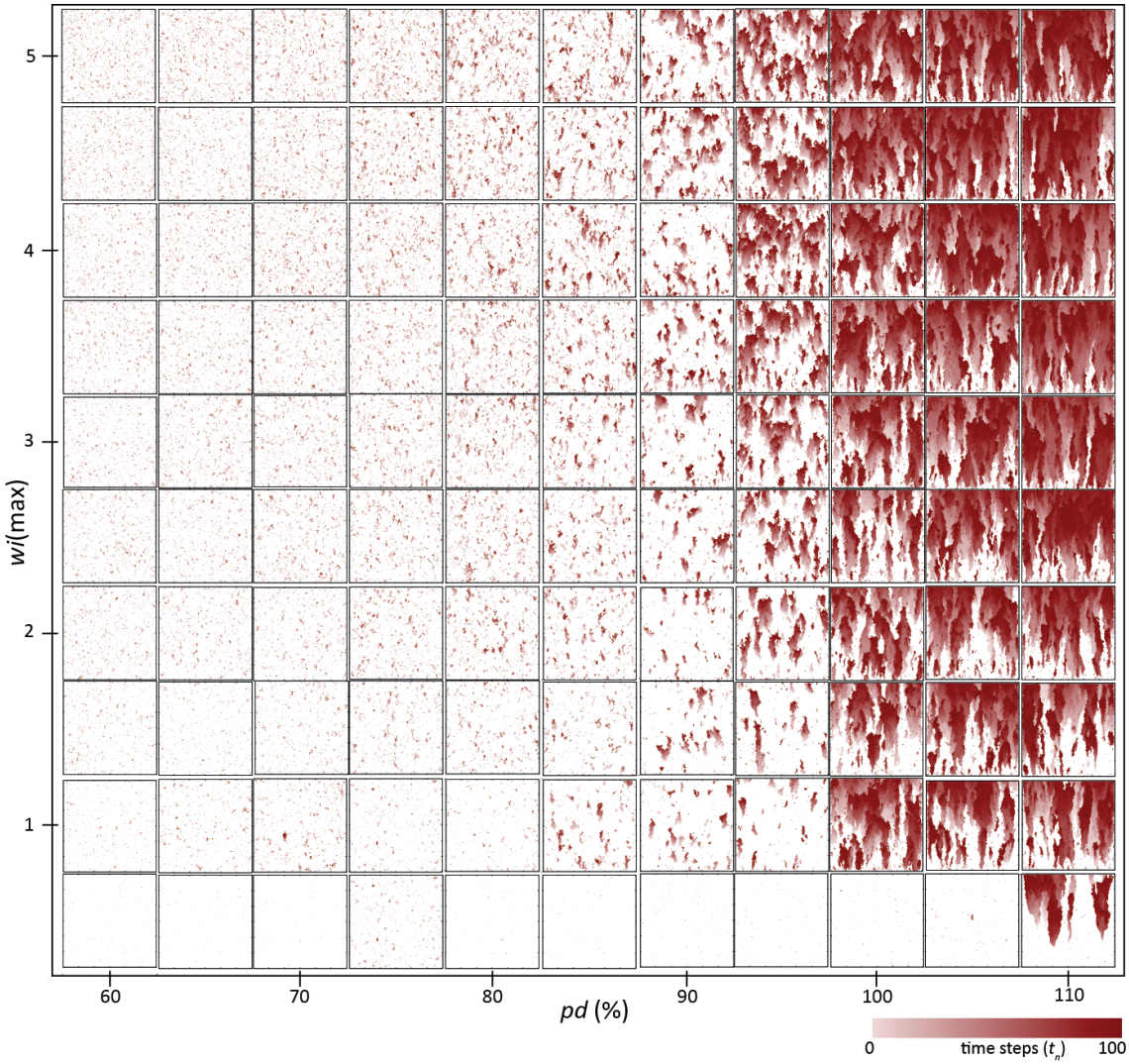

Figure 6.3: Plots of rockfalls at the rock slope surface for a range of combinations of *wi* and *pd* values. Each plot corresponds to one of the symbols in Figure 6.6a. The plots of rockfalls at the slope face depict the failures that occurred in the 100 time steps of the model from t_n = 9400 – 9500, and the failures are coloured according to the time step that they occurred in.

The range of slope profiles (Fig. 6.4) produced from a homogenous rock mass with a uniform random distribution of *wi* values, challenges the conventional understanding that slope profile form will change in response to changes in rock mass strength (lithology) or variation in external exposure to forcing or weathering (Selby, 1982), without considering internal processes. Simulating small rockfalls and their interactions, and allowing the spatial transfer of weakening, has produced a wide range of slope profiles, implying that the processes in the rockfall model beyond rock mass strength and weathering contribute to slope profile form. Consequently, this also implies that process cannot be so easily inferred from profile form

(Nunes *et al.,* 2009) and illustrates the issue of equifinality as similar profiles are observed for different *wi* and *pd* value combinations (Fig. 6.5).

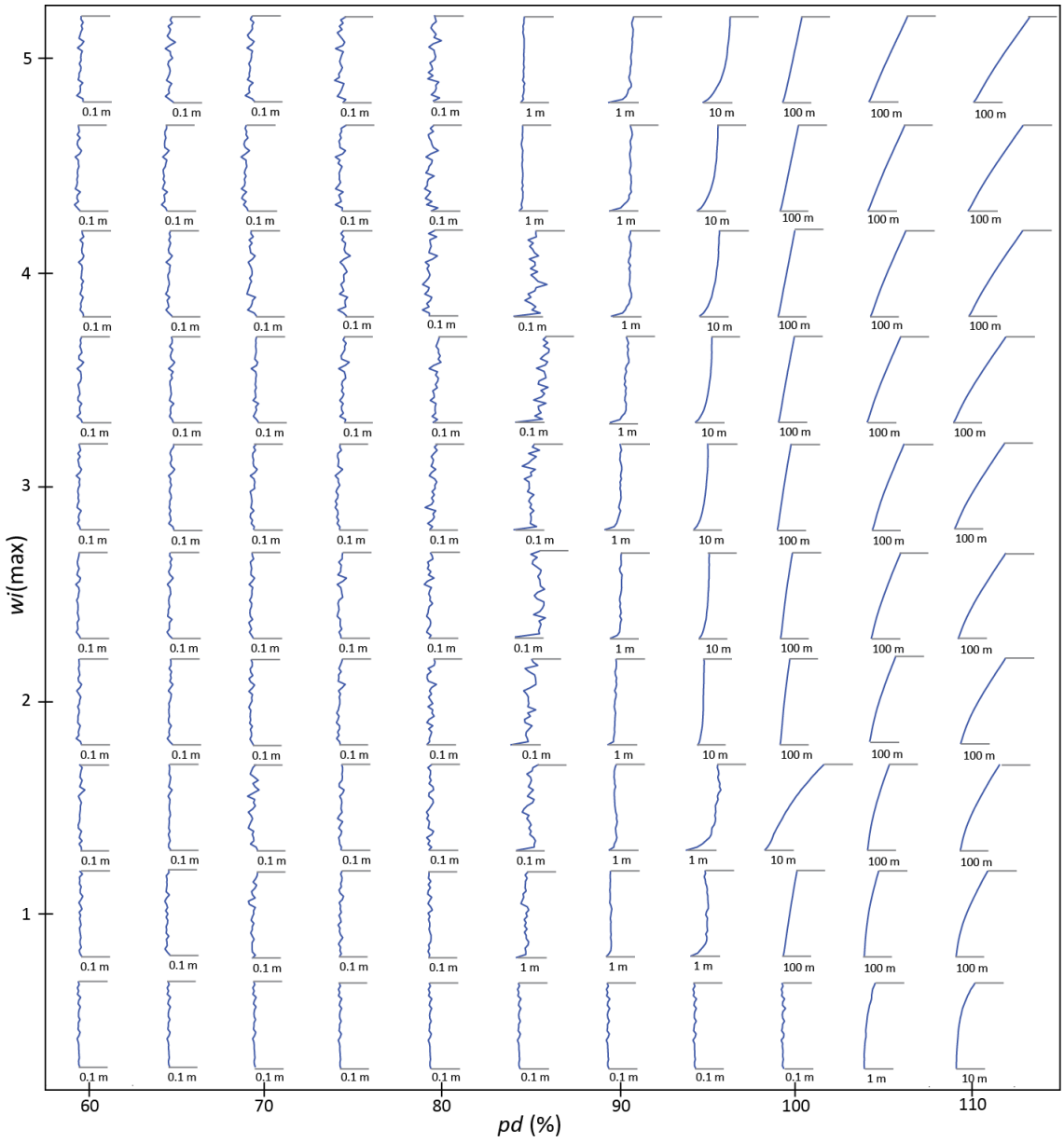

Figure 6.4: Plots of spatially averaged slope profiles for a range of combinations of *wi* and *pd* values. Each plot corresponds to one of the symbols in Figure 6.4a. The slope profiles are an average of the entire slope face at the end of the model simulation (t_n = 10,000). Each profile is 30 m high and the horizontal scale is indicated by the grey lines on each profile. Note: the horizontal scale varies in order that the profiles could be plotted within this space.

In addition to the variation in visual observations of rockfalls (Fig. 6.3) and the changes in slope profile form (Fig. 6.4), the distribution of rockfall volumes also changes with increasing *wi* and

pd values (Fig. 6.5). The five volume-frequency plots shown in Figure 6.5 are used to represent the range of volume-frequency plots produced from each of the model simulations run at different values of *wi* and *pi*. As *pd* increases the range of rockfall volumes grows, whereby the maximum rockfall volume increases from < 0.01 m^3 to > 1 m^3, and the *ß*-value also increases from -6.56 to -1.19, indicating that as *pd* increases the larger rockfalls contribute more significantly to the total material removed. As *wi* increases the range of rockfall volumes grows and the *ß*-value also increases, but the change in rockfall volumes and *ß*-value is much smaller than when *pd* is increased (Fig. 6.5). Although rock slope properties should constrain the exponents of size-frequency distributions (Barlow *et al.,* 2012), power law distributions do not always show a unique correlation to geology, climate or triggering mechanisms (Hergarten, 2003; Barlow *et al.,* 2012). Here, the plots in Figure 6.5 show that the power law distributions change with variations in *wi* and *pd,* thus the size distribution of rockfall activity appears constrained by the competition between external and internal processes acting on the rock slope.

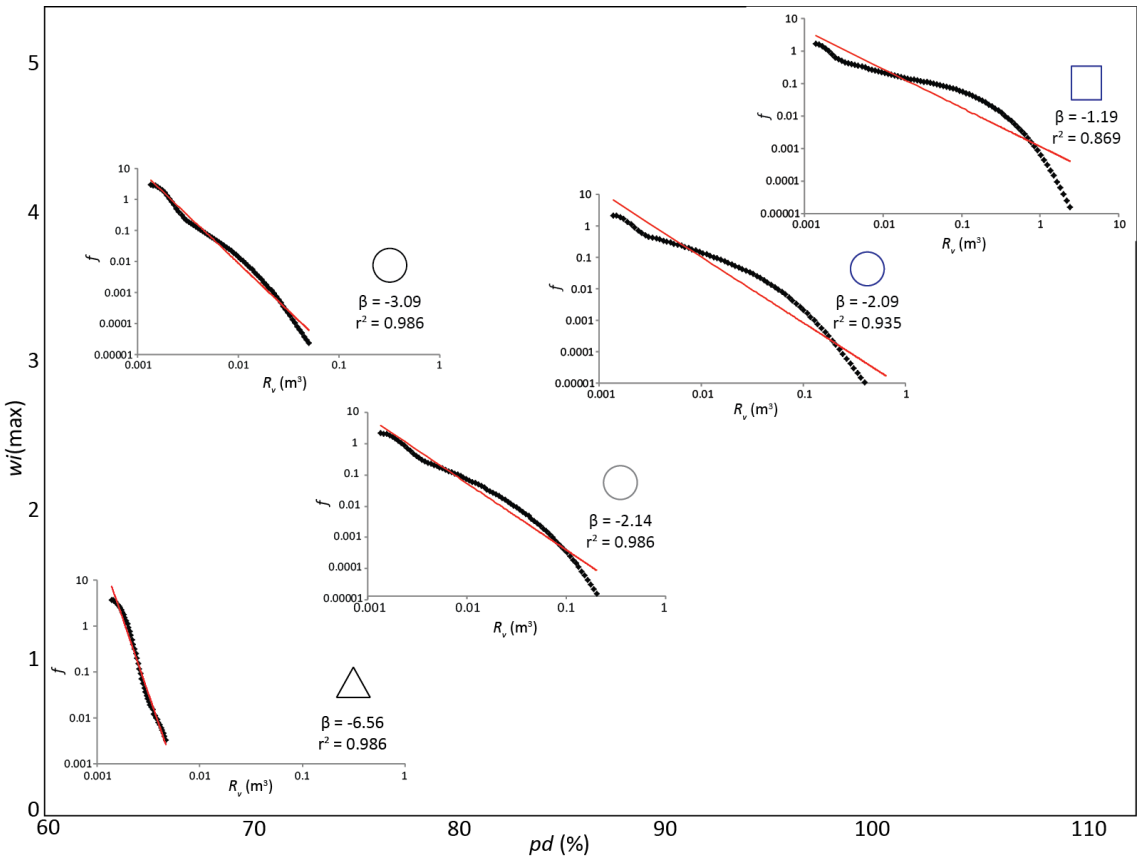

Figure 6.5: Volume-frequency plots representative of the range of vol-freq plots produced from each model simulation run at different values of *wi* and *pd*. In each plot the symbol on the right corresponds to an envelope of behaviour in Figure 6.6b.

A summary of the model results from Figures 6.3 - 6.5 is shown in Figure 6.6a, where the resulting rockfall behaviour is categorised as one of five types based on both the occurrence and size of rockfalls (Fig. 6.3 and Fig. 6.5) and the resulting slope profile (Fig. 6.4):

- *propagation controlled*, whereby the propagation of rockfalls, driven by *pd,* is the dominant, if not only evident mechanism of erosion, generating larger rockfalls and often resulting in slope collapse;
- *propagation dominant*, whereby propagation of rockfalls appears the dominant mechanism of erosion, but evidence of the role of weathering is also apparent and the slope does not collapse;
- *propagation/weathering equal,* whereby the role of both *pd* and *wi* is evident and the slope maintains a near vertical profile with small-medium sized rockfalls and evidence of surface features developing;
- *weathering dominant*, whereby *wi* appears the dominant mechanism of erosion but some evidence of propagation is seen allowing small surface features to develop;
- *weathering controlled,* whereby *wi* is the only mechanism of erosion and a slow, uniform retreat of the profile is observed as only very small rockfalls occur.

Based on these five types of rockfall behaviour, the space occupied by the range of *wi* and *pd* values has been divided into envelopes of different behaviours (Fig. 6.6b). The envelopes of different behaviours coincide with increases in *wi* and *pd* as would be expected, but the transition between envelopes is close to a vertical orientation rather than a division of the space into quadrants as would be expected if *wi* and *pd* contribute equally to rockfalls. Therefore, the envelopes of different behaviours appear more heavily weighted towards *pd* values. The divisions between envelopes are not discrete boundaries, illustrating that this data represents a continuum of change rather than discrete transitions from one distinct behaviour to another.

The space occupied by the *propagation dominant* type of behaviour appears to replicate similar behaviour to that in the field (Chapter 3). This indicates that the size distribution and spatial propagation of rockfalls, and the resulting slope profile form, that occur in the field are dominated by the mechanism of stress transfer in the rock slope. If this is an adequate representation then small changes in the intensity of external forcing should not result in a significant change to the characteristics of the rockfalls.

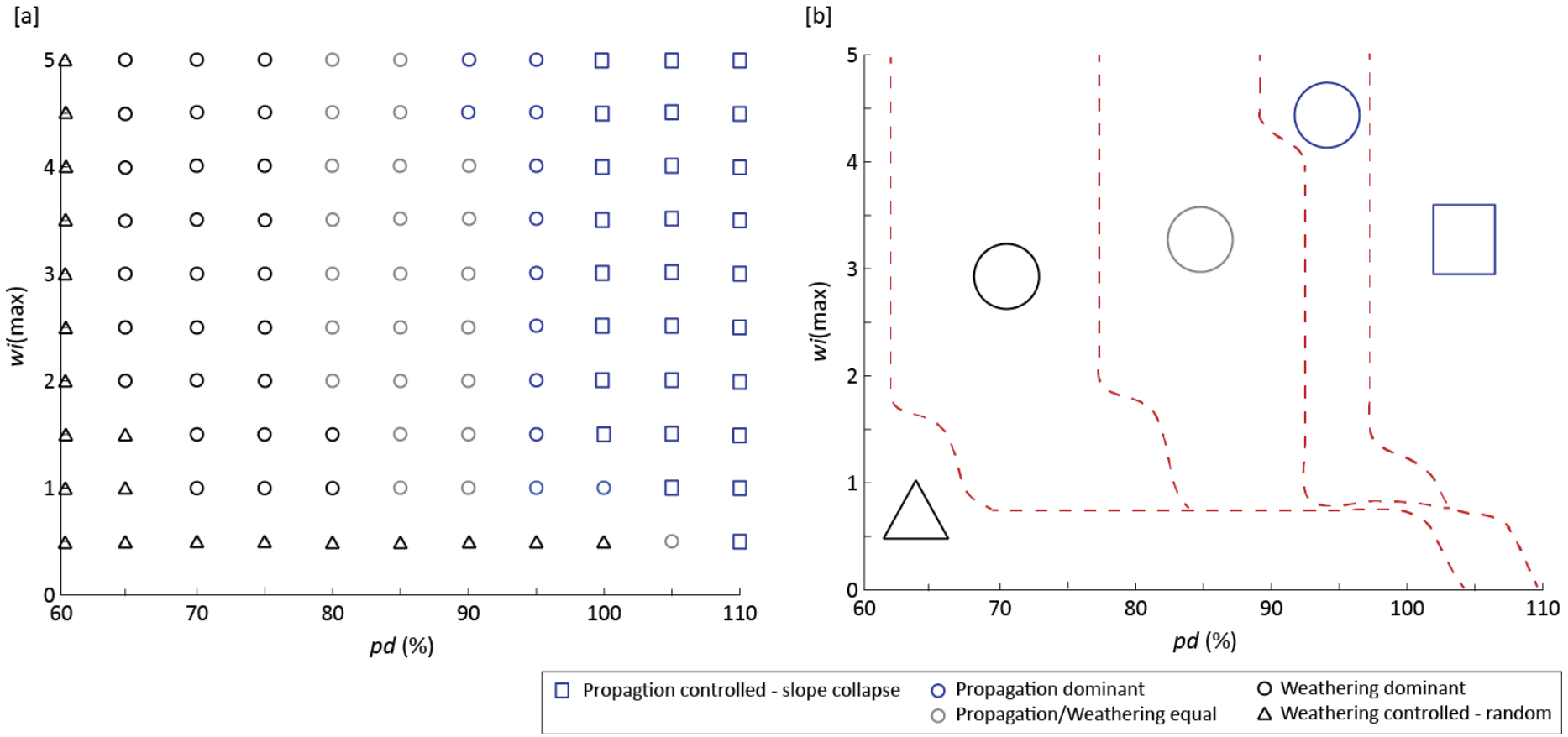

Figure 6.6: Plot of different rockfall behaviours identified for different combinations of *wi* and *pd*. [a] Rockfall behaviour observed when the rockfall model is run at a range of different *pd* and *wi* values. Each of the five symbols represents a different type of behaviour, as explained in the text; [b] Lines illustrate the boundaries of envelopes of different behaviours

The competition of internal and external processes and the resulting impact on rockfall behaviour and slope profile form considered in this modelling can be summarised by four main points:

(1) External processes such as environmental conditions that generate weathering are required to initiate and sustain rockfalls and overall rock slope erosion; however, external processes alone produce a limited distribution of rockfall sizes. In environments of intense weathering, where damage to the rock mass from external processes may outweigh that which is able to accumulate via internal processes, the overall slope profile in the model remains near vertical and recedes uniformly. The range of rockfall sizes generated will likely be small, dependent on the structural properties of the cliff, as weathering inhibits propagation generating larger rockfalls.

(2) Internal processes of stress redistribution within and across a rock mass are required to produce a larger distribution of rockfall sizes. The dependence of rockfall behaviour on the interaction laws of the model suggests some element of self-organised criticality underlying rockfalls behaviour. In a similar way to the Bak-Tang-Wiesenfeld model (Bak *et al.*, 1988), the rockfall model developed here demonstrates small instabilities that can propagate through the slope generating events of a range of sizes that adhere to a power law distribution. The variability in rockfall behaviour appears to be internally driven by time-dependent weakening within the model. In scenarios where internal stress redistribution is prevalent throughout the slope, such as within materials where crack propagation can easily occur, the slope tends to become sub-vertical through time as the upward and outward propagation of failures outpaces the removal of material directly by weathering.

(3) Environments where internal and external processes contribute equally allow a near vertical slope to be maintained whilst surface features, such as overhangs or protrusions tend to emerge on the slope face. The emergence and later failure of surface features appears to operate at a shorter timescale than any changes in the overall slope profile form.

(4) The overall rate of erosion of the rock slope varies in response to the relative contribution of internal and external processes in a multiplicative manner. For every rockfall removed by external forcing, the internal process of stress redistribution can multiply the consequences of this event by transferring stress to neighbouring areas of the rock mass surface. As a result, for any given increase in external forcing (*wi*), the resulting increase in erosion will be greater as the rate of internal processes (*pd*) increases (Fig. 6.7).

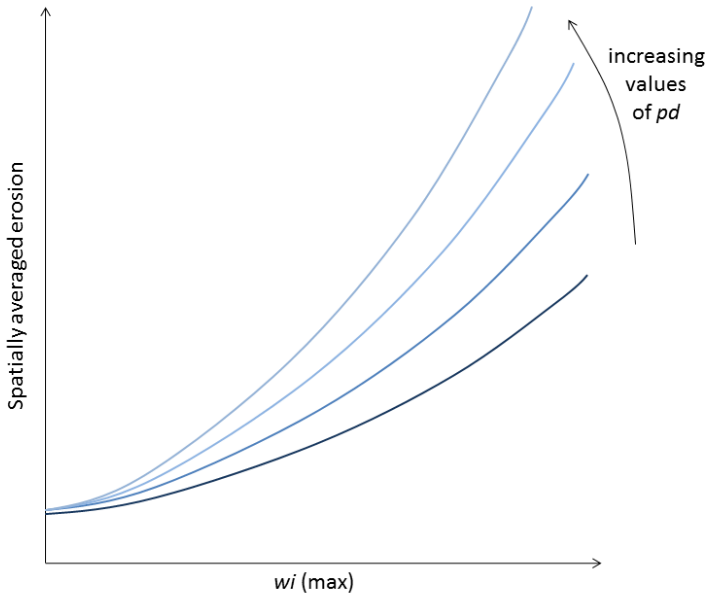

Figure 6.7: Conceptual figure illustrating the changes in spatially averaged erosion in a rock slope as a result of increasing weathering intensity (*wi*) and increasing values of damage transfer (*pd*).

6.6.1.1 Interpretation of coastal cliff profiles

Results have suggested the observable impacts of the internal and external process competition upon the surface of rock slopes in driving rockfalls. This knowledge can be used to aid interpretation of the driving processes in different rock slopes. Figure 6.8 displays four different slope profiles along a 4.2 km stretch of coastline in North Yorkshire, UK (Swirad *et al.*, 2016), which were used to demonstrate how the driving processes could be interpreted from slope profile data. These cliff profiles (Fig. 6.8) were chosen as they represent some of the variation that exists in hard rock slopes in a coastal environment and were taken from a DEM with a high spatial resolution (0.04 m^2 pixel resolution) (Swirad *et al.*, 2016).

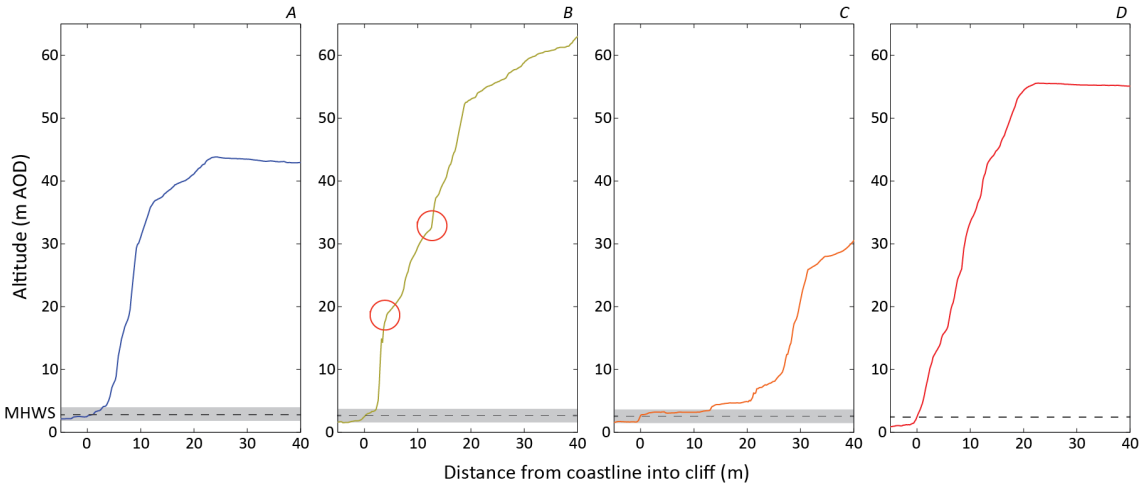

Figure 6.8: Slope profiles generated from airborne LiDAR data of the North Yorkshire coastline, UK, as published in Swirad *et al.* (2016, p.614). Each of the four profiles shown (A-D) represents a typical slope profile form from this stretch of coastline and the full range of observed profiles are shown in Swirad *et al.* (2016, p.614). The grey shaded box highlights the protruding toe where it is observed at the base of the cliff around the mean high water spring (MHWS) tide level. In profile B there is a clear lower, middle and upper section to the profile, separated by steps in the cliff face profile where there are sharp gradient changes. These steps are highlighted by the red circles on the plot.

Three of the four profiles in Figure 6.8 display a protruding toe around the height of the mean high water spring (MHWS) tide level. As demonstrated in Figure 6.4, a protruding toe develops more clearly when the ability of stress to transfer within the rock mass is increased in the model. This suggests that the rate of weathering at the base of these cliffs is outpaced by upward propagation above this, otherwise a notch may be expected to form. The presence of the cliff toe protrusion could also be a factor of differences in the rock mass properties here: the cliffs are predominantly composed of shale, but a layer of mudstone is often exposed at the base of the cliff, which may govern the slower rate of erosion in this part of the slope. In all four profiles shown, the cliff face is sub-vertical (c. 10-20° from vertical) with small scale roughness evident in the cliff profile (Figure 6.8). Similar profiles were produced by the rockfall model when *pd* was set at 100% (Figure 6.4). Despite any increases in the weathering intensity, the sub-vertical profiles were not generated at lower values of *pd*. This further supports the interpretation that *pd*, and therefore upward propagation of rockfalls, was significant for controlling rockfalls in this case. The stepped cliff profile, with three distinct sections observed in profile B (Figure 6.8) has not been generated by the rockfall model simulations undertaken or presented here, although some surface features such as overhangs have been generated. However, simple geology was represented in the model, whereas the profiles shown in Figure 6.8 are taken from cliffs with a heterogeneous lithology and a wave impacted zone at the base. Profile B suggests that there are certain features and slope profiles that cannot be explained

by the internal-external process competition and therefore require other rock mass properties and environmental factors to be accounted for, such as different sequences of rock mass strength. The following two sections of this discussion will address both environmental factors and rock mass properties.

6.6.2 The role of enhanced weathering zones for driving rockfall occurrence

The evolution and retreat of hard rock cliffs is expressed by Sunamura (1992) as the ratio between the assailing forces (F_A) and the resisting forces of the cliff material (F_R), where F_A comprise different zones of environmental forcing, for example marine and subaerial in the case of coastal cliffs. Observations of the sequencing of rockfalls across the cliff surface have challenged established conceptual models of how rock cliffs fail. In particular the models that focus on the role of the enhanced weathering at the base of coastal cliffs, or likewise cliffs undercut by other fluvial processes, such as rivers, and the resulting cantilever failure of material above (Sunamura, 1992; Young and Ashford, 2008). If established models of cliff erosion are not representative of field data then this raises two questions for how cliff profiles change in response to enhanced weathering: (1) Do zones of enhanced weathering always create a notch, especially in environments where small rockfalls dominate cliff behaviour through processes of progressive failure? (2) In cliffs where a notch is present, does the notch dominate overall cliff behaviour, in regards to rockfall occurrence and spatially averaged erosion?

Cliff profiles taken from the field dataset presented in Chapter 3 (Fig. 3.28, 3.34) do not display persistent notches at the cliff toe. Over two years of monitoring no evidence of large, cantilever-type failure is seen. Conversely, the spatial patterns of erosion show that there is a higher amount of erosion towards the cliff toe within the inundation zone, suggesting that enhanced weathering in this zone does not generate a notch feature. Evidence of rockfalls propagating across the boundary between the inundation and non-inundation zone (Case Study 1 in Chapter 3), suggests that small scale rockfall propagation inhibit the development of a persistent notch. By simulating a zone of enhanced weathering at the base of the modelled slope, the rockfall model has illustrated the magnitude of *wi* at the base that is required for a notch to develop, under different values of *pd* (Fig. 6.9). The resulting slope profiles (Fig. 6.9) show that zones of enhanced weathering do not always generate a notch in the rockfall model, supporting the field data observations (Fig. 3.28, 3.34) and illustrating the relationship between *wi* and *pd* that could explain the slope profiles observed. Additionally, the spatially

averaged erosion (Fig. 6.9), demonstrates that the interplay between *wi* and *pd* allows multiple scenarios and different profile forms to achieve the same erosion rate (Fig. 6.10).

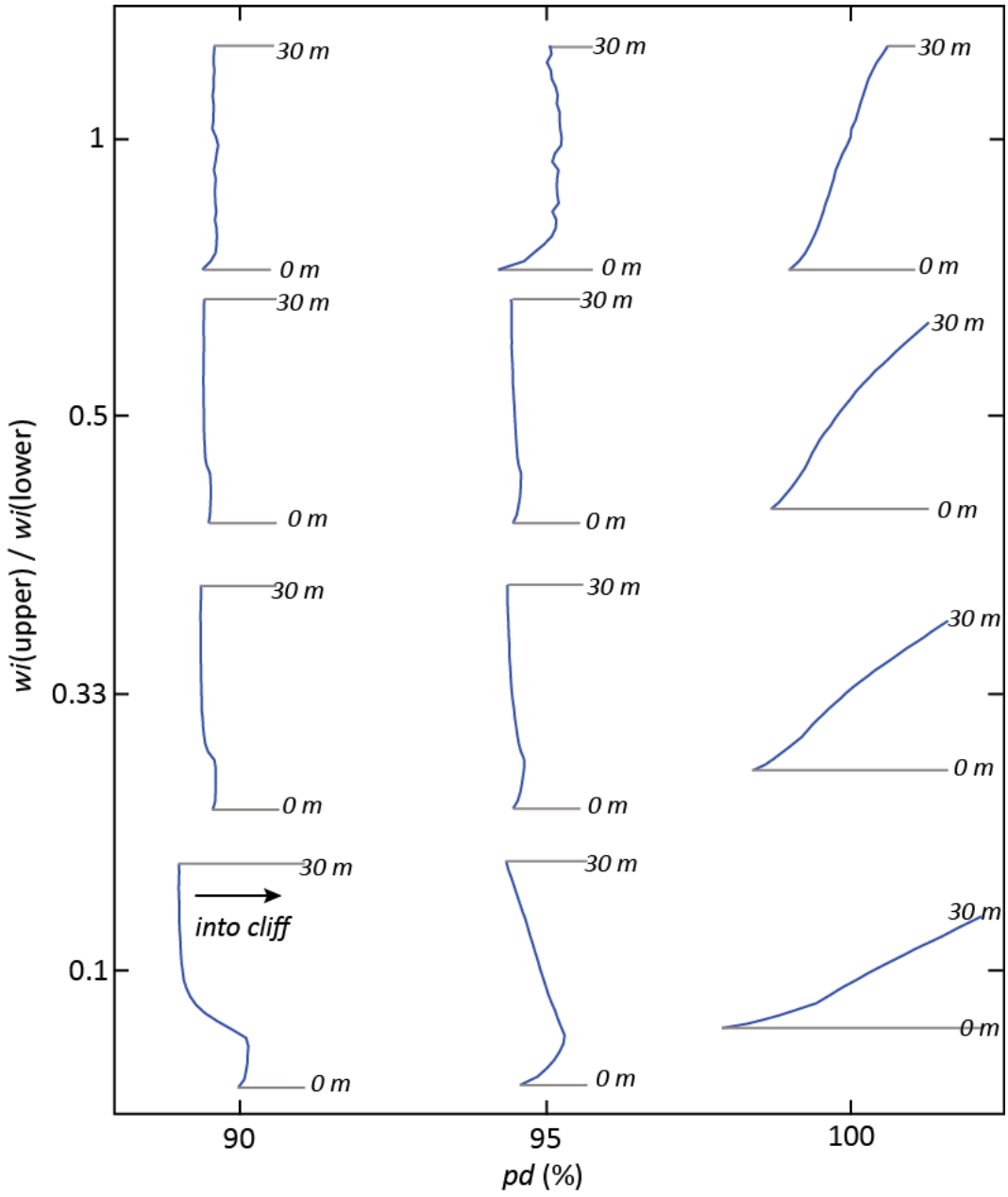

Figure 6.9: Changes to the cliff profile as a result of increasing *pd* (horizontal axis) and wi in the lower quarter of the slope (vertical axis). The vertical (y) axis denotes the ratio between wi in the upper 75% and lower 25% of the slope, such that at y = 0.1, wi in the lower 25% of the slope is 10 times higher than wi in the upper 75% of the slope; and at y = 1, wi is equal throughout the slope. Each of the profiles is 30 m high and is drawn to scale; the slope profiles are averaged over the entire cliff face. As *pd* increases, erosion increases in the upper portion of the slope and the slope begins to incline back into the cliff; when *wi* in the lower cliff is most pronounced (y = 0.1) a clear notch develops at the cliff toe, at *pd* = 90% and 95%; the notch at the cliff toe does not persist as clearly when *wi* in the lower cliff is reduced and in no scenarios where *pd* = 100%.

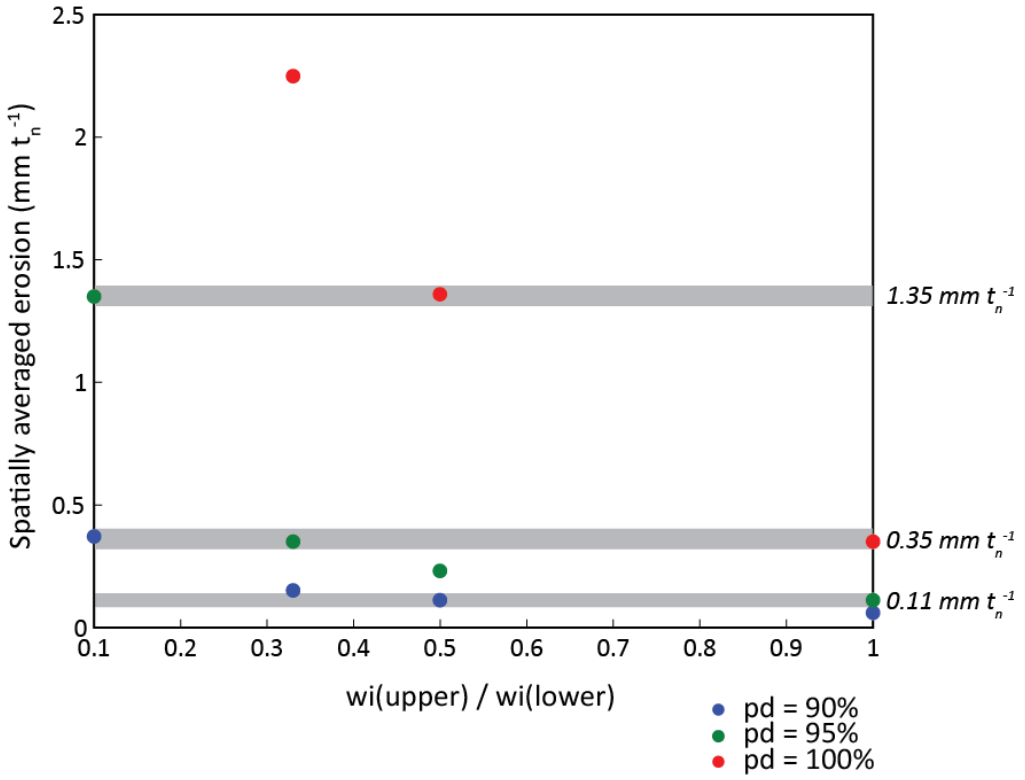

Figure 6.10: Spatially averaged erosion plotted against the *wi* ratio between the upper 75% and lower 25% of the model slope. Results are shown for model simulations run with different *pd* values. The spatially averaged erosion for *pd* = 100% and *wi* ratio = 0.1 is 5.64 mm t_n^{-1} – it is not shown on this plot so that differences between the rest of the data could be seen. Erosion rates are higher when *wi* in the lower 25% of the slope is increased, e.g. *wi* ratio = 0.1. As indicated by the grey bars, very similar erosion rates can be produced by multiple model setups, which exhibit different slope profile forms as seen in Figure 6.10. Each of the data points on this plot refers to a slope profile shown in Figure 6.9.

The development of a notch appears dependent on the combination of the *wi* intensity in the lower portion of the slope and *pd*. In the context of hard rock slopes where small rockfalls drive erosion, the development of a notch requires intensive weathering at the base of the slope coupled with a slow rate of stress transfer so that the notch has opportunity to develop. In the scenarios where notch does develop, for example *pd* = 90-95% and *wi* ratio ≤ 0.5 (Fig. 6.9), the distribution of failure sizes in the upper portion of the slope becomes more biased towards smaller failures than in the lower portion of the slope. The *ß* values of the failure size distributions are lower by an average of 0.2 in the upper portion of the slope. Alongside the evidence in the field dataset for rockfalls that propagate across the inundation/non-inundation zone boundary, this suggests that: (1) propagation out of the zone of enhanced weathering is in fact driven by small rockfalls that only appear as larger rockfalls when the temporal resolution of monitoring is lower; and (2) that if conditions permit a notch to develop to a

certain depth the erosion in the cliff above will be limited to smaller failures until block-type, cantilever failure occurs and resets the overall cliff profile (Makedon and Chatzigogos, 2012). In this case, the spatially averaged rate of erosion is higher (Fig. 6.10) owing to the high rate of erosion required to initiate and maintain the notch.

The results presented in Figures 6.9 and 6.10 have been developed in the context of hard rock, near vertical coastal cliffs and suggest that the conventional models of cliff erosion (Sunamura, 1992; Young and Ashford, 2008) do not always apply. This supports previous work (Young *et al.,* 2009; Lim *et al.,* 2010), who have shown that actively eroding coastlines often lack a concave notch at the toe; and have presented observational data that questions the dominant drivers of cliff erosion, in particular the role of marine and terrestrial forcing in a coastal environment (Lim *et al.*, 2010). The rockfall model presented here demonstrates that enhanced weathering at the cliff base increases erosion throughout the slope as shown by both the cliff profiles (Fig. 6.9) and the erosion rates presented in Figure 6.10. The observed impact of the weathered zone on overall slope erosion supports the work of Vann Jones *et al.* (2015) who established a strong relationship between microseismic data associated with marine processes and the occurrence of rockfalls across the entire rock face, indicating that the marine influences on rockfall activity could extend above the inundation zone rather than developing the classic concave toe notch. Although developed in the context of coastal cliffs, these results have implications for the erosion of steep, hard rock slopes in other environments where the slope is undercut such as waterfalls, rivers and steep gorges.

6.6.3 Structural controls and the persistence of features

Rock mass strength and the presence of discontinuities within the rock mass partly determine when and how a rockfall may occur (Stead and Wolter, 2015) and a range of studies have focused on rock mass characterisation in order to assess rockfall susceptibility (e.g. Sturzenegger and Stead, 2009a; Petley, 2012).

The role of surface topography as it interacts with the structural characteristics of the rock mass to determine failure size and location is considered by Krautblatter and Moore (2014) and identified at both large, regional scales (Leith, 2012) and at the local slope scale (Martel, 2006). However microtopographic surface features such as overhangs, protrusions and face parallel arches are not often characterised or considered with respect to rockfall susceptibility. Furthermore, many high resolution rockfall monitoring studies do not include a detailed rock

mass characterisation and therefore the consideration of rockfall occurrence in relation to structural features is lacking within our current understanding.

It is unknown how the observations of propagating contiguous rockfalls, interact with surface features on the rock slope and how surface features then impact on rock slope evolution either through promoting or reducing stability. Commonly, surface features on the rock slope emerge due to differences in rock mass strength and structural properties. Considering the observations of predominantly upward and outward propagation of rockfalls (Fig. 3.54) and that differences in rock mass properties are usually seen between different lithological bands that span across the width of a rock slope, the following questions arise: (1) If a propagating rockfall intersects a band of rock with a different strength and structural properties, how does this change the behaviour of that process zone? (2) How does the presence of a surface feature(s) impact on the size distribution of rockfalls and the overall slope evolution?

The field dataset presented in this thesis is taken from cliffs where near-horizontal bands of siltstone and sandstone and interbedded amongst weaker shale. Surface features are observed (Fig. 1.1) that form as a result of rockfall around them. These features have been observed to persist over the duration of this study and appear to drive rockfall behaviour (Fig. 3.29, 3.30). For example, the boundaries between geological layers, referred to as the transition zones, appear more active zones of the cliff as shown by the maxima of both rockfall count and failed area in these locations (Fig. 3.22 from Chapter 3). Rockfalls are seen to propagate through transition zones (Case Study Two, Chapter 3) in a manner that is potentially indicative of the role of stress transfer through the transition zone, which then generates damage within the rock mass via crack growth. The observation of the transition zones as more active zones on the cliff is supported by results of the rockfall model when a layer of stronger rock at different locations within the slope is simulated (Fig. 6.11). Once the base of the layer of stronger rock is weakened enough to fail, there is a sharp increase in rockfall activity in the transition area. This heightened activity at the transition zone is recognised in all model simulations, regardless of the size or location of the rock layer(s) (Fig. 6.11 and 6.12). By incorporating *pd*, the rockfall model has shown how propagating rockfalls can be stalled by a change in rock strength, often associated with a surface feature such as an overhang, and thus proceed to propagate outwards along this transition zone. The resulting profle form immediately above and below the more resistant layer of rock (Fig. 6.11 and 6.12) is similar to what is observed in the field. The failure notches noted in Figure 1.1c are located at a transition zone between geological layers, and overhangs in more resistant rock are observed (Fig. 1.1a). Notably, the failure notches are observed at varying elevations (Fig. 1.1c) as replicated by the model (Fig. 6.11).

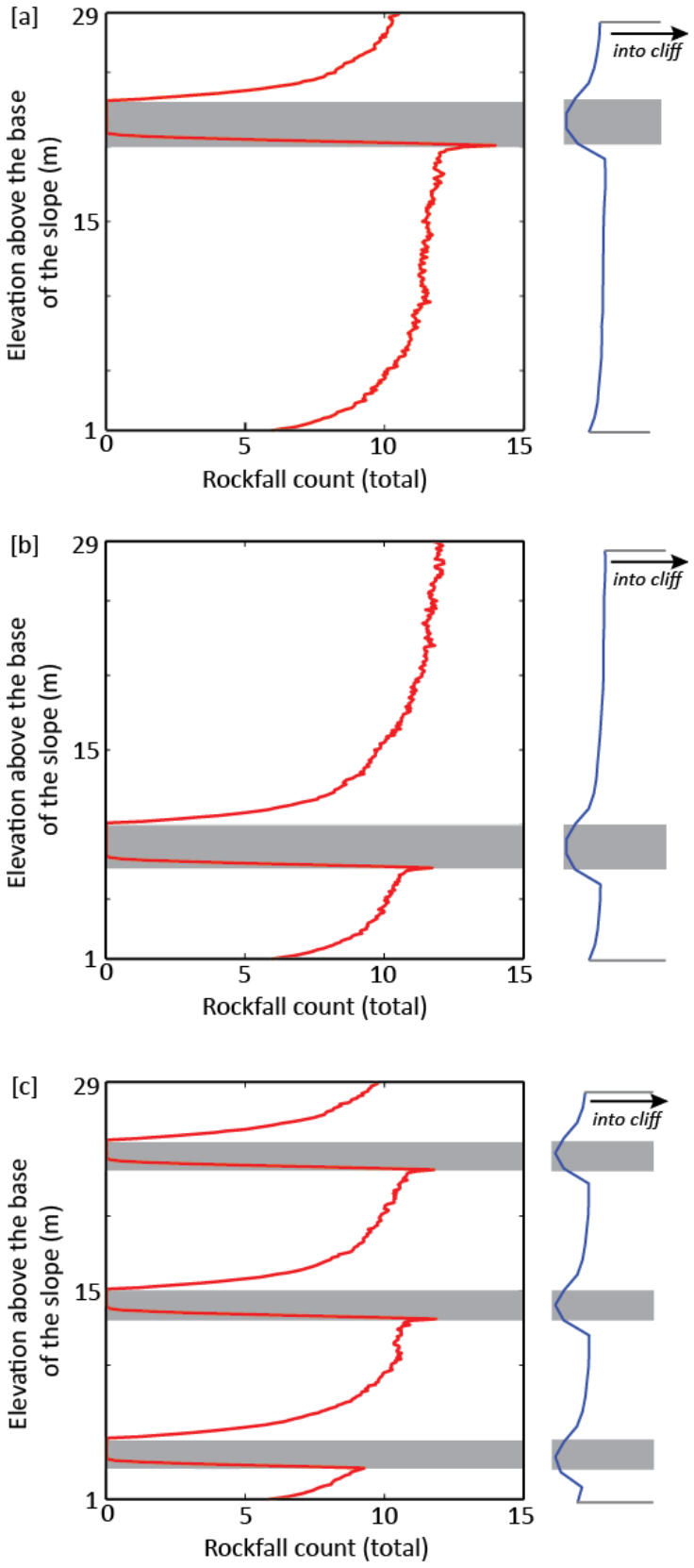

Figure 6.11: Rockfall count and resulting slope profiles for simulations run with a stronger layer of rock (GSI = 70; thickness = 3 m; 2 m in [c]) imbedded at different locations. The total rockfall count for every row (0.1 m) in the model space is shown plotted against the relative elevation above the base of the model slope (red line). The top and bottom metre are removed to avoid any boundary effects of the model. The grey shaded areas represent the layer(s) of stronger rock. The associated average cliff profile at the end of the model simulation (10,000 timesteps) is shown to the right of the plot.

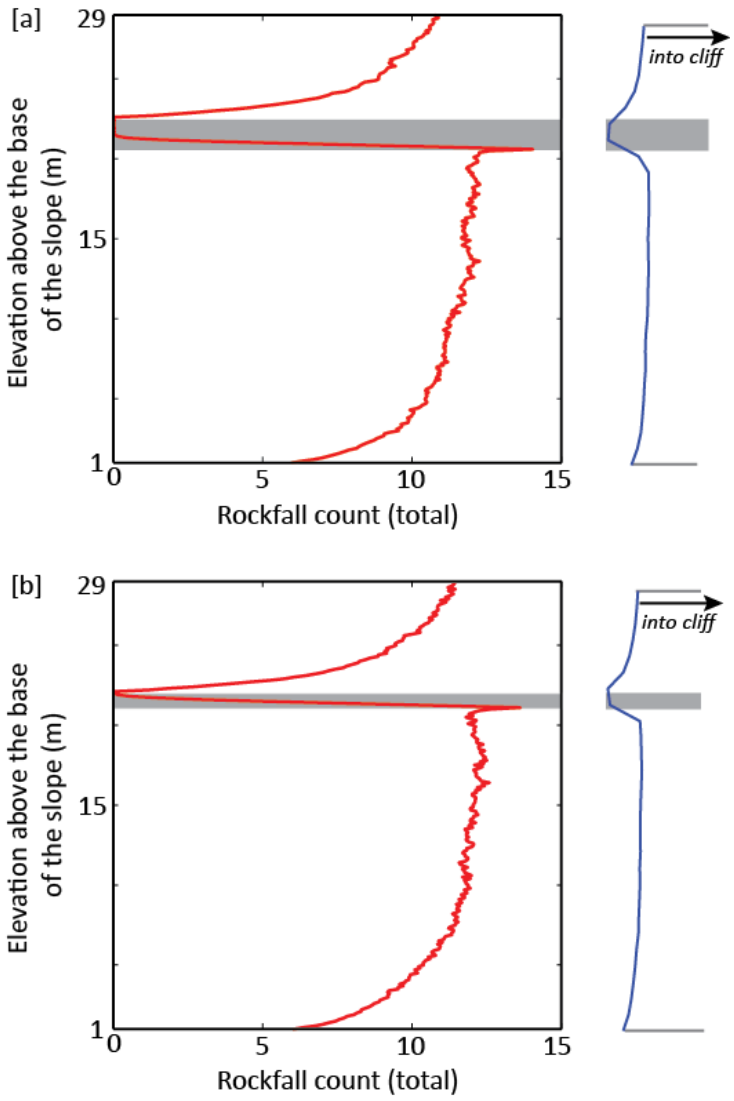

Figure 6.12: Rockfall count and resulting slope profiles for model simulations run with a stronger layer of rock (GSI = 70) of different thicknesses (a = 2 m; b = 1 m), imbedded towards the top of the model slope. Details of the plots are as given in Figure 6.12.

Including rock layers of different strengths within the rockfall model does not appear to impact significantly on the spatially averaged erosion of the slope (0.18 to 0.21 mm t_n^{-1}, where the height, strength and persistence of the layer of rock were varied). The implication of this finding is that over time, the rate of erosion of the modelled cliff is governed by the larger, weaker rock layer. This is also observed in the field data, whereby the temporal pattern in the erosion rate for the cliff is most similar to the temporal pattern in the erosion rate of the weaker, larger layers of rock (Fig. 3.38). The erosion rate in the strongest layer of rock (sandstone) displays a very different temporal pattern and does not appear to govern the overall cliff erosion rate (Fig. 3.38). The size distribution of rockfalls varies slightly as the

height, strength and persistence of the layer of stronger rock is varied and *ß* values of the size distribution power laws ranged from -1.52 to -1.68. As the weakest and largest layer of rock governs the rate of erosion in the cliff, the presence of more resistant layers of rock changes the size distribution, governing the range of failure sizes that occur. This corresponds to the notion that the exponents of size-frequency distributions should be constrained by rock slope properties (Barlow *et al.,* 2012). Although a unique correlation between the exponents of size-frequency distributions and specific lithologies is not always observed (Hergarten, 2003), the results presented here suggest that the overall distribution of different lithologies throughout the cliff do constrain the exponents.

Although the spatially averaged erosion is relatively consistent, the slope profile form changes due to the layer of more resistant rock (Fig. 6.13). Running the rockfall model with a stronger layer of rock imbedded near the top of the slope causes an overhanging surface feature to develop within this layer (Fig. 6.13). When the rockfall model is run for 40,000 time steps (Fig. 6.13), this surface feature persists through time and appears to influence the overall slope profile as the area below the surface feature retreats further than the area above.

The outputs shown in Figure 6.13 suggest either: (1) that external forcing and the interaction of small rockfalls can produce and sustain a slope morphology that would require larger rockfalls such as a block-type release (Stead and Wolter, 2015) to fail the cliff back to a uniform planar slope; or, (2) that in rock masses where sufficiently unstable joint structures do not exist, weathering and interactions within the near surface dominate the macro scale morphology of the slope face. The field data presented in Chapter 3 and in previous studies at this site (Rosser *et al.,* 2013) provide evidence for both (1) and (2) as similar surface features are seen in the more massively jointed, stronger layers of rock. These features fail predominantly as larger, block-type rockfalls, which then reset the slope profile to a near planar slope. The profiles generated by the rockfall model (Fig. 6.13) are close to those observed in the field and support the notion proposed in this study, that small scale rockfalls and their interactions can aid in explaining overall cliff behaviour, challenging the theory that overall cliff behaviour is dominated by the largest events.

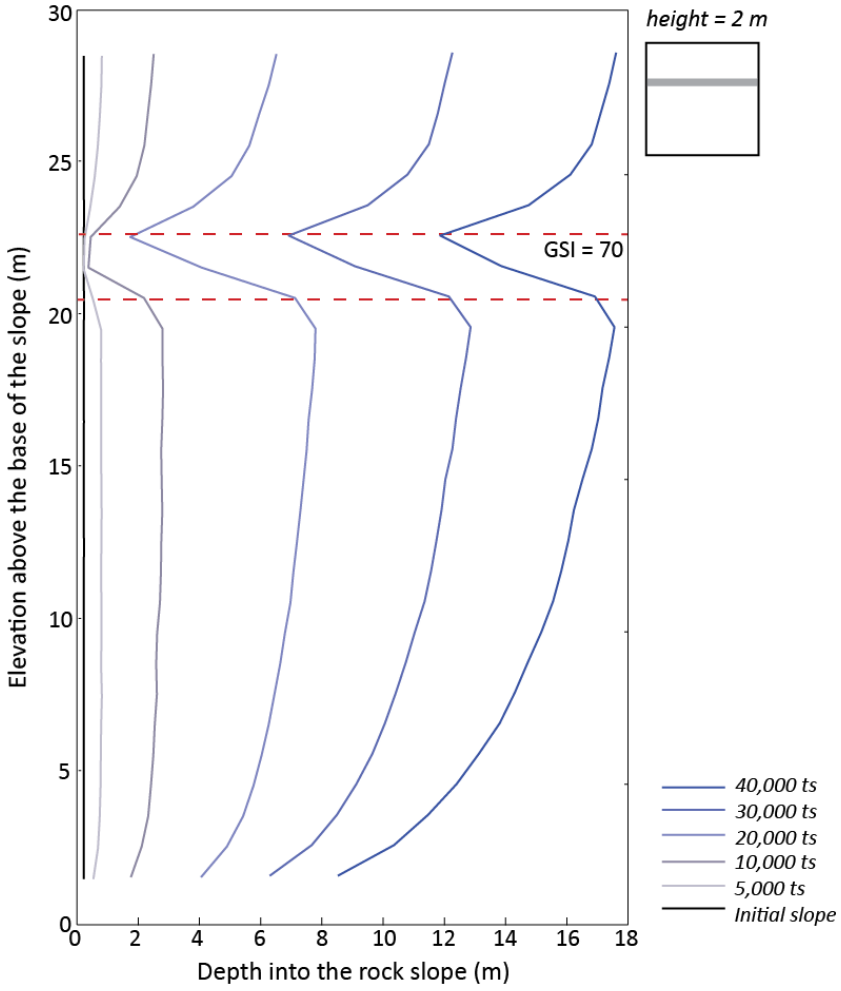

Figure 6.13: Average slope profiles for different stages within a model simulation run with a stronger layer of rock interbedded at 20.5 – 22.5 m elevation above the slope base (red dashed lines). The illustration to the right of the plot indicates the position of the layer of stronger rock on the model space (30 x 30 m). The slope profiles are averaged over the entire cliff face, and the top and bottom metre are removed to avoid any boundary effects of the model: the initial profile is shown in black and subsequent profiles shown in darkening shades of blue (see legend). The layer of stronger rock has generated a surface feature, which persists through the duration of the model simulation. The average size of the feature increases until *ts* = 20,000 and then appears to stabilise into a consistent form.

6.6.4 Are rock slopes likely to behave deterministically through time?

Monitoring of cliff erosion and the associated analysis of rockfalls is important for hazard assessment and mitigation. Assessing potential future change, particularly in light of predicted changes in climate (Murphy *et al.,* 2009), requires an understanding of how well past records can inform the future. Magnitude-frequency distributions are often used in hazard assessment and the improved resolution of monitoring data affords an accurate quantification of rockfall events and therefore more complete magnitude-frequency distributions. However, the size distribution generated from rockfall data can only be used for hazard assessment on the

assumption that the distribution is fixed through time (Dussauge *et al.*, 2003). The prediction of future events relies on the assumption that rock slopes behave in a deterministic way. Hazard assessment relies on an ability to forecast based on a subset of data and therefore the spatial and temporal extent of data that is needed to understand cliff behaviour and future patterns of change should also be estasblished. The amount of data required to accurately represent cliff behaviour can be considered from both field observations and model results.

For the cliffs in North Yorkshire, investigated in this study, it has been shown that there is little to be gained by measuring an area larger than 63 % of the full cliff size at this site over time scales ranging from one month to two years (Fig. 3.25). Whilst this result is likely to differ for different cliffs of varying sizes and rockfall characteristics, it indicates that the spatial extent of data required to understand cliff behaviour does not necessarily need to extend to the full extent of the study area. Many areas of a cliff surface fail repeatedly before a complete resurfacing would occur, as shown by Rosser *et al.* (2013). Until the cliff has completely resurfaced, any duration of the data will not be completely representative of cliff erosion and potential future change. Rosser *et al.* (2013) calculate that the cliff faces here would take an average of 28.1 years to resurface.

Variability in erosion throughout the cliff profile is demonstrated in the cliff profiles presented in Chapter 3 (Fig. 3.24), which show variability in both the failed area and rockfall count throughout the cliff profile. Likewise, profiles taken at different stages of the rockfall model simulations illustrate the variability in rock slope profile change through time for two different scenarios (Fig. 6.14). These plots show that within the simulation time of the model, the rock slope does not always retreat at a uniform rate at short timescales (10^0 to 10^1 years) and that the difference between the cliff toe, cliff top and various locations within the profile can increase through time over short timescales so that any single measure of retreat becomes less related to that of the whole slope. This highlights the potential for error in extrapolating retreat rates for future hazard assessment based on an estimation of recession of the cliff top (Young *et al.*, 2011). However, the left-hand plot in Figure 6.14 shows that when the model is run with *wi(max)* = 1, the retreat of the slope profile becomes uniform beyond 9,000 timesteps. At a higher *wi(max)* = 1.5 (right-hand plot in Fig. 6.14) this doesn't appear to happen over the duration of the model simulation time. This indicates that over longer timescales (10^1 to 10^2 years) a single measure of erosion, such as the cliff top, may be representative of the overall cliff behaviour at lower intensities of external forcing. Whilst in environments where external forcing is more intense, a single measure of erosion over the same timescales (10^1 to 10^2 years) may not be representative of cliff erosion.

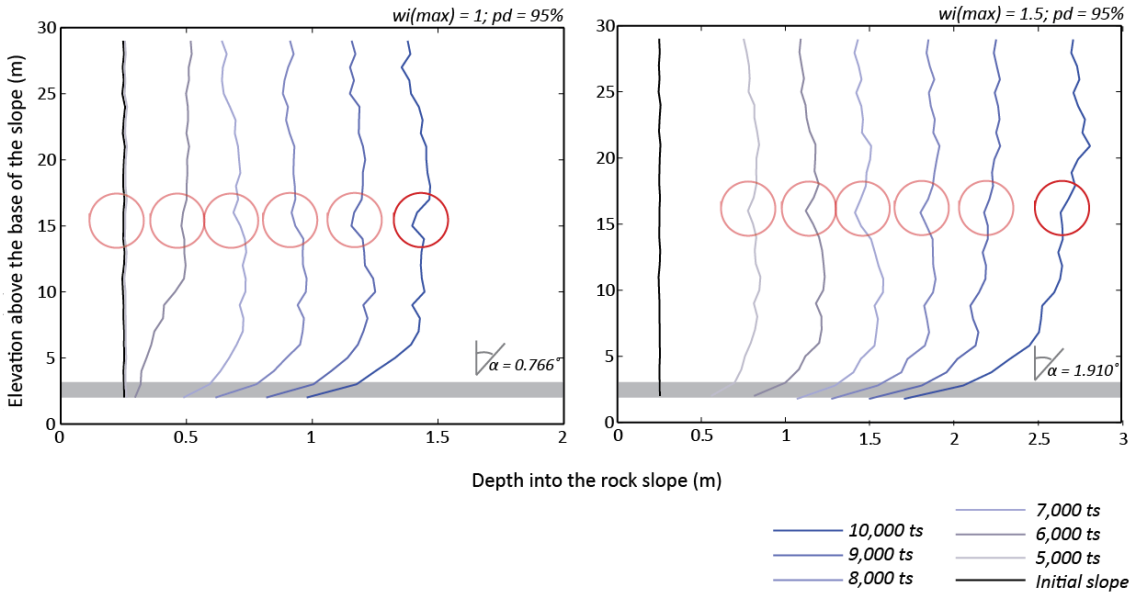

Figure 6.14: Average slope profiles for different stages in model simulations run at *pd* = 95%, with *wi* = 1 (left) and *wi* =1.5 (right). Slope profiles are averaged over the entire cliff face: the initial profile is shown in black and the subsequent profiles shown in darkening shades of blue. The final slope angle is also noted on the plot. The grey shaded area represents the bottom 1.5 m of the slope where a protruding toe can be seen to develop. The red circles highlight the development of a surface feature (overhang/protrusion).

The role of small rockfalls and their interactions upon the surface of a rock slope has been shown to provide an explanation for the observed size distribution of rockfalls. In addition, this research has been able to provide further explanation on the controls on the location and timing of rockfalls, and the resultant overall changes to slope profile form. This is evident in the results derived from the rockfall model which considers stress redistribution after small scale rockfalls and time-dependent weakening as key drivers. In doing so, the rockfall model has shown that incorporating stress redistribution in rockfall modelling increases the range of rockfall sizes generated, causing rockfalls to propagate and cluster. Simulating rockfalls based on time-dependent weakening also helps to explain the variations in the occurrence of rockfalls over time and the resulting non-parallel profile retreat of a rock slope subject to ongoing rockfall.

To summarise, the following key statements can be drawn from this research:

- Rockfall occurrence has been observed to be governed by the across-cliff growth and interaction of rockfall scars. The interactions between rockfalls at the surface may be a

controlling factor on the size, location and timing of rockfalls that can develop in any given setting.

- Stress redistribution at a sub-metre scale is a potential mechanism driving the sequencing of small rockfalls, and acts in combination with rock mass strength and environmental forcing to determine the development of rock slope profiles over longer time periods.
- Simulating rockfalls at the scale of small failures (< 0.1 m^3), rather than the overall stability of the whole slope, can reproduce the rockfall behaviour observed in the field.
- Application of the rockfall model developed here illustrates the range of slope profiles that can be produced from combinations of external and internal processes. These experiments show that the overall rate of profile erosion through time is set by the weaker and larger layers of rock in a cliff section.
- Notches generated by preferential failure at specific horizons appear in relation to variations in lithology in a cliff section, and are not always evident in relation to areas where there is an enhanced efficacy of weathering processes.
- Rock slopes appear to behave deterministically over long time scales, whilst over shorter time scales (≤ 10^1 years) the spatial and temporal extent of data that adequately represents a rock slope will vary depending on the rate and mode of rockfall generation.

7 Conclusions

7.1 Evaluation of the aim

The overall aim of this thesis has been to simulate rockfalls as a temporally- and spatially-dependent in order to better understand where, when and why rockfalls occur. This has been achieved through the four research objectives set and has resulted in a new rockfall model that simulates rockfalls as a function of accumulative damage, via spatially- and temporally-dependent sequences of events. The model outputs have demonstrated that the location of rockfalls is a function of rock mass properties, the combination of exo- and endogenic forcing, and the location of previous failures. The distribution of rockfalls across a slope indicates likely locations of future failures over short (management scale) time periods (10^{-1} to 10^{2} years). The point of failure can be simulated as a threshold of damage accumulation. Finally, the rockfall model has provided a better understanding of why rockfalls may occur, demonstrating that small rockfalls at the slope surface may be governed by the interactions between rockfalls in addition to exogenic forcing.

7.2 Conclusions

The overall conclusions of this thesis are presented here in the context of the four research objectives outlined in Chapter 1.

- O1: To look for patterns of rockfall distributions from field monitoring data that are indicative of a progressive failure mechanism.

Chapter 3 presented a two-year high resolution monitoring dataset of rockfalls in hard rock coastal cliffs in North Yorkshire, UK. Observations and analysis of this dataset revealed patterns in rockfall development across the space of the rock slope surface and through time including observations of contiguous rockfall propagation across the cliff face (Figs 3.22, 3.33); variations in the temporal patterns of rockfalls that point to a non-environmental and non-geological control (Figs 3.37 – 3.41); evidence that rockfalls cluster significantly at a range of scales in space and through time (Figs 3.47 – 3.49); and the upward and outward directionality expressed as rockfall scars grow (Figs 3.54, 3.56 – 3.57). These findings are indicative of a progressive failure process, likely driven by post-failure stress redistribution that promotes the generation of damage in neighbouring areas and subsequent rockfall propagation.

The scale at which the processes indicative of progressive failure appear to operate in these cliffs was revealed through the statistical analysis of clustering and proximity / directionality analysis. Rockfalls are observed to spatially cluster at a range of distances with a peak in the strength of clustering identified at 2 m. This distance is an indication of the spatial scale at which the mechanisms that allow rockfalls to cluster (such as stress transfer) occur. Proximity analysis revealed that rockfalls are more commonly contiguous to previous failures than a random distribution would be (Fig. 3.52), suggesting that the influence of one failure on another is seen most clearly in the immediate neighbouring areas above and alongside a failure. The statistical strength of contiguity was strongest over a time scale of four months, indicating a mean timescale over which mechanisms that drive contiguity occurs. If post-failure stress redistribution is the mechanism driving contiguous failures, then this would suggest a mean lag time of four months between initial stress transfer and subsequent failure. These spatial and temporal scales identified for the process of progressive failure also provides the necessary information to be used in developing an approach to rockfall modelling that is capable of simulating rockfall evolution in the manner observed here.

Whilst the observations and analysis presented in Chapter 3 are specific to the site of investigation, the unique methods of analysis of the data are applicable to both coastal and inland steep hard rock slopes. More broadly, the findings emphasise the need for rock slope models concerned with short-term and small-scale failure to move beyond the traditional profile perspective and consider the processes operating at the slope face in order to fully represent the mechanisms driving slope failure at the appropriate scales.

- O2: To evaluate when and under what conditions, time-dependent and spatially-dependent failure influences the characteristic scales of rockfalls.

The use of Slope Model to simulate rock slope failure at a sub-metre spatial resolution has demonstrated how the behaviour (magnitude and timing) of failures vary under different slope conditions and in relation to the development of fractures within the slope. This has been seen in the variations in timing between failure onset and critical failure under different slope conditions and in the recognition of fracture as part of the evolving failure process rather than a distinct trigger. Through these processes observed it is reasonable to determine that the timing of failure in a rock slope could be considered as a function of accumulated damage, represented by fracture. This supports the conceptual hypothesis put forward by Rosser *et al.* (2007a) that depicts the timing of failure events in response to a threshold in accumulated

damage. Furthermore, the spatial distribution of fracturing has shown that the location of failures seen at the slope surface can reflect concentrations of sub-surface fracturing but this appears restricted to larger (> 1 m^2) failures.

Taking brittle fracture as a physical representation of time-dependent failure, the simulations run in Slope Model have shown the influence of time-dependent failure on the location and timing of failure at the surface. Fracturing has been observed to concentrate above and alongside an existing rockfall, delineating the area in which subsequent rockfall then occur and therefore demonstrating how time-dependent failure can influence rockfall location. This supports the idea proposed by Stock *et al.* (2012) that spatially sequencing rockfalls are reflecting progressive stress re-distribution via sub-critical crack growth. The response of the model to altering rock mass properties has suggested that the timing of rockfalls is an internally driven process. The similar temporal behaviour seen in both fracturing and rockfall occurrence, further supports this and demonstrates the role of time-dependent failure in setting the timing of rockfall, as both fracturing and rockfall occur as part of an evolving process.

- O3: To develop an approach to simulating rockfalls as an evolving process that allows redistribution of stress and accumulation of damage through time.

The design, formulation and development of a new rockfall model was presented in Chapter 5 based on the approach of reduced complexity, interaction driven, cellular based models. Such models allow the spatial sequencing of events and have been applied to simulate other mass movement events including landslides (Hergarten, 2003) and glacier calving (Chapius and Tetzlaff, 2014). Applying these concepts to near surface rockfall dynamics allows the rockfall model to simulate rockfalls as an evolving and continuous process, at a scale commonly observed in new high resolution datasets, and allowing stress redistribution and damage accumulation to be incorporated. The rockfall model was developed based on four key criteria:

(1) Modelling at a slope face view;
(2) Modelling at a spatial resolution that the processes occur on;
(3) Considers time and operates across a range of temporal scales;
(4) Considers rockfalls as an evolving process, transferring stress from one rockfall to the neighbouring area, which can promote the generation and accumulation of damage.

The rockfall model focuses on simulating small scale (< 0.1 m^3) rockfalls as a function of damage accumulation through time and the interactions between rockfalls, which represent mechanisms of stress transfer and lateral confinement. The dominant processes operating in the model include weathering, stress transfer and damage accumulation, structural support amongst surface blocks, and time-dependent damage accumulation. Operating from a slope face perspective allows the rockfall model to consider the interactions and processes that occur across the slope face, as identified in monitoring studies where data is collected from the same perspective. By operating at a spatial resolution relative to the smallest failure size, processes of stress transfer are able to promote the generation of damage, which in turn may trigger subsequent rockfalls. This is unique to the rockfall model presented in this study and addresses the limitation of many existing rock slope models that are well suited to simulating larger scale slope failure (including 3DEC and Slope Model: Itasca, 2014), but are not applicable to simulating individual rockfalls at the slope surface and the associated failure mechanisms over the time scales and at the resolution considered here. Adopting a reduced complexity approach meant that the rockfall model was able to simulate rockfalls at a high spatial and temporal resolution, across a rock slope (10^2 – 10^3 m^2) and over relatively long time periods (10^2 years).

The approach taken in developing the rockfall model has demonstrated how the overall behaviour of a rock slope and the process of rockfalls observed in the field could be reproduced by considering small scale rockfall and the interactions between them, both as a function of accumulative damage. This supports the notion that the timing of rockfall events is governed by the accumulation of damage as a result of a variety of external and internal processes, as suggested by conceptual models of rockfalls (Rosser *et al.,* 2007a).

- O4: To use the new methodological approach to predict the evolution of rockfalls to demonstrate where and when rockfalls occur as a function of both external forcing and internal rock mass interactions.

Chapter 6 applied the rockfall model to address key research areas that apply to a wider range of research on rockfalls and rock slopes. These included: the competition of external and internal processes acting on the rock mass; the influence of enhanced weathering zones on rockfall occurrence and overall cliff profile form; the influence of rock mass structure on processes of rockfall propagation; and how rock slopes behave through time, considering whether past behaviour can inform predictions of future change.

Simulating rockfalls in a simplified and homogenous rock mass with uniform weathering conditions showed that observed rockfall behaviour is not solely the result of variability in external, environmental conditions and/or large scale rock mass structure. Rather the interaction rules that drive stress transfer and damage accumulation can govern rockfall behaviour. Application of the rockfall model to simulate variations in external, environmental conditions (*wr*) and internal stress transfer (*pd*) (Figs 6.3 – 6.6), demonstrated that external processes are required to initiate and sustain rockfalls and that these processes set the rate of spatially averaged slope erosion. In environments dominated by external processes, for example weathering limited rock slopes, the rockfall model showed that the range of rockfall sizes is small and limited to only a few grid cells as the rate of weathering inhibits large scale rockfall propagation driven by stress transfer. Conversely, the variability in rockfall behaviour appears driven by the internal processes of stress transfer and subsequent damage accumulation. In rock slopes where these internal processes outpace external, environmental processes, the model suggests that the rock slope would become sub-vertical as upward and outward propagation of larger rockfalls dominates erosion. The overall rate of erosion is shown to vary in response to internal and external processes in a multiplicative manner (Fig. 6.7); and the emergence and subsequent removal of features appears to operate at a shorter timescale than changes to the overall slope profile form.

Application of the rockfall model to simulate environments where zones of enhanced weathering exist, demonstrate that the interplay of external and internal forcing does not always generate a notch in the zone of enhanced weathering (Fig. 6.9). Instead, different slope profile forms can be achieved at the same spatially averaged erosion rate (Fig. 6.10). This demonstrates that in some cases equifinality in rock slope retreat can be explained by the interplay of external forcing and internal rock mass interactions. Furthermore, the internal stress transfer (*pd*) allows the influence of enhanced zones of weathering to extend far above their spatial extent, which is an important finding for rock slopes that are undercut such as sea cliffs, waterfalls, rivers and steep gorges.

Simulating stress transfer within the rock mass (*pd*) offered an explanation for the behaviour of rockfalls observed where a sequence of propagating rockfalls intersects a structural feature in the rock mass, such as a layer of stronger rock. Within the field dataset (Chapter 3) the transition zones at the base of a change in lithology were recognised as *active zones*, whereby rockfall count and erosion rates in these areas were higher (Fig. 3.26). Application of the rockfall model to include layers of stronger rock, demonstrated that a sequence of propagating

rockfalls can be terminated by a change in rock strength, and thus proceed to propagate outwards along this transition zone, increasing the level of rockfall activity in this area (Figs. 6.12 – 6.13). In the absence of sufficiently unstable joint structures the processes of weathering and interactions within the near surface region of the rock slope will dominate the macro scale morphology of the slope face.

7.3 Recommendations for future research

To build upon and extend the findings of this study, the recommendations for future research are outlined below in the context of both monitoring and modelling of rockfalls as an evolving process.

7.3.1 Monitoring rockfalls in hard rock slopes

Monitoring at a higher temporal resolution

The temporal resolution of the dataset presented in Chapter 3 represents an example of a high frequency monitoring study that is matched by few others (Abellán *et al.,* 2010; Stock *et al.,* 2012; Royan *et al.,* 2013) in addition to previous work at the same site (Rosser *et al.,* 2007a; Lim *et al.,* 2010; Barlow *et al.,* 2012; Vann Jones *et al.,* 2015). Despite the relatively high temporal resolution, the issue of superimposition still persists and it is probable that some of the rockfalls identified as individual events are in fact the sum of smaller failures. This leads to the assumptions that both the spatial proximity and temporal frequency of rockfall propagation is at, or above, the resolution of the dataset. To verify this assumption monitoring at a temporal frequency greater than one month is required. Constant near real-time monitoring over an extended (minimum of one year) time period, at a high spatial resolution, would provide data of rockfalls at a smaller scale. This would lead to a more accurate estimation of both the timing and spatial sequencing of rockfalls as the issue of superimposition would be negligible.

Investigating the role of surface topography

The correlation between curvature of the slope surface and the location and depth of rockfalls is not seen as clearly in larger rockfalls, where the local curvature values are calculated at a

resolution considerably finer than the failure size. The results suggest that curvature values calculated at a higher resolution to represent larger scale slope morphology might show a relationship with the occurrence of larger failures. To test this it is suggested that the slope curvature is calculated at a range of spatial scales. The results of this would be able to inform boundary conditions on curvature within a numerical model, where processes need to be represented at a spatial resolution corresponding to failure size (Stead and Coggan, 2012).

7.3.2 Numerical modelling of rockfalls

Exploring the role of surface features

Topographical surface features such as overhangs, protrusions and arches are observed to emerge on rock slopes as a result of rockfall activity, and often noted to develop to a consistent form. Subsequently, these features are observed to impact upon the location and development of rockfalls. The rockfall model has demonstrated this impact this can have on overall slope profile form. Explicit representation and detection of surface features in numerical modelling may offer further insight into the feedback process between surface features and rockfalls. For example, it is observed that areas of the rock face that form part of a larger surface feature are able to remain stable for longer periods of time, thus protruding from the cliff face without failing. To explore this and other potential feedbacks between surface features and rockfalls, further functions could be incorporated into the rockfall model to consider blocks of grid cells as distinct features and to dampen damage accumulation in these cells accordingly.

Applying the rockfall model to a wider range of environmental settings

The rockfall model has been applied to address questions pertaining to hard rock cliffs where weathering processes are uniformly distributed or where cliffs are undercut by hydrological processes, such as marine, river and waterfall environments, generating two distinct weathering zones. The rockfall model should be used to explore rock slopes where: (1) a wider variety of weathering zones operates; and (2) weathering processes are temporally variable, such as seasonal changes in high altitude environments, or diurnal temperature changes (Hales and Roering, 2007; Collins and Stock, 2016).

Both the methods of analysis and the approach to modelling rockfalls developed in this study could be applied to other geomorphological settings, in particular steep, hard rock slopes such as waterfalls, bedrock rivers and steep gorges. The spatial and temporal analysis of the rockfall dataset could be applied to rockfall datasets collected using TLS in a range of environments, in order to compare the scale at which the processes indicative of progressive failure appear to operate in different rock slopes. The exploratory approach to modelling rockfalls using cellular automata has demonstrated an alternative way to consider and simulate rockfalls. The model has demonstrated an ability to apply the concepts of interaction driven, cellular, self-organising systems to near surface rockfall dynamics. Similarly, these concepts could be applied to other geomorphological settings where surface change exhibits patterns and/or organisation to examine the potential for future change.

"There is nothing worse than a sharp image of a fuzzy concept"

A. Adams

Appendix 1: TLS rockfall data

Appendix 1.1: Summary of rockfall statistics for the two-year dataset (2012-14) collected at Boulby. 'Failure % by geology' shows the percentage of failures in each geologic unit; the percentage of the cliff area represented by each geologic unit is given in parentheses at the top of each column, and the totals given are the mean values.

Scan acquisition date	Rockfall count	Total failed area (m^2)	% cliff area failed	Total failed volume (m^3)	Surface averaged erosion (m)	Failure % by geology			
						Mudstone (24.7 %)	Shale (35.3 %)	Siltstone (26.2 %)	Sandstone (13.8 %)
19-06-2012	3149	382.5	2.4	100.6	0.0064	40.8	22.7	8.6	27.9
02-08-2012	3739	299.6	1.9	65.7	0.0042	37.2	37.1	11.8	13.9
30-08-2012	2517	222.8	1.4	58.4	0.0037	41.5	41.3	8.4	8.7
03-10-2012	4008	635.8	4.0	177.2	0.0113	37.7	31.3	12.7	18.3
15-11-2012	3870	327.1	2.1	76.2	0.0049	43.8	26.9	11.7	17.6
13-12-2012	3611	1179.5	7.5	1122.8	0.0715	9.2	13.1	14.6	63.1
16-01-2013	1850	370.7	2.4	394.3	0.0251	95.7	2.9	0.9	0.5
11-02-2013	1879	213.6	1.4	122.1	0.0078	74.0	9.6	12.7	3.7
12-03-2013	2532	203.1	1.3	70.8	0.0045	71.0	12.6	8.1	8.3
25-04-2013	2412	223.7	1.4	62.4	0.0040	61.5	18.4	12.6	7.5
25-06-2013	2088	260.2	1.7	89.1	0.0057	50.1	33.1	11.6	5.1
20-08-2013	2301	184.8	1.2	51.1	0.0033	55.6	27.6	9.7	7.1
17-09-2013	2586	262.2	1.7	76.9	0.0049	52.6	37.0	6.2	4.2
21-10-2013	1994	199.4	1.3	75.5	0.0048	77.8	16.3	2.5	3.4
18-11-2013	2288	216.2	1.4	84.6	0.0054	86.3	6.2	3.2	4.4
03-12-2013	2469	212.4	1.4	139.1	0.0089	10.1	81.8	3.3	4.8
18-02-2014	2741	1061.0	6.8	604.8	0.0385	77.6	19.0	1.8	1.5
18-03-2014	3251	300.7	1.9	97.1	0.0062	79.4	13.7	2.2	4.7
16-04-2014	2758	199.2	1.3	79.6	0.0051	50.5	37.3	4.8	7.4
14-05-2014									
18-06-2014	2032	294.8	1.9	130.3	0.0083	47.6	41.4	5.3	5.7
Total: 2012 - 14	***53805***	***7249.1***	***46.2***	***3678.7***	***0.2343***	***55.0***	***26.5***	***7.6***	***10.9***

Appendix 1.2: Summary of rockfall statistics for the two-year dataset (2012-14) collected at Section 1. 'Failure % by geology' shows the percentage of failures in each geologic unit; the percentage of the cliff area represented by each geologic unit is given in parentheses at the top of each column, and the totals given are the mean values.

Scan acquisition date	Rockfall count	Total failed area (m^2)	% cliff area failed	Total failed volume (m^3)	Surface averaged erosion (m)	Failure % by geology			
						Mudstone (10.9 %)	Shale (45.0 %)	Siltstone (40.1 %)	Sandstone (3.3 %)
19-06-2012									
02-08-2012	603	197.415	6.281481	81.14244	0.025818	9.352825	67.01941	23.29852	0.32925
30-08-2012	441	24.4225	0.777091	7.167062	0.00228	4.091879	75.69279	19.9619	0.253431
03-10-2012	500	64.94	2.066304	17.48918	0.005565	5.744963	64.96298	23.90781	5.384245
15-11-2012	256	41.8375	1.331213	12.01651	0.003823	7.649776	48.17798	42.79775	1.37449
13-12-2012	557	108.825	3.462666	47.67758	0.01517	0.686102	11.49957	5.238361	82.57596
16-01-2013	479	53.1825	1.692196	14.33608	0.004562	11.21532	28.74278	57.17491	2.866988
11-02-2013	528	60.8875	1.937359	17.62067	0.005607	1.665204	51.93984	44.5266	1.86835
12-03-2013	364	24.965	0.794353	4.870424	0.00155	8.307229	37.29349	53.42127	0.978008
25-04-2013	465	56.825	1.808095	13.81078	0.004394	2.278655	39.81317	55.37155	2.536622
25-06-2013	504	119.4	3.799148	41.21342	0.013114	2.900576	25.82902	70.44306	0.827341
20-08-2013	226	71.76	2.283307	26.58493	0.008459	1.092524	16.30988	81.22255	1.375044
17-09-2013	346	35.8125	1.139506	8.643913	0.00275	7.685593	73.36022	18.86204	0.092152
21-10-2013	356	35.955	1.14404	14.72439	0.004685	10.83422	82.21081	6.811484	0.143477
18-11-2013									
03-12-2013	285	92.895	2.955794	33.55232	0.010676	3.982557	38.04304	31.43034	26.54407
18-02-2014	523	322.405	10.25849	178.0547	0.056655	1.623501	95.693	2.515416	0.168088
18-03-2014	243	14.3475	0.456518	3.205469	0.00102	5.735428	49.38369	42.89937	1.981511
16-04-2014	463	65.3375	2.078952	22.34851	0.007111	2.312398	54.09848	41.52819	2.060933
14-05-2014	309	38.1625	1.21428	11.42956	0.003637	8.054238	55.1757	36.63827	0.131791
18-06-2014	321	45.6075	1.451169	16.08849	0.005119	7.393816	76.38961	15.66151	0.555067
Total: 2012 - 14	***7769***	***1474.983***	***46.93197***	***571.9764***	***0.181995***	***5.400358***	***52.19134***	***35.45847***	***6.949833***

Appendix 1.3: Summary of rockfall statistics for the two-year dataset (2012-14) collected at Section 2. 'Failure % by geology' shows the percentage of failures in each geologic unit; the percentage of the cliff area represented by each geologic unit is given in parentheses at the top of each column, and the totals given are the mean values.

Scan acquisition date	Rockfall count	Total failed area (m^2)	% cliff area failed	Total failed volume (m^3)	Surface averaged erosion (m)	Failure % by geology			
						Mudstone (9.2 %)	Shale (36.6 %)	Siltstone (37.8 %)	Sandstone (16.3 %)
19-06-2012									
02-08-2012	978	93.4225	1.938596	16.47853	0.003419	19.82144	17.44124	35.42353	27.29418
30-08-2012	167	12.8325	0.266285	2.323096	0.000482	25.33333	6.015983	49.87793	18.73593
03-10-2012	277	20.0075	0.415173	4.565382	0.000947	46.86611	16.73319	26.16957	10.23113
15-11-2012	337	94.245	1.955664	46.35249	0.009619	0.711645	4.361269	92.6139	2.312461
13-12-2012	500	141.7325	2.94107	52.3356	0.01086	0.596059	6.686319	77.11691	15.60071
16-01-2013	321	79.4175	1.647981	36.17902	0.007507	1.582074	5.67589	84.50438	8.235408
11-02-2013	947	111.0675	2.304745	27.18905	0.005642	12.69445	10.99965	21.59075	54.71309
12-03-2013	678	34.18	0.709264	6.070424	0.00126	4.306662	13.33829	41.75146	40.59891
25-04-2013	337	19.435	0.403293	3.165496	0.000657	7.695596	5.490613	52.32997	34.48382
25-06-2013	392	105.45	2.188177	36.02075	0.007475	0.171599	6.368314	84.78795	8.672135
20-08-2013	252	14.9075	0.309343	2.489555	0.000517	11.89914	12.32819	30.326	45.41282
17-09-2013	186	17.95	0.372478	4.822554	0.001001	1.665837	14.29391	70.79038	13.24987
21-10-2013	179	10.46	0.217054	2.301087	0.000477	28.63852	29.70827	8.103172	33.55004
18-11-2013									
03-12-2013	271	20.3375	0.42202	4.961843	0.00103	61.48981	18.54181	13.239	6.712384
18-02-2014	534	58.8025	1.220202	14.3394	0.002976	3.112302	32.44876	44.67194	19.75918
18-03-2014	260	13.1325	0.272511	3.293376	0.000683	52.80358	9.210046	24.61964	13.33283
16-04-2014	307	26.1	0.541597	7.236107	0.001502	2.037421	1.367451	71.95224	24.64289
14-05-2014	142	6.0225	0.124972	1.318246	0.000274	23.16553	4.164385	40.46021	32.20988
18-06-2014	426	40.5825	0.842121	9.295334	0.001929	4.722681	14.02204	31.76487	49.48734
Total: 2012 - 14	***7491***	***920.085***	***19.09254***	***280.7373***	***0.058255***	***16.27967***	***12.06293***	***47.47862***	***24.17026***

Appendix 1.4: Summary of rockfall statistics for the two-year dataset (2012-14) collected at Cowbar. 'Failure % by geology' shows the percentage of failures in each geologic unit; the percentage of the cliff area represented by each geologic unit is given in parentheses at the top of each column, and the totals given are the mean values.

Scan acquisition date	Rockfall count	Total failed area (m^2)	% cliff area failed	Total failed volume (m^3)	Surface averaged erosion (m)	Failure % by geology			
						Mudstone (2.3 %)	Shale (63.2 %)	Siltstone (19.4 %)	Sandstone (15.1 %)
19-06-2012	801	77.965	1.26828	47.71641	0.007762	0.23666	93.43419	1.836177	4.492971
02-08-2012	895	94.19	1.532217	26.33125	0.004283	2.020133	88.094	5.662785	4.223083
30-08-2012	752	33.335	0.542271	8.605244	0.0014	13.25703	63.01627	9.543914	14.18279
03-10-2012	648	60.4225	0.982911	37.2316	0.006057	3.956423	87.00646	6.500169	2.536944
15-11-2012									
13-12-2012	835	77.3725	1.258642	18.25901	0.00297	1.575229	64.88303	18.66866	14.87308
16-01-2013	634	116.615	1.897012	105.843	0.017218	0.189509	87.92016	10.96898	0.921349
11-02-2013	575	103.3175	1.680697	44.73441	0.007277	0.032852	92.91855	3.172386	3.876211
12-03-2013	459	43.5925	0.709132	11.09651	0.001805	1.594701	90.69532	3.712986	3.996996
25-04-2013	456	331.3325	5.389887	331.0281	0.053849	0.011865	98.84991	0.582565	0.55566
25-06-2013	920	154.2325	2.508947	47.05065	0.007654	0.609525	63.40378	19.57747	16.40922
20-08-2013	902	59.7025	0.971199	15.19129	0.002471	0.470333	76.31069	10.5422	12.67678
17-09-2013	709	54.78	0.891123	11.38305	0.001852	0.383882	69.95917	5.298366	24.35858
21-10-2013	450	61.7425	1.004384	15.30913	0.00249	0.09156	90.14133	2.710418	7.056695
18-11-2013	790	77.065	1.25364	25.83163	0.004202	0.431606	91.84192	1.949238	5.777236
03-12-2013	284	14.1625	0.230386	3.052922	0.000497	2.672111	80.23571	4.337727	12.75445
18-02-2014	1294	256.0675	4.165528	90.0456	0.014648	0.403097	94.52758	1.02678	4.04254
18-03-2014	1695	135.2725	2.200519	20.67811	0.003364	0.02613	61.43074	7.373009	31.17012
16-04-2014	840	155.465	2.528996	96.49444	0.015697	0.03662	97.15858	0.94001	1.863726
14-05-2014	724	103.415	1.682283	62.7953	0.010215	0.703011	13.98118	82.98776	2.328052
18-06-2014	674	41.7025	0.678387	15.75012	0.002562	2.627567	69.1272	8.082045	20.16319
Total: 2012 - 14	***15337***	***2051.75***	***33.37644***	***1034.428***	***0.168274***	***1.566492***	***78.74679***	***10.27368***	***9.412984***

Appendix 1.5: Elevation plots for individual monthly datasets

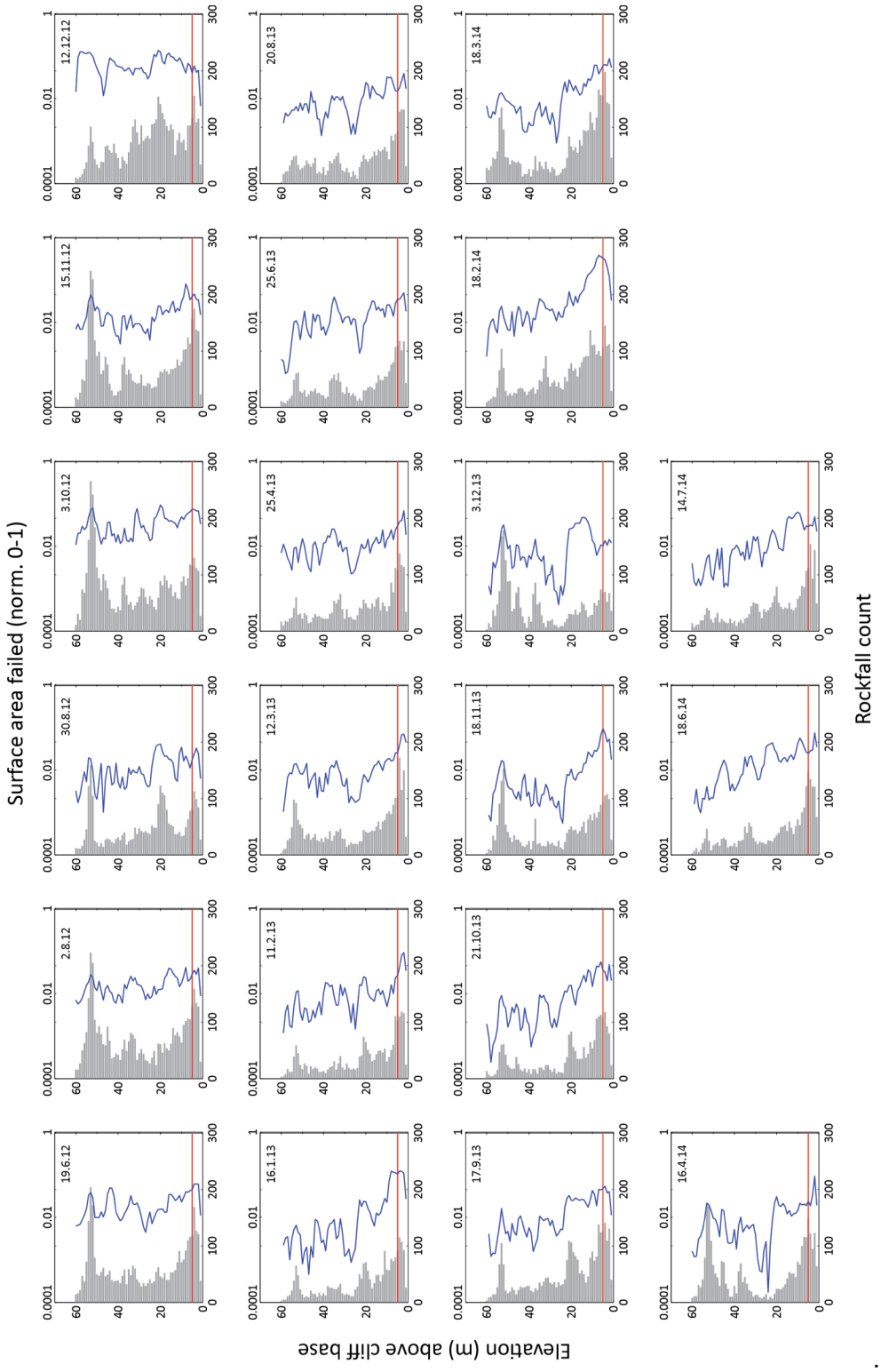

Variations in rockfall count (grey bars) and surface area (blue line) with elevation (0 m = cliff base) for ***Boulby***

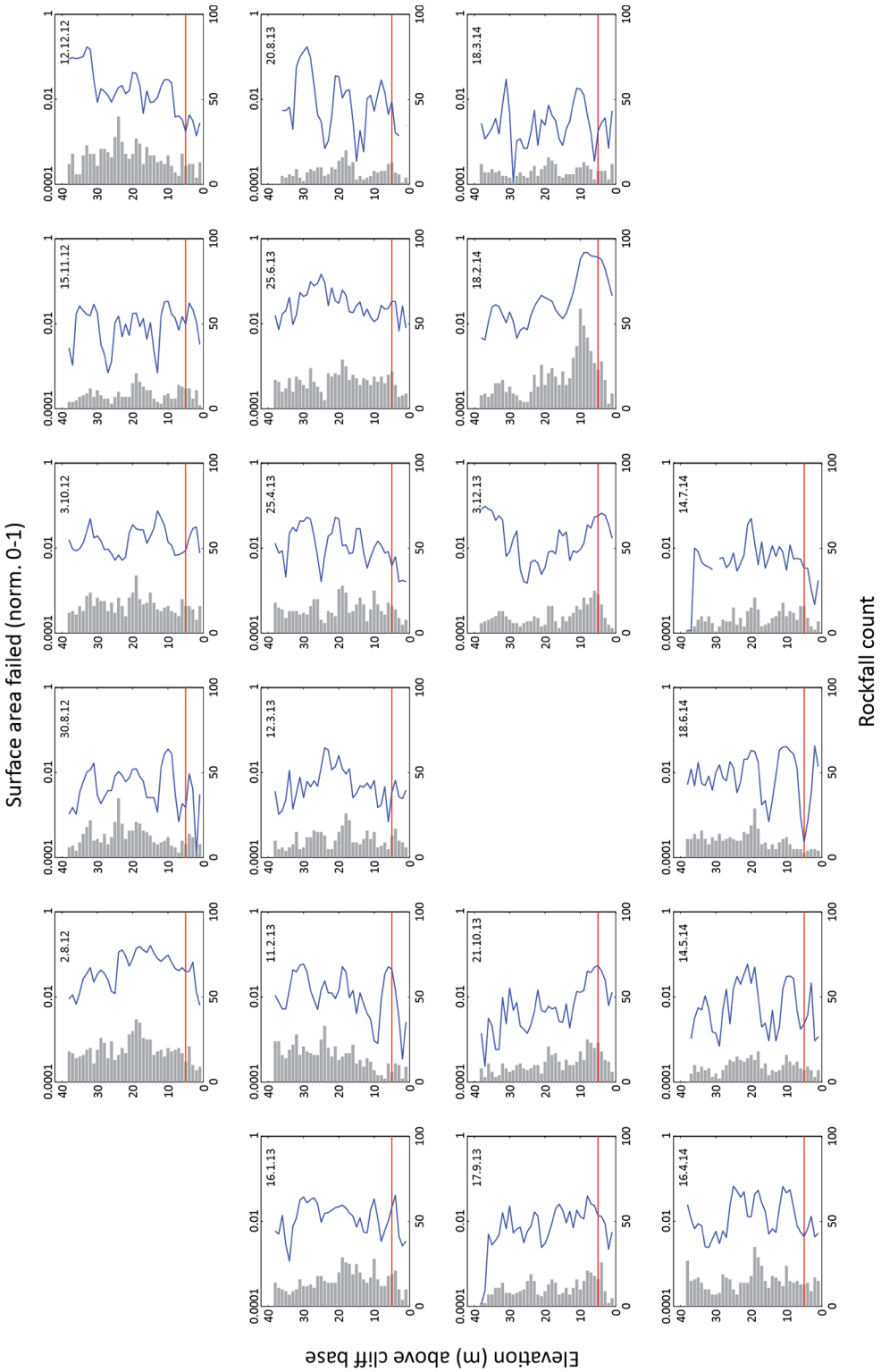

Variations in rockfall count (grey bars) and surface area (blue line) with elevation (0 m = cliff base) for ***Section 1***

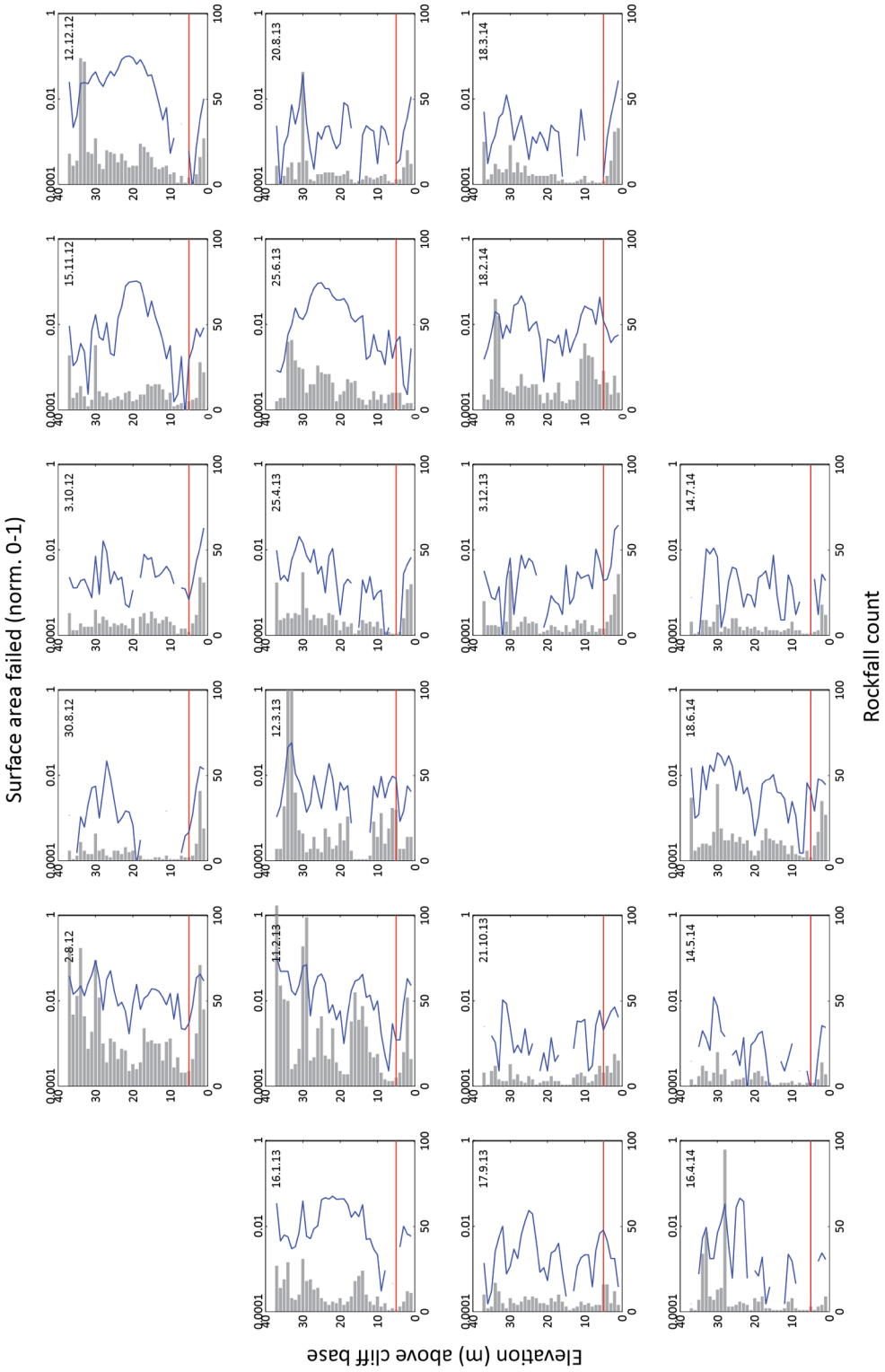

Variations in rockfall count (grey bars) and surface area (blue line) with elevation (0 m = cliff base) for ***Section 2***

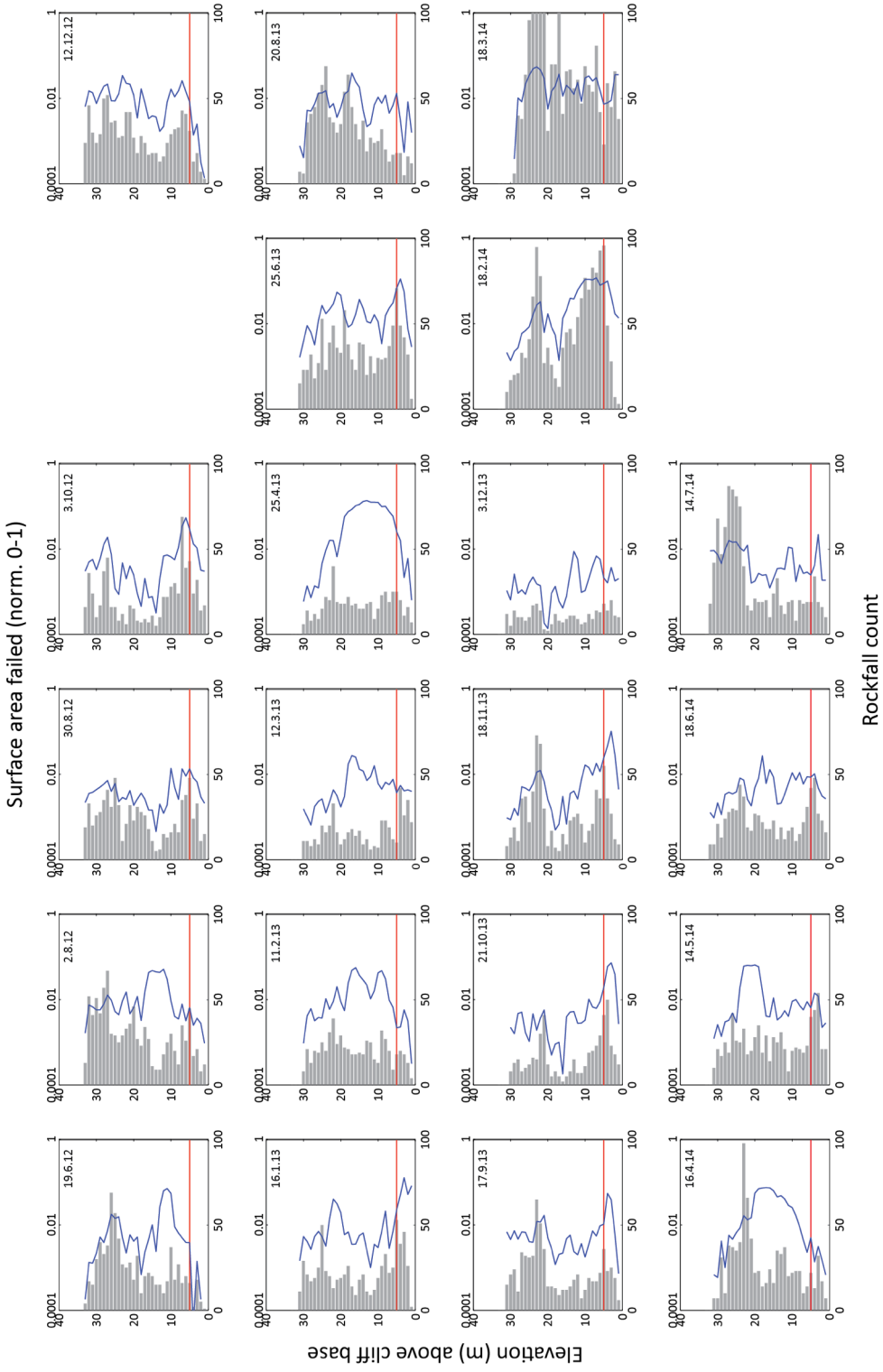

Variations in rockfall count (grey bars) and surface area (blue line) with elevation (0 m = cliff base) for ***Cowbar***

Appendix 1.6: Recurrence interval data

Temporal patterns in the rockfall behaviour can be observed by considering the recurrence interval of rockfall of different sizes. The recurrence interval of large scale geological events (> 10^7 m^3) has been shown to fit an exponential distribution in multiple environments (Korup and Clague, 2009). The rockfall data presented in this study is at a much smaller scale (< 10^2 m^3) and the exponential behaviour is still observed. The figures below show the recurrence interval (RI) plotted against rockfall volume (R_V) for the two years of monitoring data at each field site. In each plot a positive exponential relationship is seen between RI and R_V, represented by a power-law as given on the graph. The scaling coefficient (*ß*-value) is the slope of the power law and ranges from 0.6585 (Section 1) to 0.7848 (Cowbar). Overall the behaviour is similar at each field site despite any differences that may be expected owing to the differences in slope morphology and exposure at each site (Chapter 3).

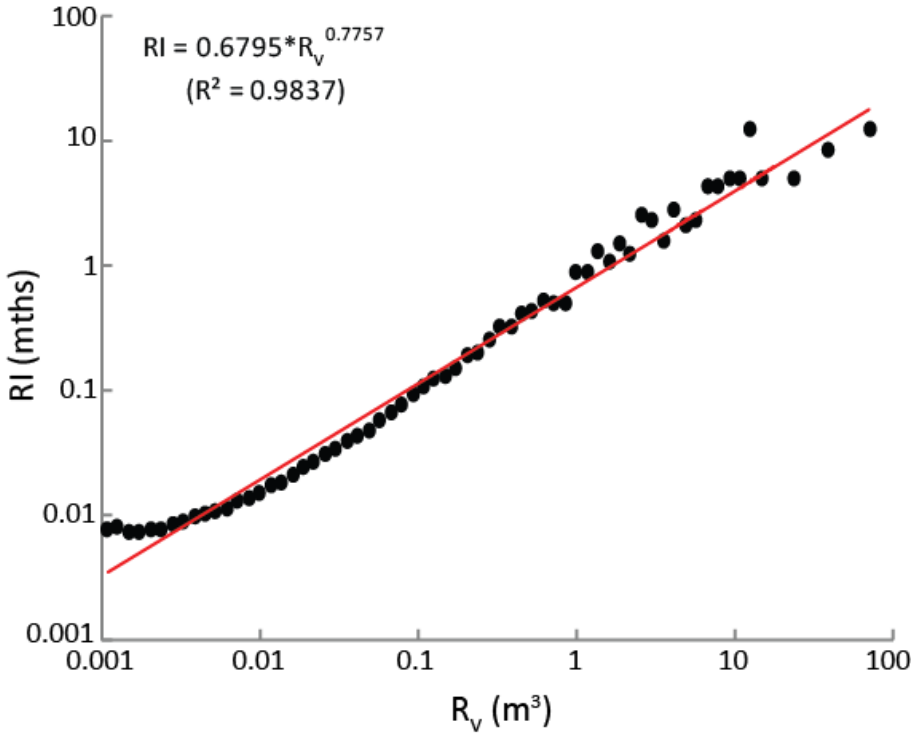

Recurrence interval (months) for different rockfall volumes (m^3) at ***Boulby*** based on 53,805 rockfalls that occurred between June 2012 and June 2014 over 15,702 m^2.

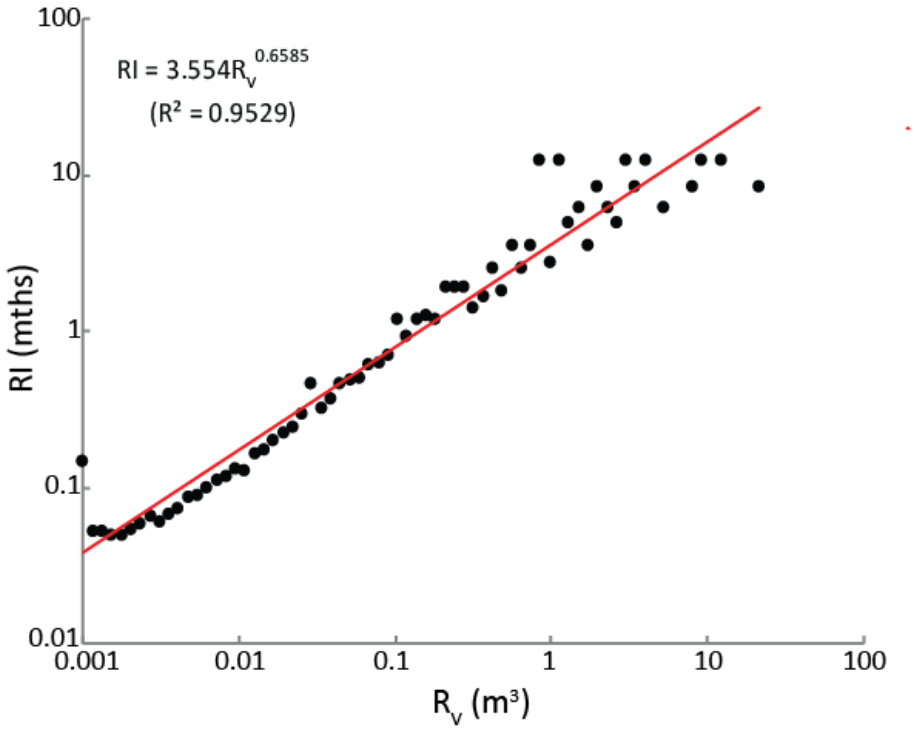

Recurrence interval (months) for different rockfall volumes (m^3) at ***Section 1*** based on 7,769 rockfalls that occurred between June 2012 and June 2014 over 3,142 m^2.

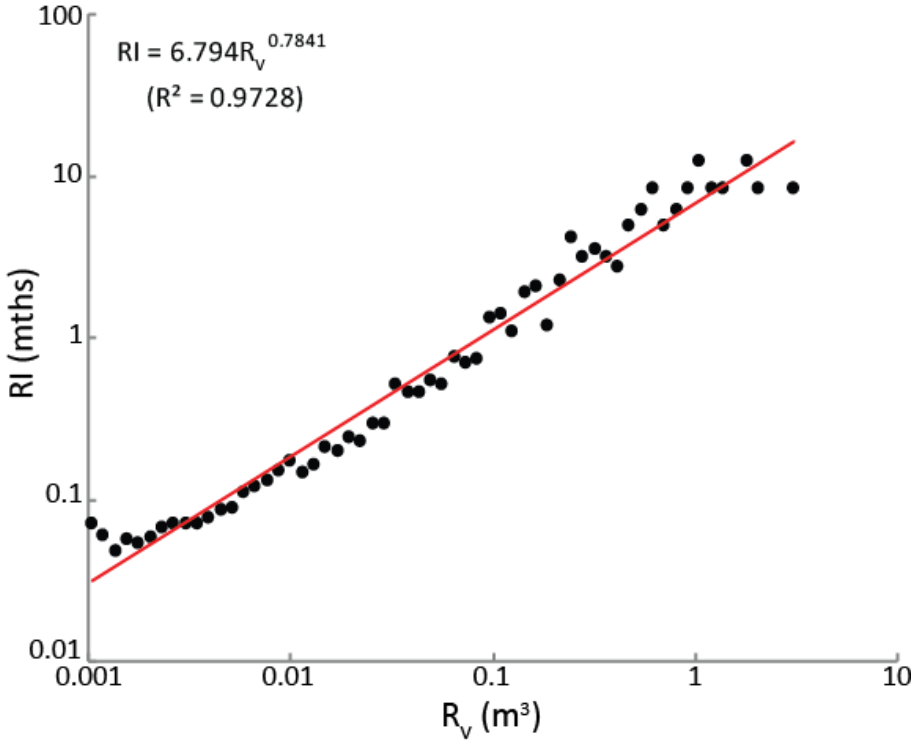

Recurrence interval (months) for different rockfall volumes (m^3) at ***Section 2*** based on 7,491 rockfalls that occurred between June 2012 and June 2014 over 4,819 m^2.

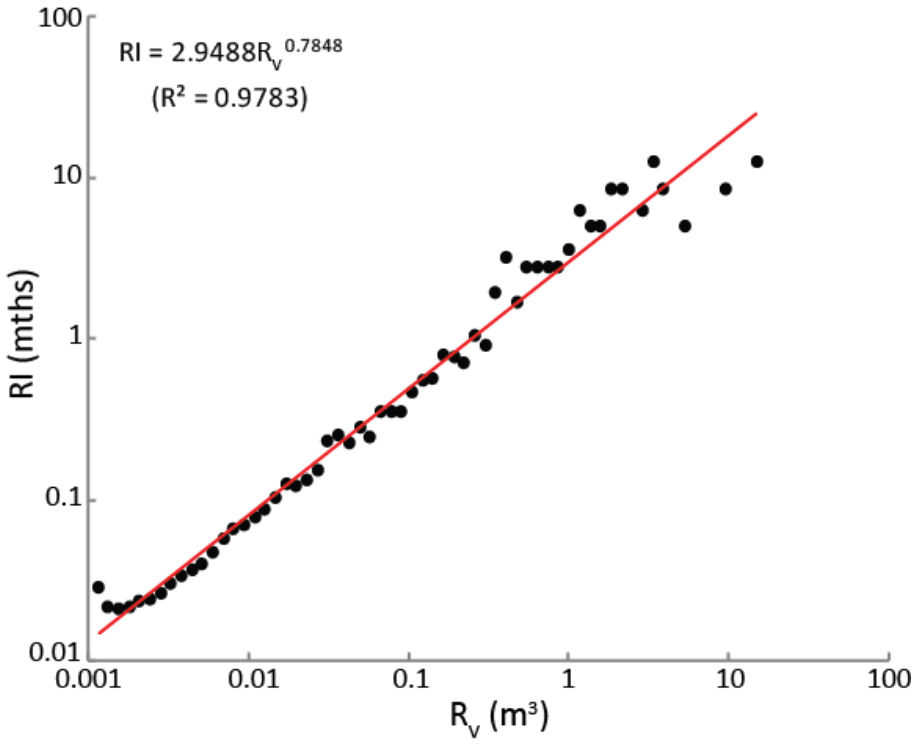

Recurrence interval (months) for different rockfall volumes (m^3) at ***Cowbar*** based on 15,337 rockfalls that occurred between June 2012 and June 2014 over 6,147 m^2.

In order to determine whether the recurrence interval behaviour is exhibited at a smaller spatial scale, three 30 x 30 m areas of interest (AOIs) were selected along the cliff at Boulby: one in the centre and two 50 m apart on either side, as shown in the figure below. In addition to examining the recurrence interval behaviour at a smaller scale, this also allowed along cliff variation in this relationship to be explored.

The resulting recurrence intervals are plotted against rockfall volume below. As shown in the three graphs, the positive exponential relationship still holds and is represented by a power-law as shown on each graph. The *ß*-value in AOI 1 is within the range of *ß*-values seen in the recurrence interval data for each field site above, whilst the *ß*-values for AOI 2 and 3 are lower. The overall variability in *ß*-values is similar to the variability seen between field sites. This suggests that the behaviour exhibited by the event size recurrence interval is similar at different spatial scales, and that the variability over 200 m along a cliff is similar to the variability seen across sites along a 2,500 m stretch of coastline.

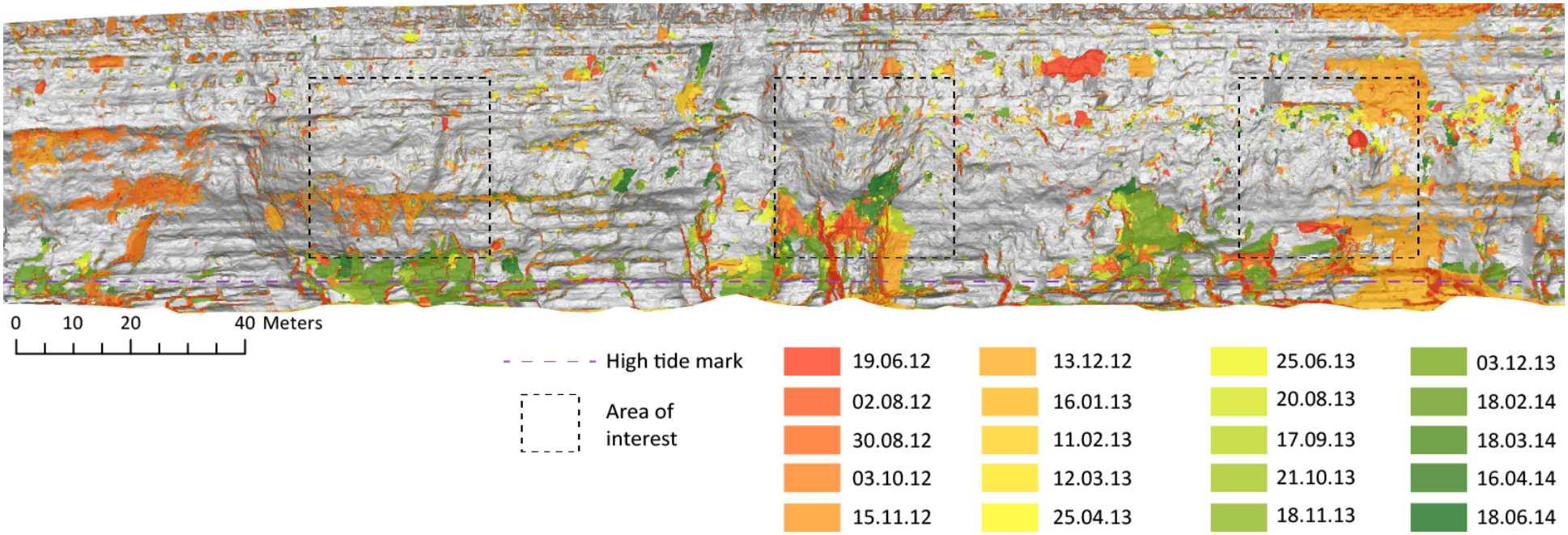

Location of 30 m x 30 m AOIs along the cliff at Boulby, outlined by the black dashed line. AOIs are numbered 1-3 moving left to right along the cliff. The base image used is the rockfall polygons colour coded by date and overlaid on a DEM of the cliff.

[a]

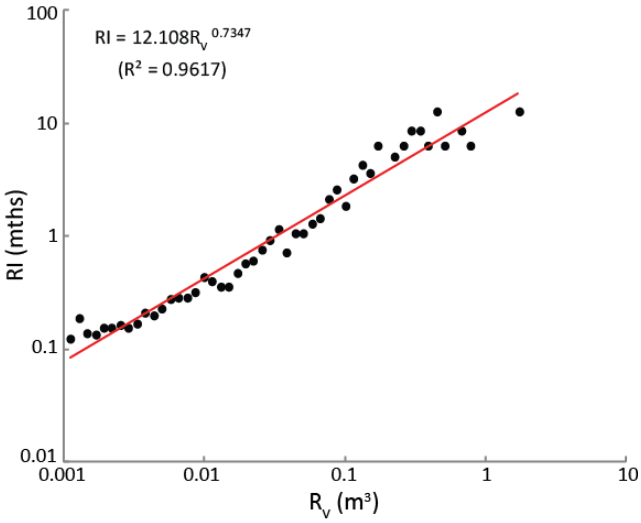

[b]

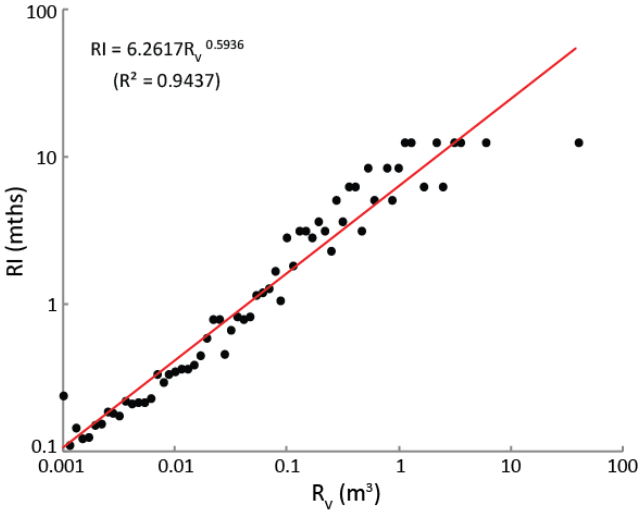

[c]

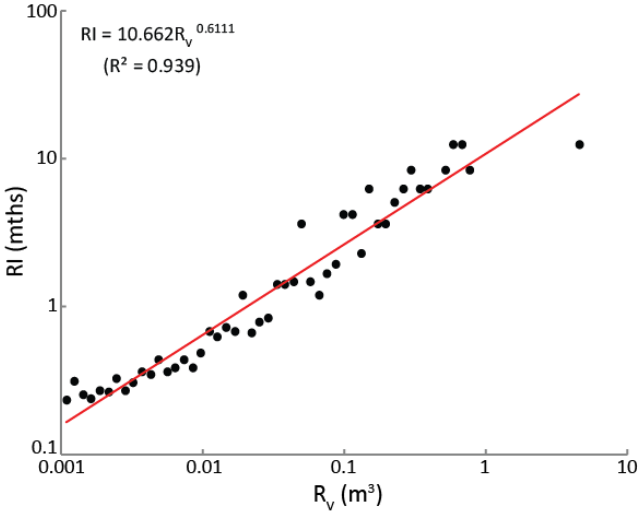

Recurrence interval (months) for different rockfall volumes (m^3) that occurred between June 2012 and June 2014 from each of the 30 m x 30 m AOIs at Boulby: [a] AOI 1; [b] AOI 2; [c] AOI 3.

Appendix 2: Slope Model

Appendix 2.1: Full numeric formulation of Slope Model

The numerical formulation of the Slope Model code presented here is reproduced from the Appendix in Cundall and Damjanac (2009).

Mechanical Formulation

The lattice used in Slope Model is an assembly of nodes and nonlinear springs. The mean distance between nodes is the model 'resolution', which is user-defined in order to control the precision a given slope is modelled with. Like other Itasca codes (Itasca, 2014) Slope Model used an explicit solution scheme, well suited to the direct simulation of highly nonlinear behaviour such as fracture, slip and opening/closing of joints. The law of motion uses the following central difference formulas for each node:

$$\dot{u}_i^{(t+\frac{\Delta t}{2})} = \dot{u}_i^{(t+\frac{\Delta t}{2})} + \sum F_i^{(t)} \Delta t/m$$

$$u_i^{(t+\Delta t)} = u_i^{(t)} + \dot{u}_i^{(t+\frac{\Delta t}{2})} \Delta t$$

(Equation A2.1)

where $\dot{u}_i^{(t)}$ and $u_i^{(t)}$ are the velocity and position respectively of vector component i (i = 13) at time t, ΣFi is the sum of all force components acting on the node of mass m, with the mechanical timestep Δt. The spins are assumed to be zero and that moments arising from shear forces do not act to cause rotations, which is equivalent to the assumption of infinite moments of inertia for nodes. These assumptions are made in the interest of code efficiency and are found to have a minimal effect on the mechanical response of the system.

After equation A4.1.1 has been applied to all nodes, a scan of all springs is performed. If a spring is unbroken, the following calculations are performed at time t (time superscript omitted for clarity):

$$\dot{u}_i^{rel} = \dot{u}_i^A - \dot{u}_i^B$$

(Equation A2.2)

where the superscript rel denotes “relative”, and A and B denote the two particles connected by the spring;

$$\dot{u}^N = \dot{u}_i^{rel} n_i$$

$$\dot{u}_i^S = \dot{u}_i^{rel} - \dot{u}^N n_i$$

(Equation A2.3)

where N denotes “normal”, S denotes “shear”, ni is the unit normal vector, and the Einstein summation convention applies to repeated indices. The normal and shear forces then are updated:

$$F^N \leftarrow F^N + \dot{u}^N k^N \Delta t$$

$$F_i^S \leftarrow F_i^S + \dot{u}_i^S k^S \Delta y$$

(Equation A2.4)

where kN and kS are the spring normal and shear stiffnesses, respectively, and the normal force is positive in tension. After calculation by equation A4.1.4, the normal force is tested for breakage: thus, if FN > FNmax, then FN = 0, FiS = 0, and a ‘fracture flag’ is set. During future calculations, the spring forces remain zero while the ‘gap’ is positive, where gap, g, is calculated as follows:

$$g \leftarrow g + \dot{u}^N \Delta t$$

(Equation A2.5)

As soon as the gap becomes zero, the spring calculation reverts to that of A4.1.4. Thereafter the spring separates again (g > 0, FN = 0) when the normal force becomes greater than zero. For a spring that is part of a joint segment, the shear force is limited to the maximum frictional force when the normal force is compressive (FN < 0):

$$If \left|F_i^S\right| > \mu |F^N| \; then \; F_i^S \neg \mu F_i^S \frac{|F^N|}{\left|F_S^i\right|}$$

(Equation A2.6)

where μ is the friction coefficient of the joint segment.

Finally, the new spring forces are added (with the appropriate signs) to the force-sums of the associated nodes:

$$\sum F_i^A \leftarrow \sum F_i^A - (F^N - pA)n_i - F_i^S$$

$$\sum F_i^B \leftarrow \sum F_i^B - (F^N - pA)n_i - F_i^S$$

(Equation A2.7)

For a regular spring (part of the intact rock material), the vector, ni is the unit normal from node A to node B – i.e. ni = (uiA – uiB)/ |(uiA – uiB)|. Should a joint plane pass through the spring, then ni is the unit normal to the joint plane rather than that of the associated spring. The terms pA in equation A4.1.7 account for the effect of fluid pressure p within the fluid element associated with the spring, where A is the apparent area of the fluid element.

Fluid Formulation

Details of the numerical formulation of fluid flow within the joints in Slope Model can be found in the Appendix of Cundall and Damjanac (2009). This option is not included in the experiments run in this study and so the details are not given here.

Flat joint model

Details of the formulation, verification and implementation of the flat joint model into Slope Model are provided in a presentation from Cundall (2014). The slides are reproduced below, with permission:

Improving the compressive/tensile strength ratio in *Slope Model*

The primary application of *Slope Model* was in representing brittle tensile failure of rock bridges between existing joints. Reproducing rock failure in compression was not originally a big priority.

Although most hard rocks exhibit ratios of unconfined compressive strength to tensile strength (UCS/Sig-t) of between 10 and 20, *Slope Model* returns ratios of around 4.

Similar behavior is exhibited by assemblies of bonded spherical particles, as modeled by *PFC3D*, although it was known that *UDEC* assemblies of angular grains show much higher ratios. The reason for the difference seemed to be that *UDEC* is able to model the partial failure of a contact between grains, providing a moment (that resists relative rotation) even when the contact has "failed" (i.e., the bond has broken).

Slide 1: (Cundall, 2014)

Accordingly, a contact model known as the "Flat Joint" was implemented in *PFC3D*, as an alternative to the parallel bond model.

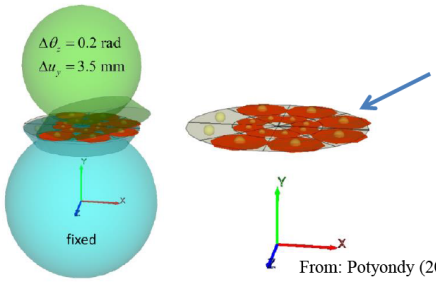

Notional contact disk, showing partial contact, due to particle rotation. The disk is divided into a number of subcontacts (Ncp)

From: Potyondy (2013): Technical Memo

The Flat Joint (FJ) model provides the following behaviors:

1. Each sub-contact point may fail (or not fail) separately;
2. Gaps may open up, and sliding may occur, at each point separately;
3. Even if all points fail, there may still be contact forces and moments, for those sub-contacts that remain touching.

Using the FJ model, *PFC3D* assemblies of bonded spheres show much higher UCS/Sig-t ratios.

Slide 2: (Cundall, 2014)

A version of the FJ model was implemented in *Slope Model*. It was assumed that the sub-contacts are arranged around the circumference of the contact disk.

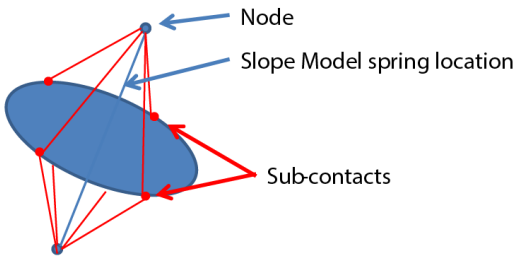

The relative motion at each sub-contact is computed from the translational and rotational motion of the two nodes, taking account of the vector directions (red lines) from nodes to contacts. The resulting normal and shear displacements at the sub-contacts give rise to forces that are compared to the tensile and shear force limits – thus: breaking, sliding or opening may occur, separately at each sub-contact. Sub-contact forces are then resolved into nodal forces and moments.

Slide 3: (Cundall, 2014)

A new option has been added to the "Solution" tab in *Slope Model*, allowing activation of the FJ model and optional specification of disk radius and number of sub-contact points. When the FJ model is used, the simulated tensile strength and modulus of the given rock are unchanged.

Tensile and compressive tests have been performed on rectangular samples, using the calibration mode of *Slope Model*. By expressing the contact shear strength as a multiplier on contact tensile strength, the following results are obtained. It is seen that:

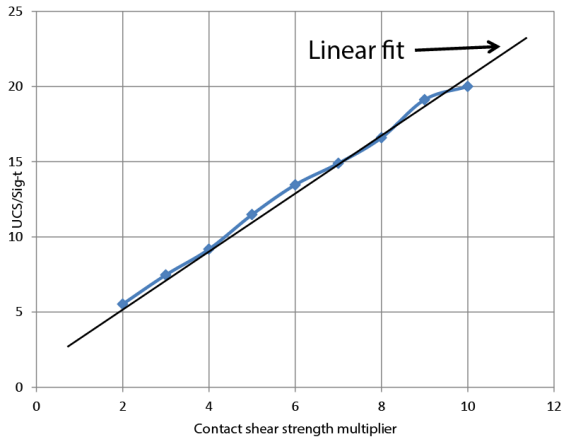

1. The UCS/Sig-t ratio is significantly increased (up to a value of 20 or more);
2. The relation between UCS/Sig-t and shear strength multiplier is almost linear.

Thus, a linear relation has been built into the code, so that a user-given UCS is translated automatically into a contact shear strength.

Slide 4: (Cundall, 2014)

Using the linear strength fit, UCS values (given by the user as rock properties) are reproduced with accuracies of around 1%.

High values of UCS/Sig-t ratios are achieved as intended.

Furthermore, the *shape* of the strength envelope for various confining stresses is quite realistic (and appears to resemble the generic Hoek-Brown curve).

The curve at right is for a series of confined compression tests performed with *Slope Model*, using a specified UCS/Sig-t ratio of 15, and a UCS of 185 MPa (for 3-point contact disks of relative radii 0.5).

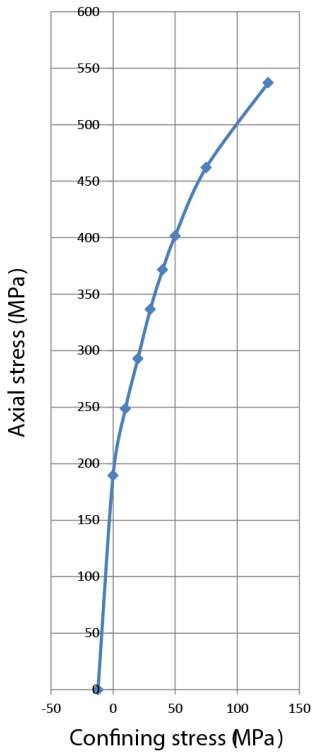

Slide 5: (Cundall, 2014)

The Flat Joint option is available in *Slope Model* for the whole rock mass and/or for selected seams. The execution-time penalty is about 1.5 (that is, a model with all springs represented by FJs executes 1.5 times slower than a model with simple springs, for 3-point contact disks).

An enhanced crack plot-item now displays (optionally) the state of each crack (fully-broken or partially broken); for example -

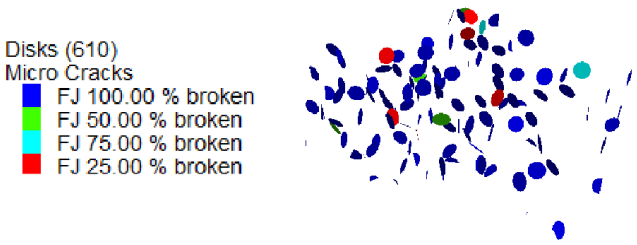

The force plot-item displays the sums of forces (either normal and shear) at all sub-contact points, for each notional spring.

Slide 6: (Cundall, 2014)

Appendix 2.2: Model performance

Model behaviour

Key aspects of the model behaviour are demonstrated with the use of a basic framework for model verification and validation (Lane *et al.,* 2005) – modified from the American Society of Mechanical Engineers (ASME, 1993). Three of the criterion in the framework, which are considered relevant to this study, are used to demonstrate the behaviour of the model in relation to changes in model resolution; mechanical equilibrium; and boundary conditions.

Model resolution

Criterion 4 in Lane *et al.* (2005) states that:

"Solutions over a range of significantly different grid resolutions should be presented to demonstrate grid independence or grid-convergent results."

In order to test this, a model scenario is set based on the conditions that satisfy a stable slope, as identified by Itasca (2010b): a 75°, 40 m high slope composed of 'test rock' (Table A2.1) is simulated, with two daylighting joint planes with dips of 40° and dip directions of 40° and 135° (Figure A2.1). The material properties of the rock and joints are given in Table A2.1. The simulation was run at four different model resolutions, represented by lattices with a node spacing (n_s) of: 0.2 m, 1 m, 2 m and 10 m, and the results are presented in Table A2.2.

Overall the results demonstrate a dependence on the model resolution (as defined by the node spacing), which is seen more clearly at larger node spacings. As shown in Table A2.2 and in the plots in Figure A2.2, increasing the node spacing generates a small increase in the maximum displacement and velocities measured. The time taken to reach mechanical equilibrium, defined as the point at which *peak* velocities in the model drop below $1e^{-4}$ m/s (Torres, 2014) varies slightly between node spacings used, and is highest at n_s = 2 m. Once the model is run at a much coarser resolution (n_s = 10 m) the model becomes unstable, never reaching equilibrium (Figure A2.2g, h).

As the results from Slope Model are shown to be dependent on the node spacing, all of the model experiments that are simulated to address the research questions (Chapter 4) are run at a single value of n_s = 0.2 m.

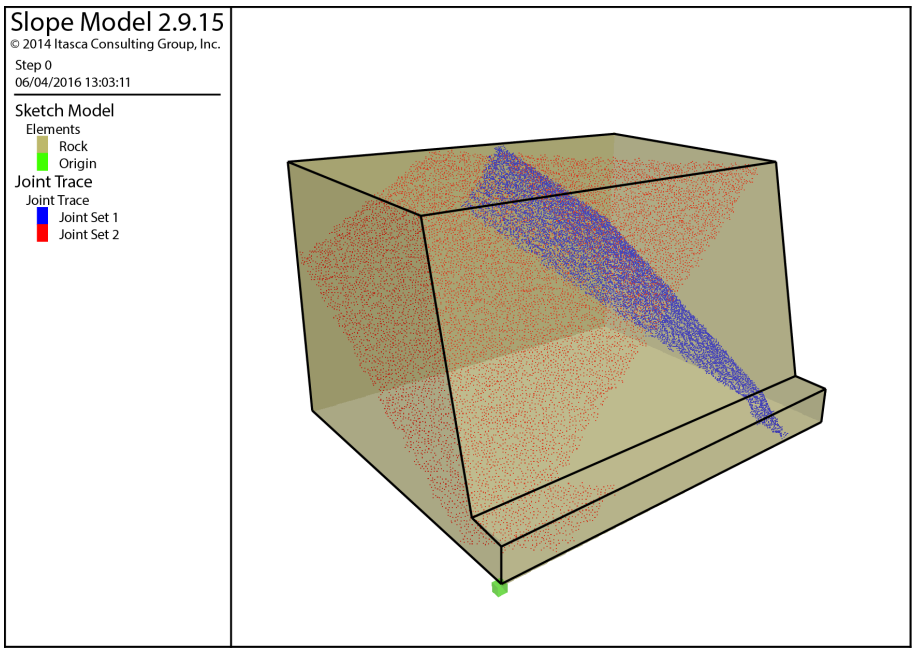

Figure A2.1: Model setup for model resolution simulations, showing two joint planes (dips of 40° and dip directions of 40° and 135°) daylighting in the 40 m high slope.

Table A2.1: Material properties for model resolution simulations

Category	**Parameter**	**Value**
Rock type: Test Rock	Density (kg/m^3)	2650
	UCS (MPa)	200
	Tensile strength (MPa)	20
	Young's modulus (GPa)	70
	Poisson's ratio	0.25
	Friction angle (°)	26.565
Joints	Tensile strength	0.5
	Friction angle	26.565

Table A2.2: Results of model resolution tests

Node spacing, n_s (m)	**Maximum displacement (m)**	**Maximum velocity (m/s)**	**Time to mechanical equilibrium (s)**
0.2	$9.05*10^{-5}$	0.0061	0.1415
1	$1.07*10^{-4}$	0.0064	0.1270
2	$1.45*10^{-4}$	0.0071	0.1652
10	∞	∞	Unstable

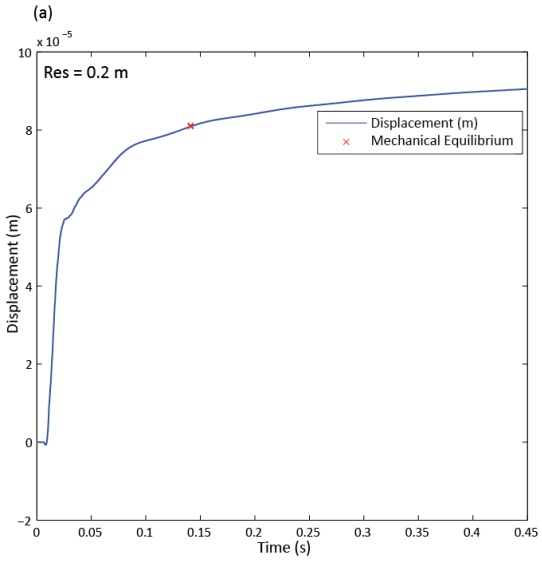
(a)
x 10 −5
Res = 0.2 m
Displacement (m)
Mechanical Equilibrium
Displacement (m)
Time (s)

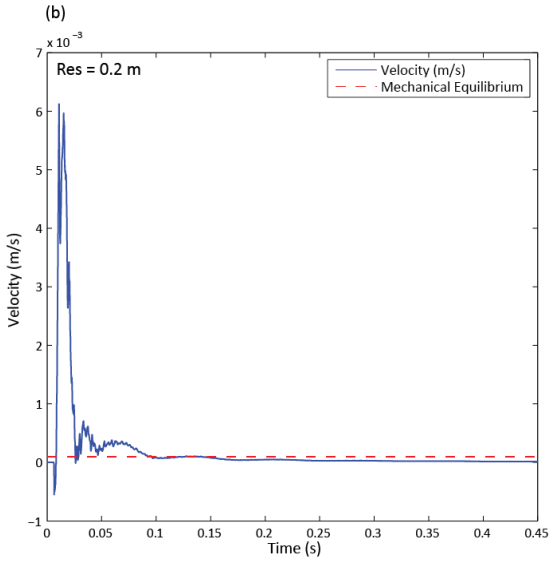
(b)
x 10 −3
Res = 0.2 m
Velocity (m/s)
Mechanical Equilibrium
Velocity (m/s)
Time (s)

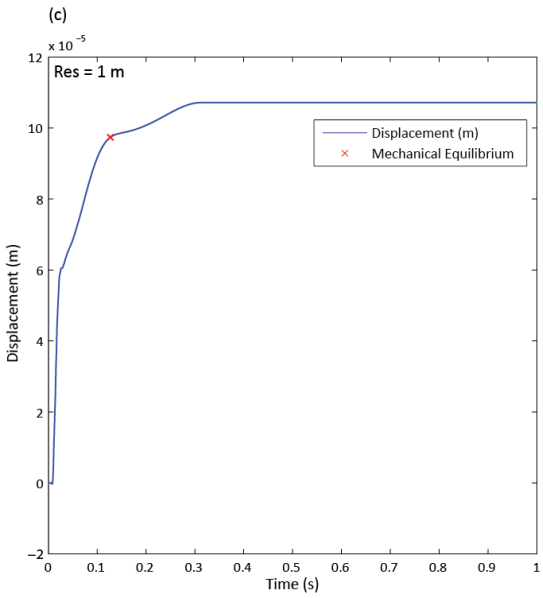
(c)
x 10 −5
Res = 1 m
Displacement (m)
Mechanical Equilibrium
Displacement (m)
Time (s)

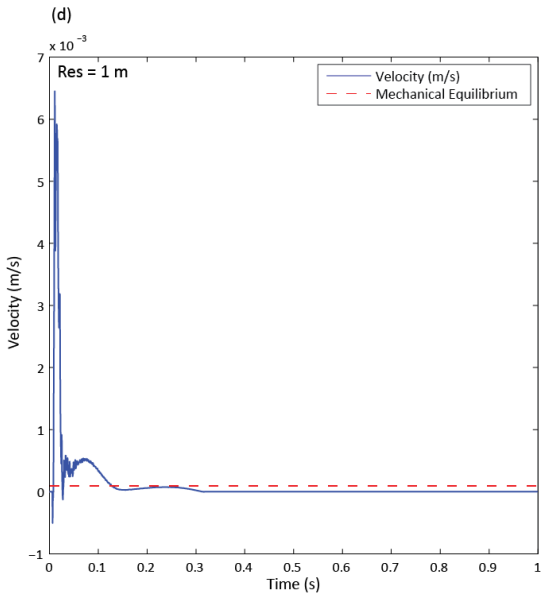
(d)
x 10 −3
Res = 1 m
Velocity (m/s)
Mechanical Equilibrium
Velocity (m/s)
Time (s)

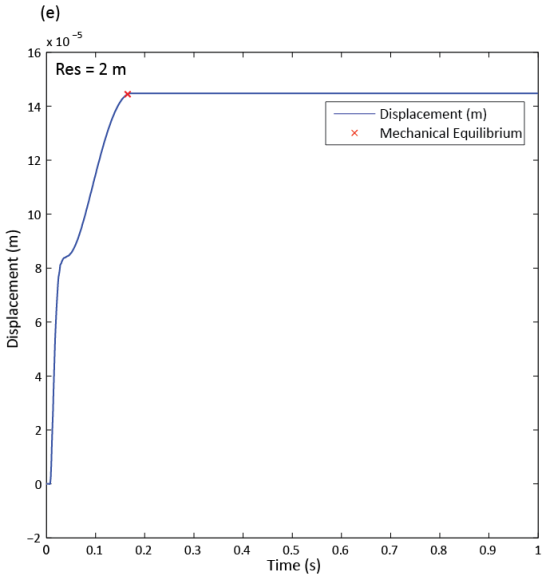
(e)
x 10 −5
Res = 2 m
Displacement (m)
Mechanical Equilibrium
Displacement (m)
Time (s)

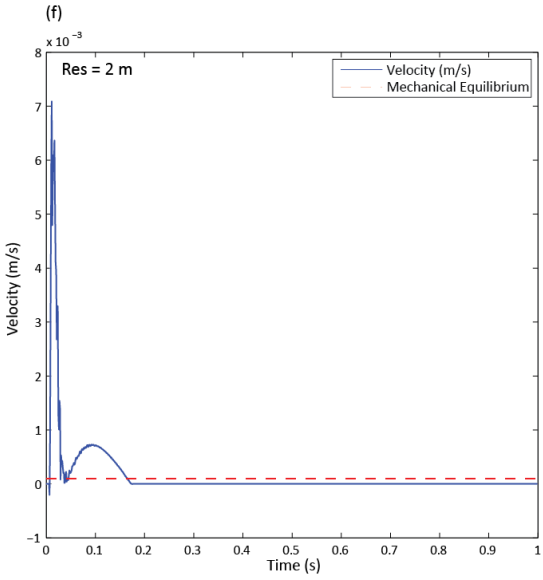
(f)
x 10 −3
Res = 2 m
Velocity (m/s)
Mechanical Equilibrium
Velocity (m/s)
Time (s)

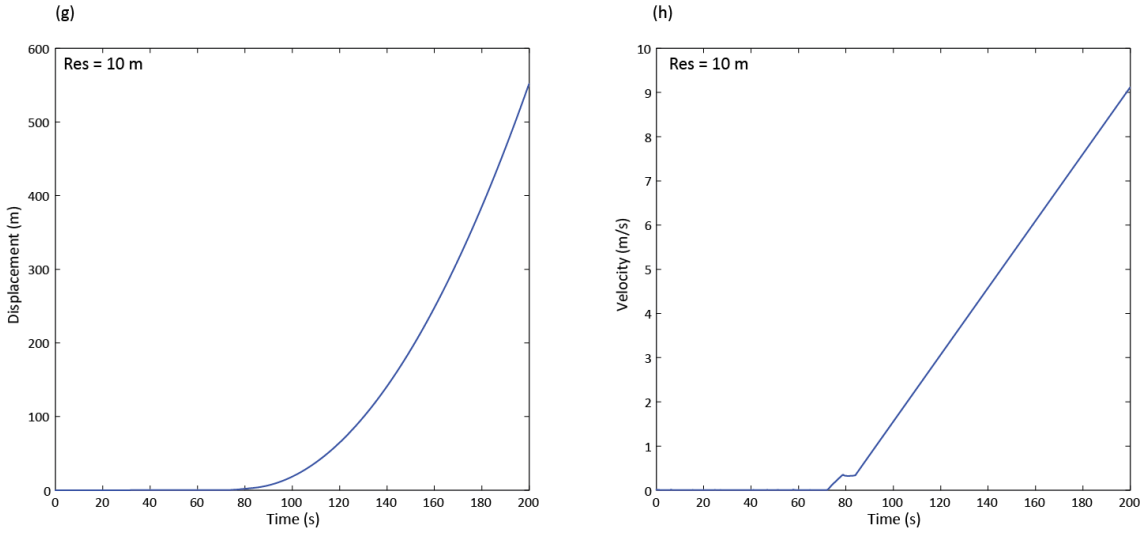

Figure A2.2: Horizontal displacement (m) and velocity (m/s) measured at the centre of the wedge (at the surface) for the model setup in figure 4.4. The plots show results from the simulations run on four different lattices with node spacing (n_s) = (a) 0.2 m, (b) 1 m, (c) 2 m and (d) 10 m. Mechanical equilibrium, defined as the point at which peak velocities in the model drop below $1e^{-4}$ m/s, is shown by the red crosses (displacement plots) and the dashed line (velocity plots).

Mechanical equilibrium

Criterion 5 in Lane *et al.* (2005) states that:

"Stopping criteria for iterative calculations need to be precisely explained. Estimates must be given for the corresponding convergence error."

In Slope Model convergence can be considered as the point when the model reaches mechanical equilibrium (Torres, 2014). The model is deemed to have reached mechanical equilibrium once *peak* velocities in the model drop below $1e^{-4}$ m/s, for slopes with a surface area greater than 10 m^2 (Torres, 2014). Figure A2.2 presents the velocity measured at the centre of the wedge (Figure A2.1), representing the location of peak velocities within this model setup. The velocity plots in Figure A2.2 have a dashed red line to indicate the velocity threshold that represents mechanical equilibrium. The time at which the model passes this threshold is indicated by the red cross on the displacement curves and is shown to be dependent on the lattice node spacing used, varying slightly as the node spacing increases (Table A2.1). At the largest node spacing simulated (10 m) the model doesn't reach mechanical equilibrium (Figure A2.2g, h).

Boundary conditions

Criterion 7 in Lane *et al.* (2005) states that:

"Clear statements defining the methods used to implement boundary and initial conditions must be presented. Typically, the overall accuracy of a simulation is strongly affected by the implementation and order of the boundary conditions."

For simulations in Slope Model the boundary conditions of the model are set by defining the slope geometry; the free surface; and the magnitude of stress applied at the top and base of the model. The slope geometry is defined using a dxf file (Chapter 4), and the slope face is always selected as the free surface in order to allow displacement outwards.

In order to demonstrate the model behaviour in response to initial stress conditions, an example from Itasca (2010b) is used whereby the model is allowed to equilibrate under different initial stresses. Firstly, a 3-bench model is set up with no initial stress (Figure A2.3) and simulation shows downward displacement as the whole model settles under gravity until equilibrium is established, as illustrated by the vertical displacement history taken from the crest of the second bench (Figure A2.4a). However, Slope Model allows initial pre-stress conditions to be set as orthogonal stress components (σ_{zz}, σ_{xx}, σ_{yy}) at the top and/or base of the model, corresponding to stresses that would exist pre-excavation (Itasca, 2010b). Assuming that the total vertical stresses are zero at the top of the model are equal to the overburden stress at the base of the model, a second simulation has been run with stresses set at the base as follows: The vertical stress component (σ_{zz}) is based on the overburden stress equation with rock density for the siltstone rock type (ρ = 2,838 kg/m^2) used in the simulation:

$$\sigma_{zz} = g\rho H$$

Equation A2.7

where g is the gravitation acceleration (10 m/s^2), ρ is the mass density of the rock (kg/m^2), and H is the maximum height of the model (m). Horizontal stresses are computed based on a horizontal to vertical stress ratio, K_0 = 0.5. Under these conditions the simulation was repeated and the vertical displacement history is shown in Figure A2.4b. Notably the downward displacement as the model settles under gravity (Fig. A2.4a) is not seen here as the appropriate overburden stresses, computed with a gravity component (Equation A2.7), have been applied.

These simulations demonstrate that Slope Model is responding to the initial stress conditions that are set and that in both cases the model does settle and reach equilibrium. For the purposes of this study stresses will be defined according to the position of the slope being simulated and the material properties of the rock.

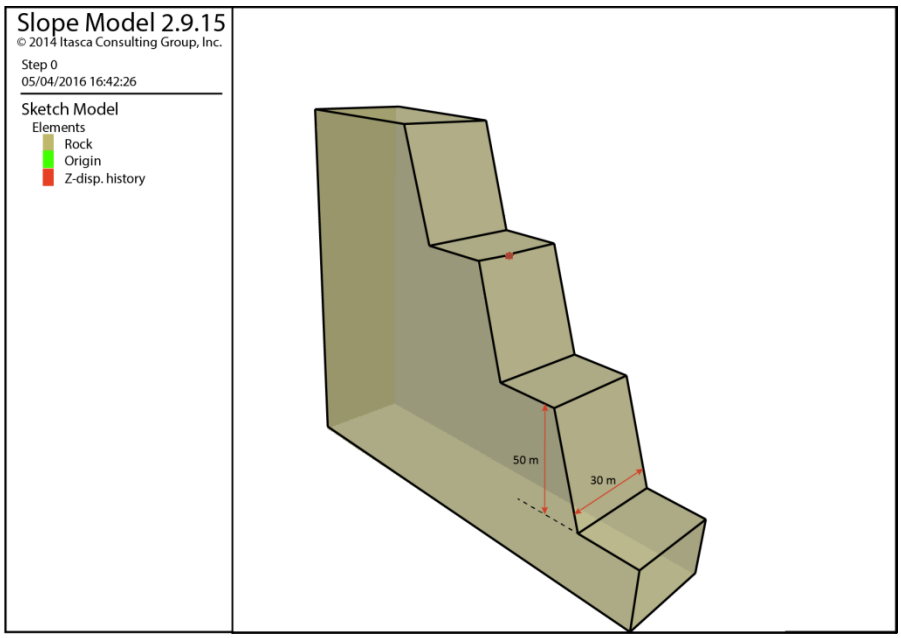

Figure A2.3: 3-bench setup in *Slope Model*. Benches are 50 m high and 30 m wide. The red square shows the point where displacement was recorded.

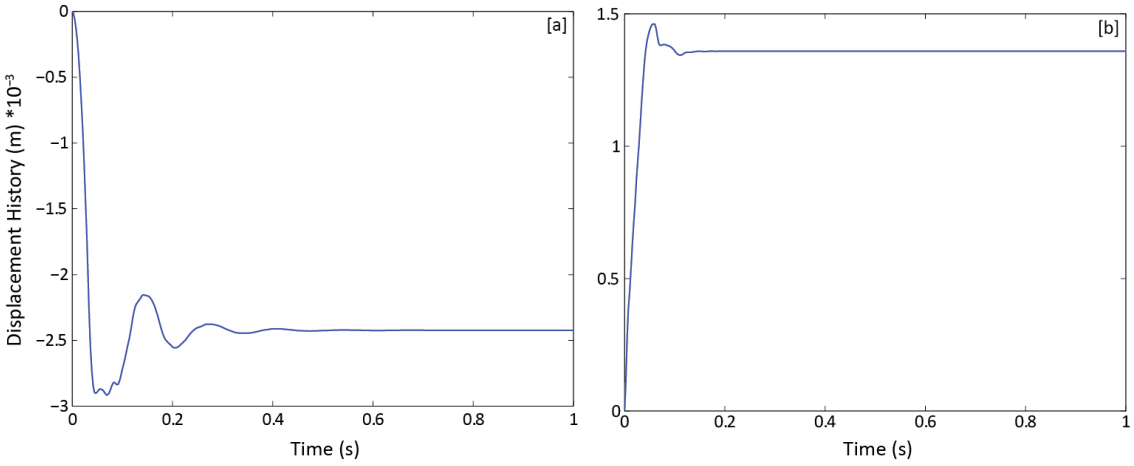

Figure A2.4: The vertical displacement history (m) at the crest of bench 2 for (a) the simulation with no initial stresses applied; and (b) the simulation with initial in situ stresses applied.

Examples of model performance

Demonstration of the confidence in the model performance is given by the examples below from Itasca (2010b), which show that the results of the model fit with fundamental process understanding and logical physical processes regarding rock slope failure.

3D wedge stability

3D wedge failure is a well-documented and investigated form of failure in jointed rock slopes. Hoek and Bray (1977) demonstrate how the stability (as expressed by the factor of safety) of a wedge can be determined under a range of conditions using stability charts. Subsequently, Kimber *et al.* (1998) have investigated the limiting conditions and geometry of the slope and wedge for different types of failure, including sliding and toppling. More recently, advances in both monitoring techniques and numerical modelling have allowed studies to examine in more detail the relationships between rock mass structure and stability. For example, Brideau *et al.* (2009) illustrate the importance of tectonic structures and associated rock mass damage on the kinematic release in large rock slopes.

Slope Model does not use continuous joint planes, as used in previous codes such as 3DEC (Itasca, 2008), and therefore the simulation of a wedge failure tested against the stability charts from Hoek and Bray (1977) is a good test of Slope Model. Itasca (2010b) present examples whereby they simulate a variety of slopes each with two joint planes that form a wedge that is symmetrical about the slope face, as shown previously in Figure A2.1. For each set of simulations the dip of the joints is varied, and within each set of simulations the dip directions of the two joints are varied until conditions are met in which the factor of safety equals 1.0, where the velocity at the centre of the slope crest tends to zero. Imposing the results on the stability chart from Hoek and Bray (1977) shows good agreement between their analytical solution and that obtained from Slope Model (Figure A2.5).

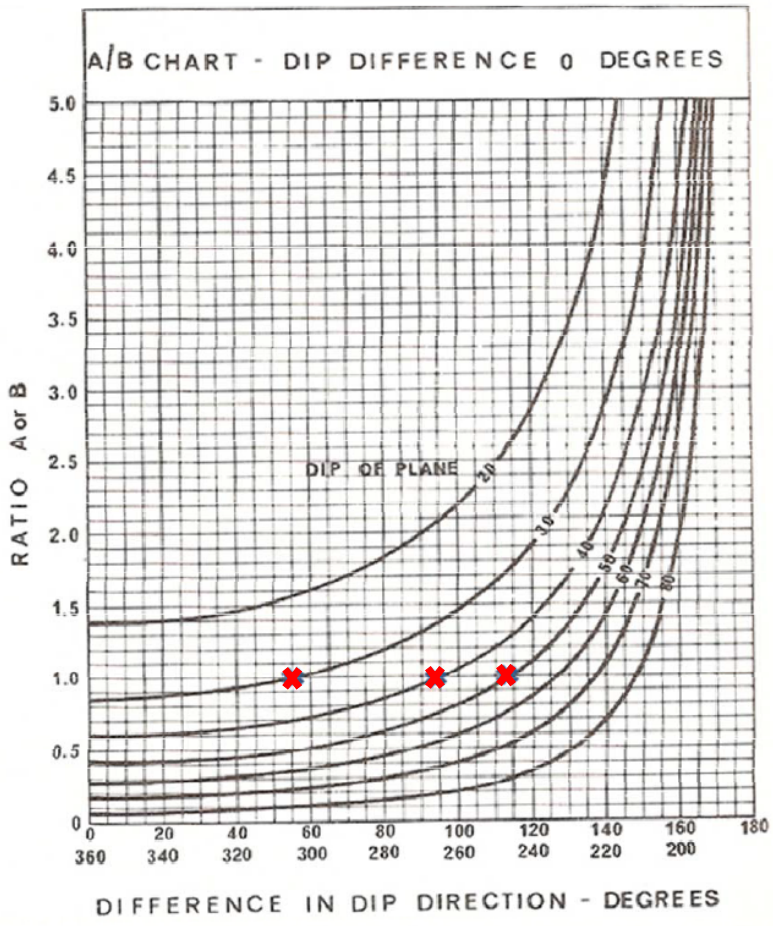

Figure A2.5: Stability chart from Hoek and Bray (1977) with red crosses superimposed for Slope Model simulation results; reproduced with permission from Itasca (2010b p.15, figure 7). *Note: the y-axis corresponds to the factor of safety when both planes have the same dip.*

Crack formation: internal damage

One of the key features of Slope Model is the ability to generate new fractures in intact rock. In order to illustrate this, and particularly to show that these fractures form links between existing discontinuities, Itasca (2010b) simulate an artificially weak rock mass with two discontinuous joint sets. The model is a 1,000 m high slope consisting of 10 benches with 70° face angles (Figure A2.6a). The material is artificially weakened to ensure that there is a large amount of initial cracking to observe both internally and at the slope face. One of the features of Slope Model is that cracks can be observed at any period selected. Figure A2.6b is a slice through the model that shows both the initial cracks that developed at the slope face (green dots) and later fractures that developed internally as a response to slope failure (black dots). The relation of these cracks to joint segments can be seen and both tension/wing cracks and bridging cracks are observed. Importantly this failure and associated internal damage would not be able to occur if the model only contained discontinuous joint planes. Further examples

of model verification relating to the fluid flow and effective stress formulation are given in Itasca (2010b) and Lorig *et al.* (2010).

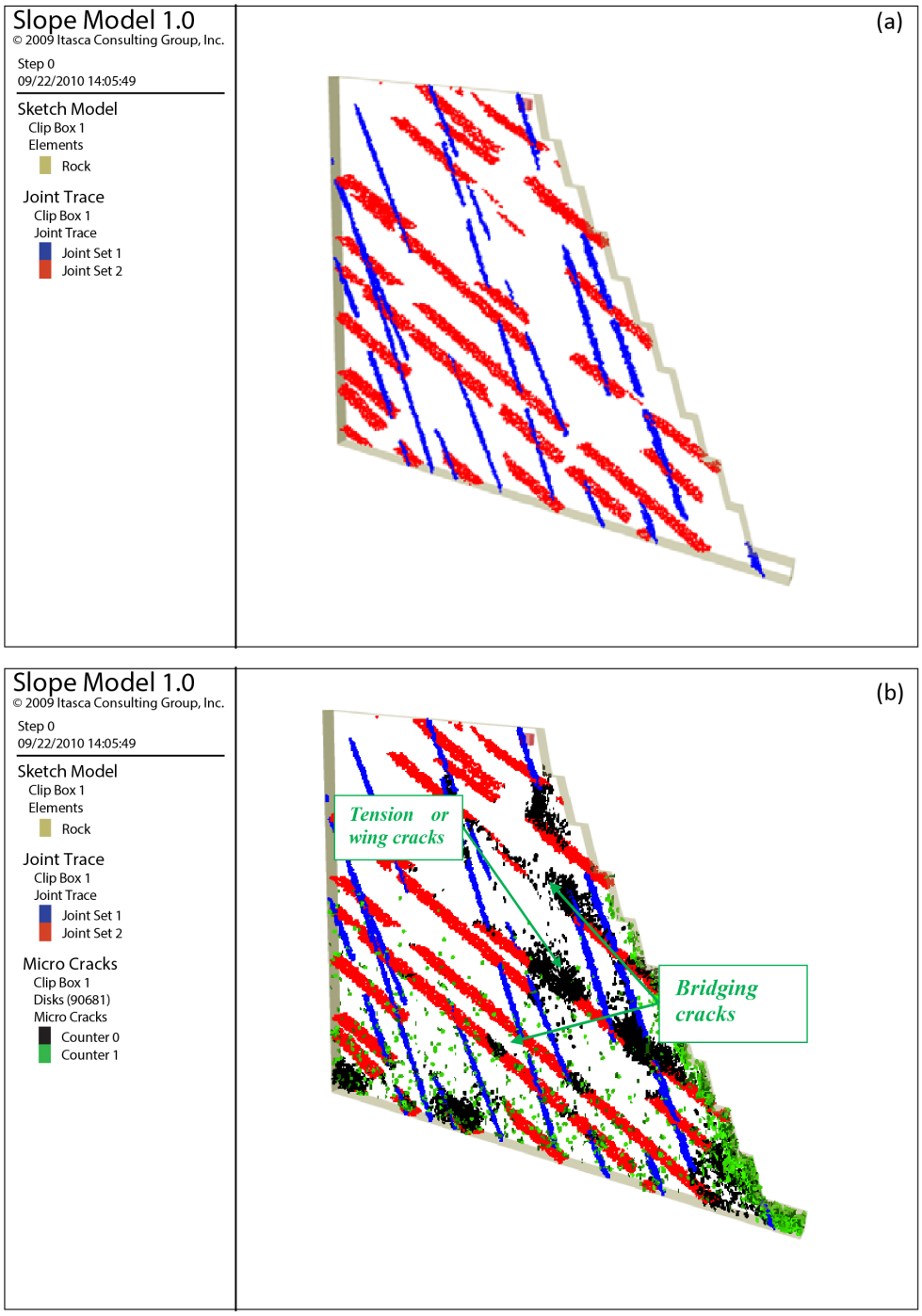

Figure A2.6: Vertical slice through the model showing a) the intersections with joint segments, and b) the cracks added. Reproduced and modified with permission from Itasca (2010b p.21, figure 15).

Appendix 2.3: Model parameters

Table A2.3: Parameters used for all model experiments in Slope Model

Parameter		**Value(s)**			
Geology (Shale)	Density, ρ	2,486 kg/m^3			
	UCS, σ_c	16.69 MPa			
	Tensile strength, σ_{ts}	3.03 MPa			
	Young's Modulus, E	2.14 GPa			
	Poisson's Ratio, ν	0.4			
	Friction Angle, ϕ	30°			
	Porosity, n	2 %			
	Permeability, k	$1*10^{-13}$ m^2			
Geometry (m)		x: 10; y: 10; z: 10			
Stress (MPa): top/base	σ1	0.72/ 0.96			
	σ2	0.36/ 0.48			
	σ3	0.36/ 0.48			
Joints	Dip (°)	6	74	78	53
	Dip direction (°)	53	118	300	268
	Spacing (m)	1.5 (0.5)	1.9 (0.6)	1.8 (0.6)	6.5 (0.5)
	Stiffness (GPa/m)	Shear = 1; Normal = 3			
Lattice node spacing (m)		0.2			
Flat Joint Model	Radius (m)	0.5			
	Contact points	3			

Table A2.4: Parameter values for each of the experiments in Slope Model. The model ID refers to those used in Section 4.2 of the thesis, where descriptions of each parameter are also found; and the morphology ID refers the images below the table.

Exp. ID	**Morph-ology**	**Joint strength**	**Rock mass Strength (MPa)**		**Spring Failure Latency**		**Add. Notes**
			σ_{ts}	σ_c	**Radius (m)**	**Timestep**	
1.1	B	Med-weak	3.03	16.69	-	-	-
1.2	B	Medium	3.03	16.69	-	-	-
1.3	B	Med-strong	3.03	16.69	-	-	-
1.4	A	Medium	3.03	16.69	-	-	-
1.5	B	Medium	3.03	16.69	-	-	-
1.6	C	Medium	3.03	16.69	-	-	-
1.7	D	Medium	3.03	16.69	-	-	-
1.8	B	Medium	1.73	9.54	-	-	-
1.9	B	Medium	1.21	6.68	-	-	-
1.10	B	Medium	0.30	1.67	-	-	-
1.11	B	Med-weak	3.03	16.69	-	-	-
1.12	B	Weak	3.03	16.69	-	-	-
1.13	B	Very weak	3.03	16.69	-	-	-
1.14	B	Med-weak	1.73	9.54	-	-	-
2.1	B	Med-weak	3.03	16.69	-	-	Model run for 20 seconds
2.2	B	Medium	1.73	9.54	-	-	
2.3	B	Med-weak	1.73	9.54	-	-	
2.4	B	Med-weak	1.73	9.54	-	-	Excavations used
2.5	B	Med-weak	1.73	9.54	5	100	-
2.6	B	Med-weak	1.73	9.54	5	1,000	-
2.7	B	Med-weak	1.73	9.54	5	10,000	-

Appendix 3: Matlab script for Rockfall Model

Parent script

```
name1 =
'N:\COBRA_V\014_Modelling\Cellular\H\H4_files\grids\GSI_50.mat';
name2 = 'N:\COBRA_V\014_Modelling\Cellular\H\H4_files\grids\z.mat';
name3 = 'N:\COBRA_V\014_Modelling\Cellular\H\H4_files\grids\w.mat';
name4 = 'N:\COBRA_V\014_Modelling\Cellular\H\H4_files\grids\k.mat';

for wmax = [% specify value];
    wmax_n = num2str(wmax);
    wmult = wmax/2;


    intro
    loop

    name_out2 =
['N:\COBRA_V\014_Modelling\Cellular\H\H4_outputs\w',wmax_n,'_110_S.mat
'];
    name_out3 =
['N:\COBRA_V\014_Modelling\Cellular\H\H4_outputs\w',wmax_n,'_110_L.mat
'];

    outputs
end
```

'intro' function

```
% 1. Model boundaries
% model runs
L = 10000;

% model size
ny = 300;
nx = 300;


% 2. Model inputs
% load GSI, topo, weath and damage initiator grid
load(name1)
load(name2)
load(name3)
load(name4)

% topo grids
z_in = z*0.5;
z_out = z_in;

% damage grids
d_in = k;
d_in = d_in.*0.2;
d_out = d_in;

%damage propagation
```

```
e1 = 3;
e2 = 3;

% damage transfer
pd = 1.1
damage = pd*0.572;

% weathering
w = w.*wmult;
wr = 10000;

% thresholds
neigh_thresh = 0.4;
sl = 0.5;           %this is the support lost in support function


% failure onset
fo = 0.9;           % onset threshold
tf = 2;             % time to failure
```

'loop' function

```
t = zeros(ny,nx);
t_fail = zeros(ny,nx);
mask_in = zeros(ny,nx);
mask_out = zeros(ny,nx);
stage_ct = zeros(L,5);
fail_mask = cell(L,1);
topo_z = cell(L,1);
diff_mask = cell(L,1);
rockfalls = cell(L,1);

for ts = 1;             %time step
    t = t+1;            %adjust time grid
    stage_ct(ts,1) = ts;


% L1. Generate slope, aspect & curvature grids
%[curv] = slope_function(ny,nx,z_in);
[p_grid] = pro_function(ny,nx,z_in);


% L2. Weathering
[d_out] = weath_function(ny,nx,d_in,d_out,w,p_grid,wr,GSI);

d_in = d_out;
stage_ct(ts,2) = sum(d_out(:) >=1);


% L3. Structural Support
[d_out] =
structural_support(ny,nx,z_in,neigh_thresh,d_in,d_out,sl,GSI);

d_in = d_out;
stage_ct(ts,3) = sum(d_out(:) >=1);
```

```
% L4. Failure Onset
[d_out,t_fail] = onset_function(ny,nx,d_out,d_in,fo,t_fail,tf,GSI);

d_in = d_out;
stage_ct(ts,4) = sum(d_out(:) >=1);


% L5. Failure
[d_in,d_out,z_in,z_out,mask_in,mask_out,t,t_fail] =
failure_function(ny,nx,d_in,d_out,z_in,z_out,e1,e2,damage,mask_in,mask
_out,t,t_fail,GSI);


% L6. Loop outputs
fail_mask{ts} = mask_out;
topo_z{ts} = z_out;

end


for ts = 2:L;           %time step
    t = t+1;            %adjust time grid
    stage_ct(ts,1) = ts;


% L1. Generate slope, aspect & curvature grids
%[curv] = slope_function(ny,nx,z_in);
[p_grid] = pro_function(ny,nx,z_in);


% L2. Weathering
[d_out] = weath_function(ny,nx,d_in,d_out,w,p_grid,wr,GSI);

d_in = d_out;
stage_ct(ts,2) = sum(d_out(:) >=1);


% L3. Structural Support
[d_out] =
structural_support(ny,nx,z_in,neigh_thresh,d_in,d_out,sl,GSI);

d_in = d_out;
stage_ct(ts,3) = sum(d_out(:) >=1);


% L4. Failure Onset
[d_out,t_fail] = onset_function(ny,nx,d_out,d_in,fo,t_fail,tf,GSI);

d_in = d_out;
stage_ct(ts,4) = sum(d_out(:) >=1);


% L5. Failure
[d_in,d_out,z_in,z_out,mask_in,mask_out,t,t_fail] =
failure_function(ny,nx,d_in,d_out,z_in,z_out,e1,e2,damage,mask_in,mask
_out,t,t_fail,GSI);

fail_mask{ts} = mask_out;
```

```
% L6. Rockfalls
[diff_mask,stage_ct,rockfalls,z_in,z_out] =
rockfall_function(diff_mask,fail_mask,stage_ct,ts,ny,nx,z_in,z_out,roc
kfalls);

topo_z{ts} = z_out;

end
```

'protrusion' function

```
function [p_grid] = pro_function(ny,nx,z_in)

p_grid = zeros(ny,nx);

z_max = max(z_in(:));
z_min = min(z_in(:));
z_range = z_max-z_min;

if z_range == 0;
    p_grid = ones(ny,nx);

else if z_range ~= 0;

% determine how far each cell protrudes or recedes from the mean
topography
z_mean = mean(z_in(:));

for i = 1:nx;
    for j = 1:ny;
        p_grid(i,j) = z_mean - z_in(i,j);
    end
end

% scale p_grid to range from 0-2, where 1 = mean topography; 0.01 =
concave; 2 = convex (protruding)
min_p = min(p_grid(:));

a = 0.01-min_p;
p_grid = p_grid + a;

max_p = max(p_grid(:));

b = 2/max_p;
p_grid = p_grid.*b;

    end
end
```

'weathering' function

```
function [d_out] = weath_function(ny,nx,d_in,d_out,w,p_grid,wr,GSI)


for i = 2:ny-1;
    for j = 2:nx-1;
        d_out(i,j) = d_in(i,j) +
(((1/wr)*w(i,j)*p_grid(i,j))^(GSI(i,j)/50));
    end
end

clear i j
end
```

'structural support' function

```
function [d_out] =
structural_support(ny,nx,z_in,neigh_thresh,d_in,d_out,sl,GSI);

% set weighting
w1 = 0.2;
w2 = 0.2;
w3 = 0.2;
w4 = 0.2;
w5 = 0.2;


% assign cells
for i = 2:ny-2;
    for j = 3:nx-2;
        c0 = z_in(i,j);
        c1 = z_in(i+1,j);
        c2 = z_in(i+1,j-1);
        c3 = z_in(i+1,j+1);
        c4 = z_in(i,j-1);
        c5 = z_in(i,j+1);

        crit = c0+neigh_thresh;
        S_L = 0;

% determine weighting of support lost using threshold
        if c1 >= crit;
            S_L = w1;
        end

        if c1 >= crit && c2 >= crit;
            S_L = w1+w2;
        end

        if c1 >= crit && c2 >= crit && c4 >= crit;
            S_L = w1+w2+w4;
        end

        if c1 >= crit && c3 >= crit;
            S_L = w1+w3;
```

```
        end

        if c1 >= crit && c3 >= crit && c5 >= crit;
            S_L = w1+w3+w5;
        end

        if c1 >=crit && c2 >= crit && c3 >= crit && c4 >= crit && c5
>= crit;
            S_L = 1;
        end


% apply the increase in damage
        d_out(i,j) = d_in(i,j) + ((S_L*sl)^(GSI(i,j)/50));

    end
end
```

'failure onset' function

```
function [d_out,t_fail] =
onset_function(ny,nx,d_out,d_in,fo,t_fail,tf,GSI);

for i = 1:ny;
    for j = 1:nx;
%query if damage is > onset threshold
        if d_in(i,j) >= fo;

%increase time beyond failure onset
            t_fail(i,j) = t_fail(i,j)+1;
        end

%fail after one time step beyond failure onset
        if t_fail(i,j) >= (tf^(GSI(i,j)/50));
            d_out(i,j) = 1;
        end
    end
end


clear i j
end
```

'failure' function

```
function [d_in,d_out,z_in,z_out,mask_in,mask_out,t,t_fail] =
failure_function(ny,nx,d_in,d_out,z_in,z_out,e1,e2,damage,mask_in,mask
_out,t,t_fail,GSI)

while max(d_in(:))>=1;                                  %until grid is
'stable'
    mask_out(d_in>=1) = mask_in(d_in>=1) + 1;           %update failure
mask
    t(d_in>=1) = 1;                                     %reset time (age)
    t_fail(d_in>=1) = 0;                        %reset time since failure
onset

    for i = 2:ny-1;
        for j = 2:nx-1;
            if d_in(i,j)>=1;
                d_out(i,j) = 0;
            end
        end
    end

% propagating damage within damage ellipse
    for i = e1+2:ny-1;
        for j = e2+2:nx-1-e2;
            if d_in(i,j)>=1;
                for r = i-e1:i;
                    for c = j-e2:j+e2;
                        if d_in(r,c)<1;
                            dist_r = ((r-i)^2)^0.5;
                            dist_c = ((c-j)^2)^0.5;
                            dist = max(dist_r,dist_c);
                            frac = (dist*4)+1;
                            d_out(r,c) = d_out(r,c) +
(((damage/(2^(dist-1))/frac))^(GSI(r,c)/50));
                        end
                    end
                end
            end
        end
    end

d_in = d_out;
z_in = z_out;
mask_in = mask_out;

clear i j r c

end
```

'rockfalls' function

```
function [diff_mask,stage_ct,rockfalls,z_in,z_out] =
rockfall_function(diff_mask,fail_mask,stage_ct,ts,ny,nx,z_in,z_out,roc
kfalls);


diff_mask{ts} = fail_mask{ts} - fail_mask{ts-1};
stage_ct(ts,5) = sum(diff_mask{ts}(:) >=1);

%each failed cell ID'd by timestep
diff_mask{ts}(diff_mask{ts}>0) = ts;
M = max(diff_mask{ts}(2:299,2:299))>0;
if max(M(:))>0;
    [count,depth,X] = eventID_function(diff_mask,ts,ny,nx);
    rockfalls{ts} = count;
    for i = 1:size(count,1);
        [r,c] = find(X==count(i,1));
        z_out(r,c) = z_in(r,c)+depth(i);
    end
end

z_in = z_out;

clear count numbers X
```

'eventID' function

```
function [count,depth,X] = eventID_function(diff_mask,ts,ny,nx)

%locating the start and end of non-zero elements of the matrix
diff_mask
X = diff(diff_mask{ts}~=0);

%add a row of zeros to the end of X to keep matrix dimensions same as
input
zrow = zeros(1,size(X,2));
X = [X;zrow];

%for failures that reach the bottom of the grid, this loop makes the
final cell in the column = -1
for c = 2:ny-1;
    if X(nx-1,c) == 1;
        X(nx-1,c) = 0;
    end
    if X(1,c) == -1;
        X(1,c) = 0;
    end

    start = find(X(1:299,c) == 1);
    finish = find(X(1:299,c) == -1);
    if length(start) > length(finish);
        X(nx-1,c) = -1;
    end

    start = find(X(1:299,c) == 1);
```

```
    finish = find(X(1:299,c) == -1);
    if length(finish) > length(start);
        X(1,c) = 1;
    end
end

clear start finish c

[rowB,colB] = find(X>0);     %indicies of beginning of non-zero groups
[rowE,colE] = find(X<0);     %indicies of ends of non-zero groups
rowB = rowB+1;               %to make the indicies the start of the
group

%give the same ID to each member (cell) of the non-zero groups
for a = 1:size(rowB,1);
    X(rowB(a):rowE(a),colB(a)) = a+1;
end

%remove identifiers of the end of the groups
X(X == 1) = 0;

clear a c

NX = size(X,1);
NY = size(X,2);


%for each non-zero cell (i.e. failed cell) assign the surrounding
failed
%cells with the same ID
for i = 2:NX-1;
    for j = 2:NY-1;
        if X(i,j)>0;
            b = X(i-1,j);
            d = X(i,j-1);
            f = X(i,j+1);
            h = X(i+1,j);

            if b>0;
                X(i-1,j) = X(i,j);
            end

            if d>0;
                X(i,j-1) = X(i,j);
            end

            if f>0;
                X(i,j+1) = X(i,j);
            end

            if h>0;
                X(i+1,j) = X(i,j);
            end

        end
    end
end

clear a b c d f g h k

for i = NX-1:-1:2;
```

```
    for j = NY-1:-1:2;
        if X(i,j)>0;
            b = X(i-1,j);
            d = X(i,j-1);
            f = X(i,j+1);
            h = X(i+1,j);

            if b>0;
                X(i-1,j) = X(i,j);
            end

            if d>0;
                X(i,j-1) = X(i,j);
            end

            if f>0;
                X(i,j+1) = X(i,j);
            end

            if h>0;
                X(i+1,j) = X(i,j);
            end

        end
    end
end

clear a b c d f g h k

%identify unique IDs in X
[numbers,r,c] = unique(X(:));
s = [300,300];
[row,col] = ind2sub(s,r);

count = hist(X(:),numbers); %count number of occurences of each ID
count = count';
count = [numbers,count];    %present in an array
count(1,:) = [];

area = count(:,2).*0.01;    %calculate the area of each failure
count = [count,area];

%volume according to vol scaling law
count(:,4) = (count(:,3).^1.1052)*0.22;
depth = count(:,4)./count(:,3);

row(1) = [];
col(1) = [];
count(:,5) = row;
count(:,6) = col;

end
```

'outputs' function

```
% OUTPUTS

% Identifying rockfall events
rf_count = zeros(L,2);

fail_end = fail_mask{L};

% Make a count of rockfall events at each time step
for i = 1:L;
    rf_count(i,1) = i;
    rf_count(i,2) = size(rockfalls{i},1);
end

% Making an age map of failures identified by the time step at which
they
% occurred
agemap = diff_mask{L};

for ts = L-1:-1:2;
    if min(agemap(:)) == 0;
        agemap(agemap==0) = diff_mask{ts}(agemap==0);
    end
end

topo_save = cell(2,1);
topo_save{1} = topo_z{1};
topo_save{2} = topo_z{5000};
topo_save{3} = topo_z{6000};
topo_save{4} = topo_z{7000};
topo_save{5} = topo_z{8000};
topo_save{6} = topo_z{9000};
topo_save{7} = topo_z{10000};

save(name_out2,'stage_ct','rf_count','agemap','d_out','fail_end','topo
_save')
save(name_out3,'rockfalls','diff_mask','-v7.3')


%% END
```

References

ABELLÁN, A., CALVET, J., VILAPLANA, J. M. & BLANCHARD, J. 2010. Detection and spatial prediction of rockfalls by means of terrestrial laser scanner monitoring. *Geomorphology,* 119**,** 162-171.

ABELLÁN, A., OPPIKOFER, T., JABOYEDOFF, M., ROSSER, N., LIM, M. & LATO, M. J. 2014. Terrestrial Laser Scanning of Rock Slope Instabilities. *Earth Surface Processes and Landforms,* 39**,** 80-97.

ADAMS, P. N., STORLAZZI, C. D. & ANDERSON, R. S. 2005. Nearshore wave-induced cyclical flexing of sea cliffs. *Journal of Geophysical Research-Earth Surface,* 110.

AGAR, R. 1960. Post-glacial erosion of the North Yorkshire coast from the Tees estuary to Ravenscar. *Proceedings of the Yorkshire Geological Society,* 32.

AGLIARDI, F., CROSTA, G. B., MELONI, F., VALLE, C. & RIVOLTA, C. 2013. Structurally-controlled instability, damage and slope failure in a porphyry rock mass. *Tectonophysics,* 605**,** 34-47.

ALLISON, R. & KIMBER, O. G. 1998. Modelling failure mechanisms to explain rock slope change along the Isle of Purbeck coast, UK. *Earth Surface Processes and Landforms,* 23**,** 731-750.

ASME 1993. Statement upon the Control of Numerical Accuracy. *Journal of Fluids Engineering,* 115**,** 339-340.

BAK, P., CHRISTENSEN, K., DANON, L. & SCANLON, T. 2002. Unified Scaling Law for Earthquakes. *Physical Review Letters,* 88.

BAK, P., TANG, C. & WIESENFELD, K. 1988. Self-organized criticality. *Physical Review A,* 38**,** 364-374.

BANKES, S., WALKER, W. E. & KWAKKEL, J. H. 2013. Exploratory Modeling and Analysis. *In:* GASS, S. I. & FU, M. C. (eds.) *Encyclopedia of Operations Research and Management Science.* Boston, MA: Springer US.

BARLOW, J., LIM, M., ROSSER, N. J., PETLEY, D. N., BRAIN, M. J., NORMAN, E. C. & GEER, M. 2012. Modeling cliff erosion using negative power law scaling of rockfalls. *Geomorphology,* 139-140**,** 416-424.

BARTON, N. 1973. Review of a new shear-strength criterion for rock joints. *Engineering Geology,* 7**,** 287-332.

BARTON, N. 2013. Shear strength criteria for rock, rock joints, rockfill and rock masses: Problems and some solutions. *Journal of Rock Mechanics and Geotechnical Engineering,* 5**,** 249-261.

BEVEN, K. 2002. *Towards a coherent philosophy for modelling the environment*.

BIENIAWSKI, Z. T. 1967. Mechanism of Brittle Fracture of Rock. *International Journal of Rock Mechanics and Mining Sciences and Geomechanics Abstracts,* 4**,** 395-406.

BIENIAWSKI, Z. T. 1989. *Engineering Rock Mass Classifications,* New York, John Wiley and Sons.

BOWMAN, A. W. & AZZALINI, A. 1997. *Applied Smoothing Techniques for Data Analysis,* New York, Oxford University Press Inc.

BJERRUM, L. 1967. Progressive failure in slopes of over-consolidated plastic clay and clay shales. *Journal of Soil Mechanics and Foundations Divisions,* 93**,** 3-49.

BÖHME, M., HERMANNS, R. L., OPPIKOFER, T., FISCHER, L., BUNKHOLT, H. S. S., EIKEN, T., PEDRAZZINI, A., DERRON, M.-H., JABOYEDOFF, M., BLIKRA, L. H. & NILSEN, B. 2013. Analyzing complex rock slope deformation at Stampa, western Norway, by integrating geomorphology, kinematics and numerical modeling. *Engineering Geology,* 154**,** 116-130.

BRAIN, M. J., ROSSER, N. J., NORMAN, E. C. & PETLEY, D. N. 2014. Are microseismic ground displacements a significant geomorphic agent? *Geomorphology,* 207**,** 161-173.

BRIDEAU, M.-A. & STEAD, D. 2010. Controls on Block Toppling Using a Three-Dimensional Distinct Element Approach. *Rock Mechanics and Rock Engineering,* 43**,** 241-260.

BRIDEAU, M.-A. & STEAD, D. 2012. Evaluating Kinematic Controls on Planar Translational Slope Failure Mechanisms Using Three-Dimensional Distinct Element Modelling. *Geotechnical and Geological Engineering,* 30**,** 991-1011.

BRIDEAU, M.-A., YAN, M. & STEAD, D. 2009. The role of tectonic damage and brittle rock fracture in the development of large rock slope failures. *Geomorphology,* 103**,** 30-49.

BRUNETTI, M. T., GUZZETTI, F. & ROSSI, M. 2009. Probability distributions of landslide volumes. *Nonlinear Processes in Geophysics,* 16**,** 179-188.

BRUTHANS, J., SOUKUP, J., VACULIKOVA, J., FILIPPI, M., SCHWEIGSTILLOVA, J., MAYO, A. L., MASIN, D., KLETETSCHKA, G. & RIHOSEK, J. 2014. Sandstone landforms shaped by negative feedback between stress and erosion. *Nature Geosci,* 7**,** 597-601.

CAI, M., KAISER, P. K., UNO, H., TASAKA, Y. & MINAMI, M. 2004. Estimation of rock mass deformation modulus and strength of jointed hard rock masses using the GSI system. *International Journal of Rock Mechanics and Mining Sciences,* 41**,** 3-19.

CHAPUIS, A. & TETZLAFF, T. 2014. The variability of tidewater-glacier calving: origin of event-size and interval distributions. *Journal of Glaciology,* 60**,** 622-634.

COLLINS, B. D. & SITAR, N. 2008. Processes of coastal bluff erosion in weakly lithified sands, Pacifica, California, USA. *Geomorphology,* 97**,** 483-501.

COLLINS, B. D. & SITAR, N. 2011. Stability of Steep Slopes in Cemented Sands. *Journal of Geotechnical and Geoenvironmental Engineering,* 137**,** 43-51.

COLLINS, B. D. & STOCK, G. M. 2016. Rockfall triggering by cyclic thermal stressing of exfoliation fractures. *Nature Geosci,* advance online publication.

COULTHARD, T. J., HICKS, D. M. & VAN DE WIEL, M. J. 2007. Cellular modelling of river catchments and reaches: Advantages, limitations and prospects. *Geomorphology,* 90**,** 192-207.

COULTHARD, T. J., RAMIREZ, J. A., BARTON, N., ROGERSON, M. & BRÜCHER, T. 2013. Were Rivers Flowing across the Sahara During the Last Interglacial? Implications for Human Migration through Africa. *PLoS ONE,* 8**,** e74834.

CSIRO, C. S. A. I. R. O. 2014. *Large Open Pit Mine Slope Stability Project* [Online]. Available: http://www.lop.csiro.au/ [Accessed 30/03/2016.

CUNDALL, P. A. Lattice Method for Modeling Brittle, Jointed Rock. 2nd International FLAC/DEM Symposium, 14-16 February 2011, 2011 Melbourne, Australia.

CUNDALL, P. A. 2014. 'Flat Joint', powerpoint presentation.

CUNDALL, P. A. & DAMJANAC, B. A comprehensive 3D model for rock slopes based on micromechanics. Slope Stability 2009 Conference, 2009 Santiago, Chile.

D'AMATO, J., HANTZ, D., GUERIN, A., JABOYEDOFF, M., BAILLET, L. & MARISCAL, A. 2016. Influence of meterological factors on rockfall occurrence in a middle mountain limestone cliff. *Nat. Hazards Earth Syst. Sci.,* 16, 719-735

DE FREITAS, M. H. & WATTERS, R. J. 1973. Some field examples of toppling failure. *Geotechnique,* 23**,** 494-513.

DEERE, D. U. 1964. Technical description of rock cores for engineering purposes. *Rock Mechanics and Engineering Geology,* 1**,** 16-22.

DEFRA 2002. Soft Cliffs: Prediction of Recession Rates and Erosion Control Techniques. *In:* DEFRA (ed.). London: DEFRA Flood Management Division.

DEWEZ, T. J. B., ROHMER, J. & CLOSSET, L. 2007. Laser survey and mechanical modelling of chalky sea cliff collapse in Normandy, France. *In:* MC INNES, R., JAKEWAYS, J., FAIRBANK, H. & MATHIE, E. (eds.) *Landslides and Climate Change - Challenges and Solutions.* London: Taylor & Francis Group.

DEWEZ, T. J. B., ROHMER, J., REGARD, V. & CNUDDE, C. 2013. Probabilistic coastal cliff collapse hazard from repeated terrestrial laser surveys: case study from Mesnil Val (Normandy, northern France). *In:* CONLEY, D. C., MASSELINK, G., RUSSELL, P. E. & O'HARE, T. J., eds. 12th International Coastal Symposium, 2013 Plymouth, England. 702-707.

DIEDERICHS, M. S. 2003. Manuel Rocha Medal Recipient Rock Fracture and Collapse Under Low Confinement Conditions. *Rock Mechanics and Rock Engineering,* 36**,** 339-381.

DIEDERICHS, M. S., KAISER, P. K. & EBERHARDT, E. 2004. Damage initiation and propagation in hard rock during tunnelling and the influence of near-face stress rotation. *International Journal of Rock Mechanics and Mining Sciences,* 41**,** 785-812.

DONG, P. & GUZZETTI, F. 2005. Frequency-Size Statistics of Coastal Soft-Cliff Erosion. *Journal of Waterway, Port, Coastal, and Ocean Engineering,* 131**,** 37-42.

DUSSAUGE-PEISSER, A., HELMSTETTER, A., GRASSO, J.-R., HANZ, D., DESVARREUX, P., JEANNIN, M. & GIRAUD, A. 2002. Probabilistic approach to rockfall hazard assessment: potential of historical data analysis. *Natural Hazards and Earth System Sciences,* 2**,** 15-26.

DUSSAUGE, C., GRASSO, J.-R. & HELMSTETTER, A. 2003. Statistical analysis of rockfall volume distributions: Implications for rockfall dynamics. *Journal of Geophysical Research: Solid Earth,* 108**,** n/a-n/a.

EBERHARDT, E., STEAD, D. & COGGAN, J. S. 2004. Numerical analysis of initiation and progressive failure in natural rock slopes - the 1991 Randa rockslide. *International Journal of Rock Mechanics and Mining Sciences,* 41**,** 69-87.

EBERHARDT, E., STEAD, D. & STIMPSON, B. 1999. Quantifying progressive pre-peak brittle fracture damage in rock during uniaxial compression. *International Journal of Rock Mechanics and Mining Sciences,* 36**,** 361-380.

EINSTEIN, H. H., VENEZIANO, D., BAECHER, G. B. & O'REILLY, K. J. 1983. The effect of discontinuity persistence on rock slope stability. *International Journal of Rock Mechanics and Mining Sciences & Geomechanics Abstracts,* 20**,** 227-236.

ELMO, D. 2006. *Evaluation of a hybrid FEM/DEM approach for determination of rock mass strength using a combination of discontinuity mapping and fracture mechanics modelling, with particular emphasis on modelling of jointed pillars.* PhD, University of Exeter.

ELMO, D., CLAYTON, C., ROGERS, S., BEDDOES, R. & GREER, S. 2011. Numerical Simulations of Potential Rock Bridge Failure within a Naturally Fractured Rock Mass. Slope Stability 2011: International Symposium on Rock Slope Stability in Open Pit Mining and Civil Engineering, 2011 Vancouver, Canada.

EMERY, K. O. & KUHN, G. G. 1982. Sea cliffs: Their processes, profiles, and classification. *Geological Society of America Bulletin,* 93**,** 644-654.

ESRI. 2016. *Curvature function* [Online]. Available: http://desktop.arcgis.com/en/arcmap/10.3/manage-data/raster-and-images/curvature-function.htm [Accessed 05/07/2016 2016].

FRAYSSINES, M. & HANTZ, D. 2009. Modelling and back-analysing failures in steep limestone cliffs. *International Journal of Rock Mechanics and Mining Sciences,* 46**,** 1115-1123.

GLOVER, J., SCHWEIZER, A., CHRISTEN, M., GERBER, W., LEINE, R. & BARTELT, P. Numerical investigation of the influence of rock shape on rockfall trajectory. EGU General Assembly Conference Proceedings, EGU 2012 Vienna, Austria. pp. 11022.

GIORDAN, D., MANCONI, A., FACELLO, A., BALDO, M., DELL'ANESE, F., ALLASIA, P. & DUTTO, F. 2015. Brief Communication: The use of an unmanned aerial vehicle in a rockfall emergency scenario. *Nat. Hazards Earth Syst. Sci.,* 15**,** 163-169.

GISCHIG, V. S. 2011. *Kinematics and failure mechanisms of the Randa rock slope instability (Switzerland).* Doctor of Science, ETH Zurich.

GISCHIG, V. S., MOORE, J. R., EVANS, K. F., AMANN, F. & LOEW, S. 2011. Thermomechanical forcing of deep rock slope deformation: 1. Conceptual study of a simplified slope. *Journal of Geophysical Research-Earth Surface,* 116.

GRIFFITH, A. A. 1921. The phenomena of rupture and flow in solids. *Philosophical Transactions of the Royal Society of London, A,* 221**,** 163-198.

GRIFFITH, A. A. 1924. Theory of rupture. Proc. First Int. Cong. appl. Mech., 1924 Delft. 55-63.

GUNZBURGER, Y., MERRIEN-SOUKATCHOFF, V. & GUGLIELMI, Y. 2005. Influence of daily surface temperature fluctuations on rock slope stability: case study of the *Rochers de Valabres* slope (France). *International Journal of Rock Mechanics and Mining Sciences,* 42**,** 331-349.

GUZZETTI, F., MALAMUD, B. D., TURCOTTE, D. L. & REICHENBACH, P. 2002. Power-law correlations of landslide areas in Central Italy. *Earth and Planetary Science Letters,* 195**,** 169-183.

HAJIABDOLMAJID, V., KAISER, P. K. & MARTIN, C. D. 2002. Modelling brittle failure of rock. *International Journal of Rock Mechanics and Mining Sciences,* 39**,** 731-741.

HALES, T. C. & ROERING, J. J. 2007. Climatic controls on frost cracking and implications for the evolution of bedrock landscapes. *Journal of Geophysical Research: Earth Surface,* 112**,** F02033.

HAMDI, P., STEAD, D. & ELMO, D. 2013. Numerical Simulation of Damage During Laboratory Testing on Rock Using a 3D-FEMM/DEM Approach. American Rock Mechanics Association.

HAVAEJ, M., COGGAN, J., STEAD, D. & ELMO, D. 2015. A Combined Remote Sensing–Numerical Modelling Approach to the Stability Analysis of Delabole Slate Quarry, Cornwall, UK. *Rock Mechanics and Rock Engineering***,** 1-19.

HAVAEJ, M. & STEAD, D. 2016. Investigating the role of kinematics and damage in the failure of rock slopes. *Computers and Geotechnics,* 78**,** 181-193.

HAVAEJ, M., STEAD, D., EBERHARDT, E. & FISHER, B. R. 2014a. Characterization of bi-planar and ploughing failure mechanisms in footwall slopes using numerical modelling. *Engineering Geology,* 178**,** 109-120.

HAVAEJ, M., STEAD, D., MAYER, J. & WOLTER, A. 2014b. Modelling the Relation Between Failure Kinematics And Slope Damage in High Rock Slopes Using a Lattice Scheme Approach. 48th US Rock Mechanics/Geomechanics Symposium, 2014. American Rock Mechanics Association.

HAVAEJ, M., WOLTER, A., STEAD, D., TUCKEY, Z., LORIG, L. J. & EBERHARDT, E. 2013. Incorporating brittle fracture into three-dimensional modelling of rock slopes. *In:* DIGHT, P. M., ed. Slope Stability, 2013 Australian Centre for Geomechanics, Perth. 625-638.

HERGARTEN, S. 2003. Landslides, sandpiles, and self-organized criticality. *Nat. Hazards Earth Syst. Sci.,* 3**,** 505-514.

HOEK, E. 1994. Strength of Rock and Rock Masses. *ISRM News Journal,* 2**,** 4-16.

HOEK, E. & BRAY, J. W. 1977. *Rock Slope Engineering,* London, The Institution of Mining and Metallurgy.

HOEK, E. & MARTIN, C. D. 2014. Fracture initiation and propagation in intact rock – A review. *Journal of Rock Mechanics and Geotechnical Engineering,* 6**,** 287-300.

HUNGR, O., EVANS, S. G. & HAZZARD, J. 1999. Magnitude and frequency of rock falls and rock slides along the main transportation corridors of southwestern British Columbia. *Canadian Geotechnical Journal,* 36**,** 224-238.

IRWIN, G. R. 1957. Analysis of Stresses and Strains Near the End of a Crack Traversing a Plate. *Journal of Applied Mechanics,* 24**,** 361-364.

ITASCA 2008. 3DEC - 3 Dimensional Distinct Element Code. Minneapolis, MN, USA: Itasca Consulting Group Inc.

ITASCA 2010a. PFC3D Version 4.0 - Smooth Joint Model. Minneapolis, MN, USA: Itasca Consulting Group Inc.

ITASCA 2010b. Slope Model, description of formulation with verification and example problems, Revision 2. Minneapolis, MN, USA: Itasca Consulting Group Inc.

ITASCA 2014. 3DEC (v. 5.0), FLAC2D (v. 7.0), FLAC3D (v. 5.0), PFC (v. 5.0), *Slope Model* (v. 2.9), UDEC (v. 6.0). Minneapolis, MN, USA: Itasca Consulting Group.

JENNINGS, J. E. 1970. A mathematical theory for the calculation of the stabilty of slopes in open cast mines. *In:* VAN RENSBURG, P. W. J. (ed.) *Symposium on the Theoretical Background to the Planning of Open Pit Mines with Special References to Slope Stability.* Johannesburg.

JING, L. & HUDSON, J. A. 2002. Numerical methods in rock mechanics. *International Journal of Rock Mechanics and Mining Sciences,* 39**,** 409-427.

JOYAL, G., LAJEUNESSE, P., MORISSETTE, A. & BERNATCHEZ, P. 2016. Influence of lithostratigraphy on the retreat of an unconsolidated sedimentary coastal cliff (St. Lawerence estuary, eastern Canada). *Earth Surface Processes and Landforms,* 41**,** 1055-1072.

KEMENY, J. 2003. The Time-Dependent Reduction of Sliding Cohesion due to Rock Bridges Along Discontinuities: A Fracture Mechanics Approach. *Rock Mechanics and Rock Engineering,* 36**,** 27-38.

KEMENY, J. 2005. Time-dependent drift degradation due to the progressive failure of rock bridges along discontinuities. *International Journal of Rock Mechanics and Mining Sciences,* 42**,** 35-46.

KIMBER, O. G., ALLISON, R. & COX, N. J. 1998. Mechanisms of failure and slope development in rock masses. *Transactions of the Insitute of British Geographers,* 23**,** 353-370.

KORUP, O. & CLAGUE, J. J. 2009. Natural hazards, extreme events, and mountain topography. *Quaternary Science Reviews,* 28**,** 977-990.

KRAUTBLATTER, M. & DIKAU, R. 2007. Towards a uniform concept for the comparison and extrapolation of rockwall retreat and rockfall supply. *Geografiska Annaler: Series A, Physical Geography,* 89**,** 21-40.

KRAUTBLATTER, M. & MOORE, J. R. 2014. Rock slope instability and erosion: toward improved process understanding. *Earth Surface Processes and Landforms,* 39**,** 1273-1278.

KULHAWY, F. H. 1975. Stress deformation properties of rock and rock discontinuities. *Engineering Geology,* 9**,** 327-350.

LAGUE, D., BRODU, N. & LEROUX, J. 2013. Accurate 3D comparison of complex topography with terrestrial laser scanner: Application to the Rangitikei canyon. *ISPRS Journal of Photogrammetry and Remote Sensing,* 82**,** 10-26.

LAJTAI, E. Z., SCHMIDTKE, R. H. & BIELUS, L. P. 1987. The effect of water on the time-dependent deformation and fracture of a granite. *International Journal of Rock Mechanics and Mining Sciences & Geomechanics Abstracts,* 24**,** 247-255.

LANE, S. N. Braided rivers and the question of sufficient physics. EGU General Assembly, 2005. Copernicus Publications, EGU05-A-01815.

LANE, S. N., HARDY, R. J., FERGUSON, R. I. & PARSONS, D. R. 2005. A framework for model verification and validation of CFD schemes in natural open channel flows. *In:* BATES, P. D., LANE, S. N. & FERGUSON, R. I. (eds.) *Computational Fluid Dynamics: Applications in Environmental Hydraulics.* Chichester, England: John Wiley & Sons, Ltd.

LARSEN, I. J., MONTGOMERY, D. R. & KORUP, O. 2010. Landslide erosion controlled by hillslope material. *Nature Geosci,* 3**,** 247-251.

LARSEN, L. G. & HARVEY, J. W. 2010. How Vegetation and Sediment Transport Feedbacks Drive Landscape Change in the Everglades and Wetlands Worldwide. *The American Naturalist,* 176**,** E66-E79.

LARSEN, L. G., THOMAS, C., EPPINGA, M. & COULTHARD, T. 2014. Exploratory Modeling: Extracting Causality From Complexity. *Eos, Transactions American Geophysical Union,* 95**,** 285-286.

LEITH, K. J. 2012. *Stress development and geomechanical controls on the geomorphic evolution of alpine valleys.* Doctor of Sciences, ETH Zurich.

LEITH, K., MOORE, J. R., AMANN, F. & LOEW, S. 2014a. In situ stress control on microcrack generation and macroscopic extensional fracture in exhuming bedrock. *Journal of Geophysical Research: Solid Earth,* 119**,** 594-615.

LEITH, K., MOORE, J. R., AMANN, F. & LOEW, S. 2014b. Subglacial extensional fracture development and implications for Alpine Valley evolution. *Journal of Geophysical Research: Earth Surface,* 119**,** 2012JF002691.

LIM, M. 2006. *Coastal cliff evolution with reference to Staithes, North Yorkshire.* Doctor of Philosophy, Durham University.

LIM, M., MILLS, J. & ROSSER, N. 2009. Laser scanning surveying of linear features: considerations and applications. *In:* HERITAGE, G. & LARGE, A. (eds.) *Laser scanning for the environmental sciences.* Wiley Blackwell.

LIM, M., PETLEY, D. N., ROSSER, N. J., ALLISON, R. J., LONG, A. J. & PYBUS, D. 2005. Combined Digital Photogrammetry and Time-of-Flight Laser Scanning for Monitoring Cliff Evolution. *The Photogrammetric Record,* 20**,** 109-129.

LIM, M., ROSSER, N. J., ALLISON, R. & PETLEY, D. N. 2010. Erosional processes in the hard rock coastal cliffs at Staithes, North Yorkshire. *Geomorphology,* 114**,** 12-21.

LORIG, L. J., CUNDALL, P. A., DAMJANAC, B. & EMAM, S. A Three-Dimensional Model for Rock Slopes Based on Micromechanics. 44th US Rock Mechanics Symposium and 5th US-Canada Rock Mechanics Symposium, 2010 Salt Lake City, UT, USA. American Rock Mechanics Association.

MAKEDON, T. & CHATZIGOGOS, N. 2012. Failure mechanism of overhanging slopes in sedimentary rocks with dissimilar mechanical properties. *Bulletin of Engineering Geology and the Environment,* 71**,** 703-708.

MALAMUD, B. D., TURCOTTE, D. L., GUZZETTI, F. & REICHENBACH, P. 2004. Landslide inventories and their statistical properties. *Earth Surface Processes and Landforms,* 29**,** 687-711.

MARTEL, S. J. 2006. Effect of topographic curvature on near-surface stresses and application to sheeting joints. *Geophysical Research Letters,* 33**,** L01308.

MARTEL, S. J. 2011. Mechanics of curved surfaces, with application to surface-parallel cracks. *Geophysical Research Letters,* 38**,** L20303.

MARTIN, C. D. & CHANDLER, N. A. 1994. The Progressive Fracture of Lac du Bonnet Granite. *International Journal of Rock Mechanics and Mining Sciences and Geomechanics Abstracts,* 31**,** 643-659.

MATASCI, B., CARREA, D., JABOYEDOFF, M. & PEDRAZZINI, A. Structural characterization of rockfall sources in Yosemite Valley from remote sensing data: toward more accurate susceptibility assessment. 2011 Pan-Am CGS Geotechnical Conference, 2011 Toronto, Ontario.

MATASCI, B., CARREA, D., JABOYEDOFF, M., STOCK, G. M., COLLINS, B. D. & PUTNAM, R. 2013. Fracturing mapping and rockfall susceptibility assessment in Yosemite Valley (California, USA). *2013 Fall Meeting, AGU.* San Fransisco, Calif.

MAZARS, J. & PIJAUDIER-CABOT, G. 1996. From damage to fracture mechanics and conversely: A combined approach. *International Journal of Solids and Structures,* 33**,** 3327-3342.

MOORE, L.J. & GRIGGS, G.B. 2002. Long-term cliff retreat and erosion hotspots along the central shores of the Monterey Bay National Marine Sanctuary. *Marine Geology, 181,* 265-283

MOORE, J. R., SANDERS, J. W., DIETRICH, W. E. & GLASER, S. D. 2009. Influence of rock mass strength on the erosion rate of alpine cliffs. *Earth Surface Processes and Landforms,* 34**,** 1339-1352.

MULLIGAN, M. & WAINWRIGHT, J. 2004. Modelling and Model Building. *In:* WAINWRIGHT, J. & MULLIGAN, M. (eds.) *Environmental Modelling: Finding Simplicity in Complexity.* England: John Wiley & Sons Ltd.

MURRAY, A. B., GOLDSTEIN, E. B. & COCO, G. 2014. The shape of patterns to come: from initial formation to long-term evolution. *Earth Surface Processes and Landforms,* 39**,** 62-70.

MURRAY, A. B. & PAOLA, C. 1994. A cellular model of braided rivers. *Nature,* 371**,** 54-57.

MURRAY, A. B. & PAOLA, C. 1997. Properties of a cellular braided-stream model. *Earth Surface Processes and Landforms,* 22**,** 1001-1025.

MURPHY, J., SEXTON, D., JENKINS, G., BOORMAN, P., BOOTH, B., BROWN, K., CLARK, R., COLLINS, M., HARRIS, G. & KENDON, L. 2009. Climate change projections. DEFRA.

NARTEAU, C., SHEBALIN, P., HOLSCHNEIDER, M., LE MOUËL, J. L. & ALLÈGRE, C. J. 2000. Direct simulations of the stress redistribution in the scaling organization of fracture tectonics (SOFT) model. *Geophysical Journal International,* 141**,** 115-135.

NICHOL, S. L., HUNGR, O. & EVANS, S. G. 2002. Large-scale brittle and ductile toppling of rock slopes. *Canadian Geotechnical Journal,* 39**,** 773-788.

NORMAN, E. C. 2012. *Microseismic monitoring of the controls on coastal rock cliff erosion.* Doctor of Philosophy, Durham University.

NUNES, M., FERREIRA, O., SCHAEFER, M., CLIFTON, J., BAILY, B., MOURA, D. & LOUREIRO, C. 2009. Hazard assessment in rock cliffs at Central Algarve (Portugal): A tool for coastal management. *Ocean & Coastal Management,* 52**,** 506-515.

OPPIKOFER, T., JABOYEDOFF, M., BLIKRA, L. H., DERRON, M.-H. & METZGER, R. 2009. Characterization and monitoring of the Aknes rockslide using terrestrial laser scanning. *Nat. Hazards Earth Syst. Sci.,* 9**,** 1003-1019.

OPPIKOFER, T., JABOYEDOFF, M. & KEUSEN, H.-R. 2008. Collapse at the eastern Eiger flank in the Swiss Alps. *Nature Geoscience,* 1**,** 531-535.

ORESKES, N., SHRADER-FRECHETTE, K. & BELITZ, K. 1994. Verification, Validation, and Confirmation of Numerical Models in the Earth Sciences. *Science,* 263**,** 641-646.

PALLESKE, C. K., HUTCHINSON, D. J., ELMO, D. & DIEDERICHS, M. S. Impacts of limited data collection windows on accurate rock simulation using discrete fracture networks. 47th US Rock Mechanics/ Geomechanics Symposium, 2013 San Francisco, CA, USA. American Rock Mechanics Association.

PALMSTRÖM, A. 1995. *RMi - A rock mass characterization system for rock engineering purposes.* Doctor Scientiarium, University of Oslo.

PARKER, R. N., DENSMORE, A. L., ROSSER, N. J., DE MICHELE, M., LI, Y., HUANG, R., WHADCOAT, S. & PETLEY, D. N. 2011. Mass wasting triggered by the 2008 Wenchuan earthquake is greater than orogenic growth. *Nature Geosci,* 4**,** 449-452.

PETLEY, D. 2012. Remote sensing techniques and landslides. *In:* CLAGUE, J. J. & STEAD, D. (eds.) *Landslides: Types, Mechanisms and Modelling.* New York: Cambridge University Press.

PETLEY, D. N., HIGUCHI, T., PETLEY, D. N. J., BULMER, M. H. & CAREY, J. 2005. Development of progressive landslide failure in cohesive materials. *Geology,* 33**,** 201-204.

PICKERING, G., BULL, J. M. & SANDERSON, D. J. 1995. Sampling power-law distributions. *Tectonophysics,* 248**,** 1-20.

PIERCE, M., CUNDALL, P. A. & POTYONDY, D. O. A synthetic rock mass model for jointed rock. *In:* EBERHARDT, E., STEAD, D. & MORRISON, T., eds. 1st Canada-US Rock Mechanics Symposium, 2007 Vancouver, Canada. Taylor & Francis, 341-350.

PINE, R. J., OWEN, D. R. J., COGGAN, J. S. & RANCE, J. M. 2007. A new discrete fracture modelling approach for rock masses. *Geotechnique,* 57**,** 757-766.

POTYONDY, D. O. A flat-jointed bonded-particle material for hard rock. *In:* ASSOCIATION, A. R. M., ed. 46th US Rock Mechanics/Geomechanics Symposium, 2012 Chicago, USA.

RAWSON, P. F. & WRIGHT, J. K. 2000. *The Yorkshire Coast: The Yorkshire Coast Geologists' Association Guide No 34,* London, UK, Geologists' Association.

RIEGL, GmbH. 2015. RIEGL VZ-1000 Datasheet. Available: http://www.riegl.com/uploads/tx_pxpriegldownloads/DataSheet_VZ-1000_2015-03-24.pdf [Accessed 01/03/2017]

RIPLEY, B. D. 1976. The Second-Order Analysis of Stationary Point Processes. *Journal of Applied Probability,* 13**,** 255-266.

ROBERT MCNEEL, A. 2014. *Rhinoceros* [Online]. Available: http://www.rhino3d.com/ [Accessed 8/12/14 2014].

ROBINSON, L. A. 1974. *Towards a process response model of cliff retreat - the case of North East Yorkshire.* Ph.D., University of Leeds.

ROCKFIELD 2013. Advanced Finite Element/Discrete Element: ELFEN. Swansea, UK: Rockfield Software Ltd.

ROCSCIENCE 2013. Rocscience Software Products. Toronto, ON, Canada: Rocscience Inc.

ROHMER, J. & DEWEZ, T. J. B. 2013. Analyzing the spatial structure of sea cliff instabilities through repeated high resolution terrestrial laser scanning surveys and point process statistics. *8th International Conference on Geomorphology.* Paris, France.

ROSE, N. D. & HUNGR, O. 2007. Forecasting potential rock slope failure in open pit mines using the inverse-velocity method. *International Journal of Rock Mechanics and Mining Sciences,* 44**,** 308-320.

ROSSER, N. J. 2002. *The geomorphology of coarse clastic surfaces in arid environments.* Doctor of Philosophy, Durham University.

ROSSER, N. J., BRAIN, M. J., PETLEY, D. N., LIM, M. & NORMAN, E. C. 2013. Coastline retreat via progressive failure of rocky coastal cliffs. *Geology,* 41**,** 939-942.

ROSSER, N. J., LIM, M., PETLEY, D. N., DUNNING, S. & ALLISON, R. 2007a. Patterns of precursory rockfall prior to slope failure. *Journal of Geophysical Research-Earth Surface,* 112.

ROSSER, N. J., PETLEY, D. N., DUNNING, S., LIM, M. & BALL, S. 2007b. The surface expression of strain accumulation in failing rock masses. *In:* EBERHARDT, E., STEAD, D. & MORRISON, T. (eds.) *Rock Mechanics: Meeting Society's Challenges and Demands: Proceedings of the 1st Canada-US Rock Mechanics Symposium, Vancouver, Canada, 27-31 May 2007.* Oxford: Taylor & Francis.

ROSSER, N. J., PETLEY, D. N., LIM, M., DUNNING, S. & ALLISON, R. 2005. Terrestrial laser scanning for monitoring the process of hard rock coastal cliff erosion. *Quarterly Journal of Engineering Geology and Hydrogeology,* 38**,** 363-375.

ROYÁN, M., ABELLÁN, A., JABOYEDOFF, M., VILAPLANA, J. & CALVET, J. 2013. Spatio-temporal analysis of rockfall pre-failure deformation using Terrestrial LiDAR. *Landslides***,** 1-13.

ROZIER, O. & NARTEAU, C. 2014. A real-space cellular automaton laboratory. *Earth Surface Processes and Landforms,* 39**,** 98-109.

SAITO, M. 1965. Forecasting the Time of Occurrence of a Slope Failure. *Proceedings of the 6th International Conference on Soil Mechanics and Foundation Engineering, Montreal, Quebec.* Oxford: Pergamon Press.

SAITO, M. Forecasting time of slope failure by tertiary creep. The 7th International Conference on Soil Mechanics and Foundation Engineering, 1969 Mexico City. 677-683.

SAKURAI, S. 2001. The monitoring of landslides by GPS. *In:* MARINOS, P. G., KOUKIS, G. C., TSIAMBAOS, G. C. & STOURNARAS, G. C. (eds.) *Engineering Geology and the Environment.* The Netherlands: Swets & Zeitlinger.

SANTANA, D., COROMINAS, J., MAVROULI, O. & GARCIA-SELLES, D. 2012. Magnitude-frequency relation for rockfall scars using a Terrestrial Laser Scanner. *Engineering Geology***,** 50-64.

SAOUMA, V. E. 2010. *Applications of fracture mechanics to rock slope stability* [Online]. Available: http://civil.colorado.edu/~saouma/FM/slope-stability.pdf.

SCAVIA, C. 1990. Fracture mechanics approach to stability analysis of rock slopes. *Engineering Fracture Mechanics,* 35**,** 899-910.

SCAVIA, C. 1995. A method for the study of crack propagation in rock structures. *Geotechnique,* 45**,** 447-463.

SELBY, M. J. 1980. A rock mass strength classification for geomorphic purposes. *Zeitschrift fur Geomorphologie,* 24**,** 31-51.

SELBY, M. J. 1982. Controls on the stability and inclinations of hillslopes formed on hard rock. *Earth Surface Processes and Landforms,* 7**,** 449-467.

SELBY, M. J. 2005. *Hillslope Materials and Processes,* Oxford, Oxford University Press.

SENFAUTE, G., DUPERRET, A. & LAWRENCE, J. A. 2009. Micro-seismic precursory cracks prior to rock-fall on coastal chalk cliffs: a case study at Mesnil-Val, Normandie, NW France. *Natural Hazards and Earth System Sciences,* 9**,** 1625-1641.

SINGH, R. N. & SUN, G. X. 1989. Fracture mechanics applied to slope stability analysis. *International Symposium on Surface Mining - Future Concepts.* Nottingham.

STACEY, T. R. 1981. A simple extension strain criterion for fracture of brittle rock. *International Journal of Rock Mechanics and Mining Sciences & Geomechanics Abstracts,* 18**,** 469-474.

STARK, C. P. & HOVIUS, N. 2001. The characterization of landslide size distributions. *Geophysical Research Letters,* 28**,** 1091-1109.

STEAD, D. & COGGAN, J. S. 2012. Numerical modeling of rock-slope instability. *In:* CLAGUE, J. J. & STEAD, D. (eds.) *Landslides: Types, Mechanisms and Modeling.* New York: Cambridge University Press.

STEAD, D., COGGAN, J. S. & EBERHARDT, E. 2004. Realistic simulation of rock slope failure mechanisms: the need to incorporate principles of fracture mechanics. *International Journal of Rock Mechanics and Mining Sciences,* 41, Supplement 1**,** 563-568.

STEAD, D., COGGAN, J. S., ELMO, D. & YAN, M. Modelling Brittle Fracture in Rock Slopes - Experience Gained and Lessons Learned. *In:* POTVIN, Y., ed. 2007 International Symposium on Rock Slope Stabilty in Open Pit Mining and Civil Engineering, 2007 Perth, Australia. Australian Centre for Geomechanics, 239-252.

STEAD, D. & EBERHARDT, E. 2013. Understanding the mechanics of large landslides. *Ital. J. Eng. Geol. Environ. Book Ser,* 6**,** 85-112.

STEAD, D., EBERHARDT, E. & COGGAN, J. S. 2006. Developments in the characterization of complex rock slope deformation and failure using numerical modelling techniques. *Engineering Geology,* 83**,** 217-235.

STEAD, D., JABOYEDOFF, M. & COGGAN, J. S. Rock slope characterization and geomechanical modelling. *In:* EBERHARDT, E., FROESE, C., TURNER, A. K. & LEROUEIL, S., eds. 11th

International and 2nd North American Symposium on Landslides and Engineered Slopes, 2012 Banff, Canada. CRC Press, 83-100.

STEAD, D. & WOLTER, A. 2015. A critical review of rock slope failure mechanisms: The importance of structural geology. *Journal of Structural Geology,* 74**,** 1-23.

STOCK, G. M., BAWDEN, G. W., GREEN, J. K., HANSON, E., DOWNING, G., COLLINS, B. D., BOND, S. & LESLAR, M. 2011. High-resolution three-dimensional imaging and analysis of rock falls in Yosemite Valley, California. *Geosphere,* 7**,** 573-581.

STOCK, G. M., MARTEL, S. J., COLLINS, B. D. & HARP, E. L. 2012. Progressive failure of sheeted rock slopes: the 2009-2010 Rhombus Wall rock falls in Yosemite Valley, California, USA. *Earth Surface Processes and Landforms,* 37**,** 546-561.

STRUNDEN, J., EHLERS, T. A., BREHM, D. & NETTESHEIM, M. 2015. Spatial and temporal variations in rockfall determined from TLS measurements in a deglaciated valley, Switzerland. *Journal of Geophysical Research: Earth Surface,* 120**,** 1251-1273.

STURZENEGGER, M. & STEAD, D. 2009a. Quantifying discontinuity orientation and persistence on high mountain rock slopes and large landslides using terrestrial remote sensing techniques. *Natural Hazards and Earth System Sciences,* 9**,** 267-287.

STURZENEGGER, M. & STEAD, D. 2009b. Close-range terrestrial digital photogrammetry and terrestrial laser scanning for discontinuity characterization on rock cuts. *Engineering Geology,* 106**,** 163-182.

STURZENEGGER, M. & STEAD, D. 2012. The Palliser Rockslide, Canadian Rocky Mountains: Characterization and modeling of a stepped failure surface. *Geomorphology,* 138**,** 145-161.

STURZENEGGER, M., YAN, M., STEAD, D. & ELMO, D. 2007. Application and limitations of ground-based laser scanning in rock slope characterization. *In:* EBERHARDT, E., STEAD, D. & MORRISON, T., eds. Rock mechanics: Meeting Society's Challenges and Demands - Proceedings of the 1st Canada-US Rock Mechanics Symposium, 2007 Vancouver, Canada. Taylor and Francis.

STYLES, T. D., COGGAN, J. S. & PINE, R. J. 2011. Back analysis of the Joss Bay Chalk Cliff Failure using numerical modelling. *Engineering Geology,* 120**,** 81-90.

SUNAMURA, T. 1992. *Geomorphology of rocky coasts*, John Wiley & Son Ltd.

SWIRAD, Z. M., ROSSER, N. J., BRAIN, M. J. & JONES, E. C. V. 2016. What controls the Geometry of Rocky Coasts at the Local Scale? *Journal of Coastal Research,* 75**,** 612-616.

TEMME, A. J. A. M., KEILER, M., KARSSENBERG, D. & LANG, A. 2015. Complexity and non-linearity in earth surface processes – concepts, methods and applications. *Earth Surface Processes and Landforms,* 40**,** 1270-1274.

TERZAGHI, K. 1950. Mechanism of Landslides. *In:* PAIGE, S. (ed.) *Application of Geology to Engineering Practice.* USA: Geological Society of America.

TERZAGHI, K. 1962. Stability of steep slopes on hard unweathered rock. *Geotechnique,* 12**,** 251-270.

THARP, T. M. & COFFIN, D. T. 1985. Field Application Of Fracture Mechanics Analysis To Small Rock Slopes. *26th US Symposium on Rock Mechanics.* Rapid City, SD: American Rock Mechanics Association.

TONINI, M. & ABELLÁN, A. 2014. Rockfall detection from terrestrial LiDAR point clouds: a clustering approach using R. *Journal of Spatial Information Science,* 8.

TONINI, M., PEDRAZZINI, A., PENNA, I. & JABOYEDOFF, M. 2013. Spatial pattern of landslides in Swiss Rhone Valley. *Natural Hazards***,** 1-14.

TORRES, M. 19/11/2014 2014. *RE: Slope Model query*

TRENHAILE, A. 2011. Predicting the response of hard and soft rock coasts to changes in sea level and wave height. *Climatic Change,* 109**,** 599-615.

TRENHAILE, A. S. 2002. Rock coasts, with a particular emphasis on shore platforms. *Geomorphology,* 48**,** 7-22.

TUCKEY, Z., STEAD, D., STURZENEGGER, M., ELMO, D. & TERBRUGGE, P. 2012. Towards a methodology for characterizing intact rock bridges in large open pits. *46th US Rock Mechanics/ Geomechanics Symposium.* Chicago, IL, USA: American Rock Mechanics Association.

VANN JONES, E. C., ROSSER, N. J., BRAIN, M. J. & PETLEY, D. N. 2015. Quantifying the environmental controls on erosion of a hard rock cliff. *Marine Geology,* 363**,** 230-242.

VARNES, D. J. 1978. Slope movement types and processes. *In:* SCHUSTER, R. L. & KRIZEK, R. J. (eds.) *Landslides: Analysis and Control.* Washington D. C.: Transportation and Road Research Board, National Academy of Science.

VILES, H. A. 2013. Linking weathering and rock slope instability: non-linear perspectives. *Earth Surface Processes and Landforms,* 38**,** 62-70.

WELLS, T., HANCOCK, G. & FRYER, J. 2008. Weathering rates of sandstone in a semi-arid environment (Hunter Valley, Australia). *Environmental Geology,* 54**,** 1047-1057.

WILLENBERG, H., SPILLMANN, T., EBERHARDT, E., EVANS, K. F., LOEW, S. & MAURER, H. R. Multidisciplinary monitoring of progressive failure processes in brittle rock slopes - Concepts and system design. *In:* RYBAR, J., STEMBERK, J. & WAGNER, P., eds. The First European Conference on Landslides, 2002 Prague, Czech Republic. A.A. Balkema Publishers, 477-483.

WOLFRAM, S. 1983. Statistical mechanics of cellular automata. *Reviews of Modern Physics,* 55**,** 601-644.

YAN, M. 2008. *Numerical Modelling of Brittle Fracture and Step-path Failure: from Laboratory to Rock Slope Scale.* Doctor of Philosophy, Simon Fraser University.

YOUNG, A. P. & ASHFORD, S. A. 2008. Instability investigation of cantilevered seacliffs. *Earth Surface Processes and Landforms,* 33**,** 1661-1677.

YOUNG, A. P., FLICK, R. E., GUTIERREZ, R. & GUZA, R. T. 2009. Comparison of short-term seacliff retreat measurement methods in Del Mar, California. *Geomorphology,* 112**,** 318-323.

YOUNG, A. P., GUZA, R. T., O'REILLY, W. C., FLICK, R. E. & GUTIERREZ, R. 2011. Short-term retreat statistics of a slowly eroding coastal cliff. *Natural Hazards and Earth System Sciences,* 11**,** 205-217.

YOUNG, A. P., OLSEN, M. J., DRISCOLL, N., FLICK, R. E., GUTIERREZ, R., GUZA, R. T., JOHNSTONE, E. & KUESTER, F. 2010. Comparison of Airborne and Terrestrial Lidar Estimates of Seacliff Erosion in Southern California. *Photogrammetric Engineering & Remote Sensing,* 76**,** 421-427.

ZHANG, L. 2016. Determination and applications of rock quality designation (RQD). *Journal of Rock Mechanics and Geotechnical Engineering,* 8**,** 389-397.

ZILIANI, L., SURIAN, N., COULTHARD, T. J. & TARANTOLA, S. 2013. Reduced-complexity modeling of braided rivers: Assessing model performance by sensitivity analysis, calibration, and validation. *Journal of Geophysical Research: Earth Surface,* 118**,** 2243-2262.

ZIMMER, V. L., COLLINS, B. D., STOCK, G. M. & SITAR, N. 2012. Rock fall dynamics and deposition: an integrated analysis of the 2009 Ahwiyah Point rock fall, Yosemite National Park, USA. *Earth Surface Processes and Landforms,* 37**,** 680-691.